

KIEL UNIVERSITY

FACULTY OF ENGINEERING

**Additive and Self-Organised
Manufacturing**

DISSERTATION

submitted to obtain the degree of

DOCTOR OF ENGINEERING (DR.-ING.)

Author:
Leonard SIEBERT

Supervisor:
Prof. Dr. Rainer ADELUNG

November 2020

Referent: Prof. Dr. Rainer Adlung
1. Koreferent: Prof. Dr. Franz Faupel
2. Koreferent: PhD Su Ryon Shin
Datum der mündlichen Prüfung: 09.07.2021
Zum Druck genehmigt: 09.07.2021

Abstract

The introduction of additive manufacturing in the wake of industry 4.0 is often seen as a substantial part of a new industrial revolution. Automated control for fabricating highly complex geometries out of almost any common engineering material gives rise to a design freedom previously inaccessible. While these engineering materials cover a wide range of beneficial properties, there are design possibilities yet to be explored. Self-organisation phenomena for example have been used to create intricate structures on the nanoscale and to exploit microscale and nanoscale material properties. Naturally, the combination of the macroscopic design freedom of additive manufacturing paired with the nanoscale design possibilities of self-organisation phenomena is very attractive. Therefore, this work deals with the investigation of novel self-organisation phenomena and their application in additive manufacturing.

By employing self-organisation phenomena such as the capillary effect, polymer composites with promising qualities for artificial heart valves have been demonstrated. The self-organised growth of metal oxide nanowires from additively manufactured metal microparticle composites led to the rapid development of low power gas sensors for the detection of acetone in breath. The functional and structural properties of self-organised tetrapod-shaped zinc oxide microparticles have also been used to create complex shaped hydrogel composites both by additive manufacturing and a template approach for medical applications. Their use prevented spinodal decomposition in immiscible monomer mixtures and they were employed as semiconducting carriers for fullerene decoration. The blending of self-reporting polymers with structurally similar, tougher polymers enabled the development of self-reporting microfibres.

The broad range of these applications hints at the potential that remains to be explored for self-organisation, and the examples demonstrated in this work may lead to even more sophisticated applications of self-organisation in additive manufacturing.

Kurzfassung

Die Entwicklung der additiven Fertigung mit der Industrie 4.0 wird oft als wesentlicher Teil einer neuen industriellen Revolution angesehen. Die automatisierte Steuerung zur Herstellung hochkomplexer Geometrien aus fast allen gängigen Konstruktionswerkstoffen ermöglicht eine bis dahin unzugängliche Designfreiheit. Obwohl diese Konstruktionswerkstoffe ein breites Spektrum an vorteilhaften Eigenschaften abdecken, gibt es noch andere mögliche Designtechniken, die noch zu erforschen sind. Selbstorganisationsphänomene wurden zum Beispiel genutzt, um komplizierte Strukturen auf der Nanoskala zu schaffen, und um mikro- und nanoskalige Materialeigenschaften auszunutzen. Daher ist die Kombination der makroskopischen Gestaltungsfreiheit der additiven Fertigung gepaart mit den nanoskaligen Gestaltungsmöglichkeiten von Selbstorganisationsphänomenen sehr vielversprechend.

Diese Arbeit befasst sich mit der Untersuchung neuartiger Selbstorganisationsphänomene und deren Anwendung in additiven Fertigungsverfahren. Unter Ausnutzung von Selbstorganisationsphänomenen wie dem Kapillareffekt konnten Polymerkomposite mit vielversprechenden Eigenschaften für künstliche Herzklappen hergestellt werden. Das selbstorganisierte Wachstum von Metalloxid-Nanodrähten aus additiv hergestellten Metall-Mikropartikel-Kompositen führte im Rahmen dieser Arbeit zur Entwicklung von Gassensoren mit geringer Leistung für die Detektion von Aceton in der Atemluft. Die funktionellen und strukturellen Eigenschaften selbstorganisierter tetrapodenförmiger Zinkoxid-Mikropartikel wurden genutzt, um komplex geformte Verbundwerkstoffe aus Hydrogelen, sowohl durch additive Herstellung als auch als Templatansatz für medizinische Anwendungen herzustellen. Ihre Verwendung verhinderte die spinodale Entmischung nicht mischbarer Monomere. Des Weiteren wurden diese Mikropartikel als Halbleiterträger für die Fulleren-Dekoration eingesetzt. Die Mischung von selbstberichtenden Polymeren mit strukturell ähnlichen, aber mechanisch festeren Polymeren ermöglichte die Entwicklung von schadensanzeigenden Mikrofasern.

Das breite Spektrum dieser Anwendungen verdeutlicht das noch zu erkundende Potenzial der Selbstorganisation und die in dieser Arbeit aufgeführten Beispiele können als Grundlage für noch anspruchsvollere Anwendungen der Selbstorganisation in der additiven Fertigung dienen.

Contents

I	Fundamentals	1
1	Introduction	3
2	Theoretical Background	9
2.1	Digital Manufacturing	9
2.1.1	Stereolithography	10
2.1.2	Fused Deposition Modelling	13
2.1.3	Direct Ink Writing	15
2.2	Self-organisation	17
2.2.1	Phase Separation	17
2.2.2	Wetting	21
2.3	Metal Oxides	23
2.4	Polymers	26
2.4.1	Polymer Physics	26
2.4.2	Polymer Synthesis	29
II	Publications	33
3	Perfect polymer interlocking by spherical particles: capillary force shapes hierarchical composite undercuts	35
4	Homogeneous polymerisation realised by only trace amounts of crushed microcrystals	49
5	Buckminsterfullerene hybridised zinc oxide tetrapods: defects and charge transfer induced optical and electrical response	75
6	3D Hydrogels Containing Interconnected Microchannels of Subcellular Size for Capturing Human Pathogenic <i>Acanthamoeba Castellani</i>	101
7	Light controlled growth factors release on tetrapodal ZnO microparticles incorporated 3D printed hydrogels for developing smart wound dressing	117
8	3D-Printed Chemiresistive Sensor Array on Nanowire CuO / Cu₂O / Cu Heterojunction Nets	173

9	Facile fabrication of semiconducting oxide nanostructures by direct ink writing of readily available metal microparticles and their application as low power acetone gas sensors	189
10	Mechanochromic Microfibres Stabilised by Polymer Blending	217
III	Summary and Outlook	271
11	Summary and Outlook	273
IV	Appendix A Additional Publications	283
	3D-Printed Sensor Array of Semiconducting Oxides	285
	Resistivity Response to Stress and Strain of a Flexible Bi ₂ Te ₃ Based Thermoelectric Material	291
	Conversionless efficient and broadband laser light diffusers for high brightness illumination applications	297
	Enhancement of antiviral drug efficacy through multimodal mechanism of Au nanoparticles complexed with ZnO tetrapods	309
	Wear behaviour of additive manufactured polymer-polymer sliding combinations	333
V	Appendix B Additional Information	347

Part I
Fundamentals

Chapter 1

Introduction

The invention and discovery of novel materials has made manufacturing a more demanding and important task than ever before. Aside from the native material properties, the manufacturing method itself can also create new functionalities by controlling structural features. This enables the creation of parts with the desired properties for most major tasks in today's industry and private applications. Two methodologies employed in the synthesis of new materials, the manufacturing of diverse composites and the building of extraordinary work pieces are self-organisation and additive manufacturing.

Often deemed as disruptive technology additive manufacturing (AM) is the set of techniques that can generate complexly shaped work pieces bottom-up with relative ease. This is done by cutting a digital work piece design into individual layers called slices and building them successively. Geometries inaccessible to other fabrication techniques and features such as undercuts, open porous or cellular structures can easily be realised. Additionally, the simplicity of this approach allows for a fast iteration, optimising specific functionalities of the parts.

Yet another benefit is the combinatorial explosion arising from merging established and novel materials with the formative possibilities of additive manufacturing. Three dimensional (3D)-printing, as additive manufacturing is often denoted, can be extended by another dimension if functional materials are employed. These approaches have been labelled 4D-printing, where, e.g, predetermined deformation [1], self-reporting materials [2] or electronic functionalities [3] are added to the structural design. Therefore, it is no surprise that additive manufacturing spans major technology branches including automotive [4], aerospace [5], therapeutics [6], electronics [7] and many more. Details on the current limitations and prospects of the existing AM approaches will be given in the theoretical background of this thesis (chapter 2).

While additive manufacturing means the spatial control over the formation of a work piece on a macroscopic scale, self-organisation phenomena belong to the other side of this spectrum. In the most general sense the terms self-organisation or spontaneous order describe processes, that lead to an overall order in a previously disordered system. Some examples include spontaneous symmetry breaking (in, e.g., crystal growth and spontaneous magnetization), phase transitions and (on a molecular level) micelle formation.

All of these processes have in common that there is some sort of positive feedback and that they are robust to random fluctuations. Specific self-organisation phenomena can be triggered by controlling thermodynamic and kinetic aspects during the formation process. For example, the extremely high temperatures during the synthesis of carbon nanotubes (between 4000 to 6000 K) lead to a preferential ordering of the carbon atoms

into these 1D-structures [8].

In nature, self-organisation is one of the main mechanisms to produce complex living beings. This ability to form almost arbitrary structures by means of self-assembly leads to many interesting qualities (e.g., Gecko's ability to climb walls) [9]. Likewise, scientists try to understand and replicate the principles of living organisms and their often very complex self-organisation phenomena. Even though there is no direct extrinsic design control over the precise architecture of self-organised structures [10, 11], their arrangement complexity is astounding.

Utilizing self-organisation phenomena for the formation of functional materials on micro- and nanoscale while precisely controlling the 3D-geometry and macroscopic architecture via additive manufacturing is an exciting possibility to generate complex and functional parts. Understanding the mechanisms behind specific self-organisation phenomena and implementing them with (additive) manufacturing opens up new and unprecedented potentials.

So far, there are many approaches to use common self-organised nanomaterials such as carbon nanotubes (CNTs) [12] and graphene [12, 13] for electronics and biomedical applications. Self-organisation as a structural element has been used by employing wetting of additively manufactured geometries [14]. Functional elements utilizing self-organisation have been additively manufactured as well. Printing with subsequent functionality has also been demonstrated with liquid crystals [15]. So while there is already a general trend towards self-organisation as a tool for heightening the value of additive manufacturing, many concepts are yet to be explored.

Since both self-organisation and additive manufacturing are wide fields with countless ongoing research topics, not every process can be discussed here. Some novel approaches applying both self-organisation phenomena and additive manufacturing individually and in combination are presented in the following.

Polymers are a very interesting and highly relevant class of materials because of the countless applications which arise from their unique molecular structure. They are often made by reacting two or more liquid monomers together in batch syntheses where mixing and phase separation play a decisive role. For homogeneous mixtures phase separation should be avoided, but the thermodynamic properties of the system favour demixing. Surfactants with both polar and non-polar group lower the interfacial energy between polar and non-polar components. However, these materials are always small and one-dimensional and have only a short-range effect. Thus they are only effective, when they form a membrane-like interfacial layer between the polar and non-polar liquids. Furthermore they are almost exclusively made from organic compounds, that would easily react with either of the reactive monomers thus significantly influencing the properties. By self-organisation amphiphilic particles can be made, that act like surfactants at the interface, called Janus particles, and form 'surfactant-free' so-called Pickering emulsions. Still, the membrane-like arrangement of these particles makes complete mixing unfavourable.

A long-ranged mixing effect has been described in chapter 4 using fractured single-crystalline ZnO tetrapods (t-ZnO). Due to the exposure of a highly polar surface upon fracturing and the rather low polarity of the side facets of these microparticles, a strong

homogenisation effect is observed for reactive monomer mixtures resulting in an increase in mechanical toughness. Exemplary, the adhesive strength of standard commercial epoxy could be improved by >32%. These findings could enable greener and cheaper polymer processing, e.g., of thermoplastic filaments for additive manufacturing.

Even for solids one restriction in many additive manufacturing approaches is the respective incompatibility when combining two materials. This can even happen when they stem from the same class (e.g., polymers). There are only very specific material combinations to be achieved to join stiff or tough materials with elastic materials. [16] A lack in miscibility, processing temperature and the overall limitations of the respective additive manufacturing technique render usual bonding techniques ineffective. Bonding two chemically incompatible materials is even more challenging. Low surface-energy polymers do not show strong interactions to any chemical treatment, thus new approaches are necessary for joining these kinds of materials. Self-organisation by utilising the capillary effect on polar polymers could provide a solution.

An example for a mechanical interlocking approach using undercuts made by self-organisation is introduced in chapter 3. Here **poly ether ether ketone** (PEEK, a high-strength polymer) and **polydimethylsiloxane** (PDMS, a low surface energy polymer) are joined with the assistance of hierarchical, self-organised undercuts on the PEEK surface. The structuring method showed that the wetting behaviour of hydrophilic, powder-based capillaries by the polar PEEK can be employed to produce hierarchical surface architectures acting as anchor points for joining a second material. These surface structures include undercuts which are capable to hold the elastic PDMS in place after bonding, resulting in high adhesion strengths between the two materials. The interlocked composite shows promising application in the field of artificial heart-valves.

Wetting as a driving force for self-organisation can also be employed to synthesise new hybrid materials with complex, open-porous architectures. In chapter 5 the decoration of C60 fullerenes on open-porous framework materials made on the structural basis tetrapodal zinc oxide (t-ZnO) can serve as another example. Here the complex shape of the t-ZnO, produced via a dendritic growth mechanism shows the capabilities of self-organisation. The simple 3D-geometry of tetrapods makes them ideal candidates for open-porous 3D-architectures. Additionally, the wetting behaviour of the solution containing the fullerenes on the polar zinc oxide leads to a homogeneous coverage. The number of coating steps dictates the density of fullerenes on the surface of the zinc oxide tetrapods. The decoration of open porous networks with nanomaterials can thus be used to grant access to a larger fraction of a nanomaterials surface. This in turn enhances the specific surface effects typically attributed to nanomaterials. In the case of the 0D fullerenes on t-ZnO, a charge transfer could be inferred from the steeper absorption band edges.

By using structural elements like the t-ZnO, a 3D arrangement on the microscale can be achieved by the random distribution of tetrapods. The tetraeder-like arrangement of t-ZnO naturally favours an open-porous structure, since any two particles are held away from each other by at least a tetrapod arm's distance. Therefore, it is possible to achieve very low densities and tune the density in a certain range by pressing the powdered

t-ZnO into tablet-like scaffolds. Packing the tetrapods closer without fracturing the arms is difficult because the individual arms hinder each other during compression. In chapter 6, this method is used to create defined, interconnected channels in hydrogels. T-ZnO networks are infiltrated with a polyacrylamide precursor to form a composite hydrogel. In a subsequent etching step, the t-ZnO is dissolved in hydrochloric acid to obtain an interconnected network of tubes inside the hydrogel. The predefined density of the tetrapodal networks dictates the density of the channels in the hydrogel and the length and thickness of the tetrapod arms determine the diameter of the tubes. This approach is used to form a scaffold for the effective capture of *Acanthamoeba Castellanii*, a human pathogenic amoeba.

By employing many of these advantages of self-organisation with the design freedom of additive manufacturing, complex and often even complementary functionalities can be easily integrated into one device. One sector where this is of high relevance is biomedical engineering. Exemplary, for the treatment of chronic wounds a multifactor approach is necessary. This means that one treatment should desirably provide all or most of the conditions for proper wound healing. In this context the semiconducting nature of the self-assembled t-ZnO leads to interesting functionalities such as light-responsiveness which is used in chapter 7 for light-induced protein release. Additionally, the particles exhibit strong antibacterial properties while simultaneously being only cytotoxic in high concentrations. Zinc oxide tetrapods combine advanced functionalities with a natural bioactivity which is used in a moisturising, 3D-printed hydrogel matrix for ideal wound treatment. Thus it is demonstrated how the decisive benefits of self-organised microparticles and additive manufacturing can lead to rapid innovation in the biomedical sector.

Using the self-organisation is an effective method to achieve structural ordering on the microscale. Many cases also require complex or precise control over the structure in 3 dimensions. By **D**irect **I**nk **W**riting (DIW) of microparticles in well-defined traces, fabrication of devices using these particles becomes much more reproducible. This is normally difficult to achieve. Adding a self-organised nanostructure on top will enable specific features. Here, an approach for ordering metal microparticles by additive manufacturing is presented in chapter 8. An added thermal annealing step causes the growth of cupric oxide (CuO) nanowires on the surface. Overlapping from wires of two particles randomly leads to junctions between two wires. The diameter of these CuO nanowires is 10 nm. When molecules of a reducing gas adsorb at the surface, the resistance drastically increases. Via this effect, the 3D-printed structures can be used as gas-sensors.

Beside the structuring advantages of additive manufacturing, the free material selection renders this technique tremendously versatile. The ubiquity of the approach enables a rapid iteration of material systems and direct implementation of electronic systems into tailor-made circuits. In chapter 9 a mixture of two metal micro particles is used to fabricate low-power gas sensors with a power consumption as low as 0.26 μ W at a gas response of 50%.

While additive manufacturing is mostly thought of for bottom-up fabrication, there exist other, well-established processes to bring materials into the desired shapes. One is the spinning of polymer fibres, which have been mass produced since the 1930 [17].

The benefits of spinning materials into fibers is their highly oriented, high aspect-ratio nature. This beneficial shape is employed in chapter **10** to produce self-reporting, stable fibers by blending of immiscible polymers. Therefore, this work adds another facet of insight into manufacturing by a bottom-up approach, which is not easily obtained by any other fabrication method.

This doctoral thesis is a cumulative thesis and is organised as follows. Part I serves as a general introduction into the relevant topics including the necessary theoretical background. In Part II publications and manuscripts related to self-organisation and additive manufacturing emerging in the scope of this thesis are presented. Part III summarizes the presented findings and will give a prospective view on ongoing research towards the combined additive and self-assembled manufacturing.

Chapter 2

Theoretical Background

This chapter deals with fundamental aspects of both the driving forces for the self-organisation phenomena presented in this work, as well as the history and current developments in additive manufacturing.

2.1 Digital Manufacturing

In order to give some perspective to the chapters 8 and 9 involving additive manufacturing, the fundamental differences between conventional and additive fabrication techniques are discussed. Additionally, the major AM techniques with their advantages and disadvantages are presented.

Digital manufacturing involves the production of work pieces or parts with the aid of computers or robotic elements. The robotic portion of the setup can be programmed to perform specific, manufacturing-related tasks in the most general sense. For instance, one of these purposes is the translation and rotation of tool heads during **Computer Numerical Control (CNC)**-milling. The necessary rotational speed of the tool head, its speed of translational movement, the depth and the width of the cut are all controlled with respect to the boundaries given by the work piece material, the milling geometry and the tool head. The milling path is predefined digitally, by loading a **Computer Aided Design (CAD)**-model of the final work piece into a path calculator. The automated nature of the machining is the decisive characteristic of a digital manufacturing method. Modern digital manufacturing is divided into two fundamentally different methods, subtractive and additive manufacturing. **CNC**-milling is a major technology of subtractive manufacturing and as such it is restrained by a fundamental limitation. Subtractive manufacturing methods, such as milling, take a solid bar stock and selectively remove material until the product has the desired shape. Necessarily, this method can only produce parts, where the cutting paths are accessible, meaning undercut, hollow or porous parts cannot be manufactured. However, these disadvantages however are compensated by unprecedented accuracy and a wide range of materials including metals and ceramics. The limitations of subtractive manufacturing do not hold for additive manufacturing. In this methodology, a **CAD**-model is digitally divided into individual slices, which can be iteratively deposited on top of each other. The bottom-up nature of this technique can therefore enable the production of parts with complex geometry such as undercuts or porous pieces with ease. While overhangs are generally difficult to achieve, many techniques use support structures that are removed after fabrication. The rapid progress made in this field in the last three decades promises strong impact on all manufacturing branches

in the future. The advantages can be seen in the design and material freedom, offering solutions for some of the most demanding fields in science and technology.

While additive manufacturing allows enables the simple construction of complex geometries, it is not suitable for mass-fabrication. Common methods like injection moulding will always have a decisive advantage: The fabrication rate is very high and can allow production of simple parts within seconds. Additive manufacturing, while still showing potential for speed improvements can only be relevant for small batch, highly complex fabrication. For example, it is unimaginable to fabricate plastic cups by additive manufacturing in a cost efficient manner. Whole motor blocks however, possessing a high geometrical complexity seem much more likely to be fabricated efficiently by additive manufacturing.

Additive manufacturing will be explored in greater detail in the following subchapters, showing the different approaches with their possibilities and limitations.

2.1.1 Stereolithography

Historically, stereolithography or the **Stereolithographic Apparatus (SLA)** is the first mainstream additive manufacturing technique. While Hideo Kodama published the first account of a three dimensional (3D)-fabricated object made from photo-hardening resin in 1981 [18], it is not the most recognized account of additive manufacturing. Instead Chuck Hull and his team, who first coined the term 'stereolithography' (greek *stereós*, "solid", *lithos*, "stone", and *gráphein*, "to write") in 1984 take most of the credit for inventing additive manufacturing. The procedure was patented [19] and this patent has become the first reference of SLA and represents the historical set point for additive manufacturing.

SLA shares its working principle with the other AM techniques:

A 3D object is designed and sliced digitally into individual layers. The differentiation between the processes happens, when the layers are fabricated. In SLA, as depicted in Figure 2.1, a liquid, photo-curable resin made of monomers, oligomers and initiators is contained in a vat and irradiated with light, triggering a cross-linking reaction. Irradiated areas harden immediately, limiting the spatial movement and ensuring a high lateral resolution. Many devices use ultra-violet light with a wavelength of around 405 nm for curing. When one layer is fully developed, the vertically displacing build platform is moved upwards and the current layer is covered with another film of uncured resin. The process is repeated, until the work piece is fabricated. Typical layer heights are between 0.01-0.1 mm.

As with most other 3D-printing, overhangs need to be supported by temporal structures, to ensure a tight connection to the building platform. Even though most of the modern fabrication methods followed, starting from 1991, SLA remains one of the most universal techniques. This is due to multiple factors. The decisive one is its high lateral resolution, meaning the minimum width of an individually printed line. Two-photon direct-laser-writing, a subset of stereolithography can offer resolutions below 500 nm [20, 21, 10, 22]. The technique uses two-photon absorption phenomena, which limit photo-

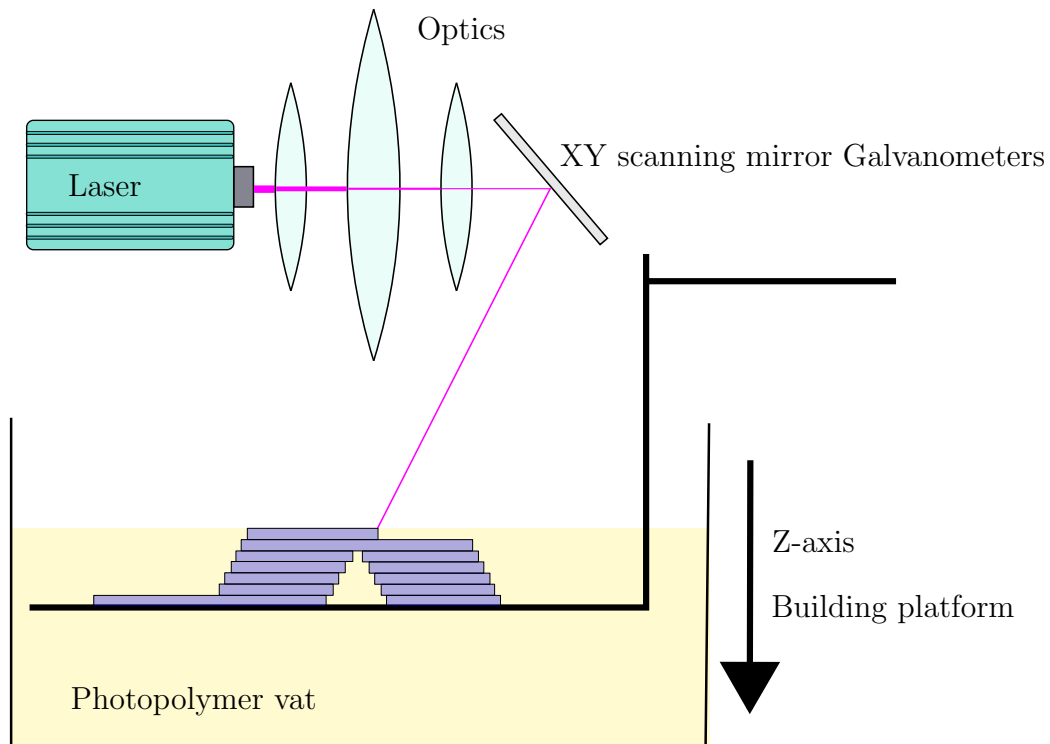


Figure 2.1: Schematic representation of a SLA process. A laser (mostly UV with $\lambda \approx 405$ nm) is focused through some laser optics and a mirror galvanometer into a specific location inside a vat filled with photosensitive resin. When the laser hits the resin, a radical polymerisation reaction is triggered and the resin solidifies. A building platform carries the solidified structures and is moved incrementally to build an object layer-by-layer. A wiper can additionally be used to provide a sufficiently thick layer of photo-resin on the part. The mirror galvanometer allows for precise and fast scanning of the laser beam and thus enables quick and reliable printing.

curing to a tiny focal volume. The typical limitations of Gaussian-distributed power and wavelength limitations do not apply. Aside from that, the SLA in general is simple to use and printers are offered as "desktop-compatible", enabling rapid prototyping in office environments. Many different commercial varieties of the photo-curable resin are available already. Mostly, the mechanical properties are tailored, the resins offered are often labeled "tough" or "flexible". Some resins are specifically used for casting applications, where the SLA-printed part is used as a negative. Aside from the commercially available resins, there are countless examples in research for innovative applications of this technique producing a large assortment of functional and structural SLA-printed work pieces. As an example, fabrication of ceramic parts has been explored since 1996 [23, 24, 25].

Although there have been some attempts at multi-material printing (cf. Choi et al. in 2011 [26]), SLA does not offer an accessible design freedom on the material side. Printing combinations of materials in one print and even switching materials between two prints are difficult to perform because of the specific requirements of the printing setup, namely the condition of the resin containing vat, laser settings, reaction kinetics and fluid dynamics of the resins and many others. Therefore, SLA remains one of the most popular techniques [27] but is not universally suitable for handling high stress, high temperature or other extreme conditions as well as other techniques. Some of the decisive disadvantages of SLA are alleviated by other techniques, e.g., extrusion based additive manufacturing. These techniques are thus presented in the next section.

2.1.2 Fused Deposition Modelling

Known as **Fused Filament Fabrication (FFF)**, **Fused Deposition Modelling (FDM)** or other terms represents the most common class of additive manufacturing methods in the private sector. S. Scott Crump developed and patented the method in 1989 [28] and also founded the company Stratasys, successfully marketing and distributing FDM printers until today. Since the patent has expired in 2009, FDM became the most prominent open-source process in additive manufacturing. The reason lies in the process itself. As depicted in Figure 2.2, the individual slices of a 3D object are fabricated by melting a thermoplastic material inside a heated printhead. The plastic is delivered in filament form with the standard diameters of 1.75 mm and 3 mm. The filament is heated inside the print-head to temperatures much higher than the melting temperature. Because of the short retention time inside the print-head, temperatures where normally decomposition occurs, can be employed. Typically, the temperature should be high enough to allow easy extrusion of filament, but low enough to provide sufficient shape retention after printing as well as avoiding decomposition. When additional filament is pushed into the upper end of the print head, molten polymer flows out of a defined opening, typically between 100 and 800 μm in diameter. Controlling the position of this print head in all dimensions and extruding polymer at a set rate yields the deposition of individual solid layers.

FDM uses solid, thermoplastic polymers for the construction of 3D-objects. Thermoplastic materials have the distinct advantage to melt when temperature is sufficiently high and rapidly solidify when cooling down again. The high base viscosity of this material class allows for deposition with shape retention after printing. Adhesion to the bed material is obligatory to achieve high quality parts. Thermoplastic polymers with semi-crystalline structure are decisively more difficult to print, due to deformation during cooling induced by crystallisation. This behaviour is called 'warping' and is one of the main reasons to predominately use amorphous thermoplastics. Apart from the standard materials which include **polylactic acid (PLA)**, **acrylonitrile-butadiene-styrene (ABS)** and **polyamide (PA/Nylon)**, special filaments are used. Exemplary thermoplastic polyurethane can be used, which exhibits the flexibility of elastomers while being melt-able. In recent research many composites have been produced by filling the polymers with solid particles made of metals or ceramics to obtain all-metal, all-ceramic parts. Nanoparticles or photochromic/mechanochromic molecules have been embedded [2] to fabricate parts with special properties like thermal/electrical conductivity [29], mechanochromism or other unusual properties. The major advantage of this approach is the easy implementation with standard printers. On the other hand, the necessity to mix the desired materials into high melting point polymers first and the relatively low maximum filling factors hamper the applicability of some procedures. For example, electronic circuits are very difficult to produce because of the high base resistance of thermoplastics. Additionally, for testing a large amount of filament has to be produced in a sophisticated process with every variation that should be tested. Quick and easy composition variations are not easily achievable, complicating the research in this field.

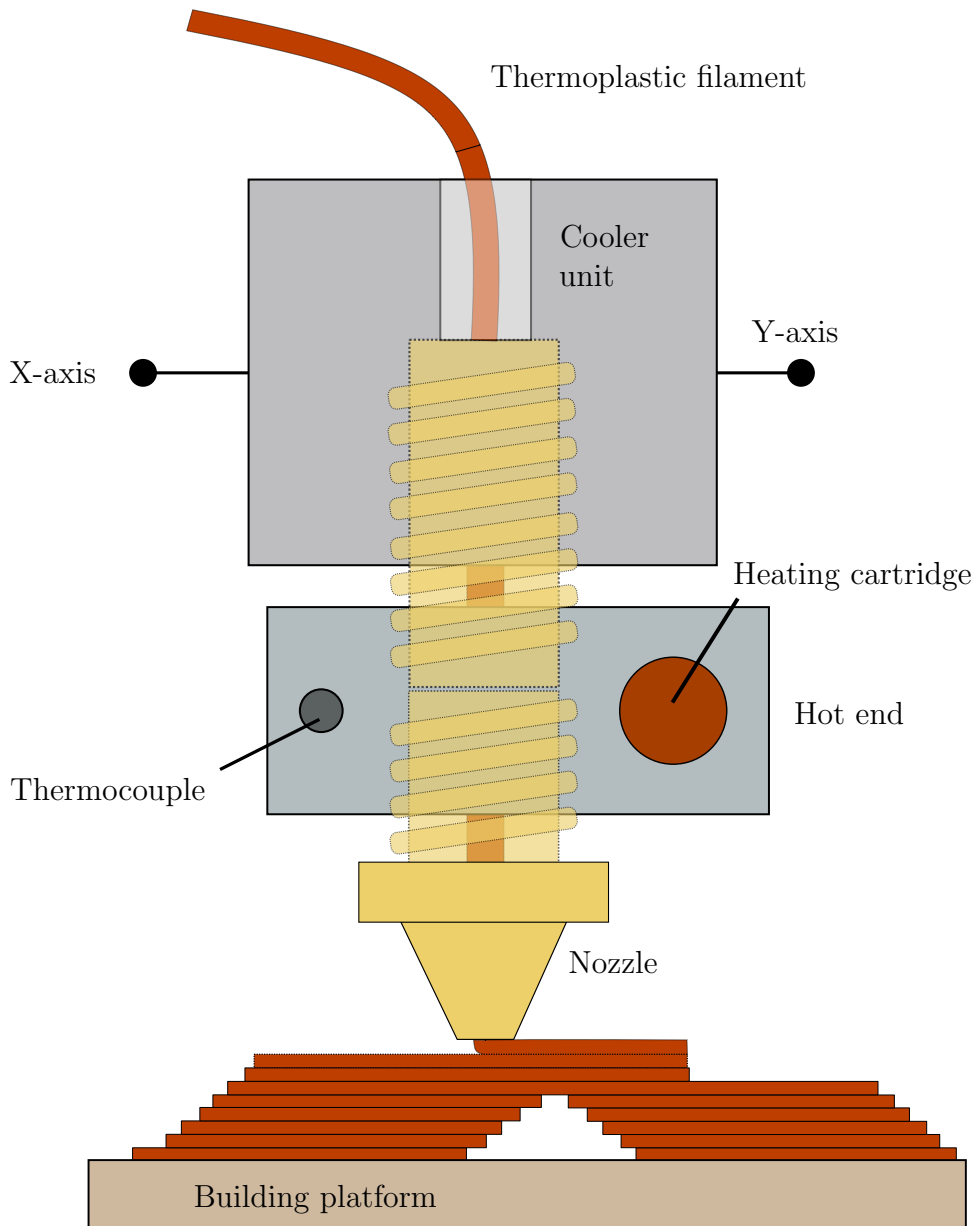


Figure 2.2: Schematic representation of a FDM process. A thermoplastic filament is fed into the printhead. The printhead is divided into a cool zone provided by a cooler unit and a hot zone, which is always heated above the melting point and below the decomposition temperature of the polymer. The temperature of the so-called hot end measured by a thermocouple and controlled electrically with a heating cartridge. A nozzle with a precise opening diameter (typically $400\ \mu\text{m}$) is fixed at the bottom of the filament path. By precisely controlled pushing and pulling on the filament with a stepper motor, polymer can be extruded from the nozzle or retracted to stop polymer flow. The printhead is then moved relative to the bed and polymer is deposited where desired.

2.1.3 Direct Ink Writing

The method described here is known as Robocasting, Direct Ink Writing, Direct-Write Assembly or Microrobotic Deposition. All of these designations describe the process of depositing viscous slurries automatically from a syringe. The essential requirement for printing with this technique is a low enough viscosity to allow extrusion of the inks through a nozzle <1 mm and subsequent solidification to ensure dimensional stability. This can then be achieved by a multitude of mechanisms including pseudoplasticity (also called shear thinning), gelation due to reaction, evaporation of the solvent or printing into viscous liquids.

The decisive benefit of this approach is the material-versatility. Many materials can be fabricated as micro- or nanoparticles, put into a slurry and printed directly. After an additional treatment step (,e.g., sintering, curing) a fully solidified metallic, ceramic or composite part can be obtained easily. Quick adaptation of the inks is possible without the necessity for sophisticated extruder machines.

It is therefore not surprising that many research teams have adapted a wide spectrum of different DIW sub-techniques to produce e.g., nanoparticle composites, ceramic or metallic parts, functional devices like electronics or sensors and many others. One of the pioneers in this field is Jennifer A. Lewis from the Harvard University with her work on functional materials assembled by DIW [11]. In this work, the fundamental relationships between viscosity and printability (that is shape retention after printing, paired with sufficiently high extrusion rates) are explored for colloid systems and demonstrated on an ink that contains SiO_2 particles and water. Additionally, many strategies for other solidifying techniques such as solvent evaporation and shear thinning are given.

The devices and parts already fabricated by this method are manifold. Exemplary, stretchable electronics [3], flexible actuators [30] and swelling- or temperature-induced shape-shifting devices [31] have been demonstrated in the last three years alone by Lewis' group.

The rapid progress ($>2,500$ publications with 'Direct Ink Writing' in the title since 2016, according to Google Scholar) can certainly be attributed to the design freedom offered by this technique. Specifically, the choice of materials available as powders through other industries like nanotechnology and powder processing manufacturing are a stepping stone towards easy implementation of almost all material classes with this printing method.

Despite the numerous advantages and possibilities of this technique, the only printers commercially available are carried under the name 'bioprinters' by companies like CELLINK. These are still mainly used for academic purposes and DIW has not found its way as a standard technique for fabrication like FDM or SLA.

One reason might lie in the versatility that is also the benefit of the approach. Designing long-term and temperature stable inks that are reproducible is difficult because of phase separation, degradation or particle settling are challenging. Without the specific inks, the approach is hard to control and does therefore not fit for arbitrary use.

Thus, some development needs to be done to integrate this fabrication method as

standard technique for additive manufacturing. In the scope of this thesis, this method has been utilized for promising applications of both self-organisation and additive manufacturing, c.f. chapters **7**, **8** and **9**.

2.2 Self-organisation

Ordering phenomena are a major method for systematically generating structures on the micro- and nanoscale. Although the advent of nanofabrication has impacted the society in an unprecedented way, the complexity in self-organisation phenomena still cannot be matched. Effects like wetting, dewetting, phase separation, other thermodynamic processes or even kinetic limitations can result in sophisticated architectures that cannot be built with any other method. The driving forces are typically present at a small scale, yet have a large scale and sometimes self-promoting effects.

Since wetting is a major part of chapters **3**, **5** and **6** and phase separation plays an important role in understanding chapters **4** and **10**, both mechanisms are discussed in greater detail here.

2.2.1 Phase Separation

Phase separation is a complex interplay between thermodynamics and kinetics.

Two constituents of a mixture with repulsive forces are kinetically stabilised, i.e. the thermodynamically driven separation processes are frozen in. Therefore, such a homogeneous mixture is metastable. When the temperature is increased, the thermodynamically driven process for phase separation is favoured and the kinetics allow demixing in a finite time. There are several mechanisms that can lead to phase separation in this manner. Spinodal decomposition is a very fast process that typically occurs, when stable systems undergo a rapid phase transformation (e.g., quenching). Slower phase transitions trigger a set of processes called nucleation, growth and Oswald ripening. Both mechanisms are discussed in the following section.

Spinodal Decomposition

Spinodal decomposition is one of the fundamental processes leading to phase separation. It is defined as the spontaneous separation of a homogeneous mixture into two separate phases [32]. Spontaneous phase separation means, that there is no Gibbs free energy barrier for the transition from a one-phase to a two-phase system. The consequence is that infinitesimal fluctuations in concentration or temperature lead to immediate phase separation in the whole mixture. The phase separation leads to a decrease in Gibbs free energy which is the driving force for the formation of distinct stable phases. To understand the principles of phase separation, a Gibbs diagram for a system with a miscibility gap is shown in Figure 2.3.

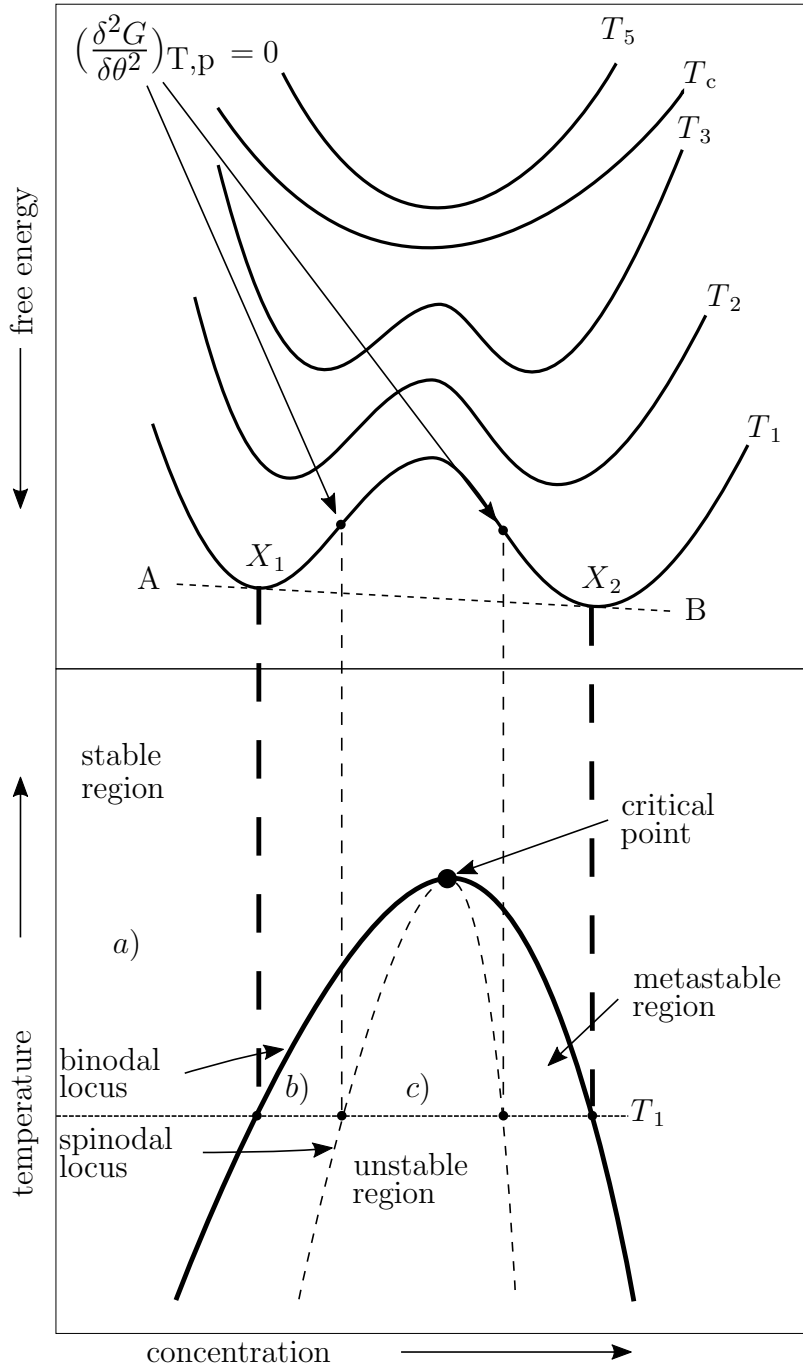


Figure 2.3: Schematic Gibbs free energy diagram for spinodal and binodal decomposition of mixture systems A and B. At low mole fractions of A in B or vice versa, the system forms one uniform and stable phase (a)). For a given temperature T_1 there is a miscibility gap, where the system can decompose into two distinct phases. These phases will then have the mean compositions X_1 and X_2 . The main growth mechanism in this metastable phase between the binodal and spinodal locus (b)) is nucleation and growth. The region in the Gibbs energy diagram where the curvature of the Gibbs energy curve with respect to concentration θ transitions from negative to positive denotes the unstable region (c)). Here, a system with the overall composition and temperature inside this curve will spontaneously form two distinct phases. When the temperature is increased, the entropic contribution to the Gibbs energy can lead to a stabilisation of the system. The temperature of the maximum of the spinodal locus is called the critical temperature T_c . Above this critical temperature, the system is always present in a single phase.

When the curvature of the Gibbs energy switches from negative to positive, the spontaneous formation of a two-phase system becomes so favorable, that infinitesimal fluctuations in the composition will lead to phase separation. This region in the Gibbs energy diagram is called the unstable region and the phase separation process is always spinodal decomposition. This signifies that when passing the critical temperature T_c , the system can not exist in a single phase. Additionally, the spinodal decomposition is an entirely kinetic process and a single phase can not be kinetically stabilized by rapid quenching. Since there is no nucleation barrier involved, this is not a statistical process and therefore the phase separation is occurring homogeneously throughout the system - not just in nucleated spots. When the composition of the system falls into the metastable range, the dominating process for phase separation is nucleation and growth which will be discussed in the following subsection.

Nucleation & Growth

While the coexistence of two distinct phases is thermodynamically favourable, kinetics might either promote or impede the formation of these phases from a single phase. In the metastable region of the Gibbs free energy diagram, the process leading to phase separation is limited by an energy barrier. The Gibbs energy plot for this process is depicted in Figure 2.4.

The energy barrier for the formation of phase separated nuclei stems from two competing energy contributions: The first contribution is the surface (or interfacial) energy $\Delta G_{\text{surface}}$ of the newly formed particles. This energy has to be invested and thus this contribution destabilises particles and it scales with the particles' radius squared. The other contribution is the released volume energy ΔG_{volume} of the newly formed nuclei which scales with the nucleus' radius cubed. For nucleus sizes below a critical size R_{crit} (also called sub-critical nuclei) the difference in Gibbs energy between surface and volume energy favours dispersed, separated atoms/molecules instead of stable nuclei. Therefore, stable nuclei (also called super-critical nuclei) can only exist from a critical size on, which limits, e.g., the formation of nanoparticles of certain materials like water under ambient conditions. Naturally, the individual contributions of the interfacial energy γ contained in $\Delta G_{\text{surface}}$ and the free energy of the volume decide the exact extent of the critical radius for particles. Both the volume and the interfacial energies are dependent on the bonding enthalpy H and the entropy S of the specific arrangement.

Without external triggers, overcoming the potential barrier is a statistical process: the formation of nuclei of a critical size can take a time between seconds and days. With the formation of the first stable nuclei however, a chain reaction can be triggered, where the growth of existing nuclei is very fast compared to the nucleation.

The growth rate however, is always a trade-off between energy decrease and mobility of the system. In super-cooled melts, the possible energy decrease upon nucleation becomes higher with lower temperatures, but the mobility of atoms in the solution also becomes lower. These two processes compete, resulting in an ideal, fastest solidification rate.

Understanding the mechanism of nucleation and growth is important for the synthesis

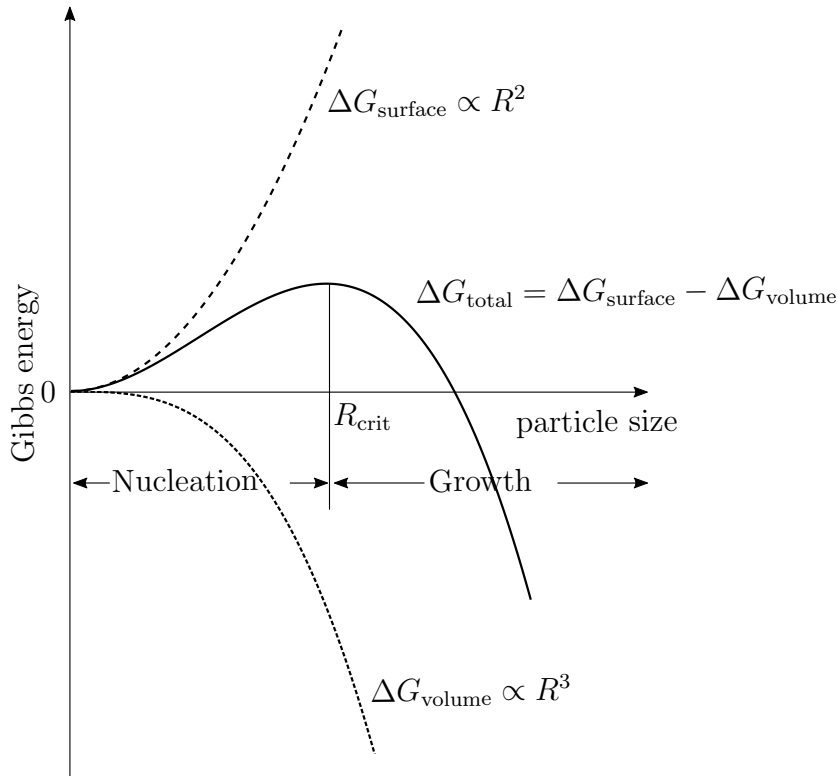


Figure 2.4: Schematic plot of the Gibbs energy barrier for the nucleation process. Two competing energy contributions lead to a critical particle size R_{crit} . Below this size, the formed particles are highly unstable and fall apart, above stable particles can exist and will start to grow. The two energies involved are the surface energy which has to be invested and the volume energy which is gained. Due to geometric reasons, spherical particles form with a R^2 surface energy and a R^3 volume energy dependency. The critical particle size is reached, when the difference between surface and volume energy contributions becomes negative.

of zinc oxide tetrapods used in chapters 4, 5, 6 and 7. Additionally, the phase separation mechanisms in general are important for the mixing and demixing of monomers and polymers in chapters 4 and 10.

2.2.2 Wetting

Wetting is the behaviour of a liquid towards a solid when both phases are in contact to one another. The tendency of a liquid to form either a thin, spread out film or maintain a spherical shape depends on the interface interactions between the solid, liquid and gas phase and the intermolecular forces of the liquid. The wetting behaviour of two materials is important for applications such as adhesion, materials synthesis and materials engineering. Exemplary, wetting can be employed to produce self-organised structures on the micro- and nanoscale as is shown in chapter 3.

Many terms for labelling surfaces and liquids are used and are sometimes interchangeable. Fundamentally, one can distinguish between polar and non-polar molecules and materials. When considering surfaces the terms of polar and non-polar are often substituted for hydrophilic and hydrophobic, respectively. The reason is that the water contact angle is used as a measure for the surface polarity of the tested surfaces. Because water itself is polar, it is attracted by polar surfaces which can then be called hydrophilic. Contrarily, non-polar surfaces lead to a contraction of a water droplet into a spherical shape, since the hydrogen-bonds inside the droplet are more favourable for the water molecules than the bonding to the surface. These surfaces are called hydrophobic.

The principle of wetting depending of the polarity is not only important for water on surfaces, but holds for all gas-liquid-solid interactions, regardless of the chemical composition of the individual partners. As is shown in chapters **3** and **6**, the wetting is also important for systems where the liquid is a polymer and the surface is a metal oxide.

To employ wetting in terms of self-organisation the capillary effect is used in both examples. Therefore, the capillary effect will be described in more detail in the following section.

Capillary Effect

When considering capillaries of a polar material in contact with a polar liquid, e.g., water, there are mainly two competing force contributions to the overall process. Firstly, depending on the orientation of the capillary, the gravitational pull of the rising liquid opposes the rising of the liquid in the capillary. Secondly, wetting of the inner surface of the capillary is energetically favourable, since the interfacial energy between water and polar surface is lower than that of air and the polar surface. The height, that the liquid rises inside the capillary results from the difference in these two forces:

$$h = \frac{2\sigma \cos\Theta}{r\rho g} \quad (2.1)$$

As can be seen from equation 2.1, the height of the capillary rise is inversely proportional to the radius of the capillary. Therefore, smaller capillaries (i.e., smaller pores inside a solid) will exhibit a higher column of liquid than wider capillaries. This phenomenon has been used to selectively produce undercut structures on polar PEEK polymer in the **3**.

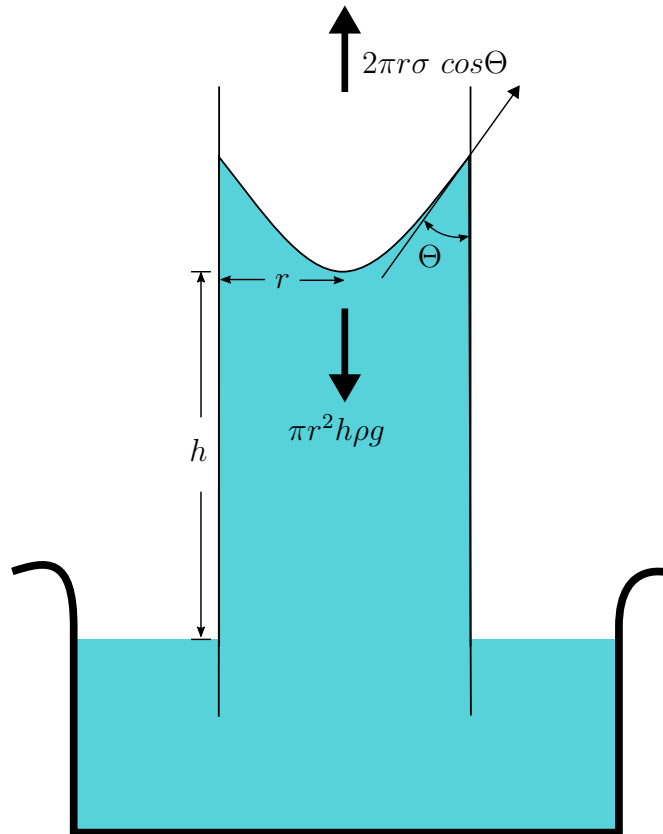


Figure 2.5: Schematic representation of the capillary action. An upwards force arising from the surface tension $2\pi r \sigma \cos\Theta$ competes with the gravitational force of the rising liquid $\pi r^2 h \rho g$. The height of the capillary rise depends mainly on the width of the capillary r and the interfacial tension σ .

2.3 Metal Oxides

Metal oxides are inherently interesting material for countless applications.

Some of their functional properties have been employed in almost all of the presented works, excluding 10. There are more than 20 metallic elements, many of which are able to form more than one stable oxide. The specific properties arise from the bonding character and the crystal structure and can be drastically different between two metal oxides. Thus, they offer a wide range of industrially relevant uses. On the one hand, they often exhibit semiconducting properties and are catalytically active, on the other hand, they find uses as biomaterials or simply as technical ceramics. Most metals belong to the group of transition metals, exhibiting a partially filled d-orbital and therefore exhibit both covalent and ionic bonding. The varying degree in this bonding character is partially the reason for the different electronic, mechanical and chemical properties of the metal oxides.

A few prominent candidates are presented in more detail in the following section.

Zinc Oxide

Zinc oxide (ZnO) is one of the most-studied compounds in the world. At the time of this thesis, there are more than 2.8 million articles about zinc oxide on Google Scholar alone. One natural reason for this is the abundance of zinc in the earth's crust (0.0075%) [33] and that it has been used evidently in brass alloys together with copper as early as the 14th century BC [34]. Although the element zinc was isolated in the 14th AD in India [35] and the 17th century AD in the west [34], evidences of the use of zinc oxide itself in ointments for open wounds as early as 500 BC in India [36]. This long-lasting knowledge of the compound together with its abundance however is only one of the reasons for the persistent interest in zinc oxide.

There are not many other materials that have such a broad spectrum of properties and applications as zinc oxide. It is often deemed 'multi-functional' and a selection of its properties includes a wide direct bandgap (around 3.37 eV), photocatalytic activity, anti-bacterial behaviour, piezoelectric capabilities and the ability to form a considerable set of micro- and nanostructures [37, 38, 39]. This last quality heightened the interest in zinc oxide once again with the advent of nano- and semiconductor technology. Many uses can be listed such as UV- and gas sensing, energy harvesting and photocatalysis. Many of the properties are found to be excellent due to the tendency of ZnO micro- and nanostructures to be single-crystalline. The periodic arrangement of Zn^{2+} and O^{2-} in the most prominent Wurtzite structure enables many of the natural qualities of the ZnO.

Some of the micro-architectures are of high technical relevance and are studied thoroughly. One interesting shape of ZnO is the tetrapod, which will be discussed in greater detail in the following subsection.

Zinc Oxide Tetrapods

The self-assembled tetrapods made from zinc oxide are the major building blocks for the applications presented in chapters 4, 6, 5 and 7 and are thus discussed here in more detail.

Tetrapods form a unique class of ZnO micro- and nanostructures. They consist of four single-crystalline Wurtzite structure arms connected via twins in a central hexagonal core [40]. Each individual arm consists of a micro- or nanorod and hence possesses all of the features of such a structure, while being connected to form a 3D-shape. The size of these tetrapods ranges from a few hundreds of nanometres [39] to a few hundreds of micrometers [38]. The single-crystalline nature of tetrapodal ZnO (t-ZnO) enables some of its important semiconductor properties, while the geometry of the tetrapods facilitate some unique applications, e.g., producing highly porous materials by using ZnO tetrapods as template material [41, 42]. One of these applications to produce self-organized micro-porous, interconnected hydrogels able to catch a pathogenic amoeba is presented in chapter 6.

The growth of ZnO tetrapods is dominated by the nucleation and growth process described in section 2.2.1. The nucleation phase is the limiting step, since the arms grow in a dendritic fashion [43]. The either zinc- or oxygen-terminated tips of each individual tetrapod are highly unstable and thus susceptible to the reaction with the respective other species. If there is enough of each educt present at the right partial pressures without a diffusion limitation in the gas-phase, very high aspect ratio zinc oxide wires grow from a centre tetrapod core. With longer duration of the reaction the individual arms get thicker because vapour atoms stick to the sides of the ZnO whiskers. Therefore, many morphology variations exist for ZnO tetrapods, most of which have found interesting applications [44].

One property nearly all metal oxides have in common is their tendency to form oxygen vacancies on the surface.

Cupric Oxide

Cupric oxide or CuO is one of the two stable oxides of copper, the other one is copper oxide (Cu₂O). This metal oxide is the more stable compound of the two and is used extensively in catalysis, e.g., to reduce polycyclic aromatic compounds [45]. Aside from that, the cupric oxide shares the tendency to form oxygen vacancies under ambient condition, resulting in an intrinsic n-doped semiconductor. This property can be used for example for gas sensing, where the adsorption of ionized oxygen changes the surface conductivity of CuO at elevated temperatures (i.e., >300 °C). When organic gas molecules react with the surface oxygen, the resistance of the surface is decreased. The extent of the resistance change depends on the surface-to-volume ratio. Therefore, small nanowires exhibit a higher reactivity towards reactive gas atmospheres than other morphologies. This effect has been utilized for the fabrication of additively manufactured sensors of self-organized nanowire networks in chapters 8 and 9 as well as in the Appendix chapter IV.

Metal Oxide Nanowires

The general growth mechanism of metal oxide nanowires will be briefly discussed as one self-organisation mechanism relevant for chapters 8 and 9 with CuO as an example [46].

A metal microparticle usually possesses a natural oxide layer on its surface with grain boundaries. At elevated temperature, metal atoms diffuse faster along the grain boundary and react with atmospheric oxygen when they reach the surface. The growth of a new oxide layer near the grain boundary is epitaxial. Therefore, the grain boundary extends into the newly formed oxide. The process continues, forming oxygen preferentially around the tip of the grain boundary. In this way, a spike grows with a grain boundary in the middle. The process is diffusion controlled and thus longer needles or spikes require a longer duration of several hours at elevated temperatures.

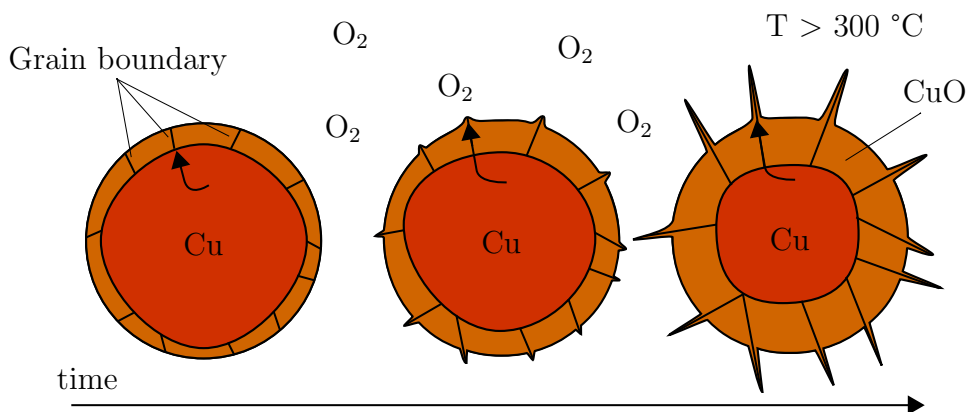


Figure 2.6: The growth of nanowires from spherical metal particles. The particles possess a native oxide layer containing grain boundaries. At elevated temperatures a faster diffusion of metal atoms occurs at these grain boundaries. At the surface the metal oxidizes and the oxide grows epitaxially, maintaining the grain boundary. Since the diffusion is preferentially higher at these grain boundaries, long spikes or wires grow. At the same time, oxygen can diffuse into the particles which increases the thickness of the oxide layer.

The length of the spikes depends on the initial size of the particles because larger particles contain more metal is available on the inside for the formation of these spikes. It was also shown that the crystallinity of the surface plays a crucial role in the density of spikes forming through thermal annealing. Hansen et al. found that nanocrystalline Cu leads to a much higher spike density hinting at a grain-boundary driven mechanism [47]. This self-organised growth of nanowires has been used in the chapters 8 and 9 to form metal oxide nanowires for volatile organic compound detection.

2.4 Polymers

Polymers form a material class that is distinctly different from metals and ceramics. The exclusive property combinations include light weight, general chemical resistance, high plasticity and ductility, high thermal and electric insulation and many others. Representatives of this class are always composed of small building blocks called monomers (greek *monos*, "one" and *meros*, "part") which form covalently bound macromolecules, also known as polymers (greek *polý*, "many" and *meros*, "part"). The arrangement of these building blocks can occur in many different ways which have high impact on the physical and chemical properties of the final properties. The physics involved in polymer engineering are relevant for almost all following chapters. Additionally, a selection of syntheses for tailoring e.g. mechanical properties relevant for chapters 4 and 10 will be presented and discussed briefly.

2.4.1 Polymer Physics

Polymer classification

The class of polymers is often divided into three main groups depending on their structure-property relationship. These groups are called thermoplasts, elastomers and thermosets. The monomers in the polymer chains are always bound covalently. In general, if the chains have no additional covalent bonds called cross-links between them, they can be melted. This because the movement of the individual chains allows them to move forward or backward inside a certain tubular volume described by the reptation model proposed by Pierre-Gilles de Gennes [48]. These polymers can be melted and are collectively described as thermoplastics. Some special thermoplastics cannot be melted but only sintered, since their melting point is too close to the decomposition point [49]. In general however, the absence of cross-links enables melting and dissolution in organic solvents, leading to easy processing and countless applications in industry, as packaging, in consumer products, pharmaceuticals and many others. In the context of this thesis, thermoplastics have been used, e.g., long-chained polyethylene oxide or polyvinylbutyral acted as viscosity agents for DIW in chapters 8, 9 and in the Appendix chapter IV. Additionally, the flow and wetting characteristics of high strength poly ether ether ketone have been utilized in chapter 3. Therefore, some specifics of the viscous flow occurring for polymers melts and solutions are relevant for this thesis and will be discussed in the next section.

Aside from cross-link-free thermoplastic, mildly cross-linked polymers exist which are classified as elastomers. They typically cannot be melted or dissolved but rather swell in suitable solvents. Due to their high elasticity called rubber elasticity, these polymers are usually applied as seals, gaskets, tires, dampeners and others. The most known relevant polymers in this class are silicones, polyurethanes or synthetic rubbers like ethylene propylene diene monomer rubber. One special subset of elastomers that easily take up multiples of their own weight in water is called hydrogels. Although there exist also thermoplastic hydrogels, many of these polymers are mildly cross-linked biopolymers. The high water uptake of these materials paired with a certain biocompatibility makes

them very attractive for biomedical engineering as tissue replacements, wound dressing, contact lenses and many others [50]. The cross-linked hydrogel gelatin methacryloyl has been used as matrix material and viscosity agent for bioprinting in chapter 7.

For high-strength and high temperature applications highly cross-linked thermosets are the most favorable. The high cross-linking density provides a much higher fracture toughness than for typical elastomers or thermoplasts. The fabrication, however, is exceedingly difficult, because once the polymer is cured it becomes very rigid. Aside from that thermosets are chemically inert and rarely swell in solvents. In general they show brittle mechanical behaviour, but this quality depends on the cross-linking density. Typical thermosets are epoxides, polyurethanes and polyesters. They find a broad range of applications for example as adhesives, circuit boards, casings or as fibre-reinforced sheets. In injection moulding they are typically used for more complex and detailed parts, since the monomer mixture has a lower viscosity before curing compared to molten thermoplastics. The reaction mechanism of thermosets are part of chapter 4, which is why common synthesis routes will be discussed in the following sections.

Polymers have a very high impact on the applicability of additive manufacturing, e.g., as viscosity agent or as printing filament/resin and have been used for many self-organisation fabrication techniques such as nanoparticle stabilisation [51], microstructuring induced by phase separation [52] and many others [53, 54].

Fluid Dynamics of Viscous Polymer Melts and Solutions

For the extrusion of material through small orifices the respective fluid's dynamics is important to consider. Apart from Newtonian fluids which exhibit a linear behaviour between shear rate and shear stress most real fluids show some kind of a shear rate dependent effect. The major classes for viscous flow are called pseudoplastic and dilatant flow behaviour. Pseudoplastic liquids exhibit a reduction in the required shear stress for extrusion at increasing shear rates. This is a very important behaviour for DIW and FDM since it allows the material to easily flow through orifices below 1 mm while exhibiting shape retention when unagitated after extrusion. Dilatant fluids on the other hand show an increase in apparent viscosity for higher shear rates, which is typically not desired when processing polymer melts or solutions. The shear rate dependent behaviour of the viscosity can be described by the so called Power Law Model:

$$\eta = K(T)\dot{\gamma}^{n-1} \quad (2.2)$$

Here, the viscosity η depends on a temperature (T) dependent flow consistency index K and the flow behaviour index n . When n is larger than 1, the fluid is described as dilatant. Values of n below one lead to the description of pseudoplastic fluids. However, this model is only an approximation, because values for n below 1 would lead to an infinite viscosity at $\dot{\gamma} = 0$ and zero viscosity for infinite shear rates. The exact fluid dynamic behaviour is therefore often measured shear rate dependently by utilizing a rheometer. The units of the viscosity η are Pas. Newtonian and Non-Newtonian shear rate dependency is depicted in Figure 2.7.

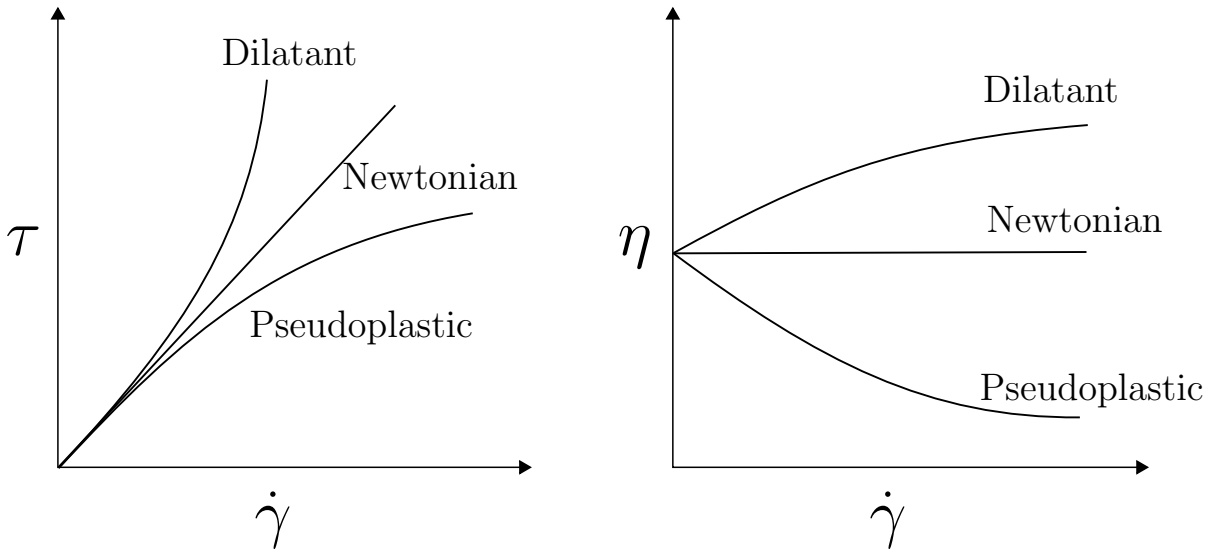


Figure 2.7: Shear rate $\dot{\gamma}$ dependency of shear modulus τ and apparent viscosity η of Newtonian and Non-Newtonian fluids. Fluids with increasing apparent viscosity η are called dilatant. The opposite behaviour is described as pseudoplastic. Fluids with shear rate independent viscosity are called Newtonian fluids.

The exact mechanisms for dilatant and pseudoplastic behaviour is not fully understood [55]. Commonly, pseudoplasticity occurs in polymer melts and solutions, but the exact fluidic properties depend on molecular weight, temperature, nature of intermolecular forces, steric chain architecture and for polymer solutions also solvent and concentration. The shear rate dependent behaviour is assumed to occur due to disentanglement and alignment of the polymer chains in solution or in the melt when sheared. At lower shear rates and at rest, the polymer chains entangle due to entropy maximization resulting in a higher shear resistance and therefore higher apparent viscosity. Pseudoplastic flow of polymer solution has been important for chapters **3**, **7**, **8**, **10** and the Appendix chapter **IV**.

Hagen-Poiseuille Law

The ideal flow characteristics for material extrusion is laminar flow where the volumetric flow for a given pressure is maximized. This ideal flow simultaneously represents the highest flow rates possible at a given pressure difference. The distinction between laminar and turbulent flow is given by the Reynolds number and is specific for any system. Laminar flow is the simplest way for describing the volumetric flow rate \dot{V} through a tube as a function of pressure difference Δp . The exact relationship is given by the Hagen-Poiseuille equation:

$$\dot{V} = \frac{\Delta p \pi r^4}{8\eta L} \quad (2.3)$$

Fundamentally, one can learn that the maximum obtainable flow rate depends on the tube's radius r to the fourth power, the viscosity η and the length of the tube L . This has important implications for the design of nozzles for FDM and DIW. When extruding a polymer melt or a stabilized colloid ink, the viscosity η cannot be varied extensively. To obtain a high enough flow rate for a given pressure, the architecture of printing nozzles can be designed to reduce the internal and interfacial friction. On the one hand tapered nozzles which gradually reduce their internal diameter can be used to reduce the influence of fourth power radius dependency and allow for smooth flow without undercuts. This has been employed for highly viscous polymer solutions containing microparticles in chapters **7**, **8** and **9** and in the Appendix chapter **IV**. On the other hand a discontinuous reduction in opening radius is used in metal FDM printing nozzles. The length of the smallest opening is reduced to below 1 mm to allow for maximum flow while enabling reasonable manufacturing of these brass nozzles. For FDM where the temperature can be used to reduce the viscosity of the polymer melts and thus provides another parameter for extrusion this approach is feasible. This architecture is used in all common FDM printers and has been employed in the frame of this thesis for the Appendix chapter **IV**. In DIW on the other hand polymer solutions are used, where the temperature dependence of the viscosity is not as pronounced as in polymer melts and the vapour pressure of the solvent has to be considered. Therefore continuous tapered nozzles are more relevant for DIW. For centrifugal fibre spinning, the volumetric flow rate has to be limited because the polymer solution often has to present a low viscosity. Therefore in chapter **10** and the Appendix chapter **IV**, straight, non-tapered nozzles have been utilised. In strict terms the Hagen-Poiseuille law in this form only holds for Newtonian liquids, since the viscosity for these liquids is not shear rate dependent. In a capillary or tube however the shear rate is not constant. Nevertheless, the implications drawn from the Hagen-Poiseuille law for the design of printing nozzles stay relevant.

2.4.2 Polymer Synthesis

The synthesis of polymers is the decisive step to obtain the desired properties of the final product. For pure polymers, the important features influencing mechanical, thermal, electrical and chemical properties are the molecular weight distribution (MWD), the tacticity, the chain configuration, the crystallinity, the chain constitution, the polydispersity and the nature and strength of intermolecular forces. With this multitude of relevant parameters, precise control over the whole synthesis is desired. Since the discovery of the first synthetic polymer made from phenolic resin by Leo Baekeland in 1907 [56] many synthesis routes for fabricating thermoplasts, elastomers and thermosets have been discovered and developed. For a clear understanding it is necessary to differentiate the reaction mechanisms of polymers from the technical polymerisation processes. While the fundamental reaction mechanisms are important to understand when trying to influence the polymer's properties, the technical reaction processes are more relevant in the scope of this thesis. Therefore, the reaction mechanisms will only be briefly named, while the following section will discuss the most prominent polymerisation processes relevant

for publications presented in this thesis. While there are distinct differences between the technical polymerisation processes, one type of process can host reactions following different reaction mechanisms.

Polymerisation reactions are generally divided into chain-growth polymerisation and step-growth polymerisation (further divided into polyaddition and polycondensation). Most of the common polymers are made from chain-growth polymerisation, which is typically employed to make thermoplastics like polyethylene, polypropylene, poly(vinyl chloride) and many others. One can differentiate this mechanism from the others by adding individual, small molecules to the active site of a growing chain. This means that there are typically only a few reaction centres depending on the number of initiating moieties. These initiating moieties can be either free radicals, anions, cations or coordination centres like the Ziegler-Natta catalyst [57]. At any point in time, there is a limited number of active reaction sites which leads to characteristically long chain length, no byproducts and fast reaction kinetics.

Another class of polymerisation reactions is the step-growth polymerisation. Instead of only few active sites, the reaction usually consists of two compatible functional groups either divided on two separate monomers or included in the same molecule. This results in a large quantity of parallel reactions leading to many small and slowly growing chains. Only at a high conversion close to 1, a high chain length can be achieved. The fundamental mechanism is shared by both the by-product-free polyaddition reaction (leading to, e.g., polyurethane or epoxy) and the by-product-producing polycondensation (forming for instance polyamide and polyethylene terephthalate).

The formation of elastomers and thermosets can be achieved by cross-linking after the polymerisation or by incorporating more than two functional groups during the step-growth reactions. The step-growth polymerisation mechanism is relevant for chapters **4** and **10**. Polymers made by chain-growth polymerisation are utilised in chapters **3** and **10** and in the Appendix chapters **IV** and **IV**.

The control over technical parameters during synthesis is essential to obtain the aforementioned qualities of the final product. This is especially true, since polymers are made in large scale processing producing several tons of product per batch. To ensure a stable quality in each batch and between individual batches and gain more control over, e.g., the MWD, different approaches have been developed. These will be briefly presented in the following to provide some insight into the advantages and disadvantages of the individual processes.

Bulk polymerisation

Historically, the process of bulk polymerisation is the oldest developed polymerisation technique. All of the educts are mixed together without additional solvents and the polymerisation is triggered. During the reaction the molecular weight and the viscosity increase. The advantages of this process partially lie in its simplicity. Because only educts are involved in the reaction, the interactions between monomers, initiators and growing polymers can be described more easily. Additionally, the obtained product is

very pure. Naturally, these systems can still be complicated. This becomes clear in chapter 4 where immiscible monomers lead to undesired phase separation and common emulsifiers cannot be used. A novel process based on solid-state emulsifiers made from crushed tetrapodal ZnO microcrystals is presented to account for this problem. For the production of injection moulded parts by reactive extrusion bulk polymerisation is very favourable, since the product is very clean and no additional cleaning or evaporation step is required. Bulk polymerisation is often used for step-growth reactions which are typically much slower than chain-growth reactions. The disadvantages of this process are obvious for chain-growth reactions. Because of the high heat released during the rapid reaction, large batches of polymer cannot be produced by this method. The heat conduction of the monomer-polymer mixture is not sufficient if amounts >1 litre should be produced. The reaction heat ultimately leads to boiling and decomposition of the monomers and polymers and the reaction is not easy to control. Especially at a high conversion when the molecular weight is already high, the solution becomes viscous, heat cannot be dissipated by convection and the reaction locally speeds up considerably. This effect is called autoacceleration, gel effect or the Trommsdorff-Norrish effect. There exist relevant applications where bulk polymerisation is the most reasonable polymerisation process like adhesives and reactive injection moulding of large parts.

Dispersion polymerisation

For the dissipation of reaction heat, liquid monomers are typically dispersed in a liquid phase, e.g., in water. If the two liquids are immiscible, droplets of monomer form in the water phase and monomer-soluble initiators can be added to the batch. These diffuse through the solvent into the monomer droplet and the reaction can occur locally inside these spheres. The heat that develops during the reaction is dissipated by the solvent phase and the viscosity does not change during conversion. Therefore, the autoacceleration cannot occur and more control over the reaction process is possible. Additionally, the constant viscosity enables an easier flow-processing instead of batch processing, facilitating continuous polymer production. By this method it is also possible to create nearly monodisperse polymer nano- and microbeads. The disadvantage is that the final polymer always contains a certain amount of solvent which may be undesirable for applications with a high purity requirement like vacuum technology or healthcare products.

Emulsion polymerisation

Emulsion polymerisation shares many of its benefits with dispersion polymerisation compared to bulk polymerisation. On top of the processing control, emulsion polymerisation contains a surfactant which hinders coalescence of the monomer particles. Therefore the MWD can be easily controlled and high molecular weight polymers can be obtained in a short time. The final product will be contaminated with solvent and with surfactants. This is the most common way to obtain polymers with high molecular weight ($>50,000$) [58].

The main distinction between these polymerisation techniques is the important background for chapters **4** and **10**.

Part II

Publications

Chapter 3

Perfect polymer interlocking by spherical particles: capillary force shapes hierarchical composite undercuts

Polymers exhibit a wide range of physical and chemical properties and often complementary properties are needed. Combining two polymers to take advantage of beneficial bulk and surface properties of the respective materials can be very challenging. Adhesion between complementary or to low surface energy polymers is a major task, since normal types of bonding may not be possible. Mechanical interlocking on the micro- and nano-scale is a relatively new approach for adhesion of complementary materials. This work shows how capillary-induced self-organisation of undercuts on the polar high-strength polymer **polyether ether ketone** (PEEK) can be used to form a strong bond to the low surface energy polymer **poly dimethyl siloxane** (PDMS). Different structuring architectures are achieved by using more than one size of particles, i.e., ZnO nanoparticles and Al microparticles. More hierarchical structuring leads to the highest bond strength between PDMS and PEEK, around 5.7 times higher than the unstructured surface. SEM and EDX investigations showed that the elastic PDMS can demold itself from non-hierarchical undercuts. On the other side cohesive failure at the PDMS occurred for hierarchical interlocking sites. Key aspects of the self-organisation process and the mechanical interlocking of soft polymers are discussed in detail. The composite between PEEK on the inside and PDMS on the outside can be used as rigid, yet blood-repelling heart valves. Blood adhesion tests on smooth PDMS show the lowest blood platelet adhesion when compared to standard heart valve materials like diamond-like carbon (DLC), titanium and titanium nitride. Due to the ubiquity of the approach and the facility of the manufacturing step, this adhesion technique can be transferred to many other complementary polymer systems.

The results have been published in the journal "Nanoscale Horizons".

Own contribution presented in this article

- Surface structuring process development, optimisation and sample preparation
- Characterisation of the structural properties by means of SEM
- Characterisation of the mechanical properties

- Data analysis
- Discussion and interpretation
- Writing and editing the Manuscript

The following content in this chapter is reproduced with permission.



Cite this: *Nanoscale Horiz.*, 2019, 4, 947

Received 12th February 2019,
Accepted 27th February 2019

DOI: 10.1039/c9nh00083f

rsc.li/nanoscale-horizons

Perfect polymer interlocking by spherical particles: capillary force shapes hierarchical composite undercuts†

Leonard Siebert,^a Tim Schaller,^b Fabian Schütt,^a Sören Kaps,^a Jürgen Carstensen,^a Sindu Shree,^a Jörg Bahr,^a Yogendra Kumar Mishra,^a Hans-Hinrich Sievers^b and Rainer Adelung^{*a}

Polymers often do not provide all necessary properties for certain applications. In this case polymer composites can be used to combine beneficial qualities of each single component. In many cases, especially for surface–bulk-composites, adhesion is an issue because polymers with complementary properties are necessary. If the chemical binding of the pristine polymers does not allow for good adhesion, advanced strategies have to be employed which most of the time lead to chemical alteration of the surface, its destruction or else low adhesion. While roughening of the surface leads to an increase in the interface area, it will not provide a stable bond, if the adhesion between the two polymers is low in the first place. By selforganized introduction of special undercuts onto one of the polymer surfaces and by applying the second polymer in a liquid form, a mechanical interlocking composite can be achieved. In these composites adhesion can be so strong that only cohesive failure in one of the polymers will occur. In this work we evaluated simple fabrication techniques for the design of simple and complex undercuts and the adhesion between the exemplary composite PEEK and PDMS. We find that by utilizing the capillary effect, spherical standard particles can be used to create a surface structure for mechanical interlocking. Additionally, we obtain a 5.6 times higher adhesion between PEEK and PDMS. We come to the conclusion that a multi-scale undercut is necessary to obtain a strong adhesion between soft polymers like PDMS and stiff polymers like PEEK by looking at the detachment mechanism for these different undercut systems. Lastly, the composite is evaluated by blood contact tests to verify the intactness of the blood repellent effects of the PDMS layer.

Conceptual insights

Polymer composites can be used to realize a combination of the special individual features of polymers, e.g. low adhesion of PDMS and high mechanical strength of PEEK. Especially in laminate like composites, a good adhesion between the polymers is important. Modifications of the interface chemistry might lead to undesired alteration of the surfaces in touch, their destruction or else low adhesion. Micro and nano scale mechanical interlocking is an effective alternative only if hook like undercut structures can be provided. However, the notched shape of interlocking particles complicates the fabrication and embedding process. Counter-intuitively, the presented strategy is based on simple spherical particles self-organizing into hook like undercuts on the polymer surface by capillary action. By applying the second, liquefied polymer on top, a mechanical interlocking composite laminates where perfect adhesion is provided, i.e. only cohesive failure will occur as failing mechanism. Thus, we obtain 5.6 times higher adhesion strength for exemplary PDMS/PEEK composites and conclude that hierarchical undercuts are necessary to obtain strongest adhesion. Lastly, the composite is evaluated by blood contact tests to verify that the blood repellent feature of the PDMS layer is still intact while the laminate exhibits the mechanical strength of PEEK.

Introduction

Multi-polymer based composite materials are key components in several state-of-art technological applications because of their simultaneously accessible cumulative properties.¹ Individual properties of different polymers play very unique roles and hence it becomes necessary to combine several polymers together in an appropriate composite form, often a requirement for many applications.² For general applications polymers based composites come in the form of interpenetrating phase composites but in some specific applications,³ the polymer layers are often adhered together using various bonding methods.^{4–6} In many cases the adhesion of the desired polymers is difficult, simply because materials with complementary properties are used.⁷ If the pristine chemical bonds do not allow for good adhesion, techniques like plasma treatment,^{8,9} ion beam treatment,¹⁰ chemical etching¹¹ or chemical grafting¹² are applied to form

^a Functional Nanomaterials, Institute for Materials Science, Kiel University, Kaiserstr. 2, D-24143, Kiel, Germany. E-mail: lesi@tf.uni-kiel.de, ykm@tf.uni-kiel.de, ra@tf.uni-kiel.de

^b Department of Cardiac and Thoracic Vascular Surgery, University of Lübeck, Ratzeburger Allee 160, D-23538, Lübeck, Germany

† Electronic supplementary information (ESI) available. See DOI: 10.1039/c9nh00083f

Communication

View Article Online
Nanoscale Horizons

reactive bonds. Although these processes are often accompanied by a reorganization¹³ or a serious chemical alteration¹⁴ of the polymer surface, the adhesion strength may still be limited to values one order of magnitude below the cohesive strength of the weakest composite partner.¹⁵

Additionally, the storage time after the surface treatment prior to the adhesion step is limited for most common practices such as plasma modification. In these cases the treated surfaces revert back to their pristine states because reactive groups react with the environment or the reactive bonds diffuse into the bulk and thus the adhesion lowers again.^{16,17} Purely mechanical surface treatments (e.g. grinding, grit-blasting) are standard methods to increase the adhesion without changing the chemical nature of the polymers by only increasing the interfacial area or additionally producing undercuts.^{9,18}

While the increase in the surface area just enhances the adhesion by providing more bonding sites (larger contact area), an undercut structure allows for mechanical interlocking¹⁹ thus replacing the adhesive bonding strength between the polymers by the cohesive bonding strength of the individual polymers. This process makes the adhesion independent of chemistry and the quality of the interlocking structures is the decisive factor for the strength of the interface.²⁰

Complex shaped nanostructures have been used by Jin *et al.*, where zinc oxide tetrapods (ZnO-T) were utilized to join the Teflon (PTFE) and silicone (PDMS) together which do not adhere directly because of their very low surface energies.²⁰ The interlocking mechanism was investigated and it has been reported that the 3D complex shape indeed plays a very important role. Using a tetrapods based interlocking approach, a peel strength of around 2 N cm⁻¹ between PTFE and PDMS layers was reported, however for certain applications, an even higher adhesion is needed. In this study no cohesive failure was found, meaning a further improvement of the core idea might raise the adhesion even further. Additionally, the necessity of complex shaped particles limits the practicability.

Here we demonstrate a simple fabrication procedure for complex shaped surfaces to promote the adhesion of two typically non-adhering materials. We utilize standard spherical nano and micro particles without any intrinsic possibility for polymer/particle undercut formation by using the capillary effect. We also assess what makes a good undercut structure by the example of joining PDMS, a low surface energy, chemically inert and soft polymer to PEEK, a high strength, high temperature, chemically inert polymer and show that hierarchical undercuts on multiple length scales are most efficient adhesion promoters allowing for only cohesive failure of the individual polymer and therefore giving the strongest possible adhesion. Different fabrication approaches and different detachment mechanisms are evaluated to obtain insight into the most promising type of undercuts and surface modifications.

For the given composite additional platelet adhesion tests have been carried out on differently prepared PDMS surfaces in order to check the hemocompatibility of the as prepared polymer composites. The results indicate that a perfectly flat silicone surface can achieve the highest blood adhesion resistances while

still keeping the hemocompatibility of pristine PDMS. This indicates the viability of the utilized fabrication methods with respect to an application as biomedical implants.

Particle interlocking approach

The model for the fabrication of a surface with interlocking sites on multiple scales is depicted in Fig. 1. In the first step the polar polymer substrate is coated with a dry powder mixture of particles. The mixture can consist of more than one different particle type (e.g. ceramic, metal) of two different sizes, preferably polar nanoparticles of 100 nm and smaller and a micron sized particle type. The layer thickness ranges from 100 μm to 500 μm and contains particle agglomerates, where the particle-particle distance is smaller than in the surrounding powder. After coating the surface with a particle layer, different regimes of varying density are present due to these agglomerates (Fig. 1a). This particle film is then heated (e.g. 500–600 °C for PEEK) from the top in order to melt the polar polymer beneath.

Dipole-(induced) dipole interactions between the polar particles and the polar polymer lead to a combination of Keesom and Debye attractive forces between these two components. Molten polymer is thereby flowing into the particle network above, preferentially into the particle agglomerates in which the medium distance between the particles is lower than in other places.

More generally, the agglomerated powder layer can be assumed as the series of dimensionally distributed interconnected capillaries. A regime of higher packing density can be regarded as a network of capillaries with low diameter, whereas the surrounding powder can be regarded as a network of high diameter capillaries. According to the laws for capillary action, sufficient wetting of the particles by the polymer is primarily given through a low contact angle of $\theta < 90^\circ$. Additionally, the surface energy γ of polymers at the liquid-air interface is usually high, reducing the tendency to wet capillaries where the particle-particle-distance is too high. The wetting becomes energetically more favorable however, when the area of the polymer-gas interface is reduced. Thus, the energy barrier E_w for an agglomerate to be wetted completely scales with the medium particle distance squared:

$$E_w \propto r^2$$

Only if the microscopic particle-particle-distance is low enough, a sufficient capillary force can be generated, enabling the molten polymer to flow easily. Thus, the denser packed agglomerates are wetted by the polymer (Fig. 1b), which leads to the formation of pillars of particle-polymer composite. Due to the different sizes of the particles and the selective embedding process, a hierarchical roughness with many polymer/particle composite undercuts is produced (Fig. 1c). The heat source is removed and the polymer cools down, solidifying the particle-polymer pillars and the surrounding polymer. The particle sites which could not draw up the polymer or are only partially-embedded are rinsed away by thorough brushing under running water.

A surface of randomly distributed, self-organized interlocking sites is obtained at the polymer surface. When another liquefied polymer is coated onto this surface, these interlocking sites will

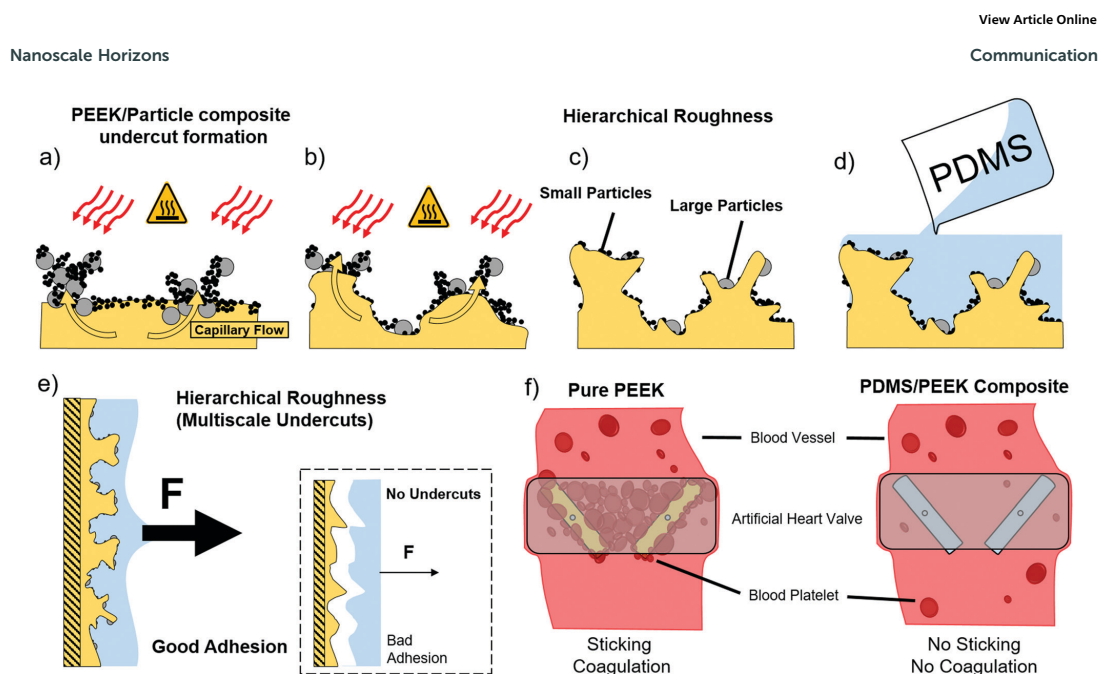


Fig. 1 Surface sculptured PEEK–ZnO composites and general working principle of the fabrication steps: (a and b) Coating of particles with regimes of different density on the surface and heat treatment to melt the underlying PEEK surface. Self-organized formation of undercut structures by capillary effect. (c) Formation of hierarchical undercuts with two different particle sizes. (d) Coating with PDMS, which multiscale interlocking sites into the undercut structures. (e) Increased adhesion by the interlocking of PDMS onto the surface undercuts, the inset shows the lower adhesion of normally roughened surfaces to PDMS, (f) decreased platelet adhesion on novel composite material in comparison to pristine PEEK in vascular implants (e.g. heart valve leaflets).

be covered completely (Fig. 1c), so that only the surface of the composite consists of the second polymer. By solidifying the second polymer a mechanical interlocking between the two polymers is achieved, creating a strong polymer composite sandwich structure.

Since the substrate polymer shows many undercuts on multiple length scales a much stronger adhesion (e.g., here shown 5.6 times stronger adhesion between PDMS and PEEK) than a surface roughened by standard techniques can be expected (inset Fig. 1e). Pulling forces can be distributed much better around the inner walls of a hierarchical undercut than on a flat surface.

By employing this novel concept we fabricated and analyzed a composite of polyether ether ketone (PEEK, a high strength, high temperature thermoplastic) and polydimethylsiloxane (PDMS, a low surface energy elastomer). The properties of both are respectively utilized in a manifold of applications such as surgical implants and many others.

Results and discussions

The adhesive properties of the fabricated composites were evaluated in terms of the three different heating approaches (described briefly in Experimental section, ESI†). Fig. 2 shows the three representative curves, one for each treatment, where the inset shows the testing geometry with the two aluminum rods and the PDMS coated PEEK samples in between them. The control

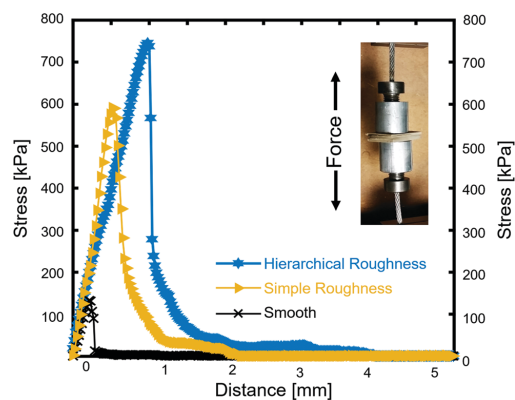


Fig. 2 Adhesive strength results for differently treated PEEK surfaces. The stress–distance–curve for differently structures samples. The values achieved for different roughness complexities are shown as well as a photograph of the testing setup.

sample was a pristine PEEK sample coated with around 1 mm of PDMS. The black curve in Fig. 2 shows the stress–distance–diagram for this sample, where the maximum adhesive strength is 133 kPa. The curve has a linear regime corresponding to the elastic deformation of the PDMS and a steep drop after the maximum

Communication

View Article Online
Nanoscale Horizons

indicating a sudden detachment from the PEEK. PDMS was only found on one side of the sandwiched sample, meaning the failure mechanism is adhesive and not cohesive. In comparison, the yellow curve representing a sample which was structured with ZnO nanoparticles only. These particles have been chosen to be big enough to rule out the reinforcement mechanisms of very small nanoparticles. The structured sample shows a factor of 4.5 stronger adhesive strength with a value of 592 kPa. Apart from the increase in adhesive strength, the curve has the same shape as the untreated sample, with a linear elastic range and a sudden decline after the maximum value. Also the failure is adhesive, since only one side of the sample was covered with PDMS, while the other side showed the structured surface. The blue curve represents a surface structured by the Al-ZnO-mixture, with a maximum adhesive strength of 745 kPa, 5.6 times the value of the unstructured sample. While the curve's shape is the same, both parts of the sandwiched sample exhibited PDMS and some parts are even covered in the same area of the sample indicating that the failure mechanism is cohesive. The shape of the curve is important, since it represents a homogeneous structuring of the surface. Inhomogeneously structured samples would exhibit parts of higher and parts of lower adhesive strength and would therefore show additional plateaus in the linear ranges, meaning that some parts of the sample already detached while others remain intact. The absence of these plateaus hints about a uniform surface with all three types of samples. The approach to sandwich the samples works well, since the adhesion test can only affect the weakest parts of the interface between PDMS and PEEK. Cohesive failure is only possible, where the PDMS is strongly attached on both sides. For elastic materials such as PDMS the mechanical adhesion is typically low, because of their ability to change the shape when stress is applied.

Understanding the involved rupture mechanisms is of key-importance for transferring the structuring approach to other polymers. The differences in the ultimate bonding strength as a result of the surface treatments is directly related to the complexity of the surface structuring. The detachment mechanisms as well as the structure's corresponding scanning electron microscopy (SEM) images are shown in Fig. 3. An unstructured sample is smooth and the attachment works by van-der-Waals bonds, hydrogen bonds and other dipole-dipole interaction. Because of the non-polar nature of PDMS it only exhibits van-der-Waals bonding which is very weak and the smooth interface can therefore easily detach (Fig. 3a). The ZnO structured sample however exhibits undercuts in the size regime of the ZnO (a few hundred nanometers) (Fig. 3b) as well as the micropillars formed by the mechanism explained in the Experimental section (ESI[†]). The small undercuts are not sufficient to hold the PDMS in place and the larger structures only rarely exhibit larger undercuts lowering the adhesion of the PDMS compared to the ideal case. EDX of detached PDMS confirmed that some zinc oxide nanoparticles were embedded by the PDMS and came off of the PEEK surface during the pull-off test (Fig. S2, ESI[†]). This process is usually expected when roundish particles are placed at an interface. A spherical particle cannot provide undercuts to both sides and the detachment of one side from the particles is due to the lack of chemical bonding (compare Fig. S2 and S3, ESI[†]).

In contrast to that, the Al-ZnO structured sample however exhibited many undercuts on multiple length scales and even showed remaining PDMS in these areas, which failed cohesively (Fig. 3c). Due to the hierarchical roughness of the sample and its complexity, necking of the PDMS is not immediately accompanied by a detachment since the force is distributed among many attachment centers inside the big undercut. With only one undercut length scale, the PDMS at the undercut would show necking

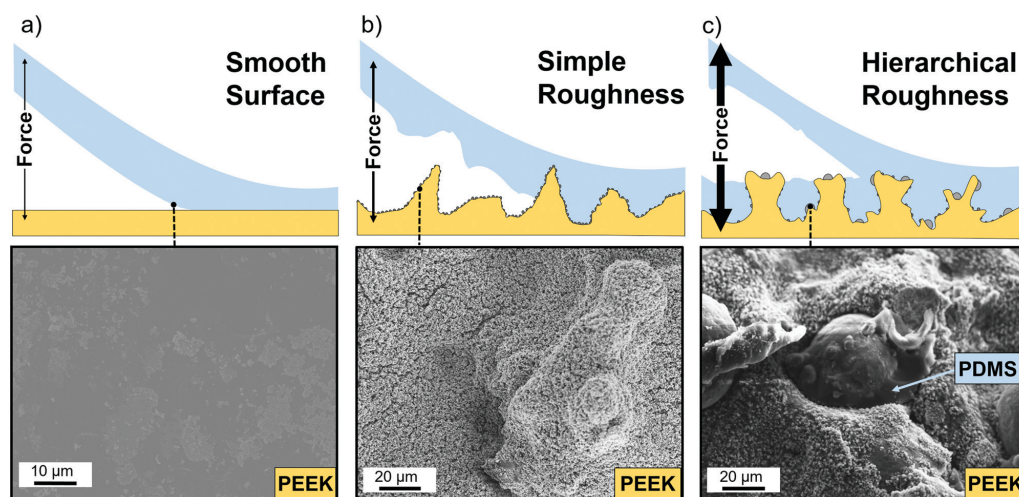


Fig. 3 Different adhesive failure mechanisms and respective SEM images after the pull-off. (a) is an unstructured PEEK surface after adhesive testing. In (b) the simple, roughly structured PEEK surface as produced by only ZnO particles is shown. In (c) the remains of ruptured PDMS around an Al particle can be seen on the complex, rough surface of the PEEK which was structured by using Al and ZnO particles.

Nanoscale Horizons

and therefore shrink, which would make a detachment inside the undercut easy. When compared to the approach by Jin *et al.*, where complex shaped linkers were used, a significant increase in the adhesive strength can be seen by the fact that cohesive failure occurred. In the former study an increased adhesion but no cohesive failure was found, indicating that the hierarchical roughness is indeed a very important feature of a mechanical interlock structure.

Since not all of the polymer has failed cohesively, however, there is potential for optimization. The undercuts have to be distributed over the whole interface, where the two polymers are supposed to be in contact. The principles investigated here therefore have to be transferred to larger area treatments. Understanding the underlying phenomena of wetting and adhesion leads to a better design of the polymer–polymer interface with respect to the nature of the undercuts. The simplicity of the approach and the manifold of particles available ensure versatile applications of the concept, not requiring difficult or expensive experimental setups but only basic equipment and chemicals.

Contact angle measurements have been performed on PEEK/PDMS samples with different coating thicknesses of PDMS (Fig. S4, ESI[†]). Structured PEEK without PDMS showed a contact angle of 0°, indicating superhydrophilic behavior. When a diluted PDMS solution was used, the contact angle showed to be superhydrophobic (> 120°) even after just one coating step. With a higher concentration of PDMS solution (1:5 parts by PDMS/thinner fluid by weights) a thicker coating of PDMS can be observed and the contact angle decreases to the pristine contact angle of PDMS of 105°. This means that the contact angle can be tailored to meet the specific application. For the blood contact tests, thickly coated PDMS/PEEK composites were used.

To show the unaltered properties of the PDMS layer on top, blood contact tests have been carried out on samples prepared with two different coating techniques. The fabrication of the coating allowed for different surface architectures, resulting on the one hand in a smooth surface, on the other hand in a crack containing surface (Fig. 4). Both of the surfaces have been tested with human blood and revealed different platelet adhesion behaviors. On average the crack containing surface has 311.4 single thrombocytes cells, 1.6 small cell heaps and 1.8 big cell heaps. Six visual fields had so many cells in more than one layer and without a clear boundary so that the number of cells could not be counted. On average the smooth surface showed 27.8 single cells, 1.3 small and 0.5 big cell heaps, indicating that the thrombogenic activity was severely reduced.

When compared with literature values in Fig. 4, the smooth PDMS surface showed the lowest platelet adhesion, even relative to other promising materials, such as diamond-like carbon (DLC). This can be readily seen in the inset of the SEM images taken of this surface after the blood contact test. On the other hand, the high number of attached cells on the cracked surface is clearly related to the introduction of anchor points for the cells by these crevices. These results are directly linked to Park *et al.* where polished titanium showed highly reduced platelet adhesion compared to normal sandpaper abraded surfaces.²² The cracks on the surface are most likely due to shrinkage upon thinner evaporation

View Article Online

Communication

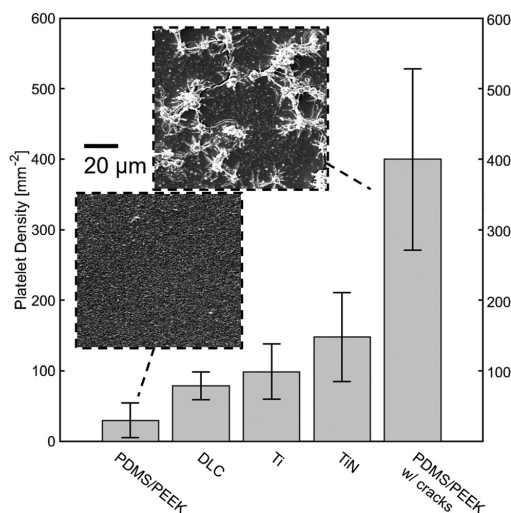


Fig. 4 Adhered platelets over several surfaces from the present work. The values for smooth PDMS are the lowest, even compared to diamond-like carbon (DLC). Titanium (Ti) and titanium nitride (TiN) showed an increased platelet adhesion, but the PDMS surface with cracks shows the highest number of adhered platelets. The insets show the SEM images for the smooth and the cracked PDMS, respectively. The very large number of blood platelets can be seen for the cracked PDMS surface.

and resulting material stresses. It is also not to rule out that the zinc oxide tetrapods in the smooth sample have an influence on the adhesion behavior. Hölken *et al.* could show a reduced biofouling activity when incorporating tetrapodal zinc oxide into polythiourethanes.^{23,24} Both of these possibilities open up a window for further investigations. Although there are more effective ways to treat the PDMS for reduced platelet adhesion (*e.g.* by grafting PEG to its surface), the results show the preservation of the inertness of the PDMS towards biological materials as well as the increase in adhesion.

Conclusions

In summary, we report on a heightening of the bond strength between the low surface energy polymer PDMS to the high strength polymer PEEK by a factor of 5.6 times by utilizing mechanical interlocking at the polymer–polymer interface. It could be shown that an increase in adhesive strength is achieved by forming undercut structures with additional hierarchical roughness. Undercuts like these can be formed and tuned through various methods proposed here and can even be influenced by considering particle architecture and surface design. Three simple structuring methods have been proposed and tested in order to verify the quality of the treatments. Additional effort has been made to confirm the strong influence of thin coatings of PDMS on the PEEK by contact angle measurements resulting in hydrophobic surfaces of formerly ultrahydrophilic structures. Both SEM and EDX have been utilized to investigate the surface and obtain a

View Article Online

Nanoscale Horizons

Communication

fundamental understanding of the underlying rupture mechanisms found through pull-off testing. Further effort can be made by employing different ways of heating the PEEK surface (e.g. microwave or laser treatment) to obtain an infiltration of PEEK into the particle sponge on its surface. Also a larger variety of particles on multiple length scales might result in even better structuring of the surface.

Author contributions

LS, TS, H-HS and RA identified the idea and planned the study. LS, SS and FS synthesized and analyzed the materials. LS and FS carried out studies. LS, SS and SK performed adhesion tests. TS and H-HS performed blood contact tests. LS, YKM, FS, JC, JB and RA analyzed the data and wrote the paper with contributions from other authors.

Conflicts of interest

There are no conflicts to declare.

Acknowledgements

R. A. gratefully acknowledges partial project funding by the Deutsche Forschungsgemeinschaft (DFG) under the grant number AD183/18-1 as well as parts of the Research Training Group "Materials for Brain" (GRK 2154). Additionally, H.-H. S. gratefully acknowledges project funding by the German Federal Ministry of Education and Research under the grant number 13GW055B.

References

- 1 S. Ramakrishna, J. Mayer, E. Wintermantel and K. W. Leong, *Compos. Sci. Technol.*, 2001, **61**, 1189.
- 2 K. G. Budinski and M. K. Budinski, *Engineering materials: properties and selection*, Pearson Education, New Jersey, 2010.
- 3 D. R. Paul and J. W. Barlow, in *Multiphase polymers*, ed. S. L. Cooper, American Chemical Society, Washington, DC, 1979, vol. 176, p. 315.
- 4 A. Wilson, I. Jones, F. Salamat-Zadeh and J. F. Watts, *Int. J. Adhes. Adhes.*, 2015, **62**, 69.
- 5 E. T. Kang, K. L. Tan, K. Kato, Y. Uyama and Y. Ikada, *Macromolecules*, 1996, **29**, 6872.
- 6 V. Sunkara, D.-K. Park, H. Hwang, R. Chantiwas, S. A. Soper and Y.-K. Cho, *Lab Chip*, 2011, **11**, 962.
- 7 J. Y. Lai, Y. Y. Lin, Y. L. Denq, S. S. Shyu and J. K. Chen, *J. Adhes. Sci. Technol.*, 1996, **10**, 231.
- 8 M. J. Owen and P. J. Smith, *J. Adhes. Sci. Technol.*, 1994, **8**, 1063.
- 9 S. I. Moon and J. Jang, *J. Mater. Sci.*, 1999, **34**, 4219.
- 10 Y. Suzuki, *Nucl. Instrum. Methods Phys. Res., Sect. B*, 2003, **206**, 501.
- 11 S. R. Kim, *J. Appl. Polym. Sci.*, 2000, **77**, 1913.
- 12 K. Kato, *Prog. Polym. Sci.*, 2003, **28**, 209.
- 13 T. Venkatesan, *Nucl. Instrum. Methods Phys. Res., Sect. B*, 1985, **7-8**, 461.
- 14 L. S. Penn and H. Wang, *Polym. Adv. Technol.*, 1994, **5**, 809.
- 15 P. Rezai, P. R. Selvaganapathy and G. R. Wohl, *J. Micromech. Microeng.*, 2011, **21**, 65024.
- 16 F. Awaja, M. Gilbert, G. Kelly, B. Fox and P. J. Pigram, *Prog. Polym. Sci.*, 2009, **34**, 948.
- 17 M. Morra, E. Occhiello, R. Marola, F. Garbassi, P. Humphrey and D. Johnson, *J. Colloid Interface Sci.*, 1990, **137**, 11.
- 18 W.-S. Kim, I.-H. Yun, J.-J. Lee and H.-T. Jung, *Int. J. Adhes. Adhes.*, 2010, **30**, 408.
- 19 M. Baytekin-Gerngross, M. D. Gerngross, J. Carstensen and R. Adelung, *Nanoscale Horiz.*, 2016, **1**, 467.
- 20 X. Jin, J. Strueben, L. Heepe, A. Kovalev, Y. K. Mishra, R. Adelung, S. N. Gorb and A. Staubitz, *Adv. Mater.*, 2012, **24**, 5676.
- 21 B. Ruben, M. Elisa, L. Leandro, M. Victor, G. Gloria, S. Marina, S. Mian, K. R. Pandiyan and L. Nadhira, *Micro Nano Lett.*, 2017, **12**, 754.
- 22 J. Y. Park, C. H. Gemmel and J. E. Davies, *Biomaterials*, 2001, **22**, 2671.
- 23 I. Hölken, M. Hoppe, Y. K. Mishra, S. N. Gorb, R. Adelung and M. J. Baum, *Phys. Chem. Chem. Phys.*, 2016, **18**, 7114.
- 24 Y. K. Mishra, S. Kaps, A. Schuchardt, I. Paulowicz, X. Jin, D. Gedamu, S. Freitag, M. Claus, S. Wille, A. Kovalev, S. N. Gorb and R. Adelung, *Part. Part. Syst. Charact.*, 2013, **30**, 775.

Electronic Supplementary Material (ESI) for Nanoscale Horizons.
This journal is © The Royal Society of Chemistry 2019

Electronic Supporting Information

Perfect polymer interlocking by spherical particles: capillary force shapes hierarchical composite undercuts

By Leonard Siebert,^{a} Tim Schaller,^b Fabian Schütt,^a Sören Kaps,^a Jürgen Carstensen,^a Sindu Shree,^a Jörg Bahr,^a Yogendra Kumar Mishra,^{a*} Hans-Hinrich Sievers,^b Rainer Adelung^{a*}*

^aFunctional Nanomaterials, Institute for Materials Science, Kiel University, Kaiserstr. 2, D-24143, Kiel, Germany.

E-mail: lesi@tf.uni-kiel.de, ykm@tf.uni-kiel.de, ra@tf.uni-kiel.de

^bDepartment of Cardiac and Thoracic Vascular Surgery, University of Lübeck, Ratzeburger Allee 160, D-23538, Lübeck, dGermany.

Keywords: Mechanical interlocking, biocompatible, low surface energy polymer, high tensile strength polymer, biocomposites.

Experimental

Materials

ZnO nanoparticles with a medium size of 100 nm were purchased from Sigma Aldrich (CAS number 1314-13-2). Zinc oxide tetrapods were obtained by employing the newly developed flame transport synthesis by Mishra et al. Victrex® PEEK 450G sheets of 5 mm thickness were purchased from RS Components GmbH and cut into small chips of 20 x 20 mm and about 2.5 mm thickness. PEEK has a melting point of 343 °C, has a decomposition onset temperature of 575 °C and a tensile strength of 98 MPa. For the blood contact test another PEEK was used (PEEK-OPTIMA, Invibio Inc., West Conshohocken, USA) because of its medical approval. The two-component PDMS elastomer Sylgard 184 by Dow Corning consists of a basis polymer and a cross linker. The given mixing ratio in weight parts is 10:1 and the cured PDMS has a tensile strength of 6.7 MPa. For the contact angle measurements, the solution was thinned down in order to produce very thin layers of PDMS by drop casting and check for a homogenous coating. The thinner used for the silicone elastomer is Q7-9180 Silicone Fluid 1 CST also purchased from Dow Corning. The thinned PDMS had a m/m mixing ratio of 1:50 PDMS elastomer to thinning fluid.

Energy Dispersive X-ray Spectroscopy

The morphology of the surface both before and after coating with PDMS and pulling off have been investigated using a scanning electron microscope (SEM) Carl Zeiss (7 kV, 10 µA). The analysis of the composition of the surface sculptures have been carried out by energy-dispersive X-ray microanalysis (EDX) equipped to the SEM. Chemical analyses by EDX were performed with a Si/Li detector (Noran, Vantage System).

Sample preparation

For adhesion testing of the sculptured PEEK surface, three distinctly different treatments of the samples were applied. As a control untreated PEEK samples were cleaned and cut. To test the impact of a multiscale undercut formation two variations of the particle powder were considered. Firstly, only ZnO nanoparticles were used. Secondly, a treatment was done with a 2:1 weight ratio mixture of ZnO and Al microparticles to provide a second length scale as well as better heat conductivity.

Both powders were applied to the smooth PEEK surface and pressed to form a semi-solid layer of approximately 200 µm thickness. The thickness varied around 100 µm for each sample and depending on the thickness, the duration of the experiment was changed. This particle layer is heated to temperatures above the melting temperature of PEEK, depending on the thickness and the heat conductivity of the samples. PEEK is a very stable polymer and can easily withstand temperatures of 600 °C and above. The temperature is applied via a brass heat element with a diameter of 16 mm and thermal insulation to make manual handling feasible. For pure ZnO powder films temperatures of up to 600 °C were necessary to significantly melt the surface. Due to the heat conductivity of aluminum the temperature for structuring the Al-ZnO-system could be reduced to 450 °C. The heating process can take somewhere between 2-10 seconds, again depending on the thickness of the particle layer and its composition. The melting of the PEEK is clearly visible and was always used as an indicator for the end of the experiment. After sculpturing the remaining, non-embedded micro particles are brushed off with a standard cleaning brush under running water and dried at room temperature.

Adhesion Tests

The area used for the adhesion strength calculation was the overlap area between two PEEK platelets of a maximum size of 2 by 2 cm. Any PDMS which is not covered by PEEK on either side is not taken into consideration. The PEEK plates have then been pressed onto a hot aluminum rod, where they melt and form a strong bond to the rod's surface. The stamps have a length of 25 mm and steel cables attached at the back which have a thickness of 3 mm and eliminate tilting forces. These prepared samples are then structured with one of the sculpturing methods stated above. Before applying the PDMS on the structured surface, the two components are mixed together and degassed to remove all the air bubbles, which would reduce the tensile strength of the PDMS film and thus decrease the adhesion to the sculptured PEEK surface. After mixing and degassing both sides of the respectively sculptured samples were covered with a thin layer of prepolymer and pressed together. Kept in this state they were stored at 80°C for 24 hours to ensure complete polymerization of the PDMS. After the hardening of the PDMS the samples were cooled down to ambient temperature. For the mechanical testing a self-built tensile

testing machine has been used with a maximum force of 500 N. The pulling speed has been set to 0.1 mm/s and the samples have been pulled until fracture. The position over the measured force has been recorded and normalized on the least adhesive area between two samples.

Contact Angle Measurement

To qualify a homogenous coating with very thin layers of PDMS, Al-ZnO-structured samples were coated with only a very thin layer of PDMS by using two differently diluted solutions (one part by weight of curing agent has been mixed with 10 parts of base polymer and further diluted with 5 or 50 parts of thinning fluid respectively) A few droplets of this solution were put onto a sculptured PEEK sample, treated with a 1:1 mixture by weight parts of ZnO and Al. The samples P1-P8 were treated multiple times with the 1:50 PDMS/thinner fluid solution and the samples P9-P11 were treated with 1:5 PDMS/thinner fluid solution. Each treatment consisted of multiple coatings, increasing with the sample number and starting from 1 coating step again for the samples P9-P11. After each treatment the samples were stored in an oven at 80 °C. After the final treatment the sample rested for 24 hours in the oven at 80 °C. The samples P9-P11 showed a thick layer of PDMS after coating, whereas the samples P1-P8 showed no change in appearance after the treatment. The samples were then put into a self-built contact angle machine. A droplet of 50 µL was dispensed on the surface of the samples and multiple images were taken from the side and the angle at the interface between droplet and substrate was measured.

Blood Contact Tests Sample Preparation

For evaluation of the blood adhesion, two sample types have been fabricated. The first sample type is a BAS PEEK sample with a 2 mm thick PDMS coating. The coating also contained 5 w.-% tetrapodal zinc oxide produced by the previously introduced flame transport synthesis^[24] to increase the stiffness of the PDMS layer. The top of the sample was covered by a glass slide, to ensure the smoothness of the resulting surface and put into a furnace for 24 h at 80 °C. The second sample was prepared using the previously mentioned silicone thinner in a thinning ratio of 1:50 by weights. The coating was applied by wetting the surface three times and letting it dry after each iteration for one hour at 80 °C.

The silicone was coated on the small medically approved PEEK plates. Before the blood contact tests, all samples were cleaned in an ultrasonic bath in acetone (Carl Roth GmbH + Co. KG, Karlsruhe, Germany), ethanol (70 % denatured, Carl Roth GmbH + Co. KG, Karlsruhe, Germany) and distilled water for 5 minutes each. The samples were fixed in a PTFE tank (4.5 cm diameter, 6 cm height, 95.4 cm³).

The blood was stored in blood collection tubes with heparin (S-Monovette 4.9 ml, Lithium-Heparin, Sarstedt AG & Co. KG, Nümbrecht, Germany). Test medium was human blood, donated by healthy and drug free volunteers in the age of 27 to 55 years. 50 ml blood from one donor was filled into the tank and covered the samples. The tank was placed on a magnetic mixer (M22/1, Franz Morat GmbH & Co. KG, Eisenbach, Germany) with an integrated heating function to ensure a constant temperature of 37 °C. For 5 minutes a mixing speed of 511 mm/s was adjusted to simulate normal blood flow condition in the aortic valve position. Afterwards the samples were rinsed in a standardized phosphate buffered saline solution (PBS-Lösung ohne CA 2+, MG 2+, Biochrom GmbH, Berlin, Germany). To fix the cells on the silicon, samples were put in a Monit-Graziadei-Solution (2 % glutaraldehyd, 0,6 % paraformaldehyde in 0,1 M cacodylat bufferer, ph 7,2, Institute for Anatomy, University of Lübeck, Germany). For analyzing the specimens with a scanning electron microscope (SEM) a thin gold layer was sputter-coated on the surface. Ten randomized visual fields were chosen from every sample (not including the fringe) of the SEM record. The pictures had a 1.200 x magnification and a size of 92 µm x 62 µm. The number of thrombocytes on each field was counted manually.

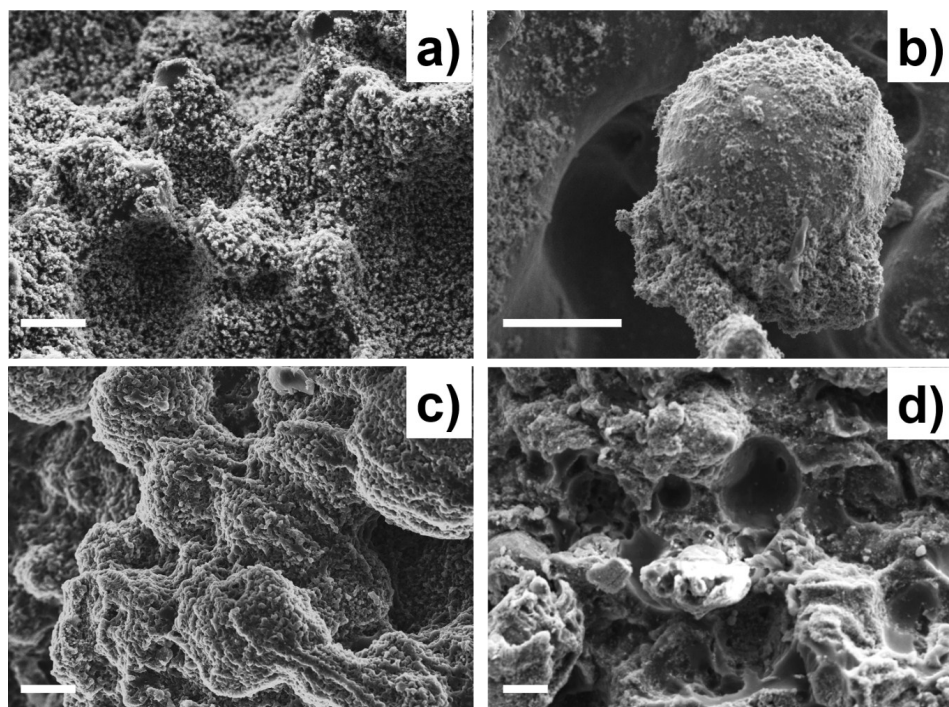


Figure S1 SEM images of various structured surfaces. Simple structures surface with ZnO nanoparticles is shown in a), b) shows a complex undercut structure made from Al and ZnO, c) and d) show the negatives of the samples seen a) and b) after the detachment experiment. The roughness of both samples can be clearly seen.

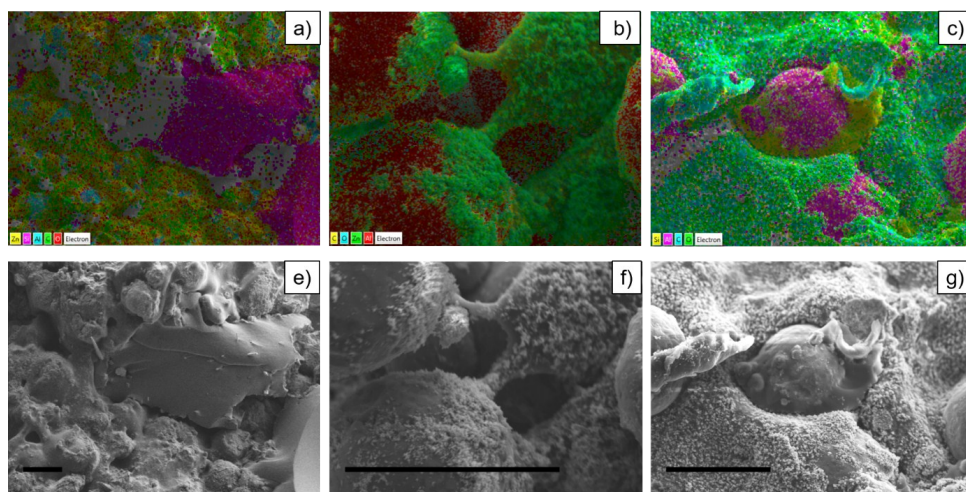


Figure S2 a) and e) show the EDX elemental map and the corresponding SEM image of a complex structured surface with cohesively failed PDMS. b) and f) show PEEK flowed through a dense network of ZnO particles and embed Al micro particles. c) and g) show an Al particle with cohesively failed PDMS around it. The scale bar is 50 μm

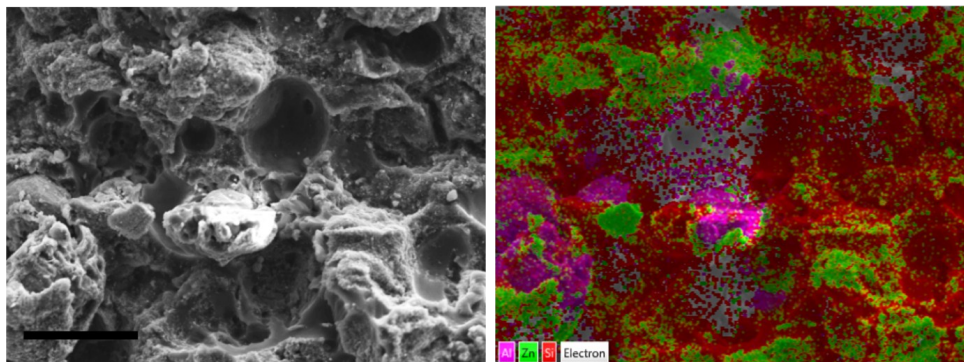


Figure S3 SEM image and EDX elemental map of a PDMS surface after detachment from a complex structured PEEK surface. Cohesively failed, flat PDMS parts can be seen as well as Al and ZnO particles detached from the PEEK.

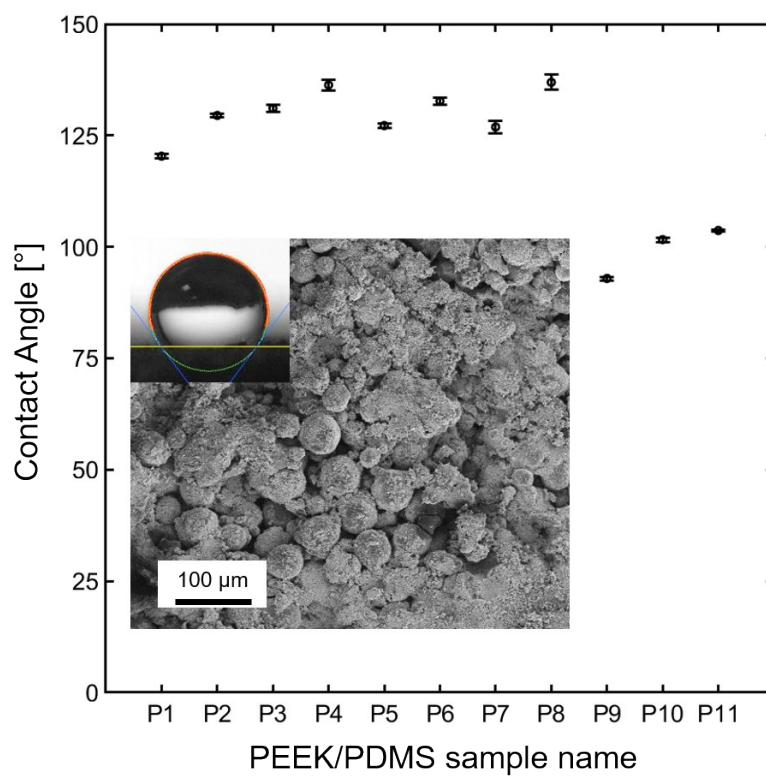


Figure S4: The contact angle in dependency of the thickness of the PDMS coating is shown. The inset shows the surface of a hierarchically structured sample and an exemplary image of a contact angle measurement on the coated surfaces.

Chapter 4

Homogeneous polymerisation realised by only trace amounts of crushed microcrystals

Polymers made from two or more reactive immiscible, liquid monomers often exhibit spatial property fluctuations. While the monomers are often designed to reproducibly ensure good quality, the mixing is often less than ideal. Micelle-based surfactants which are typically used to promote mixing of immiscible liquids cannot be used, since they would either participate in the reaction or form a separating membrane between either component. This work presents the use of highly polar, single-crystalline, fractured micro-rods based on tetrapodal zinc oxide (t-ZnO). The surfaces emerging by fracturing t-ZnO along its c-axis are extremely polar, while the side facets remain rather non-polar. By pulling a water string through oil, a possible mechanism for favourable mixing is demonstrated while the amphiphilic nature of the particles helps in stabilising reactive polar-non-polar mixtures. By utilising self-organized particles, the self-organisation into a phase separated mixture is suppressed and a stable mixture becomes favourable. Demonstrated by improving the adhesive strength of standard commercial epoxy by 32.4% with only trace amounts (<0.1 vol.-%) this concept proves high technological relevance for greener and cheaper polymer processing.

Own contribution presented in this article

- Homogenisation process investigation and sample preparation
- Planning and design of the mechanical experiments
- Data analysis
- Discussion and interpretation
- Writing the manuscript

1 Homogeneous polymerization realized by only trace amounts of crushed microcrystals

2 Leonard Siebert¹, Jürgen Carstensen¹, Philipp Schadte¹, Martha Gerhardt¹, Jörg Bahr¹,

3 Klaus Rätzke², Rainer Adelung^{1,*}

4 ¹Chair for Functional Nanomaterials, Institute for Materials Science, Faculty of Engineering, Kiel

5 University

6 ²Chair for Multicomponent Materials, Institute for Materials Science, Faculty of Engineering,

7 Kiel University

8 Abstract

9 For polymer synthesis proper and stable mixing of the two often immiscible monomers is a
10 fundamental challenge. There are no simple solutions to homogenize reactive yet immiscible
11 components and thus a mixing promoter is very significant for high quality processing. We report
12 on proper and stable mixing without membrane-forming molecules at the interface of immiscible
13 liquids promoted just by dipole-induced, long-range interaction. This is facilitated by trace
14 amounts (below 0.1 vol. %) of fractured tetrapodal zinc oxide (t-ZnO) increasing, e.g., the
15 adhesive strength of standard commercial epoxy resins by 32.4%, although composites with
16 filling factors below 1 vol.-% are generally considered useless. Fracturing the t-ZnO within the
17 polar component helps with the mixing kinetics of monomers with complementary polarity while
18 thermodynamically preventing demixing. The microparticles are mass producible and cost
19 effective and have the potential for simpler, faster, and cheaper polymer processing with less
20 additives and greener technology.

21

22

1

23

24 Introduction

25 All of the commercially available polymers nowadays have gone through thorough development
26 to perfect the polymerization during processing. An ideal processing should reproducibly lead to
27 the optimal mechanical, chemical and thermal properties in the final product. Often a
28 compromise is made to achieve the best properties for the lowest price.

29 Many materials produced by bulk polymerization involve two or more liquids with different
30 polarities¹⁻³. Polar and non-polar liquids tend to demix (cf. water and oil). Thus, a fundamental
31 mixing problem arises, which leads to inevitable spatial stoichiometry fluctuations of the final
32 polymer⁴⁻¹⁰. These might be tolerable but are less than ideal. A process with the capability to
33 improve the mixing on the sub-micron to nano scale while stabilizing final mixtures is necessary
34 for the polymers to unfold their full potential^{11,12}.

35 Many polymers are polymerized from two or more different monomers, but these monomers
36 typically exhibit opposite polarity and mixing is an issue. For polymer blends so called
37 compatibilizers are known¹³⁻¹⁶, which are mostly grafted to one of the homopolymers in the
38 blend to favor mixing. This method is not easily transferrable to arbitrary mixtures in bulk
39 polymerization (, e.g., reactive extrusion) because a modification may lead to serious property
40 changes. Emulsifiers cannot be used in reactive polymers as well, since the emulsifier's organic
41 nature easily leads to a participation in the reaction or otherwise form a membrane at the liquid-
42 liquid-interface. An ideal, cost-efficient and effective mixing with subsequent stabilization is
43 unknown.

44 As a possible solution, the here presented long-range linkers based on single-crystalline,
45 fractured, tetrapodal zinc oxide (t-ZnO) microrods, can be used to efficiently create and stabilize
46 ideal monomer mixtures, leading to improved polymerization and polymers. This is achieved by
47 a strongly amphiphilic behavior on the micron scale, enabled by fracture of the t-ZnO microrods
48 instead of chemical or physical treatments. The effect is purely based on a difference in energy
49 levels between the freshly exposed, highly polar cleaved surfaces and the as grown crystal facets
50 of the microrods. The polar liquid is attracted by long-range dipolar forces to the freshly cleaved
51 surface, while the non-polar liquid wets the sides.

52 In this paper, we will first demonstrate in a simple hand-made setup for the influence of breaking
53 ZnO single-crystals on interfacial energies and propose a mechanism for the observed effects.
54 Secondly, we will show how breaking t-ZnO improves properties of a poly(thiourethane). To
55 show the general validity, a standard epoxy system is then used and the application to gluing
56 aluminum is shown. Finally, a mechanical toughening mechanism based on lower built in stresses
57 is presented through polarization microscopy.

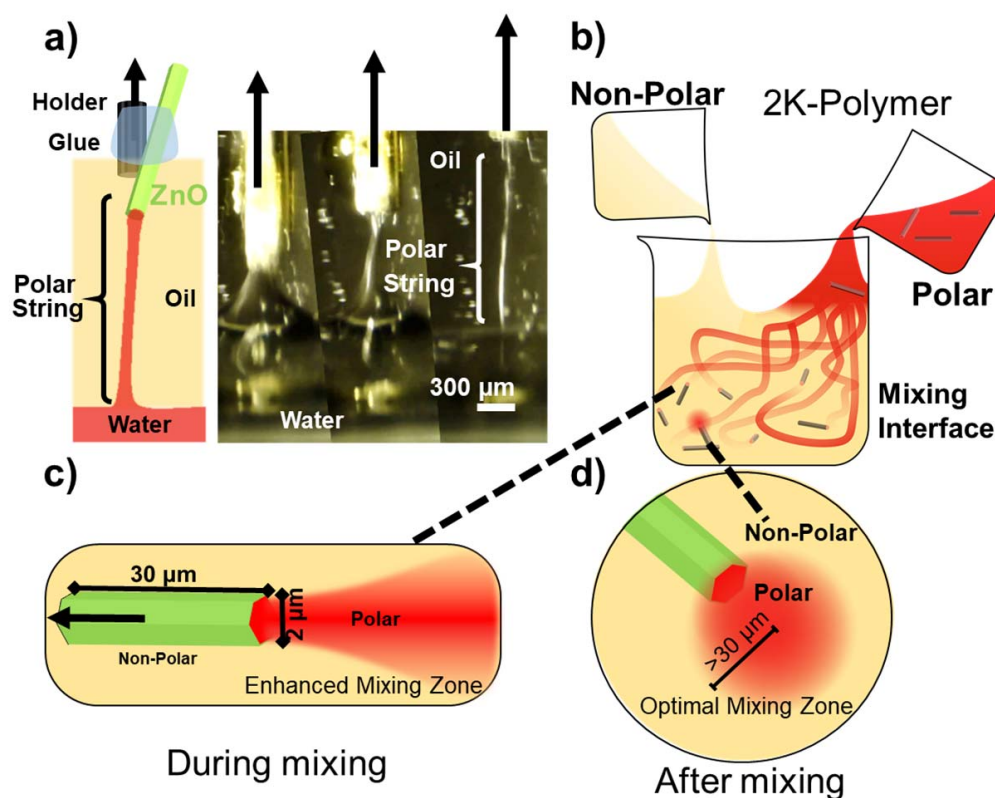
58 Results and Discussion

59 To demonstrate the strong dipole adsorption of polar liquids a large ZnO single-crystal is
60 fractured in water and dragged through oil, thus creating long high aspect ratio water ribbons, the
61 results of which are presented in Figure 1a. For that, a roughly 100 μm thick, single-crystalline
62 ZnO needle⁹ is fixed on a movable stage and filmed with a microscope camera. The needle is
63 dipped in a beaker with phase separated oil on top and water at the bottom. The needle is first
64 wetted by the oil and is then dragged multiple times through the water-oil-interface with no
65 observable effect (Supporting Video SV1).

66 The needle is then moved down and is pushed to the bottom of the beaker until it fractures inside
67 the water. After the needle is fractured at the bottom of the container (surrounded by water), it is
68 moved up through the interface of water and oil.

69 A very clear tail of water can be seen as it is pulled from the water phase into the oil phase. The
70 polar surface of a fractured ZnO needle is able to pull a string of polar water through a non-polar
71 oil. The length of the water tail is >1 mm while its width is <30 μm . This relates to a surprisingly
72 high aspect ratio of >30 . After a short time of roughly 1 s, the string splits up into smaller
73 droplets due to the Rayleigh instability¹⁷ (Supporting Video SV2 and Supporting Video SV3).

74 The droplets vary in size from roughly 100 μm to below the resolution limit of the camera setup
75 (< 30 μm). The setup and the string of water is shown in Figure 1a as both a photograph and a
76 schematic.



77

78

79 Figure 1 Single-crystal long-range linker based on zinc oxide tetrapods: a) A macroscopic ZnO
 80 needle glued to a dispensing tip with epoxy can absorb polar water so strongly that a thread of
 81 water is formed inside the non-polar oil. The water thread inside the oil is <50 μm and falls into
 82 smaller droplets when it reaches a critical length b) t-ZnO microparticles are added to the polar
 83 monomer of a reactive two-component polymer and then broken by mechanical force. The
 84 tetrapodal-shape is optimal for fracture, since shear in any direction will lead to fracture. After
 85 fracture a contact between high-energy fractured surfaces and the liquid phases occurs. The side
 5

86 facets are non-polar and the high-energy surface is strongly polar. The non-polar component is
87 adsorbed strongly on the side facets and the polar component is attracted by the high-energy
88 surface. c) During mixing of immiscible liquids this leads to a high shear at the interface of polar
89 and non-polar fluid which helps creating more and smaller interfaces. d) Once the interface width
90 reaches the length-scale of the average diffusion length of the two components respectively, a
91 homogeneous mixture is achieved. This results in a homogenization of the two phases on the
92 micrometer scale. These long-range linkers stabilize the mixture until completion of the reaction.
93 This effect can be only observed, when the ZnO needle is fractured inside the water. Fracturing
94 the needle in ambient air or not fracturing at all, will not lead to the necessary strong polar
95 interaction and the needle fails to pull a string of water.

96 This means, that the highly reactive and highly polar surface, exposed by fracturing the needle
97 will degrade or reconstruct under any normal circumstances. Only when the strong interactions
98 between the polar water and the freshly fractured ZnO needle are present, the high energy surface
99 is stable enough to act as an attracting pole for water adsorption. The adsorption is strong enough
100 to overcome the interfacial energies necessary to create more water-oil-interface.

101 One possible explanation may lie in the following mechanism. For any two-phase system the
102 spontaneous mixing or de-mixing will occur based on the change in Gibbs free energy of the
103 process which is given by equation 1:

$$(1) \Delta_{mix}G = \Delta_{mix}H - T \Delta_{mix}S$$

104 Even though the textbook knowledge prevails that entropy increases when mixing, favoring the
105 process, the opposite has been proven true. For many polar-non polar mixtures a positive change
106 in mixing enthalpy and a negative entropy change has been observed¹⁸. This means that de-

107 mixing is an entropy driven process. Such entropy barriers have been observed in other systems
108 before¹⁹. We propose that the highly polar surfaces of the t-ZnO lead to a spontaneous order, i.e.,
109 a reduction in entropy in the polar liquid. This lowers the energy barrier for the formation of
110 liquid-liquid interface, promoting and stabilizing homogeneous mixtures.

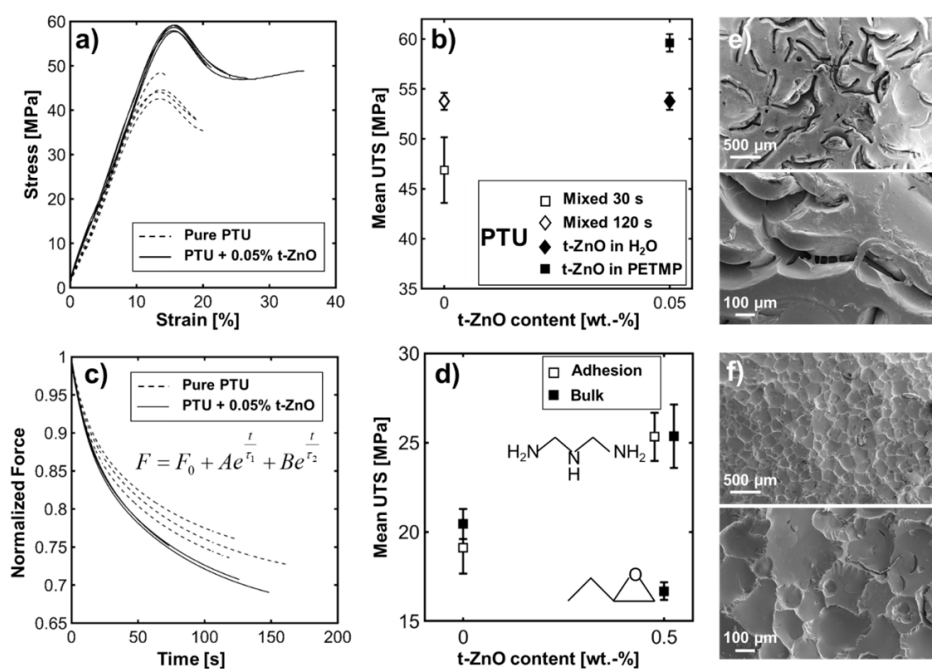
111 On this basis, a microscopic mechanism for better mixing and stabilized mixtures is proposed,
112 using microscopic tetrapodal, single-crystalline ZnO particles:

113 When microscopic t-ZnO is fractured in the polar component, many microscopic tails of polar
114 liquid can be pulled through a non-polar liquid (cf. Figure 1b). This creates a large interface
115 (Figure 1c) between the two liquids, which is beneficial for chemical reactions like bulk
116 polymerization. The t-ZnO additionally stabilizes the mixture by a reduced entropy barrier and by
117 adsorbing the non-polar liquid on the sides and the polar liquid at the fractured tip like shown in
118 Figure 1d. Therefore, coalescence will not occur as easily. This leads to a much better and more
119 stable homogenization on all length scales.

120 To demonstrate the efficiency of this approach, two-component, solvent-free systems are
121 presented, for which otherwise there is no easy way to ensure a stable mixture and homogeneous
122 properties.

123 Poly(thiourethane) (PTU) comprised of the polar tetra-functional Pentaerythritoltetrakis (3-
124 mercaptopropionat) (PETMP) and the non-polar Hexamethyldiisocyanate (HDI) is chosen as
125 member of the important polyurethane polymer family. When mixing the two components
126 without further stabilizing, demixing of individual components occurs, resulting in insufficient
127 reaction and thus insufficient mechanical properties. Thus, there is a large spread, e.g., in
128 mechanical properties.

129 To characterize the mechanical properties and the reproducibility, tensile tests on stabilized and
 130 non-stabilized PTU were performed and shown in Figure 2. Without the t-ZnO, the curves show
 131 significant scatter in their stress-strain behavior and reach only a maximum of around 48.5 MPa
 132 as ultimate tensile strength as a result of improper mixing. In strong contrast, the polymer filled
 133 with only trace amounts (0.05%) of fractured t-ZnO behaves highly reproducibly. For all tested
 134 samples it shows a higher ultimate tensile strength of 59.2 MPa and the identical stress-strain
 135 relationship. This relates to an increase 22% in ultimate tensile strength and a standard deviation
 136 reduction of 73.5%. Such additional increase, achieved by only tiny amounts of an inorganic,
 137 universal additive is very attractive for all major bulk polymerization production industries as
 138 they allow cost effective and yet greener production.



139

140 Figure 2 Mechanical properties applying trace amounts of the long-range linker. a) Stress-strain-
141 curves of pure and t-ZnO filled PTU samples. The spread in the dashed curves is considerable,
142 while all PTU with added t-ZnO (solid) shows very little deviations (, i.e., 73.5% lower scatter).
143 b) Mean ultimate tensile strength found for different processing of PTU. The tensile strength
144 increases only when the long-range linker is fractured in the polar component PETMP. Long-
145 range linker previously fractured in water and dried, shows no effect. c) Normalized stress
146 relaxation curves for pristine and t-ZnO filled PTU. The stress relaxation rate increases
147 significantly with added t-ZnO and the scatter becomes negligible. d) A plot showing mean
148 ultimate tensile strength and mean adhesion strength values for bulk (filled) and adhesion
149 samples (unfilled) of commercial epoxide with and without long-range linker. When the t-ZnO is
150 mixed into the polar hardener, the long-range linker significantly increases the tensile strength of
151 the final epoxy. When mixed into the non-polar binder, the opposite effect can be observed.
152 Likewise, a significant improvement in the adhesive strength of 32.4% is found, when 0.5% t-
153 ZnO is added to the polar hardener. e) and f) are scanning electron microscopy (SEM)
154 micrographs of unfilled PTU and t-ZnO filled PTU, respectively, after etching in concentrated
155 sulfuric acid for 24 h. In e) large etching-pits can be observed. f) shows a homogeneous
156 distribution of shallow etch pits with a mean size of 180 μm and a standard deviation of 62 μm .
157 Different fabrication variations confirm the suggested improvement mechanism, see Figure 2b.
158 As expected PTU mixed for a short duration of only 30 seconds shows large spread and low
159 ultimate tensile strength for the final polymer. Increasing the blending time naturally improves
160 the resistance towards mechanical stress. After about 60 s of mixing, further mixing does not
161 improve the mechanical properties of the PTU anymore. Thus, the samples mixed for 120 s
162 shown in Figure 2b show a higher ultimate tensile strength than the samples 30 s of mixing.
163 When blending for 120 s with additional 0.05 wt.-% of t-ZnO that has previously been fractured

9

164 in water and dried, no effect on the mechanical properties can be observed. Only fracturing the
165 tetrapods in the PETMP leads to a significant increase in the mechanical properties. With the
166 proposed mechanism in mind, the interpretation of these effects is better mixing and better
167 stabilization by adding t-ZnO fractured in the polar component. From our experiments a filling
168 factor of 0.05 wt.-% is the minimal amount of t-ZnO leading to the maximum reinforcement
169 effect. Through simple geometry this corresponds to an influenced volume with a diameter of 70
170 μm around each long-range linker. This large volume hints at the long-ranged effect and supports
171 the proposed mechanism. When fractured in water, the high energy surface can reconstruct and
172 lose their strong effect on polar liquids. Thus, for t-ZnO fractured in water, no reinforcement
173 effect can be observed.

174 The well-known reinforcement mechanism of small whiskers in polymers is dictated by the
175 mechanical properties of the whiskers and mainly depends on the filling factor and the size of the
176 whiskers. Ordinarily, mechanically stiff whiskers would lead to a stress relaxation rate decrease
177 with increasing filler content. In contrast, the stress relaxation rate of the present composite even
178 increases when blending in 0.05 wt.-% t-ZnO, as can be seen in Figure 2c. The reason might be
179 found in segregation of the polymer into a highly and an only mildly cross-linked region for the
180 unfilled polymer or a homogeneous cross-linking for the t-ZnO filled polymer. Detailed
181 description of the stress relaxation differential equation can be found in the supporting
182 information.

183 To show the general validity of the approach, a second system, namely standard two component
184 epoxy adhesive has been investigated as well. Epoxide resins are chemically very different to the
185 previously shown PTU. They typically consist of a non-polar liquid, exhibiting multiple oxirane

186 groups, whereas HDI is a diisocyanate. Both only share their non-polarity but show no chemical
187 resemblance.

188 Additionally, as binder in epoxide resins amides ($-N-H$ or $-N-H_2$) functional groups are used,
189 contrasting the mercaptan groups ($-S-H$) of the PETMP in PTU. The only similarities lie in the
190 polarity and non-polarity of the two monomers of the respective polymers.

191 In this context, similar results for the mechanical properties of epoxides have been achieved by
192 blending in t-ZnO in trace amounts and are presented in Figure 2d. Without t-ZnO under
193 otherwise ideal fabrication conditions, the ultimate tensile strength for these samples is 20.4 MPa.
194 When t-ZnO is added to the non-polar diglycidyl ether of bisphenol A (DGEBA) in trace
195 amounts of 0.5 wt.-%, the ultimate tensile strength is lowered to 16.7 MPa. This is likely due to a
196 reaction of DGEBA with the freshly fractured (100) surface of the t-ZnO. When DGEBA reacts
197 with the high energy (100) surface, the oxirane group is no longer available for reaction with the
198 polyamides. For the drastic improvement in the ultimate tensile strength, the t-ZnO needs to be
199 mixed into the polar amide component. In this case the filled epoxy shows a ultimate tensile
200 strength of 25.4 MPa, an increase of 24.5%. similar to above a possible explanation is the
201 occupation of the polar surface of the t-ZnO, leading to a homogenization between DGEBA and
202 the polyamides in the final mixture.

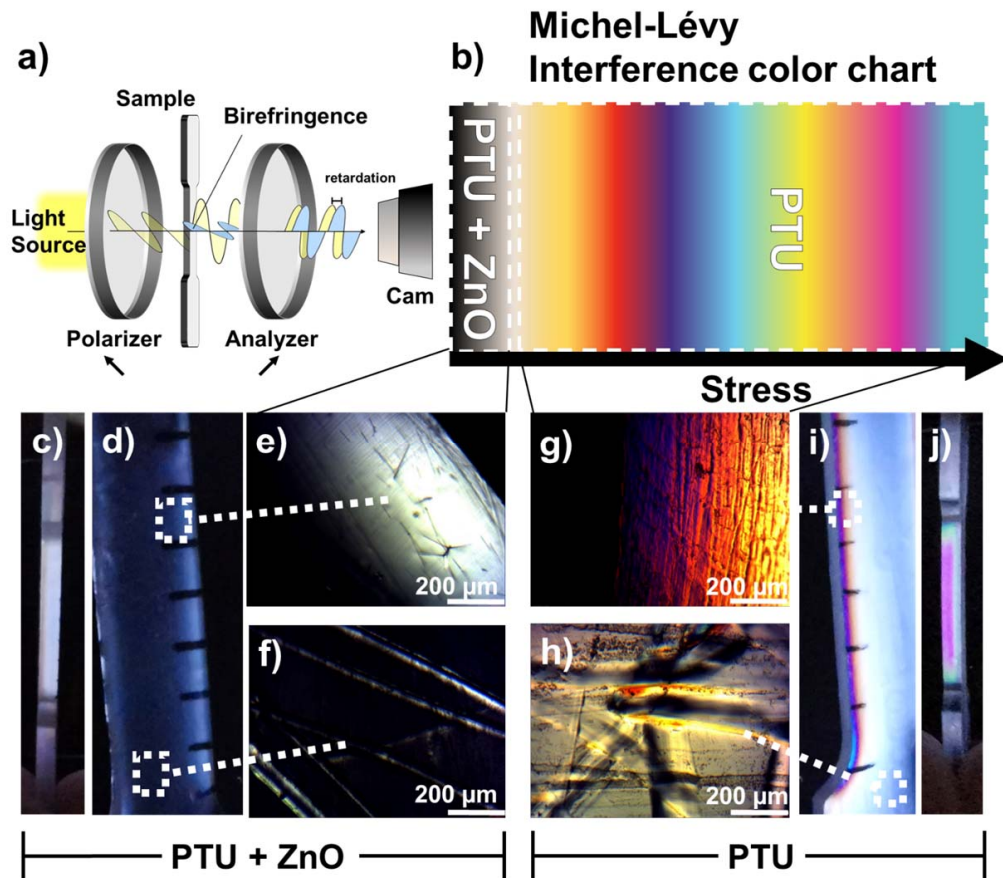
203 The approach shows high technological relevance, when the epoxy is used as a glue between two
204 smooth aluminum surfaces. The adhesive strength of the interface increases from 4.8 to 6.3 MPa,
205 which corresponds to an increase of around 32%. Additionally, the unfilled samples all failed
206 adhesively, while 0.5% of t-ZnO resulted in cohesive failure of the epoxy. Usually, the ideal
207 processing conditions (heating the glue to >80 °C for >30 min) cannot be kept and there is no
208 easy way to improve the adhesive strength any further. When adding the long-range linker in

209 trace amounts, a significantly stronger adhesion is possible with a minimum additional effort. The
210 mechanism might be an accumulation of the polar binder at the likewise polar aluminum oxide,
211 leading to a phase separation and a weakened interface. Adding the long-range linker then results
212 in a more homogeneous mixture, preventing accumulation of either component at the interface.

213 To investigate the length-scale on which phase separation may occur in unfilled samples, micro-
214 Raman (length-scale $\sim 10 \mu\text{m}$) and x-ray diffraction (XRD) (length scale $< 5 \text{ nm}$) have been
215 performed. The results are depicted in Figure S1. Neither experiment showed significant
216 chemical or structural fluctuations on the respective length scale.

217 Another method for revealing heterogeneities in e.g. the crosslinking density on all length scales
218 is etching. In this manner, structural variations were made visible after etching unfilled PTU and
219 PTU filled with 0.05% t-ZnO for 24 h in concentrated sulfuric acid (Figure 2e-f). While the
220 unfilled PTU sample shows large crazes sized $> 200 \mu\text{m}$, the sample containing t-ZnO shows a
221 distribution of shallow etch-pits with diameters of $\sim 180 \mu\text{m}$ and low depth. The crazes in unfilled
222 PTU most likely originate from regions with a lower cross-linking density due to an excess of
223 either component, while the remaining structures are likely much higher cross-linked regions.
224 When t-ZnO is blended in, a more uniform distribution of both components is achieved and the
225 polymer is etched more homogeneously. The etching pits observed may arise from preferential
226 etching, when the acid touches the t-ZnO and the etching is radially increased in these regions.

227 Significant changes have been found, however, in the internal stress of tensile testing samples.
228 The influence of ZnO on the concentration of internal stresses can be seen in Figure 3. Here, the
229 unfilled PTU exhibits a high concentration of built in stresses, that would ultimately lead to a
230 lower fracture toughness of these samples. Contrarily, samples filled with 0.05% ZnO exhibit a
231 much lower stress concentration, often close to zero.



232

233 Figure 3 Birefringence Setup and representative birefringence photographs of PTU tensile test
 234 specimens prior to mechanical testing. a) The testing geometry: a sample is placed between a
 235 polarizer and an analyzer with an angular difference of 90° in their polarizing axes. The
 236 birefringence measurements are photographed either directly or through a magnification lens. b)
 237 A schematic of the Michel-Lévy interference color chart, where the colors change upon increased
 238 residual stress in the samples. c-j) Birefringence photographs of PTU samples with t-ZnO (c-e)
 239 and without t-ZnO (g-j). c) and d) show side and top views of filled samples, respectively. The

240 low brightness and the absence of color indicates low internal stress. e) a magnified view of an
241 edge of a sample filled with t-ZnO. The fractured and partially aligned t ZnO can be observed as
242 well as some minor residual stresses at the edge. f) Magnified view on a surface of t-ZnO filled
243 PTU scratched with tweezers. Only minor residual stress can be observed at the edges of each
244 scratch. g) Magnified view on the edge of a PTU tensile testing sample without ZnO. A strong
245 coloration is evident, indicating high residual stresses. h) Magnified view on a surface of unfilled
246 PTU scratched with tweezers. High residual stresses are visible at the scratch fringes. The image
247 i) shows the top view and j) shows the side view of a sample without t ZnO, exhibiting strong
248 coloration.

249

250 This is likely due to the decreased stress relaxation rates observed for unfilled samples. Stresses
251 occurring during sample preparation and curing cannot be relaxed as easily on samples which are
252 more heterogeneous. Such stresses may come from local defects or may be due to variable
253 shrinkage during polymerization. The embedded stress fields will lead to a decreased ability to
254 relax external stresses. Lower stress relaxation leads to a concentration of stress on local defects
255 and therefore increased crack formation and propagation.

256 When ZnO is added to the polymer in the described manner, fluctuations in the local
257 concentration of either component are reduced and occurring stresses can be relaxed more easily.
258 This is also the case, when the samples are scratched. In unfilled PTU, the high stresses at the
259 fringes of the scratches cannot be relieved. Therefore, even minor defects will have a strong
260 impact on the toughness of the whole material. These results are also consistent to the relaxation
261 curves shown in Figure 2c and may serve as a microscopic explanation for the difference in the
262 stress strain curves in Figure 2a.

263 Better mixing may be the reason for the reduction in internal stresses. Based on the above stated
264 entropy barrier mechanism, the long-range of the effect is the reason for the efficiency (, i.e.
265 filling factors below 0.1 vol.-%) of the fractured particles. Strong enthalpic attraction of polar
266 liquids to the strongly polar, freshly fractured t-ZnO surfaces lead to long-ranged entropy
267 reduction (, i.e., order) which enables a reduction of the energy barrier of entropy-limited
268 processes like mixing of many polar and non-polar substances. Instead of zero- or one-
269 dimensional additives like salts or surfactants, the fractured plains translate a two-dimensional
270 enthalpic effect into a large volume by dipole-induced ordering, which is a highly efficient
271 process. The benefits of these approach have also been observed for surfactant-free dispersion of
272 carbon nanotubes in water, which will be discussed in detail in a follow-up paper.

273 Conclusion

274 In conclusion, we have demonstrated an efficient processing method for multicomponent
275 polymer systems based on trace amounts of crushed micro-crystals. The amphiphilic nature of
276 these particles and the strong polarity of the crushing-induced high surface energy facets enable a
277 thorough mixing of incompatible liquids while stabilizing the mixture after preparation. The
278 improved mixing shows significant results in two-component polymers, like an increased stress
279 relaxation and higher mechanical strength without preparation-induced stresses. A stabilization
280 mechanism based on decreased entropy barriers is proposed. The process is easily adaptable for
281 large-scale polymer production and may be used to synthesize ¹⁷polymers like epoxides,
282 polyamides, polyethylene terephthalate, polyesters, polyurethanes and many others in a much
283 more controlled manner.

284 References

- 285 1. Jin, F.-L., Li, X. & Park, S.-J. Synthesis and application of epoxy resins. A review. *Journal of*
286 *Industrial and Engineering Chemistry* **29**, 1–11; 10.1016/j.jiec.2015.03.026 (2015).
- 287 2. Akindoyo, J. O. *et al.* Polyurethane types, synthesis and applications – a review. *RSC Adv.* **6**, 114453–
288 114482; 10.1039/C6RA14525F (2016).
- 289 3. Forsythe, J. S. *et al.* Rheological properties of high melt strength poly(ethylene terephthalate) formed
290 by reactive extrusion. *J. Appl. Polym. Sci.* **100**, 3646–3652; 10.1002/app.23166 (2006).
- 291 4. Dušek, K., Pleštil, J., Lednický, F. & Luňák, S. Are cured epoxy resins inhomogeneous? *Polymer* **19**,
292 393–397; 10.1016/0032-3861(78)90243-4 (1978).
- 293 5. Krakovský, I., Bubeniková, Z., Urakawa, H. & Kajiwara, K. Inhomogeneous structure of polyurethane
294 networks based on poly(butadiene)diol. 1. The effect of the poly(butadiene)diol content. *Polymer* **38**,
295 3637–3643; 10.1016/S0032-3861(96)00897-X (1997).
- 296 6. Matsuo, E. S., Orkisz, M., Sun, S.-T., Li, Y. & Tanaka, T. Origin of Structural Inhomogeneities in
297 Polymer Gels. *Macromolecules* **27**, 6791–6796; 10.1021/ma00101a018 (1994).
- 298 7. Chung, J., Munz, M. & Sturm, H. Stiffness variation in the interphase of amine-cured epoxy adjacent
299 to copper microstructures. *Surf. Interface Anal.* **39**, 624–633; 10.1002/sia.2571 (2007).
- 300 8. Takahama, T. & Geil, P. H. Structural inhomogeneities of cured epoxy resins. *Makromol. Chem.*,
301 *Rapid Commun.* **3**, 389–394; 10.1002/marc.1982.030030603 (1982).
- 302 9. Hrkac, S. B. *et al.* Tunable Strain in Magnetolectric ZnO Microrod Composite Interfaces. *ACS Appl.*
303 *Mater. Interfaces* **9**, 25571–25577; 10.1021/acsami.6b15598 (2017).
- 304 10. Meyer, F., Sanz, G., Eceiza, A., Mondragon, I. & Mijović, J. The effect of stoichiometry and thermal
305 history during cure on structure and properties of epoxy networks. *Polymer* **36**, 1407–1414;
306 10.1016/0032-3861(95)95918-Q (1995).
- 307 11. Gupta, V. B., Drzal, L. T., Adams, W. W. & Omlor, R. An electron microscopic study of the
308 morphology of cured epoxy resin. *J Mater Sci* **20**, 3439–3452; 10.1007/BF01113751 (1985).
- 309 12. Aoki, M., Shundo, A., Kuwahara, R., Yamamoto, S. & Tanaka, K. Mesoscopic Heterogeneity in the
310 Curing Process of an Epoxy–Amine System. *Macromolecules* **52**, 2075–2082;
311 10.1021/acs.macromol.8b02416 (2019).
- 312 13. Kalfoglou, N. Comparison of compatibilizer effectiveness for PET/HDPE blends. *Polymer* **36**, 4453–
313 4462; 10.1016/0032-3861(95)96853-Z (1995).
- 314 14. Sadiku, E. R. & Ogunniran, E. S. in *Nanostructured polymer blends*, edited by T. Sabu, R. Shanks &
315 S. Chandrasekharakurup (William Andrew an imprint of Elsevier, Amsterdam, Boston, Heidelberg,
316 2014), pp. 101–131.
- 317 15. Sabu, T., Shanks, R. & Chandrasekharakurup, S. eds. *Nanostructured polymer blends* (William
318 Andrew an imprint of Elsevier, Amsterdam, Boston, Heidelberg, 2014).
- 319 16. Aparna, S., Purnima, D. & Adusumalli, R. B. Review on Various Compatibilizers and its Effect on
320 Mechanical Properties of Compatibilized Nylon Blends. *Polymer-Plastics Technology and*
321 *Engineering* **56**, 617–634; 10.1080/03602559.2016.1233280 (2016).
- 322 17. Papageorgiou, D. T. On the breakup of viscous liquid threads. *Physics of Fluids* **7**, 1529–1544;
323 10.1063/1.868540 (1995).
- 324 18. Silverstein, T. P. The Real Reason Why Oil and Water Don't Mix. *J. Chem. Educ.* **75**, 116;
325 10.1021/ed075p116 (1998).
- 326 19. Gösele, U., Frank, W. & Seeger, A. An entropy barrier against vacancy-interstitial recombination in
327 silicon. *Solid State Communications* **45**, 31–33; 10.1016/0038-1098(83)90878-5 (1983).
- 328

329

330 Methods

331

332 Water string experiments were carried out with distilled water and grocery grade sunflower oil. Single
333 Crystalline ZnO needles with a thickness $>50\ \mu\text{m}$ were glued with epoxy to 0.4 mm tapered dispersing
334 tips. While filming with an USB microscope, the needles were dipped through the water oil interface
335 multiple times. Subsequently, they were fractured on the bottom of the vessel surrounded by water.
336 Then they were dragged through the interface again.

337 Tensile samples were made with custom dogbone-shaped molds. These molds were vacuum-sealable
338 and the polymer was vacuum-casted under a desiccator to avoid gas bubbles. PETMP and HDI were
339 provided by Fluid & Prozesstechnik (Waltershausen, Germany). UHU Endfest 300 was bought from the
340 hardware store. Unfilled samples were prepared by mixing the two components by hand for at least 1
341 minute, if not stated otherwise. The prepolymer was filled into a syringe without piston which was
342 connected to the vacuum mold. By pulling a vacuum into the mold through the prepolymer, bubble free
343 polymer was obtained after venting the desiccator. All samples were stored at $80\ ^\circ\text{C}$ for 24 h, if not
344 stated otherwise. Zinc oxide tetrapods were crushed inside the polar component of the polymer by
345 either ultrasonication with a Bandelin SONOPULS HD 4100 for 30 s at 30% amplitude (PTU) or by
346 crushing with mortar and piston for 5 minutes (epoxy). Adhesion tests were carried out by glueing two
347 flat aluminum stamps front-end to each other with a fixed gap of $500\ \mu\text{m}$. To prevent tilting forces, a
348 setup using UHMWPE ropes was used to pull the samples apart. The maximum force per area was taken.

349 Stress relaxation tests were performed by rapid deformation to a predefined elongation. The position
350 was held and the force measured over time. All curves were normalized to the respectively occurring
351 maximum force. Tensile tests were carried out at a deformation rate of $1\ \text{mm}/\text{min}$ until fracture
352 occurred. Adhesion tests were carried out with a deformation rate of $0.1\ \text{mm}/\text{min}$ until fracture.

353 Author contribution statement

354 L.S. and J.C. and R.A. conceived the research and designed the experiments. R.A. supervised the work.

355 L.S. and P.S. performed the mechanical characterization. P.S. and M.G. prepared the samples. J.B.

356 developed and built the technical setup for mechanical and birefringence characterization. M.G. and

357 L.S. performed the water string and the birefringence experiments. K.R., J.C. and R.A. provided

358 theoretical background and developed the idea of the mechanism with L.S.. All authors participated in

359 writing and editing the manuscript.

360

361 Acknowledgement

362 We thank T. Spratte and A. Kuntze for assistance in mechanical testing. We also thank O.

363 Riemenschneider for fruitful scientific discussion. Funding from the EU network FLAG-ERA is

364 gratefully acknowledged under the proposal number (GRMH2TANK; Ad 183/18-1).

365

366 Competing interests

367 Patent Cooperation Treaty (PCT) patent applications have been filed under the numbers

368 PCT/DE2020/100693 and PCT/DE2020/100693 by L.S., J.C., P.S., J.B. and R.A..

1 **Supporting Information**

2 Homogeneous polymerization realized by only trace amounts of crushed microcrystals

3 Leonard Siebert¹, Jürgen Carstensen¹, Philipp Schadte¹, Martha Gerhardt¹, Jörg Bahr¹,

4 Klaus Rätzke², Rainer Adelung¹

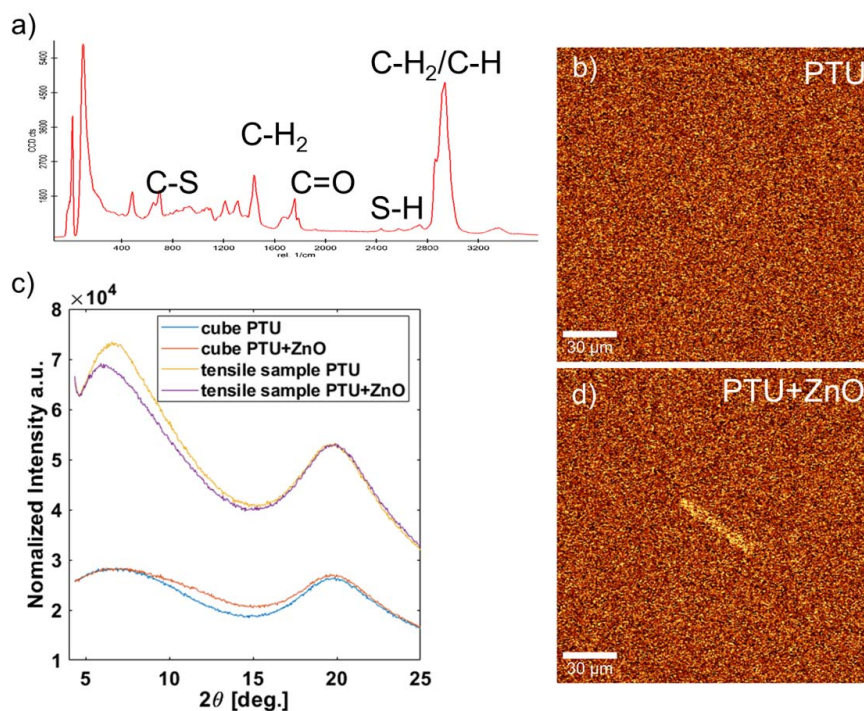
5 ¹Chair for Functional Nanomaterials, Institute for Materials Science, Faculty of Engineering,

6 Kiel University

7 ²Chair for Multicomponent Materials, Institute for Materials Science, Faculty of Engineering,

8 Kiel University

9

10 **Microstructural Characterization**

11

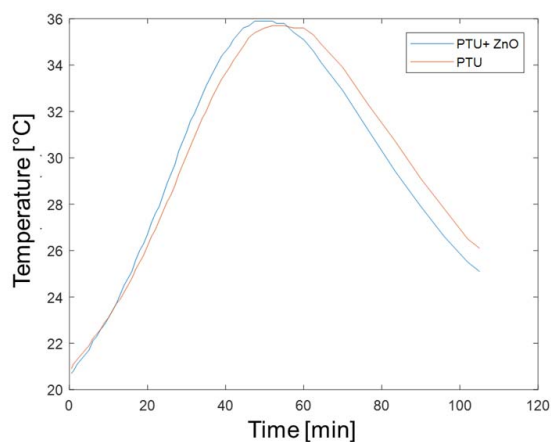
12 Supporting Figure S1 Microstructural characterization and influence of t-ZnO a) Raman
 13 spectra of a representative PTU sample. The S-H peak has been used to create the image of
 14 unfilled PTU in b) and a t-ZnO peak has been used for the map of the filled sample in d). b)
 15 shows Raman maps of unfilled PTU. Even at maximum resolution, no local differences in
 16 chemical composition are visible on the micron-scale. c) XRD patterns of filled and unfilled
 17 PTU both as Cubes with 20 mm edge length and as a tensile testing sample. d) shows Raman
 18 maps of PTU filled with 0.05% fractured t-ZnO.

19

20

21 **Thermal analysis**

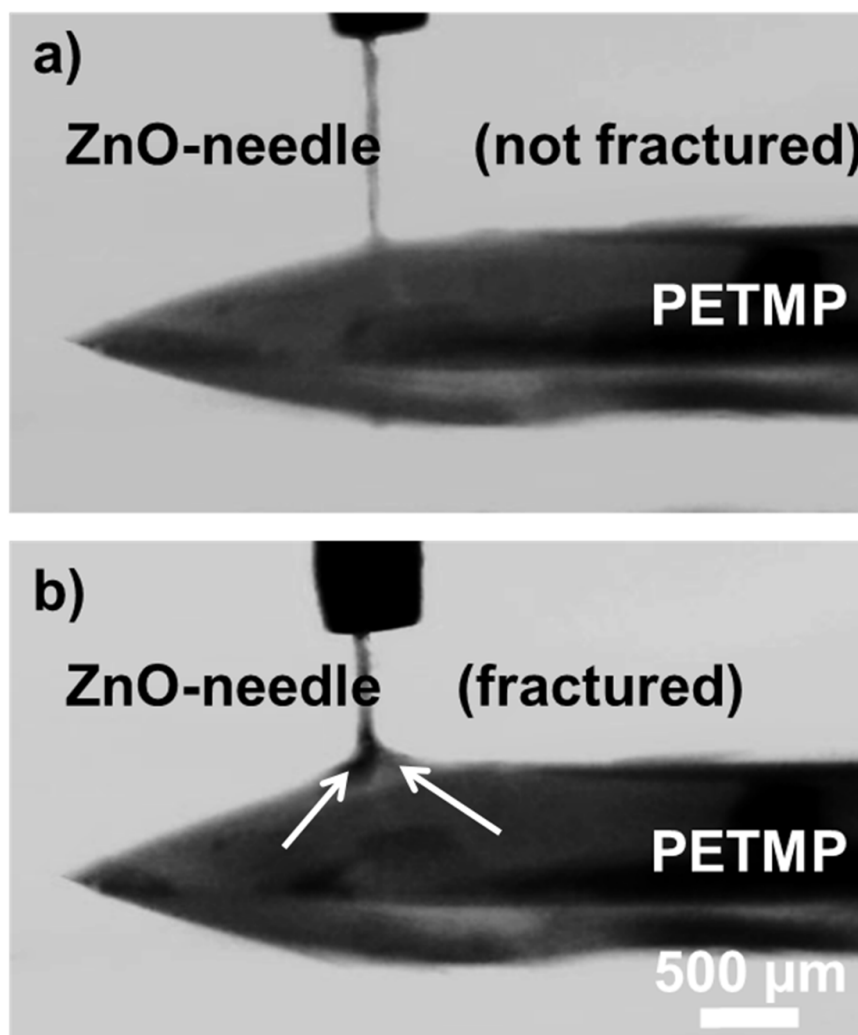
22 In order to investigate a possible catalysis by the fractured t-ZnO, temperature curves of the
23 reaction to PTU have been measured both with and without t-ZnO, depicted in Figure S2. The
24 area under the curves relate to the integral heat of reaction released. For both curves, the area
25 is equal, hinting at an equal conversion. On the time axis, the curve for the system containing
26 fractured t-ZnO was slightly faster. This could hint at a faster conversion rate due to proper
27 mixing, but the evidence is not strong, since fluctuations of a few degree centigrade can occur
28 naturally the thermocouples used for this experiment. Therefore, it can be assumed that there
29 is no decisive catalysis induced by fracturing the t-ZnO as would be obvious in either a much
30 higher conversion rate or more complete reaction, i.e., more area under the curves.



31

32 Supporting Figure S2: Time-temperature curve of the curing process of PTU. Over the
33 duration of 105 minutes, the temperature of a filled sample and an unfilled sample is at a
34 maximum of 1 °C. The difference is well inside the measurement noise of the type K
35 thermocouples used. Still, the reaction with t-ZnO occurs a few minutes faster. The area under
36 the curve is equal for both filled and unfilled PTU, indicating an equal heat of reaction and
37 therefore equal conversion.

3

38 **Interaction and necking of ZnO and PETMP**

39

40 Supporting Figure S3 from Supporting Video SV4: Photographs of the interaction between a
41 ZnO needle and the polar PETMP monomer of PTU before and after fracturing. In a) the
42 needle is not fractured and there is little adsorption of the PETMP to the needle. In b) the
43 strong necking occurring from adhesion of the PETMP to the fractured surface of the ZnO
44 needle can be seen (arrowed, see video).

4

45 **Stress Relaxation**

46 The stress relaxation curves in Figure 2c can be fitted by the equation (S1):

47
$$(S1) \quad F = F_0 + Ae^{\frac{t}{\tau_1}} + Be^{\frac{t}{\tau_2}}$$

48 Remarkably, the time constants are equal for all samples, both filled and unfilled, with
49 $\tau_1 = 11$ s and $\tau_2 = 80$ s. The difference between filled and unfilled samples arises from the
50 linear coefficients F_0 , A and B . When t-ZnO is added, a larger portion of the relaxation is
51 dominated by the fast process related to A and τ_1 , whereas without ZnO, there is more
52 residual stress, related to F_0 . The general validity of the two time constants can be interpreted
53 as two different stress relaxation processes in parallel, while the pre-factors could show one
54 portion of the polymer follows the behavior described by A and τ_1 , while the rest follows F_0
55 or B and τ_2 .

56 When the t-ZnO is ground by hand, it requires longer duration until all arms are fractured.
57 The more strongly polar facets are created, the less initial t-ZnO is necessary. When too much
58 t-ZnO is added, the effect nullifies, as can be observed in Supporting Figure S4.

59

60

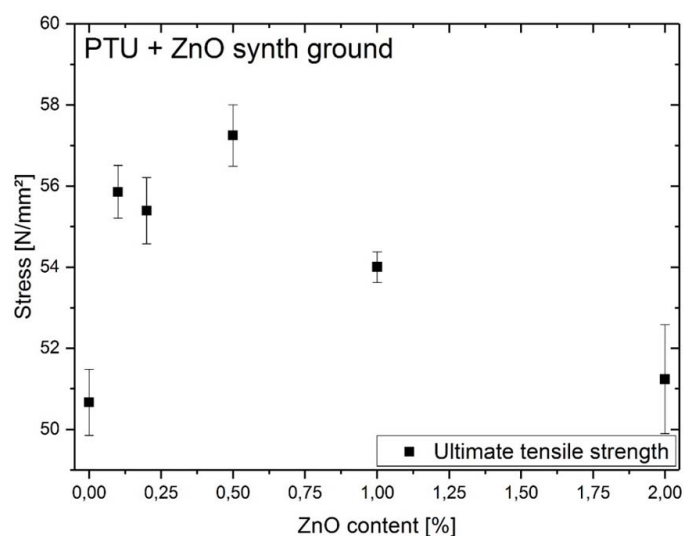
61

62

63

64

65

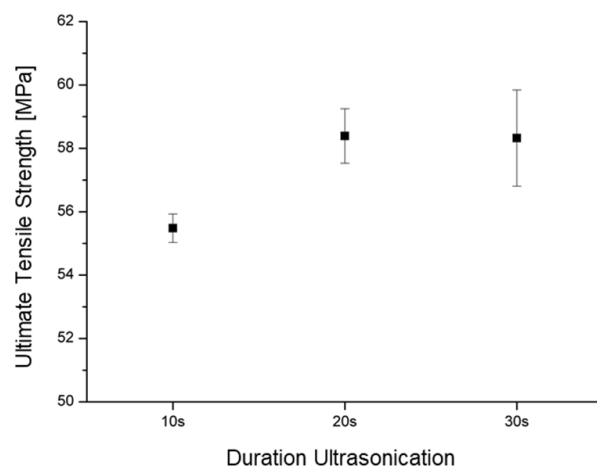
66 **Influence of preparation conditions**

67

68 Supporting Figure S4: Plot of the ultimate tensile strength of PTU for increasing t-ZnO
69 concentration. When crushed by hand, a maximum effect is observed at 0.5% (by weight). At
70 higher concentration of t-ZnO, the effect decreases.

71 The ratio of fractured t-ZnO arms is a decisive parameter for the effect fully develop.

72 Different PTU tensile samples with 0.05% t-ZnO have been prepared with increasing
73 durations of ultrasonication, with the intent to fracture more t-ZnO arms (Supporting
74 Figure S5). The ultimate tensile strength increases from 55 MPa to 58 MPa when increasing
75 the duration of ultrasonication from 10 s to 20 s. Longer durations of ultrasonication do not
76 increase the UTS further. The scatter increases, which may be linked to heating up and
77 degradation of the PETMP component.



78

79 Supporting Figure S5: Plot of the ultimate tensile strength of PTU with 0.05% t-ZnO for

80 increasing duration of ultrasonication.

Chapter 5

Buckminsterfullerene hybridised zinc oxide tetrapods: defects and charge transfer induced optical and electrical response

The very high surface-to-volume ratio of nanomaterials is the key aspect of their special properties. Surface-related effects and quantisation can only arise for materials, where the surface is the main contributor. Because of strong Van-der-Waals interaction, nanoparticles often tend to agglomerate in solutions when not separated by some sort of surface treatment. In their solid form, e.g., as a powder, the presented surface is significantly reduced due to clumping of particles. An arrangement of quasi 2D-layers in 3D is necessary to present more of the nanomaterial's surface. However, it is impossible to efficiently order nanomaterials into 3D by direct external manufacturing. Instead, self-organisation phenomena need to be employed to favour the formation of 3D-architectures made of nanomaterials. One approach is presented here, where 0D carbon nanoparticles known as fullerenes are coated onto the surface of open-porous 3D ZnO architectures. Van-der-Waals interactions between the fullerenes and the surface of the ZnO lead to strong attraction upon drying of the solvent. The resulting hybrid material between fullerenes and ZnO was investigated by photoluminescence and a possible charge transfer between both materials is strongly indicated. Additionally, gas-sensing properties are measured, where the hybrid material shows a reaction towards ethanol.

The results have been published in the journal "Nanoscale".

Own contribution presented in this article

- Scientific discussion and modelling
- Editing the manuscript

The following content in this chapter is reproduced with permission.



Nanoscale

PAPER

View Article Online
View Journal | View Issue



Cite this: *Nanoscale*, 2018, **10**, 10050

Buckminsterfullerene hybridized zinc oxide tetrapods: defects and charge transfer induced optical and electrical response†

Daria Smazna,^a Joana Rodrigues,^{id} b Sindu Shree,^a Vasile Postica,^{id} c Gero Neubüser,^a A. F. Martins,^b N. Ben Sedrine,^b Naresh K. Jena,^d Leonard Siebert,^a Fabian Schütt,^a Oleg Lupan,^{a,c} Rajeev Ahuja,^d M. R. Correia,^b Teresa Monteiro,^{*b} Lorenz Kienle,^{*a} Ya Yang,^{id} e Rainer Adelung^{*a} and Yogendra Kumar Mishra^{id} ^{*a}

Buckminster fullerene (C₆₀) based hybrid metal oxide materials are receiving considerable attention because of their excellent fundamental and applied aspects, like semiconducting, electron transfer, luminescent behaviors, etc. and this work briefly discusses the successful fabrication of C₆₀ decorated ZnO tetrapod materials and their detailed structure–property relationships including device sensing applications. The electron microscopy investigations indicate that a quite dense surface coverage of ZnO tetrapods with C₆₀ clusters is achieved. The spectroscopy studies confirmed the identification of the C₆₀ vibrational modes and the C₆₀ induced changes in the absorption and luminescence properties of the ZnO tetrapods. An increased C₆₀ concentration on ZnO results in steeper ZnO bandgap absorption followed by well-defined free exciton and 3.31 eV line emissions. As expected, higher amounts of C₆₀ increase the intensity of C₆₀-related visible absorption bands. Pumping the samples with photons with an energy corresponding to these absorption band maxima leads to additional emission from ZnO showing an effective charge transfer phenomenon from C₆₀ to the ZnO host. The density of states model obtained from DFT studies for pure and C₆₀ coated ZnO surfaces confirms the experimental observations. The fabricated C₆₀–ZnO hybrid tetrapod based micro- and nanodevices showed interesting ethanol gas sensing characteristics.

Received 21st February 2018,
Accepted 24th April 2018

DOI: 10.1039/c8nr01504j

rsc.li/nanoscale

Introduction

Since its discovery, buckminsterfullerene (C₆₀), among all the low dimensional carbon allotropes, has always introduced new fundamental and applied research paradigms in various disciplines due to its unique physical and chemical properties.¹ Together with other fullerenes (such as C₇₀, C₈₄ etc.), buckyballs belong to the semiconductor family with a bandgap energy from 1.5 to 1.98 eV, which makes them attractive for optical and electrical applications.² Taking into account their

excellent charge extraction and accommodation capabilities,³ diverse applications in photovoltaics,^{1b} photocatalytic water purification,⁴ as a photocorrosion protective layer,⁵ energy⁶ or even as an antibacterial barrier,⁷ have been proposed. Generally, in most of the applications, fullerenes were immersed in a hybrid layer in the form of fullerene agglomerates. In this strategy, fullerenes were involved as the bulk phase, allowing only a small fraction of individual fullerene molecules to be accessible for interaction with the other phases/materials. Surface accessibility is the most important criterion towards many applications. To achieve a higher surface accessibility compared to conventional methods, advanced synthesis strategies in adequate hierarchical forms need to be developed. In this context, three-dimensional (3D) architected substrates play an important role as they can support nanocrystals (or several monolayers) of fullerenes on their surface, thereby increasing the overall accessibility. An appropriate highly porous and non-conductive 3D cellular material in which fullerenes can be homogeneously decorated on the surface would provide new fundamental research scopes in the direction of the fundamental structure–property relationship and can also lead to a large number of advanced

^aInstitute for Materials Science, Kiel University, Kaiserstr. 2, D-24143, Kiel, Germany. E-mail: lk@tf.uni-kiel.de, ra@tf.uni-kiel.de, ykm@tf.uni-kiel.de

^bDepartamento de Física & I3N, Universidade de Aveiro, 3810-193 Aveiro, Portugal. E-mail: tita@ua.pt

^cDepartment of Microelectronics and Biomedical Engineering, Technical University of Moldova, 168 Stefan cel Mare Blvd., MD-2004, Chisinau, Republic of Moldova

^dCondensed Matter Theory, Materials Theory Division, Department of Physics and Astronomy, Uppsala University, Box 516, SE-751 20, Uppsala, Sweden

^eCAS Center for Excellence in Nanoscience, Beijing Institute of Nanoenergy and Nanosystems, Chinese Academy of Sciences, Beijing, 100083, China

†Electronic supplementary information (ESI) available. See DOI: 10.1039/c8nr01504j

applications because of high surface accessibility and simplicity of use.

Nanoarchitected porous materials in the 3D form are the most adequate candidates for such desired applications, boosting their research focus in the last couple of years. Various physical, chemical, and biologically inspired and other innovative strategies have been adopted for their fabrication. However, issues like versatile fabrication, cost effective process, upscalability, *etc.*, have been the main concerns for the advanced materials community. Structural aspects of nanomaterials could play a very important role in this context, since a macroscopic porous network material can be easily built out of complex shaped nanostructures, for example from nanosearchins, tetrapods, multipods, *etc.*, in a cost-effective way which could be rather efficient in contrast to complex multistep processes or clean room technologies.⁸ Because of its unique crystalline nature, zinc oxide (ZnO) is a remarkable candidate for complex nanostructuring and the usually flame based process offers the possibility of a large scale growth of nano- and micro-tetrapods.^{8a,b} These tetrapods are formed with four interconnected arms *via* a central core, facilitating the easy accessibility of 1D nanoscale features in a complex 3D shape and offering large technological opportunities.^{8b,9} Additionally, these zinc oxide tetrapods can be used as building blocks for synthesizing highly porous 3D interconnected networks, which can be used as solid backbones for fabricating hybrid materials or as sacrificial templates¹⁰ for developing a new class of porous 3D materials.^{8a,b,11}

With n-type conductivity, ZnO is one of the most active materials from the II–VI metal oxide semiconductor family because of its hexagonal-wurtzite crystal structure, featuring a high polarity along the *c*-axis, supported versatile growth nature and unique physical (*e.g.* optical and electrical) properties.^{1e,12} The complex shapes additionally facilitate ZnO nanomaterials with many structural aspects, thereby making tetrapods from ZnO a very relevant nanomaterial candidate for various technological applications.^{8b} In order to enhance or even tune their properties, the ZnO nanostructures need to be hybridized with other nanostructured materials. For the successful fabrication of any hybrid materials, two necessary requirements should be fulfilled, (i) structural appropriateness of the underneath backbone, and (ii) desired properties of the nanostructures utilized for hybridization. Three dimensional networks consisting of interconnected ZnO tetrapods, which can be synthesized in large amounts by the flame transport synthesis, are a very adequate choice as the template.¹¹ Owing to the three dimensional shape of the tetrapodal microparticles, highly porous networks can be fabricated. Due to the super-hydrophilic properties of such templates and the large free volume, these networks can be homogeneously coated using any kind of nanoparticle dispersion.¹¹ Fullerene C₆₀ exhibits remarkable properties such as strong UV absorption, excellent electron accepting, charge transfer, *etc.*¹⁶ when used in the form of a very thin coating. Therefore, the characteristic features of individual C₆₀ molecules are very useful for the

desired functionalities. Both being very unique nanomaterials in terms of physical properties, accordingly we aimed to synthesize a 3D hybrid material in the form of C₆₀ coated ZnO tetrapods and investigate its optical, electronic, and sensing properties in detail.

Actually, ZnO and C₆₀ are very complementary, because they can significantly enhance each other's functionalities, thus making the hybrid system a very interesting candidate in terms of technological relevance.¹³ For example, ZnO is a very important gas sensing material and its sensitivity as well as selectivity can be further improved by decorating the ZnO surface with carbon nanostructures.^{12c,14} On the other hand, ZnO-fullerene based hybrid structures have shown increased electron mobility leading to an enhanced efficiency of solar cells.^{1b} Several hybrid material systems based on carbon-ZnO have been synthesized towards different applications^{14a,15} but to the best of our knowledge, the effect of fullerene layers on the ZnO surface has been less explored, and mainly with studies of its properties at room temperature (RT).¹⁶ A temperature dependent investigation might reveal more about the mutual effects of ZnO and C₆₀ with respect to each other's properties, for example, electron transfer behaviors,^{1a} optical responses and electrical conductivity changes, *etc.*

ZnO inherits n-type electrical conductivity due to unavoidable defects which can be easily enhanced by doping with group III elements.¹⁷ For optoelectronics applications, *e.g.*, LEDs, a p–n junction is required which provides the necessity to make ZnO p-type as well. But achieving p-type conductivity in ZnO is really difficult and has been a topic of discussion since ever.¹⁸ Although a successful p-doping of ZnO utilizing N,¹⁹ As or P sources has been reported, its stability and reproducibility are still an open topic. In general, p-type conductivity is achieved by doping with acceptor elements and this requirement is nicely fulfilled by fullerene molecules due to their strong charge ejecting properties.²⁰ Inspired by the unique properties of ZnO material and C₆₀, we have fabricated a C₆₀–ZnO tetrapod based hybrid 3D porous networked material, where fullerene molecules are strongly attached to the surface of nano-microscale arms of ZnO tetrapods by using a simple infiltration technique.¹¹ ZnO itself exhibits exceptional optical properties and the addition of C₆₀ introduces additional states within the bandgap, which promotes further advanced applications. In the present work, we successfully varied the amount of C₆₀ on ZnO tetrapods and investigated the samples' morphological, structural and optical properties in detail, under various conditions. The C₆₀ decorated ZnO samples have also been explored *via* low temperature photoluminescence (PL) studies, which indicate electron transfer processes from C₆₀ to ZnO. The computational modeling for the density of states of the C₆₀–ZnO hybrid system also supports the experimental results and preliminary gas sensing studies hinted its potential towards technological applications, showing excellent ethanol sensing properties. Since ethanol is one of the main products of alcoholic fermentation in winemaking processes,²¹ various studies have been

performed to develop cost-effective ethanol sensors for continuous monitoring of the ethanol concentration during the wine production.²²

Motivated by the abovementioned features, we synthesized hybrid composites using flame based ZnO tetrapods covered with different C₆₀ floodings in a simple strategy.¹¹ The hybrid composites were fully characterized by morphological, structural, optical and electrical techniques. Optical spectroscopy investigations highlighted the effect of the C₆₀ addition on the absorption and luminescence properties of ZnO. Noticeable differences were observed in the near band edge (NBE) region with the amount of the C₆₀ floodings, namely an increase in the relative intensity of the free exciton (FX) and 3.31 eV emission line. Furthermore, exciting the composite samples at the maximum of the C₆₀ absorption band led to the observation of the ZnO green luminescence, evidencing the occurrence of charge transfer processes. Further rationalization of the interaction of C₆₀ with ZnO and the related charge transfer process was also supported by density functional theory (DFT) calculations.

Experimental

ZnO network synthesis

For the scaffold material for deposition of fullerenes a newly developed flame transport synthesis^{8a,23} was further modified. For this purpose a conventional muffle furnace,^{8a} with a metal crucible, is preheated up to 950 °C, and a nitrogen rich atmosphere is achieved using a N₂ gas flow of 41 L h⁻¹. After that, a simple Zn wire (of a total weight of 10–15 g, with a purity of approx. 99.95%) was inserted and placed into the metal crucible. After the temperature stabilization, pressured air was let into the furnace leading to a rapid Zn oxidation and thus to the formation of a large amount of ZnO 3D structures. In the next step, 3D ZnO pellets were formed out of the produced ZnO powder by compressing and sintering it at 1150 °C for 5 hours (Fig. 1a and S1a†).

Fullerene solution preparation

A water-based solution of fullerene powder (with 99.5% purity purchased at Sigma Aldrich) was prepared based on the

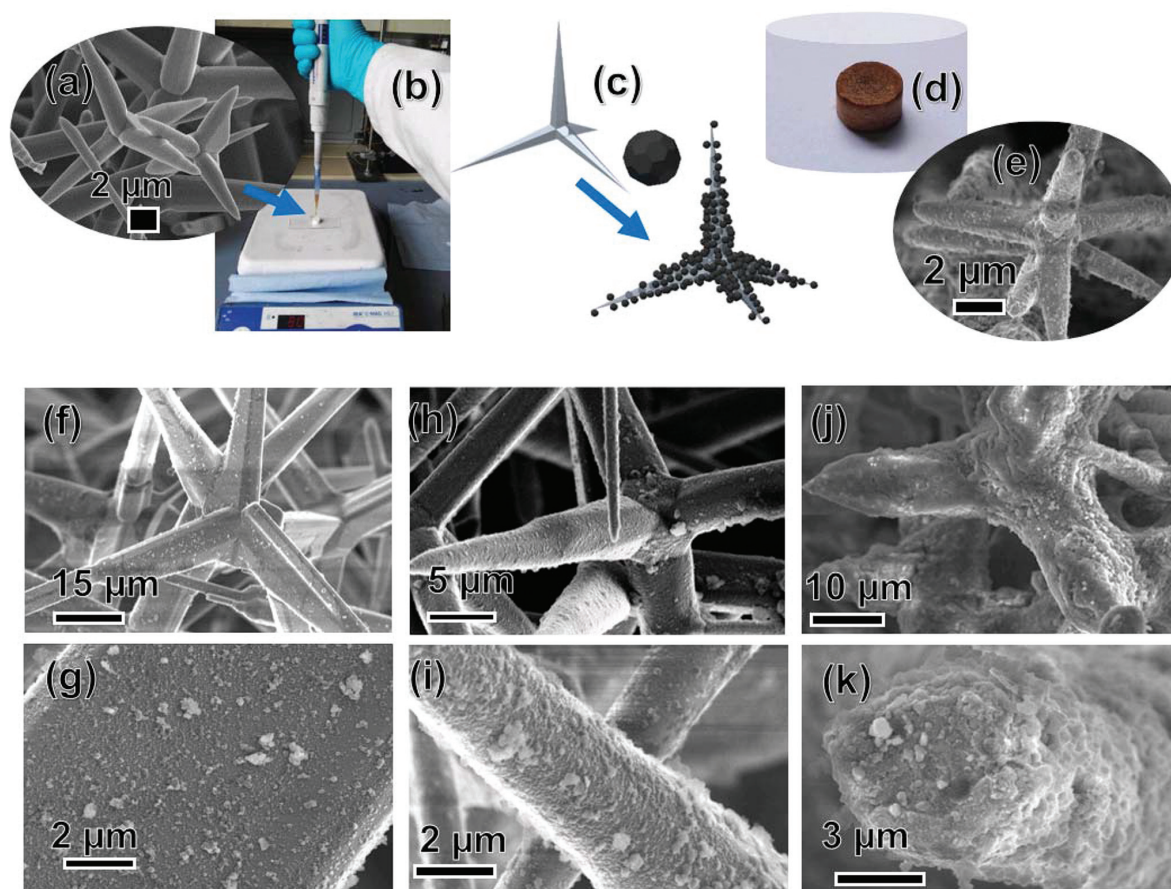


Fig. 1 ZnO microstructures and the process scheme: (a) SEM image of a ZnO-tetrapodal network after sintering. (b) Actual drop-coating process with a C₆₀ solution. (c) Schematics of the surface after a flooding process was performed. (d) Camera image of a ZnO pellet after the coating. (e) SEM image of the ZnO network coated with C₆₀. (f)–(k) SEM images of the density variation of C₆₀ on ZnO. (f,g) – 10 floodings, (h,i) – 20 floodings, (j,k) – 60 floodings.

method proposed,²⁴ where toluene was taken as a solvent (C_{60} exhibits excellent solubility in toluene).²⁵ First fullerene powder was diluted into toluene and then an identical amount (fullerene + toluene) of water was added into the solution and sonicated for several hours (typically 4 to 5 hours) until all the toluene was evaporated. Mixing the C_{60} in the toluene, with a slightly lower concentration (2.0 mg ml^{-1}) than the maximum reported solvable concentration (3.8 mg ml^{-1}),²⁴ and dispersing it with an ultrasonic tip, resulted in a dark purple solution with no visible precipitation of fullerenes. Additionally, the beaker with C_{60} -toluene solution was placed into the ultrasonic bath and the same amount of distilled water was rapidly added to the pristine solution. During the preparation of the solution with toluene no visible C_{60} precipitates were observed, however when the distilled water was added to the mixture and the sonication process started, two clear phases were visible: a dark purple phase (standing for toluene + C_{60}) and a white phase (representing the possible hydrogenation of C_{60}).²⁶ After several hours when the toluene was evaporated, the color of the solution changed to a yellowish-brown^{5,27} and a water based solution of fullerenes was successfully produced.

Drop-coating of the ZnO network

The so prepared C_{60} solution was subsequently drop-cast onto fresh sintered pellets of ZnO that were kept on a hot plate ($\sim 80 \text{ }^\circ\text{C}$), as shown in Fig. 1b. The moderate density of the pellets was chosen (0.3 g cm^{-3}) to guarantee a high porosity of the template for the optimal accessibility of the tetrapod surface for the C_{60} molecules. For the small size of the cylindrical pellets (3 mm in thickness and 6 mm in diameter), 50 μL of the solution was taken per round. A hot plate maintaining a temperature of $65 \text{ }^\circ\text{C}$ was utilized to accelerate the evaporation process. Intervals of 1.5 hours were kept between the rounds to let the water and the remaining solvents present in the solution evaporate (ESI Video, V1†). The total number of coating cycles was varied from 5–60, thus resulting in the total amount of fullerenes on the ZnO surface in the range of 0.5–6 mg, respectively. In the final step the C_{60} coated ZnO templates were dried in a vacuum furnace (at $65 \text{ }^\circ\text{C}$, 100 mbar, for at least 8 hours). Even though some drop-casting procedures took several weeks, the solution remained unchanged and formed no visible precipitates. Fresh sintered ZnO pellets revealed extreme hydrophilic properties, allowing a fast penetration of the droplet of the water solution of C_{60} , while the pellets that were kept for several weeks in the room with the typical humidity and the absence of UV light turned out to be hydrophobic. Performing a heating treatment of these templates at $600 \text{ }^\circ\text{C}$ in the ambient atmosphere for 30 min solves the problem of hydrophobicity.

Characterization

The produced ZnO/ C_{60} composites were characterized by scanning and transmission electron microscopy (SEM, TEM), Raman spectroscopy, absorption, photoluminescence, PL-excitation (PLE) and electrical measurements. SEM analysis was performed in a Zeiss Supra 55 V with a working voltage of 15

kV and a working current of 10 μA . For TEM characterization a Tecnai F30 STwin was used (with FEG, accelerating voltage of 300 kV, $C_s = 1.2$ and an EDAX EDX detector). A small amount of the hybrid network, consisting mostly of single tetrapods or even of only the tetrapod part, was placed on a Cu grid with a carbon mesh sample holder. In order to evaluate the chemical and structural composition of the ZnO/ C_{60} composites, RT Raman spectra were obtained by using an alpha300 RA, WITec system, with a triple grating spectrometer (600 gr mm^{-1}) and a CCD detector. The measurements were performed in a back-scattering geometry using the 532.2 nm line of a cw laser. The spot size of the laser on the sample was $\sim 1.41 \text{ } \mu\text{m}$, the maximum power at the sample was $\sim 52 \text{ mW}$ and the entire scattered beam was collected by an optical fiber with a diameter of 50 μm . The spectra were taken with a spectral resolution of 1 cm^{-1} . Additional measurements were performed in a Jobin Yvon HR800 spectrometer, using the 442 nm wavelength radiation from a cw He–Cd laser, a $\times 100$ magnification lens and a 1800 gr mm^{-1} diffraction grating.

The RT samples absorption was recorded in a UV/Vis JASCO V-560 system equipped with deuterium and halogen lamps and a ISV-469 integrated sphere. Steady state PL spectroscopy was performed as a function of temperature (from 10 K to RT) using a cold finger He cryostat. The 325 nm line of a cw He–Cd laser (power density $I_0 < 0.6 \text{ W cm}^{-2}$) was used as the excitation source, corresponding to an energy of $\sim 3.8 \text{ eV}$. The luminescence radiation was dispersed using a Spex 1704 monochromator (1 m, 1200 gr mm^{-1}), then it was detected with a cooled Hamamatsu R928 photomultiplier. All the measurements were conducted using a neutral density ND1 filter to avoid damaging the samples by overheating with the UV radiation. The RT PLE was assessed in a Fluorolog-3 Horiba Scientific set-up with a double additive grating Gemini 180 monochromator (1200 gr mm^{-1} and $2 \times 180 \text{ mm}$) in the excitation and a triple grating iHR550 spectrometer in the emission (1200 gr mm^{-1} and 550 mm). As excitation source a 450 W Xe lamp was used. The PLE has been measured by setting the monochromator in the maxima of the optically active defects and the excitation has been scanned to higher energies. Additionally, the same Fluorolog-3 system was used to perform energy dependent RT PL measurements. Namely, the RT PL of the ZnO/ C_{60} was evaluated by exciting the samples with below ZnO bandgap energy, corresponding to the blue absorption maxima reached after the functionalization with C_{60} .

I-*V* measurements were performed using a self-designed setup consisting of a PC-controlled micromanipulator with Cu/Au sputtered contacts, Keithley that is controlled through a Labview program allowing to measure the current flowing through the template at the set intervals in the studied voltage ranges. (Due to the still high template resistance 2-wire measurements were performed.) Cylindrical templates of the same ZnO density with and without C_{60} coating were analyzed. Several types of electrical contacts deposited at both ends of a cylindrical template were tested: adhesive silver paste with its solvent being evaporated, or sputtered gold contacts, or sputtered Ni–Au contacts.

Device preparation and gas sensing measurements

The devices based on ZnO/C₆₀ were fabricated using the same approach reported in previous studies,²⁸ while devices based on individual hybrid microstructures were fabricated in a FIB/SEM system using the procedure reported by Lupan *et al.*²⁸ Hybrid individual microstructures were contacted with a Pt complex to Au/Cr pads (Fig. S8a†). UV measurements were performed at RT in the dark and in air (relative humidity ~ 30%) and upon UV illumination at $\lambda = 365$ nm (~3.4 eV) and an intensity of ~10 mW cm⁻², as was reported earlier.^{8b} In the case of devices based on networks, gas sensing measurements were performed in the range of 20–400 °C, in order to determine the optimal operating temperature (OPT). For the devices based on individual structures, the measurements were only performed at RT. More details on gas sensing measurements were presented in our recent work.²⁸ The gas response (*S*) was defined as, $S = \left[\frac{R_{\text{gas}} - R_{\text{air}}}{R_{\text{air}}} \right] \times 100\%$ where *R*_{gas} and *R*_{air} are the resistance of the sensor under exposure to gas and ambient air, respectively.

DFT computational modeling

Under the framework of density functional theory (DFT)²⁹ computational modeling is performed using the Vienna *ab initio* simulation package (VASP).³⁰ The projector-augmented-wave (PAW)³¹ method as implemented in VASP is used with the Perdew–Burke–Ernzerhof³² (PBE) variant of the generalized gradient approximation (GGA) as the exchange correlation functional. A plane-wave cutoff of 520 eV has been kept for the kinetic energy. We have also included van der Waals correction in the form of Grimme's semi-empirical corrections.^{32a} The hexagonal stable phase of ZnO (space group *P6₃mc*) has been considered in our modeling where each Zn atom occupies the tetrahedral void formed by 4 adjacent O atoms and a similar configuration is maintained for O atoms. We have considered a supercell of ZnO to model the surface adsorption of C₆₀ molecules on the oxide. The fullerene molecule is adsorbed on the (0 0 1) surface of ZnO. A space of 30 Å is kept along the *c*-direction to avoid any spurious interactions of the simulation cell with their periodic images. During structural relaxation, to minimize the computational cost associated with a relatively large supercell, only top one layer of ZnO along with the adsorbed molecules on it is allowed to relax keeping the bottom layers of ZnO fixed. The Brillouin zone was sampled with a *k*-mesh of within the Monkhorst-Pack³³ scheme.

Results and discussion

The fabrication strategy for the C₆₀-ZnO based hybrid composites is presented in Fig. 1(a–d). The micro- and nanoscale tetrapods with pyramidal arms (length in the range of 10 to 50 μm, base and tip diameters ~10 μm and 500 nm, respectively) as shown in the scanning electron microscopy image in Fig. 1(a) are utilized as a backbone for C₆₀ molecules

decoration. The tetrapod based 3D interconnected network tablets with a porosity of ~92%, which were achieved by post-sintering (favors interconnections), were infiltrated with commercially available C₆₀ in the solution form *via* a pipette (Fig. 1b and ESI Video, V1†). The high porosity and hydrophilicity in the network allow a homogeneous flow of C₆₀ based solution in the entire network and drying results in an attachment of C₆₀ molecules on the surface of the ZnO tetrapod arms (Fig. 1c). The amount of C₆₀ molecules decorated on ZnO tetrapods depends on the number of infiltrations and the used concentration of the dispersion. The initial ZnO templates are white in color (Fig. 1b), turning into brownish color (Fig. 1d and S1†) after C₆₀ infiltrations (~50 floodings). The number of floodings is the most important parameter deciding the C₆₀ coverage at ZnO tetrapod arms and, depending on the requirements, from well separated C₆₀ molecules to continuous C₆₀ layers (mono and multiple) on the surface of ZnO tetrapod arms can be easily achieved by the here adopted drop-cast strategy. Typical SEM images corresponding to C₆₀ coated ZnO tetrapods from the hybrid network in Fig. 1d are shown in Fig. 1e, S2 and S3.† The detailed SEM analysis of the coated templates revealed a homogeneous coverage of the ZnO tetrapods and, depending on the number of cycles (ESI Video, V1†), more or less dense distribution of C₆₀ was achieved (Fig. 1f–k, S2 and S3†). However, measuring the smallest particle at the ZnO surface, it is visible that C₆₀ is drawn together forming clusters with sizes varying from 100 nm to 1 μm (Fig. 1g, i, k and S3†).

The crystallinity of the ZnO/C₆₀ was evaluated by electron microscopy and Raman spectroscopy. In particular, transmission electron microscopy studies revealed the presence of fullerite, a crystalline solid C₆₀ modification.³⁴ In bright field mode several clusters attached to ZnO tetrapods have been identified as shown in Fig. 2(a and b). High resolution TEM studies confirmed a highly crystalline arrangement, demonstrated in Fig. 2c. The corresponding fast Fourier transform pattern (Fig. 2d) matches well with a simulated electron diffraction pattern from the cubic C₆₀³⁵ in the [1 0 2] orientation (Fig. 2e). Based on the high resolution images, the interplanar spacing corresponds to 3.23 Å for (4 0 2) (literature value: 3.17 Å (ref. 36)) and 7.89 Å for (1 1 1) (literature value: 8.18 Å (ref. 36)). The deviation for (020) indicates an increased lattice parameter *b*. Moreover, a tilt in α and γ was observed. Similar to Fig. 2a many fullerite fractions have been identified next to ZnO tetrapods. Basically, C₆₀ molecules were arranged to form spherical clusters with diameters from 50 to 1000 nm (Fig. S3 and S4a†). By a selected area electron diffraction (SAED) pattern taken from the red marked region (Fig. S4b†) it was shown that every cluster is an independent crystalline domain (Fig. S4c†) and every interface between two spheres represents a domain boundary. Thus in the beginning small clusters of C₆₀ molecules start to agglomerate. While continuously growing occasionally clusters merge and form a common boundary.

RT Raman spectra of the ZnO/C₆₀ composites are presented in Fig. 2f. Beside the vibrational modes known for the ZnO

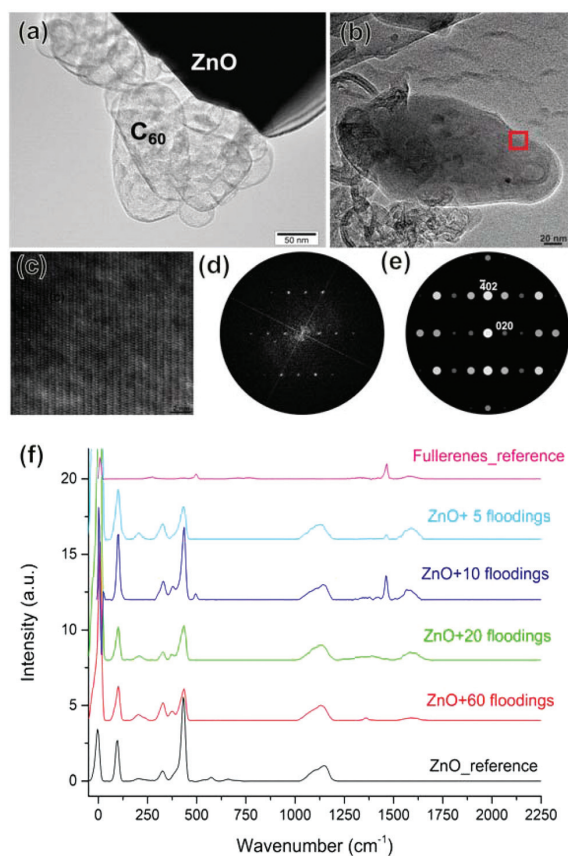


Fig. 2 (a) TEM low magnification bright field micrograph of several C_{60} clusters on top of a ZnO tetrapod surface (appearing black due to the larger thickness compared to the thickness of C_{60} clusters). (b) TEM bright field image of a single cluster of C_{60} . (c) HRTEM micrograph from the position marked in (b) aligned to [102]. (d) FFT pattern from (c). (e) Simulated ED-pattern from [102] orientation. (f) Raman spectra of reference fullerene powder (pink), reference ZnO network (black) and ZnO network coated with fullerenes. Number of floodings for the analyzed samples was: 5 (cyan), 10 (blue), 20 (green) and 60 (red). For the ZnO network with 60 floodings of C_{60} on the surface the D peak at 1350 cm^{-1} becomes sharper and more defined.

(black curve), all of the peaks have been identified and correspond to the values reported in the literature for fullerenes.³⁷ For the latter, the strongest peak at 1469 cm^{-1} , the pentagonal pinch mode (PPM) corresponding to a totally symmetric $A_g(2)$ mode,³⁸ is seen in samples having the number of floodings from 5 to 20 (cyan, blue and green curves in Fig. 2f). The samples with 10 floodings (blue curve) show most clearly the presence of the further fullerene peaks $A_g(1)$ at 495 cm^{-1} and a broader peak at $1565\text{--}1581\text{ cm}^{-1}$ that could be assigned to the $H_g(8)$ mode. An interesting phenomenon is observed for the sample with the much higher counting (60 floodings, red curve), namely the distinct D band peak at 1350 cm^{-1} , well known for the carbon materials indicating the presence of defects. Explanation for that might be the fullerene structures

building a layer on top of ZnO and producing edge defects that are Raman active.³⁸

PL and PL excitation measurements were carried out in order to investigate the influence on the optical properties of the 3D ZnO networks by the addition of C_{60} . Fig. 3a depicts the normalized PL spectra of the ZnO/ C_{60} samples (from the UV to the near infrared) obtained at RT. All samples exhibit a dominant green/yellow emission band with maxima slightly shifted between the samples. While for the samples with 10 and 20 floodings the maxima are located at $\sim 2.23\text{ eV}$, the samples with the lowest (5) and highest (60) C_{60} content evidence a high energy shift of the band maximum peak position ($\sim 2.27\text{--}2.28\text{ eV}$). As reported in the literature,^{17b} this PL band is frequently composed by the overlap of different emitting centers, which may have different relative intensities in the analyzed samples, resulting in the shift of the maxima of the overall emission. Even so, if the emission is originated from the same optical center, the $\sim 50\text{ meV}$ apart could be related to distinct band bending effects on the ZnO electronic structure and ZnO/ C_{60} interface, assuming that the green/yellow band involves effective mass described electronic states. At 14 K (Fig. 3b), spectra are also dominated by the visible band, evidencing a vibrational assisted structure, similar to the so-called structured green band, widely reported in the literature.^{17b,39} Regarding the NBE recombination that appears in the UV region (inset of Fig. 3b and Fig. S5†), noticeable changes can be observed with increasing C_{60} content, meaning that distinct interactions between the ZnO surface and C_{60} molecules occur for the different hybrid systems. In particular, a strong quenching of the NBE is seen in the sample with the lowest (5) flooding. In this case, the NBE seems to be absent when compared with the visible emission, however an ultra-violet/blue band at 3.0 eV was also detected, probably related to disorder-induced defects, as was previously observed in thin films.⁴⁰ For the samples with higher floodings (10 to 60), a well-defined NBE emission was observed (Fig. 3c and S6†). While the sample with 10 floodings exhibits NBE PL mainly dominated by the Al-donor bound exciton transition, increasing the C_{60} floodings (20 and 60) promotes changes in the dominant donor bound exciton recombination, accompanied by the observation of the emission at 3.31 eV and its phonon-replicas. This line has been widely discussed in the literature⁴¹ and associated with distinct recombination mechanisms, such as structural defect-related transitions^{41,42} or surface excitonic contribution.⁴³ Recently, this emission was studied in detail by J. Rodrigues *et al.*⁴⁴ in ZnO microrods grown by laser assisted flow deposition (LAFD). This line was seen to dominate the low temperature PL spectrum in the UV region, evidencing a spectral shape similar to the one obtained for the ZnO/ C_{60} samples with 20 and 60 floodings. The reported work suggests a strong correlation of the 3.31 eV emission line with the presence of surface states, as identified by the influence of distinct plasma treatments on the recombination line intensity. In fact, the same authors observed an increase in the relative intensity of this line when ZnO tetrapods grown by LAFD were mixed with carbon nanotubes (CNTs).⁴⁵ This fact constitutes another

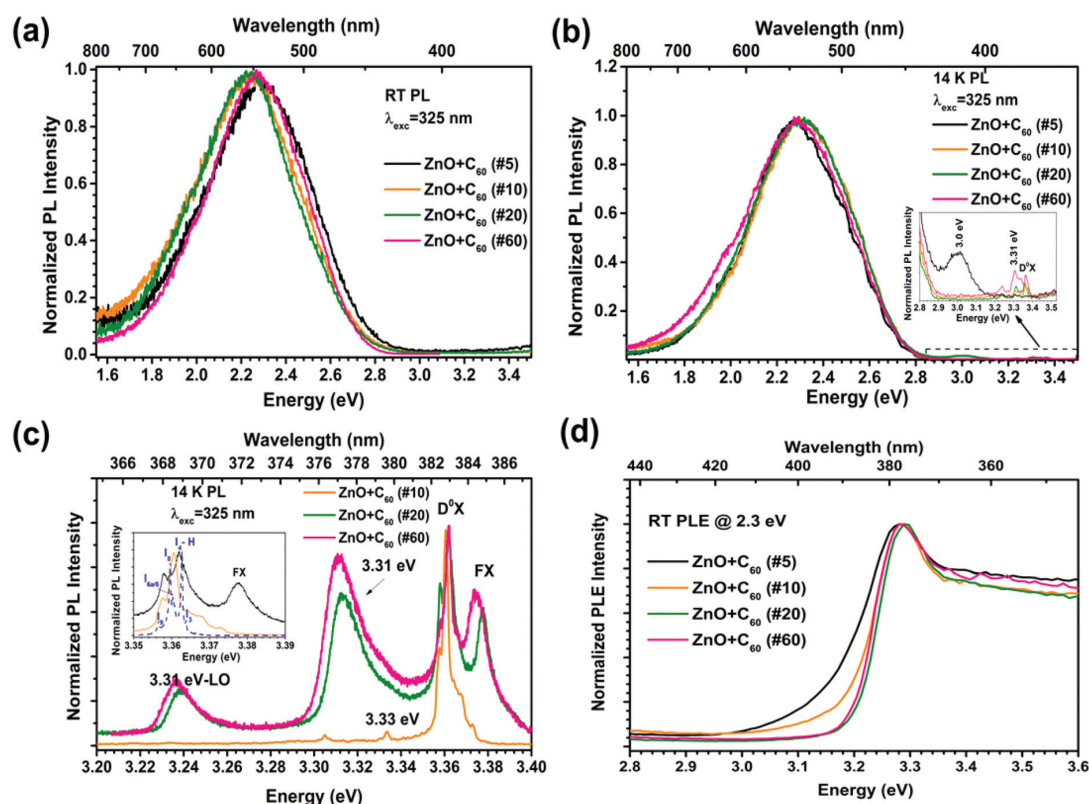


Fig. 3 (a) Normalized RT PL of the studied ZnO-T-C₆₀ samples, excited with 325 nm (3.8 eV photon energy) and using a ND1 filter. (b) Normalized 14 K PL spectra of the same samples under the same excitation conditions. The inset shows an amplification of the UV region. (c) Normalized 14 K PL spectra of the NBE region for the samples with 10, 20 and 60 floodings, evidencing a well-resolved emission. The inset includes high resolution spectra in the FX-D⁰X region and a comparison with the bulk ZnO emission (dashed line). (d) RT PLE spectra of the ZnO-T-C₆₀ samples with different floodings, monitored at 2.3 eV (visible band maximum).

indication that the 3.31 eV emission is affected by surface states. When incorporated in the CNT composite, the surface of the ZnO tetrapods was in direct contact with the functionalized CNTs, leading to a higher concentration of electron-hole pairs on the surface of the ZnO 3D structures. The enhancement of the PL intensity in ZnO/carbon composites was previously reported in the literature,^{15b,c} and attributed to the generation of a higher concentration of optically active centers, namely improving surface and excitonic related recombination. A similar phenomenon is likely to be present in the ZnO samples with a higher amount of C₆₀ on its surface and thus the enhancement of the relative intensity of the 3.31 eV emission. It is important to note that the intensity of this line increases with the increase of C₆₀, as in Fig. 3c. Moreover, besides the enhancement of the 3.31 eV emission, also the intensity of FX recombination is seen to increase (inset of Fig. 3c and Fig. S6†), accompanied by a decrease in the relative intensity of Al donor-bound exciton, meaning that with the used conditions an enhancement of free carrier concentration is favored rather than the carriers captured through the Al shallow donor. With the increase of C₆₀ floodings differences

in the electronic states band alignments are expected, inducing changes in the preferential recombination paths. Indeed, the offset between the lowest unoccupied molecular orbital (LUMO) of C₆₀ and the conduction band minimum (CBM) of ZnO defines the barrier for charge transfer between the two materials and was seen to depend on the thickness of the C₆₀ layer covering the ZnO structures.⁴⁶

These differences are also reflected in the RT PLE spectra (Fig. 3d) when monitored at the visible band maxima. The spectra show that the emission is mainly populated with photons with energy equal to or higher than the ZnO bandgap. Furthermore, it can be also shown that the ZnO bandgap absorption feature becomes slightly narrower as the C₆₀ floodings increase, exhibiting a steeper absorption and a slight shift towards the expected bandgap to pure ZnO. Such behavior indicates a suppression of the effective mass described electronic states in the population pathways of the broad emission, suggesting that a charge transfer from ZnO to C₆₀ cannot be discarded. As shown in Fig. 3d, the band tail observed below the ZnO bandgap is more pronounced for samples with lower C₆₀ floodings.

Comparing these results with the ones observed for the NBE emission, one notes that the absence of this emission in the sample with the lowest C_{60} floodings is accompanied by a more pronounced effect in the band tail states of the PLE spectra, while steeper absorption results in a well-resolved NBE (Fig. 3c and Fig. S6†). Absorption measurements (Fig. 4a) reveal, besides the ZnO bandgap, additional visible and near infrared absorption bands in the samples with C_{60} on the surface, where the band with the highest intensity is peaked at 448 nm (~ 2.77 eV). The wide absorption region appears when C_{60} is added to the ZnO tetrapods, with its intensity increasing as the C_{60} amount increases up to 20 floodings. For comparison, the RT absorption of a C_{60} sample from ref. 47 is included in Fig. 4a. As can be seen, the most intense absorption band in the visible region (dashed line in Fig. 4a) of the composite samples is not present in the C_{60} absorption spectrum, suggesting that its origin is likely related to ZnO- C_{60} interactions. The additional absorption bands are related to the C_{60} molecules.

In order to evaluate the possibility of charge transfer from the C_{60} molecules to ZnO, PL measurements were carried out exciting the samples at 448 nm (maximum of the mentioned absorption band), using a Xe flash lamp with a delay time close to the pulse lamp width in order to approach the steady-state conditions (Fig. 4b). For comparison purposes a band to band excitation was also performed using the same delay. In both cases a ZnO green band was detected, evidencing that this ZnO emission band can be populated *via* both excitation processes. The excitation at 448 nm corroborates the hypothesis of charge transfer from the C_{60} to ZnO. These results are also in line with the behavior observed for the ZnO NBE where an increase in the relative intensity of the FX and the 3.31 eV line was seen to occur with the increase of the amount of C_{60} in the ZnO surface, meaning that more electrons are being transferred to the ZnO conduction band and surface states, respectively. Fig. 4c shows a schematic representation of the possible band alignment for these materials, evidencing the two described charge transfer mechanisms suggested by the spectroscopic measurements.

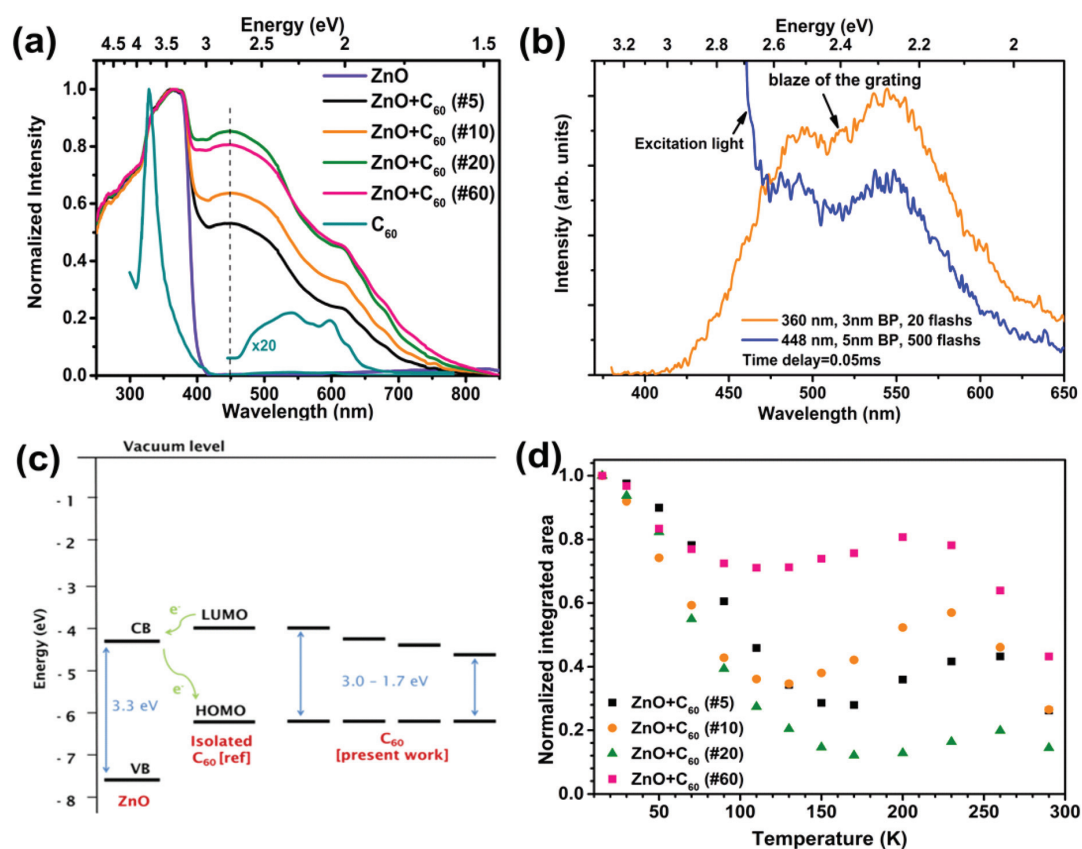


Fig. 4 (a) Absorbance spectra of the ZnO-T- C_{60} (C_{60}) absorption spectrum reproduced from ref. 56 and 57 and (b) RT TRPL of the sample with 20 floodings acquired after 0.05 ms of the pulse of a Xe flash lamp. The valley at ~ 517 nm (~ 2.40 eV) corresponds to the blaze of the grating. (c) Schematic representation of the band alignment for ZnO and C_{60} molecules, based on the spectroscopy results and ref. 3. (d) Relative intensity of the visible band as a function of the temperature for the analyzed samples.

In order to gain a better insight into the mechanisms involved in the luminescence process, temperature dependent PL studies were carried out, as can be seen in the ESI (Fig. S7†). Fig. 4d shows the dependence of the integrated green/yellow PL intensity band on the temperature. All the analyzed samples exhibited a similar behavior, with the overall intensity of the visible band decreasing up to 130–150 K followed by an increase in the intensity between these temperatures and 230–260 K and with a subsequent decrease up to RT. These results corroborate the hypothesis of having different optical active centers contributing to the broad visible emission. With increasing temperature, competitive nonradiative mechanisms start to take place, leading to a decrease in the intensity of all the emitting centers present. As the temperature rises, one of the defect states involved in green/yellow emission becomes thermally populated at the expense of another, resulting in an increase of the overall intensity. Finally, at higher temperatures, the nonradiative transitions dominate and the band intensity decreases again. A similar behavior was previously observed for ZnO with Zn_2SnO_4

and with Bi_2O_3 hybrid networks synthesized by the same method.^{39c}

Hybrid nanostructures, especially ZnO based, exhibit a very important role towards nanosensing, which also motivated us to investigate their sensing capabilities. Based upon the number of C_{60} floodings, individual micro- and nanoelectronic devices were fabricated and their detailed electrical sensing characteristics with respect to different volatile gases have been studied. Fig. 5 shows the SEM images of devices fabricated using individual zinc oxide tetrapod (ZnO-T) arms coated with C_{60} (ZnO-T-C_{60}). Three sets of devices were fabricated with relatively different contents of C_{60} on the surface of the ZnO-T arm: 10 floodings (Fig. 5a, its inset and Fig. S8a†), 20 floodings (Fig. 5b and inset) and 60 floodings (Fig. 5c and inset). The current-voltage (I - V) characteristics of the devices are presented in Fig. S8b,† showing the formation of asymmetrical double Schottky contacts, due to a higher work function of Pt contacts.⁴⁸ All individual structures have similar diameters in the range of 1–3 μm from one end to another. The calculated gas response of devices to different vapors of vola-

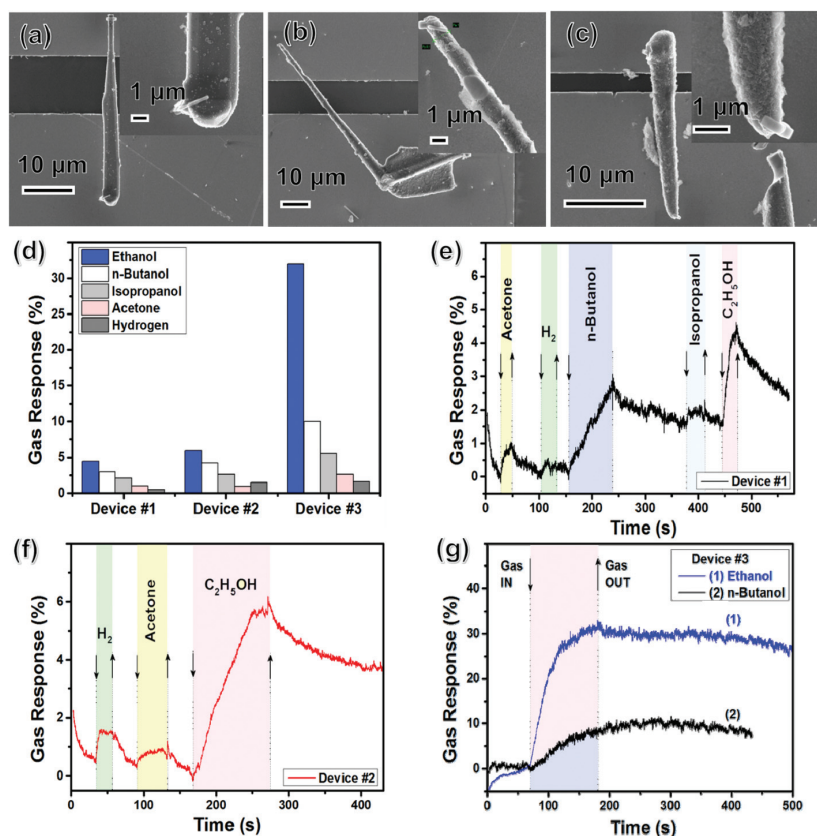


Fig. 5 SEM images of devices based on individual ZnO-T-C_{60} arms at lower and higher magnification to demonstrate the presence of C_{60} on the surface of a ZnO-T arm and electrical connections, respectively: (a) Device #1 – 10 floodings; (b) Device #2 – 20 floodings; (c) Device #3 – 60 floodings. (d) The calculated gas response at RT of fabricated devices using individual hybrid structures ZnO-T-C_{60} . The transient gas response at RT of: (e) Device #1; (f) Device #2; (g) Device #3.

tile organic compounds (VOCs) and hydrogen (H_2) gas is shown in Fig. 5d. The concentration of VOCs was 100 ppm and of H_2 gas was 1000 ppm. Actually, a previous study showed that pristine individual ZnO micro- and nanostructures showed a higher gas response to hydrogen gas (100 ppm),⁴⁹ with the highest gas response of $\sim 34\%$ (for pristine ZnO with a diameter of ~ 100 nm (ref. 49)). However, in the present case, a higher response to ethanol compared to H_2 gas is observed (see Fig. 5d).

Electrical contacts might lead to a varied sensing response and therefore nanodevices with both types (ohmic and Schottky) of contacts were fabricated and investigated, showing identical electrical/sensing characteristics. Hence, silver paste based ZnO/ C_{60} devices were chosen for the matter of simplicity. In line with the generation of more free carriers with increasing C_{60} floodings, a notable increase in the conductivity is observed (ESI, Fig. S9a†). Based on the linearity of the I - V curves, it can be assumed that an ohmic contact was achieved for the network templates and the corresponding dynamic UV sensing response is presented in Fig. S9b.† The calculated response (I_{UV}/I_{dark}) is ~ 1.6 , which is much lower compared to pristine ZnO-T networks reported earlier (>500). This can be explained based on complete covering of the ZnO tetrapod surface with C_{60} , hampering its accessibility for UV light to photogenerate the electron-hole pairs. The same situation was observed in the case of single ZnO-T- C_{60} structures (not shown here), which suggest that a lower content of fullerene on the surface of ZnO tetrapod arms would be rather preferable for gas sensing applications.

The here fabricated devices based on hybrid networks and individual structures demonstrated interesting gas sensing properties. By increasing the content of C_{60} the gas response to ethanol vapors is enhanced (taking into account that the diameter of structures is practically similar, Fig. 5). Thus, for Devices #1 (10 floodings), #2 (20 floodings) and #3 (60 floodings) the gas response to ethanol vapors is 4.43%, 6% and 32%, respectively (see Fig. 5d). The dynamic response to VOCs (100 ppm) and H_2 (1000 ppm) is shown in Fig. 5e, f and g for Devices #1, #2 and #3, respectively. Due to the operation of devices at RT, the response and recovery time are relatively high. The calculated response and recovery time (defined as the time to reach and recover the 90% of full response) of ethanol vapors are, respectively, 45 s and >350 s for Device #1, 70 s and >350 s for Device #2, 80 s and >15 min for Device #3. Thus, the evident increase in response/recovery times by increasing the content of C_{60} is confirmed, which could be related to the lower accessibility of gaseous species to the ZnO surface or to a higher influence of C_{60} on the gas response mechanism. It has been demonstrated that carbon based materials have a slow recovery at RT to VOCs or different gases such as NH_3 and NO_2 .⁵⁰ Thus, a higher content of C_{60} can improve the ethanol vapor response, but results in slower recovery.

C_{60} mainly exhibits n-type semiconductor conductivity and the oxygen content can drastically change its electrical resistance.^{14d,51} Also, previous reports showed that C_{60} thin films have good response to VOCs.^{14a,d,e} Thus, the increase in gas

response to ethanol vapors can be attributed to an increase in C_{60} content. The main mechanism can be thus explained on the basis of the interaction of VOCs and H_2 molecules with oxygen from the C_{60} layer, creating CO_2 and water, respectively,⁵² as well as charge transfer between C_{60} and gas molecules.^{14a} However, additional studies need to be performed in order to determine the nature of complex adsorption of VOC molecules (physisorption or chemisorption).^{14e} The incomplete recoveries to the initial baseline in the present devices indicate the adsorption of VOC molecules *via* chemical adsorption, *i.e.*, a comparatively strong interaction with C_{60} .^{14e} Additionally, the C_{60} crystals behave like a sponge (with nanoscale porosity) in which the possibility of intercalation of VOCs cannot be ignored.⁵³ The interactions between few VOCs and C_{60} might lead to certain weak ionic bonds which then result in localizing them within the C_{60} crystal even at RT.⁵³ Due to RT, these reactions are relatively slow, which lead to lower response and especially recovery of devices (Fig. 5e–g).

Parameters such as sensitivity and limit of detection were also investigated for Device #3. Fig. S10† shows the dependence of ethanol sensitivity at RT *versus* concentration of ethanol vapors. The sensitivity was defined as the gas response (S) divided by the concentration of ethanol, *i.e.* %/ppm.⁵⁴ The theoretical detection limit was estimated to be 5 ppm as was reported in detail by Dua *et al.*, *i.e.* using (signal/noise) ratio.⁵⁵ In general, such high response of microscale individual structures (diameter ~ 1 μm –3 μm), as in the case of Device #3 ($\sim 32\%$), can be easily explained on the basis of the C_{60} coverage on ZnO, because the surface contribution to the electron transport through the ZnO-T arm is quite lower.⁵⁶ Since both the C_{60} thin films and ZnO show n-type gas sensing behaviors,^{14d,51,57} it is very hard to distinguish which dominates the gas response in the case of the C_{60} -ZnO hybrid. However, the increased gas response to VOCs and increased recovery time hint that the C_{60} film from the surface of the ZnO-T arm is most likely a dominating factor for the here fabricated devices. In the case of ZnO-T- C_{60} networks, the degradation in response by increasing the temperature was observed. Fig. S11a† shows the gas response of networks *versus* operating temperature. The optimal temperature seems to be at 300 °C and the highest gas response was observed for the ethanol vapors. The data were calculated by applying one pulse at each operating temperature. However, by repeating measurements at the same temperature, the evident degradation in response was observed. Fig. S11b† shows the transient gas response of ZnO-T- C_{60} networks at 300 °C by exposing repeatedly to the same concentration of ethanol vapors 5 times. A large shift in the electrical baseline is observed, which also induces the change in gas response. Such behavior was observed at temperatures higher than 200 °C, which can be attributed to the destruction (conversion to amorphous structures and disintegration into icosahedral) of C_{60} molecules, as reported by Chen *et al.*⁵⁸

The adsorption behavior of C_{60} fullerene on the surface of ZnO was assessed by computing the binding energy of the system ($E_{(ZnO+C_{60})} - E_{ZnO} - E_{C_{60}}$). We obtain a binding energy of

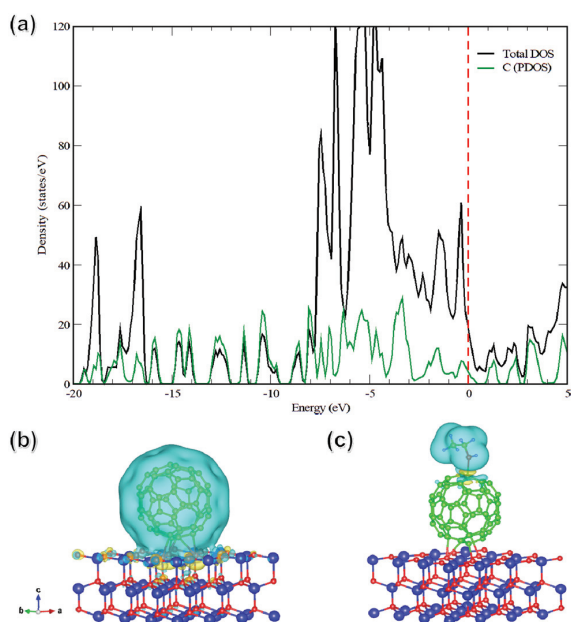


Fig. 6 (a) Total and partial DOS for fullerene (C_{60}) adsorbed on ZnO surface, (b) charge density difference isosurfaces for binding of C_{60} on ZnO surface, and (c) binding of ethanol on ZnO + C_{60} system. (The vertical red dashed line in (a) represents the Fermi energy. For isosurface, the yellow color depicts charge depletion and the cyan color charge accumulation. The isovalue used is 0.001 (a.u.). Atom color code: Zn (blue); O (red); C (green).)

−5.1 eV, which indicates relatively stronger binding of fullerene on the ZnO surface. For a deeper understanding of the binding process, we have presented the total and partial density of states (DOS) for ZnO + C_{60} in Fig. 6a. It is clear from this figure that following the adsorption of fullerene, significant states are induced which is evident from the partial DOS of C atoms from C_{60} . Moreover, states at the Fermi level with visible contribution of C_{60} are evident from this figure. This can explain the effect of C_{60} on the observed enhancement of conductivity. We have performed a Bader charge analysis of the binding process and calculated the amount of charge transfer associated with fullerene adsorption on ZnO. We have observed that there is a charge transfer from C_{60} to the ZnO surface with a net charge of +0.629 (e) on the fullerene molecule. It is known from the literature that the chemical nature of C_{60} resembles an n-type semiconductor and it is a highly electronically rich species. The stronger interaction of C_{60} with the ZnO surface and the resulting charge transfer are supportive of the above fact. To address the promising ethanol sensing properties of C_{60} covered ZnO as observed in our experiments, we further considered the adsorption of an ethanol molecule on the ZnO + C_{60} system. The adsorption energy in this case is found to be −0.39 eV, which indicates weak physisorption. The overall adsorption of C_{60} on the ZnO surface and subsequent adsorption of ethanol are pictorially depicted as isosurface plots in Fig. 6b and c. The favorable

sensing of ethanol gas on C_{60} can be attributed to the charging effect of the fullerene molecule on the ZnO surface.

Conclusions

In summary, we have demonstrated a simple strategy for cost-effective fabrication of C_{60} decorated ZnO tetrapod-based hybrid nanostructures and the corresponding 3D interconnected networks, which offer easy accessibility of features from individual as well as agglomerated C_{60} molecules in 3D space. The remarkable features from both C_{60} and ZnO tetrapods complement each other and cumulatively result in new and interesting properties in the hybrid composite form, suitable for advanced applications. Detailed photoluminescence, photoluminescence excitation and absorption studies revealed interesting optical properties, including hints about the charge transfer process between the adsorbed C_{60} molecules and underneath ZnO. The charge transfer process was additionally confirmed by density functional theory calculations. The ZnO/ C_{60} nanostructure based individual nanodevices revealed interesting sensing behaviors towards volatile organic compounds where the operating temperature plays a very crucial role. The interesting optical and electrical properties open further avenues for the application of these ZnO/ C_{60} tetrapod based hybrid materials towards advanced technologies. However, understanding further properties would be highly interesting for the fundamental materials science community.

Author contributions

DS, RA, and YKM identified the idea and planned the study. DS, SS, LS, and FS synthesized and analyzed the materials. JR, AFM, NBS, MRC and TM carried out optical studies. DSM, GN and LK performed TEM studies. O. L. fabricated the micro- and nanosensors on single C_{60} -ZnO-T and sensors based on individual structures. DS, VP, and OL performed sensing investigations. NKJ and Rajeev A finalized DFT studies. DS, TM, Rajeev A, LK, YY, RA and YKM analyzed the data and wrote the paper with contributions from other authors.

Conflicts of interest

There are no conflicts to declare.

Acknowledgements

The Kiel authors thank the Deutsche Forschungsgemeinschaft for financial support under schemes: SFB 1261 TP [(A05, RA) & (A06, LK)], and SFB 677 (C14). Additionally, a part of the work was funded by FEDER funds through the COMPETE 2020 Programme and FCT (Portuguese Foundation for Science and Technology) funds through the project UID/CTM/50025/2013. The Uppsala authors would like to thank Swedish Research

Council (Grant No. 2016-06014) for financial support and SNIC and UPPMAX, Sweden for providing the computing time. This research was partly supported by the project Institutional 45inst-15.817.02.29A funded by the Government of the Republic of Moldova.

References

- (a) S. Kirner, M. Sekita and D. M. Guldi, *Adv. Mater.*, 2014, **26**, 1482–1493; (b) T. Hu, L. Chen, K. Yuan and Y. Chen, *Nanoscale*, 2015, **7**, 9194–9203; (c) H. W. Kroto, J. R. Heath, S. C. O'Brien, R. F. Curl and R. E. Smalley, *Nature*, 1985, **318**, 162–163; (d) J. Liu, A. G. Rinzler, H. Dai, J. H. Hafner, R. K. Bradley, P. J. Boul, A. Lu, T. Iverson, K. Shelimov and C. B. Huffman, *Science*, 1998, **280**, 1253–1256; (e) D. M. Guldi and M. Prato, *Acc. Chem. Res.*, 2000, **33**, 695–703.
- (a) T. Liu and A. Troisi, *Adv. Mater.*, 2013, **25**, 1038–1041; (b) D. M. Guldi, *Chem. Soc. Rev.*, 2002, **31**, 22–36.
- J. H. Shim, K. S. Lee, J. W. Seo and D. I. Son, *J. Nanosci. Nanotechnol.*, 2016, **16**, 12017–12020.
- T. Song, J. Huo, T. Liao, J. Zeng, J. Qin and H. Zeng, *Chem. Eng. J.*, 2016, **287**, 359–366.
- J. Wu, L. B. Alemany, W. Li, L. Petrie, C. Welker and J. D. Fortner, *Environ. Sci. Technol.*, 2014, **48**, 7384–7392.
- M. Pfohl, K. Glaser, A. Graf, A. Mertens, D. D. Tune, T. Puerckhauer, A. Alam, L. Wei, Y. Chen and J. Zaumseil, *Adv. Energy Mater.*, 2016, **6**, 1600890.
- D. Virovska, D. Paneva, N. Manolova, I. Rashkov and D. Karashanova, *Mater. Sci. Eng., C*, 2016, **60**, 184–194.
- (a) Y. K. Mishra, S. Kaps, A. Schuchardt, I. Paulowicz, X. Jin, D. Gedamu, S. Freitag, M. Claus, S. Wille, A. Kovalev, S. N. Gorb and R. Adelung, *Part. Part. Syst. Charact.*, 2013, **30**, 775–783; (b) Y. K. Mishra and R. Adelung, *Mater. Today*, 2018, DOI: 10.1016/j.mattod.2017.11.003; (c) D. Gedamu, I. Paulowicz, S. Kaps, O. Lupan, S. Wille, G. Haidarschin, Y. K. Mishra and R. Adelung, *Adv. Mater.*, 2014, **26**, 1541–1550.
- I. Paulowicz, V. Postica, O. Lupan, N. Wolff, S. Shree, A. Cojocar, M. Deng, Y. K. Mishra, I. Tiginyanu, L. Kienle and R. Adelung, *Sens. Actuators, B*, 2018, **262**, 425–435.
- I. Hölken, G. Neubüser, V. Postica, L. Bumke, O. Lupan, M. Baum, Y. K. Mishra, L. Kienle and R. Adelung, *ACS Appl. Mater. Interfaces*, 2016, **8**, 20491–20498.
- F. Schütt, S. Signetti, H. Krüger, S. Röder, D. Smazna, S. Kaps, S. N. Gorb, Y. K. Mishra, N. M. Pugno and R. Adelung, *Nat. Commun.*, 2017, **8**, 1215.
- (a) Z. L. Wang, *Mater. Today*, 2004, **7**, 26–33; (b) A. B. Djurišić, Y. H. Leung, K. H. Tam, Y. F. Hsu, L. Ding, W. K. Ge, Y. C. Zhong, K. S. Wong, W. K. Chan, H. L. Tam, K. W. Cheah, W. M. Kwok and D. L. Phillips, *Nanotechnology*, 2007, **18**, 95702; (c) Z. Yang and X. Dou, *Adv. Funct. Mater.*, 2016, **26**, 2406–2425.
- D. M. Guldi, F. Zerbetto, V. Georgakilas and M. Prato, *Acc. Chem. Res.*, 2005, **38**, 38–43.
- (a) P. Bairo, K. Minami, W. Nakanishi, J. P. Hill, K. Ariga and L. K. Shrestha, *ACS Nano*, 2016, **10**, 6631–6637; (b) A. P. Saab, M. Laub, V. I. Srdanov and G. D. Stucky, *Adv. Mater.*, 1998, **10**, 462–465; (c) H.-B. Lin and J.-S. Shih, *Sens. Actuators, B*, 2003, **92**, 243–254; (d) G. Sberveglieri, G. Faglia, C. Perego, P. Nelli, R. N. Marks, T. Virgili, C. Taliani and R. Zamboni, *Synth. Met.*, 1996, **77**, 273–275; (e) Y.-C. Chao and J.-S. Shih, *Anal. Chim. Acta*, 1998, **374**, 39–46.
- (a) W.-D. Zhang, L.-C. Jiang and J.-S. Ye, *J. Phys. Chem. C*, 2009, **113**, 16247–16253; (b) J. Rodrigues, D. Mata, A. J. S. Fernandes, M. A. Neto, R. F. Silva, T. Monteiro and F. M. Costa, *Acta Mater.*, 2012, **60**, 5143–5150; (c) B. K. Gupta, V. Grover, G. Gupta and V. Shanker, *Nanotechnology*, 2010, **21**, 475701.
- M. Baibarac, I. Baltog, A. Matea and S. Lefrant, *J. Cryst. Growth*, 2015, **419**, 158–164.
- (a) A. Janotti and C. G. Van de Walle, *Rep. Prog. Phys.*, 2009, **72**, 126501; (b) Ü. Özgür, Y. I. Alivov, C. Liu, A. Teke, M. A. Reshchikov, S. Doğan, V. Avrutin, S.-J. Cho and H. Morkoç, *J. Appl. Phys.*, 2005, **98**, 41301.
- L. Liu, J. Xu, D. Wang, M. Jiang, S. Wang, B. Li, Z. Zhang, D. Zhao, C.-X. Shan, B. Yao and D. Z. Shen, *Phys. Rev. Lett.*, 2012, **108**, 215501.
- A. Tsukazaki, A. Ohtomo, T. Onuma, M. Ohtani, T. Makino, M. Sumiya, K. Ohtani, S. F. Chichibu, S. Fuke and Y. Segawa, *Nat. Mater.*, 2005, **4**, 42–46.
- H. Li and J. L. Bredas, *Adv. Mater.*, 2016, **28**, 3928–3936.
- T. B. Goriushkina, A. P. Soldatkin and S. V. Dzyadevych, *J. Agric. Food Chem.*, 2009, **57**, 6528–6535.
- (a) J. Lozano, M. Fernández, J. Fontecha, M. Aleixandre, J. Santos, I. Sayago, T. Arroyo, J. Cabellos, F. Gutiérrez and M. Horrillo, *Sens. Actuators, B*, 2006, **120**, 166–171; (b) V. Postica, I. Hölken, V. Schneider, V. Kaidas, O. Polonskiy, V. Cretu, I. Tiginyanu, F. Faupel, R. Adelung and O. Lupan, *Mater. Sci. Semicond. Process.*, 2016, **49**, 20–33; (c) O. Lupan, V. Postica, J. Gröttrup, A. K. Mishra, N. H. de Leeuw and R. Adelung, *Sens. Actuators, B*, 2017, **245**, 448–461.
- Y. K. Mishra, G. Modi, V. Cretu, V. Postica, O. Lupan, T. Reimer, I. Paulowicz, V. Hrkac, W. Benecke and L. Kienle, *ACS Appl. Mater. Interfaces*, 2015, **7**, 14303–14316.
- Y. I. Prylutskyy, V. I. Petrenko, O. I. Ivankov, O. A. Kyzyma, L. A. Bulavin, O. O. Litsis, M. P. Evstigneev, V. V. Cherepanov, A. G. Naumovets and U. Ritter, *Langmuir*, 2014, **30**, 3967–3970.
- R. Ruoff, D. S. Tse, R. Malhotra and D. C. Lorents, *J. Phys. Chem.*, 1993, **97**, 3379–3383.
- F. Cataldo and S. Iglesias-Groth, *Carbon Materials, Chemistry and Physics*, 2010, vol. 2TS–Th.
- C. N. Kramer, *Fullerene Research Advances*, Nova Science Publishers, New York, 2007.
- O. Lupan, V. Postica, M. Mecklenburg, K. Schulte, Y. K. Mishra, B. Fiedler and R. Adelung, *J. Mater. Chem. A*, 2016, **4**, 16723–16730.

View Article Online

Paper

Nanoscale

- 29 W. Kohn and L. J. Sham, *Phys. Rev.*, 1965, **140**, A1133–A1138.
- 30 (a) G. Kresse and J. Furthmüller, *Comput. Mater. Sci.*, 1996, **6**, 15–50; (b) G. Kresse and D. Joubert, *Phys. Rev. B: Condens. Matter Mater. Phys.*, 1999, **59**, 1758–1775.
- 31 P. E. Blochl, *Phys. Rev. B: Condens. Matter Mater. Phys.*, 1994, **50**, 17953–17979.
- 32 (a) S. Grimme, *J. Comput. Chem.*, 2006, **27**, 1787–1799; (b) J. P. Perdew, K. Burke and M. Ernzerhof, *Phys. Rev. Lett.*, 1996, **77**, 3865–3868.
- 33 H. J. Monkhorst and J. D. Pack, *Phys. Rev. B: Solid State*, 1976, **13**, 5188–5192.
- 34 W. Krätschmer, L. D. Lamb, K. Fostiropoulos and D. R. Huffman, *Nature*, 1990, **347**, 354.
- 35 H.-B. Bürgi, R. Restori and D. Schwarzenbach, *Acta Crystallogr., Sect. B: Struct. Sci.*, 1993, **49**, 832–838.
- 36 D. L. Dorset and M. P. McCourt, *Acta Crystallogr., Sect. A: Found. Crystallogr.*, 1994, **50**, 344–351.
- 37 (a) R. Cusc, E. Alarcon-Llad, J. Ibanez, L. Artus, J. Jimenez, B. Wang and M. J. Callahan, *Phys. Rev. B: Condens. Matter Mater. Phys.*, 2007, **75**, G3; (b) P. K. Giri, S. Bhattacharyya, D. K. Singh, R. Kesavamoorthy, B. K. Panigrahi and K. G. M. Nair, *J. Appl. Phys.*, 2007, **102**, 93515; (c) N. Rana, S. Chand and A. K. Gathania, *Ceram. Int.*, 2015, **41**, 12032–12037.
- 38 (a) S. Guha, J. Menendez, J. B. Page, G. B. Adams, G. S. Spencer, J. P. Lehman, P. Giannozzi and A. S. Baroni, *Phys. Rev. Lett.*, 1994, **72**, 3359; (b) H. Kuzmany, R. Pfeiffer, M. Hulman and C. Kramberger, *Philos. Trans. R. Soc., A*, 2004, **362**, 2375–2406; (c) H. Fu, T. Xu, S. Zhu and Y. Zhu, *Environ. Sci. Technol.*, 2008, **42**, 8064–8069.
- 39 (a) A. F. Kohan, G. Ceder, D. Morgan and C. G. Van de Walle, *Phys. Rev. B: Condens. Matter Mater. Phys.*, 2000, **61**, 15019–15027; (b) R. Dingle, *Phys. Rev. Lett.*, 1969, **23**, 579–581; (c) O. Lupan, V. Postica, J. Gröttrup, A. K. Mishra, N. H. De Leeuw, J. F. C. Carreira, J. Rodrigues, N. Ben Sedrine, M. R. Correia and T. Monteiro, *ACS Appl. Mater. Interfaces*, 2017, **9**, 4084–4099.
- 40 M. Peres, S. Magalhães, M. R. Soares, M. J. Soares, L. Rino, E. Alves, K. Lorenz, M. R. Correia, A. C. Lourenço and T. Monteiro, *Phys. Status Solidi C*, 2013, **10**, 662–666.
- 41 (a) M. Schirra, R. Schneider, A. Reiser, G. M. Prinz, M. Feneberg, J. Biskupek, U. Kaiser, C. E. Krill, K. Thonke and R. Sauer, *Phys. Rev. B: Condens. Matter Mater. Phys.*, 2008, **77**, K08; (b) D. Tainoff, B. Masenelli, P. Melinon, A. Belsky, G. Ledoux, D. Amans, C. Dujardin, N. Fedorov and P. Martin, *J. Lumin.*, 2009, **129**, 1798–1801.
- 42 K. Thonke, M. Schirra, R. Schneider, A. Reiser, G. M. Prinz, M. Feneberg, J. Biskupek, U. Kaiser and R. Sauer, *Microelectron. J.*, 2009, **40**, 210–214.
- 43 (a) J. Fallert, R. Hauschild, F. Stelzl, A. Urban, M. Wissinger, H. Zhou, C. Klingshirn and H. Kalt, *J. Appl. Phys.*, 2007, **101**, 73506; (b) S. S. Kurbanov and T. W. Kang, *J. Lumin.*, 2010, **130**, 767–770.
- 44 J. Rodrigues, T. Holz, R. F. Allah, D. Gonzalez, T. Ben, M. R. Correia, T. Monteiro and F. M. Costa, *Sci. Rep.*, 2015, **5**, 10783.
- 45 J. Rodrigues, D. Mata, A. Pimentel, D. Nunes, R. Martins, E. Fortunato, A. J. Neves, T. Monteiro and F. M. Costa, *Mater. Sci. Eng., B*, 2015, **195**, 38–44.
- 46 P. Schulz, L. L. Kelly, P. Winget, H. Li, H. Kim, P. F. Ndione, A. K. Sigdel, J. J. Berry, S. Graham, J.-L. Brédas, A. Kahn and O. L. A. Monti, *Adv. Funct. Mater.*, 2014, **24**, 7381–7389.
- 47 (a) D. M. Guldi and M. Prato, *Acc. Chem. Res.*, 2000, **33**, 695–703; (b) G. H. Sarova and M. N. Berberan-Santos, *Chem. Phys. Lett.*, 2004, **397**, 402–407.
- 48 S. N. Das, J. P. Kar, J.-H. Choi, T. I. Lee, K.-J. Moon and J.-M. Myoung, *J. Phys. Chem. C*, 2010, **114**, 1689–1693.
- 49 O. Lupan, V. V. Ursaki, G. Chai, L. Chow, G. A. Emelchenko, I. M. Tiginyanu, A. N. Gruzintsev and A. N. Redkin, *Sens. Actuators, B*, 2010, **144**, 56–66.
- 50 Z. Ting, M. Syed, V. M. Nosang and A. D. Marc, *Nanotechnology*, 2008, **19**, 332001.
- 51 A. Hamed, Y. Y. Sun, Y. K. Tao, R. L. Meng and P. H. Hor, *Phys. Rev. B: Condens. Matter Mater. Phys.*, 1993, **47**, 10873–10880.
- 52 O. Lupan, V. Cretu, V. Postica, N. Ababii, O. Polonskyi, V. Kaidas, F. Schutt, Y. K. Mishra, E. Monaico, I. Tiginyanu, V. Sontea, T. Strunskus, F. Faupel and R. Adelung, *Sens. Actuators, B*, 2016, **224**, 434–448.
- 53 B. Morosin, R. Assink, R. Dunn, T. Massis, J. Schirber and G. Kwei, *Phys. Rev. B: Condens. Matter Mater. Phys.*, 1997, **56**, 13611.
- 54 S. T. Shishiyanu, T. S. Shishiyanu and O. I. Lupan, *Sens. Actuators, B*, 2005, **107**, 379–386.
- 55 (a) V. Dua, S. P. Surwade, S. Ammu, S. R. Agnihotra, S. Jain, K. E. Roberts, S. Park, R. S. Ruoff and S. K. Manohar, *Angew. Chem., Int. Ed.*, 2010, **49**, 2154–2157; (b) J. Li, Y. Lu, Q. Ye, M. Cinke, J. Han and M. Meyyappan, *Nano Lett.*, 2003, **3**, 929–933.
- 56 V. V. Sysoev, B. K. Button, K. Wepsiec, S. Dmitriev and A. Kolmakov, *Nano Lett.*, 2006, **6**, 1584–1588.
- 57 T. Arai, Y. Murakami, H. Suematsu, K. Kikuchi, Y. Achiba and I. Ikemoto, *Solid State Commun.*, 1992, **84**, 827–829.
- 58 H. S. Chen, A. R. Kortan, R. C. Haddon, M. L. Kaplan, C. H. Chen, A. M. Muzsca, H. Chou and D. A. Fleming, *Appl. Phys. Lett.*, 1991, **59**, 2956–2958.

Electronic Supplementary Material (ESI) for Nanoscale.
This journal is © The Royal Society of Chemistry 2018

Electronic Supporting Information

Figure S1

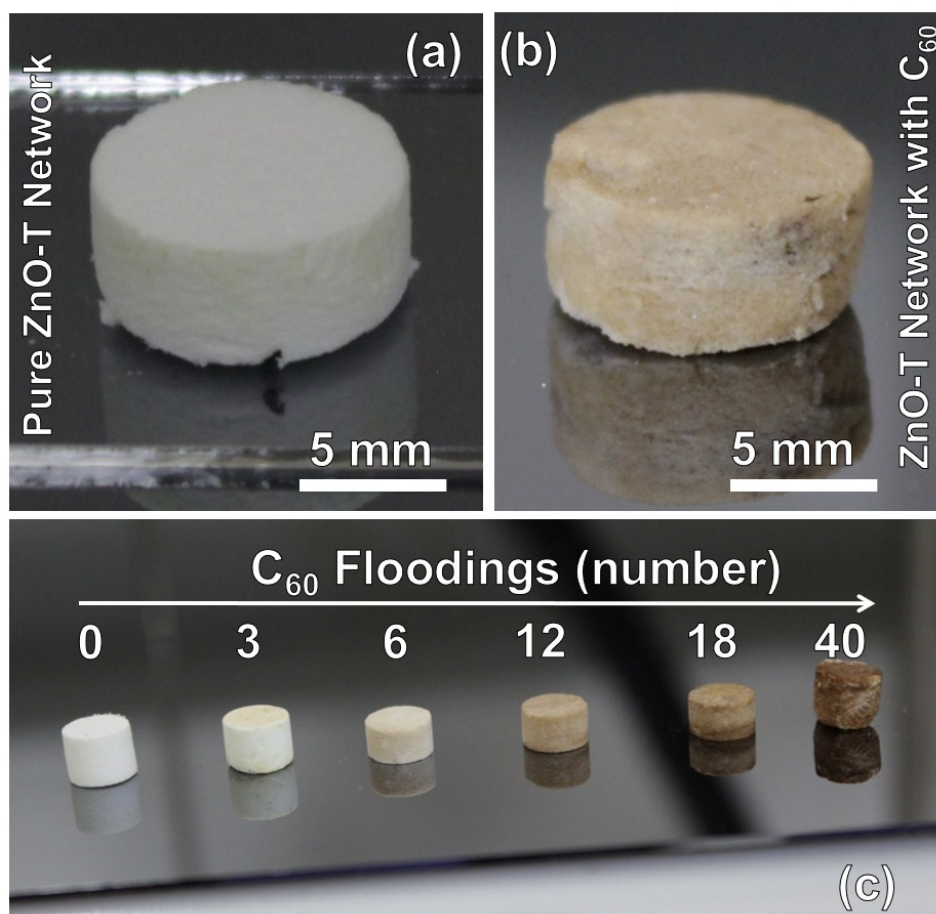


Figure S1: Camera images of the ZnO pellet before drop casting (a), and after 5 C₆₀ floodings (b). (c) Camera images of ZnO samples demonstrating their color change with increasing the amount of C₆₀ flooding times: 0-40 floodings (left to right).

Figure S2

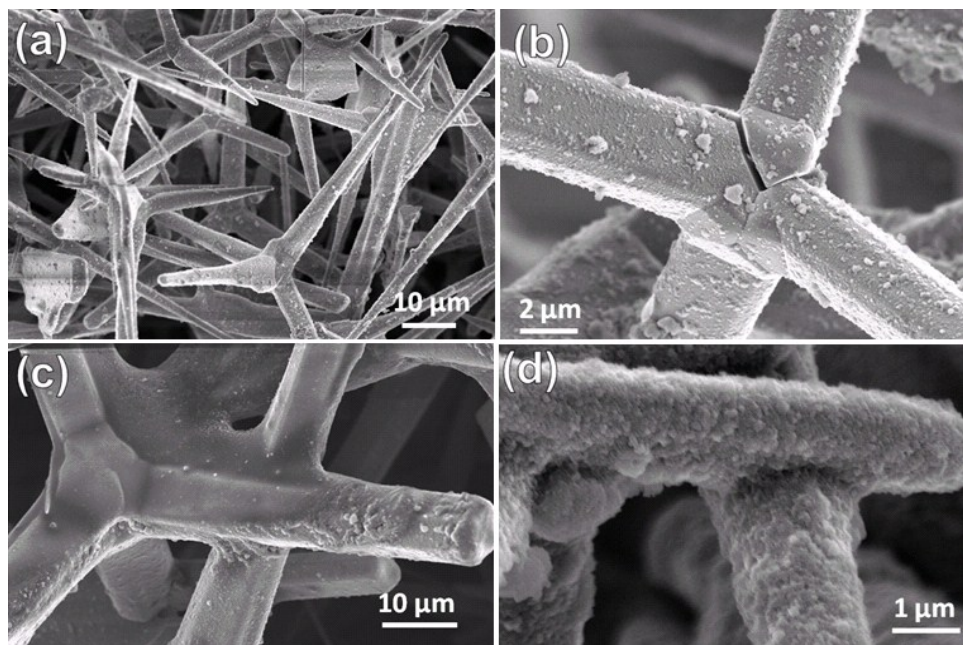


Figure S2: SEM images of ZnO networks after 10 floodings (a,b) and 40 floodings (c,d). After 40 drop-casting cycles agglomerations of C₆₀ are observed at the interconnection points between single tetrapods.

Figure S3

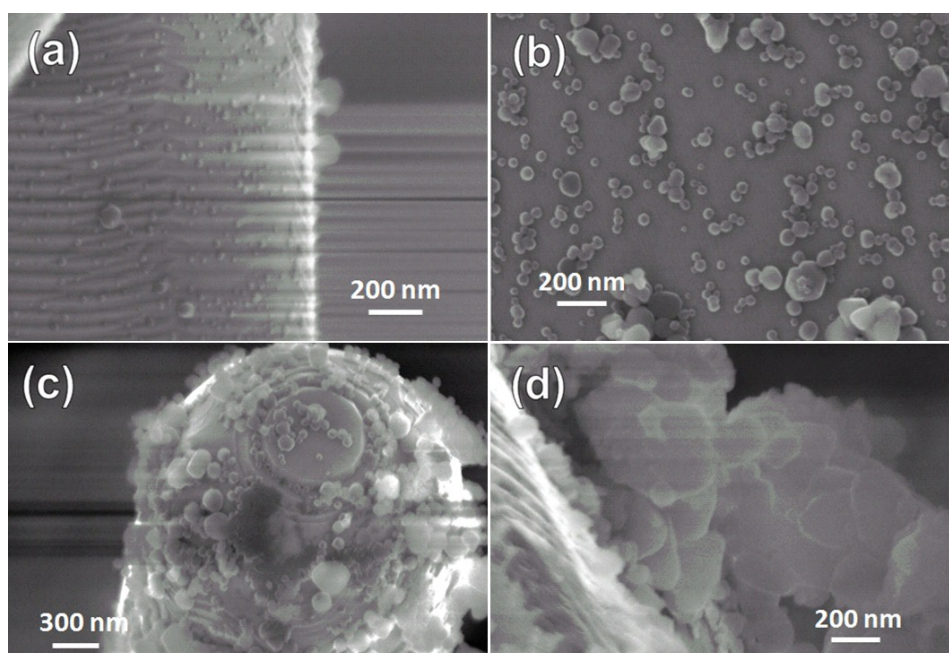


Figure S3: SEM images (higher magnification) of ZnO-T surface with C₆₀ after 3 floodings (a), 10 floodings (b), 40 floodings (c) and 60 floodings (d). For the low number of coatings with C₆₀ (3 and 10, a and b, respectively) isolated C₆₀ clusters are observed. By higher number of floodings the clusters tend to join forming a layer at the ZnO surface.

Figure S4

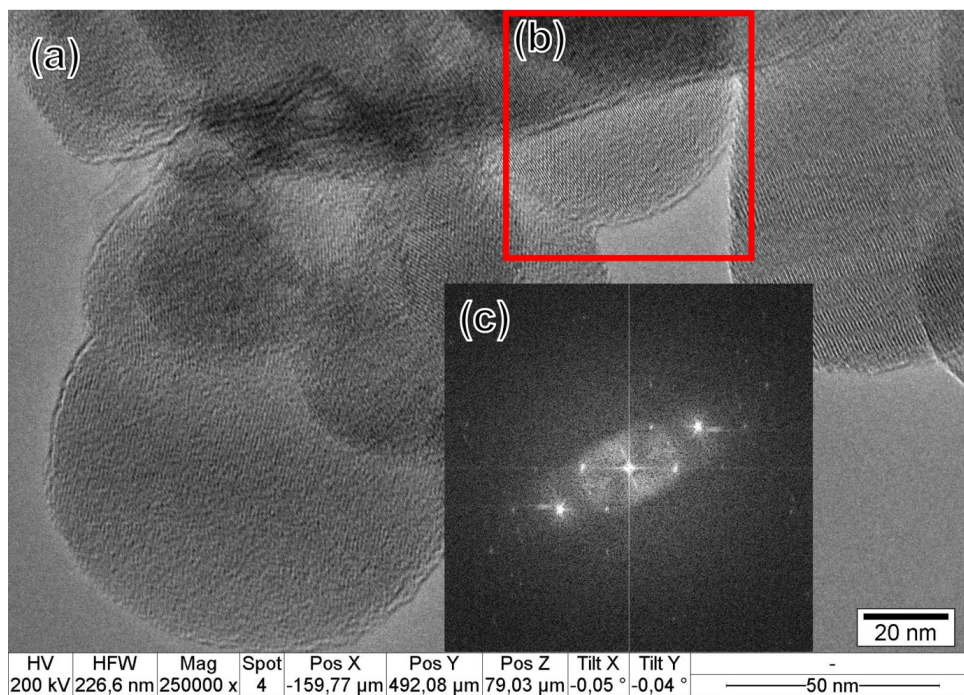


Figure S4: (a) TEM higher magnification image with an overview on fullerene clusters. From the red marked region (b) a FFT pattern was simulated (c), which indicates the crystallinity of the clusters. Also distinctive are the lines indicating the rows of the fullerene aligned into crystals.

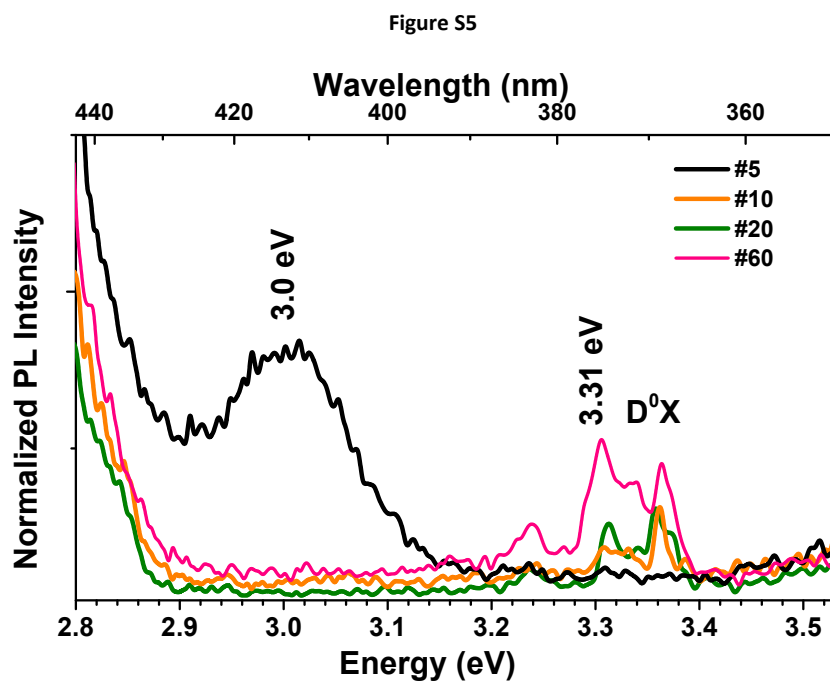


Figure S5: 14 K near band edge recombination (NBE) of the ZnO-T-C₆₀ composites. The spectra were obtained with above ZnO bandgap excitation.

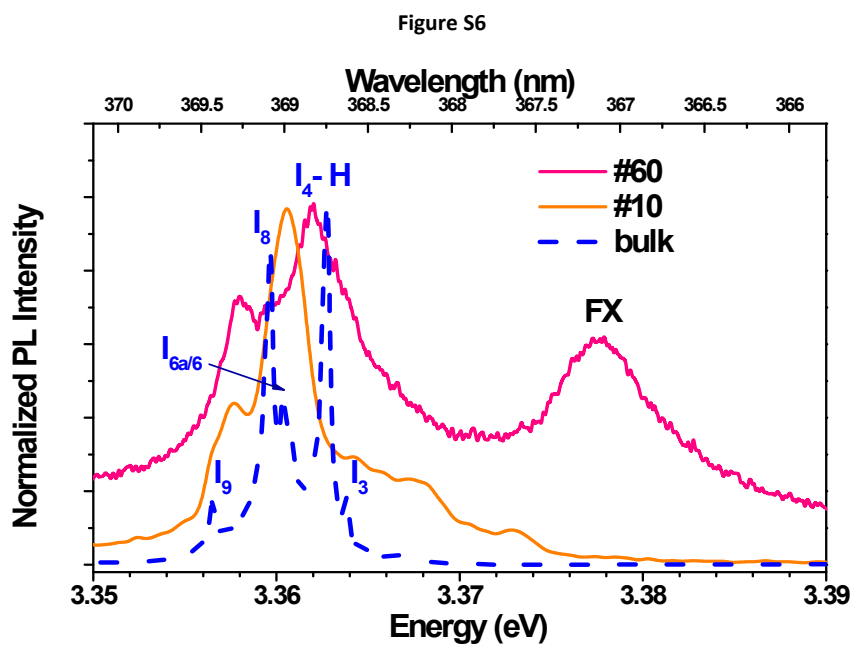


Figure S6: 14 K near band edge recombination (NBE) of the ZnO-T-C₆₀ composites: FX and bound excitons spectral regions. The spectra were obtained with above ZnO bandgap excitation.

Figure S7

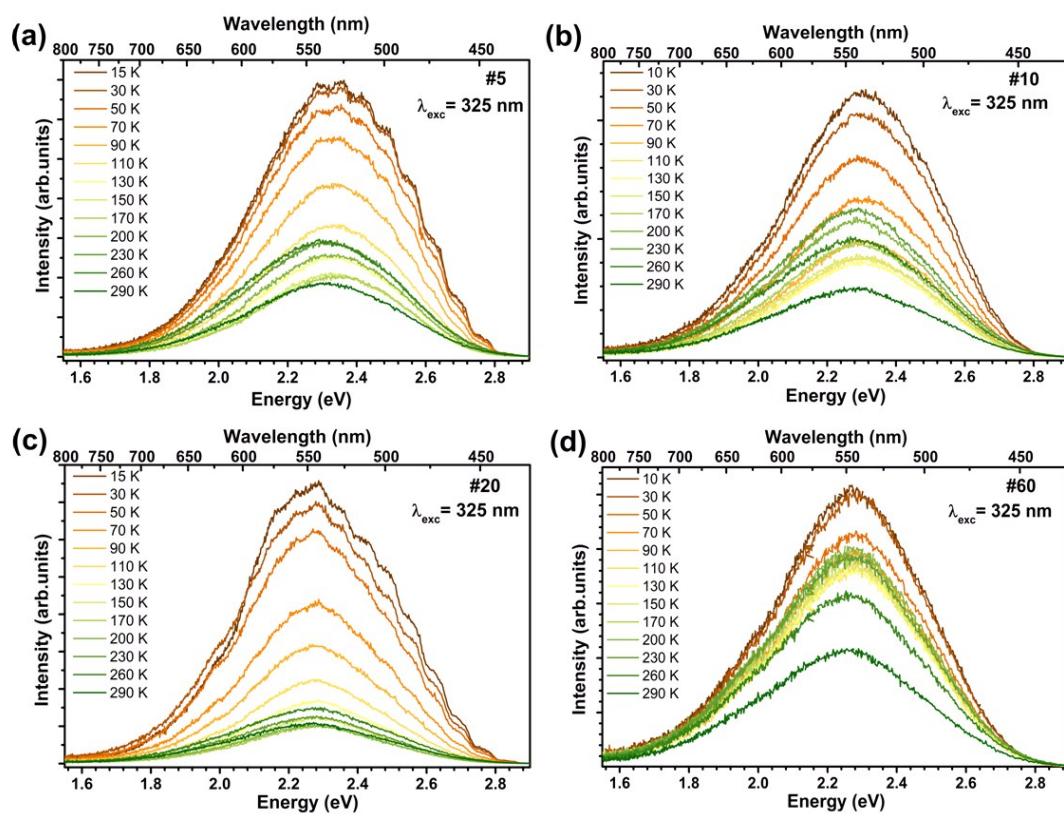


Figure S7: Temperature dependent PL spectra of the ZnO-T-C₆₀ composites. The spectra were obtained with above ZnO bandgap excitation in the interval range 10 K - RT.

Figure S8

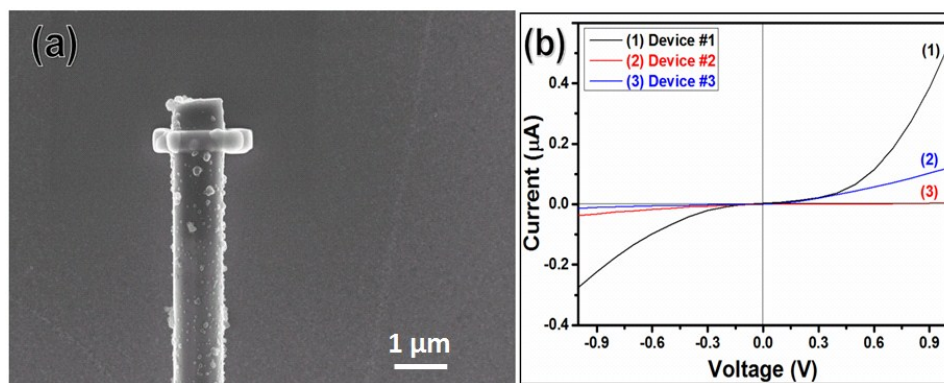


Figure S8: (a) The high magnification SEM image of Pt contacts on a nano-device 1 of a ZnO microtetrapod covered with 10 floodings of C_{60} aqueous solution. (b) Current – voltage characteristics of devices fabricated based on individual ZnO-T- C_{60} arms in the dark at room temperature.

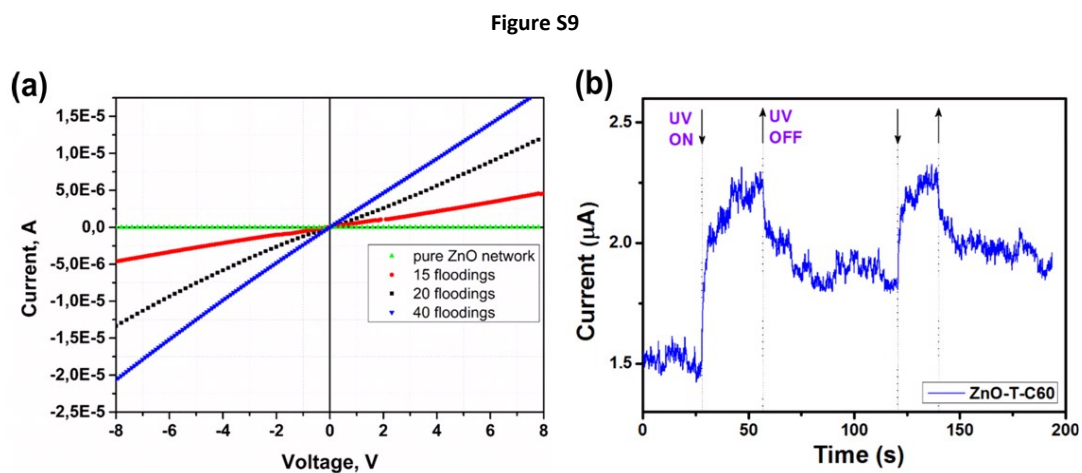


Figure S9: (a) Electrical characterization of a macroscopic template of a ZnO network and of ZnO-T-C₆₀ networks with different number of floodings. Starting with a reference network (pure ZnO), followed by networks with coatings of 15, 20 and 40 floodings of C₆₀. (b) Dynamic response of ZnO-T-C₆₀ networks to illumination with UV light at room temperature.

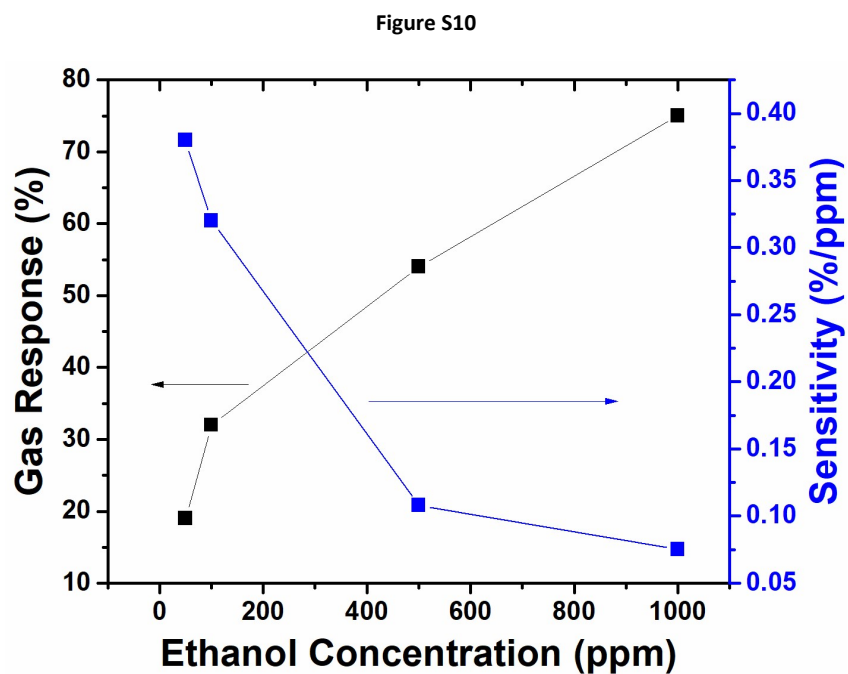


Figure S10: Dependence of room temperature gas response (%) and sensitivity (%/ppm) of Device #3 versus concentration of ethanol vapors (ppm).

Figure S11

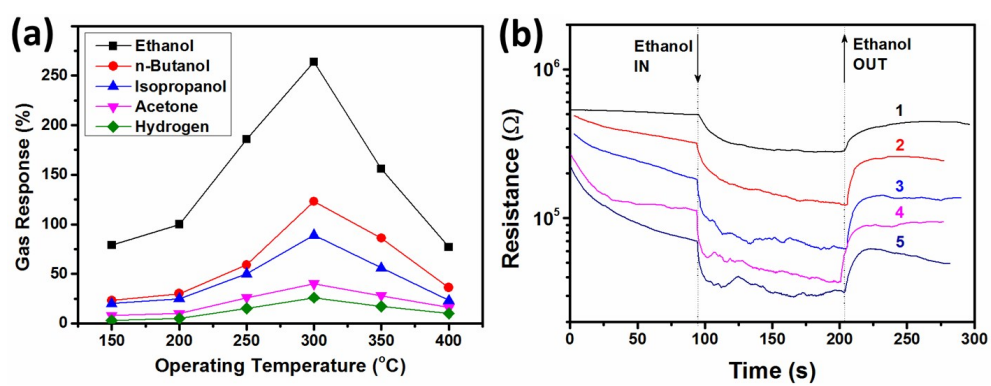


Figure S11: (a) The gas response versus operating temperature of ZnO-T-C₆₀ networks. (b) The dynamic gas response to five time exposures under ethanol vapors at 300 °C operating temperature of ZnO-T-C₆₀ networks.

Chapter 6

3D Hydrogels Containing Interconnected Microchannels of Subcellular Size for Capturing Human Pathogenic *Acanthamoeba Castellani*

Ordered microscopic holes in solids are interesting for, e.g., mimicking cellular environments or filtering applications. In this manuscript a manufacturing procedure of tubular networks in hydrogels based on highly porous ceramic ZnO scaffolds is presented. The predetermined order of the tetrapodal ZnO network and their interconnected nature is ideal as a framework for porous hydrogels. This work shows that filling a porous ZnO network with polyacrylamide hydrogel and subsequent etching of the ZnO by hydrochloric acid is a valuable subtractive approach to create guaranteed interconnected channels. It was shown that the networked channels with a diameter of less than 7 μm were able to capture the human pathogenic *Achantamoeba castelani*. The scaffolds can be used as an addition to incubation medium to capture harmful microbes.

The work was published in the journal "ACS Biomaterials Science & Engineering".

Own contribution presented in this article

- Sample preparation
- Scientific discussion
- Writing parts of the manuscript

The following content in this chapter is reproduced with permission.

This is an open access article published under an ACS AuthorChoice License, which permits copying and redistribution of the article or any adaptations for non-commercial purposes.



3D Hydrogels Containing Interconnected Microchannels of Subcellular Size for Capturing Human Pathogenic *Acanthamoeba Castellani*

Sören B. Gutekunst,[†] Katharina Siemsen,[†] Steven Huth,[†] Anneke Möhring,[†] Britta Hesseler,[†] Michael Timmermann,[†] Ingo Paulowicz,[§] Yogendra Kumar Mishra,[‡] Leonard Siebert,[‡] Rainer Adelung,[‡] and Christine Selhuber-Unkel^{*,†}

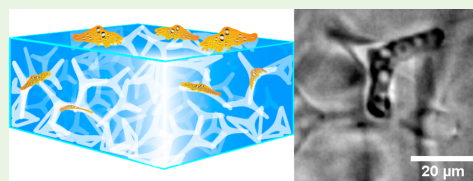
[†]Institute for Materials Science, Biocompatible Nanomaterials, and [‡]Institute for Materials Science, Functional Nanomaterials, University of Kiel, Kiel D-24143, Germany

[§]Phi-Stone AG, Kiel D-24143, Germany

Supporting Information

ABSTRACT: Porous hydrogel scaffolds are ideal candidates for mimicking cellular microenvironments, regarding both structural and mechanical aspects. We present a novel strategy to use uniquely designed ceramic networks as templates for generating hydrogels with a network of interconnected pores in the form of microchannels. The advantages of this new approach are the high and guaranteed interconnectivity of the microchannels, as well as the possibility to produce channels with diameters smaller than 7 μm . Neither of these assets can be ensured with other established techniques. Experiments using the polyacrylamide substrates produced with our approach have shown that the migration of human pathogenic *Acanthamoeba castellanii* trophozoites is manipulated by the microchannel structure in the hydrogels. The parasites can even be captured inside the microchannel network and removed from their incubation medium by the porous polyacrylamide, indicating the huge potential of our new technique for medical, pharmaceutical, and tissue engineering applications.

KEYWORDS: 3D ceramic templates, microchannels, porous hydrogel, cell migration, human pathogens



1. INTRODUCTION

The significant influence of the extracellular environment on a variety of cellular processes such as cell adhesion, proliferation, migration and differentiation has recently developed into a subject of high interest for cellular research.^{1–3} Cell migration, for instance, is controlled by the dimension^{4,5} as well as by the mechanical properties of the extracellular environment,^{6,7} where nuclear deformability, physical tissue constraints, cell stiffness, and cell adhesion are important limiting factors.^{8–10} Therefore, the manipulation and characterization of microstructural properties of materials provides novel opportunities to mimic extracellular environments in order to control cell migration.

A biomedically highly relevant application for controlling cell migration is to capture pathogenic microorganisms. For example, micron-sized lobster traps have been fabricated from silicone to capture swimming bacteria.¹¹ Such structure-based capture devices are very interesting, as they can provide cell capture without the requirement of additional chemical agents.

The medical advantages of cell-capturing materials become quickly apparent considering pathogenic cells that rely on adhesion to their surroundings. A medically dangerous,¹² adhesive,¹³ and extremely motile¹⁴ example of such pathogens is *Acanthamoeba castellanii* (*A. castellanii*). Upon contact with

the human eye, this amoeba invades the corneal tissue and leads to a painful and hard-to-treat *Acanthamoeba* keratitis, which can even cause blindness.¹⁵ This is an especially troubling issue as *A. castellanii* is found in a huge variety of environments such as water reservoirs (e.g., swimming pools or liquids for contact lens storage¹⁶) and soil, even despite disinfection procedures.¹⁷ Thus, the infection chance during everyday human life is comparably high.¹⁸ *A. castellanii* infections are especially severe as the parasite's motile trophozoite form can transform into double-walled cysts under unfavorable conditions to protect itself from medication, heat, or even radiation. This makes treatment procedures extremely long-lasting and complicated.¹⁹ Considering this, it is not only important to improve procedures that cure an *A. castellanii* infection, but also to find methods to avoid the infection in the first place. Conventional strategies to avoid *A. castellanii* infections are based on disinfection procedures,²⁰ which lack the efficiency to kill all the amoebae²¹ and strongly rely on the active cooperation of the potentially exposed person. Hence, they are prone to mistakes and

Received: August 24, 2018

Accepted: January 10, 2019

Published: January 10, 2019

capturing the amoeba using microstructured materials poses a highly promising alternative to these established methods.

Here, we introduce a novel approach to capture *A. castellanii* by the structural features of a 3D porous material. To do so, we produced bulk hydrogels containing a maze-like three-dimensional network of interconnected microchannels by embedding and subsequently dissolving microfibrillar zinc oxide (ZnO) scaffolds in Polyacrylamide (PAAm). The scaffolds are made of ZnO tetrapods, which are very unique three-dimensional structures with four arms interconnected via a central core at an angle of $\sim 109^\circ$ and with variable sizes in the micrometer regime.²² By pressing such tetrapods into a tablet and sintering them at high temperatures, a highly interconnected ZnO network can be produced that serves as sacrificial structure for microfibrillar materials.^{23,24} When employed in combination with hydrogels, a unique microchannel network is formed that can be used both for controlling *A. castellanii* migration and even for capturing these parasites from their incubation medium. Our findings indicate the high potential of this approach to lower the risk of *A. castellanii* infections on a broad scale, as it can be used to produce materials to remove the parasites from water reservoirs or to inhibit amoebae migration, giving our approach a high medical, pharmaceutical, and engineering relevance.

2. MATERIALS AND METHODS

Acanthamoeba Culture. *Acanthamoeba castellanii* trophozoites were cultured at room temperature in peptone yeast glucose (PYG) 712 medium (20 g proteose peptone (BD, Sparks, USA), 1 g of yeast extract (BD, Sparks, USA), 950 mL of distilled water, 10 mL of 0.4 M $\text{MgSO}_4 \cdot 7\text{H}_2\text{O}$ (AppliChem, Darmstadt, Germany), 8 mL of 0.05 M CaCl_2 (AppliChem, Darmstadt, Germany), 34 mL of 0.1 M sodium citrate- $2\text{H}_2\text{O}$ (Merck, Darmstadt, Germany), 10 mL of 0.005 M $\text{Fe}(\text{NH}_4)_2(\text{SO}_4)_2 \cdot 6\text{H}_2\text{O}$ (AppliChem, Darmstadt, Germany), 10 mL of 0.25 M $\text{Na}_2\text{HPO}_4 \cdot 7\text{H}_2\text{O}$ (Roth, Karlsruhe, Germany), 10 mL of 0.25 M KH_2PO_4 (Roth, Karlsruhe, Germany), and 50 mL of 2 M glucose (Sigma-Aldrich Chemie GmbH, Steinheim, Germany)). The PYG medium was exchanged at least once a week to avoid cyst formation. *Acanthamoeba* were detached from the culture flask by slight knocking, collected with a pipet and centrifuged. The generated pellet was resuspended in PYG medium and the cell number was counted using a Neubauer counting chamber.

Ceramic Porous Template Synthesis. Zinc oxide tetrapods (*t*-ZnO) were synthesized by using a single step flame transport synthesis approach.^{22,25} The tetrapods with arm diameter in the submicron regime and arm lengths ranging between 1 and 8 μm were utilized for fabrication of porous interconnected sacrificial templates for all cellular experiments. Thinner tetrapods for checking the influence of tetrapod diameter onto the resulting channel diameter were produced by adapting the flame transport synthesis: Whereas the conventional synthesis of the tetrapods presented above makes use of a sacrificial polymer (PVB) as a carbon source for zinc reduction, we now used ethanol in its stead. Furthermore, a turbulent air environment was created by applying a constant pressurized air flow of 90 L/min. Additional turbulent effects from ethanol combustion as well as a short-term temperature increase led to a faster growth of thinner and longer tetrapod arms, partly connected by nanosails.²⁵

To form the 3D sacrificial templates, tetrapods from one synthesis batch were filled and pressed into cylindrical alumina molds and the amount was chosen such that the density of the resulting network is 0.3, ~ 0.49 , 0.6, or 1.0 g/cm^3 . The templates with pressed ZnO tetrapods were annealed at high temperature (thick tetrapods at 1150 $^\circ\text{C}$ for 4.5 h; thin tetrapods at 800 $^\circ\text{C}$ for 5 h) to form interconnections. For all cell experiments, we employed scaffolds with a density of 0.49 g/cm^3 .

Template-Mediated Polymerization of Microchannel-Containing Polyacrylamide. A mixture of acrylamide (Bio-Rad, 40%, 1.00 mL), *N,N'*-methylenebis(acrylamide) (Bis, Bio-Rad, 2%, 200 μL), HEPES buffer (Sigma-Aldrich, pH 7.5, 50.0 μL), and ammonium

persulfate solution (Sigma-Aldrich, 10%, aq., 75.0 μL) were filled up to a volume of 5.00 mL with bidest. water in a small beaker and degassed for 20 min in a desiccator. The solution was poured on the *t*-ZnO tablet with *N,N,N',N'*-tetramethylethylenediamine (TEMED, Bio-Rad, 5.00 μL), and after 1 h of polymerization, the substrate was washed with and stored in bidest. water (AppliChem GmbH).

Hydrolysis of the ZnO-Template inside the Polyacrylamide. The ZnO-template was removed from the PAAm via hydrolyzation by three times incubating the hydrogel in hydrochloric acid (0.5 M, Sigma-Aldrich) for a total of at least 24 h. Afterward, the hydrogel was washed with bidest. water (AppliChem GmbH) until it had a neutral pH value (pH 6 to 7) and was swollen to equilibrium in an adenosine 3',5'-cyclic monophosphate solution (cAMP, Sigma-Aldrich, 0.01–10.0 mM), which was exchanged daily, for 2 to 4 d. Samples were sterilized in 70% ethanol for 15 min and washed under sterile conditions for 24 h with PYG 712 for *A. castellanii* experiments. Substrates were used within 48 h.

Fluorescent Staining of the Microchannels. To render the microchannels of a PAAm sample fluorescent, we removed the water from the hydrogel by washing it repeatedly in ethanol (Walter CMP, Germany) for at least 20 min, increasing the ethanol concentration with each washing step. The concentrations employed were 50, 70, 80, 90, 95, and 99%. Then, the samples were incubated in an aqueous solution of Fluorescein isothiocyanate – Dextran 500.000 – Conjugate (FITC-Dextran, 1.32 mg/mL, Sigma-Aldrich) overnight.

Imaging of the Microchannels. Fluorescent z-stack images were recorded using a confocal microscope (Olympus, IX-81), equipped with a spinning disc unit (TILL Photonics, 1203–9–1–0017), a 488 nm Laser (Topica Photonics, iCHROME-MLE LFA 3002) and an EM-CCD Digital Camera (Hamamatsu). The samples were placed upside down in glass-bottom Petri dishes (ibidi, 81218–200). The surface at the bottom of the sample was focused, and the focus plane was shifted into the sample up to a point where background fluorescence became too strong ($\sim 70 \mu\text{m}$ – $220 \mu\text{m}$ into the sample). Z-stacks were recorded between these two focus planes with a step width of 1.99 μm . The z-stack top-views were computed using the xcellence rt software (Olympus, version 1.2).

Cell Migration Experiments. The sterilized microchannel-containing PAAm samples were incubated with *A. castellanii* (ATCC 30234, 30.000 cells/mL) in PYG medium in a 6-well plate (Sarstedt). After 0.5 h - 2 h incubation time, phase contrast images (Olympus, IX-81/BX-43) and movies (1 frame per 5 s) of the trophozoites inside the microchannels were recorded with a 10 \times objective using a monochrome (Hamamatsu, C-9300) or color camera (Imaging Source, DFK 31BF03). As control experiments, bulk PAAm samples were created as described above, but without applying a ZnO template, and swollen to equilibrium in cAMP.

Image Analysis. *Acanthamoeba* images were analyzed for the resting time, cell speed, and the direction of movement of the trophozoites inside the channels. Cell speed was determined by following the track of their front and rear inside a channel. The speed of the moving amoebae and their diameter perpendicular to the direction of motion was measured using ImageJ.²⁶ The latter was interpreted as a measure for the channel diameter the cell was migrating through.

Cell Trapping Efficiency of the Microchannel-Containing Polyacrylamide Substrates. To quantify the efficiency with which our microstructured PAAm captures *Acanthamoeba* from incubation medium, we placed four PAAm substrates in one well of a 6-well-plate and incubated them with *A. castellanii* in PYG 712 medium (20000 cells per well). These experiments were performed in three technical repeats and also with blank wells as control. The number of cells in the supernatant of each well was counted with a Hemocytometer (Neubauer counting chamber, Hecht Glaswaren) after 2, 24, 48, and 120 h.

Elasticity of Bulk Samples. Bulk samples without ZnO were prepared according to the prescription above. The polymer mixture was poured in PTFE molds with a diameter of 10 and 5 mm height. The samples were polymerized at room temperature for 1 h and then treated with either dest. water, 0.5 M hydrochloric acid or 1.28 M hydrochloric acid for 2 days. Afterward, the samples were washed with dest. water

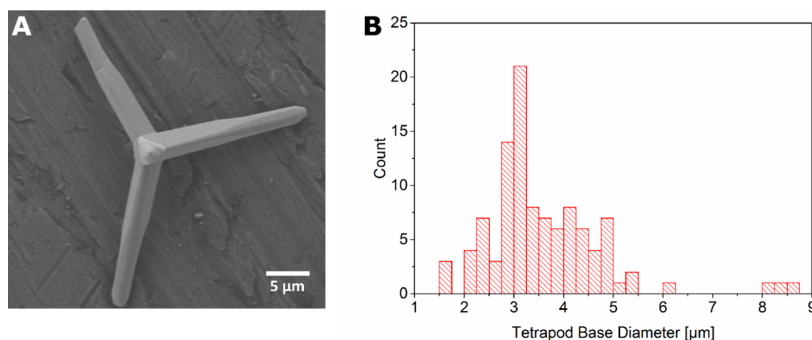


Figure 1. (A) Exemplary SEM image of a ZnO tetrapod, which serves as basic constituent of sacrificial templates for the production of microchannel-containing hydrogels. The SEM images allow the determination of the tetrapod size by image analysis. A histogram of the tetrapod diameter, measured at the base of the tetrapod arms is shown in B. The distribution ranges from 1.5 to 8.75 μm and peaks at 3 μm .

until the pH of the solution was neutral (up to 6 d). The mechanical properties of the swollen samples were determined with an indentation experiment using a modified tensile test setup. On one side, a stepper motor (M229.26S, Physik Instrumente GmbH & Co. KG, Germany) introduces a movement and on the other side, a load cell (KD24s 10N, ME-Meßsysteme GmbH, Germany) detects a force. To switch this setup to a tensile test setup, we mounted a PTFE-sphere with a diameter of 6 mm to the moving arm of the stepper motor and a flat PTFE plate to the load cell. PTFE was chosen for reducing the friction between the surfaces and the sample. For the measurement, the sphere was moved to a predefined position above the sample. Afterward, it was lowered by 3 mm with a velocity of 0.1 mm/s, resulting in an indentation of the sample. The indentation depth varied between the samples, because the start- and end point of the measurement were predefined and the sample thickness varied.

3. RESULTS

We synthesized ZnO tetrapods, pressed them into a tablet, and sintered this tablet to ensure interconnectivity of the tetrapods in the resulting ZnO network. Figure 1A shows an exemplary Scanning Electron Microscopy (SEM) image of a ZnO tetrapod, the size of which can be easily determined by image analysis. Figure 1B shows a histogram of the diameters of 105 tetrapod arms, measured at their base. These diameters range from 1.5 to 8.75 μm and their distribution peaks at 3 μm .

The ZnO tetrapod tablet was immersed in a solution of Acrylamide and BIS Acrylamide, which was then polymerized to form PAAm. A phase contrast image of the tetrapod tablet, embedded in the polyacrylamide gel, is shown in Figure 2A. When such a ZnO-containing PAAm sample was incubated in hydrochloric acid, the ZnO template dissolved, leaving microchannels in the hydrogel. In Figure 2B, the dissolving process is shown macroscopically and its final stages are captured microscopically (Figure 2C) at the center of the original tablet, showing that no ZnO tetrapods were left after the hydrolysis. The sample was then washed excessively in aqua bidest. to remove all the dissolved ZnO and other reaction products, thus resulting in microchannels inside the PAAm (Figure 2D). As the tetrapods had been pressed to high densities and were sintered at high temperatures prior to embedding them in the hydrogel, the ZnO network in the PAAm was fully interconnected and hence the microchannels, which remained in the hydrogel as a negative imprint of this ZnO network after its dissolution, were also interconnected. In other words, the hydrogel now contained a

network of cylindrically shaped, interconnected microchannels with larger cavities at the junctions of several of these channels. Figure 3 visualizes the different fabrication steps of our procedure.

For better visualization of the channels, we filled them with a FITC-Dextran conjugate (which entered the microchannels, but not the hydrogel itself), and imaged z-stacks of the samples with a confocal microscope. Exemplary top-views of z-stack composites are presented in Figure 4. For each of two different tetrapod diameter ranges (A–C and D–F, respectively), three different samples with different tetrapod densities (0.3 g/cm³ in A and D, 0.6 g/cm³ in B and E, 1 g/cm³ in C and F) were produced and for each sample, one image is given. The images show that the densities as well as diameter ranges of the resulting microchannels can be controlled by manipulating the respective property of the sacrificial scaffold. The density can be varied by adapting the amount of ZnO tetrapods added to the sample as well as by changing the pressure applied during the sintering process. More tetrapods as well as higher pressures increase the network density. The diameter ranges of the tetrapods and hence the microchannels can be varied by parameters of the tetrapod production process.²⁷

To investigate the impact of our 3D hydrogel microstructure on the migration of *Acanthamoebae*, we incubated our microchannel-containing PAAm with *A. castellanii* trophozoites, which readily adhered to the PAAm without further surface functionalization. As *A. castellanii* is responsive to adenosine 3',5'-cyclic monophosphate solution (cAMP),²⁸ the hydrogels were soaked in cAMP prior to cell experiments to accelerate migration into the hydrogel scaffold. Two very interesting and striking effects became quickly apparent: First, in spite of their typical diameter of 12 μm –35 μm ,¹² *A. castellanii* trophozoites were able to migrate through microchannels with diameters down to a few microns to explore the material (Figure 5A). Second, the trophozoites often remained immotile for much longer times when reaching larger cavities at the junctions of the microchannels inside the PAAm (Figure 5B).

To further quantify these effects, movies were taken over several hours (here, 16 h; Movie S1) and analyzed for cell migration speed, cell diameter (measured perpendicular to direction of movement, hence corresponding to the size of the microchannel that the amoeba was squeezing through) as well as the percentage of migrating and resting *A. castellanii*

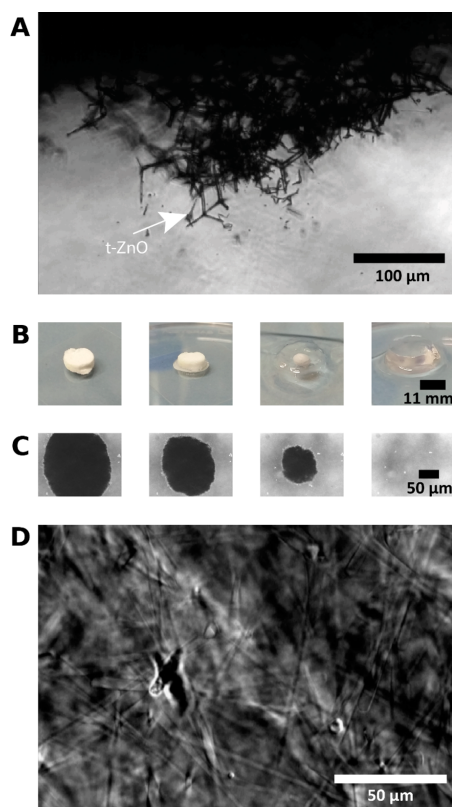


Figure 2. ZnO tetrapods are pressed and sintered into an interconnected ZnO network and embedded into an Acrylamide solution, which is then allowed to polymerize. (A) Phase contrast image of the ZnO network in the PAAm hydrogel. The ZnO network dissolves when the PAAm sample is incubated in hydrochloric acid (HCl). (B, C) both present time arrays starting from the left that recorded the dissolution process. (B) Entire process shown macroscopically. (C) Phase contrast images of the last stages of the hydrolysis, recorded microscopically every 15 min at the center of the tablet, showing that the nontransparent ZnO structures dissolve completely. The ZnO structures leave an interconnected network of microchannels in the PAAm gel, as shown in a phase contrast image in D.

trophozoites. As a control, we carried out the same analysis on *A. castellanii* migrating on bulk PAAm samples. The results are presented in Figure 6 and demonstrate that *A. castellanii* trophozoites squeezed into channels of diameters down to 6.5 μm . No migrating cells were observed in channels smaller than this. Furthermore, no apparent correlation of cell migration speed with the channel diameter was observed, but *A. castellanii* migrating on bulk PAAm samples were able to reach velocities almost twice as high as the ones in the microchannel networks (Figure 6A). Even more strikingly, we found that more than 50% of the *A. castellanii* trophozoites in microchannel-containing PAAm were resting in cavities while amoeba migrating on bulk PAAm samples were always in motion (Figure 6B), underlining the significance of the influence that our new microchannel

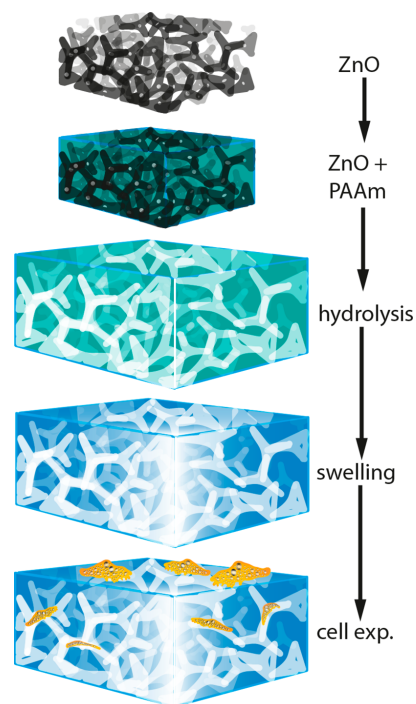


Figure 3. Synthesis of microchannel-containing polyacrylamide hydrogels. First, a sintered zinc oxide tetrapod based network template (black) with a well-defined tetrapod density is embedded into an acrylamide solution, which is then polymerized to polyacrylamide (PAAm, green). Afterward, the template is hydrolyzed with hydrochloric acid (HCl), leaving a negative of microchannels inside the PAAm (white). After complete hydrolysis of the ceramic template, the PAAm is washed and swollen to equilibrium in cAMP solution. Now, the material can be used for cell experiments (orange). As the tetrapod template was sintered and produced at high tetrapod densities, the network of microchannels in the PAAm, being a negative of this template, is highly interconnected.

network in the PAAm gels has on cell migration. An *Acanthamoeba* was defined as “resting” if it stayed inside a cavity for at least 40 s. This value was chosen heuristically due to the length of our movies. In some experiments, the trophozoites stayed inside a cavity even for several hours. It is noteworthy that *A. castellanii* trophozoites are very motile and clearly do not rest on flat, unstructured substrates.

Experiments carried out at longer time scales demonstrated that *A. castellanii* trophozoites stayed in the microchannel network inside our PAAm substrate for at least 6 days. They continued to migrate and exhibit intracellular motion while no encystment but very high trophozoite densities were observed in the channels (Figure 7). These rising cell densities motivated the idea that the specific 3D architecture of microchannels in combination with larger cavities in our hydrogels might provide the opportunity to capture *A. castellanii* from liquids with our new material. Hence, we incubated microchannel-containing PAAm samples up to 120 h with *A. castellanii* in PYG medium and repeatedly counted the number of cells in the supernatant of

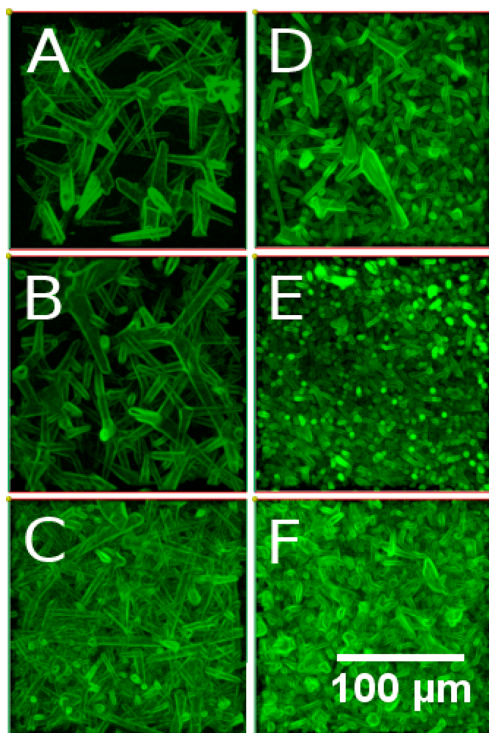


Figure 4. Top-view of a z-stack of confocal fluorescence microscopy images of the microchannels in PAAm hydrogels. The images present channels resulting from tetrapod scaffolds with different network densities and diameters. (A–C) Samples produced by using tetrapods with larger diameters, (D–F) samples produced using thinner tetrapods. Each column of images pictures samples from one ZnO density in the tetrapod template. Namely (A, D) 0.3, (B, E) 0.6, and (C, F) 1 g/cm³. It becomes clear that the ranges of channel diameters and densities are influenced by these respective parameters of the sacrificial ZnO template and can hence be controlled by adapting the template properties.

the medium (Figure 8). As a control, we repeated these experiments in cell culture dishes without PAAm. After 24 and 48 h incubation time, the amount of *Acanthamoeba* was slightly higher in the medium of the microchannel-containing PAAm, but after 120 h the presence of the microporous material had led to a significantly lower amount of *A. castellanii* in the supernatant compared to the medium of the bulk control (Figure 8).

4. DISCUSSION

We have introduced a new technique to produce microstructured 3D hydrogels as cell substrates by pressing and sintering ZnO tetrapods into an interconnected network, which is immersed in an Acrylamide solution prior to polymerization. When the solution has polymerized, the tetrapod network is removed from the resulting PAAm hydrogel by hydrolysis with HCl. We have shown that this approach produces PAAm substrates containing a network of interconnected microchannels with diameters down to only few microns and that

these porous materials can be used as 3D substrates to study and manipulate the migration behavior of *A. castellanii* trophozoites.

This, however, is just one among the many possible applications of these tetrapod-based materials in engineering and corresponding applications. In fact, following the strategy of material deposition and subsequent removal of an underlying template, 3D hollow tetrapodal networks with tunable dimensions (from nanometer to micrometer scale) and ultrahigh porosities (up to 98%) can in principle be easily realized also using many other ceramic materials. For instance, the 3D ceramic templates have already been successfully produced from several oxides, nitrides, silicon, etc. Because zinc oxide is easily hydrolyzed by acids,²⁴ it was chosen for the present experiments as the sacrificial template material. Furthermore, all polymers that withstand acidic environments can be microstructured. In other words, using our new approach, a huge variety of materials can be equipped with a network of interconnected microchannels with many different channel diameters and densities (i.e., pore sizes, pore distribution, and porosity).

We rendered the channels in the hydrogels fluorescent (Figure 4), enabling us to measure channel diameters and densities directly in the hydrogel samples. Furthermore, by analyzing confocal z-stack slices, it is possible to determine the number of junctions as well as their positions (Figure S3). This allows describing microchannel sizes and distributions in the sample (Figure S4). The porosity of the sample can also be determined using these z-stack slices. The porosity Φ is defined as the ratio of the volume of void space (i.e., of our channels) to the total sample volume.

The total channel volume directly after the ZnO dissolution process is equal to the total volume of the tetrapod network and can hence be calculated from the weight of the sacrificial ZnO template, as the density of ZnO is known. The porosity can then be expressed as²⁹

$$\Phi = \frac{V_{\text{ZnO}}}{V_{\text{PAAm}} + V_{\text{ZnO}}} = 1 - \frac{V_{\text{PAAm}}}{V_{\text{PAAm}} + V_{\text{ZnO}}} \quad (1)$$

with V_{PAAm} and V_{ZnO} as the volume of PAAm or ZnO, respectively. Hence, the initial PAAm porosity can be increased by increasing the amount of ZnO tetrapods in the sacrificial template. However, as the hydrogel continues to swell after ZnO dissolution,³⁰ and since the description in eq 1 does not take local variations of channel densities or diameters into account, it is recommendable to evaluate the microporosity at the region of interest using fluorescence images (Figure 4). Using image analysis, the fraction of fluorescent pixels to the total amount of pixels of each slice of the z-stack can be calculated and hence gives the local microporosity of the swollen gel.

In general, we suggest being careful with global descriptions of the samples produced with our approach because, as seen in Figure 1B, the tetrapods constructing the sacrificial network do not have one distinct diameter, but a distribution of diameters. The same holds for the density of the tetrapod network and indeed, different positions of the microchannel-containing PAAm samples display different channel densities. Nevertheless, the properties of the channel network can be tuned as displayed in Figure 4, but it is rather useful to consider this as an adaptation of ranges of channel densities and diameters. Another important aspect is to realize that the shape of tetrapod arms (Figure 1A) results in channels that vary their diameter across channel length.

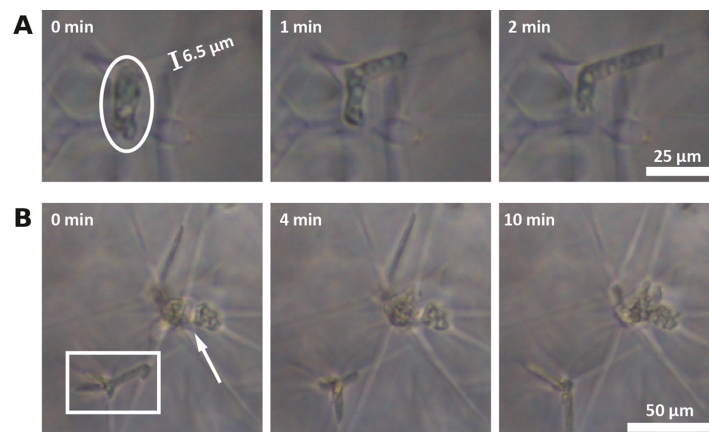


Figure 5. (A) Phase contrast images of *A. castellanii* moving through the microchannels inside the PAAm. The circle indicates an Acanthamoeba migrating into a side channel ($\varnothing = 6.5 \mu\text{m}$). (B) Several Acanthamoebae are stuck in a microchannel junction (arrow) and an Acanthamoeba is stuck inside a cavity. The Acanthamoeba probes the surrounding channels with its Acanthopodia (rectangle).

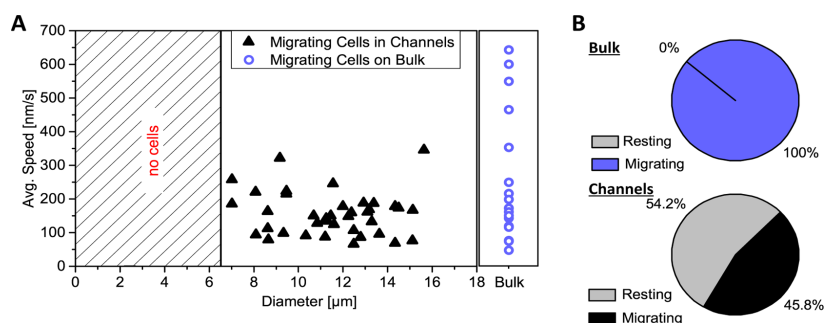


Figure 6. *A. castellanii* migration inside the microchannels of PAAm. (A) shows the migration speed plotted versus the diameter of the channel the trophozoite was squeezing through. The violet circles on the right represent the migration speeds of *A. castellanii* cells on bulk PAAm samples. It becomes clear that *A. castellanii* trophozoites can squeeze into channels with diameters as small as $6.5 \mu\text{m}$. No cells were observed below that (hatched area). Besides, there is no correlation of cell migration speed with channel diameter, but trophozoites on bulk samples can reach maximum migration speeds almost twice as high as the ones in the microchannels. (B) Percentages of resting and moving *A. castellanii* trophozoites on bulk samples (total number $N = 18$) and in the microchannel network in our PAAm sample ($N = 83$). Although all amoebae were in motion on bulk samples, 54.2% of the cells in the microchannel-containing materials were resting in cavities at the junctions of several microchannels.

In general, the fluorescent imaging of the channels is very useful to gain a quick overview of the networks' properties to optimize production parameters for specific experimental requirements. The fluorescent dextrane was chosen such that it entered the microchannels, but not the intrinsic pores of the hydrogel. This strategy can also be used to characterize the sample on many different positions and hence to apply statistical descriptions of global network properties or they can be directly taken at a specific region of interest to gain exact knowledge about sample characteristics at this region. However, it is very useful and accurate to determine the channel diameter of interest in situ during cell experiments by evaluating the cell diameter perpendicular to cellular motion while the cell is migrating through this channel. As the cells need to be optically observed anyway, this does not impose a lot of extra work, but results in the most reliable and quick determination of the relevant channel diameters during cell experiments. This

approach overcomes potential issues originating from not having channels with one distinct diameter in the sample, but rather turns this fact into an advantage, as the influence of a variety of diameters on cell migration is automatically analyzed with one experiment. Furthermore, this variety of diameters resembles in vivo situations more accurately, as physiological extracellular environments are not homogeneous at the cell scale.³¹ Similar assumptions hold for channel densities and the appropriate channel density can be chosen by simply changing the position at which experiments are carried out.

PAAm was chosen for the hereby presented experiments since hydrogels are very attractive for many biological applications,³² as they are soft³³ and can support nutrient supply due to their intrinsic nanoporosity.³⁴ Specifically, PAAm is often used in cell adhesion experiments because its elastic properties can be defined by cross-linker density in a wide and physiologically important range and its surface can easily be functionalized.³²

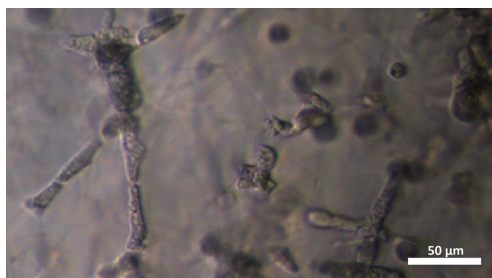


Figure 7. Phase contrast image of densely packed *A. castellanii* inside the polyacrylamide microchannel network after 1 day of incubation, revealing that the amoebae agglomerate as trophozoites in our substrate on longer time scales.

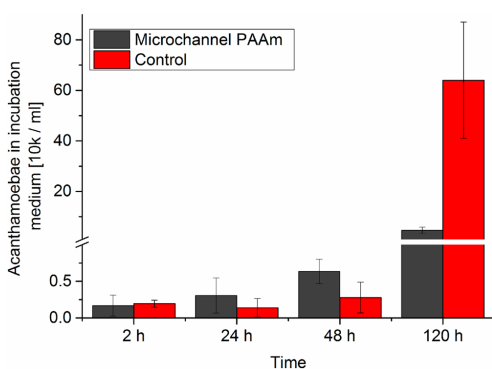


Figure 8. Number of *A. castellanii* in the medium after incubation with a microchannel-containing PAAm sample (black) or an empty cell culture dish (red) shows that although initially more trophozoites remain in the medium when incubated with the microstructured PAAm substrate, this changes strongly after 120 h incubation time, indicating the potential of our new substrate to remove amoebae from liquids.

The Young's modulus of the polyacrylamide produced in these experiments was approximately 19 kPa (Supporting Information, Table S1), thus being in the range of the matrix elasticity that ensures *A. castellanii* adhesion.³⁵

In general, the fabrication of mechanically robust 3D materials with well-defined porosities, pore shape and pore organization to control cell migration is highly desirable. However, achieving sufficient mechanical strength, and simultaneously adjustable porosities as well as interconnectivity in soft 3D architected materials is a very challenging task. Fabrication of such materials requires complicated processing steps involving high costs.^{36–38} In addition, micrometer-sized pores are often introduced into bulk materials by applying conventional salt-leaching.^{39,40} The pores generated by these conventional methods typically have diameters of several tens of micrometers, and are inverse-opal shaped so that many cells can enrich within a single pore.⁴¹ Hence, cells in such large pores rather adhere on curved 2D surfaces without being completely surrounded by the material, as it is the case in our microchannels. Furthermore, the materials fabricated by salt-based pore-leaching require large pore fractions in order to guarantee pore interconnectivity, which imposes a large structural limitation. Gas foaming techniques

lack the control of pore interconnectivity and often pose problems in the form of processing residuals in the material.⁴² Such limitations are overcome by our novel approach, because we can produce microchannels with high interconnectivity and diameters of down to only a few micrometers because of the special microstructure of the sacrificial ceramic template. Furthermore, our approach can easily be upscaled to fabricate large amounts of microstructured materials, which is challenging for many other techniques such as 3D printing or cryogelation.⁴²

It is also very interesting that most of recent advancements in microporous hydrogel concentrate on anisotropy of the pore structures or increasing the mechanical strength of structured hydrogels.⁴² Our approach concentrates on the creation of hydrogels, which cells can enter freely and in which they can migrate and proliferate without exiting the sample, so that we can study them on long time scales. Incubating *A. castellanii* cells on our new microchannel-containing PAAm revealed not only that the cells willingly enter and migrate inside the microchannels (Figure 5A), even with diameters much smaller than the cell diameter, but also that the maximum migration speed inside the channels is slower than on conventional 2D substrates (Figure 6A) and, most strikingly, that *A. castellanii* even cease migrating when reaching cavities that had formed at microchannel intersections within the network (Figure 5B). The latter is particularly interesting, because *Acanthamoebae* are always in motion on the surface of bulk polyacrylamide samples, whereas more than 50% of the amoeba in microchannel-containing materials were resting during our experiments (Figure 6B). This result is in agreement with a previous study that has reported a decrease in cell migration with increasing pore size.⁴³ Interestingly, cancer cells on the other hand have been found to increase their migration speed in narrow channels,⁴⁴ indicating the change of cell migration speed in refined spaces to be a complex phenomenon, which is worth studying. It is noteworthy that in our experiments cells accumulate in much smaller pores compared to the large pores between 96 and 151 μm in size used by Harley et al.,⁴⁵ demonstrating that the effect of cell accumulation is also present for small pores. In other words, the parasites were captured by the microchannel network structure of our material, which is highly interesting as this indicates that implementing these structures into, for example, conventional contact lens materials, whose high water contents particularly favor *A. castellanii* growth and hence pose a high infection risk on contact lens users,^{20,21} would significantly decrease this infection risk by keeping the parasites inside the material, where they cannot reach the corneal tissue. It is also important to note here that the trophozoites did not encyst, hence they might be removed without the formation of cysts, which would make them resistant against standard disinfection treatments.⁴⁵

Despite having a cell diameter of 12–35 μm ,¹² *A. castellanii* trophozoites were able to migrate through microchannels with diameters down to 6.5 μm (Figure 6A). The existence of this lower limit of diameters that *A. castellanii* can squeeze into is reminiscent of that of cells in collagen networks, where cell motion is stopped, if collagen fibers are too dense.⁹ Previous studies on mammalian cells have shown that the nuclear deformability is a critical parameter in 3D cell migration.⁸ The nucleus of *A. castellanii* trophozoites is one-sixth of the cell diameter with approximately 4.5–6.7 μm in size;⁴⁶ this can explain the abrupt absence of migrating cells in channels below approximately 6.5 μm in diameter. Another study has shown that

cancer cell migration is impeded in channels with diameters below 7 μm , which is in agreement with our results.⁴⁴

Another very striking observation we made was that the trophozoites entering and remaining in the hydrogel leads to a decreased amount of *A. castellanii* in the incubation medium, which means that our new microchannel PAAm can be applied to remove these amoebae from water reservoirs. Since the presence of *A. castellanii* in such reservoirs also enhances the invasiveness of *Legionella pneumophila*,¹² this is high of general medical relevance. In contrast to other approaches to remove pathogenic microorganisms from solutions, which are mainly based on chemical capturing⁴⁷ and magnetic capturing,⁴⁸ our approach is solely based on the structural features of the porous hydrogel. This is a clear advantage because the structure is stable, the material is nondegradable and it can be cheaply and efficiently fabricated in high-throughput mode.

CONCLUSION

In conclusion, our strategy of using porous ceramic templates to incorporate interconnected, labyrinth-like structures of microchannels into hydrogels provides novel, easy-to-fabricate 3D scaffolds for controlling and studying cell migration. As demonstrated, the specific organization and size distribution of microchannels in the material even allows to capture *A. castellanii* by structural material cues, providing an innovative high-throughput strategy for preventing Acanthamoeba-born diseases by, for example, avoiding Acanthamoeba contaminations in contact lens storage cases or water reservoirs. In addition to capturing pathogenic microorganisms, future applications in tissue engineering are highly promising, as in that case the large surface fraction of the cell–material contact in the microchannels can be exploited for controlling cell functions that are induced by this cell–material contact.

ASSOCIATED CONTENT

Supporting Information

The Supporting Information is available free of charge on the ACS Publications website at DOI: [10.1021/acsbomaterials.8b01009](https://doi.org/10.1021/acsbomaterials.8b01009).

Description and results of experiments to characterize the elastic properties as well as the swelling behavior of microchannel-containing PAAm samples; more fluorescent images are presented, which visualize the optical characterization of microchannel network properties (PDF)

Movie S1, time array of phase contrast images with a total duration of 16 h of *A. castellanii* trophozoites migrating inside the microchannels of a microstructured PAAm substrate produced with the presented technique (AVI)

AUTHOR INFORMATION

Corresponding Author

*E-mail: cse@tf.uni-kiel.de.

ORCID

Yogendra Kumar Mishra: 0000-0002-8786-9379

Christine Selhuber-Unkel: 0000-0002-5051-4822

Notes

The authors declare no competing financial interest.

ACKNOWLEDGMENTS

We acknowledge funding from the Deutsche Forschungsgemeinschaft (DFG) through the GRK 2154 and the SFB 1261, as well as from the ARVO Foundation (Vistakon Contact Lens Research Fellowship), and the European Research Council (Proof of Concept Grant 768740, Starting Grant 336104). R. A. thanks the DFG for financial support under the Scheme AD 183/17-1. We thank Matthias Leippe for providing *A. castellanii*, Supattra Paveenkittiporn for support with cell migration experiments and data acquisition, Katharina Göpfert for preparing porous substrates, Yannic Hallier for ZnO tetrapod characterization, and Manuela Lieb for support in the lab.

ABBREVIATIONS

PAAm polyacrylamide
t-ZnO zinc oxide tetrapods
pyg Peptone Yeast Glucose

REFERENCES

- (1) Doyle, A. D.; Carvajal, N.; Jin, A.; Matsumoto, K.; Yamada, K. M. Local 3D matrix microenvironment regulates cell migration through spatiotemporal dynamics of contractility-dependent adhesions. *Nat. Commun.* **2015**, *6*, 8720.
- (2) van Helvert, S.; Storm, C.; Friedl, P. Mechanoreciprocity in cell migration. *Nat. Cell Biol.* **2018**, *20* (1), 8–20.
- (3) Leach, J. K.; Whitehead, J. Materials-Directed Differentiation of Mesenchymal Stem Cells for Tissue Engineering and Regeneration. *ACS Biomater. Sci. Eng.* **2018**, *4* (4), 1115–1127.
- (4) Chang, S. S.; Guo, W.-h.; Kim, Y.; Wang, Y.-L. Guidance of Cell Migration by Substrate Dimension. *Biophys. J.* **2013**, *104* (2), 313–321.
- (5) Tayalia, P.; Mendonca, C. R.; Baldacchini, T.; Mooney, D. J.; Mazur, E. 3D Cell-Migration Studies using Two-Photon Engineered Polymer Scaffolds. *Adv. Mater.* **2008**, *20* (23), 4494–4498.
- (6) Chaudhuri, O.; Gu, L.; Klumpers, D.; Darnell, M.; Bencherif, S. A.; Weaver, J. C.; Huebsch, N.; Lee, H.-P.; Lippens, E.; Duda, G. N.; Mooney, D. J. Hydrogels with tunable stress relaxation regulate stem cell fate and activity. *Nat. Mater.* **2016**, *15* (3), 326–334.
- (7) Discher, D. E.; Janmey, P.; Wang, Y.-L. Tissue Cells Feel and Respond to the Stiffness of Their Substrate. *Science* **2005**, *310* (5751), 1139–1143.
- (8) Denais, C. M.; Gilbert, R. M.; Isermann, P.; McGregor, A. L.; te Lindert, M.; Weigel, B.; Davidson, P. M.; Friedl, P.; Wolf, K.; Lammerding, J. Nuclear envelope rupture and repair during cancer cell migration. *Science* **2016**, *352* (6283), 353.
- (9) Wolf, K.; te Lindert, M.; Krause, M.; Alexander, S.; te Riet, J.; Willis, A. L.; Hoffman, R. M.; Figdor, C. G.; Weiss, S. J.; Friedl, P. Physical limits of cell migration: Control by ECM space and nuclear deformation and tuning by proteolysis and traction force. *J. Cell Biol.* **2013**, *201* (7), 1069–1084.
- (10) Lautscham, L. A.; Kämmerer, C.; Lange, J. R.; Kolb, T.; Mark, C.; Schilling, A.; Strissel, P. L.; Strick, R.; Gluth, C.; Rowat, A. C.; Metzner, C.; Fabry, B. Migration in Confined 3D Environments Is Determined by a Combination of Adhesiveness, Nuclear Volume, Contractility, and Cell Stiffness. *Biophys. J.* **2015**, *109* (5), 900–913.
- (11) Di Giacomo, R.; Krödel, S.; Maresca, B.; Benzoni, P.; Rusconi, R.; Stocker, R.; Daraio, C. Deployable micro-traps to sequester motile bacteria. *Sci. Rep.* **2017**, *7*, 45897.
- (12) Khan, N. A. Acanthamoeba: biology and increasing importance in human health. *FEMS Microbiology Reviews* **2006**, *30* (4), 564–595.
- (13) Huth, S.; Reverey, J. F.; Leippe, M.; Selhuber-Unkel, C. Adhesion forces and mechanics in mannose-mediated acanthamoeba interactions. *PLoS One* **2017**, *12* (5), No. e0176207.
- (14) Preston, T. M.; King, C. A. Amoeboid locomotion of Acanthamoeba castellanii with special reference to cell-substratum interactions. *Microbiology* **1984**, *130* (9), 2317–23.
- (15) Moore, M. B. Acanthamoeba Keratitis. *Arch. Ophthalmol.* **1988**, *106* (9), 1181–1183.

- (16) Seal, D.; Stapleton, F.; Dart, J. Possible environmental sources of *Acanthamoeba* spp in contact lens wearers. *Br. J. Ophthalmol.* **1992**, *76* (7), 424–427.
- (17) Marciano-Cabral, F.; Cabral, G. *Acanthamoeba* spp. as Agents of Disease in Humans. *Clin. Microbiol. Rev.* **2003**, *16* (2), 273–307.
- (18) Thomas, V.; McDonnell, G.; Denyer, S. P.; Maillard, J.-Y. Free-living amoebae and their intracellular pathogenic microorganisms: risks for water quality. *FEMS Microbiology Reviews* **2010**, *34* (3), 231–259.
- (19) Lorenzo-Morales, J.; Khan, N. A.; Walochnik, J. An update on *Acanthamoeba keratitis*: diagnosis, pathogenesis and treatment. *Parasite* **2015**, *22*, 10.
- (20) Revere, J. F.; Fromme, R.; Leippe, M.; Selhuber-Unkel, C. In vitro adhesion of *Acanthamoeba castellanii* to soft contact lenses depends on water content and disinfection procedure. *Cont Lens Anterior Eye* **2014**, *37* (4), 262–266.
- (21) Coulon, C.; Collignon, A.; McDonnell, G.; Thomas, V. Resistance of *Acanthamoeba* Cysts to Disinfection Treatments Used in Health Care Settings. *Journal of Clinical Microbiology* **2010**, *48* (8), 2689–2697.
- (22) Mishra, Y. K.; Kaps, S.; Schuchardt, A.; Paulowicz, I.; Jin, X.; Gedamu, D.; Freitag, S.; Claus, M.; Wille, S.; Kovalev, A.; Gorb, S. N.; Adelung, R. Fabrication of Macroscopically Flexible and Highly Porous 3D Semiconductor Networks from Interpenetrating Nanostructures by a Simple Flame Transport Approach. *Part. Part. Syst. Charact.* **2013**, *30* (9), 775–783.
- (23) Mecklenburg, M.; Schuchardt, A.; Mishra, Y. K.; Kaps, S.; Adelung, R.; Lotnyk, A.; Kienle, L.; Schulte, K. Aerographite: Ultra Lightweight, Flexible Nanowall, Carbon Microtube Material with Outstanding Mechanical Performance. *Adv. Mater.* **2012**, *24* (26), 3486–3490.
- (24) Schütt, F.; Signetti, S.; Krüger, H.; Röder, S.; Smazna, D.; Kaps, S.; Gorb, S. N.; Mishra, Y. K.; Pugno, N. M.; Adelung, R. Hierarchical self-entangled carbon nanotube tube networks. *Nat. Commun.* **2017**, *8* (1), 1215.
- (25) Mishra, Y. K.; Adelung, R. ZnO tetrapod materials for functional applications. *Mater. Today* **2018**, *21* (6), 631–651.
- (26) Rasband, W. S. *ImageJ*; U.S. National Institutes of Health: Bethesda, MD, 2005; <http://rsb.info.nih.gov/ij/> [Online].
- (27) Paulowicz, I.; Postica, V.; Lupan, O.; Wolff, N.; Shree, S.; Cojocaru, A.; Deng, M.; Mishra, Y. K.; Tiginyanu, I.; Kienle, L.; Adelung, R. Zinc oxide nanotetrapods with four different arm morphologies for versatile nanosensors. *Sens. Actuators, B* **2018**, *262*, 425–435.
- (28) Schuster, F. L.; Levandowsky, M. Chemosensory Responses of *Acanthamoeba castellanii*: Visual Analysis of Random Movement and Responses to Chemical Signals. *J. Eukaryotic Microbiol.* **1996**, *43* (2), 150–158.
- (29) Lawrence, M.; Jiang, Y.; Porosity, Pore Size Distribution, Microstructure. In *Bio-aggregates Based Building Materials: State-of-the-Art Report of the RILEM Technical Committee 236-BBM*, Amziane, S.; Collet, F., Eds. Springer: Dordrecht, The Netherlands, 2017; pp 39–71. DOI: 10.1007/978-94-024-1031-0_2.
- (30) Peters, A.; Candau, S. J. Kinetics of swelling of polyacrylamide gels. *Macromolecules* **1986**, *19* (7), 1952–1955.
- (31) Khoshgofar, M.; Wilson, W.; Ito, K.; van Donkelaar, C. C. Influence of tissue- and cell-scale extracellular matrix distribution on the mechanical properties of tissue-engineered cartilage. *Biomech. Model. Mechanobiol.* **2013**, *12* (5), 901–913.
- (32) Engler, A. J.; Sen, S.; Sweeney, H. L.; Discher, D. E. Matrix Elasticity Directs Stem Cell Lineage Specification. *Cell* **2006**, *126* (4), 677–689.
- (33) Hadden, W. J.; Young, J. L.; Holle, A. W.; McFetridge, M. L.; Kim, D. Y.; Wijesinghe, P.; Taylor-Weiner, H.; Wen, J. H.; Lee, A. R.; Bieback, K.; Vo, B.-N.; Sampson, D. D.; Kennedy, B. F.; Spatz, J. P.; Engler, A. J.; Choi, Y. S. Stem cell migration and mechanotransduction on linear stiffness gradient hydrogels. *Proc. Natl. Acad. Sci. U. S. A.* **2017**, *114* (22), 5647.
- (34) Stellwagen, N. C. Apparent pore size of polyacrylamide gels: Comparison of gels cast and run in Tris-acetate-EDTA and Tris-borate-EDTA buffers. *Electrophoresis* **1998**, *19* (10), 1542–1547.
- (35) Gutekunst, S. B.; Grabosch, C.; Kovalev, A.; Gorb, S. N.; Selhuber-Unkel, C. Influence of the PDMS substrate stiffness on the adhesion of *Acanthamoeba castellanii*. *Beilstein J. Nanotechnol.* **2014**, *5*, 1393–1398.
- (36) Schaedler, T. A.; Jacobsen, A. J.; Torrents, A.; Sorensen, A. E.; Lian, J.; Greer, J. R.; Valdevit, L.; Carter, W. B. Ultralight Metallic Microlattices. *Science* **2011**, *334* (6058), 962–965.
- (37) Cheung, K. C.; Gershenfeld, N. Reversibly Assembled Cellular Composite Materials. *Science* **2013**, *341* (6151), 1219–1221.
- (38) Compton, B. G.; Lewis, J. A. 3D-Printing of Lightweight Cellular Composites. *Adv. Mater.* **2014**, *26* (34), 5930–5935.
- (39) Raic, A.; Rödling, L.; Kalbacher, H.; Lee-Theedieck, C. Biomimetic macroporous PEG hydrogels as 3D scaffolds for the multiplication of human hematopoietic stem and progenitor cells. *Biomaterials* **2014**, *35* (3), 929–940.
- (40) Ganji, Y.; Li, Q.; Quabius, E. S.; Böttner, M.; Selhuber-Unkel, C.; Kasra, M. Cardiomyocyte behavior on biodegradable polyurethane/gold nanocomposite scaffolds under electrical stimulation. *Mater. Sci. Eng., C* **2016**, *59*, 10–18.
- (41) Kim, J.; Bencherif, S. A.; Li, W. A.; Mooney, D. J. Cell-Friendly Inverse Opal-Like Hydrogels for a Spatially Separated Co-Culture System. *Macromol. Rapid Commun.* **2014**, *35* (18), 1578–1586.
- (42) De France, K. J.; Xu, F.; Hoare, T. Structured Macroporous Hydrogels: Progress, Challenges, and Opportunities. *Adv. Healthcare Mater.* **2018**, *7* (1), 1700927.
- (43) Harley, B. A.; Kim, H. D.; Zaman, M. H.; Yannas, I. V.; Lauffenburger, D. A.; Gibson, L. J. Microarchitecture of three-dimensional scaffolds influences cell migration behavior via junction interactions. *Biophys. J.* **2008**, *95* (8), 4013–4024.
- (44) Rolli, C. G.; Seufferlein, T.; Kemkemer, R.; Spatz, J. P. Impact of Tumor Cell Cytoskeleton Organization on Invasiveness and Migration: A Microchannel-Based Approach. *PLoS One* **2010**, *5* (1), No. e8726.
- (45) Johnston, S. P.; Sriram, R.; Qvarnstrom, Y.; Roy, S.; Verani, J.; Yoder, J.; Lorick, S.; Roberts, J.; Beach, M. J.; Visvesvara, G. Resistance of *Acanthamoeba* Cysts to Disinfection in Multiple Contact Lens Solutions. *Journal of Clinical Microbiology* **2009**, *47* (7), 2040–2045.
- (46) Khan, N. *Acanthamoeba: Biology and Pathogenesis*; Calster Academic Press: 2009.
- (47) Li, J.; Qi, C.; Lian, Z.; Han, Q.; Wang, X.; Cai, S.; Yang, R.; Wang, C. Cell-Capture and Release Platform Based on Peptide-Aptamer-Modified Nanowires. *ACS Appl. Mater. Interfaces* **2016**, *8* (4), 2511–2516.
- (48) Liu, T.-Y.; Chen, C.-L.; Lee, Y.-C.; Chan, T.-Y.; Wang, Y.-L.; Lin, J.-J. First Observation of Physically Capturing and Maneuvering Bacteria using Magnetic Clays. *ACS Appl. Mater. Interfaces* **2016**, *8* (1), 411–418.

Supporting Information to

3D Hydrogels Containing Interconnected Microchannels of Subcellular Size for Capturing Human Pathogenic *Acanthamoeba Castellanii*

Sören B. Gutekunst¹, Katharina Siemsen¹, Steven Huth¹, Anneke Möhring¹, Britta Hesseler¹,
Michael Timmermann¹, Ingo Paulowicz³, Yogendra Kumar Mishra², Rainer Adelung²,
Christine Selhuber-Unkel^{*1}.

¹ Institute for Materials Science, Biocompatible Nanomaterials, University of Kiel, D-24143
Kiel, Germany

² Institute for Materials Science, Functional Nanomaterials, University of Kiel, D-24143 Kiel,
Germany

³ Phi-Stone AG, D-24143 Kiel, Germany

Elasticity of bulk samples: Bulk samples without ZnO were prepared according to the prescription above. The polymer mixture was poured in PTFE molds with a diameter of 10 mm and 5 mm height. The samples were polymerized at room temperature for 1 h and then treated with either bidest. water or 0.5 M hydrochloric acid (HCl) for 2 d. Afterwards, the samples were washed with bidest. water until the pH of the solution was neutral (up to 6 d). The swollen samples were measured with an indentation experiment (as described in more detail in the following paragraph). The results of the analysis of the Young's modulus is

presented in table S1 and show that HCl treatment does not have a significant impact on PAAm elasticity.

Table S1. Young's modulus of PAAm bulk samples after being incubated in bidest. water or 0.5 M HCl for 2 d and subsequently washed and swollen to equilibrium in bidest. water. The results show that the acid treatment does not significantly change the elasticity of the PAAm substrate.

Incubation Medium	Young's Modulus (kPa)
Bidest. water	18.6 ± 1.32
HCl (0.5 M)	18.9 ± 0.75

Detailed Description of Indentation Experiments to Determine PAAm Elasticity: The measurement setup is a modified tensile test setup. On one side a stepper motor (M229.26S, Physik Instrumente GmbH & Co. KG, Germany) introduces a movement and on the other side a load cell (KD24s 10N, ME-Meßsysteme GmbH, Germany) detects a force. To switch this setup to a tensile test setup a PTFE-sphere with a diameter of 6 mm was mounted to the moving arm of the stepper motor and a flat PTFE plate was mounted to the load cell. PTFE was chosen to reduce the friction between the surfaces and the sample.

For the measurement the sphere was moved to a predefined position above the sample. Afterwards it was lowered 3 mm with a velocity of 0.1 mm/s, resulting in an indentation of the sample. The indentation depth varied between the samples, because start- and endpoint of the measurement were predefined and the sample thickness varied.

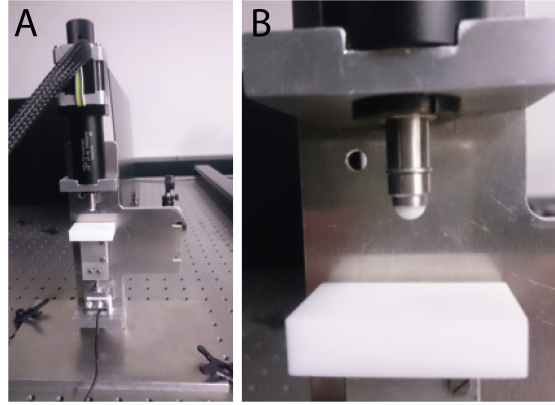


Figure S1. Photographs of the indenter setup used for the experiments. A) The complete setup is shown. On the bottom part a PTFE plate is mounted to a load cell to provide a surface for the indentation test and to measure the introduced force. On the top part a PTFE sphere is mounted to a stepper motor to introduce an indentation. B) Magnified view of sphere and surface. The sample is placed on the surface and penetrated by the sphere.

Force and indentation depth data were processed in Matlab R2015a. The mean force of the first 10% of the data points (far away from the sample) was subtracted from the force-data as a baseline. The `lsqcurvefit` function from the Matlab Curve Fitting Toolbox Version 3.5.1 was used to fit the Hertz Model to the data. The stiffness of the indenter is assumed to be much higher than that of the sample. By limiting the fitting range successively, we computed how the measured Young's modulus (E) changes with depth of indentation. We see a rapid increase of Young's modulus followed by a saturation which shows as a plateau in the E vs distance curve (see Fig. S3). Only E values in this region were assumed to present the samples properties properly. Hence the Hertz model was used for fitting the data. It is expressed as:

$$F = \frac{4E\sqrt{R}}{3(1-\nu^2)}(\delta - \delta_0)^{\frac{3}{2}}$$

With F as Force, E as Young's modulus and ν as Poisson's ratio of the hydrogel, R as indenter radius, δ as indentation depth and δ_0 as contact point. E and δ_0 are the fitting parameters. A Poisson's ratio of 0.5 is assumed for the hydrogels.¹

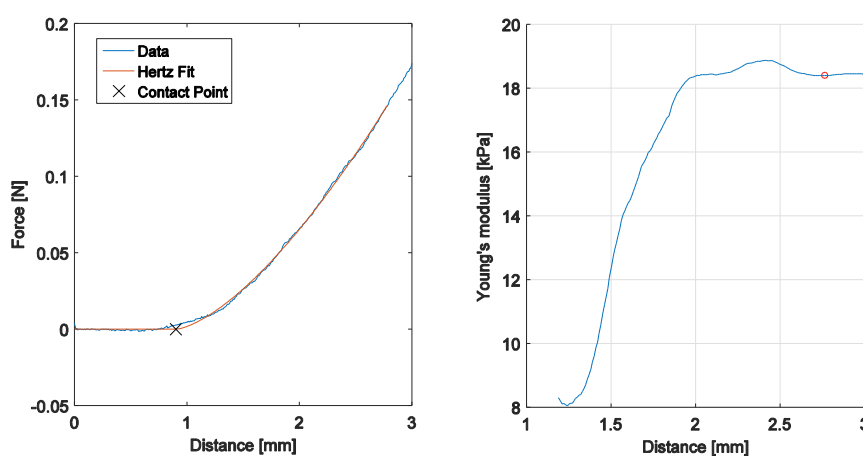


Figure S2. Left: A typical Force-distance curve of an indentation experiment. The blue line shows the measured data and the red line presents the Hertz model fit. The black X is the contact point, which is one of the fitting parameters. Right: By limiting the fitting range successively, we computed a Young's modulus-distance curve. It clearly shows an increase of Young's modulus with indentation depth. After an indentation of approximately 2 mm, a saturation can be observed and Young's modulus remains constant upon further indentation. The red circle indicates the value we chose to represent the elastic properties of the sample.

Gel content and swelling of bulk samples: For determination of the gel content and the degree of swelling bulk samples were lyophilized and weighted (W_0). The samples were treated

¹ Schwarz, U. S.; Balaban, N. Q.; Riveline, D.; Bershadsky, A.; Geiger, B.; Safran, S. A., Calculation of forces at focal adhesions from elastic substrate data: the effect of localized force and the need for regularization. *Biophysical Journal* 2002, 83 (3), 1380-1394.

either with 3 mL bidest. water or 0.5 M HCl acid for 2 d. Afterwards, the hydrogels were washed with bidest. water until the pH of the solution was neutral and weighted (W_s). The samples were lyophilized and weighted again (W_1). The gel content was calculated according to the following equation:

$$\text{Gel content (\%)} = 100 \cdot \frac{W_1}{W_2}$$

The degree of swelling was calculated by the following equation:

$$\text{Degree of swelling (\%)} = 100 \cdot \frac{W_s - W_1}{W_1}$$

The results are summarized in table S2 and show that the HCl treatment does not have a significant impact on the swelling behavior or the gel content of PAAm.

Table S2. Gel content and degree of swelling of PAAm bulk samples after being incubated in bidest. water or 0.5 M HCl for 2 d and subsequently washed and swollen to equilibrium in aqua bidest. The results show that the acid treatment does neither change the gel content nor the swelling behavior of the PAAm substrate significantly.

Incubation Medium	Gel Content (%)	Degree of Swelling (%)
Aqua Bidest.	98.2 ± 1.04	2018 ± 25
HCl (0.5 M)	98.1 ± 0.54	2048 ± 24

Supplementary Movie 1: 16 h time-lapse of *Acanthamoeba castellanii* moving through 3D hydrogel channel network with embedded cAMP solution.

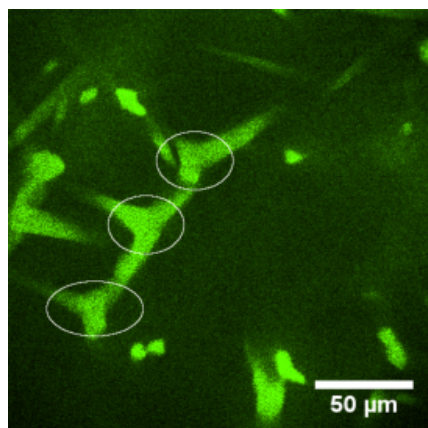


Figure S3. Fluorescence microscopy image of a microchannel-containing PAAm. The channels were filled with FITC dextran in order to render them fluorescent. The white circles indicate junctions in the microchannel network.

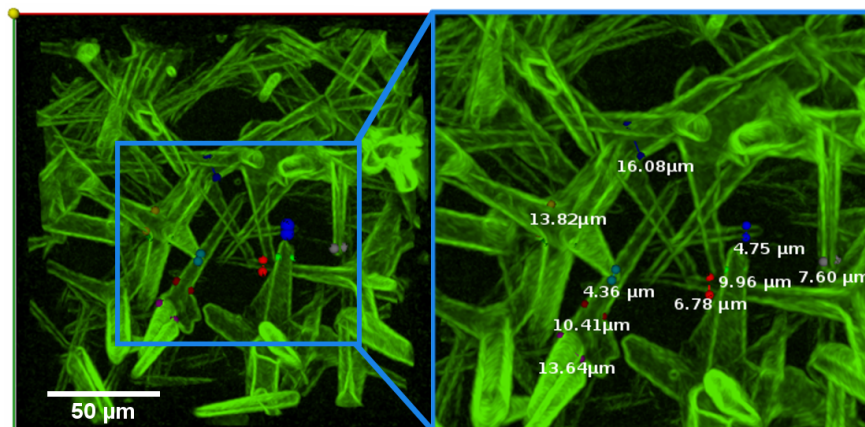


Figure S4. Top-view of a composition of z-stack images of a PAAm sample containing microchannels, which are filled with FITC dextran. Using z-stacks of fluorescent microscopy images of fluorescent microchannels, the channel diameters can be determined using image processing softwares. The zoom on the right shows exemplary results of measured channel diameters.

Chapter 7

Light controlled growth factors release on tetrapodal ZnO microparticles incorporated 3D printed hydrogels for developing smart wound dressing

For the treatment of chronic wounds a multifactor therapy is necessary to address major aspects like inflammation, bacteria infection and dehydration. The complex nature of this ailment requires precision medicine in order to ensure complete patient recovery. Often even a patient-specific treatment is necessary to account for the respective nature of the chronic wound. Smart wound scaffolds have raised attention because of the possibility to incorporate many or all components for the multifactor therapy into one system. In this work, additive manufacturing of hydrated hydrogel containing self-assembled t-ZnO particles is presented as a possible solution. The single-crystalline t-ZnO releases protein when illuminated with light and possesses anti-bacterial properties. 3D-printing allows for open-porous, patient-specific structuring of the hydrogel, which contributes to oxygenation.

Own contribution presented in this article

- Fabrication of t-ZnO hydrogel composites
- Protein release test investigation
- Mechanical and printability investigation
- Scientific analysis and discussion
- Writing the manuscript

Manuscript

1
2
3
4
5
6
7
8
9
10
11
12
13
14
15
16
17
18
19
20
21
22
23
24
25
26
27
28
29
30
31
32
33
34
35
36
37
38
39
40
41
42
43
44
45
46
47
48
49
50
51
52
53
54
55
56
57
58
59
60
61
62
63
64
65

DOI: 10.1002/ ((please add manuscript number))

Article type: Full Paper

Light-controlled growth factors release on tetrapodal ZnO-incorporated 3D-printed hydrogels for developing smart wound scaffold

By Leonard Siebert, Eder Luna-Cerón, Luis Enrique García-Rivera, Junsung Oh, JunHwee Jang, Diego A. Rosas-Gómez, Mitzi D. Pérez-Gómez, Gregor Maschkowitz, Helmut Fickenscher, Daniela Ocegüera-Cuevas, Carmen G. Holguín-León, Batzaya Byambaa, Mohammad A. Hussain, Nebras Sobahi, Anwarul Hasan, Dennis P. Orgill, Yogendra K. Mishra, Rainer Adelung, Eunjung Lee*, Su Ryon Shin**

L. Siebert, L. E. García-Rivera, E. Luna-Cerón, D. A. Rosas-Gómez, M. D. Pérez-Gómez, D. Ocegüera-Cuevas, C. G. Holguín-León, Prof. S. R. Shin.
Division of Engineering in Medicine, Department of Medicine, Brigham and Women's Hospital, Harvard Medical School, Cambridge, MA 02139, USA.
E-mail: sshin4@bwh.harvard.edu

L. Siebert, Prof. Y. K. Mishra, Prof. R. Adelung,
Functional Nanomaterials, Institute for Materials Science, Faculty of Engineering, Kiel University, Kaiserstr. 2, D-24143, Kiel, Germany.
E-mail: lesi@tf.uni-kiel.de

J. Oh, J. Jang, Prof. E. Lee
Department of Nano-biomedical Science & BK21 PLUS NBM Global Research Center for Regenerative Medicine, Dankook University, Cheonan 31116, Republic of Korea.
E-mail: leeej@dankook.ac.kr

Dr. G. Maschkowitz, Prof. H. Fickenscher
Institute for Infection Medicine, Kiel University and University Medical Center Schleswig-Holstein, Brunswiker Str. 4, D-24105 Kiel, Germany.

Dr. B. Byambaa

1
2
3
4
5
6
7
8
9
10
11
12
13
14
15
16
17
18
19
20
21
22
23
24
25
26
27
28
29
30
31
32
33
34
35
36
37
38
39
40
41
42
43
44
45
46
47
48
49
50
51
52
53
54
55
56
57
58
59
60
61
62
63
64
65

3D BioLabs, LLC, 700 Main St, Cambridge, MA 02138

Prof. M. A. Hussain, Dr. Nebras Sobahi
Department of Electrical and Computer Engineering, King Abdulaziz University, Jeddah
21569, Saudi Arabia.

Prof. A. Hasan
Department of Mechanical and Industrial Engineering, College of Engineering, Qatar
University, Doha, Qatar.
Biomedical Research Centre (BRC), Qatar University, Doha, Qatar.

Prof. D. P. Orgill
Division of Plastic Surgery, Department of Surgery, Brigham and Women's Hospital,
Harvard Medical School, Boston, MA, USA

Prof. Y. K. Mishra
Mads Clausen Institute, NanoSYD, University of Southern Denmark, Alsion 2, 6400,
Sønderborg, Denmark.

[*] L. Siebert, E. Lee, and S. R. Shin contributed equally as corresponding authors.

Key Words: Zinc oxide tetrapod, 3D Printing, Photoactive, Controlled release, Hydrogel
composites, Wound healing

Abstract

Advanced wound scaffolds that integrate active substances to treat chronic wounds have gained much attention. While wound scaffolds and advanced functionalities have been incorporated into one medical device, a wirelessly triggered release of active substances has remained the focus of many research endeavors. To combine multiple functions including light-triggered activation, anti-septic, angiogenic, and moisturizing properties, we have developed a 3D printed hydrogel patch encapsulating growth factors (GFs) decorated with photoactive and antibacterial tetrapodal zinc oxide (t-ZnO) microparticles. To achieve the smart release of GFs, t-ZnO was modified by chemical treatment and activated through UV/visible light exposure. This process would also make the surface rough and improve GF adhesion. The elastic modulus and degradation behavior of the composite hydrogels, which must match the wound healing process, were adjusted by changing t-ZnO concentrations. The t-ZnO-laden composite hydrogels can be printed with any desired micropattern to potentially create a modular elution of various GFs. The GF decorated t-ZnO-laden hydrogel patches showed low cytotoxicity and improved angiogenic properties while maintaining antibacterial functions *in vitro*. *In vivo* tests showed promising results for the printed wound patches, less immunogenicity, and enhanced wound healing.

Introduction

Chronic inflammation is a widespread complication of diabetes.^[1] Diabetic foot ulcers can lead to amputation in 14-24% of cases^[2] and 84% of amputations have been linked to extreme ulcers.^[1] Chronic wounds are described as diseased tissues that have failed to heal over a reasonable amount of time, typically within three months.^[3] Thus, treatment is important and necessary to avoid the consequences of prolonged inflammation and to reduce the probability of systemic infection. To ensure expeditious healing, a treatment that incorporates multiple factors is ideal. These factors include oxygenation, infection treatment, hydration, and the application of growth- and proliferation-related proteins. To include all of these factors, smart wound scaffold devices have gained considerable interest in the past decade.^[4] However, including synergistic therapeutic effects like antibacterial properties and proper angiogenesis in one treatment remains challenging.

To alleviate this, nanoparticle composites can be used as smart delivery platforms due to their unique physical properties, such as high surface area, the ability to respond to various stimuli (*i.e.* light, temperature, electrical signal, etc.), and the ability to control the release of bioactive molecules like growth factors (GFs) under specific conditions.^[5] Their success rate is usually hampered because nanoparticles often penetrate cell membranes by endocytosis and damage the cells through increased reactive oxygen species (ROS) concentration, etc.^[6] For example, spherical ZnO nanoparticles have been studied extensively for their antibacterial properties,^[6-7] however, due to their size, they are phagocytosed by cells and can be cytotoxic, even at low concentrations ($> \sim 25 \mu\text{g/mL}$ at around 50% viability).^[8] Tetrapod-shaped ZnO particles (t-ZnO) are nanostructured microparticles that exhibit most of the benefits of the nanoscale despite being bigger than normal cells. For example, they retain their antibacterial properties without being endocytosed, which makes them fit for

1
2
3
4 many biomedical and tissue engineering applications.^[8a, 9] Due to their unique 3D shape and
5
6 high aspect ratio, they are accessible from all dimensions, resulting in a large contact area
7
8 with the surrounding media that can facilitate the efficient loading and release of GFs. In
9
10 addition, each arm of t-ZnO is a single-crystal, thus showing unique semiconductor and
11
12 photoactive properties not inherently found in amorphous ZnO nanoparticles.^[10] The
13
14 surface's chemical and physical properties can also be altered by chemical treatment.
15
16 Therefore, by tuning the photoactive function of t-ZnO, we could achieve the controlled
17
18 release of GFs by light stimulations while maintaining the antibacterial properties.
19
20
21
22

23
24 To successfully integrate these functional microparticles into the wound area for a long
25
26 period of time, GF decorated t-ZnO particles can then be embedded into a printable hydrogel
27
28 like gelatin methacryloyl (GelMA), which is chemically functionalized and denatured
29
30 collagen. Additionally, it is possible to tune GelMA hydrogels in terms of stiffness and
31
32 elasticity, ideally matching those of the native skin, so that they degrade at a rate that supports
33
34 their replacement by the regenerating tissue to prevent scar tissue formation.^[11] The stiffness
35
36 of the gels is particularly important, as a mismatch in mechanical properties compared to
37
38 surrounding tissues can cause stress concentrations at the interface that can result in
39
40 delamination or hypertrophic scarring. Furthermore, the GelMA hydrogels have microporous
41
42 structures which allow for the uptake of a large amount of biological solutions and the release
43
44 of various biological factors, while the t-ZnO microparticles exhibit enough contact with the
45
46 wound area to effectively kill bacteria. Therefore, this t-ZnO-laden printed composite
47
48 hydrogel forms a synergistic wound healing platform, combining the unique properties of
49
50 both hydrogels and microparticles such as attractive fluid absorbance properties, tunable
51
52 mechanical properties, GF delivery capabilities and antibacterial properties.^[12]
53
54
55
56
57
58
59
60
61
62
63
64
65

1
2
3
4 In this work, we show how a combination of materials science and biomedical
5
6 engineering can drastically reduce fabrication efforts while significantly improving the
7
8 wound healing aspects of wound scaffolds. A smart wound scaffold strategy based on GF-
9
10 decorated and antibacterial t-ZnO microparticles embedded in GelMA hydrogels is
11
12 presented. Moreover, chemically-treated t-ZnO microparticles can provide denser protein
13
14 decoration, which can be released by green light stimulations. These composite hydrogels
15
16 were printed to provide open and porous 3D constructs that could assist in the release of GFs
17
18 and oxygenation penetration while maintaining hydration and having antibacterial and
19
20 angiogenic functions via GF decorated t-ZnO. The cellular behavior, *in vivo*
21
22 biocompatibility, wound healing behaviors, antibacterial functions, and the selective release
23
24 properties of the wound scaffold and the t-ZnO particles have been investigated and discussed
25
26 in detail.
27
28
29
30
31

32 33 34 35 **Results and Discussions**

36
37
38 The working concept for the smart wound scaffold and its fabrication is briefly depicted
39
40 in **Schematic 1**. We obtained t-ZnO microparticles with 30-100 μm overall size via flame
41
42 transport synthesis.^[13] The particles' unique 3D tetrapod shape and high aspect ratio
43
44 (diameter: $\sim 100\text{ nm} - 10\ \mu\text{m}$, length: $\sim 5\ \mu\text{m} - 100\ \mu\text{m}$) makes it difficult for them to penetrate
45
46 cells while allowing them to retain a large contact area with the surrounding media. Aside
47
48 from these benefits, t-ZnO also has a strong antibacterial effect. Paired with its semiconductor
49
50 nature, it can become a beneficial platform for protein and drug adhesion and release. Pristine
51
52 t-ZnO exhibits a bandgap in the UV range.^[14] To improve the release rate of GFs through
53
54 natural conditions such as visible light stimulation, which does not require specific devices
55
56 or tools, it is necessary to tune t-ZnO microparticles to become photoactive and enable them
57
58
59
60
61
62
63
64
65

1
2
3
4 to react to both UV and relatively biosafe visible light ranges, while maintaining their
5
6 antibacterial properties.
7

8
9 To do this, surface-only chemical treatments like etching t-ZnO with e.g., hydrogen
10
11 peroxide (H_2O_2) can lower its bandgap into the range of green light. This enables the t-ZnO
12
13 microparticles to interact with blue or green light and can thus allow them to deliver specific
14
15 proteins depending on the selected responsiveness towards different light sources in the
16
17 future. The t-ZnO itself can show a large bandgap and inconsistent polarity on its side facets
18
19 due to a difference in oxygen vacancy concentration. High polarity is required for strong
20
21 physical interactions with the desired GFs to ensure homogeneous and thick coating.
22
23 Converting the surface superficially into t-ZnO₂ with H_2O_2 increases protein adhesion due to
24
25 increased surface area and higher polarity. Subsequently, proteins like the vascular
26
27 endothelial growth factor (VEGF) can be used for decoration, to, e.g., increase angiogenesis
28
29 upon release. The coated t-ZnO can then be mixed into a GelMA pre-polymer solution as a
30
31 composite ink at varying concentrations, and then 3D printed into patch-like open-pore
32
33 constructs. Antibacterial activity is additionally ensured by the protruding t-ZnO from the
34
35 printed constructs.
36
37
38
39
40
41
42

43 The treatment of t-ZnO with H_2O_2 is a viable option to change the surface properties of
44
45 the t-ZnO, like protein adhesion and light responsiveness, without deteriorating the
46
47 mechanical integrity of the t-ZnO. The H_2O_2 treatment can be easily recognized by the color
48
49 change of t-ZnO from a white color to a yellowish color as shown in **Figure 1A**. The
50
51 superficial conversion of ZnO to ZnO₂ by H_2O_2 treatment was investigated by micro-Raman
52
53 spectroscopy, which is presented in **Figure 1B**. Untreated t-ZnO and H_2O_2 -treated t-ZnO
54
55 both show their respective, characteristic peaks at 100 cm^{-1} , 440 cm^{-1} , and 1140 cm^{-1} .
56
57 Additional peaks at 850 cm^{-1} and 1550 cm^{-1} , which are related to ZnO₂, were observed for
58
59
60
61

1
2
3
4 the H₂O₂-treated t-ZnO, indicating a partial conversion from ZnO to ZnO₂. The presence of
5
6 some ZnO peaks in the t-ZnO is likely due to the incomplete conversion of the ZnO to ZnO₂,
7
8 making it possible to maintain the functions of both pristine t-ZnO and H₂O₂-treated t-ZnO.
9
10 The duration of the chemical treatment dictates the degree of conversion, so the desired
11
12 amount of ZnO₂ can be tailored to the specific requirements.
13
14

15
16 The morphology of the t-ZnO before and after treatment with H₂O₂ was evaluated by
17
18 scanning electron microscopy (SEM) as shown in **Figures 1 C-i** and **D-i**, respectively. The
19
20 t-ZnO showed hexagonal arms, each with a length of roughly 30 μm and a thickness of
21
22 around 2 μm. Prior to the H₂O₂ treatment, the arms' surfaces were smooth, afterwards, the
23
24 surfaces became rough and lumpy, while pristine ZnO remained underneath. These SEM
25
26 images confirmed the results of the Raman spectroscopy, which showed an incomplete
27
28 transformation of ZnO to ZnO₂. The adhesion of the nanostructured ZnO₂ on the surfaces of
29
30 the ZnO arms was so strong that no ZnO₂ nanoparticles were released within the biological
31
32 solutions.
33
34
35
36
37

38
39 These nanostructured ZnO₂ particles also significantly increased the protein adsorption
40
41 due to their rough and porous surface morphology. To confirm the protein adhesion, the
42
43 commonly used secondary antibody IgG Alexa Fluor™ 594 (AF594) was coated on the t-
44
45 ZnO with and without H₂O₂ treatment as a model protein to easily confirm protein absorption
46
47 via fluorescence microscopy. Only a mild and inconsistent coating, indicated by the partially
48
49 expressed red fluorescence signal, was observed on the pristine t-ZnO, which expressed a
50
51 blue fluorescence signal (**Figure 1C-ii, -iii, and -iv**). In contrast, H₂O₂-treated t-ZnO showed
52
53 a thick and homogeneous coating that was confirmed by the strong red fluorescence signal
54
55 expressed on all particles, shown in **Figure 1D-ii** (high magnification) and **-iii** (low
56
57 magnification). Additionally, the bandgap of ZnO₂ (3.8 eV, visible light range) is higher than
58
59
60
61

1
2
3
4 that of ZnO, which is 3.37 eV in the UV light range.^[15] The inconsistent coating of protein
5
6 on pristine t-ZnO could be due to the varying polarity on the particles' side facets. Oxygen
7
8 vacancies on the ZnO surface are often attributed to polarity, however, their concentrations
9
10 may vary laterally and protein adsorption by polar bonding might show large lateral
11
12 deviations. The mechanism of protein adsorption can be covalent bonding between the amide
13
14 and these oxygen vacancies. This of course only holds for the first layer of protein. All
15
16 subsequent layers may be held in place by dipole forces from the polar t-ZnO to the protein.
17
18 The complicated interactions of semiconductors and liquids are often hard to predict, so the
19
20 superficial conversion to ZnO₂ helps with consistent and thick protein adsorption through
21
22 rough morphology. From the yellow color of the powder, one can also see an optical
23
24 activation of pristine ZnO underneath, which is attributed to the narrowing bandgap induced
25
26 by oxygen vacancies.^[16]
27
28
29
30
31
32

33 Protein release experiments were performed to assess the functionality of the proposed
34
35 working mechanism of H₂O₂-treated t-ZnO particles, which were produced based on their
36
37 tuned photoactive properties as well as their strong protein interactions. The ZnO₂ which
38
39 resulted from H₂O₂ treatment was much more polar than pristine t-ZnO and could therefore
40
41 bind indiscriminately yet more efficiently to the polar groups of larger proteins. Additionally,
42
43 the bandgap after H₂O₂ treatment was smaller, resulting in photoactivity in the optical
44
45 spectrum. The proposed mechanism for visible light-controlled protein release is due to the
46
47 formation of electrons and holes, resulting in the accumulation of charges on the ZnO₂ surface
48
49 as shown in **Figure 1E**. Later the increased charge density could help to release proteins via
50
51 electrostatic interaction. The energy of the electron-hole pairs needs to be low enough to
52
53 prevent photocatalysis, which destroys the adsorbed protein. In this process, the charge
54
55 carriers react with organic substances in the solution.
56
57
58
59
60
61

1
2
3
4 For the release of proteins, the binding must be light, yet efficient. A large amount of
5
6 protein loading via strong bonding to the t-ZnO surface might result in low quantities of
7
8 protein release upon illumination. To evaluate whether the H₂O₂ treatment is the best way to
9
10 efficiently load and release GFs, different surface treatments that would reduce adhesive
11
12 forces while maintaining efficient loading were tested for t-ZnO. First, different reagents
13
14 were tested to determine the most effective coating material for t-ZnO in terms of its capacity
15
16 to enhance protein adsorption. As shown in **Figure S1**, the pristine t-ZnO microparticles were
17
18 coated with bovine serum albumin (BSA), oleic acid, and streptavidin, respectively, and then
19
20 were further coated with IgG AF594. The t-ZnO particles with various coatings were exposed
21
22 to UV light for 25 seconds. The BSA-coated and the oleic acid-coated t-ZnO microparticles
23
24 showed no significant changes in the red fluorescence signal after UV light stimulation.
25
26 Moreover, protein degradation was observed on the oleic acid-coated t-ZnO microparticles
27
28 (data not shown). This could be due to the addition of ethanol during the IgG AF594 coating
29
30 process. In terms of the streptavidin-coated samples, there was no observable coating with
31
32 IgG AF594. Consequently, all treatments showed low adhesion of the protein and no visible
33
34 protein release by UV light stimulation.
35
36
37
38
39
40
41
42

43 To evaluate protein release by green light stimulation, H₂O₂-treated t-ZnO
44
45 microparticles were coated with IgG AF594 before applying UV light for 300 seconds. As a
46
47 comparison, and to differentiate protein release from protein degradation, hydrophilic and
48
49 non-photoactive SiO₂ particles were coated with IgG AF594 and exposed to UV light (**Figure**
50
51 **S2**). The negative slope despite the photo-inactivity of SiO₂ suggests degradation of the
52
53 material after it had been illuminated. The rate of degradation was around 0.008% per second,
54
55 which could be explained by photobleaching. Due to the large bandgap of SiO₂, it exhibited
56
57 no semiconductor effects.
58
59
60
61
62
63
64
65

1
2
3
4 To confirm the GF release, VEGF was coated onto H₂O₂-treated t-ZnO and was
5
6 irradiated with strong green light (527 nm at >2000 lx) for a few minutes. The VEGF-coating
7
8 on the surfaces of H₂O₂-treated t-ZnO particles was evaluated by SEM. As shown in **Figure**
9
10 **1F**, the nanostructures of ZnO₂ were entirely covered by the VEGF layer and a smooth
11
12 surface could be seen, but the texture of the surface was completely different from pristine t-
13
14 ZnO (**Figure 1C-i**). The formation of these VEGF layers has provided strong evidence for
15
16 the successful functionalization of t-ZnO with H₂O₂ treatment, which has generated a
17
18 hydrophilic ZnO₂ nanostructure that allows for uniform protein adhesion. Then ELISA assay
19
20 was performed to monitor the controlled release of VEGF in the supernatant after each
21
22 irradiation. Here, two t-ZnO groups, one with a high initial concentration during coating and
23
24 another with a lower initial protein concentration, were compared to optimize the
25
26 concentration of VEGF loading (**Figure 1G**). Both low (1 µg/mL) and high (5 µg/mL)
27
28 concentrations of coating resulted in the same release rate, indicating that the coating was
29
30 already maximized with the lower coating concentration. Even after 120 seconds with strong
31
32 green light illumination, there was no decrease in slope, which makes this technique a
33
34 promising candidate for long term protein release in natural conditions. The concentration of
35
36 VEGF released per mg t-ZnO was below 1 ng, within the efficient treatment window of
37
38 VEGF in wound healing on the order of ng/10⁶, which makes this approach suitable for
39
40 triggering proper angiogenesis without an overdose of VEGF.^[17]
41
42
43
44
45
46
47
48
49

50 When comparing the VEGF release after UV-light and green light stimulations, a
51
52 strong effect can be observed. In this experiment, the supernatants of the solutions were not
53
54 removed, and the samples were not washed after each round of illumination. The release
55
56 from treated microparticles was assessed with an ELISA. The highest concentration of VEGF
57
58 in the solution was observed after 250 seconds of green light exposure, where the released
59
60
61
62
63
64
65

1
2
3
4 concentration represented a 600% increase compared to the initial value. When exposed to
5
6 UV light, only a minor increase in protein concentration could be found. For longer durations
7
8 of the experiment, while the protein was bound to the ZnO surface, the binding may have
9
10 stabilized the protein and facilitated its integrity. The experiment was carried out at room
11
12 temperature, and sensitive proteins like VEGF are known to degenerate at higher
13
14 temperatures after some time. In any case, this set of experiments showed that fine-tuning
15
16 the semiconductor properties of a ZnO biomaterial is a viable strategy for protein adhesion.
17
18 VEGF could be successfully coated and released by utilizing both UV and green light. The
19
20 increased coating efficiency and the higher surface area after the H₂O₂-treatment could
21
22 provide a reasonable release in the effective range. This concept could be elaborated on in
23
24 future works and could be a promising candidate for light-triggered actuators for drug
25
26 delivery.
27
28
29
30
31
32

33 To develop a t-ZnO embedded wound scaffold which can protect wounds from outside
34
35 environmental conditions and infections, a GelMA hydrogel was used to facilitate the wound
36
37 scaffold due to its attractive fluid absorbance properties, biological properties similar to
38
39 collagen, structural fidelity via various microfabrication techniques, and easy to tune physical
40
41 and mechanical properties.^[12] The mechanical properties of the wound scaffold should also
42
43 match those of native skin (Elastic modulus: 100 - 210 kPa)^[18] to provide the necessary
44
45 mechanical cues for accelerated healing of the wound and to minimize scar tissue
46
47 formation.^[19] To resemble the elastic modulus of the native skin, a high concentration GelMA
48
49 hydrogel with 10% w/v which usually showed > 50 kPa compressive modulus was
50
51 selected.^[12] Furthermore, nanoparticles or microparticles have been used as reinforcing
52
53 reagents to improve the mechanical properties of hydrogels. Therefore, we studied the effect
54
55 of t-ZnO microparticles on the physical properties of hydrogels, such as the mechanical and
56
57
58
59
60
61
62
63
64
65

1
2
3
4 degradation behavior of composite hydrogels with increasing amounts of t-ZnO (from 0 to
5
6 5%). Due to the hydrophilic nature of both t-ZnO- and H₂O₂-treated t-ZnO microparticles,
7
8 thorough, yet careful vortexing of the t-ZnO particle-laden solution at 37 °C can help with
9
10 the dispersion of the particles without breaking the particles into a high concentration of
11
12 GelMA pre-polymer solution. As shown in **Figure 2A**, the t-ZnO microparticles were well
13
14 dispersed in the 10 w/v% GelMA pre-polymer solution without using additional harsh
15
16 dispersion processes (*i.e.* using ultrasonicator, strongly acidic or basic solvents, or
17
18 surfactants) due to hydrophilic nature of t-ZnO microparticles. Also at 37 °C, the increased
19
20 chain mobility and decreased viscosity of GelMA pre-polymer could help to disperse the t-
21
22 ZnO particles.
23
24
25
26
27

28
29 The surface morphology of the smart wound scaffold is of importance since it will be
30
31 in direct contact with the wound. Hence, SEM analysis was performed to investigate the
32
33 structure and morphology of the dried GelMA hydrogel. The embedded t-ZnO microparticles
34
35 were observed in the pore walls of composite hydrogels, which still maintained the porous
36
37 nature of a pristine GelMA hydrogel without any significant effect on the morphological
38
39 change by increasing the concentration of t-ZnO (**Figure 2B**). Furthermore, the tetrapodal
40
41 arms of the t-ZnO microparticles stick out on the surfaces of the hydrogels, which has been
42
43 proven to provide excellent antibacterial properties while supporting cell growth in porous
44
45 scaffolds.^[20] In **Figure 2C-i**, we observed a large number of tetrapodal arms (indicated by
46
47 red arrows) on the surfaces of the composite hydrogels. Also, we found that most of the
48
49 extruded tetrapodal arms, indicated by red arrows in **Figure 2C-ii**, were coated by the GelMA
50
51 hydrogel. These extruded tetrapodal arms significantly increased the surface roughness of
52
53 composite hydrogels, which was measured by topographic mapping using an AFM (**Figure**
54
55 **2D**). This means that the concentration of t-ZnO can be actively used to determine the number
56
57
58
59
60
61
62
63
64
65

1
2
3
4 of protruding arms, and t-ZnO microparticles could lead to an increase in the local
5
6 mechanical properties of the composite hydrogels.
7

8
9 To investigate the microscale local mechanical properties of the composite hydrogels
10 and the impact of the t-ZnO microparticles, a Derjaguin–Muller–Toporov (DMT) modulus
11 was performed using force–deformation plots to reveal the local mechanical properties of
12 different composite hydrogels (**Figures 2E and F**). With a likeness to the surface roughness
13 of composite hydrogels, a composite hydrogel laden with a high concentration of t-ZnO
14 particles showed the highest level of modulus fluctuation across the surface compared with
15 that of a pristine GelMA hydrogel. Moreover, the local elastic moduli of GelMA hydrogels
16 that incorporated 1.0 % t-ZnO (~0.5 MPa) and 3.0 % t-ZnO (~0.85 MPa) were higher than
17 that of pristine GelMA (~0.1 MPa), as shown in **Figure 2G**. The local elastic moduli of the
18 composite hydrogels increased because of the single-crystal structure of ZnO’s tetrapodal
19 arms, which themselves showed high elastic moduli in the ~70 GPa range.^[21] Here, we
20 observed a much lower elastic modulus than that of a single crystal of t-ZnO, likely because
21 the extruded tetrapodal arms were covered by the soft GelMA hydrogel around 10 μm in
22 thickness, which was confirmed by **Figure 2C-ii**. This GelMA was ordered around the arms
23 of the tetrapods and thus became stiffer than the unordered hydrogel in the rest of the
24 composite.
25

26
27 The increased local elastic modulus, which correlated with increases in the
28 concentration of t-ZnO, might have a significant effect on the macroscale mechanical
29 strength of composite hydrogels. To ensure the mechanical integrity of the constructs for
30 different concentrations of t-ZnO microparticles, compression tests were performed
31 (**Figure 2H and I**). Although fluctuations were not significantly high, the highest
32 compressive modulus was found with a 2% t-ZnO-laden GelMA hydrogel. Lower
33
34
35
36
37
38
39
40
41
42
43
44
45
46
47
48
49
50
51
52
53
54
55
56
57
58
59
60
61
62
63
64
65

1
2
3
4 compressive moduli were found for both the pristine GelMA hydrogel and the highest
5 concentrations (3% and 5%) of t-ZnO-laden composite hydrogels (**Figure 2I and Figure**
6
7 **S3**). Due to the relatively low concentration and the softness of the hydrogel, the
8 incorporation of the t-ZnO particles does not significantly impact the mechanical properties.
9
10 However, t-ZnO is a wide bandgap semiconductor, which can absorb UV-light during curing.
11
12 The absorbed light is therefore not available for crosslinking reactions at very high filling
13 factors. Induced electron-hole-pairs of the t-ZnO can significantly absorb radicals which are
14 generated by the photoinitiator under UV exposure during the photocrosslinking process.
15
16 These two competing effects may be the reason why the highest measured compressive
17 modulus was at 2% t-ZnO (**Figure S3**). In any case, the constructs showed an appropriate
18 mechanical stiffness, which enabled handling without problems.
19
20

21
22 For wound healing and protein release, the degradation of the hydrogels over time also
23 plays a crucial role. To assess the interaction between t-ZnO and the hydrogels in terms of
24 degradation, bulk hydrogel samples with varying concentrations of t-ZnO were subjected to a
25 forced degradation test by incubating them at 37 °C in a collagenase type II dissolved in PBS
26 for 24 hours (**Figure 2J**). As depicted in **Figure 2J**, the resulting measurements from the
27 degradation test confirmed that a correlation exists between the hydrogels' structural integrity
28 and the percentage of t-ZnO within the constructs. With increasing concentrations of t-ZnO,
29 the GelMA polypeptide chains have less available space to form a more solid arrangement,
30 hence, compromising the structural integrity and favoring exposition to enzymatic
31 degradation. Considering their wound healing applications, constructs with 1% t-ZnO were
32 stable enough to withstand the effects of collagenase degradation, making them feasible to
33 function efficiently for prolonged treatment times.
34
35
36
37
38
39
40
41
42
43
44
45
46
47
48
49
50
51
52
53
54
55
56
57
58
59
60
61
62
63
64
65

1
2
3
4 The high-concentration GelMA hydrogels (> 5 %) have dense structures, which, in high
5
6 concentrations might induce slow degradation behavior *in vitro* and *in vivo* and slow down
7
8 the release of biomolecules or drugs. To solve these issues, microfabricated hydrogels with
9
10 open porous microstructures, which have large surface areas compared with bulk hydrogels,
11
12 could help to adjust the degradation rate and achieve the desired release behaviors. They can
13
14 also help to flow oxygen to a wound site through open porous structures, which could
15
16 improve wound healing.^[22] To do this, a 3D printing technique was developed to fabricate
17
18 reproducible open porous 3D structures using composite hydrogel inks, such as t-ZnO
19
20 embedded GelMA hydrogels. As the inks were composed of t-ZnO-laden GelMA pre-
21
22 polymer solutions, due to the large size of the t-ZnO microparticles (Diameter: 10-100 μm),
23
24 they tended to easily settle in low concentrations of GelMA pre-polymer solutions (< 7.5
25
26 w/v%), which have low viscosities. Also, by adding t-ZnO microparticles, the viscosities of
27
28 the GelMA pre-polymer solutions at room temperature were significantly decreased (data not
29
30 shown). The hydrophilic nature of t-ZnO may decrease physical interactions within GelMA
31
32 chains, and the particles' unique 3D structures could prevent the helix-coil transition of
33
34 GelMA chains at room temperature. So, the composite ink remained in the solution phase at
35
36 room temperature without gelation and no clogging issue was observed, which has always
37
38 occurred in a pristine GelMA pre-polymer solution. Therefore, a 10% GelMA pre-polymer
39
40 solution with high viscosity has suitable conditions to prevent t-ZnO microparticles from
41
42 settling in the composite ink before and during the printing process. A higher viscosity
43
44 increases the shear force exerted on the particles and enables the extrusion of inks with high
45
46 concentrations of particles (up to 10 w/v% of t-ZnO).
47
48
49
50
51
52
53
54
55
56

57 The printing process is shown schematically in **Figure 3A**. As depicted in the schematic,
58
59 the protein-coated, H₂O₂-treated, t-ZnO suspended composite inks were successfully printed
60
61

1
2
3
4 with good shape fidelity on the print bed, which was kept at 4 °C to maintain 3D structures
5
6 before crosslinking the hydrogels by UV exposure (**Video 1**). Controlling the temperature of
7
8 the composite ink was necessary because GelMA pre-polymer solutions exhibit strong
9
10 changes in viscosity with varying temperatures.^[23] This is due to the tangling and untangling
11
12 of individual GelMA strands below ~20 °C.^[24] To prevent the fractures from occurring in the
13
14 tetrapods, a relatively large nozzle size (Inner diameter: 0.4 mm) was used due to the complex
15
16 shape and high aspect ratio of the tetrapods (some particles are up to 0.1 mm in diameter).
17
18 These measurements resulted in a successful printing as depicted in **Figures 3B** and **3C**. We
19
20 observed a homogeneous and fine dispersion of the t-ZnO particles with minimal breaking
21
22 in the printed microfibers, which is important to secure a sufficient contact area for t-ZnO in
23
24 the hydrogel. In **Figure 3B**, we also observed the protruding arms (arrows) from the printed
25
26 microfibers, which may also help to prevent separations between the scaffold and the injured
27
28 area via physical interlocking.^[25]
29
30
31
32
33
34
35

36 After optimizing the printing parameters, patch-like printed constructs with various
37
38 shapes were successfully obtained after crosslinking by UV exposure using VEGF-coated
39
40 1% H₂O₂-treated t-ZnO-laden GelMA (**Figure 3D**) and 2% t-ZnO-laden GelMA (**Figure 3E**)
41
42 inks. A fluorescence microscope image of the hydrogels was also taken, showing the blue
43
44 photoluminescence of the t-ZnO inside the gels when irradiated with UV-light. The printed
45
46 constructs with various shapes could withstand the touch, could be picked up, and were
47
48 generally easy to handle (**Figure 3F**). Patient-specific therapy might need to rely on a mixture
49
50 of multiple materials for optimal treatment. Multi-material constructs were therefore
51
52 fabricated using fluorescent dyes to demonstrate the feasibility of construction. Two printed
53
54 constructs are shown in **Figures 3G** and **3H**, possessing a cross-like and a layered pattern of
55
56 pink-colored ink with spaces filled with green colored ink, respectively.
57
58
59
60
61

1
2
3
4 In an SEM image, we observed well distributed t-ZnO microparticles within the printed
5
6 constructs with microporous structures (**Figure 3I**). Exposure to UV light triggered the
7
8 crosslinking reaction of the GelMA, and the amount of methacrylic groups and the intensity
9
10 and duration of the exposure determined the degree of crosslinking. For the treatment of
11
12 sensitive wounds, and to have a sufficient water uptake, a soft and mildly crosslinked
13
14 hydrogel is beneficial. Additionally, the UV light should not trigger the premature release of
15
16 protein. For these two reasons, the UV exposure time should be kept as short as possible. To
17
18 evaluate the swelling behavior of the hydrogels and the influence of t-ZnO, incubation
19
20 experiments in PBS at 37 °C were carried out for the 3D-printed constructs for 1 week.
21
22 Representative images of the constructs that were crosslinked for 10 to 100 seconds can be
23
24 seen in **Figure S4**. The constructs did not show significant degradation upon incubation, and
25
26 the hydrogels only swelled in the solution after 6 days. No significant impact of the added t-
27
28 ZnO could be observed.
29
30
31
32
33
34
35

36 After optimizing the printing parameters, VEGF-coated t-ZnO-laden GelMA hydrogels
37
38 were characterized to study the feasibility of cell functionality, attachment, and proliferation
39
40 on the surfaces of composite hydrogels (**Figure 4 and Figure S5**). Wound healing is
41
42 contingent upon numerous factors, such as the interactions of different cell lineages with
43
44 specific functions.^[26] Human umbilical vein endothelial cells (HUVEC), a representative cell
45
46 type involved in the key roles of angiogenesis and wound healing,^[20] were cultured and
47
48 seeded on top of hydrogels. C2C12 myoblasts, which have been previously used to measure
49
50 the cytotoxicity of t-ZnO particles, were also used to assess the cell compatibility of the t-
51
52 ZnO microparticles inside the constructs.^[27]
53
54
55
56
57

58 Cell viability was assessed on day 1 of culture for both cell types, and the results showed
59
60 a decrease in cell viability with higher t-ZnO concentrations. Previous studies regarding the
61
62
63
64
65

1
2
3
4 cytotoxic effects of t-ZnO and regular ZnO nanoparticles on different cell types, including
5 the C2C12 cell lineage, have shown similar behaviors. For the nanoparticles, this reduction
6 in viability was already observed at concentrations as low as 40 µg/mL, which is 25 times
7 lower than the concentration of t-ZnO used in this study.^[8b, 28] The primary mechanisms for
8 cytotoxicity from ZnO particles have been linked to the induction of Ca⁺² influxes, reduced
9 mitochondrial membrane potential, inactivation of key enzymatic processes, loss of
10 membrane integrity and increased levels of reactive oxygen species (ROS).^[28b] Since the first
11 influences cannot occur, because endocytosis of ZnO nanoparticles is the trigger to these
12 effects, only increased levels of ROS play a role. Therefore, the presence of elevated ROS
13 concentrations in the t-ZnO hydrogel samples compared to controls was probed, and these
14 findings may also be a contributing factor for cell toxicity (**Figure S6**). A significant increase
15 in the concentration of ROS was found when t-ZnO was incorporated into the cells, which
16 may also be the reason for their antibacterial properties. In regards to ZnO nanoparticles,
17 further studies have demonstrated that cytotoxicity was drastically increased by the cellular
18 uptake of the nanoparticles, and Zn²⁺ ions were released into the solution due to their high
19 surface area and the possibility of ZnO nanoparticles penetrating through the cells'
20 membranes.^[8b] In our approach, the particles were much bigger and could not penetrate the
21 cells. This can be observed in cell culture experiments shown in **Figure 4A**. The release of
22 reactive oxygen species (ROS) in low concentrations offers a therapeutic window for the
23 proliferation of cells and antibacterial properties.^[29]

24
25
26
27
28
29
30
31
32
33
34
35
36
37
38
39
40
41
42
43
44
45
46
47
48
49
50
51
52
53 Differences in cell viability between t-ZnO and t-ZnO-VEGF-coated hydrogels were
54 present in both cell types following different trends. In C2C12, 0.5 to 2% of groups with
55 uncoated t-ZnO had higher cell viabilities compared with VEGF-coated groups (**Figure 4B**).
56
57
58
59
60
61
62
63
64
65
66
67
68
69
70
71
72
73
74
75
76
77
78
79
80
81
82
83
84
85
86
87
88
89
90
91
92
93
94
95
96
97
98
99
100
101
102
103
104
105
106
107
108
109
110
111
112
113
114
115
116
117
118
119
120
121
122
123
124
125
126
127
128
129
130
131
132
133
134
135
136
137
138
139
140
141
142
143
144
145
146
147
148
149
150
151
152
153
154
155
156
157
158
159
160
161
162
163
164
165
166
167
168
169
170
171
172
173
174
175
176
177
178
179
180
181
182
183
184
185
186
187
188
189
190
191
192
193
194
195
196
197
198
199
200
201
202
203
204
205
206
207
208
209
210
211
212
213
214
215
216
217
218
219
220
221
222
223
224
225
226
227
228
229
230
231
232
233
234
235
236
237
238
239
240
241
242
243
244
245
246
247
248
249
250
251
252
253
254
255
256
257
258
259
260
261
262
263
264
265
266
267
268
269
270
271
272
273
274
275
276
277
278
279
280
281
282
283
284
285
286
287
288
289
290
291
292
293
294
295
296
297
298
299
300
301
302
303
304
305
306
307
308
309
310
311
312
313
314
315
316
317
318
319
320
321
322
323
324
325
326
327
328
329
330
331
332
333
334
335
336
337
338
339
340
341
342
343
344
345
346
347
348
349
350
351
352
353
354
355
356
357
358
359
360
361
362
363
364
365
366
367
368
369
370
371
372
373
374
375
376
377
378
379
380
381
382
383
384
385
386
387
388
389
390
391
392
393
394
395
396
397
398
399
400
401
402
403
404
405
406
407
408
409
410
411
412
413
414
415
416
417
418
419
420
421
422
423
424
425
426
427
428
429
430
431
432
433
434
435
436
437
438
439
440
441
442
443
444
445
446
447
448
449
450
451
452
453
454
455
456
457
458
459
460
461
462
463
464
465
466
467
468
469
470
471
472
473
474
475
476
477
478
479
480
481
482
483
484
485
486
487
488
489
490
491
492
493
494
495
496
497
498
499
500
501
502
503
504
505
506
507
508
509
510
511
512
513
514
515
516
517
518
519
520
521
522
523
524
525
526
527
528
529
530
531
532
533
534
535
536
537
538
539
540
541
542
543
544
545
546
547
548
549
550
551
552
553
554
555
556
557
558
559
560
561
562
563
564
565
566
567
568
569
570
571
572
573
574
575
576
577
578
579
580
581
582
583
584
585
586
587
588
589
590
591
592
593
594
595
596
597
598
599
600
601
602
603
604
605
606
607
608
609
610
611
612
613
614
615
616
617
618
619
620
621
622
623
624
625
626
627
628
629
630
631
632
633
634
635
636
637
638
639
640
641
642
643
644
645
646
647
648
649
650
651
652
653
654
655
656
657
658
659
660
661
662
663
664
665
666
667
668
669
670
671
672
673
674
675
676
677
678
679
680
681
682
683
684
685
686
687
688
689
690
691
692
693
694
695
696
697
698
699
700
701
702
703
704
705
706
707
708
709
710
711
712
713
714
715
716
717
718
719
720
721
722
723
724
725
726
727
728
729
730
731
732
733
734
735
736
737
738
739
740
741
742
743
744
745
746
747
748
749
750
751
752
753
754
755
756
757
758
759
760
761
762
763
764
765
766
767
768
769
770
771
772
773
774
775
776
777
778
779
780
781
782
783
784
785
786
787
788
789
790
791
792
793
794
795
796
797
798
799
800
801
802
803
804
805
806
807
808
809
810
811
812
813
814
815
816
817
818
819
820
821
822
823
824
825
826
827
828
829
830
831
832
833
834
835
836
837
838
839
840
841
842
843
844
845
846
847
848
849
850
851
852
853
854
855
856
857
858
859
860
861
862
863
864
865
866
867
868
869
870
871
872
873
874
875
876
877
878
879
880
881
882
883
884
885
886
887
888
889
890
891
892
893
894
895
896
897
898
899
900
901
902
903
904
905
906
907
908
909
910
911
912
913
914
915
916
917
918
919
920
921
922
923
924
925
926
927
928
929
930
931
932
933
934
935
936
937
938
939
940
941
942
943
944
945
946
947
948
949
950
951
952
953
954
955
956
957
958
959
960
961
962
963
964
965
966
967
968
969
970
971
972
973
974
975
976
977
978
979
980
981
982
983
984
985
986
987
988
989
990
991
992
993
994
995
996
997
998
999
1000

There may be some beneficial interaction between t-ZnO and the C2C12 proliferation, or the

1
2
3
4 presence of VEGF could put stress onto this cell type. On the other hand, for HUVEC cells,
5
6 viability was significantly increased for 1 to 3% t-ZnO VEGF-coated constructs (**Figure 4D**).
7
8 The metabolic activities of C2C12 and HUVEC cells were also different from each other.
9
10 Whereas C2C12 showed a dramatic reduction in metabolic activity after 5 days of culture on
11
12 both groups, increased metabolic activity was always maintained within the ZnO-VEGF-
13
14 coated hydrogel groups for HUVEC cells after 3 days of culture. Although VEGF has been
15
16 associated with promoting the cell growth of different cell types, this peptide has a special
17
18 tropism for endothelial cells as a mitogen and chemotactic agent.^[20, 30] These findings can
19
20 explain the differences seen which favor cell growth on VEGF-coated samples. HUVEC cells
21
22 on VEGF-coated groups showed slow proliferation at first (until day 3 of culture) but
23
24 exhibited a sustained increase in proliferation rate thereafter (**Figure 4E**). This behavior can
25
26 be explained since VEGF has been shown to experience loss of activity *in vitro* under cellular
27
28 conditions with a half-life of 40 to 96 min at 37 °C due to adaptive cellular mechanisms,
29
30 uptake, clearance, and receptor expression changes.^[31]
31
32

33
34 To evaluate cell adhesion and cell growth, area immunostainings with F-actin and CD31
35
36 were performed on days 3 and 7 of culture, respectively. The F-actin covered area showed a
37
38 decremental tendency with higher concentrations of t-ZnO, while better cell morphology and
39
40 elongation were found at lower concentrations of t-ZnO (**Figure 4C**). It has been observed
41
42 that direct contact between tetrapods and cells can increase toxicity, in comparison with
43
44 indirect contact with zinc ions from transwell models.^[8b] That means that it is feasible that
45
46 the reduction in the cell covered area was caused by direct cell damage accumulated from
47
48 contact with t-ZnO. Interestingly, the cell covered area from F-actin staining was higher at
49
50 0.5 to 2% on non-VEGF-coated samples compared with coated ones, following the same
51
52 tendency as that which occurred with metabolic activity. The local concentration of VEGF
53
54
55
56
57
58
59
60
61
62
63
64
65

1
2
3
4 on the protruding tetrapodal arms may be significantly higher than the requirement for
5
6 healthy cell activity. This is supported by the C2C12 cells, which did not show significant
7
8 differences in the cell covered area between VEGF-coated and non-coated groups.
9

10
11 CD31 is a transmembrane protein whose primary functions are promoting endothelial
12
13 cell migration, angiogenesis, and stabilization of endothelial cell-cell junctions; it also plays
14
15 an important role as a marker of endothelial cell survival and cytoprotection.^[32] These
16
17 functions are indirectly associated with endothelial integrity and are needed for successful
18
19 wound healing. HUVEC cells showed a higher CD31 covered area for 0.5 to 3% VEGF-
20
21 coated t-ZnO samples compared to non-coated ones (**Figures 4F and 4G**). The CD31 covered
22
23 area was also significantly higher in 0.5% t-ZnO VEGF-coated hydrogels compared to
24
25 controls and other groups. These results show that the presented VEGF here plays a
26
27 substantial role in endothelial cell proliferation, adhesion, and integrity. VEGF-coated t-ZnO
28
29 hydrogels at concentrations ranging from 0.5% to 1% seem to sustain an adequate
30
31 microenvironment for endothelial cell growth, a key cell lineage involved in the wound
32
33 healing process.
34
35
36
37
38
39

40
41 Although bacteria colonies are usually found on normal skin, the loss of integrity in the
42
43 epidermis may impair mechanisms associated with controlling bacterial growth and could
44
45 facilitate wound infections. Bacterial invasion leads to increased metabolic strain and a
46
47 proinflammatory state. This results in tissue injury and chronic wound formation.^[33]
48
49 Therefore, the implementation of antibacterial qualities is crucial to the proper healing of
50
51 chronic wounds. The principles of antibacterial activity of the t-ZnO are shown schematically
52
53 in **Figure 4A**. The formation of ROS species by the t-ZnO can provide a good therapeutic
54
55 window, where both antibacterial activity, angiogenesis and thus wound healing are high.
56
57
58
59 Additionally, direct bacterial contact may damage the bacteria directly. As shown in **Figures**
60
61

1
2
3
4 **2B** and **2D**, the number of penetrating arms of t-ZnO increased by increasing the
5 concentration of the microparticles, which may lead to varying degrees of antibacterial
6 activity. The antibacterial effects of both t-ZnO-laden hydrogels and t-ZnO powder were
7 evaluated by measuring the growth of different bacterial strains. Both *S. aureus* and
8 *P. aeruginosa* are common pathogens associated with infections in chronic wounds.^[34]

9
10
11
12
13
14
15
16
17
18
19
20
21
22
23
24
25
26
27
28
29
30
31
32
33
34
35
36
37
38
39
40
41
42
43
44
45
46
47
48
49
50
51
52
53
54
55
56
57
58
59
60
61
62
63
64
65

First, the mechanism of the antibacterial testing was investigated by performing an inhibition zone test. Initially, we expected the release of Zn²⁺ ions to be the main antibacterial mechanism. When too many Zn²⁺ ions are released from the t-ZnO particles, they may become cytotoxic as well. To test this, the pristine, printed GelMA hydrogel, and t-ZnO-laden composite hydrogels were placed into bacteria-seeded agar plates (**Figures 5B** and **5C**). If Zn²⁺ ions were released and killed the bacteria, an inhibition zone would form. This inhibition zone would have more definition for composites containing higher amounts of t-ZnO. Neither of the printed hydrogels formed an inhibition zone, which is a strong indication that the main mechanism for the antibacterial properties of the t-ZnO is not the release of Zn²⁺ ions from the hydrogel. This is in agreement with the *in vitro* results, where instead a larger amount of ROS was found (cf. **Figure S6**). Likewise, previous studies have found ZnO nanoparticles to release large amounts of Zn²⁺ ions due to their large surface-to-volume ratios, leading to apoptosis in, e.g., mouse macrophage Ana-1. While for the same ZnO, a certain quantity of ROS was also found, it was only believed to be harmful to the cells when the particles entered the cells.^[35] For this reason, we believe that the main antibacterial mechanism stems from ROS generation by nanoparticles. The printed composite hydrogels with and without H₂O₂ treatment as well as an additional protein coating with BSA were observed to have antibacterial properties even at low concentrations of 0.5 % t-ZnO. All hydrogels limited the bacterial growth of *S. aureus* compared to the pristine GelMA hydrogel

1
2
3
4 as control (**Figures 5D**). A similar lack of bacterial growth was also found for *P. aeruginosa*,
5
6 except for 2% H₂O₂-treated t-ZnO-laden GelMA hydrogels, which only were able to reduce
7
8 the colony formation of the pathogen while bacterial growth continued to be observable.
9

10
11 The antibacterial activity of t-ZnO powder was also evaluated over time (**Figure 5E**).
12
13 1% H₂O₂-treated t-ZnO and 1% pristine t-ZnO powders were shown to eliminate the bacterial
14
15 growth of *S. aureus* after 24 hours of culture, and significant statistical differences were
16
17 found on both powders in comparison to the control. A different behavior was found with
18
19 *P. aeruginosa*, where no significant differences were found for bacterial growth with 1%
20
21 H₂O₂/t-ZnO and 1% t-ZnO powders compared to the control. Previous studies have
22
23 demonstrated antibacterial activity from t-ZnO particles for *Salmonella*, *Listeria*
24
25 *monocytogenes*, *Escherichia coli*, *S. aureus*, and other gram-positive and negative
26
27 bacteria.^[36] Different mechanisms of t-ZnO antibacterial activity have been proposed,
28
29 including direct bacterial cell wall damage, the release of ROS and resultant DNA damage,
30
31 oxidative stress, and lipid peroxidation (in agreement with the working principle depicted in
32
33 **Figure 5A**).^[6]
34
35
36
37
38
39

40
41 *P. aeruginosa* is a pathogen often found in immunocompromised and elderly patients,
42
43 and its treatment has become problematic due to its potential to develop antibiotic
44
45 resistance.^[37] The pathogenicity of *Pseudomonas* depends on its capacity to form biofilm and
46
47 protect itself from immune defense and anti-biotic therapy. *P. aeruginosa* forms biofilm via
48
49 a dose-dependent mechanism, but it is less effective in removing pre-formed biofilm. Even
50
51 after treatment with t-ZnO, genes associated with the virulence mechanisms of this bacteria
52
53 were detected by the RT-PCR technique.^[38] These findings can explain why after seeding a
54
55 starting concentration of colony-forming units, the antibacterial activity of t-ZnO against *P.*
56
57 *aeruginosa* can be reduced but still be relevant. That means that it is possible that the impact
58
59
60
61
62
63
64
65

1
2
3
4 of ZnO antibacterial activity could increase with prompt treatment of ZnO before bacterial
5
6
7
8
9
10
11
12
13
14
15
16
17
18
19
20
21
22
23
24
25
26
27
28
29
30
31
32
33
34
35
36
37
38
39
40
41
42
43
44
45
46
47
48
49
50
51
52
53
54
55
56
57
58
59
60
61
62
63
64
65

of ZnO antibacterial activity could increase with prompt treatment of ZnO before bacterial colonization is chronically established. These results show that t-ZnO hydrogels have potential antibacterial properties and can have a great impact on the success of wound healing.

A subcutaneous *in vivo* study was performed to evaluate the biological stability of the produced hydrogels in terms of biodegradability and biocompatibility with neighboring tissues (**Figure 6A**). After subcutaneous transplantation, H&E staining was conducted to identify the reaction between the hydrogel and its surrounding tissues. Encapsulated fibrous tissue, which could be a problem during tissue remodeling, was not observed nearby for all transplanted hydrogels due to their good biocompatibility (**Figure 6B**). Especially, materials with t-ZnO were observed to have an excellent connection with neighboring tissues (**Figure 6B**). Most of the hydrogels remained 4 weeks after the transplant. 1% VEGF-coated H₂O₂/t-ZnO showed the greatest tendency for biodegradability (**Figure 6C**). The differences in biodegradability in the hydrogels are believed to be due to the different components in the hydrogels. VEGF upregulates in an inflammatory environment and induces inflammatory cells such as macrophages to contribute to wound healing.^[39] Such macrophages can play a role in accelerating the biodegradation of hydrogels.^[40] It has also been reported from earlier research that t-ZnO induced macrophages secreted enzymes, causing materials to be biodegraded faster. In **Figure 6E**, 1% t-ZnO-VEGF showed faster biodegradation than 2% t-ZnO-VEGF. This result could be due to macrophage recruitment being most active in 1% t-ZnO-VEGF, causing rapid degradation.

In order to closely observe the biological characteristics of the hydrogels *in vivo*, immunostaining was performed. The phenomenon for angiogenesis (vascularization) was observed through CD31. CD68 and CD86, markers to confirm monocytes and macrophages,

1
2
3
4 were used to analyze the immune response and inflammatory reaction, respectively. In
5
6 **Figure 6B**, the expression of CD31 in all groups was confirmed. 1% t-ZnO-VEGF especially
7
8 showed a higher level of CD31 expression compared to other groups. The CD31 expression
9
10 of the dermis per designated area (0.01 mm²) was quantified in **Figure 6D**. The expression
11
12 of CD31 in 0% t-ZnO was lower than the other groups. Interestingly, 1% t-ZnO-VEGF
13
14 showed a higher value of 10.35% ± 0.46%, compared to 2% t-ZnO-VEGF showing 4.31% ±
15
16 0.44%, indicating that angiogenesis had further proceeded in 1% t-ZnO-VEGF.
17
18
19

20
21 The CD68 expression in immunofluorescence confirms that monocytes differentiate into
22
23 macrophages and cause an immune response. The tendency of a monocyte to be located
24
25 within or induced to the tissue was confirmed through the immunofluorescence results of
26
27 CD68. A monocyte, a type of leukocyte in the blood, can differentiate into either a
28
29 macrophage or a dendritic cell that immunizes. Monocytes also produce inflammatory
30
31 cytokines.^[41] The cytokine expression acts as proof that the damaged tissues are healing. The
32
33 M1 macrophage, which performs pro-inflammatory, bactericidal, and phagocytic functions,
34
35 was identified through CD86 staining. The CD68 and CD86 expressions were noticeable in
36
37 the tissues of the hydrogels with t-ZnO (**Figure 6B**). In **Figure 6E**, CD68 was not significant
38
39 for all samples, but CD86, a macrophage marker, was significant between 0% t-ZnO and
40
41 1% t-ZnO-VEGF. The 1% t-ZnO-VEGF also showed a low intensity. This shows that 1% t-
42
43 ZnO-VEGF was more degraded than the other groups and that macrophages had a low
44
45 expression level in the neighboring tissues.
46
47
48
49
50
51

52
53 The effects of the produced hydrogel scaffold on wound healing were assessed through
54
55 changes in the wound size and histological analysis of the wound site. Two sections of a
56
57 mouse's skin were incised (0.9 cm x 0.9 cm) to compare the left, non-treated, and the right,
58
59 applied with either 0% t-ZnO or 1% t-ZnO-VEGF (**Figures 7A** and **7B**). The healing of the
60
61

1
2
3
4 wound was visually monitored for 2 weeks following surgery (**Figure 7C**). In the case of no
5
6 treatment (control), wound contraction, scab formation, and a slow healing process were
7
8 observed. This is because the exposure of the wound without the dressing could cause
9
10 excessive moisture loss in the epidermis, leading to skin damage.^[42] On the other hand, 0% t-
11
12 ZnO and 1% t-ZnO-VEGF showed fast wound healing processes without inflammatory
13
14 phenomena and scab formation, compared to the non-treated tissue. Especially, 1% t-ZnO-
15
16 VEGF revealed an excellent wound healing process without contraction. The wound healing
17
18 rate of each group was quantified by the healing time in relation to the area of the wound
19
20 (**Figure 7D**). The wound healing rate was effectively facilitated by the scaffold containing t-
21
22 ZnO and VEGF. The size of the wound treated with 1% t-ZnO-VEGF decreased to 24.90%
23
24 $\pm 4.21\%$ after 1 week and further decreased to 3.48% $\pm 6.03\%$ after 2 weeks.
25
26
27
28
29
30

31 Immunohistological staining was performed to investigate the interaction between the
32
33 wound and scaffold materials in-depth. The wound healing progress can be determined in
34
35 terms of re-epithelization and collagen deposition of the wounded tissue. In the early stages
36
37 of wound healing, re-epithelization, contraction of connective tissue, collagen formation in
38
39 the wound, and angiogenesis are needed to start the skin regeneration. In the later stages, cell
40
41 proliferation, matrix remodeling, and granulation tissue formation by re-epithelization are
42
43 required to complete wound healing.^[43] H&E staining showed the representative histological
44
45 sections of the wound healing of each group after 2 weeks (**Figure 7E**). Although a new layer
46
47 of skin tissue was generated in all groups, the non-treated case showed an incomplete wound
48
49 recovery, creating a thin epidermis and lots of keratin. The wound covered with 1% t-ZnO-
50
51 VEGF formed a thick epidermis and had relatively little keratin compared to the non-treated
52
53 wound. The measured epidermal thickness of the 1% t-ZnO-VEGF-treated wound, 101.2 μm
54
55
56
57
58
59
60
61
62
63
64
65

1
2
3
4 $\pm 12.3 \mu\text{m}$, can be confirmed to be more than twice the thickness of the non-treated wound,
5
6
7 $19.7 \mu\text{m} \pm 4.1 \mu\text{m}$ (**Figure 7F**).

8
9 In the observation of the dermis, non-treated wounds were not filled by generated tissues
10 due to incomplete dermis formation and the concentrated distribution of inflammatory cells
11 such as neutrophils around the wound. Meanwhile, the wound under 1% t-ZnO-VEGF
12 showed the densest dermal layer with $95.3\% \pm 0.5\%$ per designated area (0.3 mm^2). The
13 dermis, which is composed of dense connective tissue, plays an important role in
14 thermoregulation and cutaneous nerve signal sensing because it has a rich layer of blood,
15 lymphatic vessels, and numerous nerve endings. Therefore, the regeneration of a dense
16 dermis can be expected to greatly recover skin functions (**Figure 7G**).^[44]

17
18
19
20
21
22
23
24
25
26
27
28
29
30
31
32
33
34
35
36
37
38
39
40
41
42
43
44
45
46
47
48
49
50
51
52
53
54
55
56
57
58
59
60
61
62
63
64
65

Angiogenesis is an important process of wound repair because it allows blood vessels to provide nutrients and oxygen to the tissue and it promotes granulation tissue formation.^[24] In **Figure 7E**, the angiogenesis was most active in the wound covered by the scaffold with 1% t-ZnO-VEGF. The results showed that the CD31 expression was significantly different between the 1% t-ZnO-VEGF and the others (0% t-ZnO and control). VEGF is known as a very important growth factor that enables angiogenesis for tissue regeneration.^[39a, 45] It has been reported that chronic wounds caused by cell migration and vascularization deficiencies can be cured by VEGF treatment.^[22, 46] Zinc ions are also well known for having effective antibacterial production and angiogenesis acceleration. Therefore, it was expected for the components in the scaffold to contribute to angiogenesis. From the experiment results, it was proven that, although the existence of t-ZnO induces angiogenesis, the existence of VEGF dramatically promotes angiogenesis (**Figure 7H**).

New cell growth in the wound site was assessed by Ki67 staining (**Figure 7E**). The existence and proliferation of essential cells such as keratinocytes, fibroblasts, and

1
2
3
4 endothelial cells are very important in re-epithelialization for wound remodeling.^[47] **Figure**
5
6 **7I** shows that Ki67 appeared to have the highest activity from 1% t-ZnO-VEGF.
7
8
9 Consequently, it was confirmed through the *in vivo* study that the scaffold with 1% t-ZnO-
10
11 VEGF enhanced and anti-inflammatory reaction, angiogenesis, and cell proliferation in the
12
13 wound site, allowing for the fastest wound healing.
14
15

16 17 18 **Conclusion**

19
20
21 In summary, we have demonstrated a method that uses both materials science and
22
23 biomedical engineering for the treatment of chronic wounds. Printed GelMA hydrogels
24
25 containing tetrapodal ZnO microparticles could effectively decrease bacteria concentrations
26
27 while promoting the re-growth of C2C12 and HUVEC cells *in vitro* and wound healing *in*
28
29 *vivo*. The open porous structures of the hydrogels and their high-water content enabled the
30
31 diffusion of adsorbed, angiogenic proteins while maintaining mechanical integrity. The
32
33 printability of the gels prior to cross-linking showed excellent results, with the option of
34
35 multi-material printing for enhanced wound healing therapy with multiple growth-factors,
36
37 drugs, or other proteins. An additional treatment of t-ZnO microparticles with H₂O₂ led to
38
39 the formation of a highly protein-adsorbent surface while maintaining their biomedical
40
41 qualities. The treatment also allowed for the controlled release of VEGF with light in the
42
43 optical range over the duration of 120 seconds. The VEGF immobilized on the t-ZnO created
44
45 adequate microenvironments for improving endothelial cell growth while maintaining
46
47 antibacterial activity that can have a great impact on the success of wound healing. Through
48
49 *in vivo* studies, we confirmed that the printed scaffold with t-ZnO-VEGF showed adequate
50
51 biological stability and enhanced anti-inflammatory reaction, angiogenesis, and cell
52
53 proliferation in the wound site, resulted in achieving the fastest wound healing. All of these
54
55
56
57
58
59
60
61
62
63
64
65

1
2
3
4 factors combined make this approach an interesting candidate for future smart wound
5
6 dressing platform.
7
8
9

10 **Materials and methods**

11 **Materials**

12
13
14 Zinc oxide tetrapods (t-ZnO) were obtained by employing the newly developed flame
15
16 transport synthesis by Mishra et al.^[28] T-ZnO is pure and single-crystalline. The following
17
18 reagents were purchased from Sigma Aldrich, USA: gelatin from porcine skin, methacrylic
19
20 anhydride, hydrogen peroxide solution (30 wt. % in H₂O), trypsin solution 10X, Triton™ X-
21
22 100, bovine serum albumin (BSA); Thermo Fisher Scientific, USA: fetal bovine serum
23
24 (FBS), 100X penicillin-streptomycin, VEGF recombinant human protein, PrestoBlue™,
25
26 calcein AM, ethidium homodimer-1 (EthD-1), Alexa Fluor™ 488 Phalloidin, 4',6-
27
28 diamidino-2-phenylindole (DAPI), CD31 (PECAM-1) monoclonal antibody, goat anti-
29
30 mouse IgG2a cross-adsorbed secondary antibody Alexa Fluor™ 594; Lonza Biosciences,
31
32 USA: Dulbecco's modified eagle medium (DMEM), endothelial cell basal medium-2 (EBM-
33
34 2), endothelial cell growth medium-2 (EGM-2) SingleQuots™ kit; Electron Microscopy
35
36 Sciences, USA: paraformaldehyde aqueous solution 16% (w/v).
37
38
39
40
41
42
43
44
45
46

47 **Methods**

48
49 **GelMA synthesis:** The photo-crosslinkable gelatin methacryloyl (GelMA) hydrogel was
50
51 used as a base for a biocompatible scaffold. The synthesis method involved the reaction
52
53 between gelatin and methacrylic anhydride (MA). 10 g of porcine skin gelatin was mixed
54
55 with 100 mL sterile phosphate-buffered saline (PBS) (Thermo Fisher Scientific, USA) and
56
57 dissolved at 50 °C. Once the gelatin melted, 1.25 mL of MA was added, and the emulsion
58
59
60
61
62
63
64
65

1
2
3
4 was left in rotation (240rpm) for two hours. 100 mL of sterile PBS was added (giving a total
5
6 volume of 200 mL) and left in heating rotation (10 min at 50 °C). GelMA was transferred to
7
8 dialysis membranes (Spectro/Por molecularporous membrane tubing, MWCO 12-14,000,
9
10 Fisher Scientific) and left in distilled water for dialysis (40 °C for 5 days at 500 rpm.) Toxic
11
12 unreacted MA was removed by changing the distilled water twice a day. Once dialysis was
13
14 finalized, 200 mL of ultrapure water was added to GelMA and heated at 40 °C. The liquid
15
16 was filtered, in sterile conditions, using the vacuum Express Plus (0.22 µm) Millipore
17
18 filtration cup with a coffee filter. The sterilized polymer was transferred into 50 mL Falcons
19
20 and stored at 80 °C. GelMA was freeze-dried for 3 days at a maximum pressure of 0.13 mbar
21
22 before use.
23
24
25
26
27
28
29
30

31 **H₂O₂-treatment for improving protein adhesion:** 4 g of t-ZnO was added to 100 mL of a
32
33 30% w/v solution of hydrogen peroxide solution. The suspension was heated to around 70 °C
34
35 and left until a noticeable gas evolution occurred. The liquid phase was extracted by filtering
36
37 and the remaining t-ZnO was washed multiple times with deionized water and then dried at
38
39 80 °C in an oven. The dry t-ZnO was then filled into a container, covered with aluminum foil
40
41 for light protection, and stored under room temperature conditions.
42
43
44
45
46
47

48 **Micro-Raman spectroscopy for investigation of chemical treatment:** Both pristine and
49
50 H₂O₂ treated t-ZnO were investigated by micro-Raman (WITec, Germany) at room
51
52 temperature using a WITec system in a backscattering configuration. A Nd:YAG laser with
53
54 a wavelength of $\lambda_{\text{exc}} = 532$ nm and a power was below 4 mW was used for excitation. Each
55
56 spectrum was taken using 10 accumulations at an integration time of 0.5 sec.
57
58
59
60
61
62
63
64
65

1
2
3
4 **H₂O₂-treated ZnO coating with VEGF:** A 10% w/v solution of H₂O₂-treated t-ZnO in 10
5
6 μg/mL VEGF was prepared, protected from light with aluminum foil and incubated on ice
7
8 for 2 hours, shaking every 30 min. The solution was then centrifuged for 10 min at 5,000 rpm
9
10 and the supernatant was discarded. The remaining pellet was then washed with 1 mL of PBS
11
12 buffer (centrifugation and washing steps were repeated 3 times). After the last supernatant
13
14 was removed, the VEGF-coated H₂O₂/t-ZnO was resuspended in the PBS buffer at a 10%
15
16 w/v concentration. The solution was stored at -80 °C until further use. Both high and low
17
18 concentrations of VEGF were coated onto H₂O₂-treated t-ZnO in the following way: The
19
20 low concentration coating was done using 1 mL of 10 μg/mL VEGF/PBS solution with 50
21
22 mg of t-ZnO. The high concentration coating was done by mixing 400 μL of a 5 μg/mL
23
24 solution with 50 mg of t-ZnO. The solutions were kept in an Eppendorf container wrapped
25
26 with aluminum foil at 37 °C for 2 hours. The solutions were shaken every 30 minutes. After
27
28 coating, the t-ZnO was washed several times and the supernatant was kept for measurement
29
30 with the ELISA kit to confirm the complete removal of superfluous VEGF. Subsequently,
31
32 the 50 mg t-ZnO was transferred into 1 mL of PBS and the protein release test was performed.
33
34
35
36
37
38
39
40
41
42

43 **Protein coating experiments:** Optical protein release tests were performed by coating both
44
45 pristine t-ZnO, H₂O₂-treated ZnO, and other types of treated t-ZnO with IgG Alexa Fluor™
46
47 594. For these tests, 1 mg of the respective t-ZnO were coated in 100 μL of a 10 μg/mL
48
49 solution of the IgG Alexa Fluor™ 594. The solution was made by diluting the IgG Alexa
50
51 Fluor™ 594 obtained from Thermo Fisher to a 10 μg/mL solution with PBS. The coating
52
53 was performed at room temperature in an Eppendorf container wrapped with aluminum foil
54
55 for light protection. After coating, the t-ZnO was washed at least 3 times with PBS to remove
56
57 superfluous antibodies. The 1 mg of t-ZnO was then given into 1 mL of PBS for protein
58
59
60
61
62
63
64
65

1
2
3
4 release experiments. SiO₂ microparticles with a mean particle size of 20 μm were obtained
5
6 from Sigma Aldrich and also coated in the same fashion as the t-ZnO.
7

8
9 Oleic acid was coated onto the t-ZnO by adding 1 mg of oleic acid into 1 mL of 97%
10 ethanol. Then 1 mg of t-ZnO was added and the solution was kept for 2 hours. The coated t-
11 ZnO was washed several times with ethanol and then dried at 80 °C for 2 hours. The t-ZnO
12 was then hydrophobic and a small amount of ethanol was added into 1 mL of PBS to break
13 surface tension and to put the t-ZnO inside. Streptavidin and BSA were coated on the t-ZnO
14 in the same manner as the IgG Alexa Fluor™ 594. 10 μg/mL solutions were made in PBS
15 and then coated with 1 mg of t-ZnO in a 1 mL solution.
16
17
18
19
20
21
22
23
24
25
26
27

28 **Optical protein release experiments:** For protein release, a fluorescence microscope was
29 used with the red filter to check for the 594 nm signal of the IgG Alexa Fluor™ 594
30 fluorescence. A small lightproof box was laser-cut from black acrylic, to allow for irradiation
31 with a UV-light source while performing the protein release *in situ*. The t-ZnO/PBS
32 dispersion was placed into a confocal dish that was fitted into the acrylic box and the particles
33 were investigated from the bottom, while irradiated from the top. Fluorescence microscopy
34 was performed during *in situ* UV irradiation. Images were taken at varying intervals,
35 maintaining set parameters for exposure time and gain throughout the experiment for
36 comparability of the image series. For green-light treatment, a 1 W, 547 nm LED was
37 mounted into the acrylic box with a mean light density of 25,000 lx. During green light
38 illumination, the red fluorescence was much brighter, so those images were not considered
39 during measurement. For the release of VEGF measured with the ELISA kit, the same light
40 density of 25,000 lx with the same green LED was used. The supernatant was taken from the
41
42
43
44
45
46
47
48
49
50
51
52
53
54
55
56
57
58
59
60
61

1
2
3
4 illuminated samples and kept for ELISA 5, 20, 60, and 120 seconds. After each illumination
5
6 step, the whole solution was discarded, and fresh PBS added.
7
8
9

10
11 **Preparation of the t-ZnO hydrogels:** The t-ZnO powder was treated with 30% hydrogen
12 peroxide as previously mentioned, combined with 10 µg/mL VEGF and PBS to yield a 100
13 mg/mL VEGF-coated H₂O₂/t-ZnO stock solution. By diluting this solution and mixing it with
14 previously made GelMA, gelatin, and photoinitiator, five bioinks containing VEGF-coated
15 H₂O₂/t-ZnO were prepared, along with five more with uncoated t-ZnO. A ‘spacer’ was
16 created by building two 300 µm-height towers of stacked cover glasses, with a 5 mm distance
17 between each tower. To make the t-ZnO hydrogels, a droplet of the bioink was placed in the
18 5 mm gap in the spacer and pressed against a previously TMSPMA-coated-and-cut glass
19 slide, creating a round-shaped hydrogel with a 300 µm thickness and a 5 mm diameter.
20
21
22
23
24
25
26
27
28
29
30
31
32
33

34
35 **Mechanical properties of the t-ZnO hydrogels:** For mechanical testing, constructs
36 containing varying amounts of H₂O₂-treated t-ZnO were printed with a height of roughly 1
37 mm and 100% filling factor and subsequently crosslinked. Round biopsy punches with a
38 diameter of 8 mm were used to take multiple samples from each printed construct. The
39 samples were stored in humid conditions at 4 °C for hydration. Compression tests were
40 performed using the ADMET MTEST QUATTRO universal test machine (ADMET, Inc.,
41 USA). Compression and stress were computed using the difference in height and the area of
42 the constructs, respectively. The compressive moduli were calculated using a linear least-
43 square fit for each compression curve. The mean and the standard deviation were calculated
44 by using the values obtained from multiple samples.
45
46
47
48
49
50
51
52
53
54
55
56
57
58
59
60
61
62
63
64
65

1
2
3
4
5
6
7
8
9
10
11
12
13
14
15
16
17
18
19
20
21
22
23
24
25
26
27
28
29
30
31
32
33
34
35
36
37
38
39
40
41
42
43
44
45
46
47
48
49
50
51
52
53
54
55
56
57
58
59
60
61
62
63
64
65

Degradation test: 1cm diameter samples with 600 μ m thickness with different concentrations of t-ZnO were prepared by using the previously described protocol.^[48] Hydrogels were incubated for up to 24 hours in a solution of 1U/mL of collagenase type II (Thermo Fisher Scientific, USA) in an incubator at 37°C. At the end of each time-lapse, the supernatant was removed, and samples were washed with 1mL of PBS and then frozen overnight. After this procedure, the samples underwent lyophilization for 24 hours, and weight measurements were performed.

Scanning electron microscopy (SEM): 1 cm diameter samples with 600 μ m thickness with different concentrations of t-ZnO and VEGF coated t-ZnO were prepared by using the previously described protocol.^[49] Hydrogel samples were stored in 1.5 mL centrifuge tubes and frozen during 24 hours at -20°C. After this procedure, the samples underwent lyophilization for 24 hours, and several transversal cuts were performed in different sections of the hydrogels. Scanning electron microscopy images were obtained using an FSEM Supra55VP (Zeiss, Germany).

AFM experiments: All experiments were performed in wet conditions using in-fluid imaging set up of the AFM (Dimension Icon, Bruker, USA). ScanAsyst-Fluid+ probes having a sharpened tip with frequency 150 kHz and spring constant 0.7 N/m, ideal for high-resolution imaging and edge detection in fluid was used. Imaging was performed at a scan rate of 1 Hz with a sampling rate of 512 samples/line. Using offline AFM analysis software, images were first flattened, followed by whole image roughness and section analysis for height and DMT modulus to quantitate surface stiffness and roughness of the samples.

1
2
3
4 **Ink preparation:** The bioinks used for the experiments were composed of 10% w/v of
5
6 GelMA, 0.5% w/v of photoinitiator (Irgacure 2959, Sigma Aldrich), 2% w/v gelatin (Type
7
8 A, 300 bloom from porcine skin, Sigma Aldrich) and 0.1-10% VEGF-coated H₂O₂-treated
9
10 t-ZnO dissolved in PBS buffer (Thermo Fisher Scientific, USA) at 37 °C. The bioink was
11
12 deposited into 3 mL cartridges covered with aluminum foil to prevent premature crosslinking
13
14 and was then homogenized and stored at 4 °C.
15
16
17
18
19
20

21 **3D-printing process:** Rectangular constructs of 20 mm x 20 mm and 0.4 mm (2 layers) were
22
23 printed at 4 °C with a printing velocity of 0.1 mm/sec and an extrusion pressure of 400 kPa
24
25 using the BIOMAKER by SUNP BIOTECH (China). The nozzles were standard tapered
26
27 nozzles with orifices of 0.4 mm. Printed constructs were exposed to UV light at 100 mW/cm²
28
29 for 60 seconds.
30
31
32
33
34
35

36 **3D-printing of multi-material constructs:** The ink was prepared as before, containing 2%
37
38 w/v t-ZnO, and 0.5% w/v of green and pink fluorescence dye was added to two batches of
39
40 ink. The colored inks were then loaded into the 3 mL cartridges and printed in custom paths.
41
42 The print settings were not altered compared to the uncolored inks. One construct was a
43
44 cross-like pattern of pink ink filled with green ink. Another pattern alternated stripe-wise
45
46 between green and pink ink.
47
48
49
50
51
52

53 **Cell culture:** To culture the needed cells, vials of C2C12 and HUVEC cells were purchased
54
55 from Lonza Bioscience, along with the corresponding Dulbecco's modified eagle medium
56
57 (DMEM) and Endothelial Cell Basal Medium-2 (EBM-2). For the latter, the endothelial cell
58
59 growth medium-2 (EGM-2) SingleQuots™ Kit was also acquired to enrich the basal media
60
61

1
2
3
4 as it contains supplements and growth factors needed for HUVEC cell culture. The C2C12
5
6 cells were cultured using DMEM with 10% fetal bovine serum and 1% penicillin-
7
8 streptomycin diluted at 1X from the 100X solution. For both cell lines, only the amount of
9
10 required basal and complete media for the desired number of T-75 (Thermo Fisher Scientific,
11
12 USA) cell flasks was first aliquoted in 50 mL Falcon® (Corning, USA) tubes; media tubes
13
14 and liquid nitrogen-frozen cell aliquots containing $\sim 0.7 \times 10^6$ cells were slowly warmed up to
15
16 approximately 37 °C using a water bath. Once the cells were thawed, the volume of the
17
18 aliquot ~ 1 mL was quickly transferred to a 15 mL Falcon® tube with 9 mL of the
19
20 corresponding basal media to neutralize the freezing media containing 10% DMSO (Thermo
21
22 Fisher Scientific, USA), and the solution was centrifuged at 1,000 rpm for 5 min. Following
23
24 centrifugation, the supernatant was carefully removed, the cell pellet was resuspended in 15
25
26 mL of the proper complete media previously warmed and transferred to a T-75 flask for
27
28 incubation at 37 °C. A cell density of 0.1×10^6 was required in order to proceed with the cell
29
30 characterization assays.
31
32
33
34
35
36
37
38
39
40

41 **Cell-laden viability, proliferation, and attachment assays:** Cell viability and proliferation
42
43 of the cells seeded on hydrogels were assessed using live/dead assay (Thermo Fisher
44
45 Scientific, USA) and PrestoBlue™ kit (Thermo Fisher Scientific, USA). PrestoBlue™ assays
46
47 were performed using the manufacturer's reagent protocol and measured using a plate reader
48
49 (SpectraMax® i3, Molecular Devices, USA) by measuring absorbance at 570 nm with
50
51 reference to 600 nm. The results were normalized by day 1 of culture. For live and dead
52
53 assay, samples were stained with Calcein AM and Ethidium Homodimer-1 (EthD-1) for live
54
55 and dead cells respectively. In order to evaluate cell adhesion and cell covered area, fixation
56
57 of hydrogels was done on days 3 and 7 with 4% paraformaldehyde solution (Electron
58
59
60
61

1
2
3
4 Microscopy Sciences, USA) for 20 min and then permeabilized using 0.1% Triton X (Sigma-
5 Aldrich) in 1% BSA (Invitrogen). Alexa Fluor™ 488 Phalloidin (1:40, Invitrogen) and CD31
6
7 (PECAM-1, 1:50 Invitrogen) antibodies were added to hydrogels for staining. The hydrogels
8
9 were incubated with the primary antibody overnight at 4°C. Secondary antibody goat anti-
10 mouse Alexa Fluor™ 594 (Invitrogen) was used to image the CD31 staining and was added
11 to the hydrogels followed by incubation at 4 °C for 4 hours. DAPI (4', 6-diamino-2-
12 phenylindole, 1:300, Sigma Aldrich) was added 25 min prior to imaging with the inverted
13 fluorescence microscope. Images of all assays including phase contrast images were taken
14 by an inverted optical microscope (Nikon Eclipse TE 2000U, Japan) and processed and
15 analyzed by using ImageJ and Fiji softwares.
16
17
18
19
20
21
22
23
24
25
26
27
28
29
30

31 **Antibacterial Testing:** For the antibacterial tests we used two typical wound pathogens,
32
33 *Staphylococcus aureus* (ATCC 25923) and *Pseudomonas aeruginosa* (ATCC27853). To test
34 the pure t-ZnO, 100 µL of an overnight culture of bacteria was incubated with 5 mL LB
35 medium at 37°C. After two hours, the cell count was estimated by measuring the optical
36 density at 600 nm. 2x10⁵ bacteria/mL in 0.85% NaCl, 1% LB-medium were incubated with
37
38 1 mg/mL tetrapods for 1 hour or 24 hours at 37°C on a rotary mixer. After the incubation
39 period, the number of surviving bacteria was determined by plating serial dilutions on LB-
40 agar. For testing of the hydrogels containing t-ZnO, 100 µL of an overnight culture of bacteria
41 was incubated with 5 mL LB medium at 37°C. After two hours, the cell count was estimated
42 by measuring the optical density at 600 nm. A solution of 0.85% NaCl, 1% LB-medium and
43 6x10³ bacteria/50 µL was prepared. On a quartered hydrogel, 30 µL of the prepared solution
44 was added. The hydrogel was incubated in a Petri dish at 37 °C with moistened filter papers.
45
46
47
48
49
50
51
52
53
54
55
56
57
58
59
60 After 24 hours, the hydrogels were transferred into 5 mL 1% LB medium with 0.85% NaCl
61
62
63
64
65

1
2
3
4 and vigorously vortexed for 30 seconds. The number of surviving bacteria was determined
5
6
7 by plating serial dilutions on LB-agar.
8
9

10
11 ***In vivo* investigation of t-ZnO/GelMA:** The animal care and experimental protocols were
12
13 approved by the Animal Care and Use Committee of Dankook University, Cheonan Campus,
14
15 South Korea (DKU 17-011).^[50] The wound healing and subcutaneous model animal
16
17 experiments were conducted using 6-week-old male SKH-1 hairless mice and BALB/C mice,
18
19 each weighing 20~25 g and purchased from Orient Bio Inc. located in Seongnam, Korea. The
20
21 breeding timespan of the mice was set to 12 hours, day and night, in constant humidity and
22
23 with temperatures of RH 55% ± 5% and 25 °C ± 2 °C, respectively. Standard feed and water
24
25 were freely fed, and all experimental animal care and use committees are at Dankook
26
27 University, Republic of Korea all experimental animal care and use.
28
29
30
31

32
33 In the case of the subcutaneous model experiment, 4% avertin was used to anesthetize
34
35 the BALB/C mouse. After resecting the back of the mouse 1 cm into 4 sections, the samples,
36
37 GelMA hydrogel without t-ZnO (0% t-ZnO), GelMA with 1% coated t-ZnO (1% t-ZnO),
38
39 GelMA with 1% VEGF-coated t-ZnO (1% t-ZnO-VEGF), and GelMA with 2% VEGF-
40
41 coated t-ZnO (2% t-ZnO-VEGF) with dimensions 3 mm x 3 mm, were inserted into the
42
43 subcutaneous tissue and the incisions were sutured using 6-0 black silk (AILEE, Korea).
44
45 Histological analysis was conducted after 4 weeks.^[51]
46
47
48
49

50 In the case of the wound healing experiment, 4% avertin was used to anesthetize the
51
52 SKH-1 hairless mouse. Two circle defects with the diameter 9 mm were then created
53
54 symmetrically on the bilateral sides of the backs of mice. These defects were covered with
55
56 samples non-treated, GelMA hydrogel without t-ZnO (0% t-ZnO) and GelMA with 1%
57
58 VEGF-coated t-ZnO (1% t-ZnO-VEGF). Defects covered with samples were sealed with an
59
60
61

1
2
3
4 adhesive bandage in order to prevent wound exposures or detachment of the wound scaffold.

5
6
7 The wound healing process was monitored by an optical microscope and a confocal
8
9 microscope for up to two weeks.^[52]

10
11
12
13 **Histological analysis:** The experimental mice of the subcutaneous model and wound healing
14 model were sacrificed after 28 days and 14 days, respectively. Based on the location of the
15 wound, the tissues with samples were cut into dimensions of 1 cm x 1 cm, then fixated
16 through 4% PFA (Paraformaldehyde) solution. The fixed tissues were formed into paraffin
17 blocks and were sliced into a thickness of 5 um using the Leica rotary microtome (Leica,
18 Germany). The sliced sections were dyed using hematoxylin and eosin (H&E) and observed
19 through the CKX53 microscope (Olympus, Tokyo, Co).^[53]

20
21
22
23
24
25
26
27
28
29
30
31 In this subcutaneous *in vivo* study, the biocompatibility between the implanted material
32 and the surrounding tissue, and the biodegradation of the materials measured by the
33 remaining area of the material were evaluated through the H&E-stained histological tissue
34 sections (n=3).

35
36
37
38
39
40
41 The wound healing process with re-epithelialization was observed for 14 days through a
42 digital camera. The area of the healing from the wound compared to the initial wound was
43 measured through an image program (Image J) (n=4), and its healing rate was calculated
44 through the equation as follows:

$$45 \text{ Wound healing rate (\%)} = (A_o - A_t) / A_o \times 100$$

46
47
48
49
50
51
52
53 A_o and A_t indicate the area of the initial wound and the wound area measured in its
54 corresponding date, respectively.^[54] In the H&E staining, the thickness of the recovered
55 epidermis (n=5) and the density of the dermal layer (n=3) from the area of the dermal cells
56 in the designated area (0.3 mm²) of the dermal layer were measured.

1
2
3
4 The immunohistochemistry staining utilized for observing the vessel structures was
5
6 used to remove the paraffin from the sliced section using xylene. In order to eliminate the
7
8 endogenous peroxidase activity, the sliced sections were incubated in methanol containing
9
10 3% H₂O₂ for 30 min. Then samples were heated for 20 min in the sodium citrate buffer and
11
12 were treated as blocking (3% BSA in PBS) for 1 hour at room temperature.^[55]
13
14

15
16 In order to stain CD31 (Abcam, USA, ab28364), Ki67 (Abcam, USA, ab16667) the
17
18 primary antibodies were left overnight at 4 °C. After the antibody treatment, the samples
19
20 were further treated with 3% H₂O₂ solution, biotinylated secondary antibody,
21
22 avidinhorseradish peroxidase, and diaminobenzidine substrate. Finally, hematoxylin solution
23
24 was stained at room temperature. The stained tissues were visualized through a CKX53
25
26 microscope (Olympus, Tokyo, Co). Angiogenesis and cell proliferation levels in the
27
28 designated area (0.01 mm²) were quantifiably analyzed from the CD31-dyed area and the
29
30 number of Ki67-dyed cells, respectively (n=3). The immunofluorescence investigations were
31
32 conducted through CD68 (Abcam, USA, ab125212), and CD86 (Santacruz, USA, sc-28347)
33
34 immunostaining. The sliced sections, of which the paraffin removal and blocking were
35
36 conducted, were prepared. The prepared sliced sections (specimen) were treated with primary
37
38 antibodies at 4 °C overnight and reacted in the secondary antibody Alexa Fluor™ 555
39
40 (Invitrogen, USA) and DAPI (Thermo Fisher Scientific, Germany). After staining, all slices
41
42 were observed with an LSM700 confocal microscope (Zeiss, Germany).^[56] All quantitative
43
44 results were acquired from at least 3 specimens for analysis. Statistical analysis was
45
46 performed between the groups using t-test, and ANOVA was performed for comparison
47
48 between the groups. The value is expressed as ± SD on average. p < 0.05 difference is
49
50 considered to be statistically significant.^[57]
51
52
53
54
55
56
57
58
59
60
61
62
63
64
65

1
2
3
4 **Statistical Analysis:** The average and standard deviation were calculated in Prism8 software
5
6
7 by GraphPad. To analyze the results of protein release tests (Figure 1G, 1H) student's t test
8
9 was employed to study the presence of significant differences among groups. Mechanical
10
11 properties of t-ZnO laden hydrogels (Figure 2D,G, I, J), antibacterial tests (Figure 5D,E), *in*
12
13 *vivo* subcutaneous tests (Figure 6C,D,E) and wound healing properties of printed constructs
14
15 were analyzed by using one way analysis of variance (ANOVA) with Tukey's multiple
16
17 comparison method. The results of the PrestoBlue™ assay (Figure 4E), cell viability (Figure
18
19 4B,D), cell covered area (Figure 4C), and CD31 (Figure 4F) covered area were analyzed by
20
21 using a two-way analysis of variance method (ANOVA) to compare different treatment
22
23 groups. Error bars represented mean ± standard deviation of measurement in each group.
24
25 Statistical significance in all graphs was indicated by (ns) ($p > 0.05$), *($p < 0.05$) and ***(p
26
27 < 0.001).

32 33 34 35 **Acknowledgements**

36
37
38 The authors declare no conflict of interests in this work. All statements made herein are the
39
40 sole responsibility of the authors. This paper was funded by the National Institutes of Health
41
42 (R01AR074234 and R21EB026824), the Brigham Research Institute Stepping Strong
43
44 Innovator Award, and Qatar University grants NPR9-144-3021 funded by Qatar National
45
46 Research Foundation, a part of Qatar Foundation. This research was also supported by the
47
48 National Research Foundation of Korea (NRF) Grant funded by the Ministry of Science and
49
50 ICT for Bio-inspired Innovation Technology Development Project (NRF-
51
52 2018M3C1B7021994) and by the Research Training Group "Materials for Brain" (GRK
53
54 2154) received from the German Research Foundation (DFG). M.A. Hussain and S.R. Shin
55
56
57
58
59
60
61
62
63
64
65

1
2
3
4 extend their appreciation to the Deputyship for Research & Innovation, Ministry of Education
5
6
7 in Saudi Arabia for funding this research work through the project number (325).”
8
9

10 11 12 13 14 15 16 17 18 19 20 21 22 23 24 25 26 27 28 29 30 31 32 33 34 35 36 37 38 39 40 41 42 43 44 45 46 47 48 49 50 51 52 53 54 55 56 57 58 59 60 61 62 63 64 65

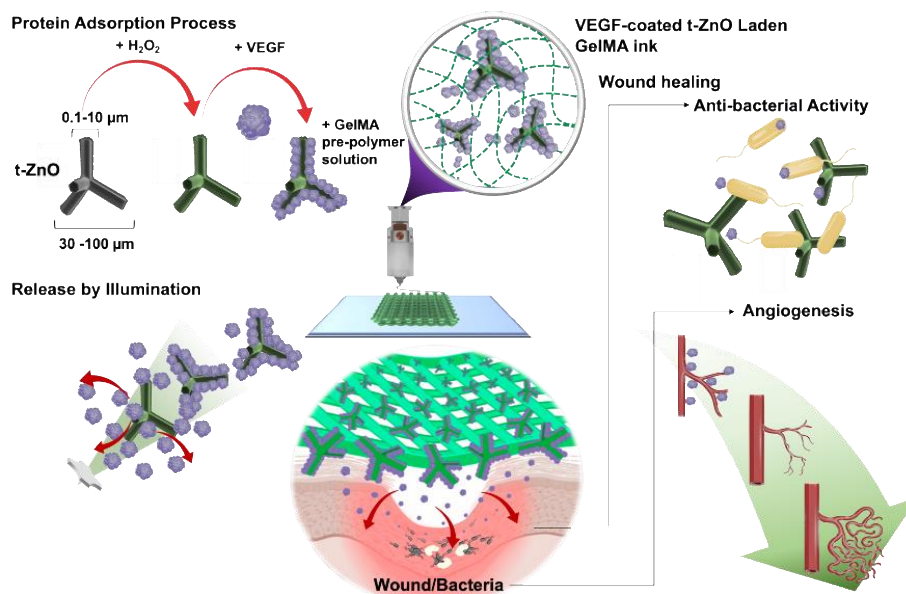
References

- [1] R. E. Pecoraro, G. E. Reiber, E. M. Burgess, *Diabetes Care* **1990**, 13, 513.
- [2] G. A. James, E. Swogger, R. Wolcott, E. Pulcini, P. Secor, J. Sestrich, J. W. Costerton, P. S. Stewart, *Wound Repair Regen* **2008**, 16, 37.
- [3] a) M. Braddock, Vol. 8, 2005, 381; b) R. Augustine, A. A. Zahid, A. Hasan, M. Wang, T. J. Webster, in *Int J Nanomedicine*, Vol. 14, 2019, 8573; c) A. A. Zahid, R. Ahmed, S. Raza Ur Rehman, R. Augustine, M. Tariq, A. Hasan, *Int J Biol Macromol* **2019**, 136, 901; d) R. Augustine, S. R. U. Rehman, R. Ahmed, A. A. Zahid, M. Sharifi, M. Falahati, A. Hasan, *Int J Biol Macromol* **2020**, 156, 153.
- [4] a) P. Kassal, J. Kim, R. Kumar, W. R. de Araujo, I. M. Steinberg, M. D. Steinberg, J. Wang, *Electrochemistry Communications* **2015**, 56, 6; b) S. Black, in *Smart Textiles for Medicine and Healthcare*, DOI: <https://doi.org/10.1533/9781845692933.1.3> (Ed: L. Van Langenhove), Woodhead Publishing **2007**, p. 3; c) S. L. Tomić, M. M. Mičić, S. N. Dobić, J. M. Filipović, E. H. Suljovrujić, *Radiation Physics and Chemistry* **2010**, 79, 643.
- [5] Z. S. Haidar, R. C. Hamdy, M. Tabrizian, *Biomaterials* **2008**, 29, 1207.
- [6] A. Sirelkhatim, S. Mahmud, A. Seeni, N. H. M. Kaus, L. C. Ann, S. K. M. Bakhori, H. Hasan, D. Mohamad, *Nanomicro Lett* **2015**, 7, 219.
- [7] R. Ahmed, M. Tariq, I. Ali, R. Asghar, P. Noorunnisa Khanam, R. Augustine, A. Hasan, *Int J Biol Macromol* **2018**, 120, 385.
- [8] a) Y. K. Mishra, R. Adelung, *Materials Today* **2018**, 21, 631; b) H. Papavlassopoulos, Y. K. Mishra, S. Kaps, I. Paulowicz, R. Abdelaziz, M. Elbahri, E. Maser, R. Adelung, C. Röhl, *PloS one* **2014**, 9, e84983.
- [9] A. Nasajpour, S. Ansari, C. Rinoldi, A. S. Rad, T. Aghaloo, S. R. Shin, Y. K. Mishra, R. Adelung, W. Swieszkowski, N. Annabi, A. Khademhosseini, A. Moshaverinia, A. Tamayol, *Advanced Functional Materials* **2018**, 28, 1870021.
- [10] A. Dejneca, I. Aulika, M. V. Makarova, Z. Hubicka, A. Churpita, D. Chvostova, L. Jastrabik, V. A. Trepakov, *Journal of The Electrochemical Society* **2010**, 157, G67.
- [11] a) C. Ghobril, M. W. Grinstaff, *Chem Soc Rev* **2015**, 44, 1820; b) S. R. U. Rehman, R. Augustine, A. A. Zahid, R. Ahmed, M. Tariq, A. Hasan, *Int J Nanomedicine* **2019**, 14, 9603.
- [12] K. Yue, G. Trujillo-de Santiago, M. M. Alvarez, A. Tamayol, N. Annabi, A. Khademhosseini, *Biomaterials* **2015**, 73, 254.
- [13] Y. K. Mishra, S. Kaps, A. Schuchardt, I. Paulowicz, X. Jin, D. Gedamu, S. Freitag, M. Claus, S. Wille, A. Kovalev, S. N. Gorb, R. Adelung, *Particle & Particle Systems Characterization* **2013**, 30, 775.
- [14] V. Srikant, D. R. Clarke, *Journal of Applied Physics* **1998**, 83, 5447.
- [15] A. L. Companion, *Journal of Physics and Chemistry of Solids* **1962**, 23, 1685.
- [16] J. Wang, Z. Wang, B. Huang, Y. Ma, Y. Liu, X. Qin, X. Zhang, Y. Dai, *ACS Applied Materials & Interfaces* **2012**, 4, 4024.

- 1
2
3
4 [17] C. R. Ozawa, A. Banfi, N. L. Glazer, G. Thurston, M. L. Springer, P. E. Kraft, D. M.
5 McDonald, H. M. Blau, *J Clin Invest* **2004**, 113, 516.
6 [18] M. Akhmanova, E. Osidak, S. Domogatsky, S. Rodin, A. Domogatskaya, *Stem Cells*
7 *Int* **2015**, 2015, 167025.
8 [19] F. Brandl, F. Sommer, A. Goepferich, *Biomaterials* **2007**, 28, 134.
9 [20] P. Bao, A. Kodra, M. Tomic-Canic, M. S. Golinko, H. P. Ehrlich, H. Brem, *J Surg*
10 *Res* **2009**, 153, 347.
11 [21] H. Kim, U. S. Jung, S. I. Kim, D. Yoon, H. Cheong, C. W. Lee, S. W. Lee, *Current*
12 *Applied Physics* **2014**, 14, 166.
13 [22] M. B. Dreifke, A. A. Jayasuriya, A. C. Jayasuriya, *Mater Sci Eng C Mater Biol Appl*
14 **2015**, 48, 651.
15 [23] M. Kirsch, L. Birnstein, I. Pepelanova, W. Handke, J. Rach, A. Seltsam, T. Scheper,
16 A. Lavrentieva, *Bioengineering (Basel)* **2019**, 6.
17 [24] T. Jungst, W. Smolan, K. Schacht, T. Scheibel, J. Groll, *Chemical Reviews* **2016**, 116,
18 1496.
19 [25] X. Jin, J. Strueben, L. Heepe, A. Kovalev, Y. K. Mishra, R. Adelung, S. N. Gorb, A.
20 Staubitz, *Advanced Materials* **2012**, 24, 5676.
21 [26] T. Velnar, L. Gradisnik, *Med Arch* **2018**, 72, 444.
22 [27] a) M. Pandurangan, D. H. Kim, *Saudi J Biol Sci* **2015**, 22, 679; b) M. Pandurangan,
23 M. Veerappan, D. H. Kim, *Appl Biochem Biotechnol* **2015**, 175, 1270.
24 [28] a) B. C. Heng, X. Zhao, S. Xiong, K. W. Ng, F. Y.-C. Boey, J. S.-C. Loo, *Food Chem*
25 *Toxicol* **2010**, 48, 1762; b) M. Pandurangan, D. Kim, *Journal of Nanoparticle*
26 *Research* **2015**, 17; c) R. J. Vandebriel, W. H. De Jong, *Nanotechnol Sci Appl* **2012**,
27 5, 61.
28 [29] M. Y. Memar, R. Ghotaslou, M. Samiei, K. Adibkia, *Infect Drug Resist* **2018**, 11,
29 567.
30 [30] a) N. Ferrara, H.-P. Gerber, J. LeCouter, *Nature Medicine* **2003**, 9, 669; b) J. M.
31 Rosenstein, J. M. Krum, C. Ruhrberg, *Organogenesis* **2010**, 6, 107.
32 [31] P. Vempati, A. S. Popel, F. Mac Gabhann, *Cytokine Growth Factor Rev* **2014**, 25, 1.
33 [32] P. Lertkiatmongkol, D. Liao, H. Mei, Y. Hu, P. J. Newman, *Curr Opin Hematol* **2016**,
34 23, 253.
35 [33] R. Warriner, R. Burrell, *Adv Skin Wound Care* **2005**, 18 Suppl 1, 2.
36 [34] I. Tom, M. Ibrahim, A. Umoru, J. Umar, M. Bakar, A. Haruna, A. Aliyu, *OALib* **2019**,
37 06, 1.
38 [35] W. Song, J. Zhang, J. Guo, J. Zhang, F. Ding, L. Li, Z. Sun, *Toxicol Lett* **2010**, 199,
39 389.
40 [36] Y. Xie, Y. He, P. L. Irwin, T. Jin, X. Shi, *Applied and Environmental Microbiology*
41 **2011**, 77, 2325.
42 [37] M. Ruffin, E. Brochiero, *Frontiers in Cellular and Infection Microbiology* **2019**, 9.
43 [38] M. Hassani, M. Moghaddam, M. M. Forghanifard, *Nanomedicine Journal* **2014**, 6,
44 121.
45 [39] a) H. Li, J. Chang, *Acta Biomater* **2013**, 9, 6981; b) S. H. Bhang, W. S. Jang, J. Han,
46 J.-K. Yoon, W.-G. La, E. Lee, Y. S. Kim, J.-Y. Shin, T.-J. Lee, H. K. Baik, B.-S.
47 Kim, *Advanced Functional Materials* **2017**, 27, 1603497.
48 [40] a) H. Gao, W. Dai, L. Zhao, J. Min, F. Wang, *Journal of Immunology Research* **2018**,
49 2018, 6872621; b) S. Zhang, J. Ermann, M. D. Succi, A. Zhou, M. J. Hamilton, B.

- 1
2
3
4 Cao, J. R. Korzenik, J. N. Glickman, P. K. Vemula, L. H. Glimcher, G. Traverso, R.
5 Langer, J. M. Karp, *Sci Transl Med* **2015**, 7, 300ra128.
6 [41] F. Geissmann, M. G. Manz, S. Jung, M. H. Sieweke, M. Merad, K. Ley, *Science* **2010**,
7 327, 656.
8 [42] X. Zhao, Q. Lang, L. Yildirimer, Z. Y. Lin, W. Cui, N. Annabi, K. W. Ng, M. R.
9 Dokmeci, A. M. Ghaemmaghami, A. Khademhosseini, *Adv Healthc Mater* **2016**, 5,
10 108.
11 [43] a) J. Deng, Y. Tang, Q. Zhang, C. Wang, M. Liao, P. Ji, J. Song, G. Luo, L. Chen, X.
12 Ran, Z. Wei, L. Zheng, R. Dang, X. Liu, H. Zhang, Y. S. Zhang, X. Zhang, H. Tan,
13 *Advanced Functional Materials* **2019**, 29, 1809110; b) X. Yao, G. Zhu, P. Zhu, J. Ma,
14 W. Chen, Z. Liu, T. Kong, *Advanced Functional Materials* **2020**, 30, 1909389.
15 [44] a) R. Carroll, in *Elsevier's Integrated Physiology* (Ed: Mosby), Elsevier **2006**, p. 7;
16 b) R. M. Ludatscher, *Virchows Arch B Cell Pathol* **1978**, 27, 347; c) M. Takeo, W.
17 Lee, M. Ito, *Cold Spring Harb Perspect Med* **2015**, 5, a023267.
18 [45] a) T. Tokatlian, C. Cam, T. Segura, *Adv Healthc Mater* **2015**, 4, 1084; b) M. Ziche,
19 L. Morbidelli, *J Neurooncol* **2000**, 50, 139.
20 [46] Q. Zeng, Y. Han, H. Li, J. Chang, *J Mater Chem B* **2015**, 3, 8856.
21 [47] G. C. Gurtner, S. Werner, Y. Barrandon, M. T. Longaker, *Nature* **2008**, 453, 314.
22 [48] H. J. Yoon, S. R. Shin, J. M. Cha, S.-H. Lee, J.-H. Kim, J. T. Do, H. Song, H. Bae,
23 *PLOS ONE* **2016**, 11, e0163902
24 [49] S. Mehrotra, B. A. G. de Melo, M. Hirano, W. Keung, R. A. Li, B. B. Mandal, S. R.
25 Shin, *Advanced Functional Materials* **2020**, 30, 2070079.
26 [50] a) C. Zhang, L. Zhang, W. Wu, F. Gao, R.-Q. Li, W. Song, Z.-N. Zhuang, C.-J. Liu,
27 X.-Z. Zhang, *Advanced Materials* **2019**, 31, 1901179; b) T.-H. Kim, M. Eltohamy,
28 M. Kim, R. A. Perez, J.-H. Kim, Y.-R. Yun, J.-H. Jang, E.-J. Lee, J. C. Knowles, H.-
29 W. Kim, *Acta Biomater* **2014**, 10, 2612.
30 [51] L. P. Yan, J. Silva-Correia, V. P. Ribeiro, V. Miranda-Gonçalves, C. Correia, A. da
31 Silva Morais, R. A. Sousa, R. M. Reis, A. L. Oliveira, J. M. Oliveira, R. L. Reis, *Sci*
32 *Rep* **2016**, 6, 31037.
33 [52] a) S. Zhang, J. Hou, Q. Yuan, P. Xin, H. Cheng, Z. Gu, J. Wu, *Chemical Engineering*
34 *Journal* **2020**, 392, 123775; b) M. Xu, A. Khan, T. Wang, Q. Song, C. Han, Q. Wang,
35 L. Gao, X. Huang, P. Li, W. Huang, *ACS Applied Bio Materials* **2019**, 2, 3329.
36 [53] J.-S. Oh, E.-J. Lee, *Mater Sci Eng C Mater Biol Appl* **2019**, 103, 109815.
37 [54] W.-Y. Chen, H.-Y. Chang, J.-K. Lu, Y.-C. Huang, S. G. Harroun, Y.-T. Tseng, Y.-J.
38 Li, C.-C. Huang, H.-T. Chang, *Advanced Functional Materials* **2015**, 25, 7189.
39 [55] H. Yu, J. Peng, Y. Xu, J. Chang, H. Li, *ACS Applied Materials & Interfaces* **2016**, 8,
40 703.
41 [56] B. P. Dos Santos, B. Garbay, M. Fenelon, M. Rosselin, E. Garanger, S.
42 Lecommandoux, H. Oliveira, J. Amédée, *Acta Biomater* **2019**, 99, 154.
43 [57] S. A. Castleberry, B. D. Almquist, W. Li, T. Reis, J. Chow, S. Mayner, P. T.
44 Hammond, *Adv Mater* **2016**, 28, 1809.
45
46
47
48
49
50
51
52
53
54
55
56
57
58
59
60
61
62
63
64
65

1
2
3
4 **Figures and Figure captions**
5
6



Schematic 1. Schematic diagram of a fabrication process of the smart wound scaffold and working principle for wound healing process: Preparation of t-ZnO microparticles by H₂O₂-treatment, subsequent VEGF adsorption, and composite ink with GelMA pre-polymer solution. Light-triggered release of VEGF on the H₂O₂-treated ZnO microparticles. Improved angiogenesis and antibacterial activity by a VEGF-coated t-ZnO embedded the open porous printing constructs at wound area.

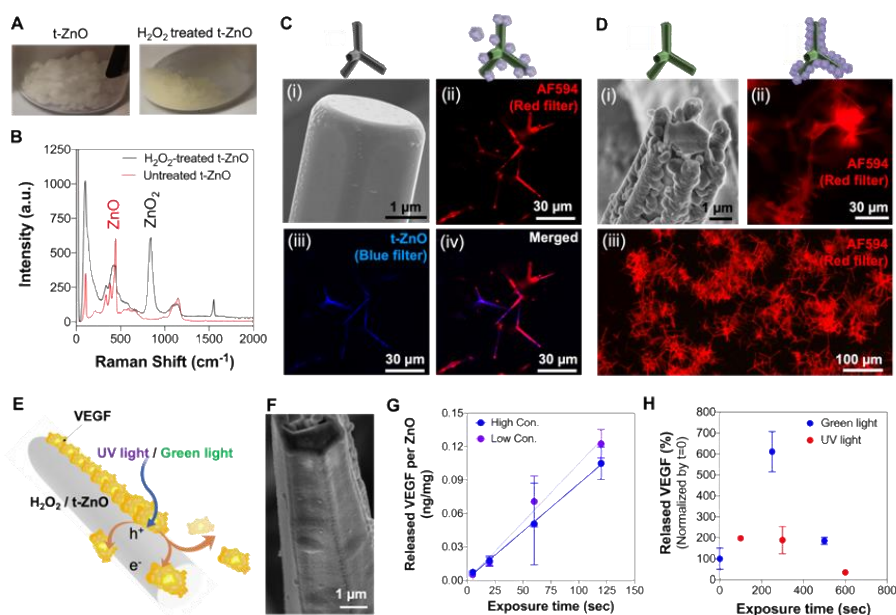


Figure 1. Tuned photoactive characterization of chemically-treated t-ZnO. (A) Photograph images showed color change from white to yellow after H₂O₂-treatment. (B) Raman spectra of t-ZnO microparticles before and after H₂O₂-treatment. (C) The pristine t-ZnO powder exhibited smooth surface of individual tetrapod in the SEM image (i) and induced low protein adhesion of IgG AF594 in the fluorescence micrograph (ii). Red and blue fluorescence signals indicated by IgG AF594 and t-ZnO, respectively. (D) The surface of the individual tetrapod of t-ZnO treated with H₂O₂ has turned to a rough and porous surface as shown in the SEM image (i). A significantly thicker coverage of t-ZnO with IgG AF594 can be observed from the fluorescence micrograph (ii). (E) SEM image showed VEGF-coated on the individual tetrapod of H₂O₂-treated t-ZnO. (F) The working principle of protein-release by UV/green light stimulations. Light induces charge carrier separation in the semiconducting t-ZnO microparticles. The charges travel to the surface and accumulate,

1
2
3
4 resulting in proteins being released from the t-ZnO microparticle surface via electrostatic
5
6 force of repulsion. (G) Released VEGF on the H₂O₂-treated t-ZnO with a low (1 µg/mL) and
7
8 high concentration of VEGF (5 µg/mL) immobilization upon green light exposure over time.
9
10
11 (n = 2). (H) Released the concentration of VEGF from H₂O₂-treated t-ZnO after green and
12
13 UV light exposure. (n = 2)
14
15
16
17
18
19
20
21
22
23
24
25
26
27
28
29
30
31
32
33
34
35
36
37
38
39
40
41
42
43
44
45
46
47
48
49
50
51
52
53
54
55
56
57
58
59
60
61
62
63
64
65

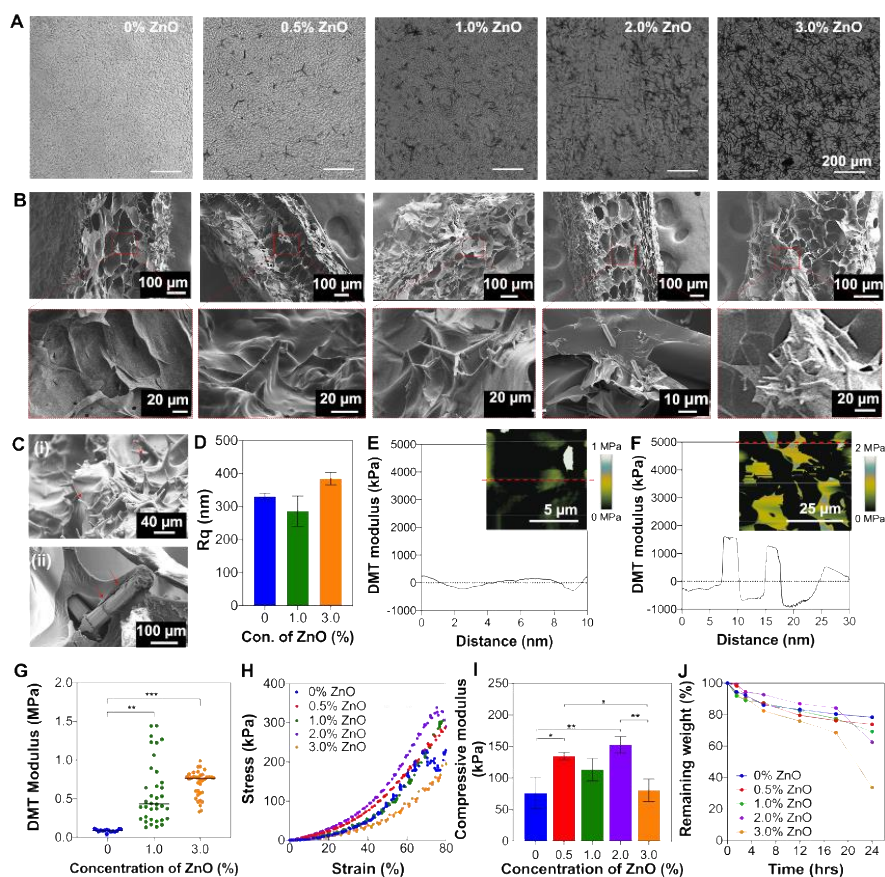


Figure 2. Mechanical properties of t-ZnO-laden hydrogel. (A) Phase contrast images to evaluate well-dispersed t-ZnO microparticles in GelMA hydrogels. (B) Cross-sectional view of SEM images of t-ZnO-laden GelMA hydrogels with increasing t-ZnO filling (0-3 w/v% t-ZnO) (C) Surface morphology of 2% t-ZnO-laden GelMA hydrogel (i) and tetrapod covered by GelMA gels. (D) Measured root mean square (RMS) roughness (Rq) of t-ZnO-laden GelMA hydrogels with various concentrations of t-ZnO. (n = 3). (E and F) DMT modulus distribution profiles of (E) pristine GelMA and (F) 1 %t-ZnO-GelMA hydrogel along with specified line in inset AFM modulus mapping images. (G) Local DMT modulus

1
2
3
4
5
6
7
8
9
10
11
12
13
14
15
16
17
18
19
20
21
22
23
24
25
26
27
28
29
30
31
32
33
34
35
36
37
38
39
40
41
42
43
44
45
46
47
48
49
50
51
52
53
54
55
56
57
58
59
60
61
62
63
64
65

of t-ZnO-laden GelMA hydrogels with various concentrations of t-ZnO measured by AFM.
(n>15) (H) Stress-strain curves and (I) microscale compressive modulus of t-ZnO-laden
GelMA hydrogels depending on the t-ZnO filling factor at 50 seconds of crosslinking time.
(n = 5) (J) Degradation behaviors of t-ZnO-laden GelMA hydrogels depending on the t-ZnO
filling factor incubated with collagenase Type II (1 U/mL). (n = 5)

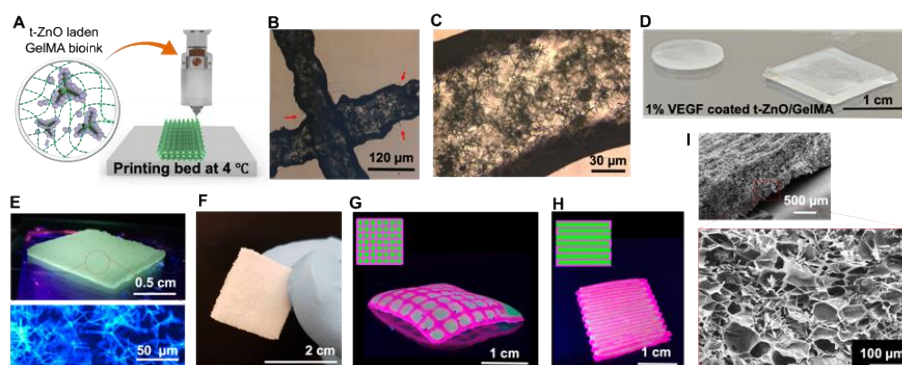


Figure 3. 3D printing of t-ZnO-laden GelMA hydrogel constructs. (A) Schematic diagram of 3D printing of t-ZnO-laden composite ink on the printing bed at 4 °C and crosslinked by UV light exposure. Phase contrast images showed (B) printed microfilaments of t-ZnO-laden GelMA hydrogels, individual tetrapods of t-ZnO that protruded out from the filaments, and (C) well-dispersed t-ZnO in the filaments. (D) Different shapes of VEGF-coated t-ZnO-laden printed hydrogel. (E) Photograph of the highly dense printed construct (3 layers) under UV and confocal micrograph of the 2% t-ZnO microparticles embedded in the printed construct. (F) Photograph showing free-standing printed construct with excellent mechanical stability to touch and grasp. (G and H) Photographs of the 3D printed constructs with grid-like (G) and layered (H) arrangements using two colored t-ZnO-laden composite inks with multi-nozzle printer in grid-like arrangement for synergetic effect of two inks. (I) SEM image of printed construct that showed microporous morphology and embedded t-ZnO microparticles.

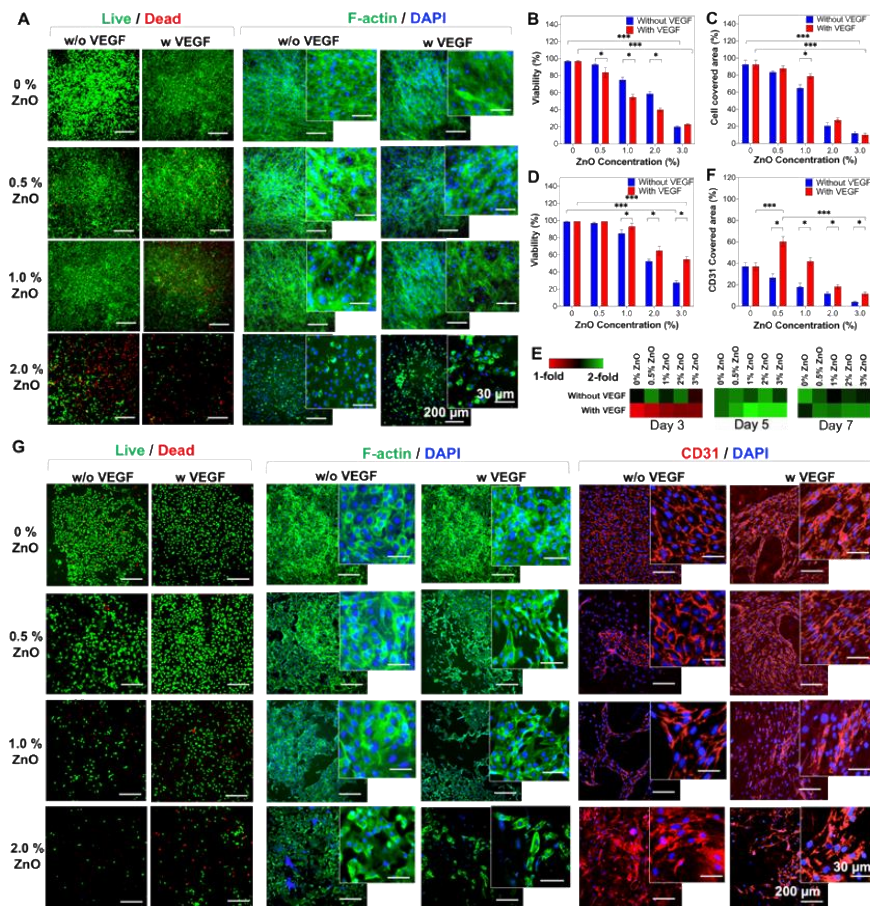


Figure 4. *In vitro* characterization of VEGF-coated t-ZnO GelMA hydrogels. (A) Live/Dead and F-Actin/DAPI staining on C2C12 behaviors cultured on the t-ZnO-laden GelMA hydrogels with and without VEGF coating at various concentrations of t-ZnO. (B) Quantified viability of cultured C2C12 cells on the constructs with and without VEGF coating and different concentrations of t-ZnO. (n = 3, 2 random images/sample, *p < 0.05, ***p < 0.001). (C) Quantified cell covered area that was calculated from F-Actin/DAPI staining images of cultured C2C12 cells on the t-ZnO-laden GelMA hydrogels obtained on

Supporting information for

Light controlled protein release in 3D printed hydrogel constructs for smart wound scaffold

By Leonard Siebert*, Eder Luna-Cerón, Luis Enrique García-Rivera, Junsung Oh, JunHwee Jang, Diego A. Rosas-Gómez, Mitzi D. Pérez-Gómez, Gregor Maschkowitz, Helmut Fickenscher, Daniela Ocegüera-Cuevas, Carmen G. Holguín-León, Batzaya Byambaa, Mohammad A. Hussain, Nebras Sobahi, Anwarul Hasan, Dennis P. Orgill, Yogendra K. Mishra, Rainer Adelung, Eunjung Lee*, Su Ryon Shin*

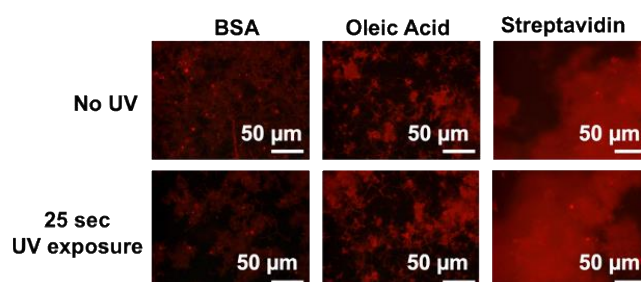


Figure S1. Fluorescence micrographs of IgG AF594 coated t-ZnO microparticles treated with BSA, oleic acid and streptavidin before and after UV exposure.

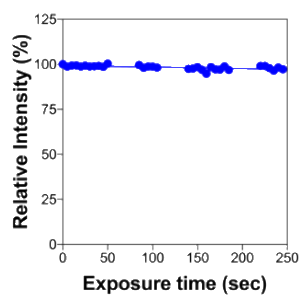


Figure S2. The relative intensity of immobilized IgG AF594 on non-photoactive SiO₂ particles overtime under UV exposure.

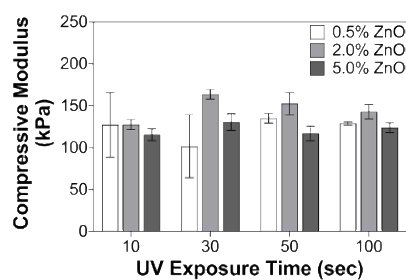


Figure S3. Compressive modulus of different t-ZnO hydrogels at different ZnO concentrations and crosslinking times.

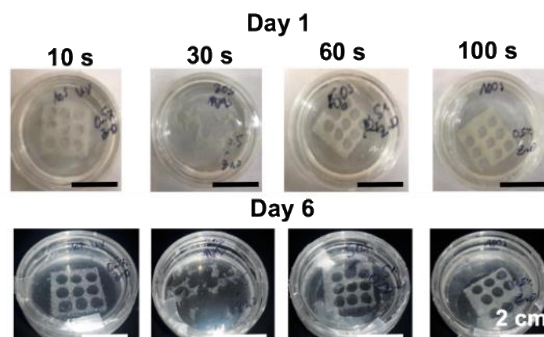


Figure S4. Degradation tests at 37 °C in PBS of 0.5% H₂O₂ treated t-ZnO-GelMA printed constructs crosslinked for times 10-100 seconds on day 1 and day 6, swelling but no visible degradation occurred.

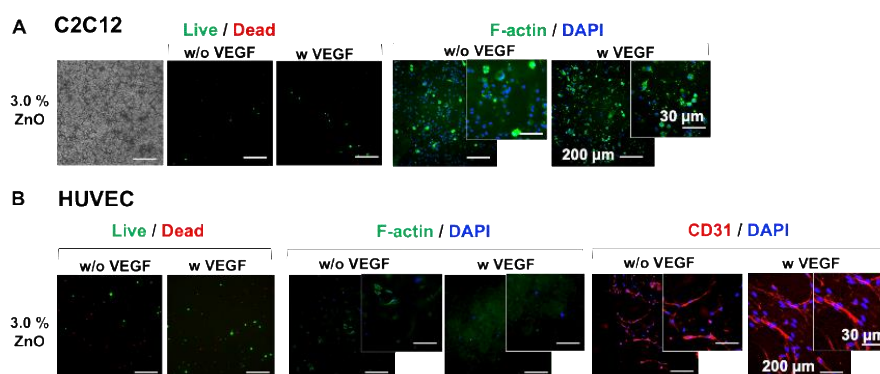


Figure S5. Effects of t-ZnO and VEGF-coated t-ZnO laden GelMA hydrogels on cell viability, attachment and proliferation of C2C12 and HUVEC cells. Live and Dead and F-Actin/DAPI and CD31/DAPI staining on HUVEC (A) and C2C12 cells (B) within different concentrations of t-ZnO laden hydrogels.

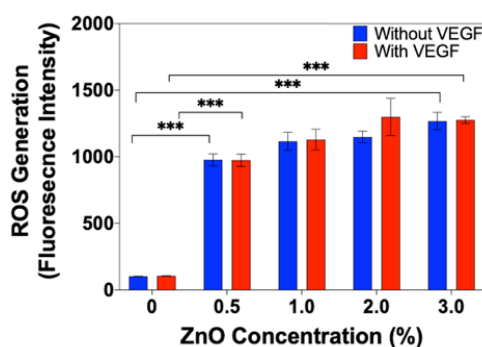
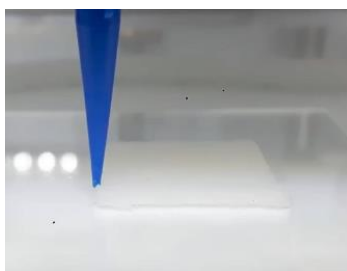


Figure S6. Reactive oxygen species (ROS) generation assay of VEGF-coated and non-coated t-ZnO-laden hydrogels at different concentrations of t-ZnO. (n = 2 per condition, ***p < 0.001).



Video 1. Video showing printing technique of t-ZnO wound scaffold.

Chapter 8

3D-Printed Chemiresistive Sensor Array on Nanowire CuO / Cu₂O / Cu Heterojunction Nets

The production procedure for semiconductor devices involves energy consuming and sophisticated clean-room technology and vacuum deposition. Despite the many benefits of these processes, they lack in materials selection, facility and are shape-limited. This work presents the combination of self-ordering of nanostructures with additive manufacturing to fabricate semiconducting metal oxide gas sensors. Direct ink writing was used to fabricate defined traces of commercially available copper microparticles. This ensures reproducibility of the printed devices while giving the particles a lateral order which is otherwise difficult to achieve. The fabrication via DIW also enables direct integration of semiconducting oxide structures onto standard circuit boards. A subsequent annealing step at 425 °C leads to the formation of nanowires on the microparticle's surfaces, resulting in so called core-spike-particles. The wires of two particles touch each other and form a junction. The wire's and the junction's resistivity change when reducing gases react with adsorbed oxygen on the surface. The devices can be used as chemiresistive gas sensors and have a gas response of 150% to 100 ppm of acetone. The general procedure in relation to the application example as gas sensors show the value of combining self-organisation with additive manufacturing.

The results were published in the journal "ACS Applied Materials & Interfaces".

Own contribution presented in this article

- Design and setup of a Direct Ink Writing printer
- Sample fabrication
- Data analysis
- Discussion and interpretation
- Writing the manuscript

The following content in this chapter is reproduced with permission.

3D-Printed Chemiresistive Sensor Array on Nanowire CuO/Cu₂O/Cu Heterojunction Nets

Leonard Siebert,[†] Oleg Lupan,^{*,†,‡,§} Mattia Mirabelli,[†] Nicolai Ababii,[‡] Maik-Ivo Terasa,[†] Sören Kaps,[†] Vasiliu Cretu,[‡] Alexander Vahl,[§] Franz Faupel,[§] and Rainer Adelung^{*,†}

[†]Institute for Materials Science—Functional Nanomaterials, Faculty of Engineering, Kiel University, Kaiserstraße 2, D-24143 Kiel, Germany

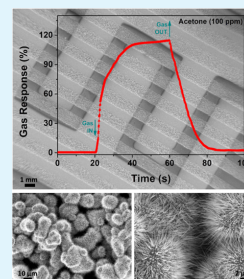
[‡]Center for Nanotechnology and Nanosensors, Department of Microelectronics and Biomedical Engineering, Technical University of Moldova, 168 Stefan cel Mare Avenue, MD-2004 Chisinau, Republic of Moldova

[§]Institute for Materials Science—Chair for Multicomponent Materials, Faculty of Engineering, Christian-Albrechts-University of Kiel, Kaiserstraße 2, D-24143 Kiel, Germany

Supporting Information

ABSTRACT: In this work, the one-step three-dimensional (3D) printing of 20 nm nanowire (NW)-covered CuO/Cu₂O/Cu microparticles (MPs) with diameters of 15–25 μm on the surface of the glass substrate forming an ordered net is successfully reported for the first time. 3D-printed Cu MP-based stripes formed nonplanar CuO/Cu₂O/Cu heterojunctions after thermal annealing at 425 °C for 2 h in air and were fully covered with a 20 nm NW net bridging MPs with external Au contacts. The morphological, vibrational, chemical, and structural investigations were performed in detail, showing the high crystallinity of the NWs and 3D-printed CuO/Cu₂O/Cu heterojunction lines, as well as the growth of CuO NWs on the surface of MPs. The gas-sensing measurements showed excellent selectivity to acetone vapor at an operating temperature of 350 °C with a high gas response about 150% to 100 ppm. The combination of the possibility of fast acetone vapor detection, low power consumption, and controllable size and geometry makes these 3D-printed devices ideal candidates for fast detection, as well as for acetone vapor monitoring (down to 100 ppm). This 3D-printing approach will pave a new way for many different devices through the simplicity and versatility of the fabrication method for the exact detection of acetone vapors in various atmospheres.

KEYWORDS: 3D-printing, Cu deposition, heterojunction, CuO/Cu₂O/Cu, gas sensing



1. INTRODUCTION

Recently, three-dimensional (3D) printing has attracted an important attention for the manufacturing of various 3D components,^{1,2} where the most important field is the fabrication of functional microstructures or even devices due to its low-cost technology and easy processing.³ In this regard, 3D-printed sensors have gained significant attention, because of novel design possibilities, for example, for innovative strain sensors³ or full electronic components.⁴ Many devices are produced with sophisticated methods like inkjet printing⁵ and lack simplicity. For this fabrication approach, inks containing metals or metal oxide nanoparticles can be easily produced but require thorough rheological optimization for becoming printable by an inkjet printer. Simpler methods such as direct ink writing (DIW) can alleviate the complexity of the fabrication by syringe-based extrusion.⁶ While not eliminating the necessity for rheological optimization, the boundary conditions are a lot less tight because of the simple extrusion process compared to inkjet printing. The DIW technology requires neither photolithography nor exposure to UV or etching processes, which allows complex functional patterns to be printed directly on sensor platforms as well as the reduction

of the final cost of fabricated sensors. All things considered, the 3D-printing shows enormous potential for use in the field of microsensing device production. However, the 3D-printing technology is designed for laboratory-scale experiments rather than for mass production yet. The synergy of the advances in gas sensing and in 3D-printing technology may open a huge potential to incorporate, for example, semiconducting oxide-based materials directly onto sensor platforms or portable devices.

Compact and portable chemiresistive sensors for breath acetone concentration are the main focus of the scientific community and are of great demand for customers because breath acetone has been shown to correlate with the level of blood glucose^{7–11} as well as with the rate of fat loss in healthy individuals.¹² Because of acetone's small size, its vapors appear in exhaled breath^{10,13,14} and are considered as a breath marker to diagnose diabetes. Historically, endogenous acetone has been measured in exhaled breath to monitor ketosis in healthy

Received: March 11, 2019

Accepted: June 19, 2019

Published: June 19, 2019



and diabetic subjects. Its level can range from <1 ppm in healthy nondieting individuals to >2–1250 ppm in diabetic ketoacidosis.¹² Thus, portable sensor devices are very important to be produced in a mass- and cost-effective manner because the number of diabetics has increased significantly (doubled¹⁵) in the past decades. In addition, acetone is a widely used reagent in household, industry, and various laboratory applications. It is greatly harmful to human health and biology; thus, its rapid identification is crucial.

In the context of a nanomaterial used in these types of sensors, copper oxide came in the focus of scientists as an important class of nanosolids that has been the main subject of intensive studies for the last decade for acetone sensors.¹⁶ Additionally, copper oxide shows considerable interest for various other applications, including optoelectronic, gas sensors, solar energy conversion, and photocatalysis.^{17–20}

In this work, we report on the one-step DIW of a 20 nm nanowire (NW)-covered CuO/Cu₂O/Cu microparticle (MP)-based sensor 3D-printed for the first time. The gas-sensing measurements showed excellent selectivity to acetone, and a mechanism for it was proposed and discussed, which is a breakthrough in acetone detection with noninvasive tools. The combination of the possibility of fast acetone vapor detection, low power consumption, and controllable size as well as geometry control, make the 3D-printing approach extremely attractive for future 3D-printed electronics or even nano-electronics. Here, we present functional Cu/Cu₂O/CuO heterojunctions made via DIW followed by thermal annealing (TA). For characterization of these, first, the results from scanning electron microscopy (SEM) (Section 3.1), subsequently the results from X-ray powder diffraction (XRD) and Raman, and then, the results of X-ray photoelectron spectroscopy (XPS) will be presented. Finally, based on the presented 3D-printed geometries and morphologies, application scenarios for the networks as well as for the CuO will be presented.

2. EXPERIMENTAL SECTION

Spheroidal copper particles (14–25 μm) obtained from Sigma-Aldrich were sonicated in distilled water for 5 min. Polyethylene oxide (PEO) powder ($M_n \approx 2\,000\,000$) from Sigma-Aldrich was added, and the solution was stirred at room temperature (see schematic Figure 1a) until an optically uniform suspension was achieved. Suspensions with different concentrations of copper and polymer according to Table 1 were produced. The suspensions were then deposited on glass substrates in single-layered traces through a custom-built DIW apparatus (see schematic Figures 1b and S1). By changing the extrusion factor and the geometry, the height, width, and the orientation of the deposited traces-strips were controlled. Conical nozzles with an orifice diameter of 0.58 mm were used throughout the deposition. Traces/strips with 22 mm length, 0.6 mm width, and 0.2 mm height were deposited for 3D-L sample sets longitudinally (L) on a glass substrate (1.0 cm × 2.5 cm) with a flow rate of 1.5 mm³/s. The sample set 3D-T was deposited transversally (T) on the glass substrate (1.0 cm × 2.5 cm) with a higher flow rate of 1.74 mm³/s, while still using the same parameters, but the stripe length was 10 mm only. 3D-T was produced with traces perpendicular to the long side of the glass substrate (Figure 1b) where 3D-L has traces parallel to the long side (see also Figure S2).

All samples presented in this paper were made from suspensions with 1.5:1.0 Cu/H₂O weight ratios. 3D-T has a base polymer solution of 6.0 wt % and 3D-L has a 6.5 wt % base polymer solution. 3D-T was deposited with a higher flow rate than 3D-L resulting in wider and higher traces.

The sample morphology was investigated by using SEM REM-ZEISS (7.0 kV, 10.0 μA). The analysis of the chemical composition of the specimens was done by energy-dispersive X-ray spectroscopy.

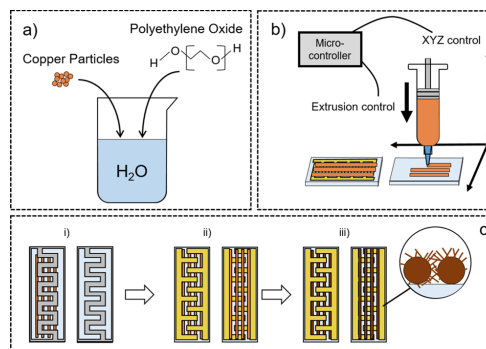


Figure 1. Fabrication process and technological flow used for 3D-printing of the Cu/Cu₂O/CuO NW heterojunction-based sensor structures: (a) ink design with copper MPs and PEO; (b) DIW of Cu-inks on glass slides with and without gold contacts; (c) masked sputter Au-deposition (i and ii) TA for Cu/Cu₂O/CuO NW heterojunction net growth (iii).

Table 1. Data for All Sample Sets Preparation

sample set	3D-T	3D-L
base solution PEO content	6%	6.5%
trace height	>0.2 mm	0.2 mm
trace width	>0.6 mm	0.6 mm
trace orientation	transversal	longitudinal

Micro-Raman studies were performed at room temperature with a WITec system in a backscattering configuration. The Nd-YAG laser power was less than 4 mW at the sample. Samples were examined with a Nd-YAG laser, $\lambda_{ex} = 532.2$ nm and for each spectrum, 10 accumulations at an integration time of 1 s were taken. Crystallographic results were measured with an XRD Seifert 3000 TT instrument unit operating at 40 kV and 40 mA, with Cu K α_1 radiation ($\lambda = 1.540598$ Å).

The CuO NW samples were investigated regarding their stoichiometry and chemical composition by applying XPS (Omicron Nano-Technology GmbH, Al-anode, 240 W). The charging effect in the recorded spectra was corrected on the basis of the C 1s line of aliphatic carbon at 285.0 eV.²¹ The evaluation was conducted using the software CasaXPS (version 2.3.16).

To investigate the electrical resistance of nonplanar CuO/Cu₂O/Cu heterojunctions, a thin film of Au (170 nm) in a meander form was deposited as electrical contact as described in our previous work.²² The gas response was obtained as the ratio $\Delta R/R_{air}$, where $\Delta R = R_{gas} - R_{air}$ and R_{air} and R_{gas} are the electrical resistances of the sensor structures in ambient air and under exposure to volatile organic compounds (VOCs) or gas, respectively. Details on the sensing experiments can be found in our previous works on gas sensing.^{8,17}

3. RESULTS AND DISCUSSION

For the reliable deposition of Cu particles, the ink must have a high base viscosity. Poly(ethylene glycol) (PEG) with a M_n of $\approx 2\,000\,000$ was used to create an ink with both a high viscosity and low concentration of less than 10 wt %. Because of the low concentration, only little PEG is present after the 3D-printing and was easily removed in the TA step. The viscosity is necessary to impart enough shearing force on the particles and thus to prevent agglomeration and clogging of the nozzle and to allow a homogeneous and controllable deposition of the ink.

For a reliable deduction of the evolution of morphological and structural properties with regard to the DIW procedure, a detailed investigation on the crystallinity and stoichiometry of the nonplanar CuO/Cu₂O/Cu heterojunctions is necessary. The results of these morphological, vibrational, and structural investigations are presented step-by-step in the following chapter.

3.1. Morphology of 3D-Printed Samples. In Figure 2, the SEM images of copper oxide nano-microspheres showing

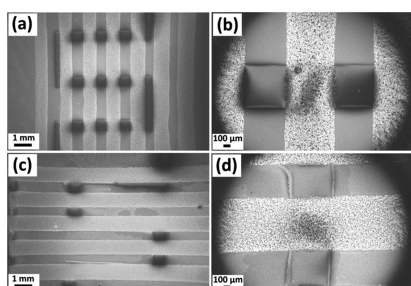


Figure 2. SEM images of CuO microspheres 3D-printed on the sensor substrate with an inset showing details of the morphology: (a) longitudinally 3D-printed stripes directly on interdigitated Au electrode contacts (set 3D-L); (b) high-magnification image to show the printed MPs; (c) transversally 3D-printed stripes directly on interdigitated Au electrode contacts (set 3D-T); (d) zoomed-in image of the transversally printed sample to show the printed MPs between the gold pads.

large view details of the morphology and geometry of the 3D-printed sensor structures are presented. The SEM images shown in Figure 2a,b are for longitudinally 3D-printed directly on interdigitated Au electrode contacts at lower and higher magnification (set 3D-L), respectively. Figure 2c,d presents images for transversal 3D-printed stripes on interdigitated Au electrode contacts (1700 μm wide) at lower and higher magnification (set 3D-T), respectively. In the case of a longitudinally sample, we have interdigit distances of about 850 μm between the Au pads and of about 800 μm between the different parallel stripes. The width of 3D-printed material is in the range of 570–610 μm. Considering that a Cu MP average size is about 20 μm, the 3D-printed results show a high shape fidelity. In the case of the transversally 3D-printed sensors, we have interdigit distances between the Au pads of about 600 and 550 μm between the different parallel transversal stripes. The width of the printed material is in the range of 850–900 μm, which can be explained by the higher flow rate of set 3D-T as well as a lower base polymer concentration of 6.0 wt % compared to the sample sets 3D-L with a 6.5 wt % base polymer solution. The lower viscosity coupled with the higher flow rate of sample set 3D-T results in wider and higher traces. Still, the shape fidelity is very high considering the size of the Cu microspheres, with a maximum deviation of 50 μm.

In Figure 3, larger view details of the NW-CuO/Cu₂O/Cu microspheres can be seen as SEM images. Figure 3b shows neighboring MPs covered with CuO NWs with lengths of 2–15 μm grown from MP CuO/Cu₂O/Cu forming stripes. Figure 3c,d shows CuO NWs bridging two neighboring CuO/Cu₂O/Cu MPs forming electrical paths for it between the Au

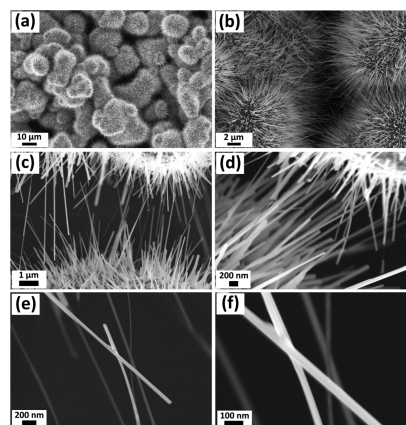


Figure 3. SEM images of NW-CuO/Cu₂O/Cu nano-microspheres showing details of morphology: (a) higher magnification images of stripes of a longitudinal 3D-L set printed directly on the sensor template; (b–f) higher magnification images of samples from (a) to show printed MPs and interpenetrated CuO NWs bridging the 3D-printed CuO/Cu₂O/Cu heterojunction MP net forming lines.

electrodes (not shown here). Figure 3e,f shows two interpenetrated NWs of CuO with diameters about 35 and 50 nm, which are bridging different microspheres and allow current flow through the sensor structure.

3.2. Crystalline Structure. Figure 4 shows the XRD pattern for the 3D-printed NW CuO/Cu₂O/Cu heterojunc-

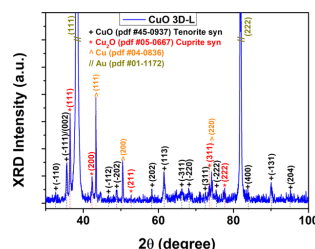


Figure 4. XRD patterns of the 3D-printed NW-CuO/Cu₂O/Cu heterojunction net on Au contacts subjected to TA at 425 °C for 120 min in air.

tion net subjected to TA at 425 °C for 120 min in air. The relative peak intensity to the background demonstrates good crystallinity of the oxide samples, which can be assigned to a Cu and Cu₂O face-centered cubic structure, CuO monoclinic structure, and also metallic Au from the contacts.

Figure 4 illustrates that the strongest reflections (*hkl*) are of cupric oxide CuO (tenorite) at 2θ values and correspond to the (-110) , $(-111)/(002)$, (-112) , (-202) , (202) , (113) , (-311) , (-220) , (311) , (-222) , (400) , (-131) , and (204) Miller planes at 32.65°, 35.65°, 46.7°, 48.8°, 58.25°, 61.5°, 68.05°, 72.6°, 75.35°, 83.85°, 90.05°, and 95.2°, respectively. The crystal structure of CuO tenorite is in the monoclinic symmetry with space group $C2/c$ ²³ with the lattice constants $a = 4.684 \text{ \AA}$, $b = 3.423 \text{ \AA}$, $c = 5.129 \text{ \AA}$, and $\beta = 99.54^\circ$.^{23,24} In

CuO, there are four Cu–O units in the unit cell and two Cu–O units in the primitive cell, and each Cu atom is located in the center of an oxygen parallelogram. Each O atom has a distorted tetrahedral copper coordination. The Cu in the CuO is in the Cu^{2+} state exhibiting antiferromagnetic ordering²⁴ and has antiferromagnetic insulating ground states.^{19,25} Reflections at 2θ of 36.5° , 42.35° , 52.75° , 73.35° , and 77.7° are assigned to (111), (200), (211), (311), and (222) of Cu_2O (cuprite). Cu_2O has a cubic structure, the cuprite type, and is of space group $T_h^2\text{-}Pn3[65W]$ or $O_h^4\text{-}Pn3[72P]$ with the following unit cell parameters: $a = 4.27 \text{ \AA}$ at $p \approx 0 \text{ GPa}$, $a = 4.18 \text{ \AA}$ at $p \approx 10 \text{ GPa}$ [82W].^{24,26} Copper has two oxygen neighbors, and the site symmetry is D_{3d} . Oxygen has four Cu neighbors, and the site symmetry is T_d .²⁶ Additionally, reflections of metallic Cu at 2θ of 43.35° , 50.5° , and 74.15° are observed for (111), (200), and (220) Miller planes, respectively, which indicate that original Cu was not completely oxidized in 2 h at 425°C . Reflections at 38.25° and 81.8° are attributed to metallic Au, which is due to sputtered contacts or external electrodes of the sensors. Relevant XRD parameters can also be found in Table S1 in the Supporting Information.

To verify the findings from the XRD studies, the Raman spectra on the 3D-printed stripes formed of the NW-CuO/Cu₂O/Cu heterojunction net were performed.

Micro-Raman can be used extensively for surface region investigations of various CuO/Cu₂O nanostructures.^{17,18} Figure 5 shows a room temperature micro-Raman spectrum

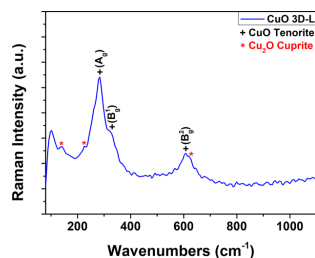


Figure 5. Raman spectrum of the 3D-printed NW-CuO/Cu₂O/Cu heterojunction net subjected to TA at 425°C for 120 min in air.

of the 3D-printed NW-CuO/Cu₂O/Cu heterojunction net in the spectral range between 70 and 1100 cm^{-1} . Coexistence of mixed phases, namely, cuprite Cu_2O and tenorite CuO , were observed in the 3D-printed samples because of the high sensitivity of the micro-Raman spectroscopy. For all samples, we observed mode peaks at around (i) 283, 332, and 610 cm^{-1} which corresponds to the CuO (tenorite) and (ii) 129, 215, and 627 cm^{-1} which corresponds to the Cu_2O (cuprite). Cuprous oxide (Cu_2O) is highly symmetrical with the space group $Pn3m$ and its unit cell contains two formula units (Cu_4O_2).¹⁸ Cu_2O has 6 atoms in the unit cell, and these 18 modes at the Γ point are¹⁹

$$\Gamma_{\text{vibr}} = A_{2u} + E_u + 3T_{1u} + T_{2u} + T_{2g} \quad (1)$$

T_{1u} modes are infrared active and are associated with the relative motion of the copper and oxygen lattices and consist of a Cu–O stretching mode and an asymmetric O–Cu–O bending mode.²⁷ T_{2g} is Raman active, the others are silent modes. The T_{1u} mode is observed around the calculated frequency.

CuO has 12 phonon branches because of four atoms in the primitive cell and a zone-center mode^{18,19}

$$\Gamma_{\text{vibr}} = A_g + 2B_g + 4A_u + 5B_u \quad (2)$$

$A_u + 2B_u$ —3 acoustic modes, $A_g + 2B_g$ —9 optical modes—Raman active, and $3A_u + 3B_u$ —6 IR-active modes.^{18,28} The IR modes involve the motion of Cu and O atoms, and the induced dipole moment is along b -axis for A_u modes and is perpendicular to it for the B_u modes.¹⁸ In the A_g and B_g Raman modes, the oxygen atoms move in the b -direction for A_g and are perpendicular to the b -axis for B_g modes.^{18,19} The results obtained from XRD and Raman indicate that the MPs have a core–shell structure with a CuO shell and $\text{Cu}_2\text{O}/\text{Cu}$ core at the present treatment's temperature and duration (2 h) in TA compared to the complete transformation into $\text{CuO}/\text{Cu}_2\text{O}$ for longer treatment durations (5 h) reported before.^{17,18} The oxidizing and growth mechanism of CuO NWs is discussed previously.^{17,29}

3.3. XPS, Chemical Studies. The overview spectrum of the NW-CuO/Cu₂O/Cu MP sample is shown in Figure 6a.

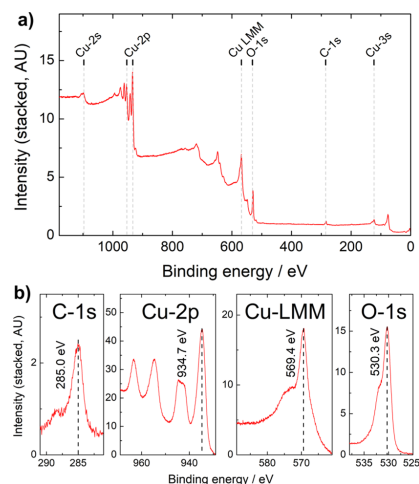


Figure 6. XPS spectra of the NW-CuO/Cu₂O/Cu MP sample: (a) overview spectrum indicating the presence of Cu, O, and C; (b) high-resolution spectra of C 1s line, Cu 2p lines (including satellite peaks), Cu-LMM Auger lines, and O 1s line. The respective peak positions are indicated by black dotted lines.

From this spectrum, the presence of Cu, O, and C can be concluded. For a more detailed investigation, the C 1s, Cu 2p, Cu-LMM, and O 1s lines are shown in Figure 6b. The signal of C originates from surface adsorbates such as atmospheric carbohydrates from the ambient atmosphere.^{30,31} The peak position of the C 1s line was used to correct charging by referencing to 285.0 eV.

In case of the Cu 2p lines, the presence of Cu^{2+} in CuO manifests in the occurrence of satellite peaks^{21,32,33} and in a slight chemical shift of the 2p-peak positions to higher binding energies. These satellite peaks can be clearly observed in the high-resolution spectra, indicating the presence of CuO rather than Cu or Cu_2O . The position of the $\text{Cu } 2p_{3/2}$ line is centered

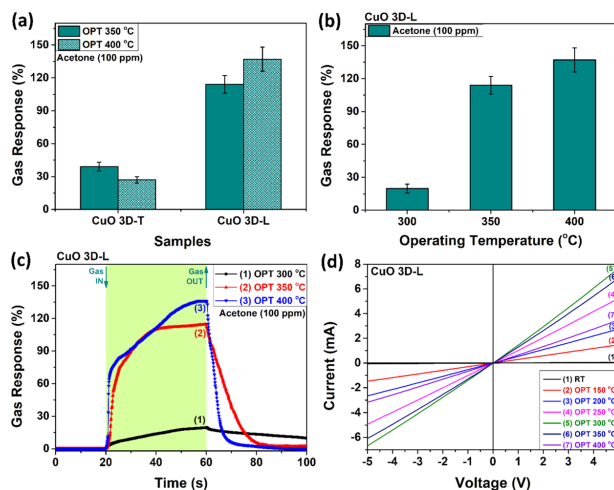


Figure 7. Gas response to 100 ppm of acetone vapors (as VOC) for the 3D-printed NW-CuO/Cu₂O/Cu heterojunction net: (a) at an OPT of 350 and 400 °C for two different sensor types (the transversal sample set 3D-T and the longitudinal one 3D-L), (b) at an OPT of 300, 350, and 400 °C for sample set 3D-L. (c) Dynamic response to 100 ppm of acetone vapors for the longitudinally 3D-printed NW-CuO/Cu₂O/Cu heterojunction net (sample set 3D-L). (d) Current–voltage characteristics of the CuO (sample set 3D-L) sensor at different OPTs.

around 934.7 eV, and the position of Cu-LMM is centered around 569.4 eV, which corresponds well with Cu²⁺ in CuO.³²

3.4. Gas-Sensing Properties. The gas response was calculated from formula $\left(S_p = \frac{R_{\text{gas}} - R_{\text{air}}}{R_{\text{air}}} \times 100\%\right)$ and the electrical conductivity showed p-type conductivity behavior.^{22,29}

Figure 7 shows the gas response to (100 ppm) acetone for two different sensor structures (CuO 3D-T and CuO 3D-L). Figure 7a presents the gas response in dependence of 3D-printing geometries used for the sensor devices at different operating temperatures (OPTs) of 350 and 400 °C, and a drop can be seen in the gas response from OPT of 400 °C versus 350 °C for CuO 3D-T. For CuO 3D-L, an increase can be observed, where the gas response was above 129% at an OPT of 400 °C. Figure 7b is the gas response of the sensor structure CuO 3D-L at three different OPTs of 300, 350, and 400 °C; it can be seen that at 400 °C the response value is higher. Figure 7b shows a diagram of the gas response values obtained for CuO 3D-L at OPTs of 300, 350, and 400 °C. In this diagram, it can be seen that the gas response increases at the increasing OPT value. Figure 7c shows the dynamic vapor response (under 100 ppm acetone) of the 3D CuO/Cu₂O/Cu heterojunction net, thermally annealed nanostructured layer-strips for 2 h. The response and recovery ranges are slightly increased. Figure 7d shows current–voltage curves for CuO 3D-L at different OPTs. Measurements were realized on several sensor structures which all demonstrate the same behavior and prove that they are Ohmic contacts; thus, they have no influence on the gas-sensing process.

The higher response of samples 3D-L in comparison with samples 3D-T can be primarily attributed to the different geometry used (L-longitudinally vs transversally-T). As the 3D-L samples have fewer and more spaced out traces connecting the gold contacts, each active site mostly acts in series, but the line segments are evenly spaced out and thus

each line segment is parallelized to the others, providing a high base resistance state. Additionally, because of the parallelization of line segments, independent active surface areas can be provided in a reliable fashion. In opposition, 3D-T samples with their connection over longer segments of the device, especially inside the traversal gaps between the gold contacts, lead to more internal shortcuts, and this therefore results in a lower base resistance. This also reduces the active sites, which can act independently. Every shortcut inside these line segments will reduce the overall resistance and resistance changes due to absorbed VOC species and therefore significantly impact the sensitivity of the overall device.

The higher concentration of the polymer in the initial suspension and its influence on the spacing of the copper particles in the final traces can also be linked to a higher base resistance. The higher the spacing between the particles, the higher will be the initial resistance of the deposited film. Additionally, if the initial spacing of the particles is slightly higher, more contributions from the interconnected NWs can be expected. Though the spacing for many of the particles is very low, because of the particles already percolating, there is 50–100 nm distance between close particles due to the polymer being present during printing. When growing the NWs, this leads to freestanding particles with interpenetrating NWs, where sometimes distances of around 1–2 μm can occur (compare Figure 3). The sparser this net is, the higher the base resistance will be and the higher the changes in resistivity there will be for each two connecting NWs. However, this also leads to a reduction in the overall amount of active sites and might shift the resistance below the detection limit of many measurement devices, rendering the here fabricated device unnecessarily complex to handle. With these considerations in mind, the optimal concentration and spacing of the copper in the solutions could still be optimized further, while our findings here show a well-functioning device with the current

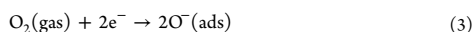
setup of many interconnecting active sites with low interparticle spacing.

In summary, for the design of a structurally optimized device, these considerations can be taken into account, where the trend seems to go to smaller and more separated individual lines, which are highly parallelized to provide many active sites for the chemiresistive response to take place. Additionally, a slight spacing between the particles very near to the percolation threshold seems to be very good for creating interconnected networks of the NWs, which predominate the chemiresistive response.

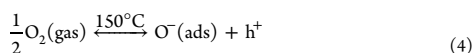
4. PROPOSED GAS-SENSING MECHANISM

The proposed gas-sensing mechanism is based on physico-chemical reactions on the sensor surface, which take place at different OPTs. The proposed sensing mechanism is based on ionosorption and decomposition and/or oxidation of gas vapor molecules as proposed and discussed in our recent works on the surface of copper oxide.^{17,30} In the case of p-type sensing, the mechanism can be explained by the modulation of the hole accumulation layer (HAL) in each of the CuO/Cu₂O/Cu MPs, which are more sensitive to gas.^{34–36}

Recent results showed that sensors with a higher selectivity and sensitivity can be obtained based on p-type semiconductors formed from NW/nanostructure networks with a high surface area of contacts.³⁰ At the exposure of the sensor to ambient air, a HAL is formed on its surface, both on the surface of the NWs and of the CuO/Cu₂O/Cu MPs³⁰

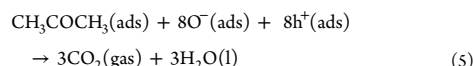


If the OPTs are increased to values higher than 150 °C, the oxygen species are adsorbed on the surface of the p-type copper oxide as follows^{30,31}



where O₂(gas) is the oxygen molecules from ambient air and O[−](ads) is the adsorbed and ionized atomic oxygen species (on CuO surface), and h⁺ is the holes in the CuO NWs and on surface of CuO MPs. This top layer HAL (represented by the blue transparent region in Figure 8a) created on the surface of

the 3D-printed material is characterized by a lower electrical resistance compared to the middle part (represented by the darker region in center) of the NWs or MPs,³⁰ which is considered to be an insulating region.^{37–39} The electrical current will flow through the surface layer (HAL). Thus, the conduction is determined by parallel currents through the outermost conducting shell (HAL) and to a lesser degree of other components of the 3D-net, which are connected in series. As a result, a larger current will flow through the HAL,³⁰ when a sensor is exposed to ambient air. According to computations reported in our recent work, the HAL region for CuO is about 5.2–16.6 nm (for different values of qV_{el} in the range 0.1 and 1.0 eV).³⁰ After introducing acetone vapors in the test chamber, the surface of the structure will react with it as follows^{37,40}



After exposure to acetone, the adsorbed oxygen at the surface of the structures will react with the vapor and captured electrons will be released to the conduction band. Thus, the HAL width will be reduced, and the electrical resistance of the 3D structures will be increased. This is mainly due to the release of eight electrons followed by their recombination with eight holes.^{16,37–39} Therefore, in such a sample with an ultrathin CuO top layer, the interface CuO/Cu₂O will be strongly affected by surface reactions, which will play a crucial role in acetone detection.^{16,37–39}

The HAL region can extend up to half of the NW radius of CuO ($r = D/2$) ≈ 25 nm. Following this, the response will be comparatively large enough to be explained by a high surface-to-volume ratio of the NWs. According to calculations in the literature,^{22,30,41} the width of the HAL region is estimated to be about 4.4–14 nm for Cu₂O and in the range of 5.2–16.6 nm for CuO nanocrystals. Because in our XRD and Micro-Raman studies a mixed phase was detected forming a 3-layered structure, it needs more investigations to propose a more reliable mechanism of acetone sensing by a nonplanar NW-CuO/Cu₂O/Cu heterostructure. Especially, the interaction and effect of the CuO/Cu₂O interface in dependence of the thickness of the CuO top layer needs further investigations because in the current experiments, the duration of TA was only 2 h compared to previous works (5 h).¹⁷

In the case of networks of MPs which are covered with NWs of CuO, the efficiency of such a sensing mechanism based on modulation of a HAL region will decrease because some current will flow through the internal region Cu₂O with a lower resistance.

Figure 8 schematically shows the internal structure of the microparticles at different ambients to explain the proposed sensing mechanism. A charge transfer from the CuO surface to an acetone molecule produces a competitive adsorption of acetone and oxygen on the surface and was comprehensively investigated previously. Additionally, the adsorption of an acetone molecule on the CuO surface which is already covered with a preadsorbed oxygen molecule is possible. At the elevated temperatures of around 400 °C, the preadsorbed oxygen molecules are dissociated from the surface, and instead, the acetone molecules with the competition are adsorbed on the surface according to quantum molecular dynamic calculations reported before.⁴² Also, at high temperature, a new adsorption geometry for acetone was found from

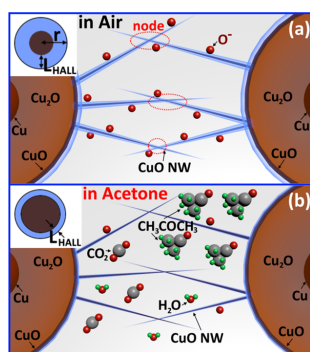


Figure 8. Schematic of the internal structure of the CuO/Cu₂O/Cu microparticles covered with CuO NWs in air (a) and in acetone (b) helping to explain the proposed mechanism through bridging CuO NWs grown driven by grain-boundary diffusion.

molecular dynamic calculations with a lower energy than the structure.⁴²

Adsorption and desorption which affect the sensor electrical resistance, that is a gas-sensing property, are absolutely surface phenomena.^{43–45} Because of the larger surface-to-volume ratio of the CuO NWs, adsorption and desorption occur faster and rapid changes of resistance values occur at higher OPT. At higher OPT, the response is higher because of the availability of sufficient adsorbed ionic species of oxygen on the CuO surface which will react much more efficiently and rapidly with acetone molecules at this temperature,^{43–45} producing a larger number of change carrier exchange, and hence, the response is higher.

5. CONCLUSIONS

The one-step 3D-printing of CuO/Cu₂O/Cu MPs, which possess diameters of 15–25 μm on the sensors substrate surface, is successfully reported for the first time. 3D-printed Cu MP-based stripes with high shape fidelity formed nonplanar NW-CuO/Cu₂O/Cu heterojunctions after TA at 425 °C for 2 h in air and were fully covered with a dense 20 nm thick NW net. The morphological, vibrational, chemical, and structural investigations were performed in detail, showing the high crystallinity of the NWs and 3D-printed CuO/Cu₂O/Cu heterojunction lines, as well as the growth of CuO NWs on the surface of the MPs. The gas-sensing measurements showed an excellent selectivity to acetone vapor at OPT at 350 °C with a high gas response ($S_p = \frac{R_{gas} - R_{air}}{R_{air}} \times 100\%$) $\approx 150\%$ to 100 ppm. The combination of the possibility of fast acetone vapor detection, low power consumption, and controllable size-geometry makes these devices ideal candidates for fast detection, as well as acetone vapor monitoring (down to 100 ppm). This 3D-printing approach will pave a totally new way to the exact detection of acetone vapors in various atmospheres as well as for developing new types of chemiresistive sensors and other electronic devices.

■ ASSOCIATED CONTENT

Supporting Information

The Supporting Information is available free of charge on the ACS Publications website at DOI: 10.1021/acsami.9b04385.

Experimental Section on the 3D-printer developed and used in this work, digital image of the 3D-printed Cu-MPs based stripes, and structural measurements, figures showing SEM images of CuO spheres 3D-printed on the sensor substrate, and figures showing the gas response versus the OPT (at 300, 350, and 400 °C) for two different sensor types (PDF)

■ AUTHOR INFORMATION

Corresponding Authors

*E-mail: ollu@tf.uni-kiel.de, oleg.lupan@mib.utm.md (O.L.).

*E-mail: ra@tf.uni-kiel.de (R.A.).

ORCID

Leonard Siebert: 0000-0001-5316-7240

Oleg Lupan: 0000-0002-7913-9712

Franz Faupel: 0000-0003-3367-1655

Notes

The authors declare no competing financial interest.

■ ACKNOWLEDGMENTS

This work was financially supported by the German Research Foundation (DFG) via the research unit FOR 2093 “Memristive devices for neuronal systems” through project A2, as well as the project “Hot End” (grant number: 16KN021247), funded by the Federal ministry for Economic Affairs and Energy. Moreover, this research was partly supported by the project Institutional inst-15.817.02.29A funded by the Government of the Republic of Moldova and by the Technical University of Moldova. Dr. Lupan acknowledges the Alexander von Humboldt Foundation for the research fellowship for experienced researchers 3-3MOL/1148833 STP at the Institute for Materials Science, Kiel University, Germany. The authors would like to thank J. Bahr for the technical assistance and Prof. Sontea for fruitful scientific discussions.

■ REFERENCES

- (1) MacDonald, E.; Wicker, R. Multiprocess 3D Printing for Increasing Component Functionality. *Science* **2016**, *353*, aaf2093.
- (2) Xu, Y.; Wu, X.; Guo, X.; Kong, B.; Zhang, M.; Qian, X.; Mi, S.; Sun, W. The Boom in 3D-Printed Sensor Technology. *Sensors* **2017**, *17*, 1166.
- (3) Muth, J. T.; Vogt, D. M.; Truby, R. L.; Mengüç, Y.; Kolesky, D. B.; Wood, R. J.; Lewis, J. A. Embedded 3D Printing of Strain Sensors within Highly Stretchable Elastomers. *Adv. Mater.* **2014**, *26*, 6307–6312.
- (4) Wu, S.-Y.; Yang, C.; Hsu, W.; Lin, L. 3D-Printed Microelectronics for Integrated Circuitry and Passive Wireless Sensors. *Microsyst. Nanoeng.* **2015**, *1*, 15013.
- (5) Liu, X.; Tarn, T.-J.; Huang, F.; Fan, J. Recent Advances in Inkjet Printing Synthesis of Functional Metal Oxides. *Particuology* **2015**, *19*, 1–13.
- (6) Kim, J. H.; Chang, W. S.; Kim, D.; Yang, J. R.; Han, J. T.; Lee, G.-W.; Kim, J. T.; Seol, S. K. 3D Printing of Reduced Graphene Oxide Nanowires. *Adv. Mater.* **2015**, *27*, 157–161.
- (7) Blaikie, T. P. J.; Couper, J.; Hancock, G.; Hurst, P. L.; Peverall, R.; Richmond, G.; Ritchie, G. A. D.; Taylor, D.; Valentine, K. Portable Device for Measuring Breath Acetone Based on Sample Preconcentration and Cavity Enhanced Spectroscopy. *Anal. Chem.* **2016**, *88*, 11016–11021.
- (8) Lupan, O.; Postica, V.; Wolff, N.; Polonskyi, O.; Duppel, V.; Kaidas, V.; Lazari, E.; Ababii, N.; Faupel, F.; Kienle, L.; et al. Localized Synthesis of Iron Oxide Nanowires and Fabrication of High Performance Nanosensors Based on a Single Fe₂O₃ Nanowire. *Small* **2017**, *13*, 1602868.
- (9) Kim, I.-D.; Choi, S.-J.; Kim, S.-J.; Jang, J.-S. Exhaled Breath Sensors. In *Smart Sensors for Health and Environment Monitoring*; Kyung, C.-M., Ed.; Springer Netherlands: Dordrecht, 2015; pp 19–49.
- (10) Tassopoulos, C. N.; Barnett, D.; Russell Fraser, T. Breath-Acetone and Blood-Sugar Measurement in Diabetes. *Lancet* **1969**, *293*, 1282–1286.
- (11) Turner, C.; Walton, C.; Hoashi, S.; Evans, M. Breath Acetone Concentration Decreases with Blood Glucose Concentration in Type I Diabetes Mellitus Patients during Hypoglycaemic Clamps. *J. Breath Res.* **2009**, *3*, 046004.
- (12) Anderson, J. C. Measuring Breath Acetone for Monitoring Fat Loss: Review. *Obesity* **2015**, *23*, 2327–2334.
- (13) Göschke, H.; Lauffenburger, T. Aceton in der Atemluft und Ketene im Venenblut bei vollständigem Fasten normal- und übergewichtiger Personen. *Res. Exp. Med.* **1975**, *165*, 233–244.
- (14) Righettoni, M.; Tricoli, A. Toward Portable Breath Acetone Analysis for Diabetes Detection. *J. Breath Res.* **2011**, *5*, 037109.
- (15) World Health Organization *Global Report on Diabetes*, 2016.
- (16) Hien, V. X.; Minh, N. H.; Son, D. T.; Nghi, N. T.; Phuoc, L. H.; Khoa, C. T.; Vuong, D. D.; Chien, N. D.; Heo, Y.-W. Acetone Sensing

Properties of CuO Nanowalls Synthesized via Oxidation of Cu Foil in Aqueous NH_4OH . *Vacuum* **2018**, *150*, 129–135.

(17) Lupan, O.; Postica, V.; Cretu, V.; Wolff, N.; Duppel, V.; Kienle, L.; Adelung, R. Single and Networked CuO Nanowires for Highly Sensitive p-Type Semiconductor Gas Sensor Applications. *Phys. Status Solidi RRL* **2016**, *10*, 260–266.

(18) Cretu, V.; Postica, V.; Mishra, A. K.; Hoppe, M.; Tiginyanu, I.; Mishra, Y. K.; Chow, L.; de Leeuw, N. H.; Adelung, R.; Lupan, O. Synthesis, Characterization and DFT Studies of Zinc-Doped Copper Oxide Nanocrystals for Gas Sensing Applications. *J. Mater. Chem. A* **2016**, *4*, 6527–6539.

(19) Debbichi, L.; Marco de Lucas, M. C.; Pierson, J. F.; Krüger, P. Vibrational Properties of CuO and Cu_4O_3 from First-Principles Calculations, and Raman and Infrared Spectroscopy. *J. Phys. Chem. C* **2012**, *116*, 10232–10237.

(20) Wang, M.; Xie, F.; Xie, W.; Zheng, S.; Ke, N.; Chen, J.; Zhao, N. Device Lifetime Improvement of Polymer-Based Bulk Heterojunction Solar Cells by Incorporating Copper Oxide Layer at Al Cathode. *Appl. Phys. Lett.* **2011**, *98*, 183304–183307.

(21) Moulder, J. F.; Chastain, J. *Handbook of X-Ray Photoelectron Spectroscopy: A Reference Book of Standard Spectra for Identification and Interpretation of XPS Data, illustrate*; Chastain, J., Ed.; Physical Electronics Division, Perkin-Elmer Corporation, 1992.

(22) Lupan, O.; Cretu, V.; Postica, V.; Polonskyi, O.; Ababii, N.; Schütt, F.; Kaidas, V.; Faupel, F.; Adelung, R. Non-Planar Nanoscale p – p Heterojunctions Formation in $\text{Zn}_x\text{Cu}_{1-x}\text{O}_y$ Nanocrystals by Mixed Phases for Enhanced Sensors. *Sens. Actuators, B* **2016**, *230*, 832–843.

(23) Åsbrink, S.; Norrby, L. J. A Refinement of the Crystal Structure of Copper(II) Oxide with a Discussion of Some Exceptional e.s.d.'s. *Acta Crystallogr., Sect. B: Struct. Crystallogr. Cryst. Chem.* **1970**, *26*, 8–15.

(24) Tiginyanu, I. M.; Lupan, O.; Ursaki, V. V.; Chow, L.; Enachi, M. Nanostructures of Metal Oxides. In *Comprehensive Semiconductor Science and Technology*; Bhattacharya, P., Fornari, R., Kamimura, H., Eds.; Elsevier: Amsterdam, 2011; Vol. 1–6, pp 396–479.

(25) Wu, D.; Zhang, Q.; Tao, M. LSDA+U Study of Cupric Oxide: Electronic Structure and Native Point Defects. *Phys. Rev. B: Condens. Matter Mater. Phys.* **2006**, *73*, 235206–235212.

(26) Cuprous Oxide (Cu_2O) Crystal Structure, Lattice Parameters. In *Non-Tetrahedrally Bonded Elements and Binary Compounds I*; Madelung, O., Rössler, U., Schulz, M., Eds.; Springer-Verlag: Berlin/Heidelberg, 1998; pp 1–3.

(27) Elliott, R. J. Symmetry of Excitons in Cu_2O . *Phys. Rev.* **1961**, *124*, 340–345.

(28) Kliche, G.; Popovic, Z. V. Far-Infrared Spectroscopic Investigations on CuO. *Phys. Rev. B: Condens. Matter Mater. Phys.* **1990**, *42*, 10060–10066.

(29) Lupan, O.; Postica, V.; Ababii, N.; Hoppe, M.; Cretu, V.; Tiginyanu, I.; Sontea, V.; Pauporté, T.; Viana, B.; Adelung, R. Influence of CuO Nanostructures Morphology on Hydrogen Gas Sensing Performances. *Microelectron. Eng.* **2016**, *164*, 63–70.

(30) Lupan, O.; Cretu, V.; Postica, V.; Ababii, N.; Polonskyi, O.; Kaidas, V.; Schütt, F.; Mishra, Y. K.; Monaco, E.; Tiginyanu, I.; et al. Enhanced Ethanol Vapour Sensing Performances of Copper Oxide Nanocrystals with Mixed Phases. *Sens. Actuators, B* **2016**, *224*, 434–448.

(31) Hübner, M.; Simion, C. E.; Tomescu-Stănoiu, A.; Pokhrel, S.; Barsan, N.; Weimar, U. Influence of Humidity on CO Sensing with P-Type CuO Thick Film Gas Sensors. *Sens. Actuators, B* **2011**, *153*, 347–353.

(32) Naumkin, A. V.; Kraut-Vass, A.; Stephen, W.; Gaarenstroom, C. J. P. NIST X-Ray Photoelectron Spectroscopy Database; National Institute of Standards and Technology, NIST Stand. Ref. Database Number 20. (2000) 20899. NIST X-ray Photoelectron Spectrosc. Database, NIST Stand. Ref. Database 20, Version 4.1 2017 (accessed 20 12, 2017).

(33) Pauly, N.; Tougaard, S.; Yubero, F. Determination of the Cu 2p Primary Excitation Spectra for Cu, Cu_2O and CuO. *Surf. Sci.* **2014**, *620*, 17–22.

(34) Barsan, N.; Simion, C.; Heine, T.; Pokhrel, S.; Weimar, U. Modeling of Sensing and Transduction for P-Type Semiconducting Metal Oxide Based Gas Sensors. *J. Electroceram.* **2010**, *25*, 11–19.

(35) Wan, X.; Wang, J.; Zhu, L.; Tang, J. Gas Sensing Properties of Cu_2O and Its Particle Size and Morphology-Dependent Gas-Detection Sensitivity. *J. Mater. Chem. A* **2014**, *2*, 13641–13647.

(36) Yoon, J.-W.; Choi, J.-K.; Lee, J.-H. Design of a Highly Sensitive and Selective $\text{C}_2\text{H}_5\text{OH}$ Sensor Using P-Type Co_3O_4 Nanofibers. *Sens. Actuators, B* **2012**, *161*, 570–577.

(37) Zoolfakar, A. S.; Ahmad, M. Z.; Rani, R. A.; Ou, J. Z.; Balendhran, S.; Zhuiykov, S.; Latham, K.; Wlodarski, W.; Kalantarzadeh, K. Nanostructured Copper Oxides as Ethanol Vapour Sensors. *Sens. Actuators, B* **2013**, *185*, 620–627.

(38) Kim, H.-J.; Lee, J.-H. Highly Sensitive and Selective Gas Sensors Using P-Type Oxide Semiconductors: Overview. *Sens. Actuators, B* **2014**, *192*, 607–627.

(39) Kamble, V. B.; Umarji, A. M. Gas Sensing Response Analysis of p-Type Porous Chromium Oxide Thin Films. *J. Mater. Chem. C* **2013**, *1*, 8167–8176.

(40) Qin, L.; Xu, J.; Dong, X.; Pan, Q.; Cheng, Z.; Xiang, Q.; Li, F. The Template-Free Synthesis of Square-Shaped SnO_2 Nanowires: The Temperature Effect and Acetone Gas Sensors. *Nanotechnology* **2008**, *19*, 185705.

(41) Hoppe, M.; Ababii, N.; Postica, V.; Lupan, O.; Polonskyi, O.; Schütt, F.; Kaps, S.; Sukhodub, L. F.; Sontea, V.; Strunskus, T.; Faupel, F.; Adelung, R. $\text{CuO-Cu}_2\text{O}/\text{ZnO:Al}$ Heterojunctions for Volatile Organic Compound Detection. *Sens. Actuators, B* **2018**, *255*, 1362–1375.

(42) Sadeghian Lemraski, M.; Nadimi, E. Acetone Gas Sensing Mechanism on Zinc Oxide Surfaces: A First Principles Calculation. *Surf. Sci.* **2017**, *657*, 96–103.

(43) Sahay, P. P.; Tewari, S.; Jha, S.; Shamsuddin, M. Sprayed ZnO Thin Films for Ethanol Sensors. *J. Mater. Sci.* **2005**, *40*, 4791–4793.

(44) Nath, S. S.; Choudhury, M.; Chakdar, D.; Gope, G.; Nath, R. K. Acetone Sensing Property of ZnO Quantum Dots Embedded on PVP. *Sens. Actuators, B* **2010**, *148*, 353–357.

(45) Vahl, A.; Dittmann, J.; Jetter, J.; Veziroglu, S.; Shree, S.; Ababii, N.; Lupan, O.; Aktas, O. C.; Strunskus, T.; Quandt, E.; Adelung, R.; Sharma, S. K.; Faupel, F. The impact of O_2/Ar ratio on morphology and functional properties in reactive sputtering of metal oxide thin films. *Nanotechnology* **2019**, *30*, 235603.

Supporting Information

for

3D-Printed Chemiresistive Sensor Array on Nanowires CuO/Cu₂O/Cu Heterojunction Net

Leonard Siebert,¹ Oleg Lupan,^{1,2,*} Mattia Mirabelli,¹ Nicolai Ababii,² Maik-Ivo Terasa,¹
Sören Kaps,¹ Vasilii Cretu,² Alexander Vahl,³ Franz Faupel,³ Rainer Adelung,^{1,*}

¹ *Institute for Materials Science – Functional Nanomaterials, Faculty of Engineering, Kiel University, Kaiserstraße 2, D-24143 Kiel, Germany*

² *Center for Nanotechnology and Nanosensors, Department of Microelectronics and Biomedical Engineering, Technical University of Moldova, 168 Stefan cel Mare Av., MD-2004 Chisinau, Republic of Moldova*

³ *Institute for Materials Science – Chair for Multicomponent Materials, Faculty of Engineering, Christian-Albrechts-University of Kiel, Kaiserstraße 2, D-24143 Kiel, Germany*

*Corresponding authors

Prof. Dr. Eng. Lupan,
E-mails: ollu@tf.uni-kiel.de oleg.lupan@mib.utm.md
Institute for Materials Science, Kiel University, Germany

Prof. Dr. Adelung
ra@tf.uni-kiel.de

The custom-built direct ink writing setup was mechanically based on a Velleman K8200 3D-printed, which was equipped with a RUMBA control unit and a custom made syringe pump. The setup is depicted in **Figure S1**.

The printer consisted of this custom-built syringe extruder (1) designed for high pressures up to 40 bar. The spatial movement is done by both a Z-axis, where the syringe pump is attached and the independent XY-printbed (3). A USB microscope was attached to the printer to obtain live videos of the 3D-printed structures for both troubleshooting and quality control (4).

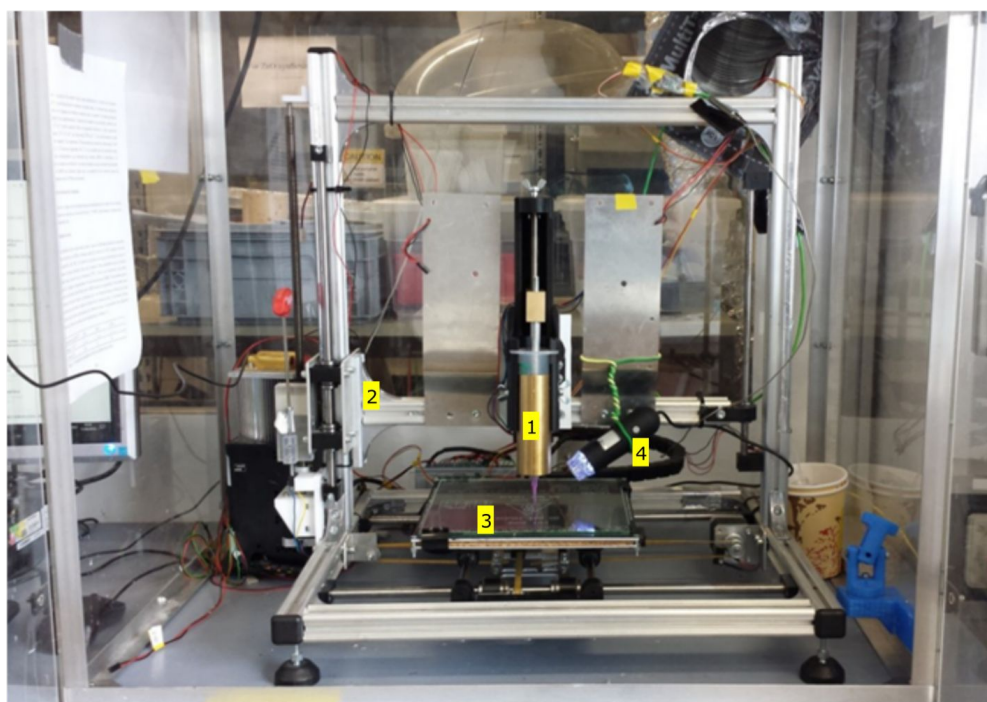


Figure S1. Digital image of a 3D-printer developed and used in this work. 1) Syringe based extruder; 2) Z-axis carrier, controlling the relative distance from nozzle with regard to the printed; 3) printbed, controlling XY-axis movements of the deposition process; 4) optical microscope used for real time feedback and evaluation of the deposition process.

Meandering lines can be produced via the Repetier Host slicing software using a rectangular infill with a density of 10-20% depending on the line thickness. This influences line spacing and can be tailored to obtain the desired geometry. Apart from using a slicing software, the machine code can be written manually.

Characteristic lines printed in the fashion are depicted in **Figure S2**, where they were printed on a glass slide. Gold can be sputtered onto the samples and the copper can be converted to the nanowire-CuO/Cu₂O/Cu MPs-net observed in **Figure S3**. Various stages of magnification, increasing from a) to d) can be observed.

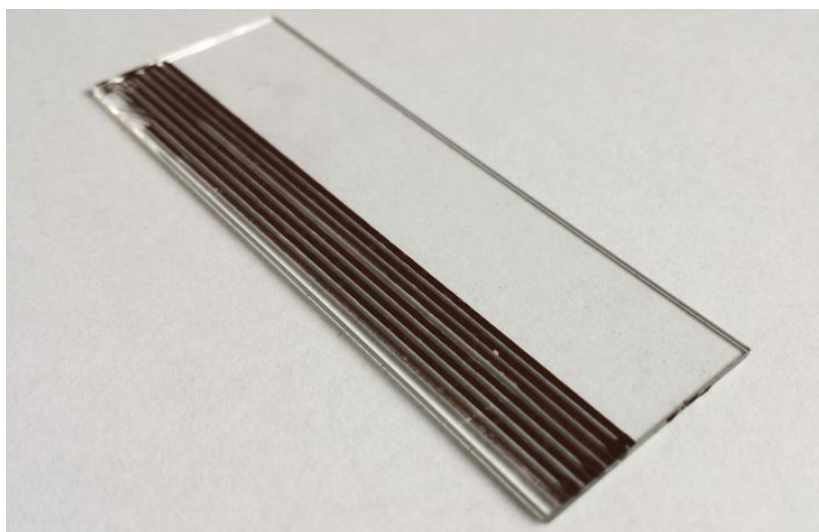


Figure S2. Digital image of a 3D printed Cu-MPs based stripes on glass substrate developed and used in this research

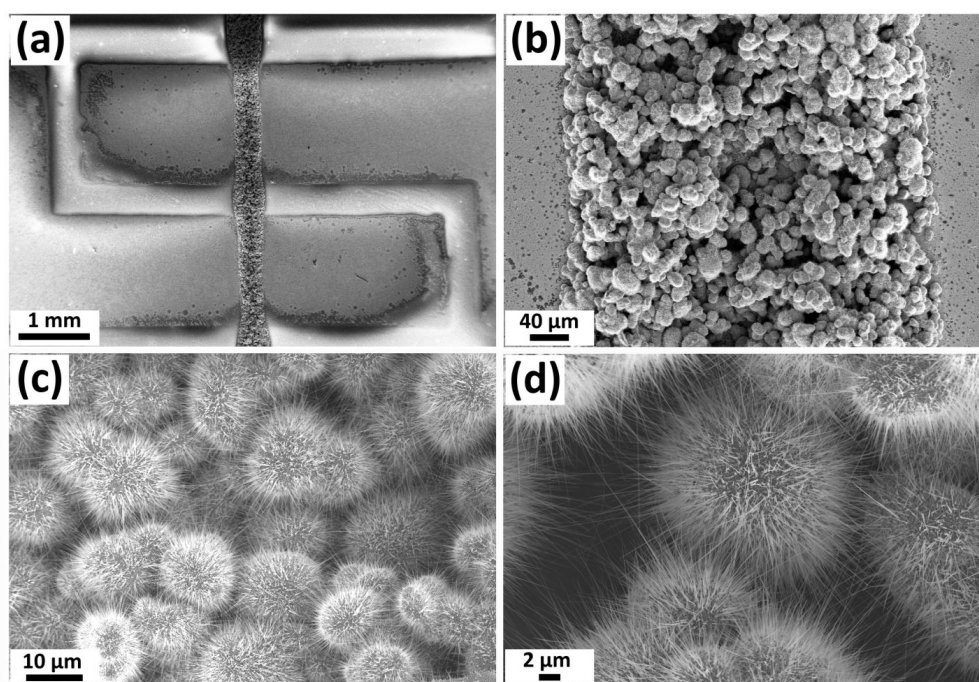


Figure S3. Scanning electron microscope (SEM) images of CuO spheres 3D-printed on sensor substrate with an inset showing details of morphology: (a) longitudinally 3D-printed stripes directly on interdigitated Au-electrodes-contacts; (b-d) images with progressive zooming into the 3D-printed microparticle lines details down to the nanoscale can be observed.

For the obtaining crystal structure, XRD-parameters for the converted CuO/Cu₂O/Cu were obtained and are collected in **Table S1**.

Table S1. XRD parameters for obtained CuO, Cu₂O and Cu – based 3D-printed stripes.

Phases	Peak Position 2 θ	FWHM Degrees	d -spacing [Å]	Rel. Int. [%]	Plane index (hkl)
CuO	35,65	1,1069	2,5195	74,34	(111)
	48,8	4,6010	1,8638	24,65	(-202)
	58,25	46,2874	1,5815	26,16	(202)
	61,5	36,2018	1,5063	57,89	(133)
	90,05	53,5538	1,0894	38,23	(-131)
Cu ₂ O	36,5	0,3612	2,4602	165,2	(111)
	42,35	16,2710	2,1320	48,95	(200)
Cu	43,35	0,2562	2,0834	195,34	(111)
	50,5	0,6287	1,8055	78,32	(200)
	74,15	15,4554	1,2776	57,24	(220)

Since a high selectivity towards acetone is beneficial for the quality of a sensor, **Figure S4** shows the gas response of not only acetone but other VOCs. It can clearly be seen, that the sensors show the highest selectivity towards acetone at 350 °C, for longitudinally 3D-L printed lines.

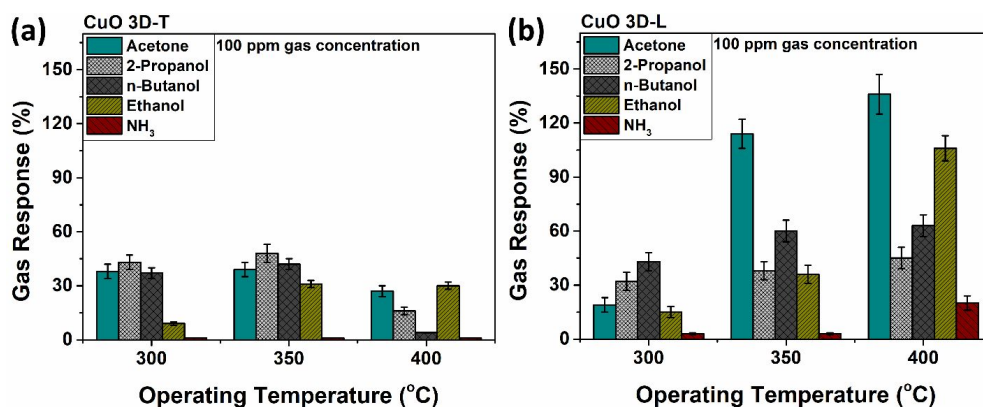


Figure S4. Gas response versus operating temperature (OPT at 300, 350 and 400 °C) for 2 different sensor types: (a) transversally printed sample set CuO 3D-T; and (b) longitudinally printed sample set CuO 3D-L.

More details on 3D-printing for increasing component functionality and on copper oxides based sensors can be found in references 1-10.

Acknowledgements

This work was financially supported by the German Research Foundation (DFG) via the research unit FOR 2093 "Memristive devices for neuronal systems" through project A2, as well as the project "Hot End" (grant number: 16KN021247), funded by the Federal ministry for Economic Affairs and Energy. Moreover, this research was partly supported by the project Institutional inst-15.817.02.29A funded by the Government of the Republic of Moldova and by the Technical University of Moldova. Dr. Oleg Lupan acknowledges the Alexander von Humboldt Foundation for the research fellowship for experienced researchers 3-3MOL/1148833 STP at the Institute for Materials Science, Kiel University, Germany. The authors would like to thank J. Bahr for the technical assistance and Prof. Sontea for fruitful scientific discussion.

References

- (1) MacDonald, E.; Wicker, R. Multiprocess 3D Printing for Increasing Component Functionality. *Science*. **2016**, *353* (6307), aa2093–aaf2093.
- (2) Lupan, O.; Postica, V.; Wolff, N.; Polonskyi, O.; Duppel, V.; Kaidas, V.; Lazari, E.;

- Ababii, N.; Faupel, F.; Kienle, L.; et al. Localized Synthesis of Iron Oxide Nanowires and Fabrication of High Performance Nanosensors Based on a Single Fe₂O₃ Nanowire. *Small* **2017**, *13* (16), 1602868.
- (3) Lupan, O.; Postica, V.; Cretu, V.; Wolff, N.; Duppel, V.; Kienle, L.; Adelung, R. Single and Networked CuO Nanowires for Highly Sensitive *p*-Type Semiconductor Gas Sensor Applications. *Phys. Status Solidi - Rapid Res. Lett.* **2016**, *10* (3), 260–266.
- (4) Cretu, V.; Postica, V.; Mishra, A. K.; Hoppe, M.; Tiginyanu, I.; Mishra, Y. K.; Chow, L.; de Leeuw, N. H.; Adelung, R.; Lupan, O. Synthesis, Characterization and DFT Studies of Zinc-Doped Copper Oxide Nanocrystals for Gas Sensing Applications. *J. Mater. Chem. A* **2016**, *4* (17), 6527–6539.
- (5) Lupan, O.; Cretu, V.; Postica, V.; Polonskyi, O.; Ababii, N.; Schütt, F.; Kaidas, V.; Faupel, F.; Adelung, R. Non-Planar Nanoscale *p* – *p* Heterojunctions Formation in Zn_xCu_{1-x}O_y Nanocrystals by Mixed Phases for Enhanced Sensors. *Sensors Actuators B Chem.* **2016**, *230*, 832–843.
- (6) Tiginyanu, I. M.; Lupan, O.; Ursaki, V. V.; Chow, L.; Enachi, M. Nanostructures of Metal Oxides. In *Comprehensive Semiconductor Science and Technology*; Bhattacharya, P., Fornari, R., Kamimura, H., Eds.; Elsevier: Amsterdam, **2011**; 1-6, 396–479. DOI: 10.1016/B978-0-44-453153-7.00105-X
- (7) Lupan, O.; Postica, V.; Ababii, N.; Hoppe, M.; Cretu, V.; Tiginyanu, I.; Sontea, V.; Pauporté, T.; Viana, B.; Adelung, R. Influence of CuO Nanostructures Morphology on Hydrogen Gas Sensing Performances. *Microelectron. Eng.* **2016**, *164*, 63–70.
- (8) Lupan, O.; Cretu, V.; Postica, V.; Ababii, N.; Polonskyi, O.; Kaidas, V.; Schütt, F.; Mishra, Y. K.; Monaco, E.; Tiginyanu, I.; et al. Enhanced Ethanol Vapour Sensing Performances of Copper Oxide Nanocrystals with Mixed Phases. *Sensors Actuators B Chem.* **2016**, *224*, 434–448.
- (9) Hoppe, M.; Ababii, N.; Postica, V.; Lupan, O.; Polonskyi, O.; Schütt, F.; Kaps, S.; Sukhodub, L. F.; Sontea, V.; Strunskus, T.; et al. (CuO-Cu₂O)/ZnO:Al Heterojunctions for Volatile Organic Compound Detection. *Sensors Actuators B Chem.* **2018**, *255*, 1362–1375.
- (10) Vahl, A.; Dittmann, J.; Jetter, J.; Veziroglu, S.; Shree, S.; Ababii, N.; Lupan, O.; Aktas, O. C.; Strunskus, T.; Quandt, E.; Adelung, R.; Sharma, S. K.; Faupel, F. The impact of O₂/Ar ratio on morphology and functional properties in reactive sputtering of metal oxide thin films *Nanotechnology* **2019**, *30*(23), 235603.

Chapter 9

Facile fabrication of semiconducting oxide nanostructures by direct ink writing of readily available metal microparticles and their application as low power acetone gas sensors

Based on the design concepts of chapter 8, this work aims at exploring the possibilities of materials selection in Direct Ink Writing. The manufacturing technique proves that a facile variation of complex, open porous semiconducting devices is possible via printing of readily available metal microparticles combined with the subsequent annealing step. Printing of mixed iron and copper microparticles allows for the formation of p-n-junctions on the nanoscale while controlling the shape macroscopically. The structural, morphological and chemical properties of the CuO nanowires and the Fe₂O₃ were investigated in detail. It was found that the annealing step is crucial to fully oxidise the metal microparticles to ensure a short-circuit free particle system. The printed devices can then be employed as low-power gas sensors with a power consumption as low as 0.26 μ W at a gas response of 50% to 100 ppm of acetone vapour.

The results were published in the journal "Nano Energy".

Own contribution presented in this article

- Design and setup of the Direct Ink Writing printer
- Sample fabrication
- Data analysis
- Discussion and interpretation
- Writing the manuscript

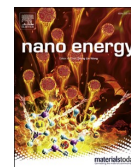
The following content in this chapter is reproduced with permission.

Nano Energy 70 (2020) 104420



Contents lists available at ScienceDirect

Nano Energy

journal homepage: <http://www.elsevier.com/locate/nanoen>

Facile fabrication of semiconducting oxide nanostructures by direct ink writing of readily available metal microparticles and their application as low power acetone gas sensors

Leonard Siebert^a, Niklas Wolff^b, Nicolai Ababii^c, Maik-Ivo Terasa^a, Oleg Lupan^{a,c,**}, Alexander Vahl^d, Viola Duppel^e, Haoyi Qiu^a, Maik Tienken^a, Mattia Mirabelli^a, Victor Sontea^c, Franz Faupel^d, Lorenz Kienle^b, Rainer Adelung^{a,*}

^a Chair for Functional Nanomaterials, Institute for Materials Science, Kiel University, Kaiserstr. 2, D-24143, Kiel, Germany

^b Chair for Synthesis and Real Structure, Institute for Materials Science, Kiel University, Kaiserstr. 2, D-24143, Kiel, Germany

^c Department of Microelectronics and Biomedical Engineering, Center for Nanotechnology and Nanosensors, Technical University of Moldova, 168 Stefan cel Mare Av., MD-2004, Chisinau, Republic of Moldova

^d Chair for Multicomponent Materials, Institute for Materials Science, Kiel University, Kaiserstr. 2, D-24143, Kiel, Germany

^e Nanochemistry, Max Planck Institute for Solid State Research, Heisenbergstr. 1, D-70569, Stuttgart, Germany

ARTICLE INFO

Keywords:

Direct ink writing
Cu-Fe deposition
Heterojunction
Fe₂O₃-CuO/Cu₂O/Cu
Gas sensing
Transmission electron microscopy

ABSTRACT

In this work, a facile two-step fabrication and characterization of printed acetone sensors based on mixed semiconducting metal oxides is introduced. The devices are fabricated by Direct Ink Writing metal microparticle (MP) stripes of commercially available pure iron and copper particles onto the surface of a glass substrate, forming a bridging multi-phase semiconducting oxide net by subsequent thermal annealing. The open, highly porous bridging structures consist of heterojunctions which are interconnected via non-planar CuO/Cu₂O/Cu nanowires and Fe₂O₃/Fe nanospikes. Morphological, vibrational, chemical and structural studies were performed to investigate the contact-forming Fe₂O₃-CuO nanostructures on the surface of the MPs. The power consumption and the gas sensing properties showed selectivity to acetone vapor at an operating temperature of around 300 °C with a high gas response of about 50% and the lowest operating power of around 0.26 μW to a concentration of 100 ppm of acetone vapor. The combination of the possibility of acetone vapor detection, the controllable size and geometry and their low power make these printed structures important candidates for next developments of accessible detection devices, as well as acetone vapor monitoring (even below 1 ppm). The printing of MPs in general paves the way for a new generation of printed different devices, even in "home-made" conditions, for a manifold of applications tailored by the composition and geometry of the printed MP stripes, enabled through the simplicity and versatility of the fabrication method.

1. Introduction

The increased demand towards individual devices in the Internet-of-Things (IoT) era with selected and often special sets of properties requires both sophisticated multipurpose materials as well as new methods to fabricate devices out of these materials.

Multifunctional materials, including semiconducting oxides of both n- and p-type conductivity with tunable properties are highly demanded in most semiconductor-powered devices. Producing such hybrid

materials however is often demanding with respect to shape and size control on a macroscopic level. Standard techniques include vacuum deposition, controlling the shape in 2D through a manifold of micro-fabrication techniques, all of them requiring costly and energy consuming clean room technology. A more facile technological approach to produce hybrid systems in all three spatial dimensions as well as highly complex geometries is required.

Especially direct ink writing (DIW), a subset of additive manufacturing (AM), also known as 3D-printing, as mentioned in

* Corresponding author.

** Corresponding author.

E-mail addresses: ollu@tf.uni-kiel.de, oleg.lupan@mib.utm.md (O. Lupan), ra@tf.uni-kiel.de (R. Adelung).

<https://doi.org/10.1016/j.nanoen.2019.104420>

Received 20 November 2019; Received in revised form 19 December 2019; Accepted 19 December 2019

Available online 3 January 2020

2211-2855/© 2020 Elsevier Ltd. All rights reserved.

different works, enables time and cost effective fabrication of state-of-the-art structures and systems with different levels of complexity for applications in many major fields of technology [1–5]. Such applications range from biomedical devices, mechanical parts and functional to electronic and sensor applications [2,5,6]. The decisive benefits include high flexibility in the design of both the geometry and the desired materials paired with the simplicity of the respective additive manufacturing technique. Pairing these qualities with the wide assortment of treatment and fabrication methods from materials science leads to an ever increasing popularity of 3D-printing processes manufacturing novel devices.

As one important subset, 3D-printed electronics range from fully integrated electronics to sensor applications, e.g., to be used in the field of breath analysis to diagnose and monitor diabetes mellitus [7,8] or strain sensors [9]. This holds true especially for DIW, where rheologically optimized inks can be combined with micro- and nanoparticles to achieve specific functionalities. These systems can even outperform classic microfabrication techniques [9,10], eliminating the necessity for clean room technology such as photolithography, exposure to ultraviolet radiation or sophisticated etching processes. Beyond that, the 3D-printing technology offers potential to integrate complex shaped semi-conducting metal oxide-based materials directly onto circuit boards of standardized portable devices, e.g., for medical application. Additional treatment steps can be used to refine certain qualities of the as-printed devices, like their base resistance or their sensitivity towards outside stimuli.

As an application example, a facile fabrication of portable sensors based on the chemiresistive effect for breath analysis is highly demanded by both the medical industry and patients suffering from diabetes.

Conventional tests of blood glucose levels suffer from inaccuracies by the individual fat loss rate, health condition and diet [7,8] in contrast to the concentration of breath acetone which is < 1 ppm for healthy individuals, while it ranges from >2 ppm to even 1250 ppm for patients with diabetic ketoacidosis [11–13]. This biological fingerprint motivates the use of acetone as a biological marker for reliable diagnosis and monitoring of diabetic conditions over breath analysis rather than testing the blood glucose level with pain for the patient. The increasing number of registered diagnoses with diabetes [14] and the amount of people suffering from anxiety of venipuncture [15] motivate the development of direct and gentle medical diagnostic pathways [16–19].

Possible candidates for sensing acetone vapors include ZnO and single component iron oxide and copper oxide nanostructures [10, 20–22], but mixed oxides of copper and iron were not studied extensively so far. Their chemical and physical properties, especially related to interfacial phenomena, can be improved by forming hybrid structures of p- and n-type semiconducting oxides. These nanocomposites in such a combination are important for fundamental studies and for practical advanced applications in portable sensor devices [18,19].

In this contribution, we report on printed low power, functional

nanomaterial nets consisting of nanowires and nanospikes bridging microparticles (MP) of CuO/Cu₂O/Cu and Fe₂O₃/Fe heterojunctions made by combining DIW with thermal annealing.

The fabricated printed mixed metal oxide networks will be presented with respect to acetone vapor sensors featuring a flexible design concept proving this approach to be highly attractive for the near future.

2. Materials and methods

2.1. Ink fabrication and DIW

The fabrication steps of the acetone sensor devices are depicted in Fig. 1. The first step is the production of a rheologically optimal ink containing the respective materials (Fig. 1a). Copper and iron microparticles as well as 96 vol% ethanol were purchased from Sigma Aldrich, polyvinylbutyral (PVB) was kindly supplied by Kuraray. The mean particle diameter for the copper and iron microparticles were 15–25 and 45–60 μm , respectively.

The mixing ratios of the final ink were 3:1:1 (ethanol:PVB:metals) by weights and the metal MPs were mixed in a 1:1 ratio by weights. The ink was prepared by sonicating the metal particles with the Ethanol for 3 min with a Bandelin Sonoplus HD 4100 ultrasonic rod at 30% power. The PVB was then added and the solution was stirred, until it became homogeneous. The ink was filled into a 30 cm³ polypropylene cartridge (Fig. 1a) and left over night before printing. The cartridge was then loaded into a custom built direct ink writing setup. For printing a tapered nozzle with a diameter of 0.58 mm was used and samples with various layer heights were printed on standard glass slides (Fig. 1b, 25 mm \times 75 mm) at a speed of around 0.4 mm³ s⁻¹. Each line had a height of 0.1 mm and a width of 0.6 mm.

After the printing step, the samples were dried for 24 h at room temperature to evaporate all of the ethanol remaining.

After drying, the printed devices were rapidly annealed in a series of annealing steps at both 425 °C and 650 °C in air at a heating rate of 40 °C s⁻¹ and kept at this temperature for varying time lengths (Fig. 1c). This leads to the formation of a net of nanowires and nanospikes between the particles as well as completing the oxidation inside of the MPs, leading to a higher base resistance. After cooling down, multiple meandering gold contacts (Fig. 1d) (thickness \sim 170 nm) were sputtered onto each sample using a sputtering mask. This is done for contacting and the samples were cut down into individual sensors. Each sensor is made of two interdigitating electrodes with a gap size of 1 mm. The utilization of gold was done to enable reliable testing of the gas sensing and low power qualities of the sensors. To completely obviate the need for vacuum technology, one can fabricate an all printed device. The contacts may be made from conducting inks containing materials like graphene, CNTs, silver flakes or conducting polymers like PEDOT:PSS [41].

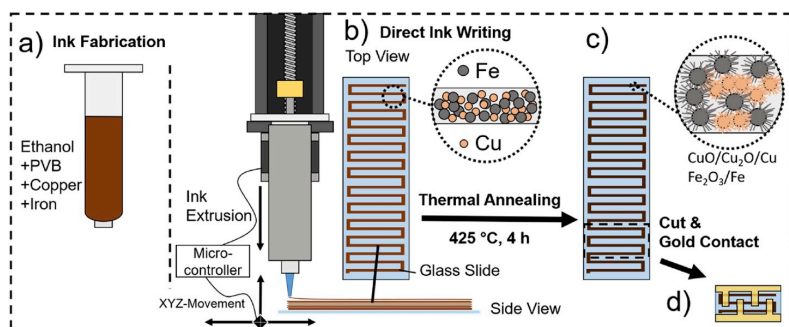


Fig. 1. Schematic sensor fabrication process: (a) ink fabricated by mixing copper and iron microparticles in ethanol, stirring in PVB until homogeneous, then the ink is filled into the printer cartridge; (b) direct ink writing via piston-driven syringe pumps in a 3D-printing setup. Layer by layer building of meandering copper-iron stripes. (c) The glass slide with the printed object is placed in an oven at air at 425 °C for 4 h where the metal oxide nanostructures form. (d) Single sensor devices are gold coated and then cut for further electrical and sensor investigations.

2.2. Morphological, chemical and Real Structure characterization

The samples geometry and morphology was investigated by using digital camera and scanning electron microscopy (SEM) REM-ZEISS (7 kV, 10 μ A). The analysis of the chemical composition of the specimens was done by energy dispersive X-ray (EDX) spectroscopy. Micro-Raman investigations were realized at room temperature with a WITec system in a backscattering configuration. The Nd:YAG laser power was less than 4 mW at the printed samples, which were examined with a Nd:YAG laser, $\lambda_{ex} = 532$ nm and for each spectrum 10 accumulations at an integration time of 10 s were taken. The measurements on a $25 \mu\text{m} \times 25 \mu\text{m}$ scanning area, 50 points per line, and 50 lines per image were conducted on the sample surface to visualize the heterojunction net.

An integral characterization was performed by an X-ray powder diffraction (XRD) Seifert 3000 TT unit operating at 40 kV and 40 mA, with $\text{CuK}\alpha 1$ radiation ($\lambda = 1.540598 \text{ \AA}$) [23].

Three sensor samples of the $\text{CuO}/\text{Cu}_2\text{O}/\text{Cu}$ $\text{Fe}_2\text{O}_3/\text{Fe}$ system were investigated by X-ray photoelectron spectroscopy (XPS, Omicron Nano-Technology GmbH), operating with an Al-anode at a power of 240 W. Main peaks were measured with a 25 eV pass energy. The recorded spectra were charge referenced to the aliphatic carbon C-1s peak at 284.9 eV (atmospheric contamination) and the software "CasaXPS" in version 2.3.16 [24,25].

Analytical methods of transmission electron microscopy (TEM) have been performed on a Tecnai F30 microscope equipped with an EDAX Si-Li drift detector for chemical analysis via energy dispersive X-ray spectroscopy (EDX) and a Gatan Imaging Filter (GIF) unit for collecting electron energy-loss spectra (EELS) and energy-filtered (EF)TEM images. For these TEM sample preparation, iron oxide and copper oxide nanostructures were scratched off the substrate and transferred to a carbon lacey film of a gold grid. Energy-loss spectra were collected on both type of oxides using the oxygen K-edge feature beginning at 532 eV and the $L_{3,2}$ edges located at 708 eV (Fe) and 931 eV (Cu). The inelastic background was subtracted with the EELS plug-in for the Digital-Micrograph software and individual spectra were corrected by an energy shift according to the position instability of the zero-loss peak (ZLP). The electron energy loss spectra were collected with an energy resolution of about 3 eV full-width at half maxima of the ZLP. Additional local crystallographic information was collected using precession electron diffraction (PED) performed on a Philipps CM 30 ST microscope.

By contacting the gold layers on the printed samples the gas response was obtained as the ratio $\Delta R/R_{\text{air}}$, where R_{air} and R_{gas} and $\Delta R = R_{\text{gas}} -$

R_{air} , are the electrical resistances of the sensor structures in ambient air (R_{air}) and under exposure to VOCs or gas (R_{gas}), respectively [26,27]. This ratio is different for the chemical composition and the concentration of the respective species in air. The VOC species sensing performances were investigated by a two-probe method after mounting sensors inside a test chamber connected to gas flow instrumentation. The test gases were permanently circulated through the test chamber at a flow rate of 110 sccm. Details on the sensing experiments can be found in our previous works [23,26].

3. Results

3.1. Morphology of the printed sensors

In Fig. 2a the photograph of the printed devices based on Cu-Fe-MPs on a standard glass substrate ($25 \text{ mm} \times 75 \text{ mm}$) used for further research is presented. Additionally, sputtered gold contacts, subdividing the glass slide into multiple individual sensor devices can be observed in Fig. 2b. Digital as well as scanning electron microscopy (SEM) micrographs of the meandering stripes and the interdigitated gold contacts are displayed in Fig. 2c and d.

It is pointed out, that the direct print of the stripes onto a glass substrate offers the potential application as flexible and free-standing precursor stripes by gently detaching them from the glass substrate. The detachment occurs after gold deposition and before thermal annealing. The stripes still contain the elemental iron and copper particles as well as the polymer binder, meaning they are not suited for sensing in this state. In this state the detached stripes could be potentially used for conformal attachment of the sensor on curved surfaces. The structures presented in Fig. 3 show the directly printed and semi-detached freestanding stripes produced by breaking away the glass slide on one side.

The morphological details of the interpenetrated $\text{Fe}_2\text{O}_3\text{-CuO}$ NWs bridging the $\text{CuO}/\text{Cu}_2\text{O}/\text{Cu}$ and $\text{Fe}_2\text{O}_3/\text{Fe}$ microparticles are presented in Fig. 4 by showing SEM micrographs obtained at multiple steps of magnification (increasing magnification from (a) to (d)). The morphologies of the individual species are described as flake-like spikes and long nanowires both in the range of just a few tens of nanometers, which are made of Fe_2O_3 and CuO , respectively. A peculiarity of this printed microstructure is the occasional touching of these two nanostructures, which is inferred from the SEM micrographs (Fig. 4c and d).

A more detailed view onto both the $\text{CuO}/\text{Cu}_2\text{O}/\text{Cu}$ and Fe_2O_3

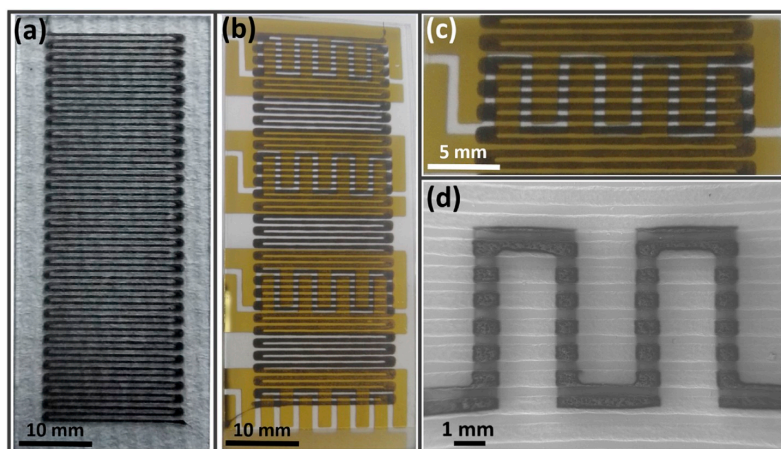


Fig. 2. Photograph of meandering printed stripes based on Cu-Fe-MPs on glass slide used for further research: (a) representative sample after printing and prior to gold deposition; (b) sample divided into individual sensors by interdigitating gold contacts; (c) the back side of a sensor element in higher magnification. (d) The SEM micrograph of the sensor element from (c).

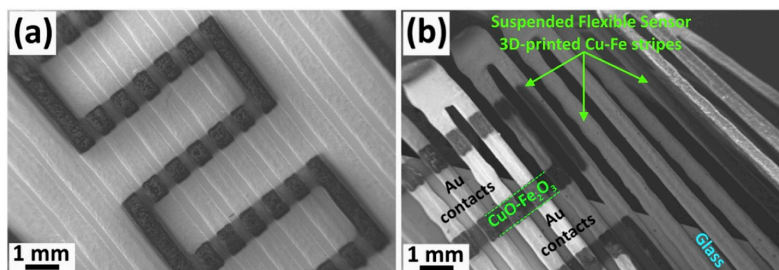


Fig. 3. SEM micrograph of the sensor element printed Cu-Fe mixed MPs: (a) on glass with Au contacts on top (brighter area); (b) suspended on the glass slide edge of flexible sensor printed Cu-Fe stripes with Au contacts on top.

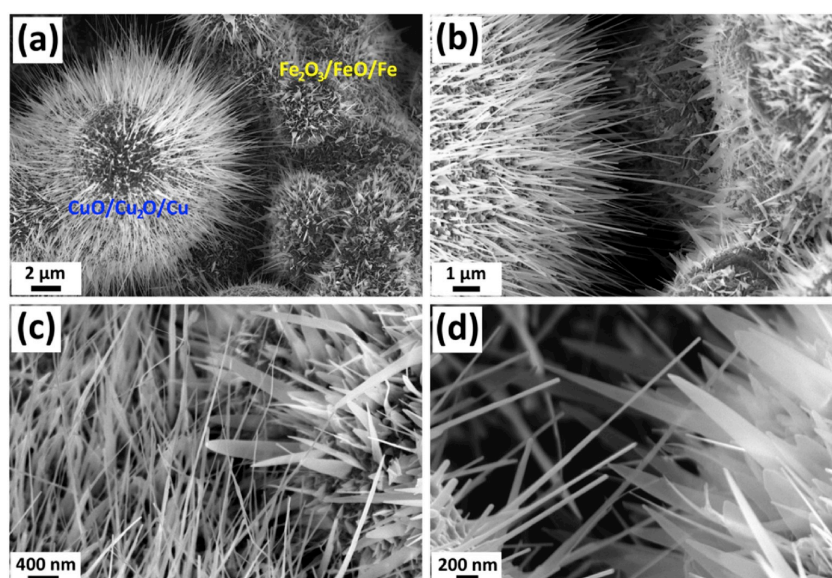


Fig. 4. SEM micrograph of the printed Cu-Fe mixed MP stripes forming CuO/Cu₂O/Cu and Fe₂O₃/Fe junction contacts: (a) lower magnification of the spike-covered MPs; (b–d) higher magnification of the area between the printed microparticles with CuO/Cu₂O nanowires and Fe₂O₃ nanospikes bridging the MPs. The thinner CuO/Cu₂O can clearly be distinguished from the broader Fe₂O₃ nanospikes.

nanostructures is presented in the SEM images included in Fig. S1 and Fig. S2. Also, a morphological comparison is presented for samples annealed with different temperature ramping. As seen in Fig. 4 and the Supporting Figs. S1 and S2, the nanostructures arrange in an open, readily accessible net-like microstructure, which is hard to achieve for planar thin film structures fabricated by standard techniques. For most gas sensors the accessibility (e.g. by high porosity) of the structures is important [23,24], since the active surface area is increased and the gas diffusion is easier resulting in an enhanced gas response. The high free volume of these structures paired with the macroscopic design freedom shows that 3D printing approaches like these will become more important for various technological applications, including gas sensors. In particular, the co-existence of p- and n-type semiconducting oxides are expected to improve the selectivity and sensitivity to weakly reactive gas species.

3.2. Crystalline structure of the nanowire/nanospike-covered microparticles

A detailed structural analysis of Fe and Cu particles, both before and

after thermal annealing respectively as well as one sample of a mixed powder after thermal annealing was performed via XRD. The results suggest that primitive cubic Cu₂O, as well as CuO in its monoclinic structure have formed from oxidation of metallic Cu in its face-centered cubic structure. Additionally, the only Fe-related species observed for the iron containing samples was Fe₂O₃. When heated at 425 °C for 4 h leftover metallic phases can be observed in the diffractograms. The samples that were re-heated at 650 °C for 2 h, did not show any metallic remains in the diffractograms, indicating a complete oxidation of the samples. Details on the results as well as the respective diffractograms can be found in the Supporting Information (Fig. S3).

In order to verify the findings from XRD studies, additional Raman spectra on the printed stripes were made and are presented in Fig. 5.

Due to the high sensitivity of Micro-Raman, it can be used extensively for surface investigations of the formed nanostructures. Fig. 5a shows micro-Raman spectra at room temperature for the printed structures finished by thermal annealing: (1) nanowire CuO/Cu₂O/Cu; (2) nanowire CuO/Cu₂O/Cu - nanospike Fe₂O₃/Fe; and (3) nanospike Fe₂O₃/Fe in the range of 100–1000 cm⁻¹. The presence of CuO as Tenorite and Cu₂O as Cuprite on the MPs as well as the existence of

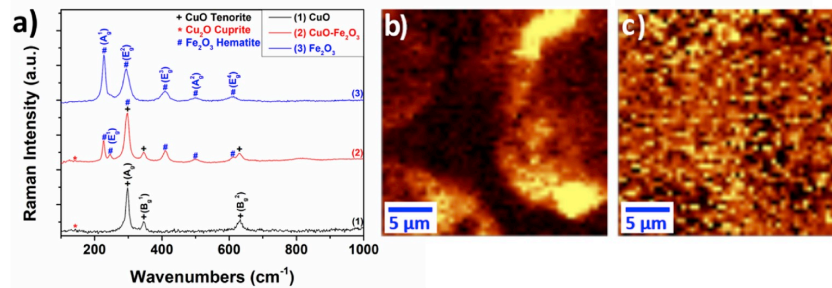


Fig. 5. Raman spectra of the 3D-printed stripes: (a) spectrum (1) nanowire-covered CuO/Cu₂O/Cu; curve (2) nanowire CuO/Cu₂O/Cu - nanospike Fe₂O₃/Fe; and curve (3) nanospike Fe₂O₃/Fe. Filtered Raman images of Fe₂O₃/Fe - CuO/Cu₂O/Cu heterojunction nets in terms of: (b) mode A_{1g} (227 cm⁻¹) corresponding to α -Fe₂O₃ (Hematite); and (c) mode B_{1g} (345 cm⁻¹) corresponding to CuO (Tenorite).

α -Fe₂O₃ (Hematite) was confirmed by the detected vibrational modes. The details on the Raman modes are described in the [Supporting Information](#).

3.3. XPS, chemical analysis

The XPS spectra of three sensor sample sets with different compositions are compared in [Fig. 6](#). The structures are either based on MPs of Cu (black line), Fe (blue line) or mixed Cu and Fe (red line) oxides. In the overview spectra ([Fig. 6a](#)) the elements Cu, Fe, O, Na and C were identified. The presence of Cu, Fe and partially O originates from the printed structures after thermal annealing whereas the signal related to carbon stems from surface contamination by atmospheric carbon (e.g. from carbohydrates) [26,28]. Accordingly, adventitious carbon (high

resolution spectrum of C-1s line in [Fig. 6b](#)) was used to correct charging effects. The signal corresponding to Na is a result of the glass substrate, on which the sensor stripes were deposited, and the heat treatment step [29]. The peak position of the C-1s line was used in order to correct charging by referencing to 285.0 eV.

The high resolution spectra of the Cu-2p_{3/2} and Fe-2p lines are shown in [Fig. 6b](#). The Cu-2p_{3/2} line reveals clear satellite peaks in case of the Cu and mixed metal sensor structures. The satellite peaks are shifted to higher binding energies with respect to the peak position of the Cu-2p_{3/2} line. The observation of satellite peaks is commonly regarded as signature for the presence of Cu²⁺ (in CuO) [24,30,31]. Accordingly, this Cu signal arising in all spectra and samples can be attributed to the presence of CuO.

A close look at the Fe-2p lines indicates different signal strengths of Fe in the different sensor structures. In case of the Fe and the mixed sensor structures the presence of Fe is clearly identified. The corresponding peak position of the Fe-2p_{3/2} line is located around 711.6 eV, which indicates the presence of Fe³⁺ in Fe₂O₃ (typically located between 710.4 eV and 711.6 eV) rather than Fe²⁺ in FeO (between 709.3 eV and 710.6 eV) or metallic Fe (between 706.5 eV and 707.7 eV) [28,30].

In conclusion, the mixed metals sensor nanostructure contains mostly CuO as well as Fe₂O₃. The quantification based on the XPS high resolution spectra reveals a Cu/Fe ratio of roughly 1.4.

3.4. Real Structure analysis of the nanospikes/nanowires

Transmission electron microscopy investigations on the structure and chemical details were performed on the CuO nanowires and Fe₂O₃ nanospikes having the described morphologies (cf. [Fig. 4](#)) shown in the STEM image of [Fig. 7a](#).

Despite from their geometry, a direct identification of copper and iron containing nanostructures was enabled by using EFTEM using electrons from the L-loss features to create element specific contrast images. The superimposed and colored EFTEM images are depicted in [Fig. 7b](#). EELS was used for the identification of the metal oxidation state and oxide phases present at three positions labeled A, B and C in [Fig. 7a](#). The respective core-loss signals of the oxygen-K edge and Fe-, Cu-L edges including their near-edge fine structures (ELNES) are presented in [Fig. 6c-f](#) and are compared with standard references [32]. For the Cu-oxide nanowire (label A) the ELNES resembles very well the one of the reference for Cu²⁺ present in the CuO phase [32,33] and for the Fe-oxide nanospikes (label B and C) excellent coincidence is observed with Fe³⁺ present in Hematite Fe₂O₃. Small differences in the ELNES between the experimental signals and the reference spectra concerning the low intensity missing third feature around 550 eV may be related to the presence of oxygen vacancies [34].

Further, ED experiments were performed on the structures labeled A and C to validate the results of the spectroscopic measurements on a

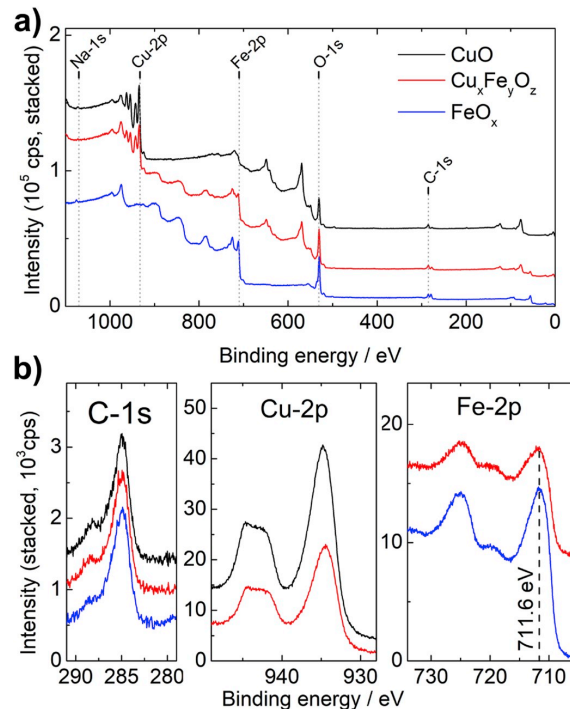


Fig. 6. XPS spectra of the mixed metal oxide sensors: (a) overview spectra; (b) high resolution spectra of C-1s, Cu-2p_{3/2} and Fe-2p lines.

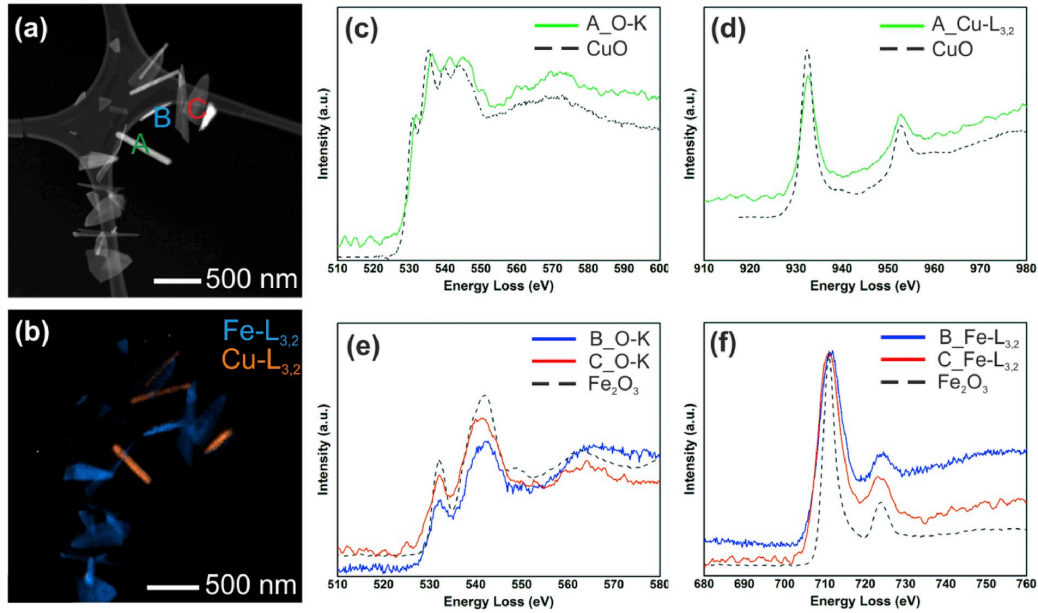


Fig. 7. Spectroscopic analyses of inelastic scattered electrons in the TEM. (a) Scanning TEM image; positions of EELS measurements are indicated with capital letters A-C. (b) EFTEM map showing the spatial distribution of Fe and Cu core loss signals. Please note, that there is a small offset of the stage tilt between images (a) and (b). (c) Core loss features of oxygen and Cu (d). (e) Core loss features of oxygen and Fe (f).

single point with crystallographic data. These investigations are summarized showing a ZLP filtered image in Fig. 8a including indicators for the positions of the virtual diffraction aperture. The experimental and simulated ED pattern of the positions A and C are depicted in Figs. 7b and 8c. Indeed, the ED patterns shown in Fig. 8b and c are assigned to the [101] zone axis pattern of monoclinic CuO and the [110] pattern of trigonal Fe₂O₃, coinciding with the EELS results. The ED pattern of the CuO nanowire presented in (b) shows diffuse streaks along the reciprocal [11-1]* direction, an effect which arises due to structural disorder. Structural peculiarities of CuO nanowires showing defects such as stacking faults, polysynthetic twinning or intergrowth of two CuO components are further demonstrated in Fig. S4 of the Supporting Information. With respect to Fe₂O₃ pattern (c) additional reflections arise in discrepancy to the trigonal space group of Hematite R-3c (yellow circles). In congruence to previous studies on iron oxide nanowires [21] a modified Hematite structure with space group R-3 (Ilmenite-type structure) may rationalize these reflections in a kinematic simulation. The reduced space group symmetry is interrelated to the elimination of the zonal reflection condition, i.e., for the 00l reflections the condition $l = 6n$ (R-3c) changes to $l = 3n$ (R-3), and for the h-kl reflections the condition $l = 2n$ (R-3c) is broken. For the interpretation of the ED pattern a pure kinematic approach is insufficient since dynamic scattering effects can be strongly significant. However, double diffraction is ruled out as an explanation for these yellow circled reflections (cf. Fig. 8c) because of the low thickness of the specimen and former precession electron diffraction experiments excluding such effects [21,35]. Since no indication for impurities were traced with EDX (not shown) on the nanospike (label C), the symmetry reduction may be rationalized with local ordering of oxygen vacancies, which are known to incorporate into Hematite nanostructures [34,36]. High-resolution TEM is capable to provide evidence on possible vacancy ordering or local structure variations. A representative HRTEM micrograph is presented in Fig. 8d together with a Fast Fourier Transformation (FFT) pattern. The interpretation of several FFT pattern calculated at different positions on the Fe₂O₃ nanospike (label C) suggest local strain variations most feasible

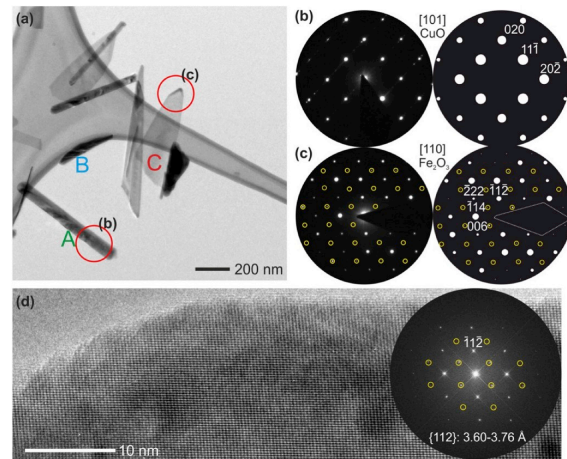


Fig. 8. (a) TEM bright-field image showing the respective oxide nanostructures with indication of the locations for electron diffraction experiments and high-resolution imaging. (b) Electron diffraction pattern of monoclinic CuO in [101] orientation and simulated pattern. Scattered intensities along the reciprocal [11-1]* direction indicate planar defects parallel to the growth direction. (c) Electron diffraction pattern of a Fe₂O₃ nanospike in [110] orientation. Reflections marked with yellow circles appear in deviation from the ideal Hematite structure and are explainable by a reduction in symmetry. (d) High-resolution TEM micrograph and FFT analysis from the area highlighted as region (c). The evaluation of local FFT pattern shows a variation of the {112} lattice parameter (standard: 3.68 Å) in the range between 3.60 and 3.76 Å, indicating a locally strained environment.

L. Siebert et al.

Nano Energy 70 (2020) 104420

from the range of d-spacings 3.60–3.76 Å measured for the $\{-11-2\}$ planes (in Hematite 3.68 Å).

In conclusion, the TEM study demonstrates the growth of defect-rich CuO nanowires and Fe₂O₃ nanospikes, described with a modified Hematite-type structure which is possibly based on ordering of oxygen vacancies.

3.5. Gas sensing properties

The plot in Fig. 9a shows the gas response to various volatile organic compound (VOC) gases (acetone, ethanol, 2-propanol and n-butanol) with 100 ppm gas concentration for printed sensor structures based on CuO/Cu₂O/Cu - Fe₂O₃/Fe. These samples were thermally annealed at 425 °C for 4 h with a ramp of about 40 °C/min to grow nanowire-nanospike nets and re-heated at 650 °C for 1 h to increase its electrical resistance. From Fig. 9 we can see that at all operating temperatures (OPTs) the printed sensor structures are selective to acetone vapor and the optimal OPT is 300 °C with a gas response to 100 ppm of about 50%.

Fig. 9b shows the typical dynamic response curves of the printed stripes exposed to 100 ppm of acetone in air. The response is about 50% with response and recovery/decay times of $\tau_r = 14.4$ s and $\tau_d > 50$ s, respectively.

For a series of VOC vapor concentration (0.5–1000 ppm), see Fig. S6 of the Supporting Information.

In Fig. 9c the current-voltage (I-V) characteristics for CuO/Cu₂O/Cu - Fe₂O₃/Fe printed sample sets are depicted at different operating temperatures. From Fig. 9c it can be seen that from room temperature up to 250 °C there is a non-linear current-voltage relation, indicating the dominance of an energy barrier-driven conductivity effect. Possible candidates for the room temperature conductivity could be a Poole-Frenkel or a Trap Assisted Tunneling effect. At higher temperatures the I-V-characteristics become ohmic, which means that the remaining series resistance is dominating the resistivity. The high current values can be explained based on the non-oxidized Fe and Cu micro-particles at the central or bottom parts [21].

For a more detailed characterization of the acetone sensing properties of the printed sensors, the plot in Fig. 10a shows the gas response to acetone vapor (100 ppm and 1000 ppm). At OPTs of 300 °C, 325 °C and 350 °C gas responses at 100 ppm are about 50%, 37% and 35%, respectively, and at a concentration of 1000 ppm the measured gas responses were about 50%, 52% and 53%, respectively.

Gas sensors are typically selective towards one gas but still show reactivity towards other gas species. This can lead to an unclear evaluation when mixed atmospheres are investigated with one sensor type. A means to correctly detect specific gases is by using multiple sensors in one platform and by cross-correlating their signals to find a specific compound. These preliminary results hint at a good selectivity for acetone. A good selectivity for a compound at a certain temperature can be used to create a sensor array with multiple sensors kept at different temperatures, where a linear combination of each signal enables the identification of a specific compound in a gas mixture.

In Fig. 10b the gas response versus concentration of acetone vapors is represented from 0.5 ppm to 1000 ppm at OPT of 300 °C. From Fig. 10 one can see that at low concentrations, the response is quite high and increasing with the concentration. The respective gas responses at 0.5, 1.0, 5.0 and 10 ppm, are, 12%, 14%, 15% and 16%. For more details on selectivity for low concentrations see Fig. S6 of the Supporting Information.

Fig. 10c shows the dynamic response at OPT of 300 °C to 1, 10 and 100 ppm acetone vapors. As can be seen, at lower vapor concentrations the value of the practical response does not change significantly, thus obtaining the values at 1, 10 and 100 ppm gas concentration of about 14%, 16% and 50%, respectively, and the response/recovery times of $\tau_r = 11.1$ s, 11.6 s, 14.4 s and $\tau_d = 10.33$ s, 11.9 s, >50 s, respectively.

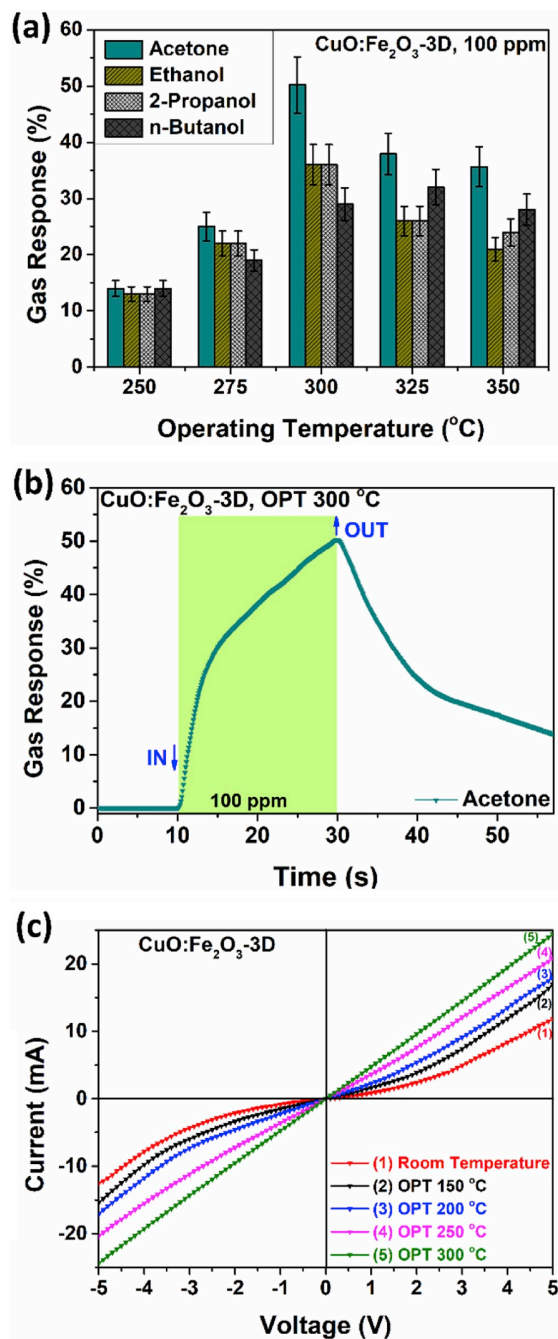


Fig. 9. (a) Gas response to various gases (100 ppm) versus operating temperature for the printed sensors based on CuO/Cu₂O/Cu - Fe₂O₃/Fe after thermal annealing at 425 °C for 4 h. (b) Dynamic response to 100 ppm of acetone vapor of the same sensor. (c) I/V-characteristics for different operating temperatures for the CuO/Cu₂O/Cu - Fe₂O₃/Fe sensors.

L. Siebert et al.

Nano Energy 70 (2020) 104420

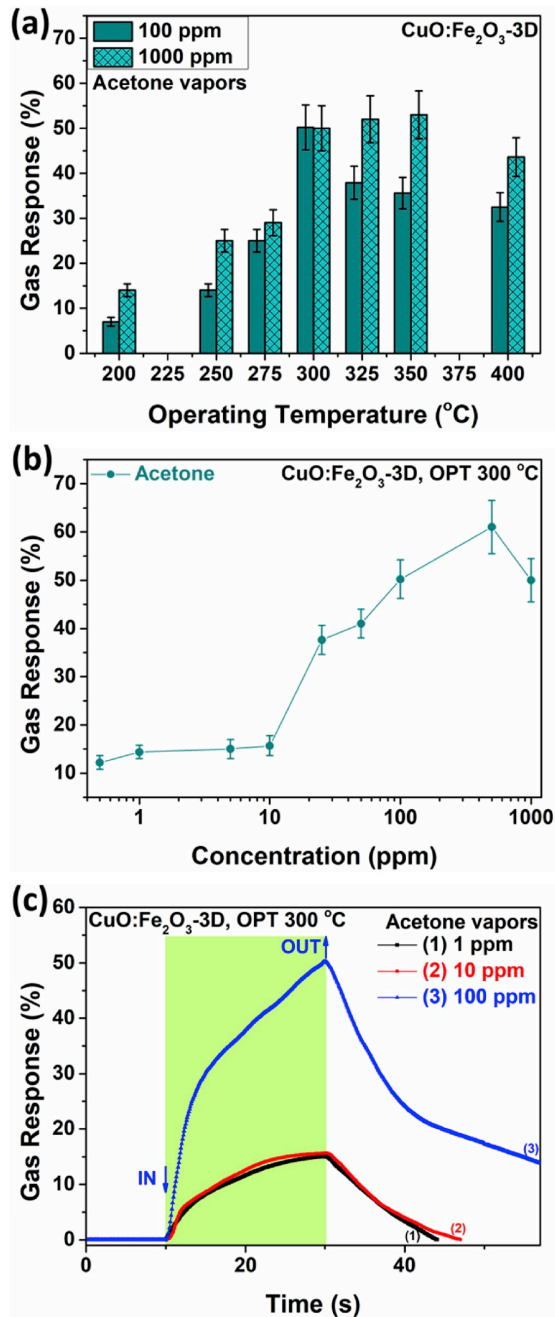


Fig. 10. (a) Gas response to acetone vapor (100 ppm and 1000 ppm) for the printed sensors measured at OPT from 200 °C to 400 °C. (b) Concentration dependency of the gas response for the printed sensors at an operating temperature of 300 °C (c) Dynamic response at OPT of 300 °C to 1, 10 and 100 ppm of acetone vapor.

3.6. Power consumption

By increasing the time and temperature of the thermal annealing, the level of oxidation of the MPs can be tailored, which can lead to the removal of electrical shortcut, increasing the sensitivity while lowering the power consumption.

In Fig. 11a the dependence of the power consumption and the response to acetone versus type of thermal annealing for printed samples of CuO:Fe₂O₃-3D is represented. The samples were treated in the following way: #1: 425 °C for 4 h; #2: 425 °C for 8 h; #3: 425 °C for 4 h and 650 °C for 1 h; #4: 425 °C for 4 h and 650 °C for 3 h.

It is observed that as the temperature and time of treatment increase, the power consumption decreases, and the highest value of the gas response is for the thermal annealing # 3, which included a 4-h treatment at 425 °C followed by a shorter 650 °C treatment. This indicates that for the correct formation of the nanowire and nanopike nets, a long duration of lower temperatures is necessary, which is in good agreement with the current model of the NW formation [37]. Additional heating at 650 °C leads to a much higher base resistance, which coincides with a higher gas response. This effect is likely caused by complete oxidation of the microparticles, forcing the current through the nanowires and nanopikes, while not changing their structure and therefore their conductivity mode. This can also be observed from the characterization, where Fig. S3 in the supporting information shows the XRD diffractogram of samples only heated once at 425 °C for 4 h. This sample shows a significant amount of remaining elemental copper and iron. When re-heated at 650 °C for 2 h no more elemental phases are visible in the diffractogram, further strengthening the hypothesis of a more complete oxidation in this second heating step. The complete oxidation is likely due to higher diffusion rates of oxygen into the metal microparticles at these elevated temperatures.

There is a trade-off however between the gas response and the power consumption, when the duration of the treatment at 650 °C is increased in time. The gas response lowers, which shows that the temperature also has an influence on the structure and the mode of conductivity of the NWs, which is not beneficial for the surface sensitive gas sensing mechanism proposed in the following section.

The possibility to tailor the quality of the sensors by simple thermal annealing adds an additional degree of freedom in designing electronic devices like the acetone vapor sensor presented here.

Fig. 11b shows the dependence of the power consumption and the response to acetone versus operating temperature of CuO:Fe₂O₃-3D samples. It can be seen that the operating temperature of OPT 300 °C leads to the highest response of ~50% with the power consumption of around 0.26 μW, which represents the optimal operating temperature for the developed devices. This is most likely due to the processes established on the NW surfaces during the experiment, which is proposed as a model in the following section. This calculation however does not include the necessary operation temperature and the corresponding power consumption. This issue has to be addressed in further iterations of such sensor systems by integrating a current-driven heating into the nanowires by employing high voltages and thermally insulating the substrate underneath. This could be realized by printing porous SiO₂ nanoparticles as an insulating layer. Another option would be to find a composition of nanowire covered particles and the corresponding conductivity modes that would alleviate the necessity of a higher operation temperature altogether.

The long-term stability of metal oxide semiconductors is also often discussed. Typically, sensors of this kind do not show any significant sensor drift in individual measurements, but drift can occur over longer durations of operation. While metal oxide semiconductors do not easily fail and are very robust, they need re-calibration after some time to account for this kind of thermal drift [42].

In summary, this concept of manufacturing allows for many different new concepts for such sensors and can easily be adopted, hinting at much more potential for developing a sensor with the desired properties.

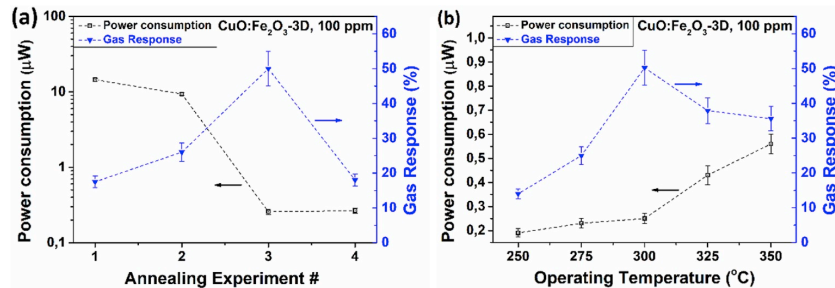


Fig. 11. (a) Dependence of the power consumption and the response to acetone versus type of thermal annealing for samples of CuO:Fe₂O₃-3D; (b) Dependence of the power consumption and the response to acetone versus operating temperature of CuO:Fe₂O₃-3D samples.

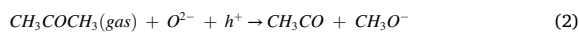
4. Proposed gas sensing mechanism

The proposed gas sensing mechanism is based on physico-chemical reactions on the sensor surface, which take place at different operating temperatures [38,39]. Under exposure to air oxygen species are adsorbed on the surface of CuO nanowires and ionized in dependence of the operating temperature. For example, at temperatures around 200–250 °C, O⁻ is formed in the following manner [22,38]:



Besides O⁻, depending on the OPT, also O₂⁻ and O²⁻ can be formed. The consequence for the mechanism is the same, as all ions will take up electrons leading to the accumulation of positively charged holes.

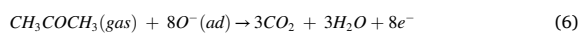
The negative charge will promote the formation of a hole accumulation layer (HAL) in the CuO nanowires acting as a conduction channel. The size of this conduction channel critically depends on the temperature, since the amount of adsorbed oxygen ions sinks with increasing temperature, resulting in an increase in sensitivity towards the concentration of the adsorbed gas molecules. After exposure to acetone vapor, the acetone molecules react with the adsorbed O⁻ and the HAL width will decrease, increasing the electrical resistance again. The proposed reactions facilitating the detection will be done as follows [22, 38].



For Fe₂O₃, the opposite mechanism as for CuO is proposed, where under exposure to air the reaction towards adsorbed oxygen is the reduction in conductivity via the formation of a depletion layer at the Fe₂O₃ surface a lightly doped n-type semiconductor oxide following manner [21,40]:



but after exposure to acetone vapor, gas molecules will react with the chemisorbed oxygen ions at the Fe₂O₃ nanopikes surface to form CO₂ and H₂O according to the following equation [21,40]:



Both of these mechanisms will lead to a p-n-junction formation at the interface of the CuO NWs and the Fe₂O₃ nanopikes, where at some connections, an additional resistance will be in place due to insufficient contacting between the two materials. When a p-n-junction at the interfaces between the p-type CuO and the n-type Fe₂O₃ is formed, a depletion region WD1 and an accumulation region WA1 will be present with the exposure of atmospheric O₂ (see Fig. S10 from the Supporting

Information). The introduction of acetone leads to a reduction in both the accumulation layer of the CuO, as well as the depletion layer in Fe₂O₃. Additionally, acetone adsorbed at the interface between CuO and Fe₂O₃ increases the contact resistance. This might lead to an increase in the potential barrier at the interface of the two materials (see Fig. S10 from the Supporting Information), making the junctions resistance higher. An increase in resistance of the CuO will then lead to an increase in the overall resistance. Both Fe₂O₃ and CuO are responsive to VOCs, so in order to maximize the effect of the junctions, the number of junctions has to be maximized. The density of iron is slightly higher than that of copper and the average particle size of the iron is larger. The amount of particles in contact when mixed in a 1:1 wt ratio should be approximately equal. A higher tendency towards one particle system will change the mechanism more to the pure particle system and will not lead to a higher sensitivity based on the junction effect.

Aside from this, the increase of the operation temperature leads to both an increase in the intrinsic charge carrier concentrations for both materials and therefore an increased conductivity, as well as it provides more energy for crossing the potential barriers at the interface between the two materials.

5. Summary and outlook

A facile 3D-printing based fabrication of otherwise clean room dependent structures made of mixed metal microparticles for gas sensing applications was demonstrated for the first time. Printed Cu and Fe MPs with diameters of 45–60 μm and 15–25 μm, respectively, were mixed and the MPs formed bridging non-planar CuO/Cu₂O/Cu - Fe₂O₃/Fe nanostructures after thermal annealing at 425 °C for 4 h in air. The contacts touching at the interface between the particles showed a highly open porous structure, which is beneficial for gas sensing applications. Morphological, vibrational, chemical and structural investigations were performed in detail. The TEM study demonstrates the growth of defect rich CuO nanowires and Fe₂O₃ nanopikes, described with a modified Hematite structure which is possibly based on ordering of oxygen vacancies. The gas sensing measurements showed excellent selectivity to acetone vapor at an operating temperature of 300 °C with high gas response of 50%–100 ppm which occurred after an additional annealing step of 650 °C for 1 h. The power consumption was low at 0.26 μW. The combination of the possibility of fast acetone vapor detection and controllable size and geometry, makes these devices ideal candidates for fast detection, as well as acetone vapor monitoring (down to 1 ppm).

More generally the mixing of easily obtained metal micro particles, their macroscopic alignment in real sensor devices via printing and their interplay in the gas sensing opens new ways for other such sensor systems. This demonstration represents the ground work for 3D-printing of semiconducting oxides of both types' n- and p-conductivity with tunable properties as an alternative for clean room technology and microfabrication.

L. Siebert et al.

Nano Energy 70 (2020) 104420

Declaration of competing interest

The authors declare that they have no known competing financial interests or personal relationships that could have appeared to influence the work reported in this paper.

Acknowledgements

This work was financially supported by the German Research Foundation (DFG) via the research unit FOR 2093 “Memristive devices for neuronal systems” through project A2, as well as within the CRC1261, gratefully acknowledged by NW and LK. LK thanks Prof. Bettina Lotsch from the Max Planck Institute for Solid State Research for enabling additional TEM measurements. Additional funding was provided under the project “Hot End” (grant number: 16KN021247), by the Federal ministry for Economic Affairs and Energy. This research was sponsored in part by the NATO Science for Peace and Security Programme (SPS) under grant G5634, “Advanced Electro-Optical Chemical Sensors” AMOXES. Dr. Oleg Lupan acknowledges the Alexander von Humboldt Foundation for the research fellowship for experienced researchers 3-3MOL/1148833 STP at the Institute for Materials Science, Kiel University, Germany. The authors would like to thank J. Bahr for the technical assistance and Prof. Tiginyanu for fruitful scientific discussions.

Appendix A. Supplementary data

Supplementary data to this article can be found online at <https://doi.org/10.1016/j.nanoen.2019.104420>.

References

- 1] E. MacDonald, R. Wicker, Multiprocess 3D printing for increasing component functionality, *Science* 353 (2016), aaf2093, <https://doi.org/10.1126/science.aaf2093>.
- 2] J.J. Schwartz, A.J. Boydston, Multimaterial actinic spatial control 3D and 4D printing, *Nat. Commun.* 10 (2019) 791, <https://doi.org/10.1038/s41467-019-08639-7>.
- 3] M. Nadgorny, A. Ameli, Functional polymers and nanocomposites for 3D printing of smart structures and devices, *ACS Appl. Mater. Interfaces* 10 (2018) 17489–17507, <https://doi.org/10.1021/acsami.8b01786>.
- 4] T.D. Ngo, A. Kashani, G. Imbalzano, K.T.Q. Nguyen, D. Hui, Additive manufacturing (3D printing): a review of materials, methods, applications and challenges, *Compos. B Eng.* 143 (2018) 172–196, <https://doi.org/10.1016/j.compositesb.2018.02.012>.
- 5] Y. Xu, X. Wu, X. Guo, B. Kong, M. Zhang, X. Qian, S. Mi, W. Sun, The boom in 3D-printed sensor technology, *Sensors* 17 (2017) 1166, <https://doi.org/10.3390/s17051166>.
- 6] G.I. Peterson, M.B. Larsen, M.A. Ganter, D.W. Storti, A.J. Boydston, 3D-Printed mechanochromic materials, *ACS Appl. Mater. Interfaces* 7 (2015) 577–583, <https://doi.org/10.1021/am506745m>.
- 7] V. Saasa, T. Malwela, M. Beukes, M. Mokgotho, C.-P. Liu, B. Mwakikunga, Sensing technologies for detection of acetone in human breath for diabetes diagnosis and monitoring, *Diagnostics* 8 (2018) 12, <https://doi.org/10.3390/diagnostics8010012>.
- 8] D. Smith, P. Španěl, A.A. Fryer, F. Hanna, G.A.A. Ferns, Can volatile compounds in exhaled breath be used to monitor control in diabetes mellitus? *J. Breath Res.* 5 (2011), 022001 <https://doi.org/10.1088/1752-7155/5/2/022001>.
- 9] M.T. Rahman, R. Moser, H.M. Zbib, C.V. Ramana, R. Panat, 3D printed high performance strain sensors for high temperature applications, *J. Appl. Phys.* 123 (2018), 024501, <https://doi.org/10.1063/1.4999076>.
- 10] L. Siebert, O. Lupan, M. Mirabelli, N. Ababii, M.-I. Terasa, S. Kaps, V. Cretu, A. Vahl, F. Faupel, R. Adelung, 3D-Printed chemiresistive sensor array on nanowire CuO/Cu₂O/Cu heterojunction nets, *ACS Appl. Mater. Interfaces* 11 (2019) 25508–25515, <https://doi.org/10.1021/acsami.9b04385>.
- 11] J.C. Anderson, Measuring breath acetone for monitoring fat loss: review, *Obesity* 23 (2015) 2327–2334, <https://doi.org/10.1002/oby.21242>.
- 12] Z. Wang, C. Wang, Is breath acetone a biomarker of diabetes? A historical review on breath acetone measurements, *J. Breath Res.* 7 (2013), 037109, <https://doi.org/10.1088/1752-7155/7/3/037109>.
- 13] C. Wang, A. Mbi, M. Shepherd, A study on breath acetone in diabetic patients using a cavity ringdown breath analyzer: exploring correlations of breath acetone with blood glucose and glycohemoglobin A1C, *IEEE Sens. J.* 10 (2010) 54–63, <https://doi.org/10.1109/JSEN.2009.2035730>.
- 14] W.R. Rowley, C. Bezold, Y. Arikian, E. Byrne, S. Krohe, Diabetes 2030: insights from yesterday, today, and future trends, *Popul. Health Manag.* 20 (2017) 6–12, <https://doi.org/10.1089/pop.2015.0181>.
- 15] J.H. Simmons, K.K. McFann, A.C. Brown, A. Rewers, D. Follansbee, R.E. Temple-Trujillo, G.J. Klingensmith, Reliability of the diabetes fear of injecting and self-testing questionnaire in pediatric patients with type 1 diabetes, *Diabetes Care* 30 (2007) 987–988, <https://doi.org/10.2337/dc06-1553>.
- 16] D. Guo, D. Zhang, N. Li, L. Zhang, J. Yang, in: D. Zhang, M. Sonka (Eds.), *Diabetes Identification and Classification by Means of a Breath Analysis System BT - Medical Biometrics*, Springer Berlin Heidelberg, Berlin, Heidelberg, 2010, pp. 52–63.
- 17] D. Zhang, D. Guo, K. Yan, A breath analysis system for diabetes screening and blood glucose level prediction, in: D. Zhang, D. Guo, K. Yan (Eds.), *Breath Anal. Med. Appl.*, Springer Singapore, Singapore, 2017, pp. 259–279, https://doi.org/10.1007/978-981-10-4322-2_14.
- 18] C. Sun, G. Maduraveeran, P. Dutta, Nitric oxide sensors using combination of p- and n-type semiconducting oxides and its application for detecting NO in human breath, *Sens. Actuators B Chem.* 186 (2013) 117–125, <https://doi.org/10.1016/j.snb.2013.05.090>.
- 19] C. Turner, C. Walton, S. Hoashi, M. Evans, Breath acetone concentration decreases with blood glucose concentration in type 1 diabetes mellitus patients during hypoglycaemic clamps, *J. Breath Res.* 3 (2009), 046004, <https://doi.org/10.1088/1752-7155/3/4/046004>.
- 20] O. Lupan, V. Postica, J. Gröttrup, A.K. Mishra, N.H. de Leeuw, J.F.C. Carreira, J. Rodrigues, N. Ben Sedrine, M.R. Correia, T. Monteiro, V. Cretu, I. Tiginyanu, D. Smazna, Y.K. Mishra, R. Adelung, Hybridization of zinc oxide tetrapods for selective gas sensing applications, *ACS Appl. Mater. Interfaces* 9 (2017) 4084–4099, <https://doi.org/10.1021/acsami.6b11337>.
- 21] O. Lupan, V. Postica, N. Wolff, O. Polonskyi, V. Duppel, V. Kaidas, E. Lazari, N. Ababii, F. Faupel, L. Kienle, R. Adelung, Localized synthesis of iron oxide nanowires and fabrication of high performance nanosensors based on a single Fe₂O₃ nanowire, *Small* 13 (2017) 1602868, <https://doi.org/10.1002/sml.201602868>.
- 22] S. Park, H. Kheel, G.-J. Sun, T. Ko, W.I. Lee, C. Lee, Acetone gas sensing properties of a multiple-networked Fe₂O₃-functionalized CuO nanorod sensor, *J. Nanomater.* 2015 (2015) 1–6, <https://doi.org/10.1155/2015/830127>.
- 23] N. Ababii, M. Hoppe, S. Shree, A. Vahl, M. Ulfa, T. Pauporté, B. Viana, V. Cretu, N. Magariu, V. Postica, V. Sontea, M.-I. Terasa, O. Polonskyi, F. Faupel, R. Adelung, O. Lupan, Effect of noble metal functionalization and film thickness on sensing properties of sprayed TiO₂ ultra-thin films, *Sensors Actuators A Phys* 293 (2019) 242–258, <https://doi.org/10.1016/j.sna.2019.04.017>.
- 24] J.F. Moulder, J. Chastain, *Handbook of X-ray Photoelectron Spectroscopy: A Reference Book of Standard Spectra for Identification and Interpretation of XPS Data*, Illustrate, Physical Electronics Division, Perkin-Elmer Corporation, 1992, <https://books.google.md/books?id=A-XGQgAACAAJ>.
- 25] A. Vahl, J. Dittmann, J. Jetter, S. Veziroglu, S. Shree, N. Ababii, O. Lupan, O. C. Aktas, T. Strunskus, E. Quandt, R. Adelung, S.K. Sharma, M. Sharma, The impact of O₂/Ar ratio on morphology and functional properties in reactive sputtering of metal oxide thin films, *Nanotechnology* 30 (2019) 235603, <https://doi.org/10.1088/1361-6528/ab0837>.
- 26] O. Lupan, V. Cretu, V. Postica, O. Polonskyi, N. Ababii, F. Schütt, V. Kaidas, F. Faupel, R. Adelung, Non-planar nanoscale p–p heterojunctions formation in ZnxCu1–xOy nanocrystals by mixed phases for enhanced sensors, *Sens. Actuators B Chem.* 230 (2016) 832–843, <https://doi.org/10.1016/j.snb.2016.02.089>.
- 27] M. Hoppe, N. Ababii, V. Postica, O. Lupan, O. Polonskyi, F. Schütt, S. Kaps, L. F. Sukhodub, V. Sontea, T. Strunskus, F. Faupel, R. Adelung, (CuO-Cu₂O)/ZnO:Al heterojunctions for volatile organic compound detection, *Sens. Actuators B Chem.* 255 (2018) 1362–1375, <https://doi.org/10.1016/j.snb.2017.08.135>.
- 28] O. Lupan, L. Chow, T. Pauporté, L.K. Ono, B. Roldan Cuenya, G. Chai, Highly sensitive and selective hydrogen single-nanowire nanosensor, *Sens. Actuators B Chem.* 173 (2012) 772–780, <https://doi.org/10.1016/j.snb.2012.07.111>.
- 29] O. Lupan, V. Cretu, V. Postica, N. Ababii, O. Polonskyi, V. Kaidas, F. Schütt, Y. K. Mishra, E. Monaico, I. Tiginyanu, V. Sontea, T. Strunskus, F. Faupel, R. Adelung, Enhanced ethanol vapour sensing performances of copper oxide nanocrystals with mixed phases, *Sens. Actuators B Chem.* 224 (2016) 434–448, <https://doi.org/10.1016/j.snb.2015.10.042>.
- 30] Y. Shimizu, T. Maekawa, Y. Nakamura, M. Egashira, Effects of gas diffusivity and reactivity on sensing properties of thick film SnO₂-based sensors, *Sens. Actuators B Chem.* 46 (1998) 163–168, [https://doi.org/10.1016/S0925-4005\(97\)00247-5](https://doi.org/10.1016/S0925-4005(97)00247-5).
- 31] N. Pauly, S. Tougaard, F. Yubero, Determination of the Cu 2p primary excitation spectra for Cu, Cu₂O and CuO, *Surf. Sci.* 620 (2014) 17–22, <https://doi.org/10.1016/j.susc.2013.10.009>.
- 32] O. Lupan, V. Postica, V. Cretu, N. Wolff, V. Duppel, L. Kienle, R. Adelung, Single and networked CuO nanowires for highly sensitive p-type semiconductor gas sensor applications, *Phys. Status Solidi Rapid Res. Lett.* 10 (2016) 260–266, <https://doi.org/10.1002/psrr.201510414>.
- 33] J.P. Ngantcha, M. Gerland, Y. Kihn, A. Rivière, Correlation between microstructure and mechanical spectroscopy of a Cu-Cu₂O alloy between 290 K and 873 K, *Eur. Phys. J. Appl. Phys.* 29 (2005) 83–89, <https://doi.org/10.1051/epjap:2004200>.
- 34] T. Li, H. Feng, Y. Wang, C. Wang, W. Zhu, L. Yuan, G. Zhou, Formation of modulated structures induced by oxygen vacancies in α-Fe₂O₃ nanowires, *J. Cryst. Growth* 498 (2018) 10–16, <https://doi.org/10.1016/j.jcrysgro.2018.05.031>.
- 35] P.A. Midgley, A.S. Eggeman, Precession electron diffraction – a topical review, *IUCr J* 2 (2015) 126–136, <https://doi.org/10.1107/S2052252514022283>.
- 36] Z. Chen, U. Cvelbar, M. Mozetič, J. He, M.K. Sunkara, Long-range ordering of oxygen-vacancy planes in α-Fe₂O₃ nanowires and nanobelts, *Chem. Mater.* 20 (2008) 3224–3228, <https://doi.org/10.1021/cm800288y>.

L. Siebert et al.

- [37] L. Xiang, J. Guo, C. Wu, M. Cai, X. Zhou, N. Zhang, A brief review on the growth mechanism of CuO nanowires via thermal oxidation, *J. Mater. Res.* 33 (2018) 2264–2280, <https://doi.org/10.1557/jmr.2018.215>.
- [38] N. Barsan, U. Weimar, Conduction model of metal oxide gas sensors, *J. Electroceram.* 7 (2001) 143–167, <https://doi.org/10.1023/A:1014405811371>.
- [39] D.R. Miller, S.A. Akbar, P.A. Morris, Nanoscale metal oxide-based heterojunctions for gas sensing: a review, *Sens. Actuators B Chem.* 204 (2014) 250–272, <https://doi.org/10.1016/j.snb.2014.07.074>.
- [40] D.H. Kim, Y.-S. Shim, J.-M. Jeon, H.Y. Jeong, S.S. Park, Y.-W. Kim, J.-S. Kim, J.-H. Lee, H.W. Jang, Vertically ordered hematite nanotube Array as an ultrasensitive and rapid response acetone sensor, *ACS Appl. Mater. Interfaces* 6 (2014) 14779–14784, <https://doi.org/10.1021/am504156w>.
- [41] G. Postiglione, G. Natale, G. Griffini, M. Levi, S. Turri, Conductive 3D microstructures by direct 3D printing of polymer/carbon nanotube nanocomposites via liquid deposition modeling, *Compos. Appl. Sci. Manuf.* 76 (2015) 110–114.
- [42] A.C. Romain, J. Nicolas, Long term stability of metal oxide-based gas sensors for e-nose environmental applications: an overview, *Sens. Actuators B: Chem.* 146 (2) (29 April 2010) 502–506.



Leonard Siebert is a Ph.D. student at the chair for Functional Nanomaterials at the Institute for Materials Science at Kiel University, Germany. In his work, he focuses on novel fabrication techniques for extreme polymer composites, additive manufacturing and metal oxide semiconductor gas sensors. Having developed multiple 3D-printing setups, he seeks to apply innovative and unconventional means for manufacturing new materials.



Niklas Wolff is a Ph.D. student in materials science at Kiel University, Germany. He studied materials science and engineering at Kiel University and focused on functional materials for sensing application using transmission electron microscopy. His current research interest is on the nanoscale structural and chemical aspects of piezoelectric and magnetostrictive materials for magnetoelectric composite sensors and metal oxides for gas sensing applications.



Nicolai Ababii is at present a Ph.D. candidate in the group “Nanotechnology and nanosensors” of Prof. Dr. Oleg Lupan, Department of Microelectronics and Biomedical Engineering, TUM, Moldova. He worked in the field of copper oxide nanocomposite and its surface control for his Engineering degree diploma. He received his M.Sc. in microelectronics and nanotechnologies from the Technical University of Moldova in 2016. He was awarded with a fellow for 2018–2019 from the Government of the Republic of Moldova as an Excellence Ph.D. student. His current research interests are nanostructuring of semiconducting oxide thin films and nanowires for gas sensors.



Maik-Ivo Terasa is currently working as a Ph.D. student at the chair for Functional Nanomaterials (Prof. Dr. Rainer Adelung) at the Institute for Materials Science, Faculty of Engineering, Kiel University, Germany. He received his M.Sc. degree in materials science and engineering in 2017 from the Kiel University. His current research is focused on the junction of memristive and sensitive components for neuromorphic applications.



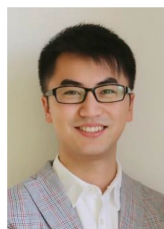
Oleg Lupan is an invited scientist at the research group “Functional Nanomaterials” of Professor Adelung, Germany. He received his Ph.D. from the Institute of Applied Physics, Academy of Sciences of Moldova (ASM) in 2005. His postdoctorate research activities were carried out at the French, CNRS, Paris, France and the University of Central Florida, USA. He is a Professor and research scientist in solid state electronics and nanoelectronics at TUM. His current research interests include sensors, nanosensors, optoelectronic devices, LEDs, semiconducting oxides, nanotechnologies, and nanodevices.



Alexander Vahl studied Materials Science at Kiel University (2009–2014). He wrote his dissertation at the Chair of Prof. F. Faupel (Multicomponent Materials) on the topic of memristive switching and memsensor devices and obtained his Ph.D. from the Faculty of Engineering in 2019. Since 2019 he is working as postdoc in the group “Multicomponent Materials” of Prof. F. Faupel at Faculty of Engineering at Kiel University. His field of study includes memristive and memsensitive thin film devices with a special focus on nanoparticle composites.



Viola Duppel works as a technician in the field of electron microscopy at the Max Planck Institute for Solid State Research, in the group of Prof. Bettina Lotsch.



Haoyi Qiu is a Ph.D. candidate in the group of Functional Nanomaterials (Prof. Dr. Rainer Adelung) at Kiel University, Germany. He obtained his M.Sc. in Materials Science and Engineering (2017) from Kiel University. His current research is focused on the development of eco-friendly polymer coatings for reduction of the marine biofouling.

Nano Energy 70 (2020) 104420

L. Siebert et al.



Maik Tienken is a master student in materials science at Jena University, Germany. He completed his bachelor degree in materials science at Kiel University, Germany. During his bachelor thesis he worked on direct ink writing of tetrapodal zinc oxide. Afterwards he continued his research on the printability of microparticles for functional inks. In Jena he is also working as a research assistant at the Fraunhofer IOP.



Franz Faupel received his Ph.D. in physics from the University of Göttingen in 1985. He was postdoctoral fellow at the IBM Research Center Yorktown Heights and got his habilitation in 1992. Since 1994, he holds the Chair for Multicomponent Materials at Kiel University. Prof. Faupel is Chairman of the North German Initiative Nanotechnology and has served on various editorial boards including Journal of Materials Research, SN Applied Sciences, Materials, Applied Physics Letters and Journal of Applied Physics. He published more than 300 papers (h = 54, Google Scholar, 12/2019). His research interests include functional nanocomposites, magnetoelectric sensors and plasma deposition.

Nano Energy 70 (2020) 104420



Mattia Mirabelli studied materials science and engineering between the University of Calabria in Italy and the Kiel University in Germany. His main research field has been the development and application of direct ink writing 3D printing technologies. Since June 2019 he works as 3d printing process engineer at BigRep GmbH, Berlin.



Lorenz Kienle is Professor for Synthesis and Real Structure at the Faculty of Engineering at tKiel University, Germany. Moreover, he is heading the center for transmission electron microscopy at the Faculty of Engineering. His research focuses on the synthesis of novel bulk- and nanomaterials by chemical approaches and thin film deposition techniques as well as their characterization by state of the art nanoanalytical methods, including transmission electron microscopy, X-ray diffraction and others. Presently, the materials under investigation are thermoelectrics, battery materials, complex alloy nanoparticles, piezoelectrics and superlattice nanostructures.



Victor Sontea received his M.S. degree in microelectronics and semiconductor devices from the Polytechnic Institute of Chisinau, Moldova, in 1973. He received his Ph.D. degree in semiconductor physics from the Institute of Applied Physics of the Academy of Sciences of Moldova of U.S.S.R. in 1982. He was promoted to Professor in 1996. He is appointed as Full Professor at Department of Microelectronics and Biomedical Engineering (MBE). He holds the position of Head of the MBE Department at TUM. His research interests are in microelectronics, physics and technology of materials, semiconductor devices and micro-nano-electronics, engineering of micro-nano-electronics and biomedical devices.



Rainer Adelung is full professor and chair holder of the Functional Nanomaterials group established in 2007 at the Institute for Materials Science, Kiel University, Germany. He received his Ph.D. (rer. nat.) in physics in 2000 from the Institute of Experimental and Applied Physics, Kiel University, and during 2001–2002 he was at Case Western Reserve University in Cleveland (USA) as Feodor Lynen (Alexander von Humboldt) research fellow. In 2006 he finished his habilitation at the Institute for Materials Science in Kiel and then continued as Heisenberg Professor (DFG grant) with his own Functional Nanomaterials group in 2012. More information at <https://www.tf.uni-kiel.de/matwis/fnano/de>.

Supporting Information

Facile Fabrication of Semiconducting Oxide Nanostructures by Direct Ink Writing of Readily Available Metal Microparticles and their application as Low Power Acetone Gas Sensors

Leonard Siebert^a, Niklas Wolff^b, Nicolai Ababii^c, Maik-Ivo Terasa^a, Oleg Lupan^{a,c,*}, Alexander Vahl^d, Viola Duppel^e, Haoyi Qiu^a, Maik Tienken^a, Mattia Mirabelli^a, Victor Sontea^c, Franz Faupel^d, Lorenz Kienle^b, Rainer Adelung^{a,*}

^a *Chair for Functional Nanomaterials, Institute for Materials Science, Kiel University, Kaiserstr. 2, D-24143, Kiel, Germany*

^b *Chair for Synthesis and Real Structure, Institute for Materials Science, Kiel University Kaiserstr. 2, D-24143 Kiel, Germany*

^c *Department of Microelectronics and Biomedical Engineering, Center for Nanotechnology and Nanosensors, Technical University of Moldova, 168 Stefan cel Mare Av., MD-2004 Chisinau, Republic of Moldova*

^d *Chair for Multicomponent Materials, Institute for Materials Science, Kiel University, Kaiserstr. 2, D-24143, Kiel, Germany*

^e *Nanochemistry, Max Planck Institute for Solid State Research, Heisenbergstrasse 1, Stuttgart 70569, Germany*

Corresponding author:

*Rainer Adelung (ra@tf.uni-kiel.de)

Keywords: 3D printing, Cu-Fe deposition, heterojunction, Fe₂O₃-CuO/Cu₂O/Cu, gas sensing, Transmission electron microscopy

In **Figure S1 a)** larger view details of the nanowires-CuO/Cu₂O/Cu microspheres can be seen as SEM images. Figure S1 b) shows neighboring microparticles covered with a dense net of CuO NWs with length of 2-15 μm grown from microparticle CuO/Cu₂O/Cu bridging each other. Figure S1c and d shows CuO NWs bridging two neighboring CuO/Cu₂O/Cu microparticles forming a bridge or paths for electrical current between it. Figure S1d shows several interpenetrated nanowires of CuO with diameters about 25 to 50 nm, which are bridging different microspheres and allow current flow through the sensor structure.

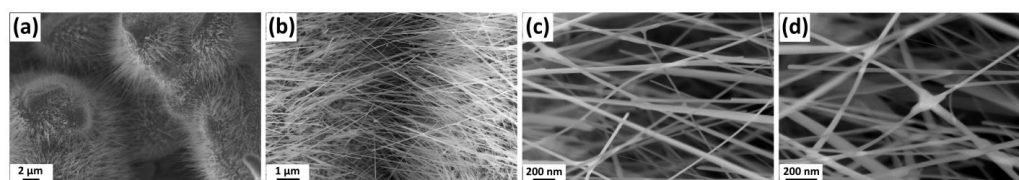


Figure S1. SEM images of nanowires-CuO/Cu₂O/Cu nano-microspheres thermally annealed at 425 °C for 4 h with ramp of about 40 °C/min showing details of morphology: a) lower magnification images of microparticles deposited directly on sensor template; b-d) higher magnification images of samples from (a) to show microparticles and interpenetrated CuO nanowires bridging CuO/Cu₂O/Cu heterojunctions net forming sensor structure.

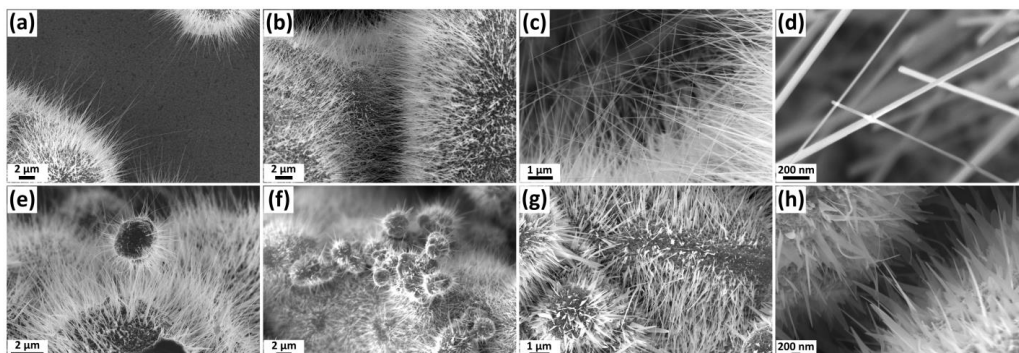


Figure S2. SEM images of nanowire networks of CuO thermally annealed at 425 °C for 4 h with a temperature ramp of 3.4 °C/min at increasing magnification starting with the lowest magnification at a) and the highest at b). e-h) show the CuO-Fe₂O₃ nanowires-nanospikes networks with increasing magnifications. The wider nature of the Fe₂O₃ nanostructures can be seen in h).

Figure S2 shows SEM images of Cu MPs oxidized at 425 °C for 4 h with ramp 3.4 °C/min. Figures S2, a, shows SEM images of two oxidized MPs where can be clearly seen nanowires grown at 425 °C. From Figures S2, b, can be seen a high density of nanowires on the surface of MPs. From Figures S2, c, d, we can see interconnections of nanowires CuO at different magnifications. Figures S2, e, f shows SEM images of Cu and Fe MPs (mass ratio 1:1, and Fe MPs size was 10 μm) thermally annealed at 425 °C for 4 h. From Figure S2, g, h, it can be distinguished interpenetrated CuO and Fe₂O₃ at low and higher magnifications.

Figure S3 shows the XRD pattern for the 3D printed devices. The relative peak intensity to the background demonstrates the crystallinity of the oxide-metal samples, which can be assigned to Cu and Cu₂O face-centered cubic (fcc) structure, as well as CuO monoclinic structure. When heating the samples for 4 hours at 425 °C a significant development of

oxidizes phases can be observed (Figure S3 a), (2-4)). Remaining metallic copper and iron can also be observed. When the sensors were additionally heat treated a second time at 650 °C for 2 h, the metal peaks vanish, indicating a complete oxidation of both copper and iron (Figure S3 b), (2)).

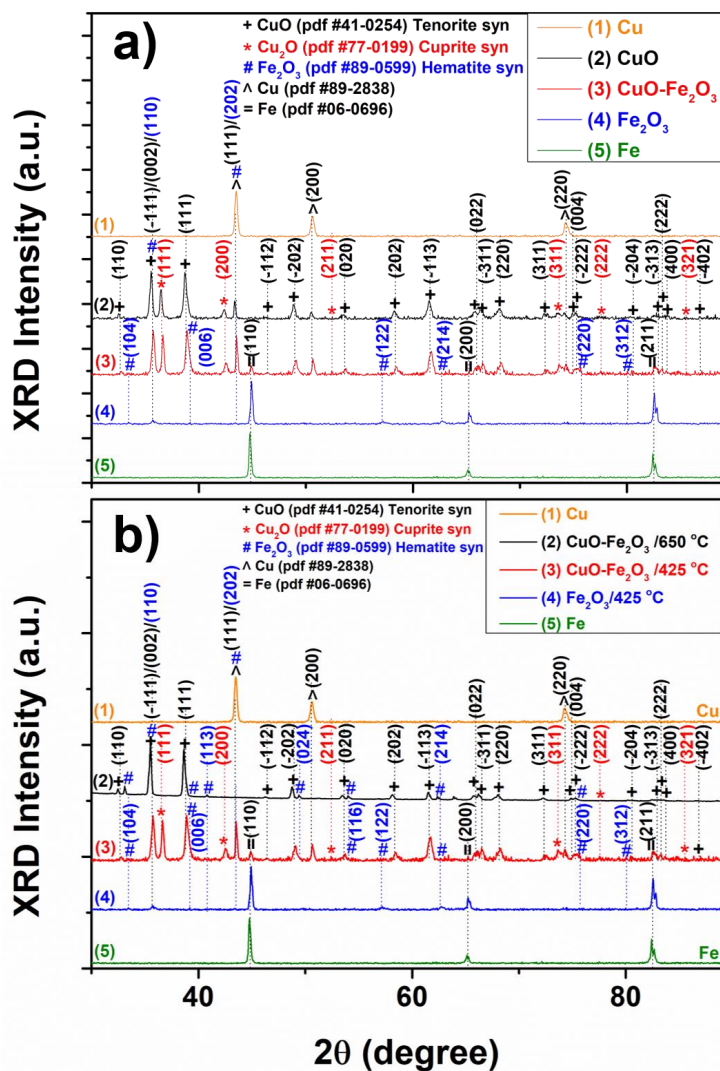


Figure S3. a) XRD patterns of the Cu and Fe powders before annealing: (1) Cu and (5) Fe. XRD diffractograms of the CuO/Cu₂O/Cu and Fe₂O₃/FeO/Fe heterojunctions microparticles stripes subjected to thermal annealing TA at 425 °C for 4 h in air: (2) CuO/Cu₂O/Cu; (3) CuO/Cu₂O/Cu and Fe₂O₃/FeO/Fe; and (4) Fe₂O₃/FeO/Fe.

The b) part shows the CuO/Cu₂O/Cu and Fe₂O₃/Fe powders after re heating at 650 °C for 2 h in air (2), where the metallic phases have disappeared and are likely oxidized to CuO and Fe₂O. (3) shows the diffractogram of a 425 °C 4 h heated sample as comparison, as well as a pure Fe₂O₃ heat treated for 4 h at 425 °C (4).

Reflections of metallic copper can be seen in the diffractogram (**Figure S3**) at 2θ of 43.35°, 50.5° and 74.15° observed for (111), (200) and (220) Miller planes, respectively, which proves the purity of original Cu before being oxidized in air. The strongest reflections (*hkl*) in diffractogram 2 are of cupric oxide CuO (Tenorite) at 2θ values and correspond to the (-110), (-111)/(002), (-112), (-202), (202), (113), (-311), (-220), (311), (-222), (400), (-131) and (204) Miller planes at 32.65°, 35.65°, 46.7°, 48.8°, 58.25°, 61.5°, 68.05°, 72.6°, 75.35°, 83.85°, 90.05° and 95.2°, respectively. Reflections at 2θ of 36.5°, 42.35°, 52.75°, 73.35° and 77.7°, are assigned to (111), (200), (211), (311) and (222) of Cu₂O (Cuprite) [31]. XRD diffractogram #3 is related to the CuO/Cu₂O/Cu and Fe₂O₃/Fe microparticles lines after thermal annealing.

Micro Raman was performed on both the individual iron and copper particles and the mixed phase system after thermal annealing. Modes were found at A_g (297 cm⁻¹), B_g¹ (345 cm⁻¹) and B_g² (633 cm⁻¹), which belongs to CuO (Tenorite) [31]. The mode at 143 cm⁻¹ corresponds to Cu₂O (Cuprite) [42]. Modes A_g¹ (227 cm⁻¹), E_g¹ (246 cm⁻¹), E_g² (297 cm⁻¹), E_g³ (408 cm⁻¹), A_g² (498 cm⁻¹) and E_g⁴ (612 cm⁻¹) from **Figure 4** corresponds to α -Fe₂O₃ (Hematite) [43]. Coexistence of CuO, Cu₂O and α -Fe₂O₃ in the MPs was confirmed by A_g (297 cm⁻¹), B_g¹ (345 cm⁻¹) and B_g² (633 cm⁻¹) for CuO (Tenorite) and mode at (143 cm⁻¹) corresponds to

Cu_2O , but also appears peaks at A^1_g (227 cm^{-1}), E^1_g (246 cm^{-1}), E^2_g (297 cm^{-1}), E^3_g (408 cm^{-1}), A^2_g (498 cm^{-1}) and E^4_g (612 cm^{-1}), which are associated to $\alpha\text{-Fe}_2\text{O}_3$ (Hematite) [20,21]. Intensity maps created by filtering the Raman modes A^1_g (227 cm^{-1}) and B^1_g (345 cm^{-1}) shown in Figure 4b-c illustrate the local distribution of the $\alpha\text{-Fe}_2\text{O}_3$ (Hematite) and the CuO (Tenorite) phases represented by high intensity in Figure 4b and Figure 4c, respectively.

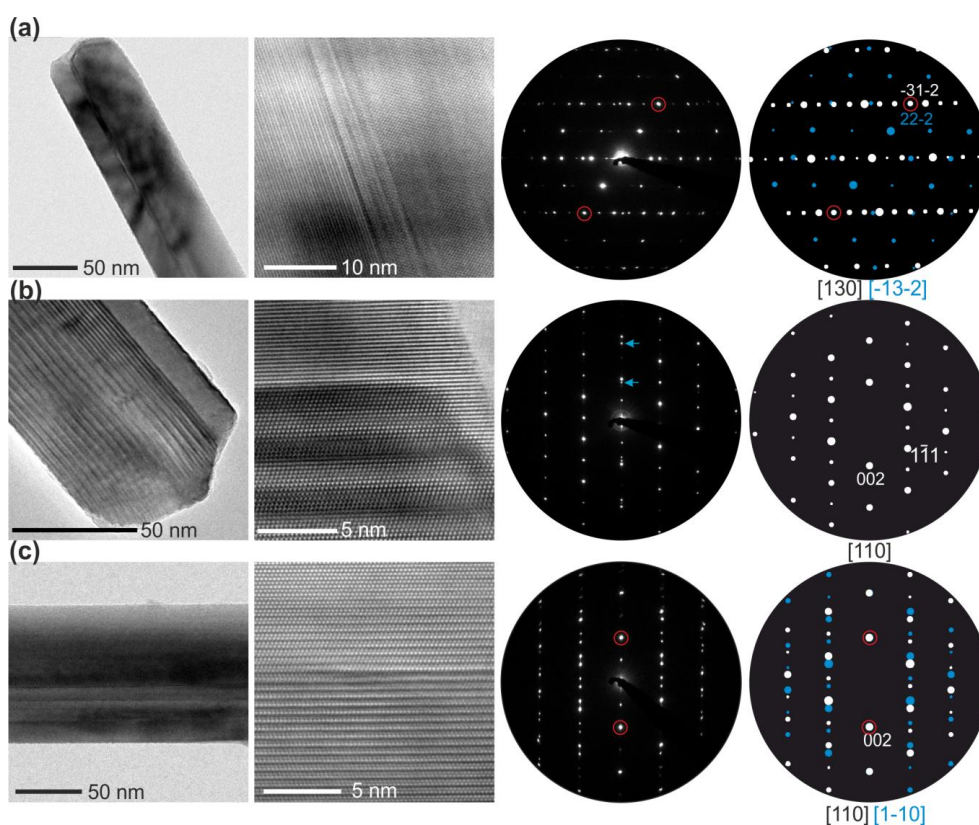


Figure S4. Structure of CuO nanowires: TEM image, high-resolution micrograph, precession electron diffraction pattern, simulation (from left to right). (a) Edge-on view onto an intergrowth boundary of $- (31-2)$ and $(22-2)$ planes of a two component CuO

nanowire. (b) Moirée contrast established by the superposition of two different orientated lattices due to structural intergrowth. The blue arrows in the PED pattern indicate the reflections belonging to a low order zone axis orientation of the second component. (c) Polysynthetic twinning on the (002) planes is observed parallel to the nanowire growth direction.

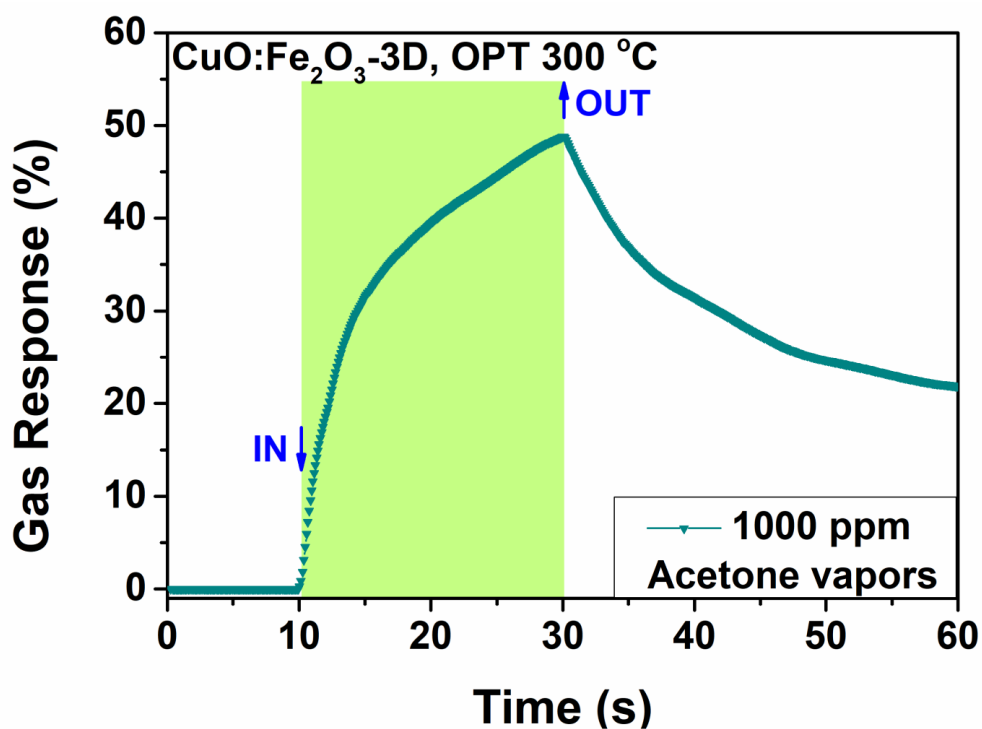


Figure S5. Dynamic response to 1000 ppm of acetone vapors of $\text{CuO}/\text{Cu}_2\text{O}/\text{Cu}$ and $\text{Fe}_2\text{O}_3/\text{Fe}$ based sensor structure.

Figure S5 shows the typical dynamic response curves of the 3D-printed stripes exposed to 1000 ppm of acetone in air. The response is about 50% with response and recovery/decay times of $\tau_r = 14.9$ s and $\tau_d > 50$ s, respectively.

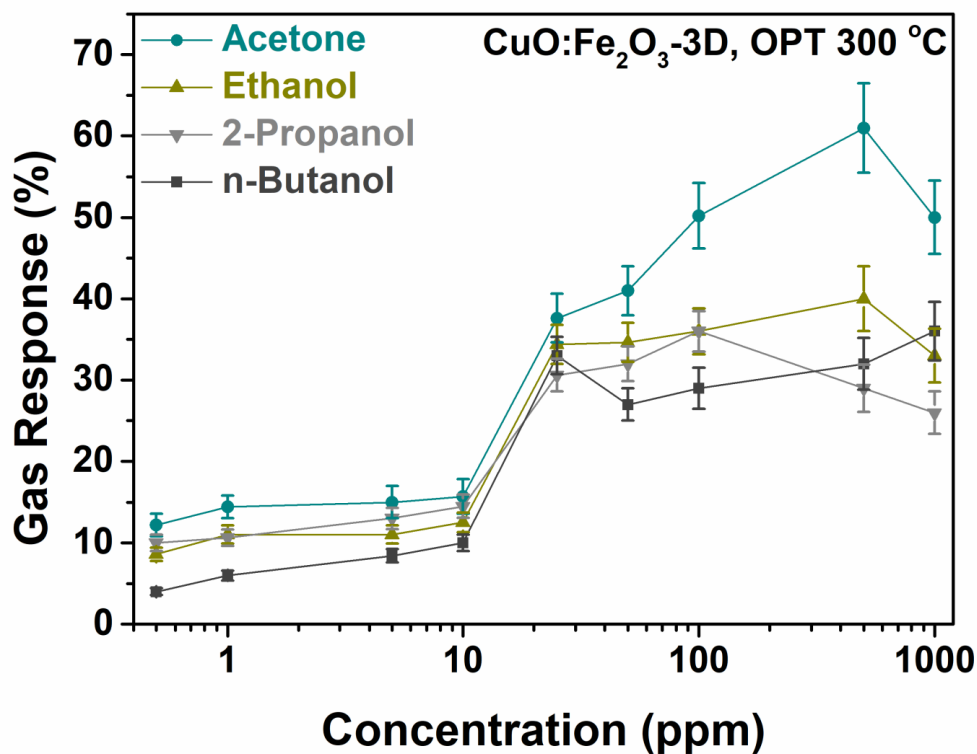


Figure S6. Gas response versus concentration of the 3D-printed CuO/Cu₂O/Cu and Fe₂O₃/Fe based sensor structure for different gases (Acetone, Ethanol, 2-Propanol and n-Butanol).

Figure S6 shows the gas response versus concentration from 0.5 ppm to 1000 ppm of the 3D-printed sample with of CuO/Cu₂O/Cu and Fe₂O₃/Fe structure of different gases (Acetone, Ethanol, 2-Propanol and n-Butanol) at OPT 300 °C. As can be observed, samples are selective to acetone vapor at all concentration values.

The gas response was calculated from formula ($S_p = \frac{R_{gas}-R_{air}}{R_{air}} * 100\%$) and electrical conductivity showed *p*-type conductivity behavior.

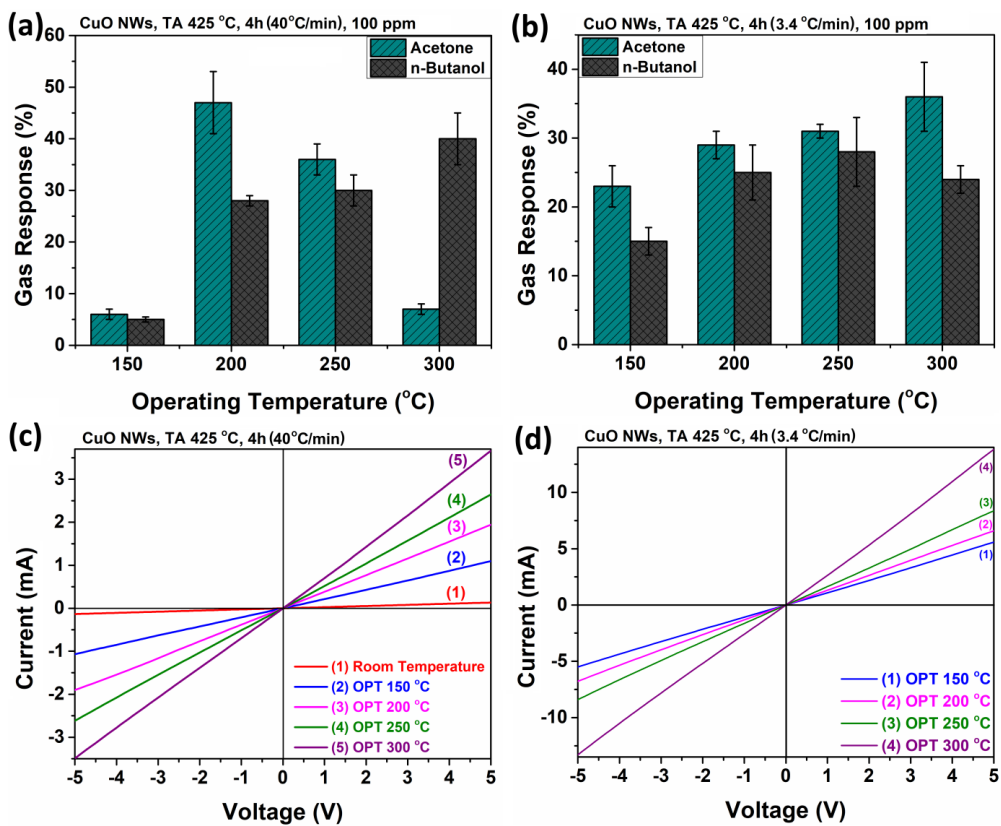


Figure S7. Gas response to 100 ppm of acetone and *n*-Butanol vapors (as volatile organic compounds) for the nanowire CuO/Cu₂O/Cu heterojunction net thermally annealed at: (a) 425 °C for 4 h with a temperature ramp of 40 °C/min for sensor types longitudinally sample set 3D-L; (b) 425 °C for 6 h with a temperature ramp of 3.40 °C/min. Current-voltage characteristics of samples from (c) belong to (a) and (d) belong to (b) at different operating temperatures, respectively.

Figure S7 shows the gas response to (100 ppm) acetone *n*-Butanol vapors and current-voltage characteristics for sensor structure CuO. Figure S7(a-b) presents the gas response in dependence of OPT for two sensor types, namely TA with temperature ramp of 40 °C/min and 3.40 °C/min, respectively. For CuO from Figure S7(a), an increase above 47% at OPT of 200 °C can be observed in the gas response for acetone vapor, but at higher OPT it decreased below 7%. Thus, such sample sets are more selective to acetone at OPT range 150-200 °C. As well as, response to *n*-Butanol vapors increased to about 40% at OPT range 250-300 °C. It means that for sample with ramp of 40 °C/min by using different OPT can be controlled selectivity or changed from acetone at 200 °C to *n*-Butanol vapor at 300 °C. These responses were calculated by using formula ($S = \frac{R_{gas} - R_{air}}{R_{air}} * 100\%$). Figure S7b is the gas response of sensor structure CuO with ramp of 3.40 °C/min at four different OPT of 150 °C, 200 °C, 250 °C and 300 °C, it can be seen that at 300 °C the response value is higher. Figure S7b shows a diagram of the gas response values to acetone obtained for such CuO is higher at all OPT with respect to *n*-Butanol. It should be pointed out that gas response to acetone was increased for such samples to about 23 % at OPT of 150 °C. Figure S7c-d shows the current-voltage curves in dependence of thermal annealing temperature ramp of 40 °C/min and 3.40 °C/min for sensor types sample set, respectively. Measurements were realized on several sensor structures which all demonstrate the same Ohmic behavior.

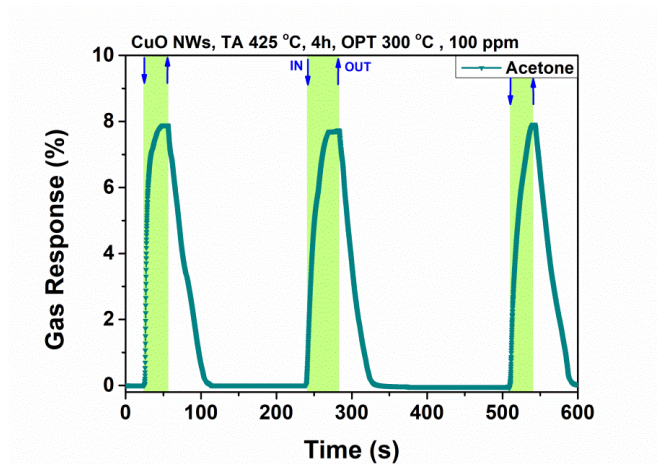


Figure S8. Dynamic gas response at OPT of 300 °C to acetone vapor with concentration of 100 ppm for CuO nanowire nets treated TA at 425 °C for 4 h.

Figure S8 shows dynamic gas response at OPT of 300 °C to acetone vapor with concentration of 100 ppm for CuO nanowire nets treated TA at 425 °C for 4 h with response ramp of about 40 °C/min with $\tau_r = 6.8$ s and $\tau_d = 76.4$ s, respectively.

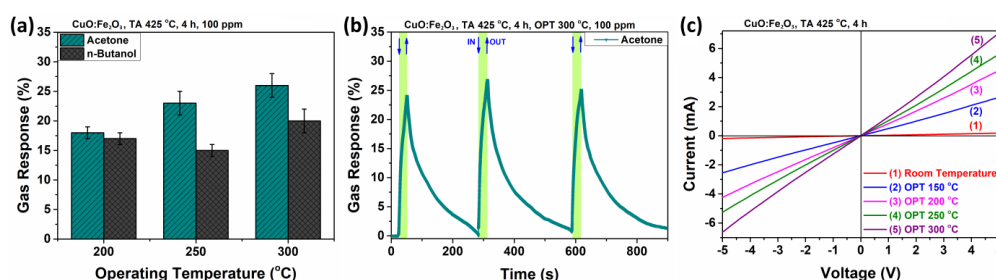


Figure S9. Gas response to 100 ppm of acetone and *n*-Butanol vapors (as volatile organic compounds) for the nanowire-nanospikes CuO:Fe₂O₃ heterojunction stripes thermally annealed at: (a) 425 °C for 4 h. (b) Dynamic response to 100 ppm of acetone vapors for nanowire CuO:Fe₂O₃ heterojunction stripes. (c) current-voltage characteristics of CuO:Fe₂O₃ sensors at different operating temperatures.

Figure S9a presents the gas response in dependence of different OPT in the range 200 °C to 300 °C of CuO:Fe₂O₃ heterojunction stripes used for the sensor devices at and an increase can be seen in gas response from OPT of 200 °C versus 300 °C for CuO:Fe₂O₃. Thus, by mixing Cu with Fe microparticles in such samples it is possible to maintain the response at higher OPT, too. Figure S9b shows the dynamic vapor response (under 100 ppm acetone) of CuO:Fe₂O₃ heterojunction net, thermally annealed nanostructured oxide. The response and recovery range is slightly increased. Figure S9c shows current-voltage characteristics of CuO:Fe₂O₃ sensor at different operating temperatures. Measurements were realized on several sensor structures which all demonstrate the same behavior.

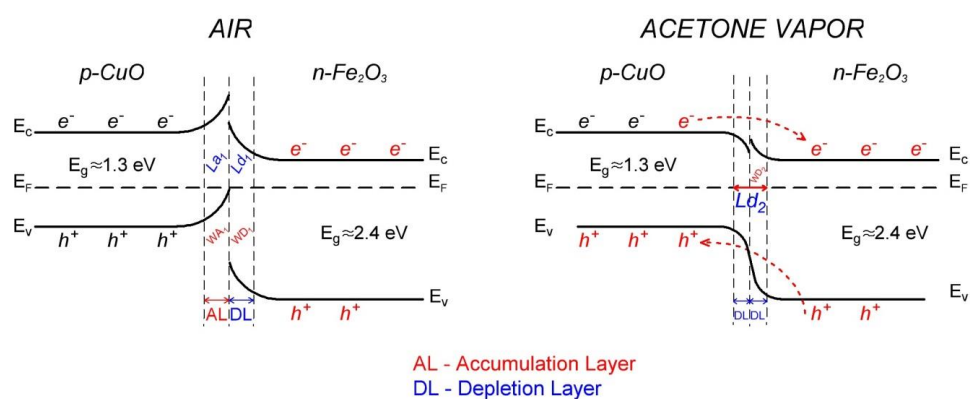


Figure S10. Schematic energy band diagrams of 3D CuO/Cu₂O/Cu - Fe₂O₃/Fe heterojunction nano structures indicating potential barrier formed at the interface between nanowires-nanospikes upon exposure to air and then to acetone vapor.

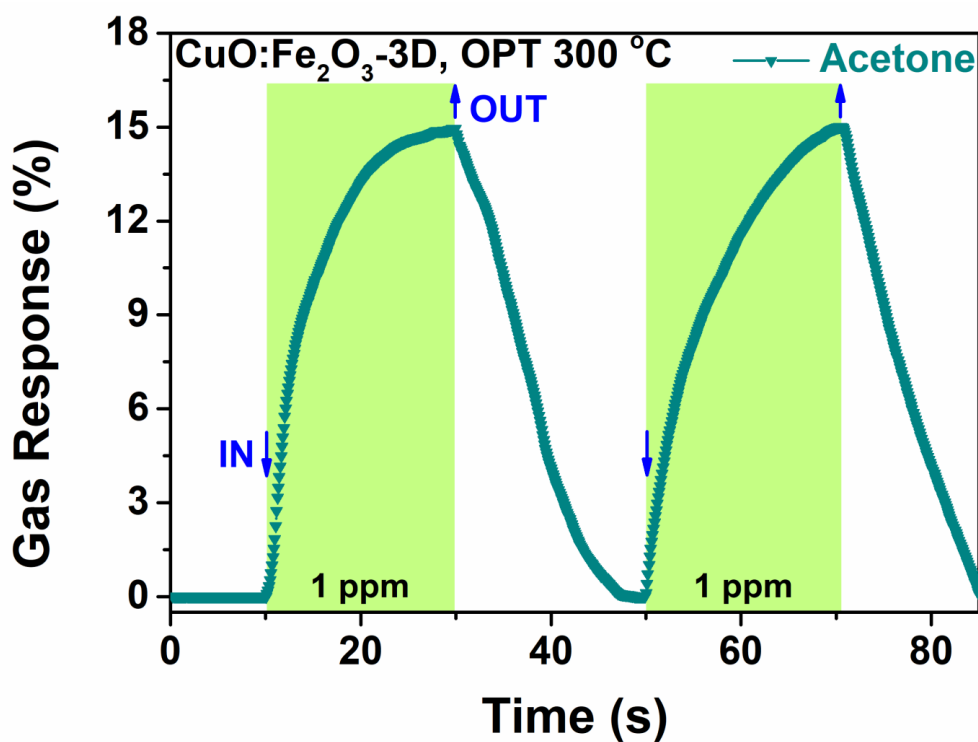


Figure S11. Dynamic response to 1 ppm of acetone vapors of CuO/Cu₂O/Cu and Fe₂O₃/Fe based sensor structure.

Figure S11 shows the typical dynamic response curves of the 3D-printed stripes exposed to 1 ppm of acetone in air. The response is about 14% with response and recovery times of $\tau_r = 11.1$ s and $\tau_d = 10.3$ s, respectively.

Chapter 10

Mechanochromic Microfibres Stabilised by Polymer Blending

An immediately obvious optical response to mechanical stress is important for many applications. Complex and important parts of vital machines like aeroplanes must be damage-free under all circumstances. The necessary costs and effort to detect by common methods such as ultrasonic testing however is a burden for manufacturers and service alike. A self-reporting material could warn of occurred or impending damage and would be highly desired. Mechanochromic materials can help to overcome this problem. They are specially designed to change their colour when enough stress is applied in a specific way. Spiropyranes are among the most prominent materials and are used in this work covalently bound to a poly(methyl acrylate) (PMA) backbone. The resulting soft polymer is blended with the stiff poly (methyl methacrylate) (PMMA) to increase the mechanical properties and allowed spinning microfibres by centrifugal spinning. The resulting microfibres were tested for their self-reporting capabilities and mechanical properties. Different blend ratios have been tested and investigated for their spinning behaviour.

The results have been published in the journal "ACS Applied Polymer Materials".

Own contribution presented in this article

- Design and setup of the centrifugal spinning machine
- Discussion and interpretation
- Writing and editing of the manuscript

The following content in this chapter is reproduced with permission.

Mechanochromic Microfibers Stabilized by Polymer Blending

Ruchira Colaco, Sindu Shree, Leonard Siebert, Clement Appiah, Mathias Dowds, Sven Schultzke, Rainer Adelung,* and Anne Staubitz*

Cite This: <https://dx.doi.org/10.1021/acsapm.0c00213>

Read Online

ACCESS |

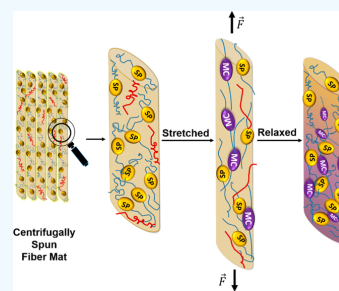
Metrics & More

Article Recommendations

Supporting Information

ABSTRACT: Stimuli-responsive polymers processed into microfibers bear the potential to be fabricated as systems detecting stress-induced failures. Microfiber processing of spiropyran (SP)-functionalized polymer poly(methyl acrylate) (PMA), in pristine form and as a blend with poly(methyl methacrylate) (PMMA), was studied. Material inhomogeneities such as bead formation and fiber–fiber fusion affected the durability of the microfibers which were aimed to be applied as self-reporting materials. The present study investigates the effect of polymer blending to improve the structural stability, i.e., the shape of the fibers compared to the nonblended PMA fibers (NBF). Blended microfibers (BF) with <4 wt % PMMA could overcome the structural malfunctions observed in NBF. Rheological analyses confirmed that there were no drastic alterations in the mechanical properties due to blending with a low amount of PMMA. We report the mechanoactivation in the structurally stable and durable BF processed via centrifugal force spinning (CFS). These fibers detected high strain deformations and retained the mechanochromic response after unloading. The color change in the BF confirms strain-induced isomerization of SP which will further assist in the visual inspection of damage before failure. The microfibers also showed reversible photochromism upon irradiation with ultraviolet (UV) light (360–370 nm) and green light (520–530 nm). The outstanding benefit of processing microfibers from polymer blends is the ease of obtaining structurally stable, self-reporting material with longer durability.

KEYWORDS: blended microfibers (BF), centrifugal force spinning (CFS), mechanochromic, nonblended microfibers (NBF), poly(methyl acrylate) (PMA), poly(methyl methacrylate) (PMMA), spiropyran (SP)



INTRODUCTION

Self-reporting polymers have garnered a growing interest in the past decade due to their ability to signal material failures.^{1–5} The polymers are functionalized with chemical species known as *mechromes*, which impart a stress sensing ability by altering their optical properties in response to the induced force.^{6–8} Spiropyran (SP), which is yellow to colorless, is the best researched stimuli-responsive specie that reversibly isomerizes to the highly colored, purple merocyanine (MC) form.^{9–12} SP is the primary choice for syntheses of a wide range of functional polymers as the switching properties are retained when incorporated either covalently or noncovalently.^{1,3,8,13–16} SP has been reported to respond to light and impact force in polymeric materials when dispersed in an amount as low as 0.5 wt %.^{16,17} Additionally, a wide range of SP-doped polymers such as poly(L-lactic acid) (PLLA),¹⁸ poly(methyl methacrylate) (PMMA),¹⁹ and poly(methacrylic acid) (PMAA)²⁰ have been fabricated into microfibers. Because of the random distribution of mechanochromes in the material, the above studies focused mainly on the fabrication processes and the photochromic sensitivity of the microfibers. For effective force translation from polymer chains to the molecular switch, covalent functionalization in the elastomeric poly(methyl acrylate) (PMA) polymer showed

effective mechanoactivation.² The optimum macroscopic force should align the polymer chains as well as sufficient number of SP in the direction of the applied force, which can be further isomerized to MC.^{14,17}

Further processing of functional polymers into nano- or microfibers adds unique structural characteristics such as high surface to volume ratio and porosity in the materials.^{19,22} The synergy of the mechanochromic and structural properties has the potential to enhance the existing applications of fibers, which are widely used in textiles,¹⁹ membranes,²³ scaffolds in tissue engineering,^{24–26} and as reinforcements in composite materials.²⁷ Only a limited number of SP-functionalized polymeric microfibers have been assessed for their mechanochromic activity. One such study reported the low-strain mechanoactivation in nanofibers with SP in the repeating unit of a brittle polymer.²⁸ The efficient color change was due to

Received: March 5, 2020

Accepted: April 10, 2020

Published: April 10, 2020

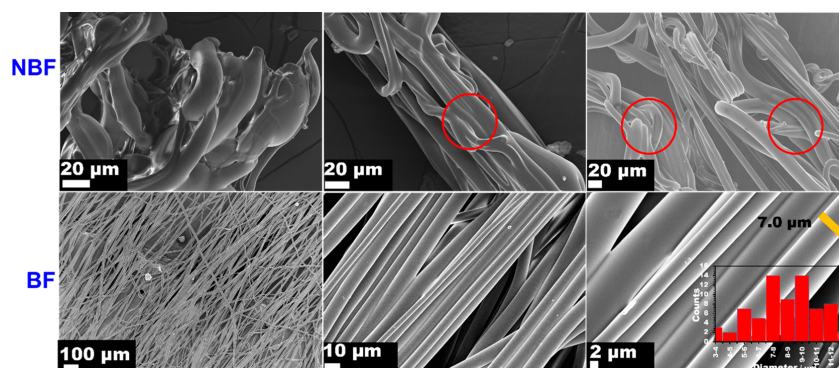


Figure 1. Top: SEM images of the nonblended fibers (NBF) of PMA in 22, 25, and 33 wt % concentration (left to right). Bottom: bead-free SEM images of blended fibers (BF) having 3 wt % PMMA with increasing magnification (inset: histogram plot indicating fiber diameter distribution of BF). The fibers were spun at 5000 rpm from a 0.20 mm diameter nozzle. The regions marked (red) show the fused NBF and (yellow) point out a single fiber diameter of the BF.

the high amount of SP, in turn making it a highly expensive method. For the large-scale applications of mechanochromic materials for damage identification, cost effectivity is integral.¹⁷

The focus of the research presented here was placed on mechanochromic sensitivity in blended microfibers. The functionalized PMA polymer had a single SP in the long polymer chain. The high-throughput processing of fibers was performed by using a self-designed centrifugal force spinning (CFS) machine. The method of polymer blending with PMMA was used to overcome structural inhomogeneities in the PMA fibrous network due to its low glass transition temperature (T_g). An easy, low-cost method was developed to fabricate structurally stable microfibers with longer durability. Finally, the response of the fibers to mechanical force and UV irradiation was studied to demonstrate their use as self-reporting fibers (SRF).

RESULTS AND DISCUSSION

Polymer Blending for Structurally Stable Microfibers.

The microfibers obtained from pure SP-functionalized PMA are labeled as nonblended fibers (NBF) and from the blend of PMA with PMMA as blended fibers (BF). The detailed fabrication process is reported in the [Materials and Methods](#) section. All fibers were examined under a scanning electron microscope (SEM). The outcome of the centrifugal force-spinning (CFS) process has been observed to produce either beads only, fused fibers, or the desired bead-free fibers.^{29,30} The NBF processed from PMA were either beads only at low concentration (<20 wt %; see [Figure S1](#)) or deformed due to fiber–fiber fusion at higher concentrations (20–33 wt %) ([Figure 1](#), top).

Additional increase in the concentration above 33 wt % limited the laminar volumetric flow at the smallest nozzle diameter (0.15 mm) due to the Hagen–Poiseuille law, whereas the larger sized nozzle (0.20 mm) gave thicker fibers (see [Figure S2](#)).³¹ Therefore, the solution optimization shows reduced bead formation but increased fiber fusion. Such deformations in fibers may be due to the incomplete solvent evaporation, which is crucial for high quality fibers and takes place in two stages. First, the mass transfer of the solvent takes place at the surface of the jet in flight, before reaching the

collectors. Second, the remaining solvent diffuses into the polymer matrix and evaporates post-fiber formation.³² However, the thermogravimetric analyses (TGA) of the NBF fibers (see [Figure S3](#)) showed no sign of residual solvent in the fibers.

Therefore, we suspected that the low glass transition temperature (T_g) of the elastomeric PMA (14–17 °C)³¹ might be a reason for the structural degradation in the fibers (see [Figure S4](#)). Because of this, even at a higher polymer concentration (33 wt %), fiber–fiber fusion ([Figure 1](#), bottom) could not be avoided due to the intrinsic property (low T_g) of PMA. To enhance the durability and impart structural stability, the PMA was blended with PMMA. Atactic PMMA has a T_g of 106–114 °C,³¹ which should stabilize the structural integrity of the fibers at ambient temperatures. The T_g of the commercially purchased PMMA was measured to be 110 °C (see [Figure S5](#)). The SEM analyses of the BF clearly revealed a bead-free fiber matrix ([Figure 1](#), bottom, and [Figure S6](#)). They were structurally stable and showed no fiber–fiber deformation in comparison to the NBF. Addition of PMMA up to merely 3 wt % reduced the skeletal deformities compared to fibers from pure PMA solutions. For further applications of the fibers as a self-reporting composite layer,²⁸ a stable structure and the durability of microfibers are essential, which according to our knowledge has not been investigated. A comparison between the fiber matrix of NBF and BF immediately after the spinning process and after a year is shown in [Figure 2](#). The NBF matrix coalesced into bulk, in contrast to the well retained fibrous network of the BF. The fiber fusion in NBF as previously seen in ([Figure 1](#), top), escalated into deterioration of the entire microscopic structure over time. The optical images after day 400 of NBF showed only a reminiscent thick fiber strand at the sample border. Coalescence of the NBF occurred due to environmental conditions such as temperature and humidity. The NBF lost their characteristic shape and structure due to low T_g , which is an intrinsic property of the polymer. This limits the utilization of the material as self-reporting fibers, although the polymer is SP functionalizable and also processable into microfibers. On the other hand, the BF shows a structurally stable fiber matrix. The stable and durable BF are promising candidates to investigate the mechanochro-

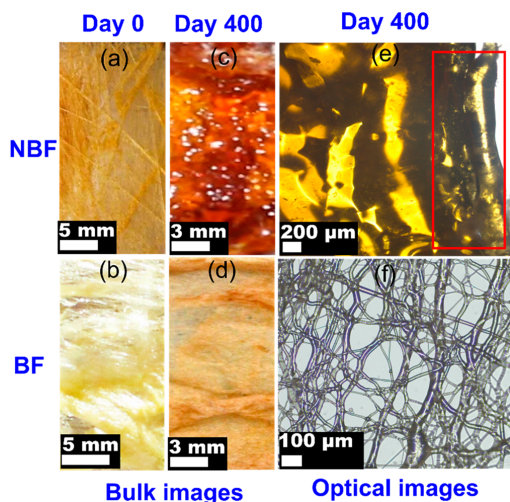


Figure 2. Bulk and optical images of nonblended fiber (NBF) and blend fibers (BF), respectively. (a, b) Digital images after spinning (day 0) and (c, d) after day 400. (e, f) Optical images after day 400 of NBF and BF, respectively. The optical images were taken under identical conditions.

mic effect as they retain the microscopic fiber network in contrast to the NBF

Mechanochromism of Blended Fibers. To examine the mechanochromic activation in polymers, the orientation of mechanophores in the direction of the applied force is pivotal.¹⁴ Aligned molecular chains are ideal to mechanically induce isomerization of SP covalently incorporated in the polymer backbone.¹⁴ Force translation to the mechanophore was induced by an uniaxial tensile force applied parallel to the aligned BF (Figure 3). The fibers ($l_0 = 25$ mm) were stretched in the tensile test apparatus by using a 10 kN load cell at the rate of 1 mm/s. Several methods of sample preparation had to be optimized to overcome fiber breakage and slippage from clamping sites (see Figures S7 and S8). For every cycle, the elongation was increased by 20 mm, and the sample was cycled between the extended position and the reference position. With increasing strain, necking was observed in the fibers (see Figures S9 and S10). Consequently, the microfibrils underwent excessive thinning, rendering the detection of color change with bare eyes. After an elongation of 145 mm, i.e., 480% strain, the first appearance of color change from yellow to light pink could be visually identified in the relaxed sample (see the marked area in Figure 3a). The mechanochromic response suggests sufficient alignment of polymer chains in the direction of the applied force. As the polymer was amorphous, the initial chain alignment may be correlated to the yielding strength of the fibers. Beyond the yielding point, plastic deformation sets in and the fibers do not recoil to the original position.

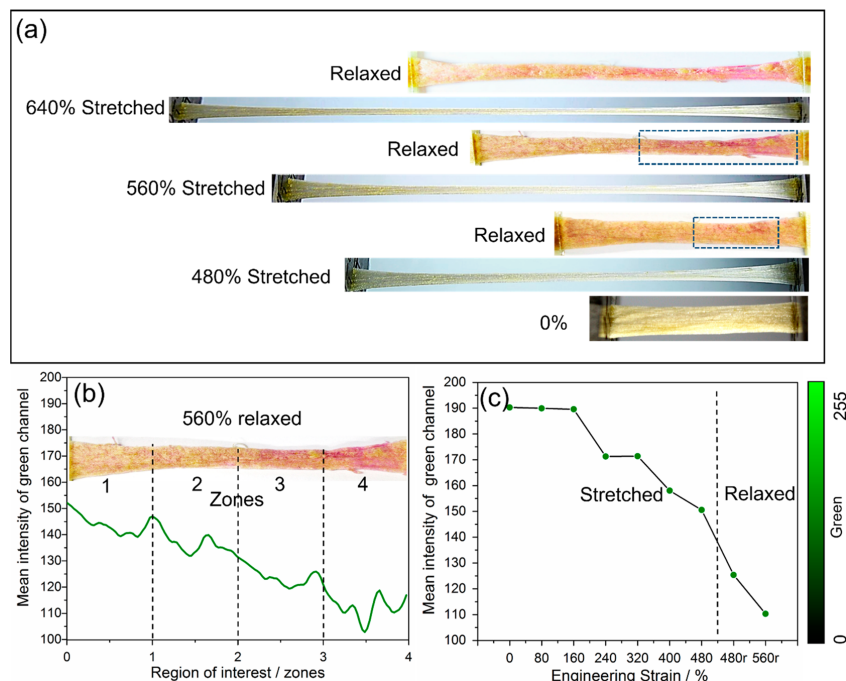


Figure 3. (a) Mechanochromic response of BF visible to the bare eye after an elongation of 480%, 560%, and 640%. (b) Mean intensity of green channel (I_g) by ImageJ analysis of 560% relaxed sample divided in four zones. (c) I_g values from zone four of fibers stretched from 0% to 480% (for the images of periodic elongation of the fibers, see Figure S8) and of the relaxed samples 480r and 560r.

C

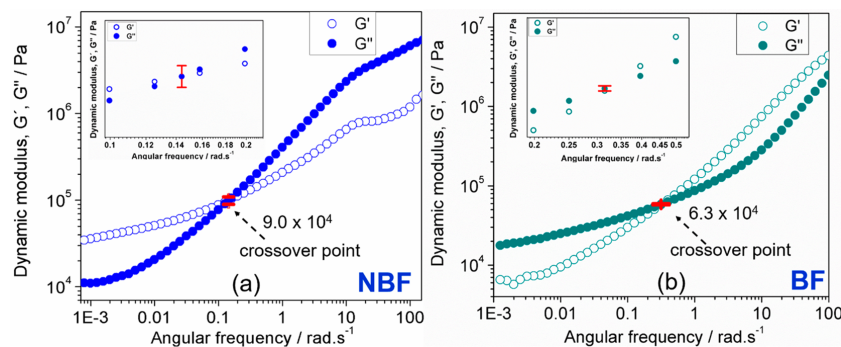


Figure 4. (a, b) Frequency dependence of the storage (G') and loss (G'') moduli at 25 °C for the NBF and BF (inset: plot of error bar for the crossover point of NBF and BF).

To demonstrate the robustness at higher deformations, the BF were further stretched to 165 mm, i.e., 560%. The relaxed sample showed enhanced color change in the bottom half of the sample (see marked area in Figure 3a). The elongation cycles were continued until 185 mm, i.e., 640% (Figure 3a), withstanding cyclic loading up to five times before failure. The fibers were further stretched until breaking point, where even the fragments had switched and retained the color visible to the bare eye, postrupture (see Figure S9). Thus, we conclude that BF makes an ideal stress indicator over a wide range of elongations. Such a system has the potential to be applied as a self-reporting material before failure.

For comparison and analyses of the mechanochromic response, the relaxed sample after 560% elongation was divided into four zones (Figure 3b). Visually, the indication of color change to deep pink is most prominent in the zones three and four of the sample relaxed after 560% elongation. The mechanochromic analyses of a polymeric matrix reported the sensitivity of the green channel (among the RGB channel) to record strain induced color change of SP from yellow to pink.¹⁷ Considering this, the mechanoactivation in the BF was also investigated in relation to the mean intensity of the green channel (I_g) by using the ImageJ software (for details see the Supporting Information). A plot of the change in the I_g values across the four zones of 560% relaxed sample was traced and provided with a standardized green color bar for reference (Figure 3b). The I_g values across the zones (one to four) demonstrated a gradual decrease in the mean intensity which related to a greater amount of chain alignment. The lowest I_g value correlated to the distinct and enhanced color change in zone four of the sample (Figure 3b). The extent of damage at higher deformations in the BF was thus clearly evident by the change in the I_g values and by visual inspection of the fibers. This raised the question of whether mechanoactivation of SP to MC sets in before 480% strain, which could not be visually detected. To qualitatively trace the development of mechanoisomerization, the I_g values of zone four were tracked and plotted in relation to the induced elongation from 0% to 480% (Figure 3c).

For the initial extensions from 0% to 160%, the I_g values recorded were constant, suggesting that the force was utilized to align the polymer chains of the fibers in the direction of the applied stress (Figure 3c). The effect can be attributed to the role of chain entanglement, which is a dominant prerequisite

for processing a bulk polymer into microfibers.¹⁴ As the strain increased from 160% to 320%, a stepwise drop in the I_g value was observed, illustrating further orientation of the polymer chains in the direction of the applied stress.¹⁷ Similarly, with increase in the induced strain, the intensity profile displays a gradual drop until 480% in the stretched sample. This demonstrates that the force was sufficient to induce SP to MC mechanoisomerization at 480% elongation, which was difficult to observe in the stretched state due to excessive thinning of the sample. The retention of the color change in the relaxed state makes fibers applicable in detecting mechanically induced deformations even after unloading the stress.

Rheology of Microfibers. To study the influence of PMMA blending on the mechanical properties of the functional PMA polymer, room temperature rheological measurements were investigated. The frequency-dependent storage (G') and loss (G'') moduli were compared between the NBF (33 wt %) and BF consisting PMMA (3 wt %), respectively (Figure 4). All other BF (1–5 wt %) showed the same viscoelastic behavior (see Figure S11). It was found that the mechanical response of the blends was dominated by G' at low angular frequency (elastic part, $G' \gg G''$) and by G'' at higher angular frequency (viscous part, $G'' \gg G'$) presenting them as viscoelastic systems. A viscoelastic transition regime ($G' \approx G''$) was identified between angular frequencies of 0.1–1 rad/s. The viscoelastic transition regime (crossover point) increases slightly from 1 wt % PMMA to 5 wt % PMMA incorporation (see Figure S11). It is worth mentioning that the blends showed no Newtonian flow at low frequencies. A plateau was not clearly observed at low frequencies for the complex viscosity (see Figure S11); however, an ever increasing viscosity as the frequency approaches zero was observed. This implies the blends do not flow, but are rather solid like material.

As previously investigated by Callies et al.,³³ increasing the concentration of a material within the stoichiometric polymer mixture should induce a more elastic behavior at small deformations and a stronger cohesion at large deformations (general theory of rubber elasticity).³³ Thus, if the introduction of the different PMMA had a significant influence on the concentration of the blends, then an expected change in the elastic modulus (G') of the blends at lower frequencies with the increasing wt % of the PMMA fraction should be

D

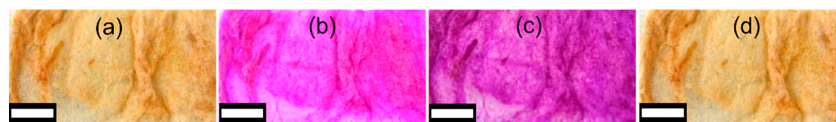


Figure 5. Digital image of BF indicating reversible switching between SP to MC (a) before irradiation, (b) during UV irradiation, (c) after UV for 5 min on each side, and (d) after green irradiation for 3 min on each side (white scale bar = 3 mm).

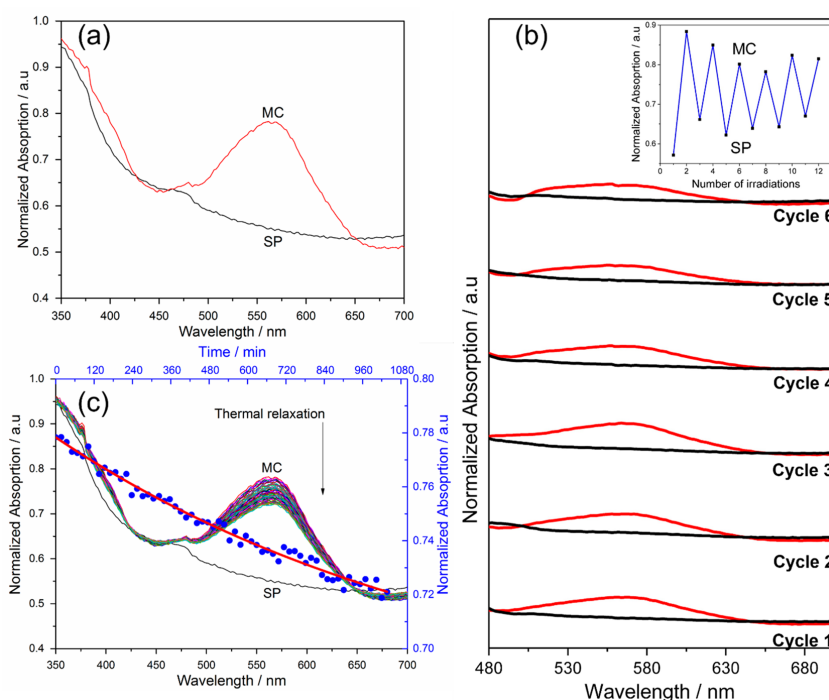


Figure 6. (a) UV-vis absorption spectra of the BF fibers for the open MC form (red line) and the closed SP form (black line) on irradiating with UV light and green light on each side for 5 and 3 min, respectively. (b) SP and MC absorption UV-vis absorption spectra peaks for six cycles. Inset is the absorption intensity (at $\lambda_{\max} = 564$ nm) from the cyclic measurements. (c) Thermal relaxation of MC-SP was monitored for 17 h after irradiating the sample with UV light for 5 min on each side. The absorption values ($\lambda_{\max} = 564$ nm) are fitted exponentially (red line with blue spots) to procure the half-life time of the fibers.

noticeable in Figure 4. However, according to Figure S11, no significant change in the modulus of the blends was observed with increasing PMMA wt %. This implies that the fraction of the PMMA from 1 to 5 wt % was insignificant to cause any major difference in the modulus of elasticity of the polymer blends. The absolute values of G' for all the blends are within the orders of magnitude of 10 kPa. This equivalence value of magnitude of modulus for all the blends is an indication that the mechanical properties (modulus of elasticity) of the blends were not modified on PMMA introduction.

Photochromism in Microfibers. The photochemical studies of the BF fiber mat were performed by UV illumination to isomerize the closed SP moieties and convert them to their open MC isomer.¹ The transformation of SP to MC is due to the cleavage of the heterolytic C–O bond,¹⁰ giving rise to an intense color change from light yellow to purple in the fibers (Figure 5). The isomerization is also plausible from the

fluorescence of the MC form observed during UV irradiation.¹⁰ The highly colored MC form (Figure 5c) switches back to light yellow coloration upon irradiation with green light (Figure 5d).

The formation of the highly colored, open-ring MC form is a result of the extended conjugation of the π -system, shifting the characteristic absorption into the visible region ($\lambda = 550$ – 570 nm) (Figure 6a). On illumination with green light, the MC signal ($\lambda_{\max} = 564$ nm) disappeared, which confirmed MC to SP back-switching behavior in the fibers (Figure 6a).

Spiropyrans undergo photodegradation when subjected to multiple back and forth UV and green light irradiations.^{10,34} To examine the cyclic photochemical activity of SP in fibers, the BF fibers were illuminated with alternating UV and green light for six cycles, and the corresponding spectra were measured after each irradiation (Figure 6b). The inset in Figure 6b represents absorption intensities recorded at 564 nm

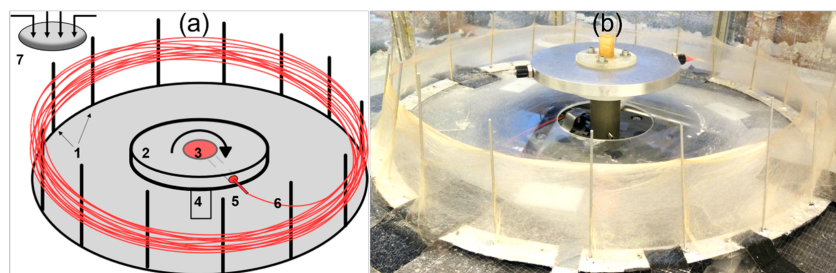
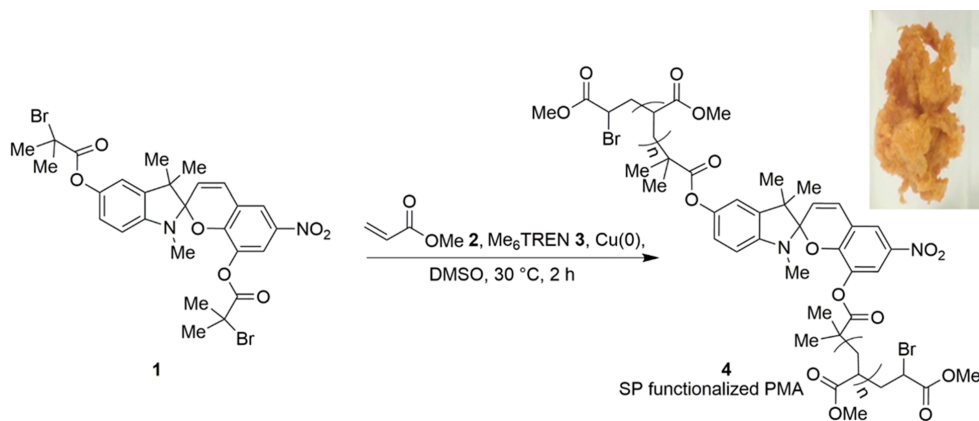
Scheme 1. Synthesis of the Mechanophore-Linked Polymer PMA via the ATRP Method³

Figure 7. (a) Schematic and (b) self-designed centrifugal spinning machine: (1) radially placed collector rods; (2) spinneret; (3) solution injection inlet and reservoir; (4) DC motor; (5) junction for nozzle attachment; (6) fibers; (7) exhaust to remove the solvent vapors produced during spinning.

to verify the photochemical stability of the molecular switch in the fibers. There was no substantial photodegradation detected in the fibers for 12 irradiations. The reversible ring-closing reaction from MC to SP can also occur via spontaneous thermal relaxation over time (Figure 6c).³⁴ The thermal back-conversion of MC to SP was monitored for 17 h after irradiating the fibers with UV light for 5 min on each side. At an interval of every 17 min, absorption spectra were recorded at 20 °C (Figure 6c). The study revealed a very gradual decrease in the absorption intensity with time. After 17 h of thermal relaxation, the intensity of absorption was reduced by 20% from that measured at 0 h, indicating slow transformation of the specimen toward the photostationary equilibrium. The exponential decay revealed a half-life time of $\tau = 15 \text{ h } 12 \text{ min} \pm 3 \text{ h}$. As a result, this system was well-suited to retain the color change and communicate the damage of UV light treatment in fibers for a substantial amount of time.

MATERIALS AND METHODS

If not stated otherwise, all chemicals were commercially available, of analytical grade, and used without further purification. The monomer methyl acrylate (MA, 99%, inhibitor MEHQ (100 ppm)) was purchased from Sigma-Aldrich Ltd., and the poly(methyl methacrylate) (PMMA, $M_n = 100 \text{ kDa}$, a colorless coarse powder) was purchased from Kunststoff-und Farbensgesellschaft mbH. For the list

of chemicals with purity and supplier, see Tables S1 and S2 in the Supporting Information.

The covalent incorporation of SP into the polymer backbone of PMA was performed with the spiroyranyl-functionalized α -bromoester **1** (Scheme 1), as an initiator. Using methyl acrylate (MA) as the monomer (2), elemental copper as transition metal catalyst Cu(0), and the ligand tris[2-(dimethylamino)ethyl]amine (Me₆TREN) (3), we performed the atom transfer radical polymerization (ATRP) in dimethyl sulfoxide (DMSO) as the solvent at 30 °C.² The synthetic route^{1,3} of the precursor molecules to **1** is shown in Scheme S1. For the details of all the analytical instruments used for characterization, see the Supporting Information. All experimental procedures with the corresponding chemical characterizations (¹H NMR, ¹³C {¹H}NMR, IR, and HRMS (EI-TOF)) and the melting points from DSC measurements are given in the section 9 of the Supporting Information. The corresponding DSC plots, GPC plots, and ¹H NMR and ¹³C {¹H}NMR plots of the synthesized products are given in sections 10–12 of the Supporting Information, respectively.

Microfiber Processing. In CFS (Figure 7), a concentrated polymer solution is rapidly ejected through a rotating nozzle, and the fibers are collected on the radially placed rods. During the spinning process, both the centrifugal force and the air frictional force act on the solution.²⁷ However, only when the rotating speed exceeds a critical value does the centrifugal force overcome the surface tension of the solution, and the liquid jet is ejected from the nozzle tip. The solvent evaporates in flight, and the polymer fiber is finally caught on the collector rods.²⁹ The fiber characteristics such as fiber diameter and morphology depend on the fluid properties such as viscosity and

ACS Applied Polymer Materials

pubs.acs.org/acscapm

Article

solution concentration as well on the operating parameters, namely nozzle–collector distance, nozzle diameter, and rotating speed.³⁵

The nonblended polymer solutions were processed into fibers by using a self-designed centrifugal spinning machine at 5000 rpm equipped with a 0.15 or 0.20 mm diameter nozzle (Figure 7).

Fluid properties such as solution viscosity, concentration, surface tension along with the rotational speed, and the centrifugal force acting on the solution jet predominantly influence the resulting fiber morphologies.²⁹ The type of morphology obtained can be correlated to the polymer solution concentration spun at a constant rotational speed.³⁰ Therefore, the concentrations (wt %) of the polymer solutions were controlled and optimized to yield uniform and bead-free microfibers at a rotational speed of 5000 rpm through the smallest nozzle diameter (0.15 mm) available. For the PMA solutions, it was observed that the low-concentrated solutions (11, 15, and 18 wt %) spun into a beads-only network (see Figure S1). It has been shown in the literature that a low polymer concentration and hence low viscosity are insufficient to achieve the critical chain entanglement, essential for spinning bead-free fibers.³⁰ To reduce the bead formation, the viscosity and thereby the polymer chain entanglement were increased by using higher solution concentration. The increase in concentration to 22 wt % changed the fiber morphology from beads-only to beaded-fibers; however, multiple fibers fused together on contact with other fibers. Additional operating parameters are given in section 4, Supporting Information.

CONCLUSIONS

In conclusion, using the high production rate technique of CFS, we fabricated bead-free and aligned fiber mats from polymer blends. The blend constituted of a mechanophore-linked polymer PMA imparting the switching functionality and PMMA to improve structural stability of the fibers. The method of polymer blending reduced the physical deformations in fibers of functional polymer PMA by merely adding up to 3 wt % PMMA. Most importantly, the blended microfibers (BF) were structurally stable and durable over a year. Stimuli-responsive properties of SP were successfully imparted in the resulting blend, and active mechanochemical and photochemical isomerization of SP to MC was observed. The BF withstand high pre-elongations of ~480%, after which uniform switching was observed with a color change ideal for visual inspection. The fibers reversibly respond to UV and green light for at least six cycles with negligible photodegradation, making it suitable for sensing history of light exposure. Such structurally stable BF may have exceptional applications as durable components in composite materials for active stress monitoring.

ASSOCIATED CONTENT

Supporting Information

The Supporting Information is available free of charge at <https://pubs.acs.org/doi/10.1021/acscapm.0c00213>.

Spectroscopic data, GPC data, and thermal analyses of all compounds and polymers; tensile sample preparation, SEM, and rheology data of microfibers (PDF)

AUTHOR INFORMATION

Corresponding Authors

Rainer Adelung – Institute for Materials Science, Functional Nanomaterials, Kiel University, 24143 Kiel, Germany;
Email: ra@tf.uni-kiel.de

Anne Staubitz – Institute for Organic and Analytical Chemistry and MAPEX Center for Materials and Process, University of Bremen, 28359 Bremen, Germany; Institute for Materials

Science, Functional Nanomaterials, Kiel University, 24143 Kiel, Germany; orcid.org/0000-0002-9040-3297;
Email: staubitz@uni-bremen.de

Authors

Ruchira Colaco – Institute for Organic and Analytical Chemistry and MAPEX Center for Materials and Process, University of Bremen, 28359 Bremen, Germany; orcid.org/0000-0002-5317-9273

Sindu Shree – Institute for Organic and Analytical Chemistry, University of Bremen, 28359 Bremen, Germany; Institute for Materials Science, Functional Nanomaterials, Kiel University, 24143 Kiel, Germany

Leonard Siebert – Institute for Materials Science, Functional Nanomaterials, Kiel University, 24143 Kiel, Germany;
orcid.org/0000-0001-5316-7240

Clement Appiah – Institute for Organic and Analytical Chemistry and MAPEX Center for Materials and Process, University of Bremen, 28359 Bremen, Germany

Mathias Dowds – Otto-Diels-Institute for Organic Chemistry, University of Kiel, 24098 Kiel, Germany

Sven Schultzke – Otto-Diels-Institute for Organic Chemistry, University of Kiel, 24098 Kiel, Germany

Complete contact information is available at:

<https://pubs.acs.org/10.1021/acscapm.0c00213>

Notes

The authors declare no competing financial interest.

ACKNOWLEDGMENTS

This work was funded by the German Research Foundation (DFG) in the context of the Collaborative Research Center 677 “Function by Switching”, Project C14. C.A. and A.S. also thank the Volkswagen (VW) Foundation for their support with the Project 93416.

REFERENCES

- Lee, C. K.; Davis, D. A.; White, S. R.; Moore, J. S.; Sottos, N. R.; Braun, P. V. Force-Induced Redistribution of a Chemical Equilibrium. *J. Am. Chem. Soc.* **2010**, *132* (45), 16107–16111.
- Davis, D. A.; Hamilton, A.; Yang, J.; Cremar, L. D.; Van Gough, D.; Potisek, S. L.; Ong, M. T.; Braun, P. V.; Martínez, T. J.; White, S. R.; Moore, J. S.; Sottos, N. R. Force-Induced Activation of Covalent Bonds in Mechanoresponsive Polymeric Materials. *Nature* **2009**, *459* (7243), 68–72.
- Potisek, S. L.; Davis, D. A.; Sottos, N. R.; White, S. R.; Moore, J. S. Mechanophore-Linked Addition Polymers. *J. Am. Chem. Soc.* **2007**, *129* (45), 13808–13809.
- Degen, C. M.; May, P. A.; Moore, J. S.; White, S. R.; Sottos, N. R. Time-Dependent Mechanochemical Response of SP-Cross-Linked PMMA. *Macromolecules* **2013**, *46* (22), 8917–8921.
- Caruso, M. M.; Davis, D. A.; Shen, Q.; Odom, S. A.; Sottos, N. R.; White, S. R.; Moore, J. S. Mechanically-Induced Chemical Changes in Polymeric Materials. *Chem. Rev.* **2009**, *109* (11), 5755–5798.
- O'Bryan, G.; Wong, B. M.; McElhanon, J. R. Stress Sensing in Polycaprolactone Films via an Embedded Photochromic Compound. *ACS Appl. Mater. Interfaces* **2010**, *2* (6), 1594–1600.
- Li, M.; Zhang, Q.; Zhou, Y. N.; Zhu, S. Let Spiropyran Help Polymers Feel Force! *Prog. Polym. Sci.* **2018**, *79*, 26–39.
- Sommer, M.; Komber, H. Spiropyran Main-Chain Conjugated Polymers. *Macromol. Rapid Commun.* **2013**, *34* (1), 57–62.
- Schulz-Senft, M.; Gates, P. J.; Sönnichsen, F. D.; Staubitz, A. Diversely Halogenated Spiropyran - Useful Synthetic Building Blocks

G

<https://dx.doi.org/10.1021/acscapm.0c00213>
ACS Appl. Polym. Mater. XXXX, XXX, XXX–XXX

for a Versatile Class of Molecular Switches. *Dyes Pigm.* **2017**, *136*, 292–301.

(10) Klajn, R. Spiropyran-Based Dynamic Materials. *Chem. Soc. Rev.* **2014**, *43* (1), 148–184.

(11) Minkin, V. I. Photo-, Thermo-, Solvato-, and Electrochromic Spiroheterocyclic Compounds. *Chem. Rev.* **2004**, *104* (5), 2751–2776.

(12) Berkovic, G.; Krongauz, V.; Weiss, V. Spiroprans and Spirooxazines for Memories and Switches. *Chem. Rev.* **2000**, *100* (5), 1741–1754.

(13) Schmidt, S. B.; Kempe, F.; Brügger, O.; Walter, M.; Sommer, M. Alkyl-Substituted Spiroprans: Electronic Effects, Model Compounds and Synthesis of Aliphatic Main-Chain Copolymers. *Polym. Chem.* **2017**, *8* (35), 5407–5414.

(14) Beiermann, B. A.; Kramer, S. L. B.; Moore, J. S.; White, S. R.; Sottos, N. R. Role of Mechanophore Orientation in Mechanochemical Reactions. *ACS Macro Lett.* **2012**, *1* (1), 163–166.

(15) Lee, C. K.; Beiermann, B. A.; Silberstein, M. N.; Wang, J.; Moore, J. S.; Sottos, N. R.; Braun, P. V. Exploiting Force Sensitive Spiroprans as Molecular Level Probes. *Macromolecules* **2013**, *46* (10), 3746–3752.

(16) Shree, S.; Schulz-Senft, M.; Alslieben, N. H.; Mishra, Y. K.; Staubitz, A.; Adelung, R. Light, Force, and Heat: A Multi-Stimuli Composite That Reveals Its Violent Past. *ACS Appl. Mater. Interfaces* **2017**, *9* (43), 38000–38007.

(17) Shree, S.; Dowds, M.; Kuntze, A.; Mishra, Y. K.; Staubitz, A.; Adelung, R. Self-reporting mechanochromic coating: a glassfiber reinforced polymer composite that predicts impact induced damage. *Mater. Horiz.* **2020**, *7*, 598–604.

(18) Kinashi, K.; Suzuki, T.; Yasunaga, H.; Tsuchida, H.; Sakai, W.; Tsutsumi, N.; Yamane, H. Carrier-Assisted Dyeing of Poly(L-Lactic Acid) Fibers with Dispersed Photochromic Spiropyran Dyes. *Dyes Pigm.* **2017**, *145*, 444–450.

(19) Doan, H. N.; Tsuchida, H.; Iwata, T.; Kinashi, K.; Sakai, W.; Tsutsumi, N.; Huynh, D. P. Fabrication and Photochromic Properties of Forcespinning® Fibers Based on Spiropyran-Doped Poly(Methyl Methacrylate). *RSC Adv.* **2017**, *7* (53), 33061–33067.

(20) De Sousa, F. B.; Guerreiro, J. D. T.; Ma, M.; Anderson, D. G.; Drum, C. L.; Sinisterra, R. D.; Langer, R. Photo-Response Behavior of Electrospun Nanofibers Based on Spiropyran-Cyclodextrin Modified Polymer. *J. Mater. Chem.* **2010**, *20* (44), 9910–9917.

(21) Black, A. L.; Lenhardt, J. M.; Craig, S. L. From Molecular Mechanochemistry to Stress-Responsive Materials. *J. Mater. Chem.* **2011**, *21* (6), 1655–1663.

(22) Deitzel, J. M.; Kleinmeyer, J.; Harris, D.; Beck Tan, N. C. The Effect of Processing Variables on the Morphology of Electrospun Nanofibers and Textiles. *Polymer* **2001**, *42* (1), 261–272.

(23) Yanilmaz, M.; Zhang, X. Polymethylmethacrylate/Polyacrylonitrile Membranes via Centrifugal Spinning as Separator in Li-Ion Batteries. *Polymers (Basel, Switz.)* **2015**, *7* (4), 629–643.

(24) Barnes, C. P.; Sell, S. A.; Boland, E. D.; Simpson, D. G.; Bowlin, G. L. Nanofiber Technology: Designing the next Generation of Tissue Engineering Scaffolds. *Adv. Drug Delivery Rev.* **2007**, *59* (14), 1413–1433.

(25) Ellison, C. J.; Phatak, A.; Giles, D. W.; Macosko, C. W.; Bates, F. S. Melt Blown Nanofibers: Fiber Diameter Distributions and Onset of Fiber Breakup. *Polymer* **2007**, *48* (11), 3306–3316.

(26) Li, W. J.; Laurencin, C. T.; Catterson, E. J.; Tuan, R. S.; Ko, F. K. Electrospun Nanofibrous Structure: A Novel Scaffold for Tissue Engineering. *J. Biomed. Mater. Res.* **2002**, *60* (4), 613–621.

(27) Huang, Z.-M.; Zhang, Y.-Z.; Kotaki, M.; Ramakrishna, S. A Review on Polymer Nanofibers by Electrospinning and Their Applications in Nanocomposites. *Compos. Sci. Technol.* **2003**, *63* (15), 2223–2253.

(28) Raisch, M.; Genovese, D.; Zaccheroni, N.; Schmidt, S. B.; Focarete, M. L.; Sommer, M.; Gualandi, C. Highly Sensitive, Anisotropic, and Reversible Stress/Strain-Sensors from Mechano-chromic Nanofiber Composites. *Adv. Mater.* **2018**, *30*, 1802813.

(29) Zhang, X.; Lu, Y. Centrifugal Spinning: An Alternative Approach to Fabricate Nanofibers at High Speed and Low Cost. *Polym. Rev.* **2014**, *54* (4), 677–701.

(30) Ren, L.; Pandit, V.; Elkin, J.; Denman, T.; Cooper, J. A.; Kotha, S. P. Large-Scale and Highly Efficient Synthesis of Micro- and Nano-Fibers with Controlled Fiber Morphology by Centrifugal Jet Spinning for Tissue Regeneration. *Nanoscale* **2013**, *5* (6), 2337–2345.

(31) Wen, J. Poly(Methyl Acrylate). *Polymer Data Handbook*; Oxford University Press: 1999; pp 641–644.

(32) Golecki, H. M. L.; Yuan, H.; Glavin, C.; Potter, B.; Badrossamay, M. R.; Goss, J. A.; Phillips, M. D.; Parker, K. K. Effect of Solvent Evaporation on Fiber Morphology in Rotary Jet Spinning. *Langmuir* **2014**, *30*, 13369–13374.

(33) Callies, X.; Véchambre, C.; Fonteneau, C.; Herbst, F.; Chenal, J. M.; Pensec, S.; Chazeau, L.; Binder, W. H.; Bouteiller, L.; Creton, C. Effects of Multifunctional Cross-Linkers on Rheology and Adhesion of Soft Nanostructured Materials. *Soft Matter* **2017**, *13* (43), 7979–7990.

(34) Paine, M. F.; Hart, H. L.; Ludington, S. S.; Haining, R. L.; Rettie, A. E.; Zeldin, D. C. *NIH Public Access.* **2008**, *34* (5), 880–886.

(35) Ren, L.; Ozisik, R.; Kotha, S. P.; Underhill, P. T. Highly Efficient Fabrication of Polymer Nanofiber Assembly by Centrifugal Jet Spinning: Process and Characterization. *Macromolecules* **2015**, *48* (8), 2593–2602.

Supporting Information

Mechanochromic Micro-fibers Stabilized by Polymer Blending

Ruchira Colaco,^{§, ¥} Sindu Shree,^{§, †} Leonard Siebert,[†] Clement Appiah,^{§, ¥} Mathias Dowds,[‡]

Sven Schultze,[‡] Rainer Adelung,^{†,} and Anne Staubitz^{§, ¥, †,*}*

§ University of Bremen, Institute for Analytical and Organic Chemistry, Leobener Straße 7, D-28359 Bremen, Germany

¥ University of Bremen, MAPEX Center for Materials and Processes, Bibliothekstraße 1, D-28359 Bremen, Germany

† Institute for Materials Science, Functional Nanomaterials, Kiel University, Kaiserstr. 2, D-24143 Kiel, Germany

‡ Otto-Diels-Institute for Organic Chemistry, University of Kiel, Otto-Hahn-Platz 4, D-24098 Kiel, Germany

AUTHOR INFORMATION

Corresponding Authors

*Rainer Adelung: ra@tf.uni-kiel.de

*Anne Staubitz: staubitz@uni-bremen.de; orcid.org/0000-0002-9040-3297

1. Abbreviations

ATRP	atom transfer radical polymerization
ATR	attenuated total reflection
BF	blended fibers
calcd	calculated
DCM	dichloromethane
DMAP	4- <i>N,N</i> -dimethylaminopyridine
DMSO	dimethylsulfoxide
DSC	differential scanning calorimetry
EI	electron ionization
ESI	electron spray ionization
GPC	gel permeation chromatography
G'	shear storage modulus
G''	shear loss modulus
HRMS	high resolution mass spectrometry
IR	infrared
I_{MC}	absorption intensity of MC
I_{SP}	absorption intensity of SP
MA	methacrylate
MC	merocyanine
Me ₆ TREN	tris[2-(dimethylamino)ethyl]amine
MEHQ	hydroquinone monomethyl ether
M_n	number average molecular weight
M_w	weight average molecular weight
NBF	non-blended fibers
PDI	polydispersity index
PMA	poly(methyl acrylate)

PMMA	poly(methyl methacrylate)
PTFE	poly(tetrafluoroethylene)
Py	pyridine
R_f	retention factor
RI	refractive index
SEM	scanning electron microscopy
SP	spiropyran
SPS	solvent purification system
SRF	self-reporting fibers
T_g	glass transition temperature
TGA	thermogravimetric analysis
THF	tetrahydrofuran
TLC	thin layer chromatography
TOF	time-of-flight
TREN	tris(2-aminoethyl)amine
UV	ultraviolet
UV-vis	ultraviolet-visible
wt %	weight percent

2. Chemicals and Solvents

All chemicals and solvents were commercially available and were used as received unless noted otherwise **Table S1**. The dry solvents were either purchased or dried with a solvent purification system (SPS), from Inert Innovative Technology, Inc. Company. Inert reactions were carried out using Schlenk techniques under a dry, inert nitrogen atmosphere. The copper catalyst was stored in the glove box from the Inert, Innovative Technology, Inc. Company (0.1 ppm O₂ and 0.1 ppm H₂O).

Table S1. List of supplies and purities of the solvents used.

Solvent	Supplier	Purity
Acetic acid	Grüssing	99.5%
Chloroform-d	Euriso-top	99.8% D
Dichloromethane	VWR	HPLC grade, dry from SPS
Dimethyl sulfoxide	VWR	HPLC grade, dry from SPS
Dimethyl sulfoxide-d ₆	Euriso-top	99.8%
Ethanol	Sigma-Aldrich	>99.8%
Ethanol (dry)	Acros Organics	99.5%, extra dry
Ethyl acetate	VWR	99.9%
<i>n</i> -Heptane	AlfaAesar	>99%
<i>n</i> -Hexane	Sigma-Aldrich	>99.9%, HPLC grade
Tetrahydrofuran	VWR	HPLC grade

If not noted otherwise, all reagents were used as received **Table S2**.

Table S2. List of supplies and purities of the chemicals used.

Reagent	Supplier	Purity	Comments
2-Bromo-2-methylpropionyl bromide	Sigma-Aldrich	98%	stored in the glove box
3-Methyl-2-butanone	TCI	99%	
4-Dimethylaminopyridine	Acros Organics	99%	
4-Methoxy-phenyl hydrazine hydrochloride	TCI	>98%	
Ammonium chloride	Carl Roth	>99.7%	
Copper (Cu (0))	Sigma-Aldrich	>99.8%	stored in the glove box
Formaldehyde	Sigma-Aldrich	aq. 37% ACS, Reag. Ph. Eur	10-15% Methanol as stabilizer
Formic acid	Sigma-Aldrich	97%	
Hydrobromic acid (aq.)	Sigma-Aldrich	48%	
Hydrochloric acid in 2-propanol	Acros Organics	5-6 M	
Iodomethane	Sigma-Aldrich	97%	
Nitric acid	Sigma-Adrich	100% (fuming)	
Magnesium sulfate	Grüssing	99%	
Methylacrylate	Sigma-Aldrich	99%	inhibitor MEHQ (100 ppm)
Methyleneindolene	Sigma-Aldrich	97%	
Methylisopropylketone	Alfa Aesar	98%	
<i>o</i> -Vanillin	Sigma-Adrich	99%	
Poly(methyl methacrylate)	Kunststoff und Farbengesellschaft mbH		M_n : 100 kDa
Potassium hydroxide	Sigma-Aldrich	>85%	

Pyridine	Acros Organics	99.5%	
Piperidine	Acros Organics	99%	dried with CaH ₂ and stored in a J. Young's tube under nitrogen atmosphere
Sodium hydroxide	VWR	98.5%	
Sodium hydrogen carbonate	VWR	ACS, Reag. Ph. Eur	
Sodium sulphate	Sigma-Aldrich	>99%	
Silica gel 60	Merck		
Tris(2-aminoethyl)amine	Alfa Aesar	97%	

3. Analytical Equipment

The fiber samples for scanning electron microscopy (SEM) analyses were collected immediately after spinning. The samples were sputtered with gold to avoid sample charging and were examined under a Ultra 55 Zeiss SEM (8-10 kV) at varying magnifications to determine the fiber characteristics.

The tensile tests to characterize the mechanochromic behavior as well as the stress-strain relationship were recorded on the tensile test machine Zwick 1445 with a 10 kN capacity load cell.

The images were taken using a Canon EOS 700D camera with a 18-55mm lens. The ImageJ software was used to analysed the sample images and to obtain the mean intensity of the green channel (I_g). Small areas over the length of the sample were tracked and the I_g value were extracted.

Rheology experiments were carried out on a rheometer from Kinexus Pro+ MAL1196589. A parallel plate system with a plate diameter of ~8 mm diameter was used. The sample temperature was controlled by passive heating/cooling exchanger under an atmosphere of dry oxygen. The sample thickness was between 0.3 and 0.5 mm. The lower plate was connected to the passive heat exchanger and controlled the sample temperature. All measurements were performed in a dynamic mode with an angular frequency ranging from 0.0001 to 100 rad/s. Samples were equilibrated for 15 min between the two plates at constant temperature before beginning the measurements. Five repetition of measurements confirmed the reproducibility of the results. For the evaluation of data the rspace software was used.

The gel permeation chromatography (GPC) was performed on a PSS (polymer standard service) SECurity GPC system after a conventional calibration using polystyrene standards (PS). The polymer PMA was dissolved in THF (1.5 mg/mL) and GPC spectra was recorded. The number average molecular weight (M_n) of PMA was found to be 89.5 kDa.

Dynamic scanning calorimetry measurements (DSC) were performed on a Mettler Toledo DSC3+ instrument in aluminum crucibles (40 μ L, 100 μ L), under nitrogen (N_2) at a flow rate of 20 mL/min and heating rates of 10 K/min or 5 K/min.

Thermogravimetric analysis (TGA) was performed on a Mettler Toledo TGA/DSC3+ instrument in aluminum crucibles (100 μ L), under nitrogen (N_2) at a flow rate of 20 mL/min.

The UV-vis absorption measurements of the fibers (collected on the rods) were recorded at 20 $^{\circ}$ C in a Perkin Elmer UV/VIS NIR Spectrometer Lambda 900. The irradiation experiments were carried out using UV light (central wavelength = 360-370 nm; optical power = 680 mW; intensity = 2.2 mW/cm²) and green light (central wavelength = 520-530 nm; optical power = 20 W; intensity = 64 mW/cm²). The absorption of each sample was measured after 10 min of UV and 6 min of green light irradiation.

Nuclear magnetic resonance spectroscopy (NMR) spectra (¹H NMR, ¹³C{¹H} NMR) were either recorded on a Bruker Avance NEO 500 (500 MHz, 126 MHz) or on a Bruker Avance II HD 600 (600 MHz and 155 MHz) spectrometer. The NMR spectra were referenced against the solvent residual proton signals (¹H) or the solvent itself (¹³C{¹H}).

Mass spectrometric (MS) measurements were performed in the positive ion mode using a JEOL-Accu TOF 4GGCV EI mass spectrometer or on the double focusing mass spectrometer MAT 95+ or Mat 8200 from Finnigan Mat. Electron ionization (EI) was performed using an ionization potential of 70 eV. High-resolution accurate-mass electrospray ionization (ESI) spectra were recorded on a Bruker Daltonics microTOF II mass spectrometer.

Infrared spectroscopy (IR) spectra were recorded on a NICOLET iS10 IR spectrometer with a diamond-attenuated total reflectance (ATR) unit. Relative intensities of the IR bands were described by vs = very strong, s = strong, m = middle or w = weak, b = broad.

4. Polymer Solution Optimization for Centrifugal Spinning and Processing

To determine the ideal concentration for centrifugal spinning of the fibers, six different solutions of the synthesized PMA (11 wt %, 15 wt %, 18 wt %, 22 wt %, 25 wt %, 33 wt %) were prepared by dissolving the polymer in tetrahydrofuran ($\rho = 0.889 \text{ g/cm}^3$, b.p = 66 °C). Furthermore, five polymer blends with (1 to 5 wt %) of PMMA polymer were prepared. All solutions were stirred at 30 °C for 24 h followed by stirring for 15 min at 50 °C prior to spinning; this increase in temperature was used to induce faster in-flight solvent evaporation.

These solutions were processed into fibers using a self-designed centrifugal spinning machine. The machine was operated on a DC motor (430 W, 33 V), equipped with a spinneret, having a shaft length of 75 mm and rotational speeds that were adjustable between 2000-6500 rpm. With a centrally located sample reservoir, the spinneret was also harnessed with a junction for attaching dispensing needles of different sizes. The opening diameters for these needles ranged from 0.15 - 1.0 mm. The collectors were positioned concentrically to the spinneret. The collectors were at a fixed distance of 10 cm from the periphery of the spinneret, which was kept constant for all the spinning processes. The entire setup was encased in a rectangular acrylic glass chamber. The fibers were processed by spinning a batch of 2 mL solution per spin cycle and rotation speeds of 3000, 4000 and 5000 rpm respectively. The solvent vapors were simultaneously vented out at the rate of 170 m³/h through an exhaust during the spinning process.

5. Fiber Morphology Monitored by SEM of Non-Blended PMA Fibers (NBF)

Scanning electron microscopy was used to characterize the physical nature of the fibers at a microscopic scale. Surface features such as texture and pore formation, outcome of spinning parameters such as fiber branching, variation of fiber diameter and bead formation were observed under SEM. This technique played the most significant role in optimizing the solutions to achieve bead free fibers. The effect of low solution concentrations on fiber morphology and bead formation can be seen in the non-blended fibers (NBF) of PMA (**Figure S1**).

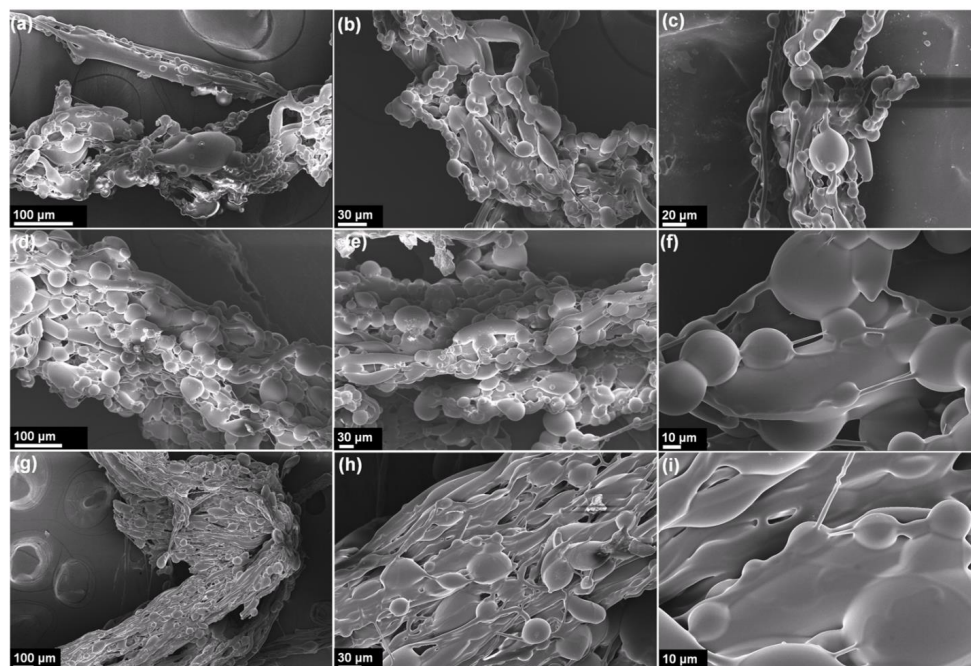


Figure S1. SEM images of fibers spun at 5000 rpm with a nozzle of 0.15 mm diameter were: (a)-(c) 11 wt %, (d)-(f) 15 wt % and (g)-(i) 18 wt % in three magnifications respectively.

As a result, the throughput of the fibers was reduced and because of this, the nozzle diameter was changed to 0.20 mm. The increased nozzle size yielded fibers with uneven diameter distribution, some very large PMA fibers (71 μm), along with some sites of inter-fiber fusion. The increase in the fiber diameter of 33 wt% solution due to large nozzle diameter (0.20 mm) is shown in **Figure S2**.

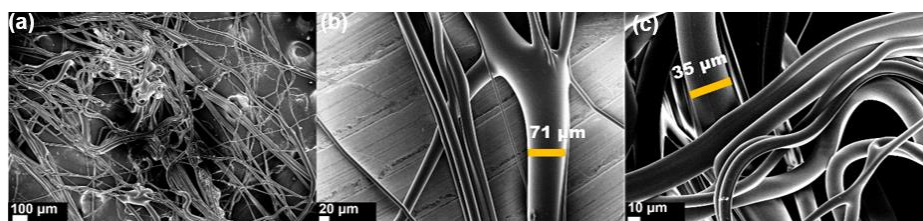


Figure S2. SEM images of NBF spun from 33 wt% solution at 5000 rpm, 0.20 mm nozzle diameter in three magnifications respectively. The marked region (yellow) indicate single fiber diameter.

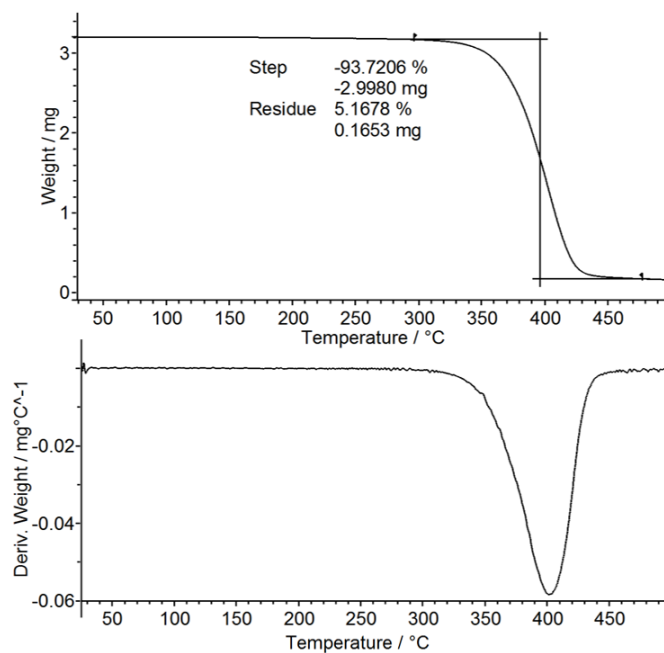


Figure S3. TGA plot of NBF spun from 33 wt% solution indicating no traces of residual solvent.

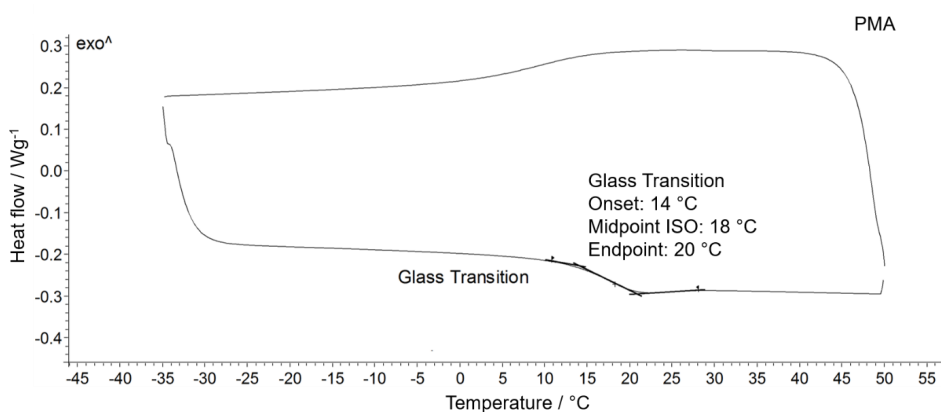


Figure S4. DSC plot of the elastomeric PMA polymer indicating the glass transition temperature (T_g). The measurement was cycled between -35 to 50 °C at the heating rate of 10 K/min under N_2 with a flow rate of 20 mL/min and sample weight of 11.35 mg

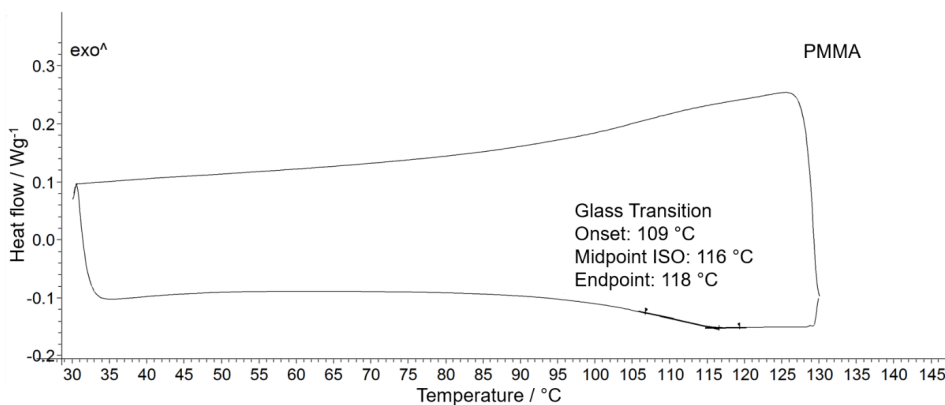


Figure S5. DSC plot of the commercial PMMA polymer indicating the glass transition temperature (T_g). The measurement was cycled between -35 to 130 °C at the heating rate of 10 K/min under N_2 with a flow rate of 20 mL/min and sample weight of 8.344 mg.

6. Fiber Morphology by SEM of Blended Fibers (BF)

Polymer blends were prepared by adding increasing amount of PMMA (1 wt % to 5 wt %) with respect to the PMA polymer. The solutions with an overall constant blend concentration of (28 wt %) were prepared by dissolving the polymer mixtures in THF. The solutions were stirred at 30 °C for 24 h followed by stirring for 15 min at 50 °C prior to spinning. The increase in the amount of PMMA in the blends 4 wt % and 5 wt %, led to bead formation (**Figure S6**). The fibers obtained from the polymer blend 1 wt% PMMA were stable even when spun in a strongly twisted orientation, indicating a significant effect of PMMA for imparting mechanical stabilities on the fibers. Two more sets of bead-free fibers 2 wt % and 3 wt % of PMMA were obtained. Further increase of the amount of PMMA, the solutions of the blends 4 wt % and 5 wt % formed fibers with large beads indicating low amount of PMMA the ideal blending range for efficiently obtaining bead-free micro-fibers.

The average diameters of 15 fibers could only be calculated for 1 wt %, 2 wt % and 3wt % **BF**, are $8.0 \mu\text{m} \pm 1.5 \mu\text{m}$, $9.8 \mu\text{m} \pm 4.0 \mu\text{m}$ and $8.4 \mu\text{m} \pm 2.1 \mu\text{m}$ respectively. The histogram (**Figure 1**) for fiber distribution was plotted after measuring diameters of 70 fibers. Among the **BF**, a high amount of fibers could be collected for 3 wt % of PMMA. This high yield was required for further photochemical and mechanochemical investigations. Additionally, the fibers appeared to be unidirectional compared to the 1 wt % and 2 wt% sample, which either spun in a twisted fashion or branched networks of fibers. For efficient mechano-switching, the alignment of both, the fibers and the mechochrome (SP) are crucial. Therefore, it was the 3 wt % fibers, which were further analyzed.

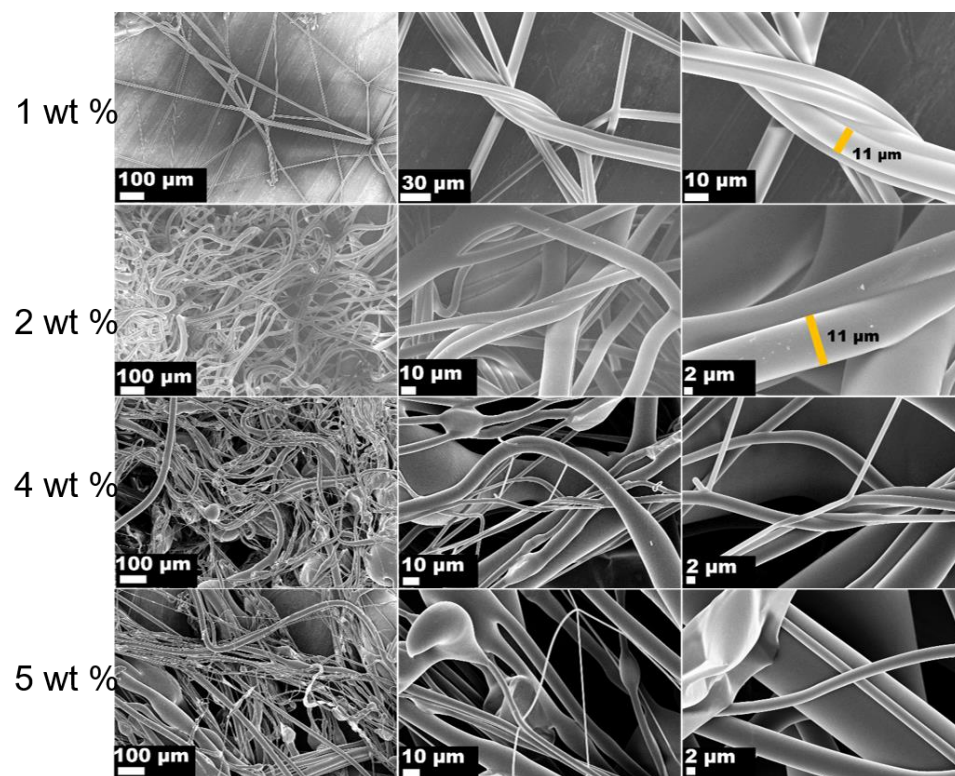


Figure S6. Blended fibers spun at 5000 rpm from a 0.20 mm nozzle diameter.

7. Mechanical Testing

The process of sample preparation is explained below. All samples were collected from the same spinning batch to maintain the density of fibers per area / cm^2 . The fiber-mat formed between the collector sticks were cut in a dimension of approximately $\sim 10 \text{ cm}^2$. The fiber-mats were then folded into a bar shape and clamped to carry out tensile measurements (method 1). As the fiber were stretched to high strain, slippage of the fibers from the grips or sample breakage at the clamping site was a common problem. To overcome this, the fibers were taped at the sample ends (method 2) (**Figure S7**). The samples did not break anymore, but the problem of sample slippage continued. To avoid the slippage, the fibers were then glued with two component adhesive glue between two pieces of glass fiber laminates (**Figure S7**). The tests were performed at a speed of 1 mm/sec on samples with a gauge length of 20 mm.

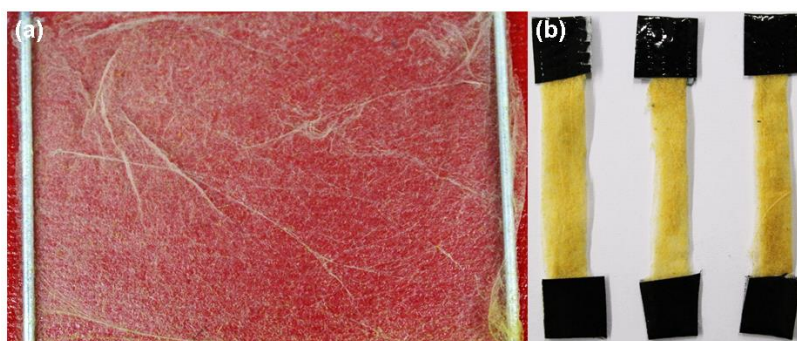


Figure S7. Method 2 of tensile sample preparation by clamping the ends of the fibers in adhesive tapes. Image (a) was taken on a red background and shows the fiber mat between two collector rods. Image (b) shows three folded fiber specimen.

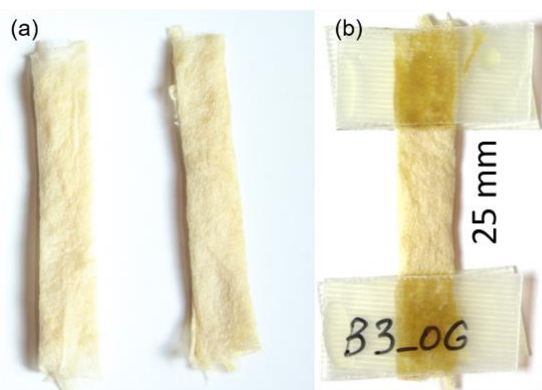


Figure S8. Method 3 of tensile sample preparation by fixing the fibers in between glass fiber laminates with a two component adhesive glue.

To observe the mechanochromic behavior in micro-fibers, uniaxial tensile measurements were carried out on the **BF** (**Figure S9**).

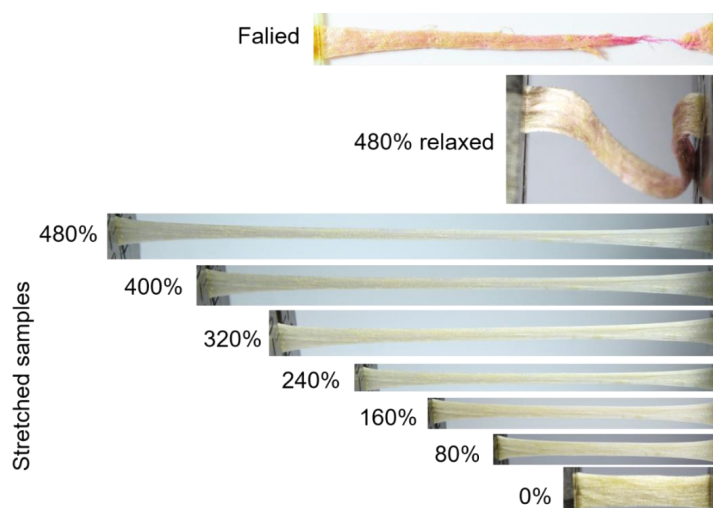


Figure S9. Images of **BF** stretched at 0%; 80%; 160 %; 240 %; 320 % and 480%; relaxed sample after 480% shows first sign of color change visible to the naked eye; sample after failure.

The stress-strain relationship of the **BF** (3 wt%) is shown **Figure S10**.

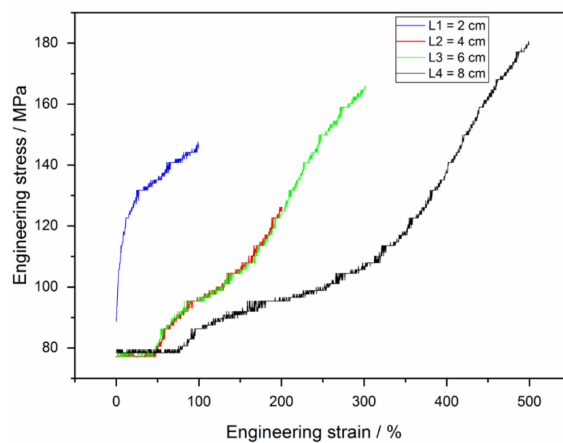


Figure S10. Stress-strain behavior of 3 wt % fiber when stretched under tensile force at a rate of 1 mm/sec.

8. Rheology

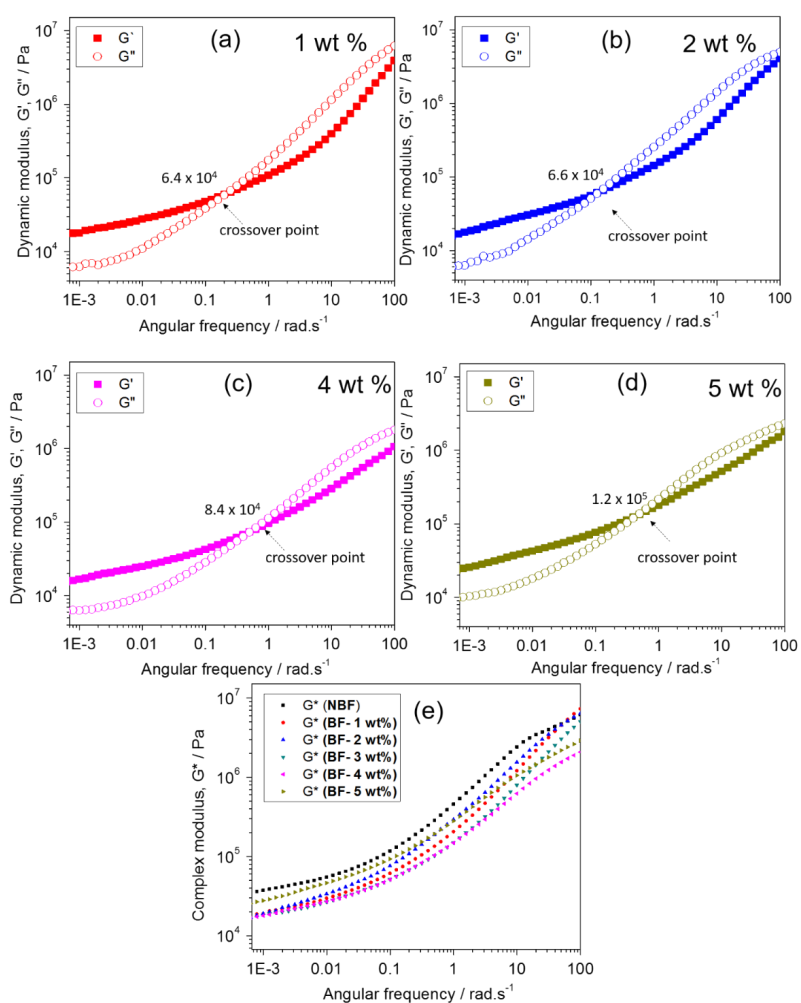
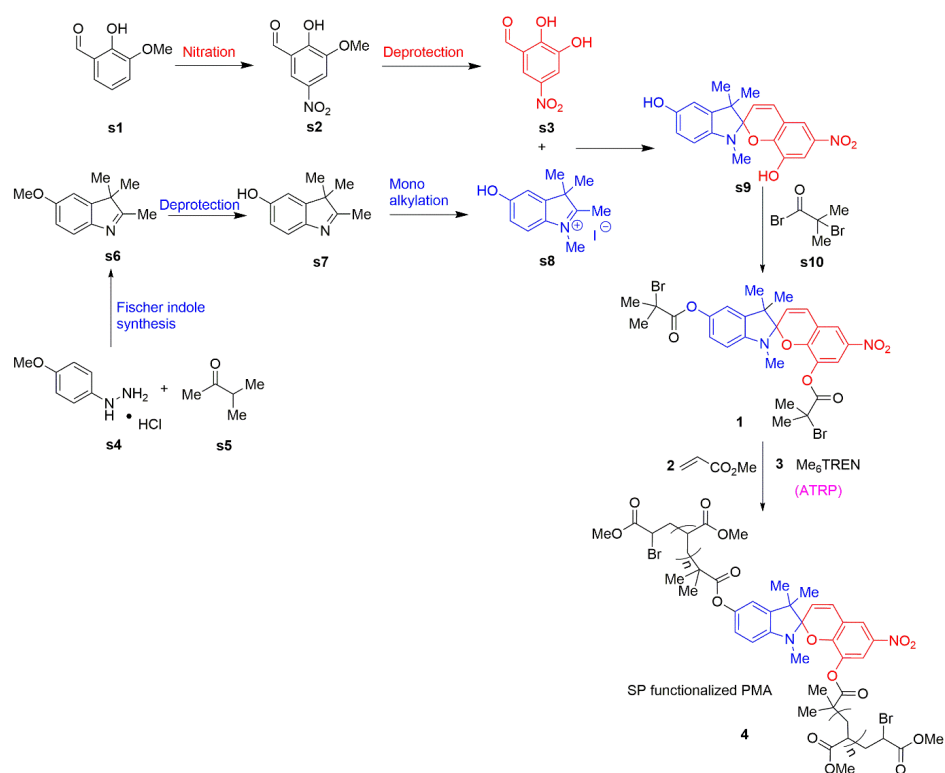


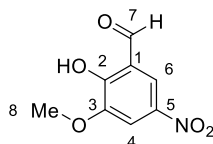
Figure S11. Frequency dependence of the storage (G') and loss (G'') moduli at 25 °C for all the investigated fibers (a-d) and (e) frequency dependence of the complex viscosity η^* for all the fibers.

9. Experimental Procedure

The synthetic route (**Scheme S1**) was designed by Potisek et al.¹ and Davis et. al.² to incorporate spiropyran (SP) covalently into the polymer backbone of poly(methyl acrylate) (PMA). The precursors of SP have been previously synthesized,¹⁻³ followed by the functionalization of SP at position 5' and 8 using 2-bromo-2-methylpropionyl bromide.^{1,2} The reported polymerization reaction was optimized to synthesis SP linked polymer (PMA) by a copper-catalyzed atom transfer radical polymerization (ATRP) method.¹ x

Scheme S1. Synthetic route to obtain SP covalently incorporation in the polymer backbone.¹



2-Hydroxy-3-methoxy-5-nitrobenzaldehyde (s2)³

To glacial acetic acid (138 mL) and water (7 mL), *o*-vanillin (30.0 g, 197 mmol) was added and the reaction mixture was cooled to 15 °C. A mixture of glacial acetic acid and fuming nitric acid (v/v), (2/1, 30 mL) was added over the course of 45 min and the reaction mixture stirred at 15 °C for another 90 min. Thereafter, the solution was diluted with water (300 mL). The formed yellow precipitate was filtered and washed with water (20 mL). The precipitate was then washed with diethyl ether (30 mL) and the obtained powder was dried in vacuum (~ 1 mbar) to obtain the product 2-hydroxy-3-methoxy-5-nitrobenzaldehyde (**s2**) as a beige solid (20.1 g, 102 mmol, 52%, Lit.:³ 56%).^a

¹H NMR (500 MHz, DMSO-*d*₆, 300 K): δ = 10.32 (s, 1 H, H-7), 8.09 (d, ⁴*J* = 2.7 Hz, 1 H, H-6), 7.92 (d, ⁴*J* = 2.7 Hz, 1 H, H-4), 3.99 (s, 3 H, H-8) ppm.

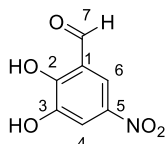
¹³C{¹H} NMR (126 MHz, DMSO-*d*₆, 300 K): δ = 189.3 (C-7), 156.4 (C-5), 149.1 (C-3), 139.4 (C-2), 121.6 (C-1), 115.7 (C-6), 110.3 (C-4), 56.8 (C-8) ppm.

IR (ATR): $\tilde{\nu}$ = 3093 (m), 2880 (w), 1667 (s), 1518 (s), 1480 (s), 1446 (s), 1393 (s), 1340 (vs), 1267 (vs), 1198 (s), 1092 (vs), 953 (vs), 884 (s), 765 (s), 721 (vs) cm⁻¹.

HRMS (EI-TOF): *m/z* (%): [M]⁺ calcd. for [C₈H₇NO₅]⁺ 197.0324; found 197.03120 (100); 151.0276 (38) [M-NO₂]⁺.

Melting point: T = 138 °C.

^a The ¹H NMR, ¹³C{¹H} NMR, IR, HRMS and mp data are in agreement with the reported.³

2,3-Dihydroxy-5-nitrobenzaldehyde (s3)³

A solution of 2-hydroxy-3-methoxy-5-nitrobenzaldehyde (**s2**) (21.5 g, 109 mmol) in aq. hydrobromic acid (48%, 363 mL, 6.70 mol) was heated to 140 °C for 5 h. Then, the solution was allowed to cool to 20 °C, diluted with water (500 mL), and then cooled to 0 °C and the precipitate that had formed was collected by filtration. It was washed with water (100 mL) and was dried at 5×10^{-2} mbar to yield 2,3-dihydroxy-5-nitrobenzaldehyde (**s3**) as a brown powder (18.2 g, 99.4 mmol, 92%, Lit.:³ 95%).^b

¹H NMR (126 MHz, DMSO-*d*₆, 300 K): δ = 11.10 (s, -OH), 10.31 (s, 1 H, H-7), 7.99 (d, ⁴*J* = 2.8 Hz, 1 H, H-6), 7.79 (d, ⁴*J* = 2.8 Hz, 1 H, H-4) ppm.

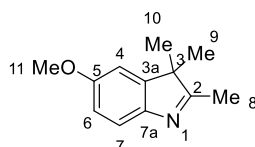
¹³C{¹H} NMR (126 MHz, DMSO-*d*₆, 300 K): δ = 189.8 (C-7), 155.9 (C-2), 147.2 (C-3), 139.2 (C-5), 121.8 (C-1), 114.6 (C-6), 113.2 (C-4) ppm.

IR (ATR): $\tilde{\nu}$ = 3252 (b), 3088 (w), 1665 (s), 1624 (w), 1522 (s), 1461 (s), 1346 (vs), 1273 (vs), 1185 (s), 1094 (m), 951 (s), 903 (s), 756 (s), 743 (vs), 722 (s), 678 (s) cm⁻¹.

HRMS (EI-TOF): *m/z* (%): [M]⁺ calcd. for [C₇H₅NO₅]⁺ 183.0167; found 183.0158 (100).

Melting point: T = 231 °C.

^b The ¹H NMR, ¹³C{¹H} NMR, IR, HRMS and mp data are in agreement with the reported.³

5-Methoxy-2,3,3-trimethyl-3H-indole (s6)³

In dry ethanol (260 mL), (4-methoxy)-phenyl hydrazine hydrochloride (**s4**) (10.0 g, 57.3 mmol) and 3-methyl-2-butanone (**s5**) (4.93 g, 57.3 mmol) were dissolved and heated to 80 °C under a nitrogen atmosphere. After 5 h, the solution was cooled to 20 °C, and filtered through silica gel (eluent: EtOAc). Purification by column chromatography gave the product 5-methoxy-2,3,3-trimethyl-3H-indole (**s6**) as dark brown solid (8.30 g, 43.9 mmol, 77%, Lit.:³ 78%).^c

TLC (UV): $R_f = 0.5$ (DCM/EtOAc = 0.5).

¹H NMR (500 MHz, CDCl₃, 300 K): $\delta = 7.46$ (d, $^3J = 8.3$ Hz, 1 H, H-7), 6.84 - 6.81 (m, 2 H, H-4, H-6), 3.82 (s, 3 H, H-11), 2.28 (s, 3 H, H-8), 1.29 (s, 6 H, H-9, H-10) ppm.

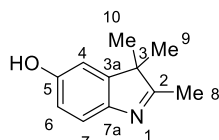
¹³C{¹H} NMR (126 MHz, CDCl₃, 300 K): $\delta = 186.4$ (C-2), 158.3 (C-5), 147.1 (C-7a), 146.2 (C-3a), 120.0 (C-7), 112.3 (C-4), 108.3 (C-6), 55.8 (C-11), 53.9 (C-3), 23.3 (C-9, C-10), 15.3 (C-8) ppm.

IR (ATR): $\tilde{\nu} = 2963$ (m), 2930 (m), 2865 (m), 2835 (m), 1614 (m), 1579 (m), 1462 (vs), 1432 (s), 1379 (m), 1289 (s), 1212 (vs), 1179 (s), 1145 (m), 1068 (vs), 1030 (vs), 943 (m), 900 (m), 866 (m), 820 (vs), 747 (m), 698 (m), 616 (m), 587 (m) cm⁻¹.

HRMS (EI-TOF): m/z (%): $[M^+]$ calcd. For $[C_{12}H_{15}NO]^+$ 189.1148, found 189.1147 (100), 174.1 (80) $[M-CH_3]^+$.

Melting point: T = 46 °C.

^c The ¹H NMR, ¹³C{¹H} NMR, IR, HRMS and mp data are in agreement with the reported.³

5-Hydroxy-2,3,3-Trimethyl-3H-indole (s7)³

To aq. hydrobromic acid (48 %, 146 mL, 1.29 mol), 5-methoxy-2,3,3-trimethyl-3H-indole (**s6**) (8.30 g, 43.9 mmol) was added and the solution was heated to 140 °C for 2 h. The solution was cooled to 20 °C, diluted with water (200 mL) and neutralized with solid NaHCO₃ until the solution was basic (pH = 10). The aqueous solution layer was extracted with dichloromethane (4 x 100 mL). The combined organic layers were washed with brine (300 mL), dried over Na₂SO₄, filtered, and concentrated in vacuum to yield 5-hydroxy-2,3,3-trimethyl-3H-indole (**s7**) as a brown solid (7.52 g, 43.0 mmol, 98%, Lit.³: 79%).^d

¹H NMR (500 MHz, CDCl₃, 300 K): δ = 7.32 (d, ³J = 8.3 Hz, 1 H, H-7), 6.85 (d, ⁴J = 2.3 Hz, 1 H, H-4), 6.78 (dd, ³J = 8.3 Hz, ⁴J = 2.3 Hz, 1 H, H-6), 2.27 (s, 3 H, H-8), 1.29 (s, 6 H, H-9, H-10) ppm.

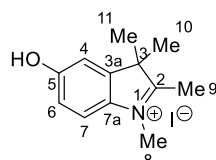
¹³C{¹H} NMR (126 MHz, CDCl₃, 300 K): δ = 186.2 (C-2), 155.7 (C-5), 147.3 (C-7a), 145.0 (C-3a), 120.0 (C-7), 114.3 (C-6), 109.9 (C-4), 53.8 (C-3), 23.3 (C-9, C-10), 15.1 (C-8) ppm.

IR (ATR): $\tilde{\nu}$ = 2967 (m), 2928 (m), 1713 (w), 1613 (m), 1592 (m), 1582 (s), 1462 (vs), 1423 (m), 1387 (m), 1360 (s), 1293 (s), 1270 (m), 1200 (s), 1191 (s), 1061 (m), 846 (m), 816 (vs), 764 (m), 622 (m), 460 (m) cm⁻¹.

HRMS (EI-TOF): *m/z* (%): [M]⁺ calcd. for [C₁₁H₁₃NO]⁺ 175.0997; found 175.0995 (100); 160.0 (95) [M-CH₃]⁺.

Melting point: T = 178 °C.

^d The ¹H NMR, ¹³C{¹H} NMR, IR, HRMS and mp data are in agreement with the reported.³

5-Hydroxy-1,2,3,3-tetramethyl-3*H*-indolium iodide (s8)³

To iodomethane (75.0 mL, 1.20 mol), 5-hydroxy-2,3,3-trimethyl-3*H*-indole (**s7**) (7.52 g, 43.0 mmol) was dissolved under nitrogen atmosphere and the solution was heated to 40 °C for 15 h. The solution was cooled to 20 °C and was diluted with Et₂O (15 mL) and filtered. The crude product was purified by recrystallization from ethanol (20 mL) to yield 5-hydroxy-1,2,3,3-tetramethyl-3*H*-indolium iodide (**s8**) as a light brown solid (13.2 g, 41.6 mmol, 96%, Lit.:³ 94%).^c

¹H NMR (500 MHz, DMSO-*d*₆, 300 K): δ = 10.24 (s, 1 H, -OH), 7.68 (d, ³*J* = 8.7 Hz, 1 H, H-7), 7.12 (d, ⁴*J* = 2.3 Hz, 1 H, H-4), 6.94 (dd, ³*J* = 8.7 Hz, ⁴*J* = 2.3 Hz, 1 H, H-6), 3.90 (s, 3 H, H-8), 2.67 (s, 3 H, H-9), 1.47 (s, 6 H, H-10, H-11) ppm.

¹³C{¹H} NMR (126 MHz, DMSO-*d*₆, 300 K): δ = 191.9 (C-2), 159.0 (C-5), 143.7 (C-3a), 134.1 (C-7a), 116.0 (C-7), 115.0 (C-6), 110.3 (C-4), 53.4 (C-3), 34.5 (C-8), 21.8 (C-10, C-11), 13.6 (C-9) ppm.

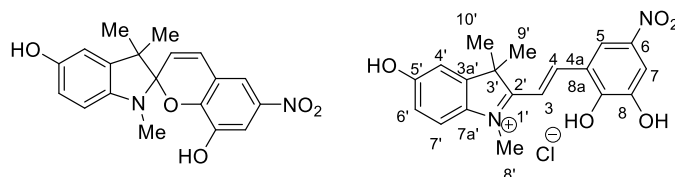
IR (ATR): $\tilde{\nu}$ = 3127 (s), 2970 (s), 1610 (m), 1478 (m), 1447 (m), 1283 (m), 1218 (vs), 1128 (w), 1058 (w), 892 (m), 869 (m), 822 (vs), 648 (s), 553 (m) cm⁻¹.

HRMS (ESI-TOF): *m/z* (%): [M-HI]⁺ calcd. for [C₁₂H₁₅NO]⁺ 190.1226; found 190.1227 (35); 174.0 (100) [M-HI-CH₃]⁺.

Melting point: T = 250 °C.

^c The ¹H NMR, ¹³C{¹H} NMR, IR, and HRMS data are in agreement with the reported.³

1',3',3'-Trimethyl-6-nitrospiro[chromene-2,2'-indoline]-5',8-diol (s9**)³**



To dry ethanol (180 mL), 5-hydroxy-1,2,3,3-tetramethyl-3*H*-indolium iodide (**s8**) (2.86 g, 9.02 mmol) and 2,3-dihydroxy-5-nitrobenzaldehyde (**s3**) (1.67 g, 9.02 mmol) were added. Under a nitrogen atmosphere, dry piperidine (1.8 mL, 18.0 mol) was added. The reaction was heated to 80 °C for 3 h. After cooling down to -30 °C, the product **s9** was filtered. A dark green solid was obtained (2.94 g, 8.3 mmol, 92%, Lit.:³ 98%).^f

¹H NMR (500 MHz, DMSO-*d*₆, 300 K): δ = 8.50 (d, ⁴*J* = 2.7 Hz, 1 H, H-7), 8.29 (d, ³*J* = 16.5 Hz, 1 H, H-4), 7.95 (d, ⁴*J* = 2.7 Hz, 1 H, H-5), 7.71 (d, ³*J* = 16.5 Hz, 1 H, H-3), 7.70 (d, ³*J* = 8.7 Hz, 1 H, H-7'), 7.21 (d, ⁴*J* = 2.3 Hz, 1 H, H-4'), 7.06 (dd, ³*J* = 8.7, ⁴*J* = 2.3 Hz, 1 H, H-6'), 4.07 (s, 3 H, H-8), 1.67 (s, 6 H, H-10', H-9') ppm.

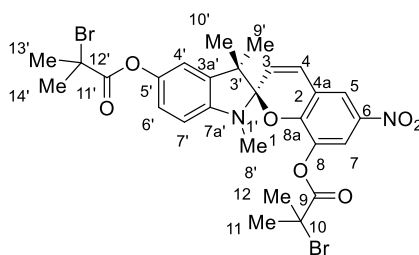
¹³C{¹H} NMR (126 MHz, DMSO-*d*₆, 300 K): δ = 178.5 (C-4a), 160.1 (C-5'), 153.3 (C-6), 146.6 (C-3a'), 146.0 (C-8), 143.9 (C-4), 139.9 (C-8a), 134.0 (C-7a'), 121.3 (C-2'), 116.8 (C-7, C-7'), 116.0 (C-6'), 114.8 (C-3), 112.1 (C-5), 110.0 (C-4'), 51.9 (C-3'), 34.9 (C-8'), 25.9 (C-9', C-10') ppm.

IR (ATR): $\tilde{\nu}$ = 3206 (w, b), 2981 (w), 1627 (w), 1596 (m), 1512 (m), 1454 (m), 1412(s), 1273 (s), 1246 (s), 1214 (vs), 1180(vs), 1065 (s), 962(s), 864 (m), 814 (m), 801 (m), 765 (m), 740 (m), 545 (m) cm⁻¹.

HRMS (EI-TOF): *m/z* (%): [M]⁺ calcd. [C₁₉H₁₈N₂O₅]⁺ 354.36, found 354.120 (50), 175(100).

^f The ¹H NMR, ¹³C{¹H} NMR, IR, and HRMS data agree with the reported data.³ The compound started to decompose at 260 °C without a melting peak (see section 10).

1',3',3'-Trimethyl-6-nitrospiro[chromene-2,2'-indoline]-5',8-diylbis(2-bromo-2-methylpropanoate) (1)¹



In a 2-necked flask, 1',3',3'-trimethyl-6-nitrospiro[chromene-2,2'-indoline]-5',8-diol (**s9**) (1.50 g, 4.20 mmol) and DMAP (259 mg, 2.12 mmol) were combined. Under a nitrogen atmosphere, dry DCM (30.0 mL) was added. After 10 min, pyridine (1.40 mL, 17.0 mmol) was added, and the solution was cooled to 0 °C. 2-Bromo-2-methylpropionyl bromide (2.10 mL, 17.0 mmol) was added dropwise within the course of (0.05 mL/min) via a syringe pump into the cooled solution. The solution was stirred at 0 °C for 90 min. The cooling bath was removed and the reaction mixture stirred at 28 °C for 1 h before heating it to 50 °C for 2 h. The reaction was quenched with water (50 mL) and the organic layer was separated. The combined aqueous layers were extracted with EtOAc (3 x 60 mL) to collect remaining organic product. The combined organic layers were washed with aq. NH₄Cl (2 x 70 mL), with aq. NaHCO₃ (3 x 50 mL) and then with brine (2 x 70 mL). The organic layer was dried over MgSO₄, filtered and concentrated. The remaining solution of EtOAc (~ 10 mL) was overlaid with *n*-pentane (100 mL) to induce crystallization of the product overnight. After addition of another portion of *n*-pentane (200 mL), the solution was filtered to obtain the product **1** as brown powder (1.60 g, 4.51 mmol, 58%, Lit.:¹ 50%).^g

^g The product **1** was prepared by modification of synthesis previously reported.¹ The ¹H NMR, ¹³C{¹H} NMR, HRMS and mp data are in agreement with the reported.¹ IR data was not reported.

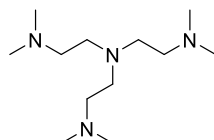
¹H NMR (500 MHz, CDCl₃, 300 K): δ = 7.98 (d, ⁴*J* = 2.6 Hz, 1 H, H-5), 7.92 (d, ⁴*J* = 2.6 Hz, 1 H, H-7), 7.10 (d, ³*J* = 10.4 Hz, 1 H, H-4), 6.88 (dd, ³*J* = 8.3 Hz, ⁴*J* = 2.3 Hz, 1 H, H-6'), 6.80 (s, ⁴*J* = 2.3 Hz, 1 H, H-4'), 6.48 (d, ³*J* = 8.3 Hz, 1 H, H-7), 5.92 (d, ³*J* = 10.4 Hz, 1 H, H-3), 2.68 (s, 3 H, H-8'), 2.07 (s, 6 H, H-13', H-14'), 1.59 (s, 2 H, H-12 or H-11, two overlapping singlets), 1.26 (s, 3 H, H-9'), 1.21 (s, 3 H, H-10') ppm.

¹³C{¹H} NMR (126 MHz, CDCl₃, 300 K): δ = 170.8 (C-11'), 169.3 (C-9), 150.9 (C-8a), 145.7 (C-7a'), 144.7 (C-5'), 140.3 (C-8), 137.5 (C-3a'), 137.3 (C-6), 128.7 (C-4), 121.1 (C-3), 120.5 (C-5), 120.0 (C-6'), 119.6 (C-4a), 119.2 (C-7), 115.1 (C-4'), 107.9 (C-2), 107.5 (C-7'), 55.8 (C-12'), 54.1 (C-10), 52.1 (C-3'), 30.9 (C-13', C-14'), 30.4 (C-11), 30.3 (C-12), 29.0 (C-8'), 25.9 (C-10'), 19.5 (C-9') ppm.

IR (ATR): $\tilde{\nu}$ = 2971 (w), 1752 (s), 1522 (m), 1485 (w), 1453 (m), 1390 (w), 1333 (s), 1258 (s), 1179 (m), 1132 (s), 1101 (vs), 1079 (s), 902.7 (s), 785 (m), 770 (m), 743 (s).

HRMS (EI-TOF): *m/z* (%): [M⁺] calcd. for C₂₇H₂₈⁸¹Br₂N₂O₇⁺ 652.0065, found 652.0091 (100), 650 (50) [M-⁷⁹Br₂]⁺.

Melting point: T = 175 °C.

Tris[2-(dimethylamino)ethyl]amine (3)⁴

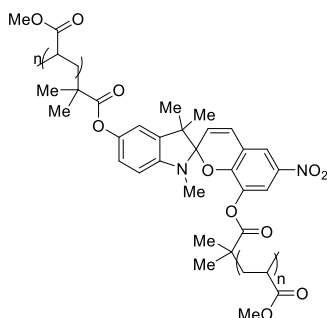
Tris(2-aminoethyl)amine (TREN) was dissolved in dry methanol (150 mL). Then, hydrochloric acid in 2-propanol (21.0 mL, 5-6 M) was added over the course of 20-30 min using a syringe pump. The reaction mixture was stirred for 1 h at 24 °C, before the precipitate was filtered and washed with methanol (3 x 100 mL). The solvent was removed under vacuum and the slightly beige TREN-hydrochloride salt was dried (yield: 6.84 g). This intermediate (6.84 g) was added to a mixture of water (12.0 mL), formic acid (56.0 mL, 1.40 mol) and formaldehyde solution (56.0 mL) and were heated to 120 °C for 6 h. The residue was obtained by removing the volatile component via rotary evaporation and aqueous solution of NaOH (5 M, 100 mL) was added until complete dissolution was achieved. Solid KOH (50.0 g, 0.90 mol) was slowly added until the solution had a pH value of 14. The aqueous phase was extracted with EtOAc (5 x 75 mL). The combined organic phases were dried over solid KOH and the solvent was removed under vacuum, followed by fractioning vacuum distillation (52 °C, 5.7 x 10⁻² mbar) under a nitrogen atmosphere. The product Tris[2-(dimethylamino)ethyl]amine (**3**) was obtained as a liquid (6.96 g, 30.2 mmol, 83%, Lit.:⁴ 91%).^h

¹H NMR (500 MHz, CDCl₃, 300 K): δ = 2.50-2.18 (m, 12 H, -CH₂), 2.08 (m, 18 H, -CH₃).

¹³C{¹H} NMR (126 MHz, CDCl₃, 300 K): δ = 57.3(-CH₂), 52.9 (-CH₂), 45.8 (-CH₃).

IR (ATR): $\tilde{\nu}$ = 2940 (m), 2850 (w), 2814 (m), 2762 (s), 1455 (s), 1263 (w), 1153 (s), 1122 (m), 1030 (s) cm⁻¹.

^h The product **3** was prepared by a modification of synthesis previously reported.^{4,5} The shift of ¹H NMR and ¹³C{¹H} NMR data are in agreement with the reported. As the molecule fragments during the mass measurement, the [M⁺] could not be measured. The fragments were in agreement with the structure.

PMA 4¹

To the spiropyran initiator **1** (131 mg, 200 μmol), dimethyl sulfoxide (30 mL) was added and the reaction mixture was stirred until the compound had dissolved. The chelating ligand, Me₆TREN, (184 mg, 800 μmol , 4 eq.) was added. The catalyst, Cu(0), (50.8 mg, 800 μmol , 4 eq.) was added and the flask was sealed inside the glovebox. The monomer, methyl acrylate (MA), (18.1 mL, 200 mmol, 1000 eq.) was added at the rate of 2 mL/min. The reaction was stirred at 30 °C for 2 h under nitrogen atmosphere. The reaction flask was opened to air and THF (100 mL) was quickly added to the viscous polymer solution. The reaction mixture was filtered through a PTFE (0.45 μm) syringe filter to remove the catalyst particles. It was purified by precipitation into diethyl ether (1 L) stirring vigorously, in five batches of 20 mL polymer solution per 200 mL of Et₂O. The viscous polymer was re-dissolved in THF and the precipitation step was carried out three times. The polymer was collected and was dried at 5×10^{-2} mbar for 24 h. The polymer **12** slight yellow in color (13.9 g, 77%).

¹H NMR (500 MHz, CDCl₃, 300 K): δ = 3.66 (s, 3 H, -OCH₃), 2.30 (s, -CH-), 1.94 – 1.39 (m, -CH₂-) ppm.

¹³C{¹H} NMR (126 MHz, CDCl₃, 300 K): δ = 175.1 (-carboxyl C), 51.9 (-OCH₃), 41.2 (-CH₂) ppm. IR (ATR): $\tilde{\nu}$ = 2954 (m), 2918 (w), 1727 (vs), 1436 (m), 1195 (m), 1157 (vs).

GPC (THF, 1 mL/min): M_n = 89.5 kDa, M_w = 161 kDa, PDI = M_w/M_n = 1.8.

DSC: T_g = 14 °C.

10. Differential Scanning Calorimetry (DSC)

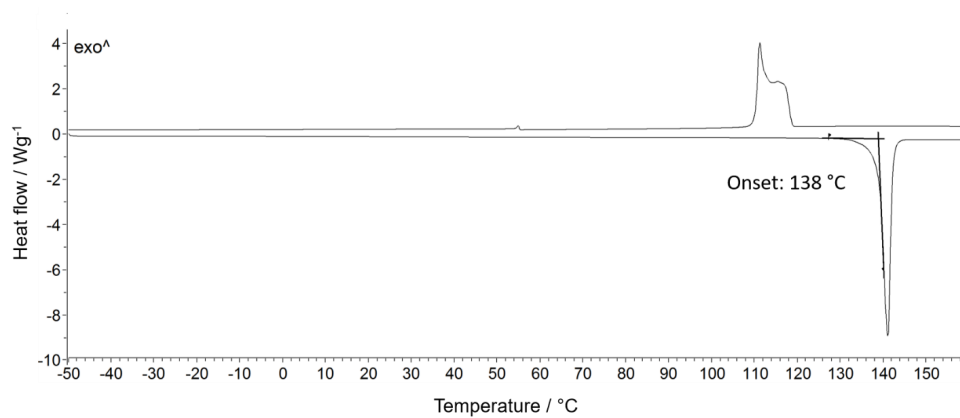


Figure S12. DSC plot of 2-hydroxy-3-methoxy-5-nitrobenzaldehyde (**s2**).

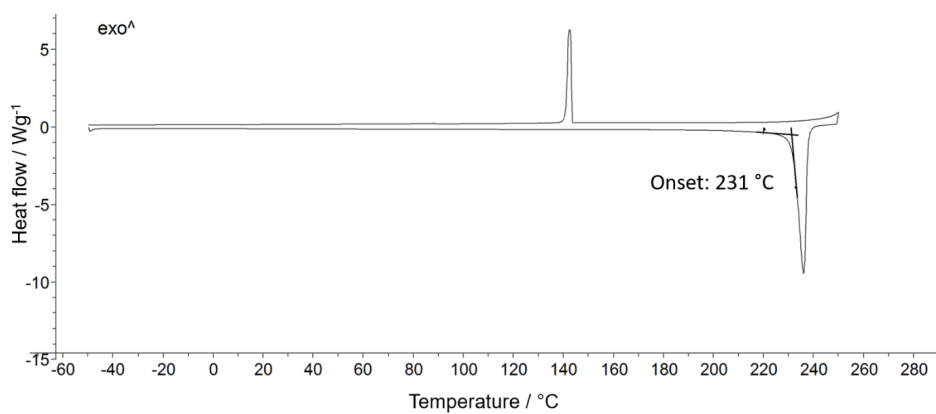


Figure S13. DSC plot of 2,3-dihydroxy-5-nitrobenzaldehyde (**s3**).

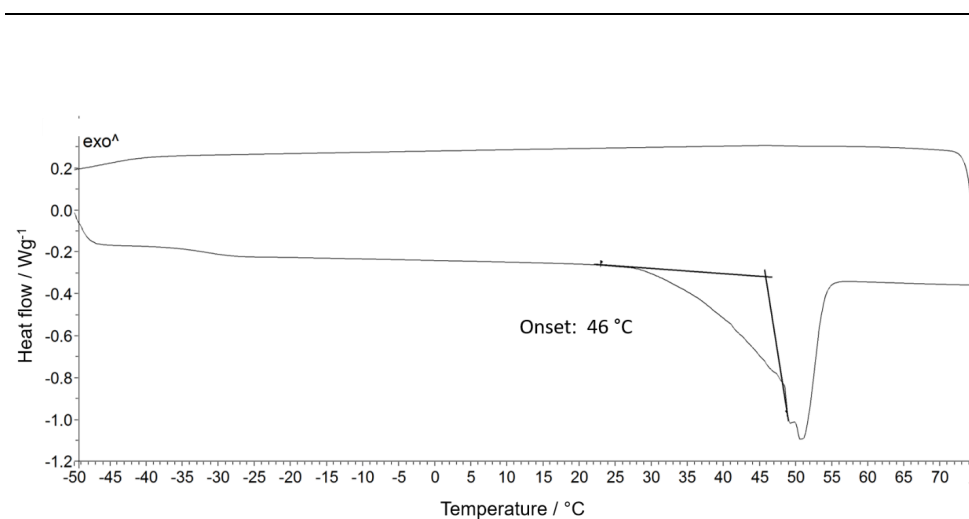


Figure S14. DSC plot of 5-methoxy-2,3,3-trimethyl-3H-indole (s6).

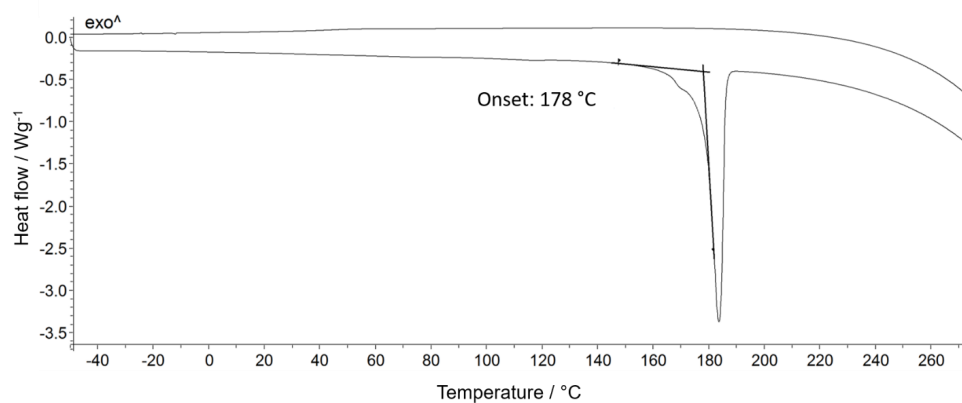


Figure S15. DSC plot of 2,3,3-trimethyl-3H-indol-5-ol (s7).

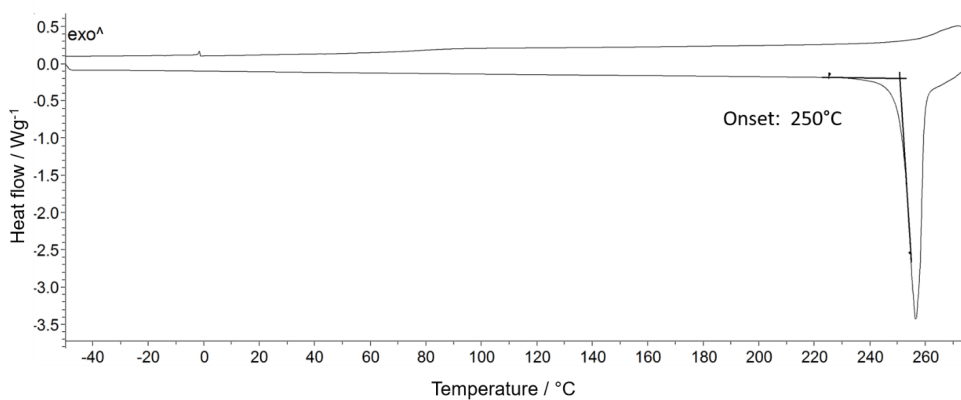


Figure S16. DSC plot of 5-Hydroxy-1,2,3,3-tetramethyl-3*H*-indolium iodide (**s8**).

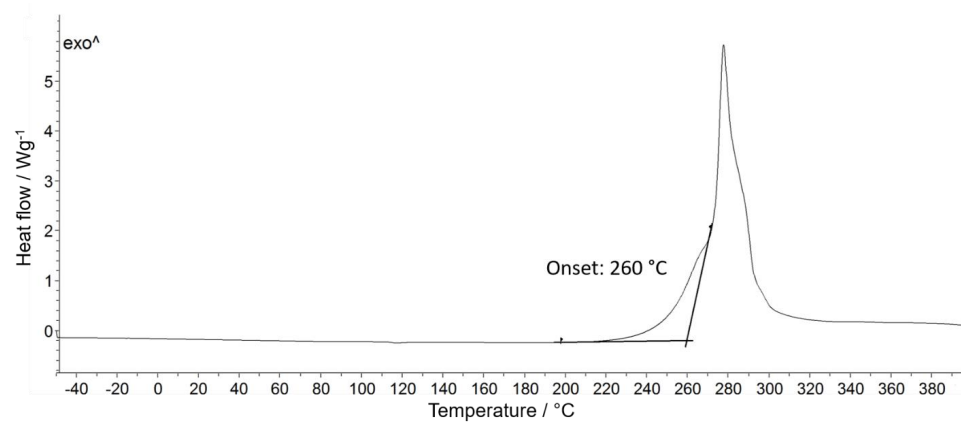


Figure S17. DSC plot of 1',3',3'-trimethyl-6-nitrospiro[chromene-2,2'-indoline]-5',8-diol (**s9**). The compound started to decompose at 260 °C without a melting peak.

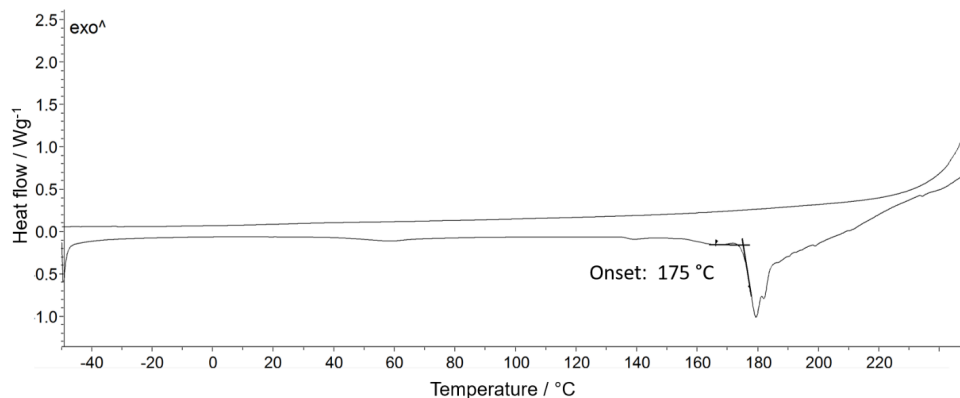


Figure S18. DSC plot of 1',3',3'-trimethyl-6-nitrospiro[chromene-2,2'-indoline]-5',8-diylbis(2-bromomethyl propanoate) (**1**).

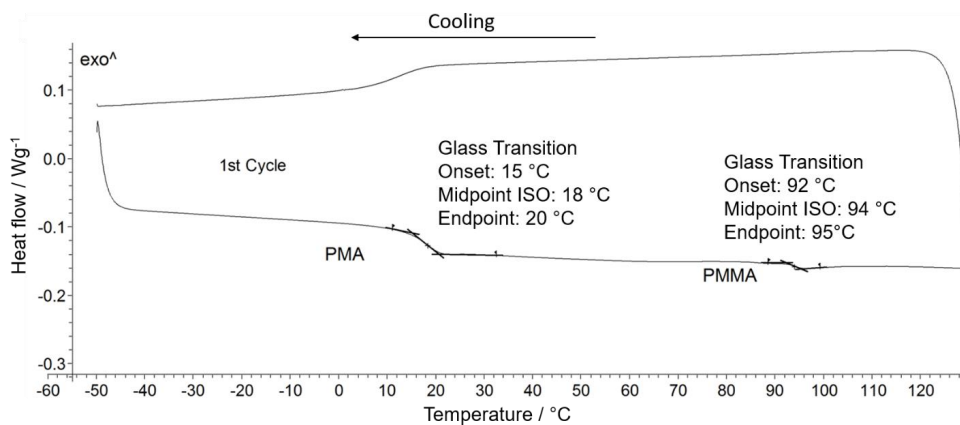


Figure S19. DSC plot of **BF** fibers indicating the glass transition temperatures (T_g) for PMA and PMMA. The measurement was cycled between -50 to 130 $^{\circ}\text{C}$ at the heating rate of 20 K/min under N_2 with flow rate of 20 mL/min and sample weight of 43.09 mg.

11. Gel Permeation Chromatogram of the Synthesized PMA

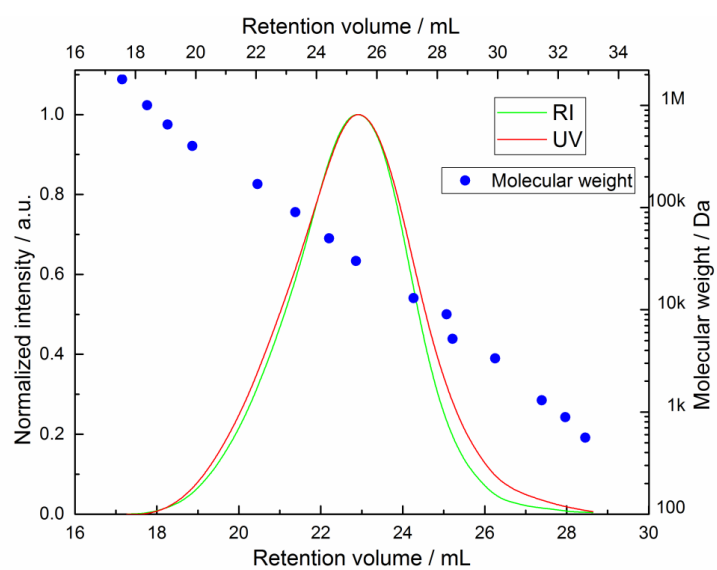
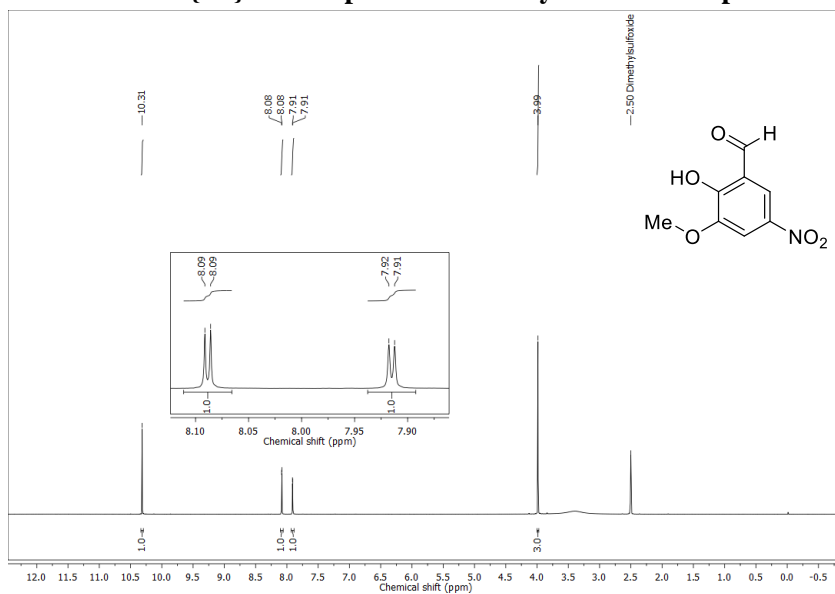
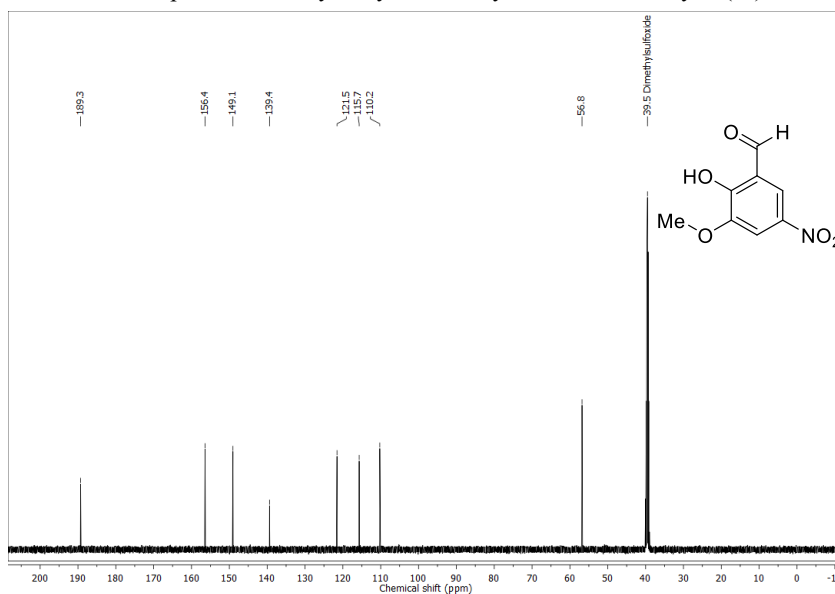


Figure S20. GPC plots of PMA with the normalized intensity of RI (green) and UV (red) detector signal vs the retention volume/mL. Conventional calibration of the GPC with polystyrene standards and their molecular weight (blue).

12. ^1H NMR and $^{13}\text{C}\{^1\text{H}\}$ NMR Spectra of the Synthesized CompoundsFigure S21. ^1H NMR spectrum of 2-hydroxy-3-methoxy-5-nitrobenzaldehyde (**s2**) in $\text{DMSO-}d_6$.Figure S22. $^{13}\text{C}\{^1\text{H}\}$ NMR spectrum of 2-hydroxy-3-methoxy-5-nitrobenzaldehyde (**s2**) in $\text{DMSO-}d_6$.

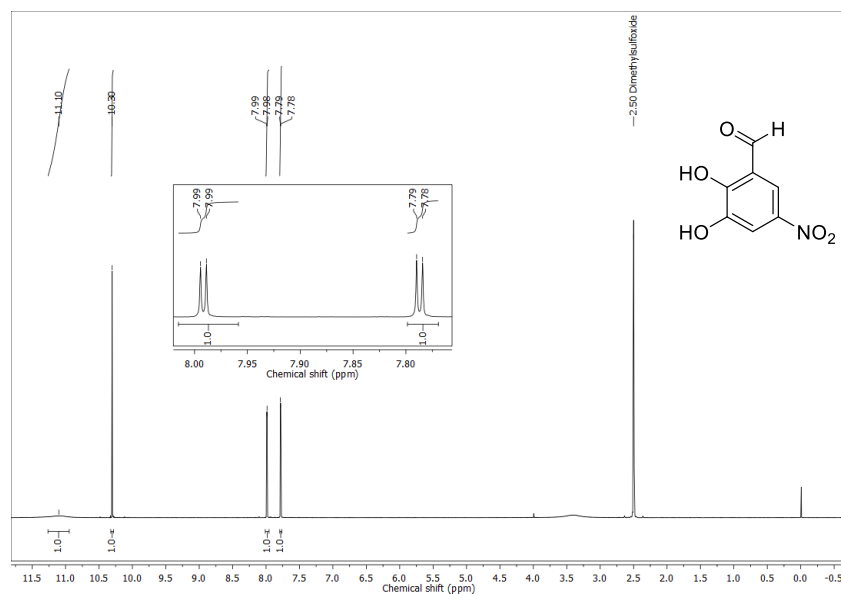


Figure S23. ^1H NMR spectrum of 2,3-dihydroxy-5-nitrobenzaldehyde (**s3**) in $\text{DMSO-}d_6$.

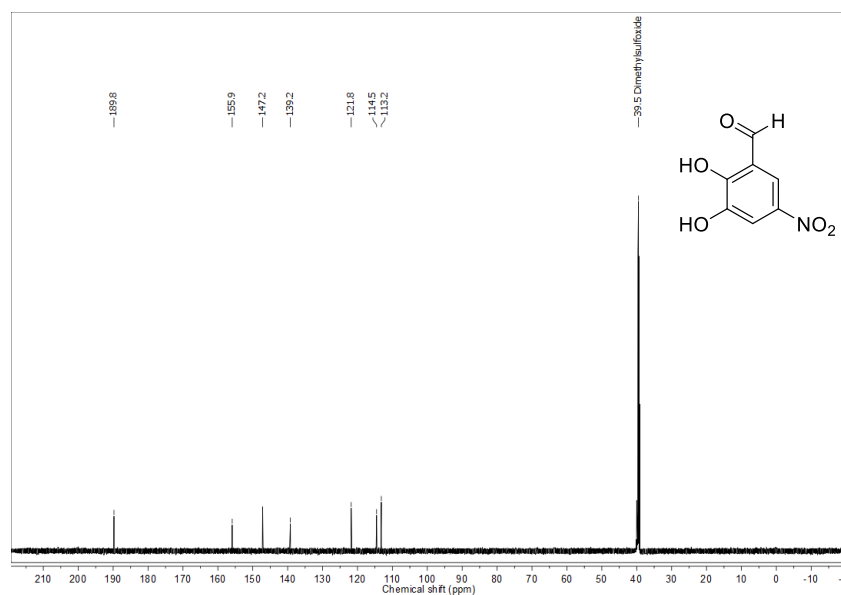


Figure S24. $^{13}\text{C}\{^1\text{H}\}$ NMR spectrum of 2,3-dihydroxy-5-nitrobenzaldehyde (**s3**) in $\text{DMSO-}d_6$.

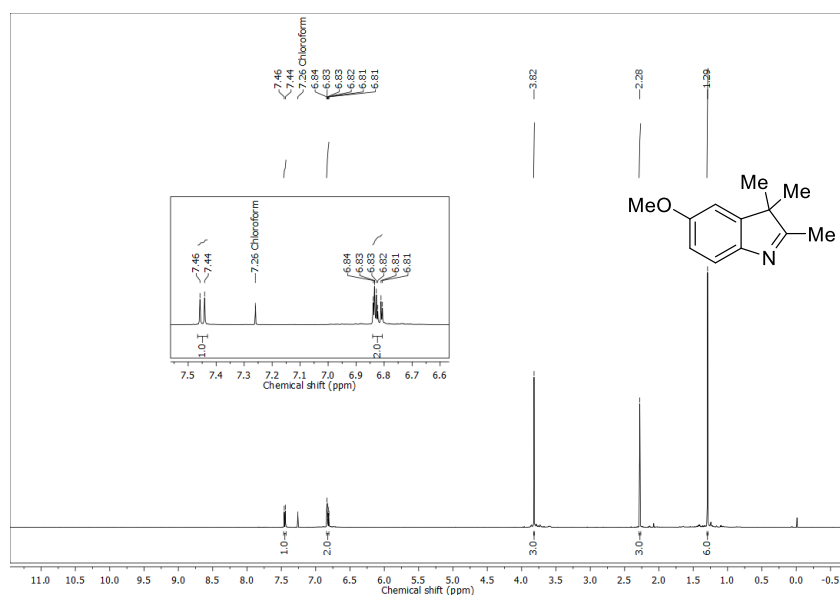


Figure S25. ¹H NMR spectrum of 5-methoxy-2,3,3-trimethyl-3H-indole (**s6**) in CDCl₃.

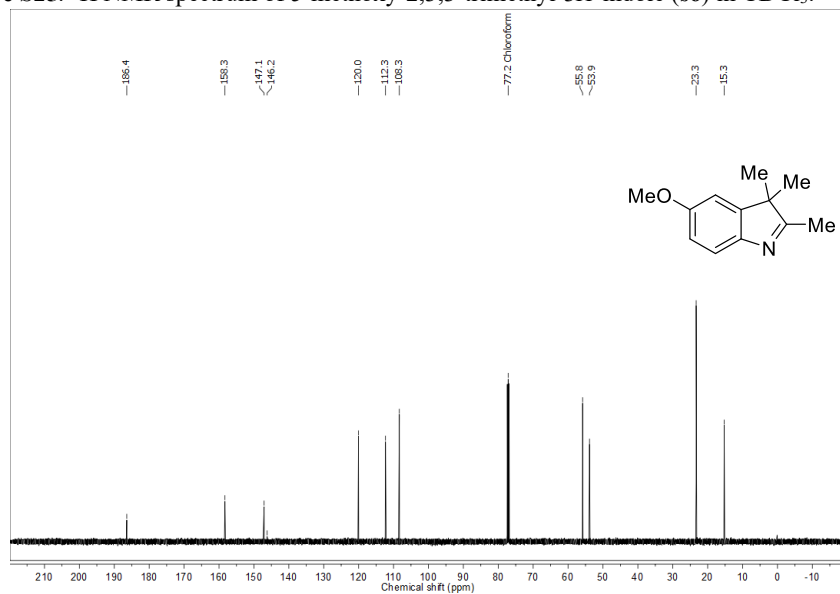


Figure S26. ¹³C{¹H} NMR spectrum of 5-methoxy-2,3,3-trimethyl-3H-indole (**s6**) in CDCl₃.

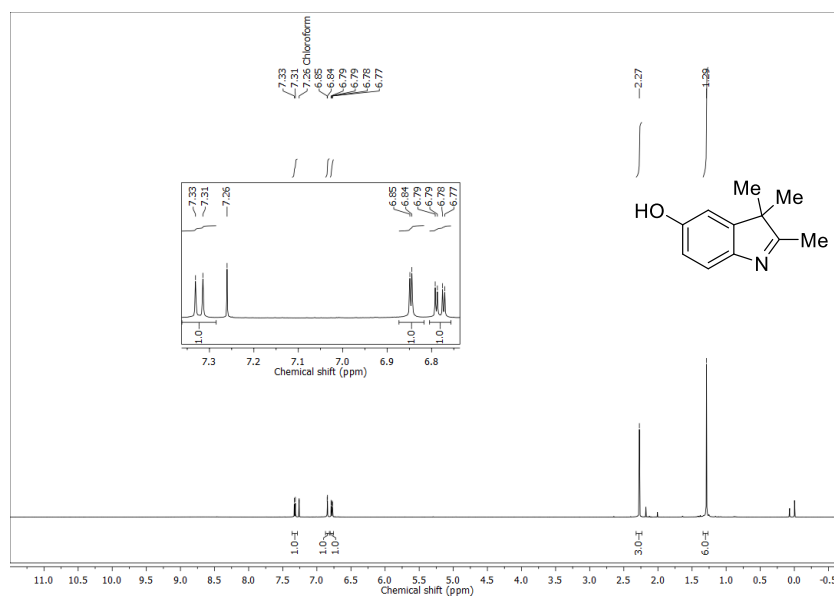


Figure S27. ^1H NMR spectrum of 5-hydroxy-2,3,3-trimethyl-3H-indol-5-ol (s7) in CDCl_3 .

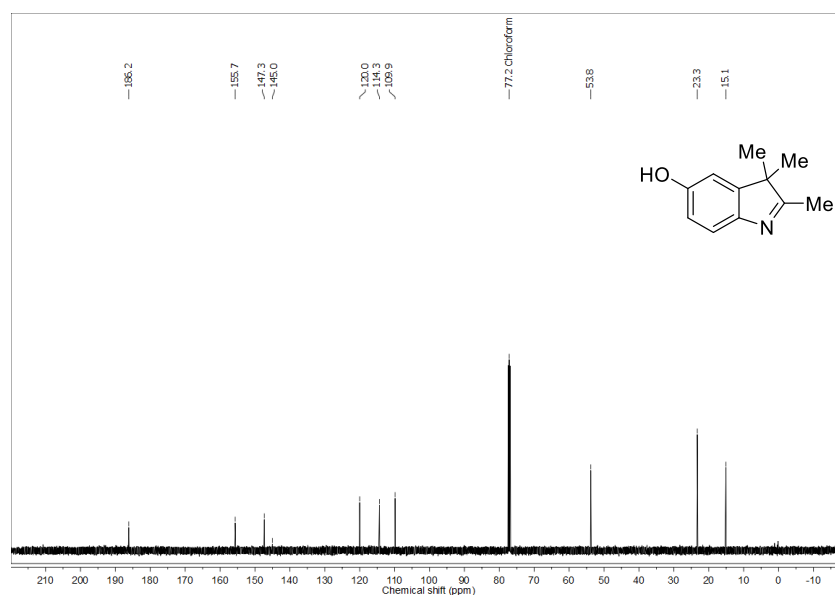


Figure S28. $^{13}\text{C}\{^1\text{H}\}$ NMR spectrum of 5-hydroxy-2,3,3-trimethyl-3H-indol-5-ol (s7) in CDCl_3 .

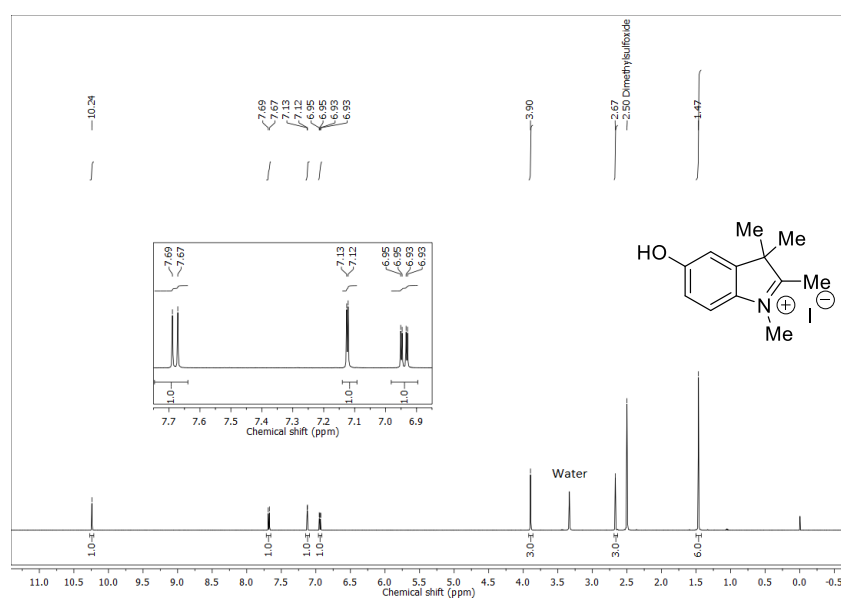


Figure S29. ^1H NMR spectrum of 5-hydroxy-1,2,3,3-tetramethyl-3*H*-indolium iodide (**s8**) in $\text{DMSO-}d_6$.

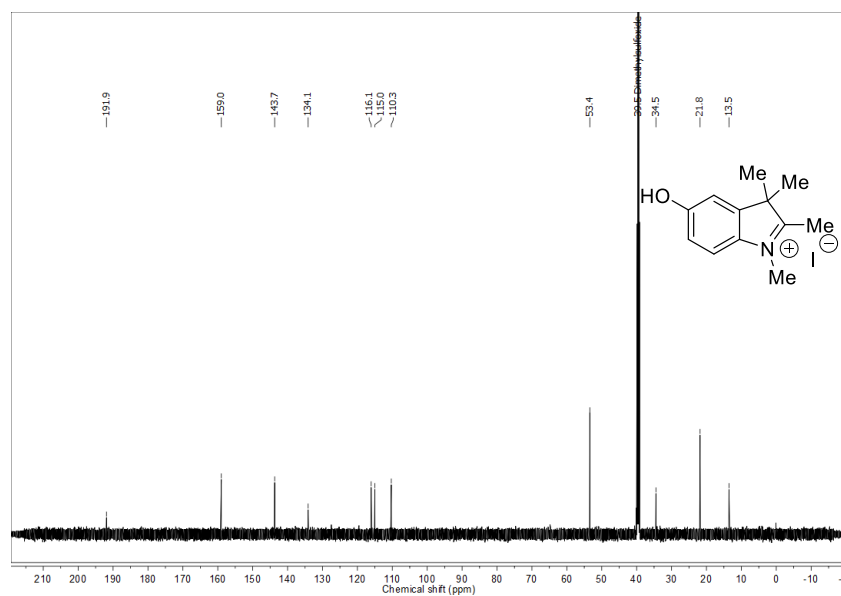


Figure S30. $^{13}\text{C}\{^1\text{H}\}$ NMR spectrum of 5-hydroxy-1,2,3,3-tetramethyl-3*H*-indolium iodide (**s8**) in $\text{DMSO-}d_6$.

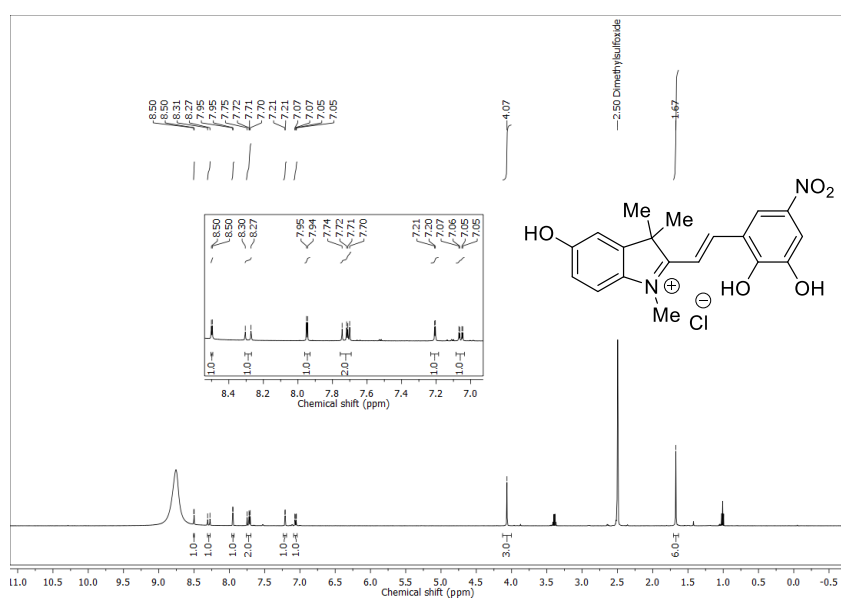


Figure S31. ^1H NMR spectrum of 1',3',3'-trimethyl-6-nitrospiro[chromene-2,2'-indoline]-5',8-diol (**s9**) in $\text{DMSO-}d_6$.

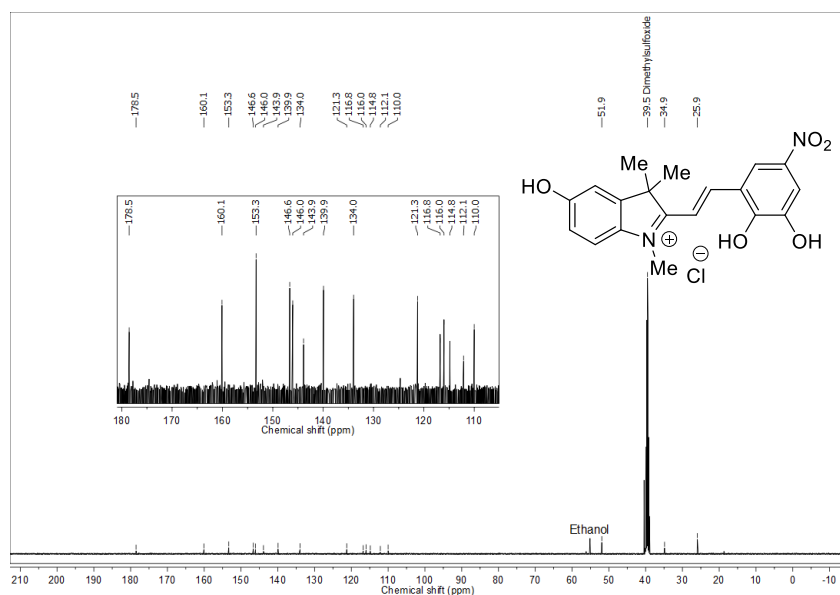


Figure S32. $^{13}\text{C}\{^1\text{H}\}$ NMR spectrum of 1',3',3'-trimethyl-6-nitrospiro[chromene-2,2'-indoline]-5',8-diol (**s9**) in $\text{DMSO-}d_6$.

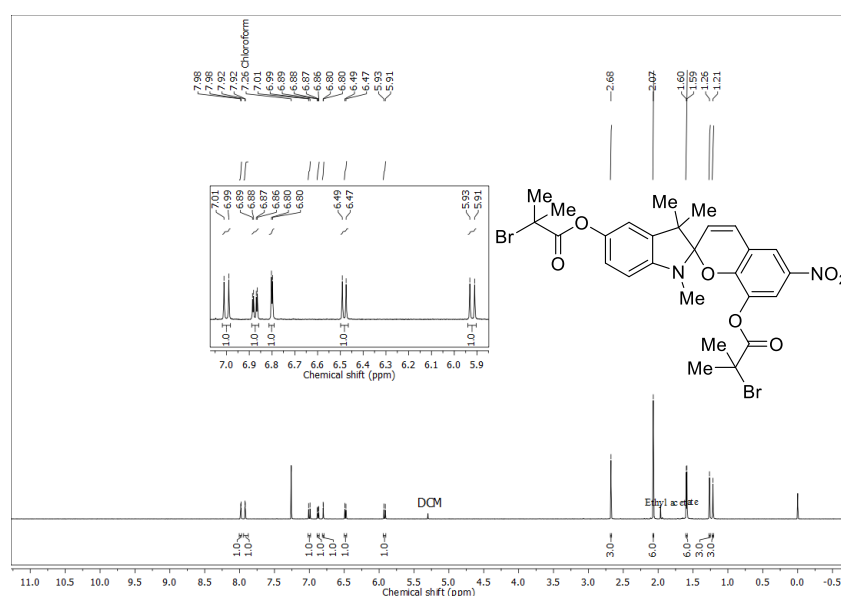


Figure S33. ^1H NMR spectrum of 1,3,3'-trimethyl-6-nitrospiro[chromene-2,2'-indoline]-5',8'-diylbis(2-bromomethylpropanoate) (1) in CDCl₃.

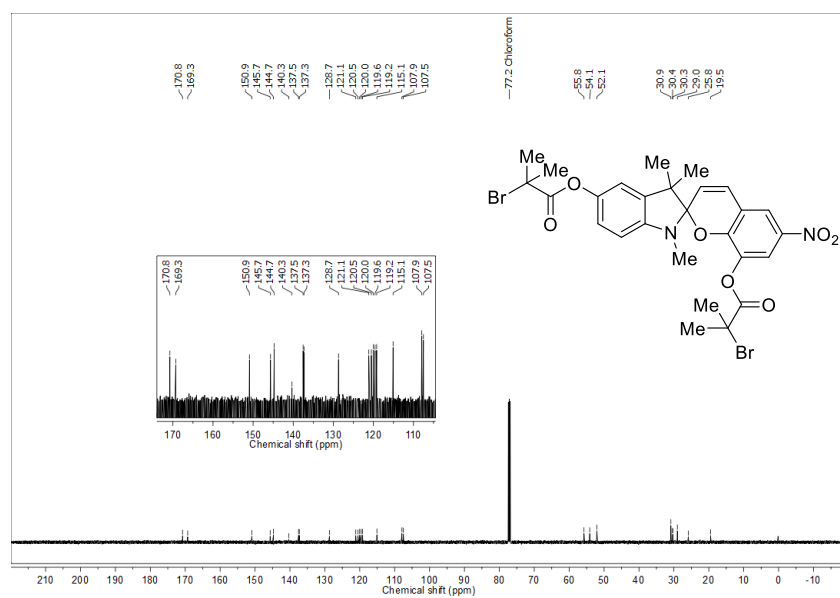


Figure S34. $^{13}\text{C}\{^1\text{H}\}$ NMR spectrum of 1,3,3'-trimethyl-6-nitrospiro[chromene-2,2'-indoline]-5',8'-diylbis(2-bromomethylpropanoate) (1) in CDCl₃.

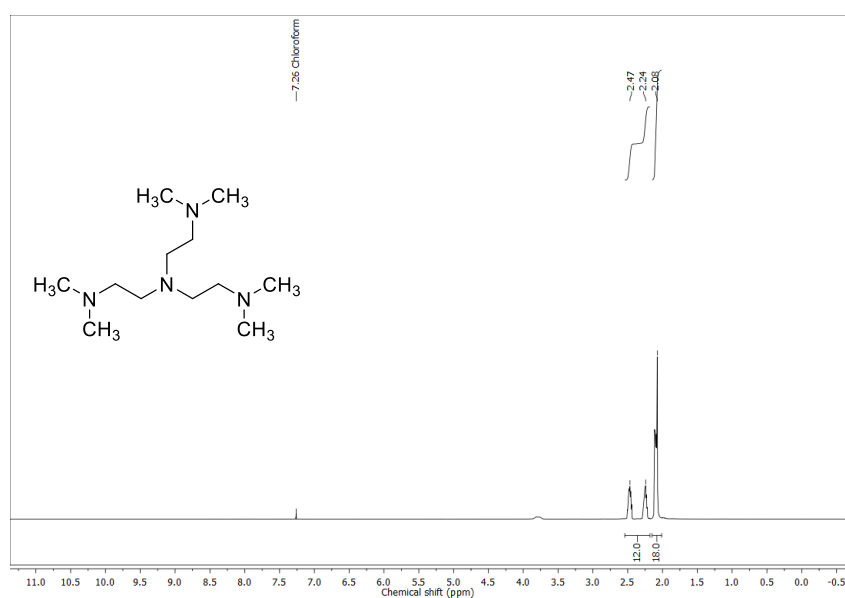


Figure S35. ¹H NMR spectrum of tris[2-(dimethylamino)ethyl]amine (3) in CDCl₃.

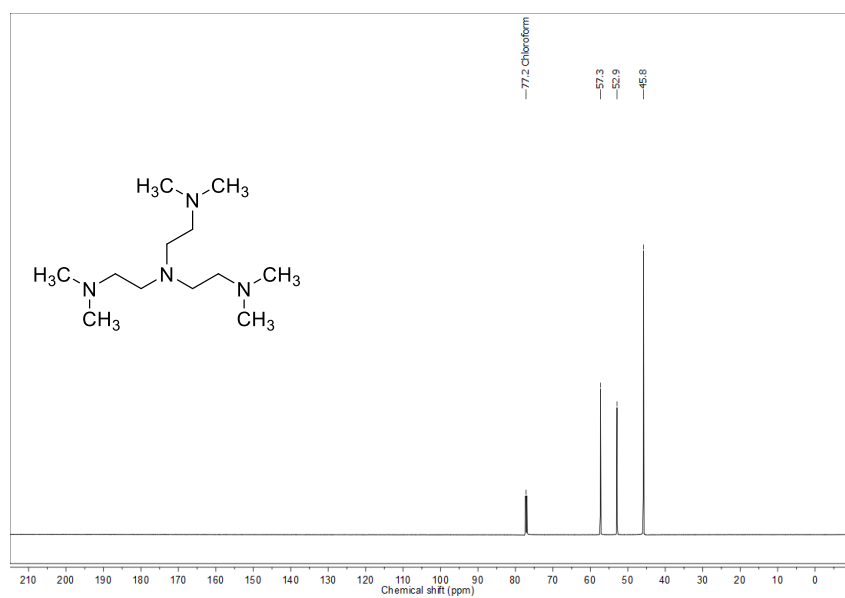


Figure S36. ¹³C{¹H} NMR spectrum of tris[2-(dimethylamino)ethyl]amine (3) in CDCl₃.

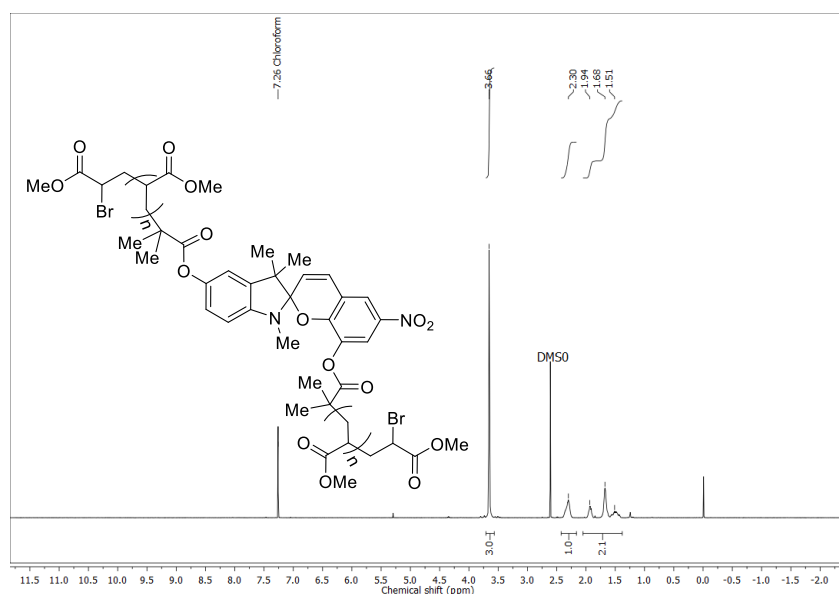


Figure S37. ^1H NMR spectrum of SP functionalized polymethylacrylate PMA 4 in CDCl_3 .

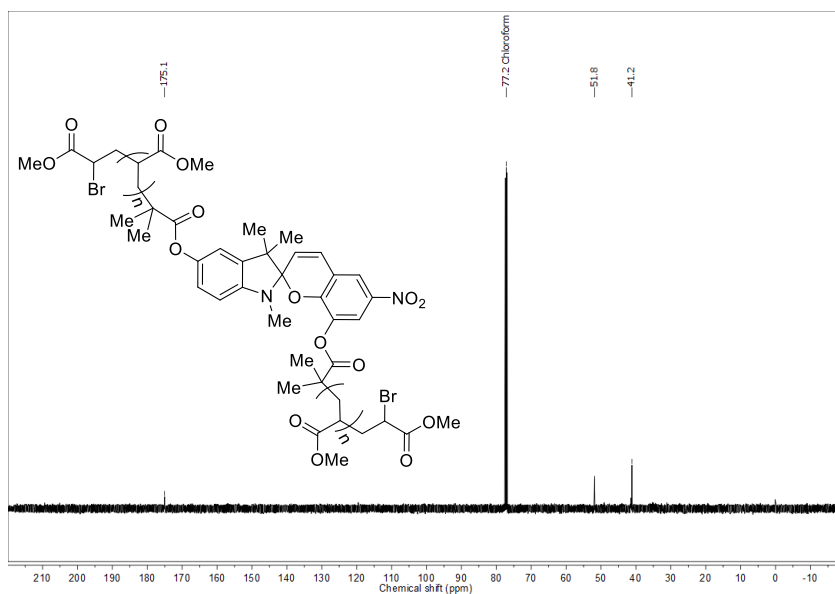


Figure S38. $^{13}\text{C}\{^1\text{H}\}$ NMR spectrum of SP functionalized polymethylacrylate PMA 4 in CDCl_3 .

References

- (1) Potisek, S. L.; Davis, D. A.; Sottos, N. R.; White, S. R.; Moore, J. S. Mechanophore-Linked Addition Polymers. *J. Am. Chem. Soc.* **2007**, *129* (45), 13808–13809. <https://doi.org/10.1021/ja076189x>.
- (2) Davis, D. A.; Hamilton, A.; Yang, J.; Cremar, L. D.; Van Gough, D.; Potisek, S. L.; Ong, M. T.; Braun, P. V.; Martínez, T. J.; White, S. R.; Moore, J. S.; Sottos, N. R. Force-Induced Activation of Covalent Bonds in Mechanoresponsive Polymeric Materials. *Nature* **2009**, *459* (7243), 68–72. <https://doi.org/10.1038/nature07970>.
- (3) Schulz-Senft, M.; Gates, P. J.; Sönnichsen, F. D.; Staubitz, A. Diversely Halogenated Spiropyran - Useful Synthetic Building Blocks for a Versatile Class of Molecular Switches. *Dye. Pigment.* **2017**, *136*, 292–301. <https://doi.org/10.1016/j.dyepig.2016.08.039>.
- (4) Ciampolini, M.; Nardi, N. Five-Coordinated High-Spin Complexes of Bivalent Cobalt, Nickel, and Copper with Tris(2-Dimethylaminoethyl)Amine. *Inorg. Chem.* **1966**, *5* (1), 41–44. <https://doi.org/10.1021/ic50035a010>.
- (5) Fu, Q.; McKenzie, T. G.; Tan, S.; Nam, E.; Qiao, G. G. Tertiary Amine Catalyzed Photo-Induced Controlled Radical Polymerization of Methacrylates. *Polym. Chem.* **2015**, *6* (30), 5362–5368. <https://doi.org/10.1039/c5py00840a>.

Part III

Summary and Outlook

Chapter 11

Summary and Outlook

The scope of this thesis involved the exploration of synergistic capabilities of additive manufacturing and self-organisation phenomena. Precise control over features on the mm-, μm - and nm-scale enables facile design and manufacturing of advanced material concepts for nearly all important sectors. The benefits of such a combinatorial approach have been demonstrated exemplary for biomedical applications in the chapters **3**, **6**, **7** and **9**. The main research topics and their classification is depicted in Figure 11.1.

One can divide the research topics presented in the scope of this thesis into three categories. The first one is utilising self-organisation phenomena to manufacture composites for advanced biomedical applications. Wetting as a driving force for self-organisation has been employed in chapters **3**, **5** and **6** to assemble complex-shaped architectures on the μm -scale. Although these processes did not involve additive manufacturing, the self-organisation phenomena can also be used in respective DIW systems. Exemplary, complex undercuts can be made by using selective wetting. Polar particle agglomerates of varying sizes induce dissimilarly strong capillary action, soaking up more or less polymer and thus create complex-shaped undercuts for adhesion of low surface energy polymers. As demonstrated in chapters **8** and **9**, microparticles can be deposited by DIW. By leaving the particles agglomerated during the printing process (i.e., refraining from a dispersion process), defined macroscopic patterns of complex-shaped undercut structures on the nano- and microscale could be realised on e.g. PEEK.

The second research topic involves complex-shaped microparticles formed by self-organisation utilising the unique features like their shape or semiconducting properties these particles exhibit. In chapters **4** and **7** properties from the single-crystalline zinc oxide tetrapods have been used in polymer composites to harness semiconductor qualities (i.e., large space charge region made by surface defects) especially found in microscopic single crystals. This approach is useful for, e.g., the biomedical sector. On the one hand, complex, interrelated matters like personalised medicine lead to a tight set of limitations. These restrictions include cell compatibility, tissue regeneration, antibacterial properties, hydration, oxygenation and many others. However, this thesis showed that even tight sets of restrictions can be fulfilled by a combination of self-organised microparticles and additive manufacturing of biomaterials in chapter **7**.

The same holds for the third research item, where additive manufacturing was used for determining macroscopic and subsequent self-organisation steps created micro- and nanoscopic features. In this way the facile fabrication of highly sensitive acetone sensors in chapters **8** and **9** have been presented. The concept can be generalised for a multitude of electronic circuits, that involve semiconducting oxide nanostructures, like diodes or

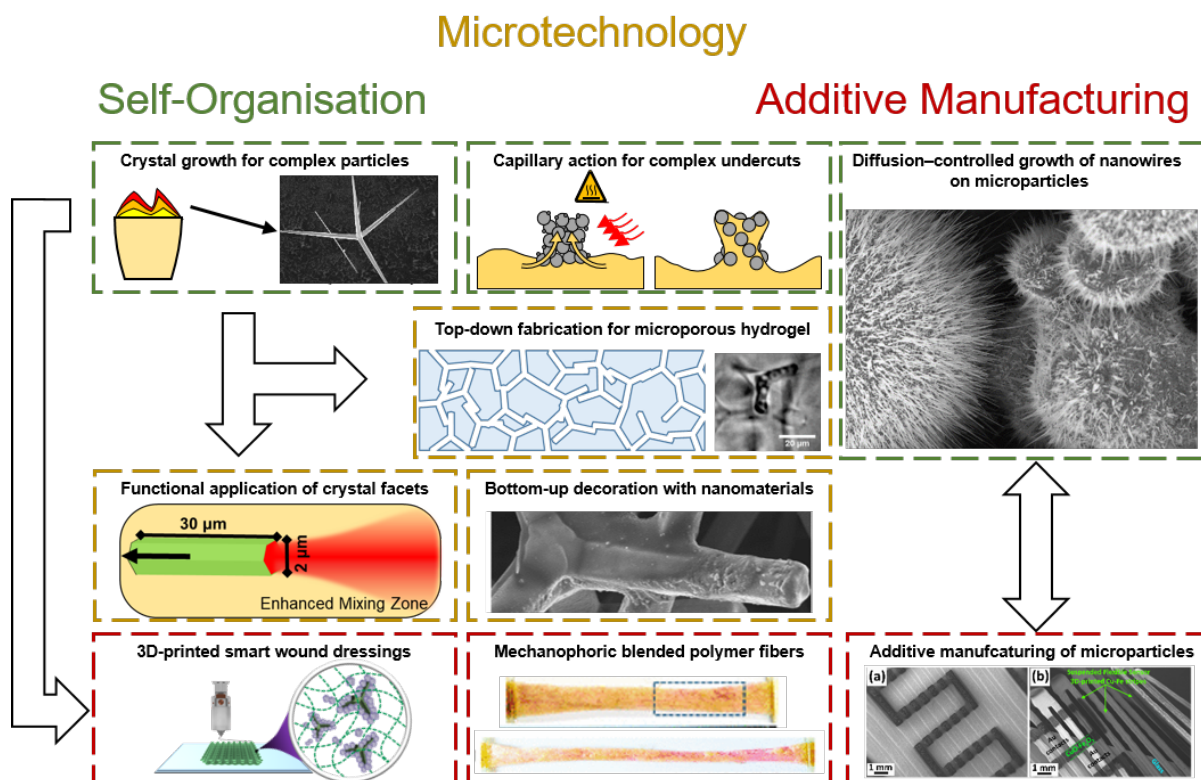


Figure 11.1: The main research items of this thesis summarised in one graphic. The topics of this thesis can be divided into three parts. Self-organisation phenomena were investigated and applied for fabrication of micro- and nanostructures. Some of these complex-shaped microparticles were employed in microtechnological processes (i.e. drop-casting or etching) for bottom-up and top-down fabrication of interesting novel materials. Finally, additively manufactured systems were investigated by either direct printing of self-organised complex-shaped particles, the self-organisation of polymer blends during spinning or additive manufacturing of microparticles with subsequent growth of nanostructures by means of self-organisation.

transistors. Therefore, not only biomedical applications can be realised by this approach but also general sensor concepts in consumer or industrial electronics. For metal oxide core-spike particles like $\text{CuO}/\text{Cu}_2\text{O}/\text{Cu}$ a simple yet versatile manufacturing has been demonstrated to lead to highly sensitive devices. The method is also applicable for mass fabrication. One future idea is to use the wetting behaviour of ZnO sea-urchin type particles to create a superhydrophilic, rapid evaporator. This high evaporation rate can be achieved by ultra-fast spreading of a water droplet on many parallel whisker surfaces. By controlled deposition of Zn particles via DIW, selective surface-bound fluidics can be manufactured easily. The concept of rapid evaporation by this method has already been proven and the current research involves understanding the fundamental processes which

involve many of the mechanisms presented in this thesis, e.g., wetting, capillary action and the nucleation and mechanism.

Another interesting research item to be expanded upon in the future builds on the experience from DIW of micro- and nanoparticles. This concept can be described as the laser-assisted DIW. High power lasers can be used for sintering or melting of ceramic or metal particles. DIW can be used to deposit inks containing these particles and each layer can be sintered individually. Multimaterial prints could then be achieved by printing more than one ink. The laser's power can be varied depending on the material demands and thus complex ceramic, metal, polymer or composite parts can be sintered together.

Bibliography

- [1] A. Sydney Gladman et al. ‘Biomimetic 4D printing’. In: *Nature materials* 15.4 (2016), pp. 413–418. ISSN: 1476-1122. DOI: 10.1038/nmat4544.
- [2] Gregory I. Peterson et al. ‘3D-printed mechanochromic materials’. In: *ACS applied materials & interfaces* 7.1 (2015), pp. 577–583. DOI: 10.1021/am506745m.
- [3] Alexander D. Valentine et al. ‘Hybrid 3D Printing of Soft Electronics’. In: *Advanced materials (Deerfield Beach, Fla.)* 29.40 (2017). DOI: 10.1002/adma.201703817.
- [4] R. Leal et al. ‘Additive manufacturing tooling for the automotive industry’. In: *The International Journal of Advanced Manufacturing Technology* 92.5-8 (2017), pp. 1671–1676. ISSN: 0268-3768. DOI: 10.1007/s00170-017-0239-8.
- [5] Milan Brandt, ed. *Laser additive manufacturing: Materials, design, technologies, and applications*. Vol. number 88. Woodhead Publishing series in electronic and optical materials. Amsterdam: Elsevier/Woodhead Publishing Woodhead Publishing is an imprint of Elsevier, 2017. ISBN: 9780081004333.
- [6] Mohd. Javaid and Abid Haleem. ‘Additive manufacturing applications in medical cases: A literature based review’. In: *Alexandria Journal of Medicine* 54.4 (2018), pp. 411–422. ISSN: 2090-5068. DOI: 10.1016/j.ajme.2017.09.003.
- [7] Nitipon Saengchairat, Tuan Tran and Chee-Kai Chua. ‘A review: Additive manufacturing for active electronic components’. In: *Virtual and Physical Prototyping* 12.1 (2017), pp. 31–46. ISSN: 1745-2759. DOI: 10.1080/17452759.2016.1253181.
- [8] Neha Arora and N. N. Sharma. ‘Arc discharge synthesis of carbon nanotubes: Comprehensive review’. In: *Diamond and Related Materials* 50 (2014), pp. 135–150. ISSN: 09259635. DOI: 10.1016/j.diamond.2014.10.001.
- [9] Bharat Bhushan. ‘Adhesion of multi-level hierarchical attachment systems in gecko feet’. In: *Journal of Adhesion Science and Technology* 21.12-13 (2007), pp. 1213–1258. ISSN: 0169-4243. DOI: 10.1163/156856107782328353. URL: <https://doi.org/10.1163/156856107782328353>.
- [10] Joachim Fischer, Georg von Freymann and Martin Wegener. ‘The materials challenge in diffraction-unlimited direct-laser-writing optical lithography’. In: *Advanced materials (Deerfield Beach, Fla.)* 22.32 (2010), pp. 3578–3582. DOI: 10.1002/adma.201000892.
- [11] J. A. Lewis. ‘Direct Ink Writing of 3D Functional Materials’. In: *Advanced Functional Materials* 16.17 (2006), pp. 2193–2204. DOI: 10.1002/adfm.200600434.
- [12] K. Gnanasekaran et al. ‘3D printing of CNT- and graphene-based conductive polymer nanocomposites by fused deposition modeling’. In: *Applied Materials Today* 9 (2017), pp. 21–28. ISSN: 23529407. DOI: 10.1016/j.apmt.2017.04.003.

- [13] Qiangqiang Zhang et al. ‘3D Printing of Graphene Aerogels’. In: *Small* 12.13 (2016), pp. 1702–1708. ISSN: 16136810. DOI: 10.1002/smll.201503524.
- [14] Jinchun Chi et al. ‘3D Printing of Self-Organizing Structural Elements for Advanced Functional Structures’. In: *Advanced Materials Technologies* 3.5 (2018), p. 1800003. ISSN: 2365709X. DOI: 10.1002/admt.201800003.
- [15] Arda Kotikian et al. ‘3D Printing of Liquid Crystal Elastomeric Actuators with Spatially Programed Nematic Order’. In: *Advanced materials (Deerfield Beach, Fla.)* 30.10 (2018). DOI: 10.1002/adma.201706164.
- [16] Conor G. Harris et al. ‘Additive Manufacturing With Soft TPU – Adhesion Strength in Multimaterial Flexible Joints’. In: *Frontiers in Mechanical Engineering* 5 (2019), p. 172. ISSN: 2297-3079. DOI: 10.3389/fmech.2019.00037.
- [17] Pap A. Ndiaye and Elborg Forster. *Nylon and Bombs: DuPont and the March of Modern America*. Studies in Industry and Society. Baltimore, MD: Johns Hopkins University Press, 2007. ISBN: 9780801884443. URL: <http://gbv.ebib.com/patron/FullRecord.aspx?p=4398441>.
- [18] Hideo Kodama. ‘Automatic method for fabricating a three-dimensional plastic model with photo-hardening polymer’. In: *Review of Scientific Instruments* 52.11 (1981), pp. 1770–1773. ISSN: 0034-6748. DOI: 10.1063/1.1136492.
- [19] Charles W. Hull. ‘Method of and apparatus for production of three dimensional objects by stereolithography’. 1993.
- [20] Michael S. Rill et al. ‘Photonic metamaterials by direct laser writing and silver chemical vapour deposition’. In: *Nature materials* 7.7 (2008), pp. 543–546. ISSN: 1476-1122. DOI: 10.1038/nmat2197.
- [21] S. Kawata et al. ‘Finer features for functional microdevices’. In: *Nature* 412.6848 (2001), pp. 697–698. ISSN: 0028-0836. DOI: 10.1038/35089130.
- [22] Markus Deubel et al. ‘Direct laser writing of three-dimensional photonic-crystal templates for telecommunications’. In: *Nature materials* 3.7 (2004), pp. 444–447. ISSN: 1476-1122. DOI: 10.1038/nmat1155.
- [23] Michelle L. Griffith and John W. Halloran. ‘Freeform Fabrication of Ceramics via Stereolithography’. In: *Journal of the American Ceramic Society* 79.10 (1996), pp. 2601–2608. ISSN: 0002-7820. DOI: 10.1111/j.1151-2916.1996.tb09022.x.
- [24] Gabriel T-M. Chu et al. ‘Ceramic SFF by Direct and Indirect Stereolithography’. In: *MRS Proceedings* 542 (1998). ISSN: 0272-9172. DOI: 10.1557/proc-542-119.
- [25] G. Allen Brady and John W. Halloran. ‘Stereolithography of ceramic suspensions’. In: *Rapid Prototyping Journal* (). DOI: 10.1108/13552549710176680.
- [26] Jae-Won Choi, Ho-Chan Kim and Ryan Wicker. ‘Multi-material stereolithography’. In: *Journal of Materials Processing Technology* 211.3 (2011), pp. 318–328. ISSN: 09240136. DOI: 10.1016/j.jmatprotec.2010.10.003.

- [27] Terry Wohlers et al. *Wohlers report 2019: 3D printing and additive manufacturing state of the industry*. Fort Collins, Colo.: Wohlers Associates, 2019. ISBN: 099133325X.
- [28] S. Scott Crump. ‘Apparatus and method for creating three-dimensional objects’. US5121329A. 1989.
- [29] Valentina Guerra, Chaoying Wan and Tony McNally. ‘Fused deposition modelling (FDM) of composites of graphene nanoplatelets and polymers for high thermal conductivity: a mini-review’. In: *Functional Composite Materials* 1.1 (2020). DOI: 10.1186/s42252-020-00005-x.
- [30] Ryan L. Truby et al. ‘Soft Somatosensitive Actuators via Embedded 3D Printing’. In: *Advanced Materials* 30.15 (2018), p. 1706383. ISSN: 09359648. DOI: 10.1002/adma.201706383.
- [31] J. William Boley et al. ‘Shape-shifting structured lattices via multimaterial 4D printing’. In: *Proceedings of the National Academy of Sciences* 116.42 (2019), pp. 20856–20862. ISSN: 0027-8424. DOI: 10.1073/pnas.1908806116.
- [32] Miloslav Nič et al., eds. *IUPAC Compendium of Chemical Terminology*. Research Triangle Park, NC: IUPAC, 2009. ISBN: 0-9678550-9-8. DOI: 10.1351/goldbook.
- [33] John Emsley. *Nature’s building blocks: An A-Z guide to the elements*. Reprinted with corrections. Oxford: Oxford Univ. Press, 2003. ISBN: 978-0-19-850340-8.
- [34] Norman N. Greenwood and Alan Earnshaw. *Chemistry of the elements*. 2. ed., repr. Amsterdam: Elsevier-Butterworth-Heinemann, 2010. ISBN: 978-0-7506-3365-9.
- [35] Irfan Habib and D. P. Chattopadhyaya. *Economic history of Medieval India, 1200 - 1500*. Vol. Pt. 1. History of science, philosophy and culture in Indian civilization Economic history of India. New Delhi: Centre for Studies in Civilizations, 2011. ISBN: 978-81-317-2791-1.
- [36] P. T. Craddock, ed. *2000 years of zinc and brass*. Vol. 50. British Museum [London]. London: British Museum Press, 1998. ISBN: 978-0-86159-124-4.
- [37] Yi Zhou et al. ‘Synthesis of sea urchin-like ZnO by a simple soft template method and its photoelectric properties’. In: *Materials Science in Semiconductor Processing* 27 (2014), pp. 1050–1056. ISSN: 13698001. DOI: 10.1016/j.mssp.2014.09.010.
- [38] Motoi Kitano et al. ‘Growth of large tetrapod-like ZnO crystals’. In: *Journal of Crystal Growth* 102.4 (1990), pp. 965–973. ISSN: 00220248. DOI: 10.1016/0022-0248(90)90867-K.
- [39] Dawit Gedamu et al. ‘Rapid Fabrication Technique for Interpenetrated ZnO Nanotetrapod Networks for Fast UV Sensors’. In: *Advanced Materials* 26.10 (2014), pp. 1541–1550. ISSN: 09359648. DOI: 10.1002/adma.201304363.
- [40] C. Ronning et al. ‘Nucleation mechanism of the seed of tetrapod ZnO nanostructures’. In: *Journal of Applied Physics* 98.3 (2005), p. 034307. ISSN: 0021-8979. DOI: 10.1063/1.1997290.

- [41] Fabian Schütt et al. ‘Hierarchical self-entangled carbon nanotube tube networks’. In: *Nature Communications* 8.1 (2017), p. 830. ISSN: 2041-1723. DOI: 10.1038/s41467-017-01324-7.
- [42] Fabian Schütt et al. ‘Conversionless efficient and broadband laser light diffusers for high brightness illumination applications’. In: *Nature Communications* 11.1 (2020), p. 72107. ISSN: 2041-1723. DOI: 10.1038/s41467-020-14875-z.
- [43] Ye Zhang et al. ‘Synthesis, Microstructure, and Growth Mechanism of Dendrite ZnO Nanowires’. In: *The Journal of Physical Chemistry B* 107.33 (2003), pp. 8289–8293. ISSN: 1520-6106. DOI: 10.1021/jp034834q.
- [44] Yogendra Kumar Mishra and Rainer Adelung. ‘ZnO tetrapod materials for functional applications’. In: *Materials Today* 21.6 (2018), pp. 631–651. ISSN: 13697021. DOI: 10.1016/j.mattod.2017.11.003.
- [45] Jun Zhang and H. Wayne Richardson. ‘Copper Compounds’. In: *Ullmann’s encyclopedia of industrial chemistry*. Chichester: Wiley, 2010, pp. 1–31. ISBN: 9783527306732. DOI: 10.1002/14356007.a07{\textunderscore}567.pub2.
- [46] Lijun Xiang et al. ‘A brief review on the growth mechanism of CuO nanowires via thermal oxidation’. In: *Journal of Materials Research* 33.16 (2018), pp. 2264–2280. ISSN: 0884-2914. DOI: 10.1557/jmr.2018.215.
- [47] Benjamin J. Hansen et al. ‘Short-circuit diffusion growth of long bi-crystal CuO nanowires’. In: *Chemical Physics Letters* 504.1-3 (2011), pp. 41–45. ISSN: 00092614. DOI: 10.1016/j.cplett.2011.01.040.
- [48] Pierre-Gilles de Gennes. ‘Entangled polymers: Physics Today, 36(6), 33-39’. In: (1983). DOI: 10.1063/1.2915700.
- [49] T. Tervoort et al. ‘Melt-Processable Poly(tetrafluoroethylene)’. In: *Macromolecules* 33.17 (2000), pp. 6460–6465. DOI: 10.1021/ma000747+.
- [50] Marta Calvo Catoira et al. ‘Overview of natural hydrogels for regenerative medicine applications’. In: *Journal of Materials Science: Materials in Medicine* 30.10 (2019), pp. 1–10. ISSN: 1573-4838. DOI: 10.1007/s10856-019-6318-7.
- [51] P. Alexandridis. ‘Gold Nanoparticle Synthesis, Morphology Control, and Stabilization Facilitated by Functional Polymers’. In: *Chemical Engineering & Technology* 34.1 (2011), pp. 15–28. ISSN: 09307516. DOI: 10.1002/ceat.201000335.
- [52] Fei Wang et al. ‘Progress Report on Phase Separation in Polymer Solutions’. In: *Advanced materials (Deerfield Beach, Fla.)* 31.26 (2019), e1806733. DOI: 10.1002/adma.201806733.
- [53] Chih-Wei Chiu and Jiang-Jen Lin. ‘Self-assembly behavior of polymer-assisted clays’. In: *Progress in Polymer Science* 37.3 (2012), pp. 406–444. ISSN: 00796700. DOI: 10.1016/j.progpolymsci.2011.07.007.

- [54] K. Y. Suh and H. H. Lee. ‘Capillary Force Lithography: Large-Area Patterning, Self-Organization, and Anisotropic Dewetting’. In: *Advanced Functional Materials* 12.6-7 (2002), pp. 405–413. DOI: 10.1002/1616-3028(20020618)12:6/7{\textless}405::AID-ADFM405{\textgreater}3.0.CO;2-1.
- [55] C. E. Chaffey. ‘Mechanisms and equations for shear thinning and thickening in dispersions’. In: *Colloid and Polymer Science* 255.7 (1977), pp. 691–698. ISSN: 0303-402X. DOI: 10.1007/BF01550058.
- [56] L. H. Baekeland. ‘The Synthesis, Constitution, and Uses of Bakelite’. In: *Journal of Industrial & Engineering Chemistry* 1.3 (2002), pp. 149–161. ISSN: 0095-9014. DOI: 10.1021/ie50003a004.
- [57] Hansjörg Sinn and Walter Kaminsky. ‘Ziegler-Natta Catalysis’. In: *Advances in Organometallic Chemistry*. Ed. by F.G.A Stone and Robert West. Vol. 18. Academic Press, 1980, pp. 99–149. ISBN: 0065-3055. DOI: 10.1016/S0065-3055(08)60307-X.
- [58] G. Billuart et al. ‘Free Radical Emulsion Polymerization of Ethylene’. In: *Macromolecules* 47.19 (2014), pp. 6591–6600. DOI: 10.1021/ma5012733.

Part IV

Appendix A

Additional Publications

3D-Printed Sensor Array of Semiconducting Oxides

The combinatorial concept of additive manufacturing of metal microparticles and subsequent self-organised growth of nanowires has been explored for cupric oxide and a cupric oxide - ferric oxide hybrid system in chapters 8 and 9. The main application demonstrated was biomedical breath analysis based on acetone vapour sensing at small nanowires junctions between oxidised metal microparticles. Additive manufacturing provided the necessary control over the track width to ensure reproducible devices. The application is not limited to acetone vapours but it works with most reducing gases. In this work the previously presented nanowire assemblies are tested for their sensitivity against other common volatile organic compounds, namely ethanol and 2-propanol vapours. It is found that the pure cupric oxide shows a significant selectivity towards 2-propanol compared to ethanol with a gas response of 50% at an operating temperature of 350 °C. The cupric oxide - ferric oxide hybrid system however is more selective towards ethanol with a slightly lower gas response of 24% at an operating temperature of 300 °C. The processes established in this thesis can therefore be used for quick permutation of various metal oxide nanowire-based gas sensors resulting in the facile fabrication of highly selective gas sensing devices without the need for sophisticated and expensive clean room technology. The results were presented at the "International Conference on Nanotechnologies and Biomedical Engineering".

Own contribution presented in this article

- Design and setup of the Direct Ink Writing printer
- Sample fabrication
- Data analysis
- Discussion and interpretation
- Writing the manuscript



3D-Printed Sensor Array of Semiconducting Oxides

L. Siebert, M. I. Terasa, N. Ababii, O. Lupan, and R. Adelung

Abstract

Sensors start to play an ever increasing role in human life and new technologies for their cost-effective mass production are required. In this work, the one-step 3D-printing of nanoflakes—nanowire covered $\text{Fe}_2\text{O}_3/\text{Fe}-\text{CuO}/\text{Cu}_2\text{O}/\text{Cu}$ microparticles (MPs) with diameters of $\sim 10 \mu\text{m}$ on the surface of glass substrate successfully forming an ordered net is reported for the first time. 3D-printed Fe–Cu and only Cu MPs-based stripes formed non-planar $\text{CuO}/\text{Cu}_2\text{O}/\text{Cu}$ and $\text{Fe}_2\text{O}_3/\text{Fe}-\text{CuO}/\text{Cu}_2\text{O}/\text{Cu}$ heterojunctions after thermal annealing at 425°C for 4 h in air and were fully covered with nanoflakes of Fe_2O_3 and CuO nanowire net bridging MPs with external Au-contacts. The morphological, chemical and structural investigations were performed in detail, showing the high crystallinity of the 3D printed material. This concept proves to be easily translatable to other semiconducting, metallic or functional microparticles for the rapid fabrication of sensor devices.

Keywords

3D printing • Cu–Fe deposition • Heterojunction • $\text{Fe}_2\text{O}_3-\text{CuO}/\text{Cu}_2\text{O}/\text{Cu}$ • Gas sensing

1 Introduction

Nowadays, three-dimensional (3D) printing has attracted a significant amount of attention, for example, for the manufacturing of custom devices or complex and functional parts [1, 2]. Another very important field is the fabrication built from functional nanomaterials or as macro- or microdevices via 3D-printing technologies due to the low-cost and easy processing [3–5].

In this field of biomedical engineering, 3D-printed components or biosensors have gained a significant attention, due to novel design possibilities e.g. for innovative strain sensors [6–8] or full electronic components [9]. The reason for this boom in this new and quite efficient technology is the compatibility with standard techniques from materials science for both the materials preparation as well as the post processing after 3D printing.

In this regard, Direct Ink Writing (DIW) has become a prominent technology, focusing on the fabrication of devices and particle systems from a viscous liquid ink [10, 11]. With this technique, even complex-shaped micro- and nanoparticles can be arranged in 3D or as 2D traces for micro- and nanoelectronics [12]. Here we present the simple integration of semiconducting oxides by DIW of metal particles with subsequent heat treatment to form sensor nets for volatile organic compound (VOC) detection.

2 Experimental

Spheroidal copper particles ($\sim 10 \mu\text{m}$) and spheroidal iron particles ($\sim 10 \mu\text{m}$) were obtained from Sigma-Aldrich. For the copper based sensor, the 3 parts by weight of Cu particles were sonicated in 2 parts distilled water for 5 min after which polyethylene oxide (PEO, $M_v = 2,000,000$), obtained from Sigma-Aldrich was added. The solution was stirred until a homogeneous, viscous state was reached for the ink.

L. Siebert (✉) · M. I. Terasa · O. Lupan (✉) · R. Adelung
Functional Nanomaterials, Faculty of Engineering, Institute for
Materials Science, Kiel University, Kaiserstraße 2, Kiel, Germany
e-mail: lesi@tf.uni-kiel.de

O. Lupan
e-mail: ollu@tf.uni-kiel.de

N. Ababii · O. Lupan
Department of Microelectronics and Biomedical Engineering,
Center for Nanotechnology and Nanosensors, Technical
University of Moldova, Chisinau, Republic of Moldova

The concentration of PEO in the final ink was 6% by weights.

For the Cu–Fe based sensor array, both copper and iron particles were sonicated in 96% Ethanol for 5 min. Polyvinyl butyral (PVB) was kindly provided by Kuraray Co. Ltd. and was added and the solution was stirred at room temperature until a homogeneous mixture was obtained. The mixing ratios of the final ink by weights were 3:1:0.5:0.5 (Ethanol:PVB:Fe:Cu). Both inks were printed in a custom-built DIW apparatus. The Cu-based ink was printed with a tapered nozzle (diameter $d = 0.41$ mm) with a constant printing speed of $0.6 \text{ mm}^3 \text{ s}^{-1}$, while the Cu–Fe-based ink was printed with a nozzle diameter of $d = 0.58$ at a speed of $0.46 \text{ mm}^3 \text{ s}^{-1}$. One layer was printed for both variations with a layer height of 0.1 mm. The printing substrate was a standard glass slide. After printing, the objects were dried at room temperature overnight and subsequently heat-treated for 4 h at $425 \text{ }^\circ\text{C}$ in air.

Micro-Raman, X-Ray Diffraction and Scanning Electron Microscopy were done to investigate the structural and morphological properties of the printed constructs.

Micro-Raman was performed at room temperature using a WITec system. A Nd:YAG laser was used which power was set to less than 4 mW.

The wavelength of the laser was $\lambda_{ex} = 532.2$ nm and each spectrum was taken with 10 accumulations at an integration time of 1 s.

XRD was performed on a Seifert 3000 TT unit at 40 kV and 40 mA, with $\text{CuK}\alpha_1$ radiation ($\lambda = 1.540598 \text{ \AA}$).

Additionally, interdigitated gold contacts were sputtered onto the samples (~ 170 nm), to measure the sensor properties. By determining the resistance ratios $\Delta R/R_{air}$, where R_{air} and R_{gas} and $\Delta R = R_{gas} - R_{air}$ are the electrical resistances of the printed sensor in ambient air and under exposure to VOCs, respectively. More details on the sensing experiments can be found in previous works on gas sensing [13, 14].

For all further results and the discussion, the copper-based sample set will be named CuO 3D and the copper-iron-based sample set will be named CuO– Fe_2O_3 3D.

3 Results and Discussion

In Fig. 1a is presented XRD for CuO 3D sample annealed TA at $425 \text{ }^\circ\text{C}$ for 4 h, where detected three phases (CuO monoclinic, Cu_2O and Cu cubic). In XRD was detected mainly CuO (Tenorite) at 2θ of 32.65° , 35.65° , 46.7° , 48.8° , 58.25° , 61.5° , 68.05° , 72.6° , 75.35° , 83.85° , 90.05° and 95.2° , respectively. Reflections at 2θ of 36.5° , 42.35° , 52.75° , 73.35° and 77.7° , are due to Cu_2O (Cuprite) phase. Also, at 2θ of 43.35° , 50.5° and 74.15° were detected reflections of metallic Cu, accordingly.

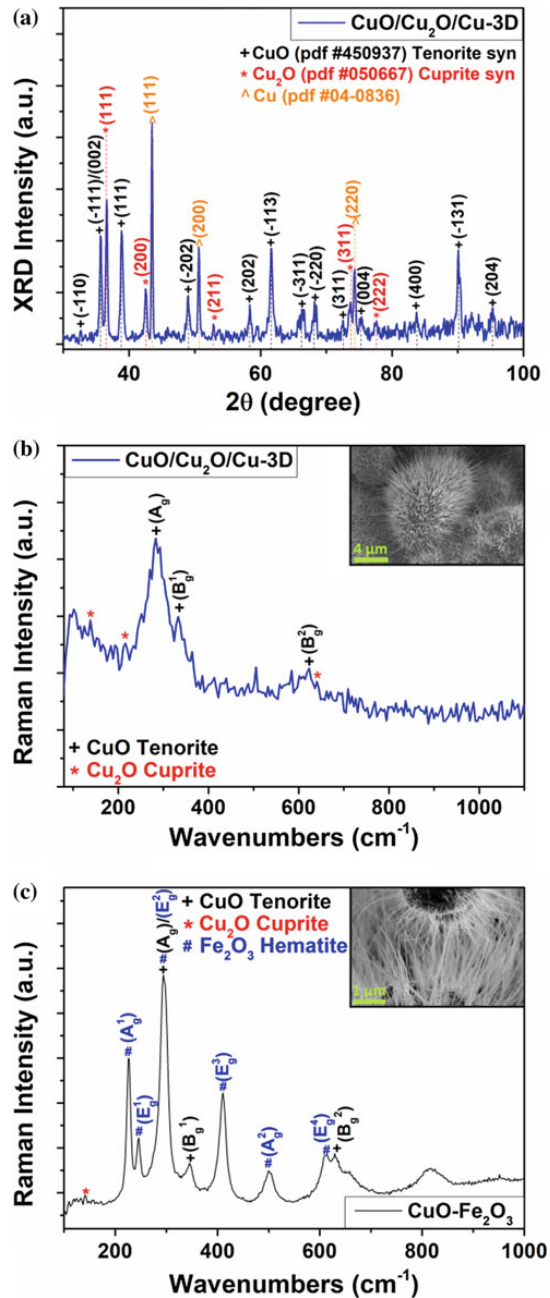


Fig. 1 a XRD patterns of the 3D printed nanowire CuO/Cu₂O/Cu heterojunction net after thermal annealing at $425 \text{ }^\circ\text{C}$ for 4 h in air for CuO 3D-T sample set; b Raman spectra for CuO 3D-T sample set from (a), in insertion is SEM for CuO 3D-T; c Raman spectrum of the 3D printed nanoflakes—nanowire covered $\text{Fe}_2\text{O}_3/\text{Fe}-\text{CuO}/\text{Cu}_2\text{O}/\text{Cu}$ microparticles (MPs) heterojunction net after TA at $425 \text{ }^\circ\text{C}$ for 2 h in air

In Fig. 1b is shown micro-Raman for CuO 3D annealed TA at 425 °C for 4 h which confirms Cu₂O and CuO in the printed samples after annealing, where intense modes at 283, 332 and 610 cm⁻¹ are due to CuO (Tenorite) and weaker peaks at 129, 215 and 627 cm⁻¹ are due to Cu₂O (Cuprite). In insertion you can see SEM for CuO 3D samples covered with nanowires on top of CuO/Cu₂O/Cu microparticles (MPs).

In Fig. 1c is shown micro-Raman for CuO–Fe₂O₃ samples TA at 425 °C for 4 h, where modes of Cu₂O, CuO and Fe₂O₃ phases in MPs are observed, namely modes A_g (297 cm⁻¹), B_g¹ (345 cm⁻¹) and B_g² (633 cm⁻¹) corresponds to CuO (Tenorite), mode (143 cm⁻¹) corresponds to Cu₂O as well as A_g¹ (227 cm⁻¹), E_g¹ (246 cm⁻¹), E_g² (297 cm⁻¹), E_g³ (408 cm⁻¹), A_g² (498 cm⁻¹) and E_g⁴ (612 cm⁻¹) which are due to α-Fe₂O₃ (Hematite). In the insertion of Fig. 1c, SEM images can be seen for CuO–Fe₂O₃ nanowires—nanoflakes, which are covering the Cu and Fe MPs.

The gas sensing results are presented in Fig. 2.

Figure 2a shows the gas response for ethanol and 2-propanol on CuO 3D samples. A higher selectivity for 2-propanol can be observed at the operating temperature

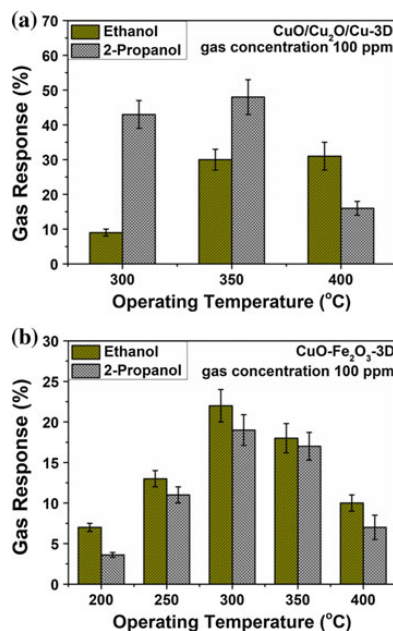


Fig. 2 Gas response to 100 ppm of ethanol and 2-propanol vapors for the 3D-printed sensor on: **a** nanowire CuO/Cu₂O/Cu heterojunction net at OPT of 300, 350 and 400 °C for sensor on CuO 3D; **b** nanoflake-nanowire Fe₂O₃-CuO/Cu₂O/Cu microparticles (MPs) with diameters of 15–25 μm heterojunction net at OPT of 200 °C up to 400 °C for sample set CuO–Fe₂O₃ 3D

(OPT) of 300 °C, whereas ethanol only invokes a low change in resistance. At 350 °C the gas response for 2-propanol slightly increases, while the increase in gas response for the ethanol is a lot higher. When the OPT is set to 400 °C, the gas response for ethanol does not change, while the response for 2-propanol strongly decreases. This shows, that the selectivity towards either VOC can be switched by increasing or decreasing the OPT for 3D printed sensor.

A reason for this behavior might be the desorption of more volatile 2-propanol at higher temperatures, while the less volatile ethanol can still attach onto the nanowires of CuO. Details on the proposed gas sensing mechanism is given in previous works [14, 15].

For the CuO–Fe₂O₃ 3D samples, no such trend can be observed. The selectivity towards either component is not very pronounced and the gas response is generally lower, than for the Cu 3D samples. However, a constant increase of the gas response is found to an OPT of 300 °C. After that, it constantly decreases. Around 300 °C seems to be the optimal temperature range for the detection of VOC for the Fe₂O₃/Fe–CuO/Cu₂O/Cu samples.

Figure 3a shows the dynamic gas response of the optimal OPT for the CuO–Fe₂O₃ 3D samples. The response to the inlet of the gas is immediate, as well as the response to the

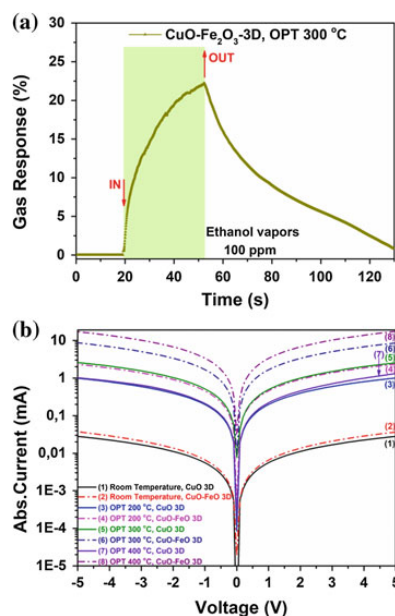


Fig. 3 a Dynamic response to 100 ppm of ethanol vapors 3D-T printed nanoflakes—nanowire covered Fe₂O₃/Fe–CuO/Cu₂O/Cu MPs heterojunction net (sample set 3D). **b** Current-voltage characteristics of Fe₂O₃/Fe–CuO/Cu₂O/Cu and CuO 3D sensor at different operating temperature

gas reduction. As can be expected the time constants for both reactions are different, shown by the sharper increase upon gas inlet and the slow decrease on the gas outlet. This is related to the ad- and desorption mechanism, respectively, indicating that the desorption of gas is slower than the adsorption.

In Fig. 3b the I-V-curves with logarithmic display are shown for all samples tested for their gas response with their respective OPT. For the CuO 3D samples, a strong increase in the conductivity can be observed, when the temperature is raised from RT to 200 °C. Another increase can be observed, when the temperature is raised to 300 °C, however a lower conductivity is observed, when the temperature is at 400 °C. This means, that for the nanowire net, the intrinsic conductivity is reached at 300 °C, with no further increase in charge carrier concentration upon temperature increase.

When no higher charge carrier concentration can be reached, the classic mechanism for the temperature dependence in conducting materials is dominant which include scattering of electrons on the vibrating lattice (phonons). With the maximum conductivity at an OPT of 300 °C, it seems obvious that the highest gas response at the same temperature is related to the conductivity. The base conductivity gets lowered by the adsorption of the gas molecules, thus increasing this conductivity results in a higher change in resistance. The same mechanism is not as easily applicable to the CuO-Fe₂O₃ 3D sample set, as its conductivity steadily increases with increasing temperature, indicating that the iron oxide is not in its intrinsic state at 400 °C. The maximum of the sensitivity at 300 °C with respect to the proposed mechanism for the CuO 3D samples indicates that the absorption of gas is mainly governed by the CuO/Cu₂O/Cu heterojunctions and not by the iron oxide. With higher temperatures, the iron oxide shortcuts the copper oxide, leading to conductive pathways not afflicted by the adsorbed gas species.

4 Conclusions

The rapid 3D-printing of CuO/Cu₂O/Cu microparticles (MPs), which possess diameters of 15–25 μm on the sensors substrate surface is successfully reported for the first time. 3D-printed Cu and Cu-Fe MPs-based stripes with high shape fidelity formed non-planar heterojunctions after thermal treatment at 425 °C in air and were fully covered with dense 20 nm thick nanowire or nanoflakes net. The morphological, chemical and structural investigations were performed in detail, showing the high crystallinity of the NWs and 3D-printed CuO/Cu₂O/Cu heterojunctions lines, as

well as the growth of CuO NWs on the surface of microparticles MPs. The gas response can be mainly related to the ability to absorb VOC onto the surface and the general conductivity of the semiconducting parts. When the adsorption is low, an increase in the conductivity can shortcut the gas response on those parts, where the VOCs are adsorbed.

Acknowledgements This work was financially supported by the German Research Foundation (DFG) via the research unit FOR 2093 “Memristive devices for neuronal systems” through project A2. Additional funding was provided under the project “Hot End” (grant number: 16KN021247), by the Federal ministry for Economic Affairs and Energy. Moreover, this research was partly supported by the project Institutional inst-15.817.02.29A funded by the Government of the Republic of Moldova and by the Technical University of Moldova. Dr. Oleg Lupan acknowledges the Alexander von Humboldt Foundation for the research fellowship for experienced researchers 3-3MOL/1148833 STP at the Institute for Materials Science, Kiel University, Germany. The authors would like to thank J. Bahr for the technical assistance and Prof. Tiginyanu for fruitful scientific discussion. Conflict of Interest The authors declare no competing interests.

References

- Xu, Y., Wu, X., Guo, X., Kong, B., Zhang, M., Qian, X., Mi, S., Sun, W.: *Sensors* **17** (Basel, Switzerland) (2017)
- MacDonald, E., Wicker, R.: *Science* **353** (New York, N.Y.) (2016)
- Zhu, W., O'Brien, C., O'Brien, J.R., Zhang, L.G.: *Nanomedicine* **9**, 859 (London, England) (2014)
- Sultan, S., Siqueira, G., Zimmermann, T., Mathew, A.P.: *Curr. Opin. Biomed. Eng.* **2**, 29 (2017)
- Campbell, T.A., Ivanova, O.S.: *Nano Today* **8**, 119 (2013)
- Gowers, S.A.N., Curto, V.F., Seneci, C.A., Wang, C., Anastasova, S., Vadgama, P., Yang, G.-Z., Boutelle, M.G.: *Anal. Chem.* **87**, 7763 (2015)
- Roda, A., Guardigli, M., Calabria, D., Calabretta, M.M., Cevenini, L., Michelini, E.: *The Anal.* **139**, 6494 (2014)
- Muth, J.T., Vogt, D.M., Truby, R.L., Mengüç, Y., Kolesky, D.B., Wood, R.J., Lewis, J.A.: *Adv. Mater.* **26**, 6307 (Deerfield Beach, Fla.) (2014)
- Wu, S.-Y., Yang, C., Hsu, W., Lin, L.: *Microsyst Nanoeng* **1**, 609 (2015)
- Lewis, J.A., Smay, J.E., Stuecker, J., Cesarano, J.: *J. Am. Ceram. Soc.* **89**, 3599 (2006)
- Lewis, J.A.: *Adv. Funct. Mater.* **16**, 2193 (2006)
- Skylar-Scott, M.A., Gunasekaran, S., Lewis, J.A.: *Proc. Natl. Acad. Sci. U.S.A.* **113**, 6137 (2016)
- Lupan, O., Postica, V., Wolff, N., Polonskyi, O., Duppel, V., Kaidas, V., Lazari, E., Ababii, N., Faupel, F., Kienle, L., Adelung, R.: *Small* **13**, 1602868 (Weinheim an der Bergstrasse, Germany) (2017)
- Lupan, O., Postica, V., Cretu, V., Wolff, N., Duppel, V., Kienle, L., Adelung, R.: *Phys. Status Solidi RRL* **10**, 260 (2016)
- Lupan, O., Cretu, V., Postica, V., Ababii, N., Polonskyi, O., Kaidas, V., Schütt, F., Mishra, Y.K., Monaco, E., Tiginyanu, I., Sontea, V., Strunskus, T., Faupel, F., Adelung, R.: *Sens. Actuators, B* **224**, 434 (2016)

Resistivity Response to Stress and Strain of a Flexible Bi_2Te_3 Based Thermoelectric Material

Energy harvesting becomes an ever increasing field of research since the increasing demand for electrical energy makes maximising energy usage efficiency more and more interesting. In this light thermoelectrics gain interest because of their ability to convert heat back to electrical energy by the Peltier effect. Typical thermoelectrics are often made from tellurides like bismuth telluride (Bi_2Te_3) however they are very brittle and require extreme care in handling. Therefore flexible solutions could be interesting for harvesting body heat and generating electrical power which would otherwise be wasted. This work presents the combination of high throughput centrifugal fibre spinning and subsequent coating with Bi_2Te_3 nanoparticles as a possible solution for applying thermoelectrics in wearable electronics. A time series of compression and stress tests with simultaneous resistivity measurements has been employed to investigate the fundamental mechanisms of such flexible devices. The results were presented at the "International Conference on Nanotechnologies and Biomedical Engineering".

Own contribution presented in this article

- Design and setup of the centrifugal spinning machine
- Discussion and interpretation
- Writing and editing the manuscript



Resistivity Response to Stress and Strain of a Flexible Bi₂Te₃ Based Thermoelectric Material

L. O. Akinsinde, S. Scheitz, L. Zimoch, J. K. Sierck, L. Siebert, R. Adelung, U. Schürmann, M. A. Rübhausen, T. Dankwort, and L. Kienle

Abstract

Here we report about the synthesis of Bi₂Te₃ based flexible thermoelectric materials and the response of the electrical resistivity to tensile and compressive stress. As a template fiber spun polymers have been used onto which a thin composite film of graphene and Bi₂Te₃ nanoplates was deposited. The Bi₂Te₃ nanoplates were synthesized using the polyol method. Upon straining the material, the resistivity dropped which is attributed to the increased contact between the individual wires.

Keywords

Bi₂te₃ • Flexible thermoelectric materials • Composite materials • Polyol process • Wet chemical method • Polymer fibers

1 Introduction

Bismuth Telluride (Bi₂Te₃), belonging to the chalcogenide-based thermoelectrics is well known for its high efficiency with respect to room temperature applications [1–3]. To obtain thermoelectric devices, conventional high temperature synthesis routes are used. Afterwards the material is ball milled to obtain powders, which in a consecutive step are sintered and compacted to obtain thermoelectric legs [4, 5]. Thus, the processing is technically costly and time consuming. An alternative synthesis route was found using wet chemical approaches. With the polyol method [6], it was

possible to grow nanoplates (nanoflakes) of various relevant thermoelectric materials [7, 8] including Bi₂Te₃ [9] at moderate temperatures. The obtained materials can be dried and sintered [10]. However, thermoelectric generators (TEGs) using sintered Bi₂Te₃ thermoelectric legs are brittle which limits the applicability of these generators. In recent years, flexible TEGs have been designed using e.g. Bi₂Te₃ suspensions, which were deposited on various types of flexible substrate materials [11, 12]. These types of thermoelectric materials have also attracted attention as self-powered pressure and temperature sensors [13].

In this contribution, we report about the synthesis of Bi₂Te₃ nanoplates and an infiltration method using these nanoplates to obtain flexible thermoelectric materials. As a template fiber spun polymers have been used. To enhance the conductivity and facilitate sticking of the Bi₂Te₃ nanoplates, graphene has been introduced. Furthermore, the response of the electrical resistivity to external stress and strain was investigated.

2 Experimental

The synthesis of stoichiometric single crystalline Bi₂Te₃ nanoplates was carried out via a simple wet chemical polyol method. The high-quality grade precursors used were purchased from Sigma Aldrich. To achieve an ideal stoichiometric Bi:Te ratio of 2:3 chemicals are weighted to 485 mg of Bi(NO₃)₃ · 5H₂O (98%, Sigma Aldrich), 0.5 g of polyvinylpyrrolidone (PVP) (30 K, Roth), 415 mg K₂TeO₃ · H₂O (97%, Alfa Aesar), 0.4 g NaOH (98%, Merck) and 50 ml of Ethylene glycol (EG) (>99.5%, Roth). The salts as well as the surfactants are dissolved in EG in a glass beaker on a hot plate set at a temperature of 65 °C while slightly stirring the mixture. The dissolved solution was then transferred via a long funnel into a three-neck round bottom flask connected to a water-cooled reflux. The flask remained closed during the entire synthesis with septum. The solution was stirred at 450 rpm with a Teflon bar and slowly heated

L. O. Akinsinde · S. Scheitz · M. A. Rübhausen
Center for Free Electron Laser Science (CFEL), Institute for Nanostructures and Solid State Physics (INF), University of Hamburg, Luruper Chaussee 149, 22761 Hamburg, Germany

L. Zimoch · J. K. Sierck · L. Siebert · R. Adelung · U. Schürmann · T. Dankwort (✉) · L. Kienle
Institute for Materials Science, Kiel University, Kaiserstrasse 2, Kiel, Germany
e-mail: td@tf.uni-kiel.de

to allow the substance to mix homogeneously. This procedure further ensures proper nucleation of the seeds that later grow to form the nanoplates. After a duration of roughly 10 min, the solution reached the preset temperature of 180 °C and turned to a black color. The nanoplates were allowed to grow at 180 °C for 22 h. The solution was left to cool down to room temperature. Apparently, small black precipitates have formed. The isolation of the Bi_2Te_3 precipitates was achieved through centrifugation in acetone and isopropanol to remove the core-shell-like structures of the residual PVP as well as EG from the synthesis and then stored inside a vial. The Bi_2Te_3 nanoplates are dispersed in high purity isopropanol to avoid the agglomeration of the nanoplates.

In order to obtain a macroscopic flexible thermoelectric device, graphene-coated polymer composite fiber mesh was adopted and infiltrated with the Bi_2Te_3 nanoplates. The infiltration of the fiber mesh consisting of Polycaprolactone (PCL) template with Bi_2Te_3 nanoplates was achieved by dip-coating (soaking) simultaneously different fiber-meshes in 5 ml solution of Bi_2Te_3 and Isopropanol for 24 h as well as 48 h under ambient conditions.

The morphology, shape and degree of infiltration of the samples were investigated using a commercial field emission scanning electron microscopy (FE-SEM), Sigma from Zeiss Company, Germany.

Nanostructural investigation were performed using a transmission electron microscope (TEM), FEI Tecnai F30 G² STwin equipped with an 300 kV field emission gun.

A custom-build setup was used to validate the electrical response of each sample, which allows to apply stress and strain to the sample while simultaneously measure the resistivity changes. Therefore, a constant DC-voltage was applied, and the electrical conductivity measured. According to ohm's law the resistivity was calculated. Further, the applied stress was measured with a load cell.

3 Results and Discussion

Nanoplates of Bi_2Te_3 were synthesized by a reduction of a stoichiometric mixture in EG in the presence of PVP. PVP is very important due to its function as a capping agent as well as a trigger for crystal growth, i.e., it facilitates a uniform uniaxial growth [14–16]. More to this, PVP bonds to the polar basal planes of the crystal structure of Bi_2Te_3 and suppresses the growth dynamic of the crystals in the c-axis direction [16]. The thin PVP core-shell layer is determined to be in the range of 2–5 nm and is mostly not completely removed through centrifugation. A complete PVP removal is detrimental and might be achieved at the expense of the Bi_2Te_3 nanoplate being partly etched during the process. The transition between PVP- Bi_2Te_3 nanoplate is not readily determined.

To investigate the nanostructure of the Bi_2Te_3 nanoplates TEM was used. Figure 1 depicts representative nanoplates of Bi_2Te_3 . The different nanoplates extend over 3–5 micrometers, while their thickness is in the range of a few nanometers. Further, large particles are often decorated with smaller particles as also depicted in Fig. 1. The nanoplates were crystalline and exhibit rotational disordering [14, 15], thus the zone axis varies within a few nanometers and produces characteristic diffraction contrast (not shown here). This observation might be the result of a screw dislocation promoted growth [16].

Electron diffraction (ED) patterns in zone axis [001] exhibited additional reflections (not shown here), which indicates a lowering of the symmetry. Thus, it was concluded that due to slight variation in the stoichiometry a transition from $R\bar{3}m$ to $P\bar{3}m1$ crystal structure is observed.

The HRTEM micrograph and corresponding Fourier Transform (FFT) in Fig. 1 highlight rotational disorder resulting in weak satellite reflections (marked in yellow) in the FFT and pronounced Moiré contrast.

The chemical composition of the nanoplates was characterized using energy dispersive X-ray spectroscopy (EDX) in scanning TEM mode. It was observed, that the stoichiometry slightly deviates from the ideal ratio of Bi:Te = 2:3. In our system the ratio was found to be 1.8:3.2, thus this deviation presumably might be attributed to impurities in the system.

The obtained nanoplates were deposited on a graphene-coated PCL fiber mesh. FESEM images (Fig. 2), revealed a strong adhesion of the Bi_2Te_3 nanoplates on the coated fiber-meshes as seen in the long percolation network

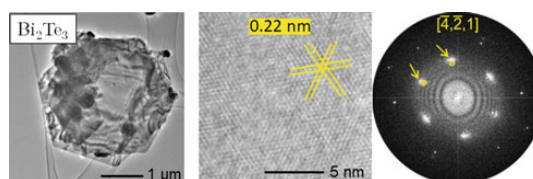


Fig. 1 Bright field image, HRTEM micrograph and corresponding FFT of a Bi_2Te_3 flake in zone axis $[-4\bar{2}1]$. In the FFT satellite reflections are observed which can be attributed to rotational disorder

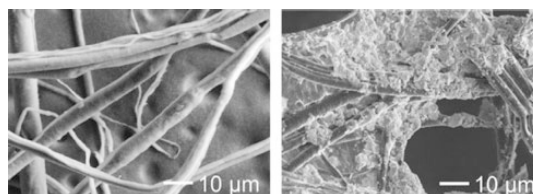


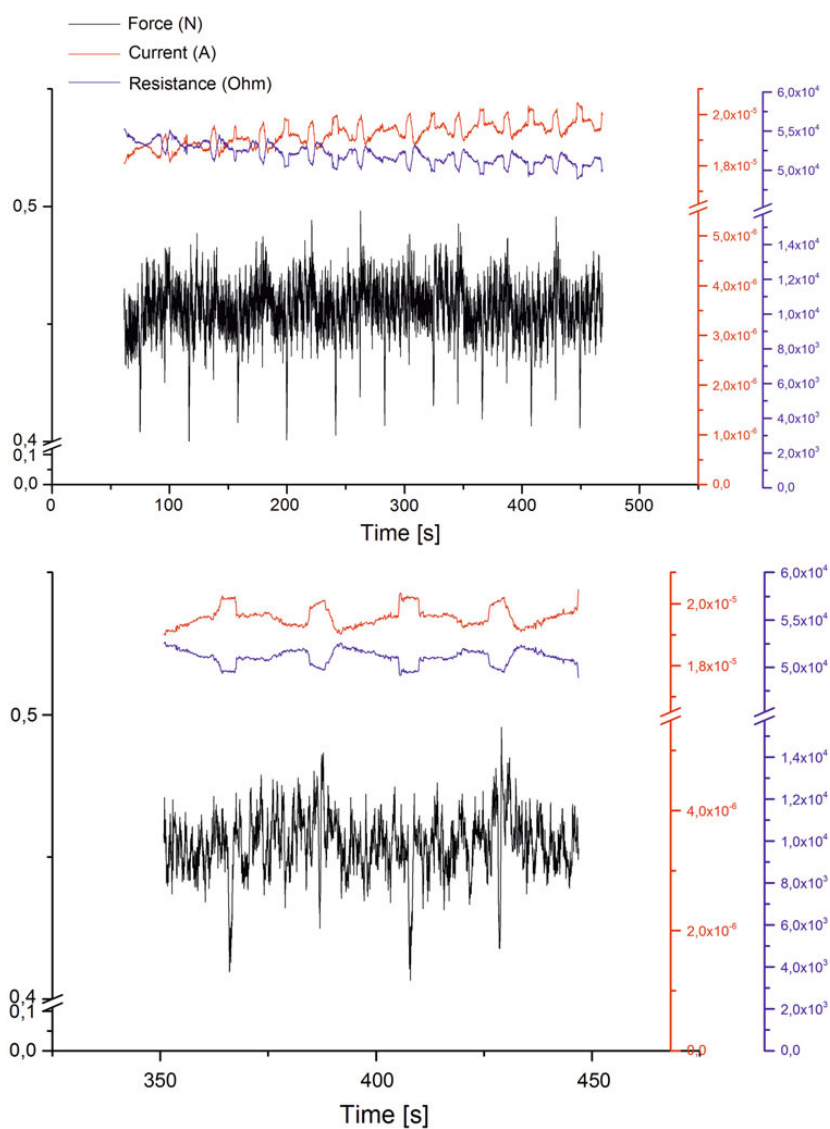
Fig. 2 FESEM micrographs of polymer fibers before and after coating with Bi_2Te_3 nanoplates

formed. Thus, strongly bonded Bi_2Te_3 nanoplates are part of a closed composite film. Also, smaller 'plate-like' structures are randomly dispersed on the surface of the fiber matrix. Overall, we assume that the weak van-der-Waals forces existing at different junctions and interfaces between Bi_2Te_3 nanoplates and the polymer fiber-mesh matrix is strongly responsible for the good adhesion. However, when no additional graphene was used the adhesion of Bi_2Te_3 nanoplates was significantly reduced, thus leading to only low coverage of the fiber-mesh (not shown here).

The mass weight as well as the dimensions of the graphene coated fiber-mesh was measured before and after dipping in Bi_2Te_3 suspension. The density of nanoplates deposited on the fiber-mesh matrix increases with the dwelling time. Lowest electrical resistivity was found for the samples with longest dwelling time.

The samples were folded, and tensile and compressive stress applied. Simultaneously, the resistivity was measured. A representative result of such measurement is depicted in Fig. 3.

Fig. 3 Change of current and resistance in dependence of mechanical loading. The upper graph represents several loading cycles while the lower graph represents an enlarged section highlighting the effect of resistivity changes upon applying tensile and compressive stress



Repeatedly compressive and tensile stress were applied to the sample applying. It is observed that a decrease in resistivity and, accordingly, an increase in electrical conductivity is observed for both cases (as seen in Fig. 3). This effect can be attributed to the re-orientation and increased overlapping of different wires/nanoplates due to the stress which is applied. With the tensile stress, it allows the coated nanoplatelets to create a junction through bonding of numerous nanoplatelets contacting each other thereby, increasing locally the conductivity whereas this effect is not strong or perhaps predominates during compressive stress. The overlapping of the nanoplatelets is predominant and we assume, the bonding of the nanoplatelets might not be too strong and responsible for the light drop in the resistivity. Supposedly, the tunneling barrier of the electron mobility is thus not completely overwhelmed. Furthermore, a memory effect is observed. With increasing number of load cycles, the resistivity further decreases leading to a remnant change in the resistivity in the unloaded state. The origin for this behavior might be again the result of different wires/nanoplates getting in contact irreversibly and forming new junctions. Thus, with an increased number of loading cycles an accumulation takes place, consequently leading to a remnant change in resistivity.

4 Conclusions

In this paper, we have highlighted the polyol wet chemical process as an effective simple chemical method to synthesize high quality and good grade nanoplates of Bi_2Te_3 that are single crystalline. The obtained nanoplates exhibit areal dimensions in the range of 3–5 μm and have a thickness of a few nanometers.

Furthermore, it was found that graphene coated PCL fiber spun polymers act as an ideal substrate for the deposition of Bi_2Te_3 nanoplates forming a long-range percolation network.

In the mechano-electrical transport measurement, tensile and compressive stress lead to a decrease in resistivity while after several cycles the material exhibited a remnant change in electrical conductivity.

These results highlight the potential of flexible thermoelectric materials to be used as pressure sensors while simultaneously being able to implement a power source or a temperature sensor.

Acknowledgements The authors like to thank the Land Schleswig-Holstein and Hamburg for financial support. Further, the authors like to thank the group of Prof. Oepen for the use of the SEM.

Conflict of Interest The authors declare that they have no conflict of interest.

References

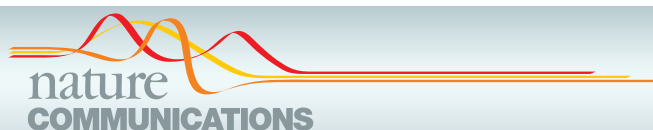
- Rowe, D.M.: Thermoelectrics Handbook: Macro to Nano. CRC Press (2005)
- Eibl, O., Nielsch, K., Peranio, N., Völklein, F.: Thermoelectric Bi_2Te_3 Nanomaterials. John Wiley & Sons (2015)
- Champness, C.H., Chiang, P.T., Parekh, P.: Influence of growth conditions and tellurium phase on the thermoelectric properties of bismuth telluride-type materials. *Can. J. Phys.* **43**, 653 (1965)
- Böttner, H., Ebling, D.G., Jacquot, A., König, J., Kirste, L., Schmidt, J.: Phys. Structural and mechanical properties of spark plasma sintered n- and p-type bismuth telluride alloys. *Status Solidi RRL—Rapid Res. Lett.* **1**, 235 (2007)
- Koenig, J., Winkler, M., Dankwort, T., Hansen, A.-L., Pernau, H.-F., Duppel, V., Jaegle, M., Bartholomé, K., Kienle, L., Bensch, W.: Thermoelectric efficiency of $(1-x)$ (GeTe) $x(\text{Bi}_2\text{Se}_{0.2}\text{Te}_{2.8})$ and implementation into highly performing thermoelectric power generators. *Dalton Trans.* **44**, 2835 (2015)
- Dong, H., Chen, Y.-C., Feldmann, C.: Polyol synthesis of nanoparticles: status and options regarding metals, oxides, chalcogenides, and non-metal elements. *Green Chem.* **17**, 4107 (2015)
- Weller, D.P., Stevens, D.L., Kunkel, G.E., Ochs, A.M., Holder, C. F., Morelli, D.T., Anderson, M.E.: Thermoelectric performance of tetrahedrite synthesized by a modified polyol process. *Chem. Mater.* **29**, 1656 (2017)
- Yang, L., Hng, H.H., Cheng, H., Sun, T., Ma, J.: Thermoelectric properties of p-type CoSb_3 nanocomposites with dispersed CoSb_3 nanoparticles. *Mater. Lett.* **62**, 2483 (2008)
- Anderson, M.E., Bharadwaja, S.S.N., Schaak, R.E.: Modified polyol synthesis of bulk-scale nanostructured bismuth antimony telluride. *J. Mater. Chem.* **20**, 8362 (2010)
- Soni, A., Yanyuan, Z., Ligen, Y., Aik, M.K.K., Dresselhaus, M.S., Xiong, Q.: Enhanced thermoelectric properties of solution grown $\text{Bi}_2\text{Te}_{(3-x)}\text{Se}_{(x)}$ nanoplatelet composites. *Nano Lett.* **12**, 1203 (2012)
- Yadav, A., Pipe, K.P., Shtein, M.: Fiber-based flexible thermoelectric power generator. *J. Power Sources* **175**, 909 (2008)
- Du, Y., Xu, J., Paul, B., Eklund, P.: Flexible thermoelectric materials and devices. *Appl. Mater. Today* **12**, 366 (2018)
- Zhang, F., Zang, Y., Huang, D., Di, C., Zhu, D.: Flexible and self-powered temperature–pressure dual-parameter sensors using microstructure-frame-supported organic thermoelectric materials. *Nat. Commun.* **6**, 8356 (2015)
- Eising, G., Niebuur, B.-J., Pauza, A., Kooi, B.J.: Competing crystal growth in Ge–Sb phase-change films. *Adv. Funct. Mater.* **24**, 1687 (2014)
- Kolosov, V.Y., Thölén, A.R.: Transmission electron microscopy studies of the specific structure of crystals formed by phase transition in iron oxide amorphous films. *Acta Mater.* **48**, 1829 (2000)
- Zhuang, A., Li, J.-J., Wang, Y.-C., Wen, X., Lin, Y., Xiang, B., Wang, X., Zeng, J.: Transmission electron microscopy studies of the specific structure of crystals formed by phase transition in iron oxide amorphous films. *Angew. Chem. Int. Ed.* **53**, 6425 (2014)

Conversionless efficient and broadband laser light diffusers for high brightness illumination applications

Laser diodes are of high interest for numerous applications in spectroscopy, imaging, materials processing and others. Their interesting characteristics like low spectral width, coherence, high power density and the highly collimated beam become disadvantages for solid state lighting. The high efficiency of laser diodes attracts interest but inorganic phosphor materials are necessary for laser light conversion and scattering. These materials decrease the efficiency and reduce the lifetime and lead to low irradiance levels. The direct, isotropical scattering in three-dimensional light diffusers made of boron nitride is presented in this work. Due to the high binding energy and the low absorbance the boron nitride architecture can withstand approx. 10 times higher irradiance levels than the phosphor materials. Additionally, no light conversion takes place. Rather the incident beams are losslessly scattered with an efficiency of around 98%. The results have been published in "Nature Communications".

Own contribution presented in this article

- Discussion and interpretation
- Editing the manuscript












ARTICLE


<https://doi.org/10.1038/s41467-020-14875-z>

OPEN

Conversionless efficient and broadband laser light diffusers for high brightness illumination applications

Fabian Schütt¹ [✉], Maximilian Zapf², Stefano Signetti³ , Julian Strobel⁴, Helge Krüger¹, Robert Röder² , Jürgen Carstensen¹, Niklas Wolff⁴, Janik Marx^{5,13}, Tian Carey^{6,7}, Marleen Schweichel¹, Maik-Ivo Terasa¹, Leonard Siebert¹, Hyo-Ki Hong⁸, Sören Kaps¹, Bodo Fiedler⁵ , Yogendra Kumar Mishra⁹ , Zonghoon Lee^{8,10} , Nicola M. Pugno^{3,11,12} , Lorenz Kienle⁴, Andrea C. Ferrari⁶, Felice Torrisi^{6,7}, Carsten Ronning² [✉] & Rainer Adelung¹ [✉]

Laser diodes are efficient light sources. However, state-of-the-art laser diode-based lighting systems rely on light-converting inorganic phosphor materials, which strongly limit the efficiency and lifetime, as well as achievable light output due to energy losses, saturation, thermal degradation, and low irradiance levels. Here, we demonstrate a macroscopically expanded, three-dimensional diffuser composed of interconnected hollow hexagonal boron nitride microtubes with nanoscopic wall-thickness, acting as an artificial solid fog, capable of withstanding ~10 times the irradiance level of remote phosphors. In contrast to phosphors, no light conversion is required as the diffuser relies solely on strong broadband (full visible range) lossless multiple light scattering events, enabled by a highly porous (>99.99%) non-absorbing nanoarchitecture, resulting in efficiencies of ~98%. This can unleash the potential of lasers for high-brightness lighting applications, such as automotive headlights, projection technology or lighting for large spaces.

¹Functional Nanomaterials, Institute for Materials Science, Kiel University, Kaiserstr. 2, 24143 Kiel, Germany. ²Institute for Solid State Physics, Friedrich-Schiller-University Jena, Max-Wien-Platz 1, 07743 Jena, Germany. ³Laboratory of Bio-inspired, Bionic, Nano, Meta Materials & Mechanics, Department of Civil, Environmental and Mechanical Engineering, University of Trento, via Mesiano 77, I-38123 Trento, Italy. ⁴Synthesis and Real Structure, Institute for Materials Science, Kiel University, Kaiserstr. 2, 24143 Kiel, Germany. ⁵Institute of Polymers and Composites, Hamburg University of Technology, Denickestr. 15, 21073 Hamburg, Germany. ⁶Cambridge Graphene Centre, University of Cambridge, 9, JJ Thomson Avenue, Cambridge CB3 0FA, UK. ⁷Department of Chemistry, Molecular Sciences Research Hub, Imperial College London, White City Campus, Wood Lane, London W12 0BZ, UK. ⁸School of Materials Science and Engineering, Ulsan National Institute of Science and Technology (UNIST), Ulsan 44919, Republic of Korea. ⁹SDU NanoSYD, Mads Clausen Institute, University of Southern Denmark, Alsion 2, 6400 Sønderborg, Denmark. ¹⁰Center for Multidimensional Carbon Materials, Institute for Basic Science (IBS), Ulsan 44919, Republic of Korea. ¹¹School of Engineering and Materials Science, Queen Mary University of London, Mile End Road E1 4NS, London, UK. ¹²Ket-Lab, Edoardo Amaldi Foundation, via del Politecnico snc, I-00133 Roma, Italy. ¹³Deceased: Janik Marx. ✉email: fas@tf.uni-kiel.de; ra@tf.uni-kiel.de

ARTICLE

NATURE COMMUNICATIONS | <https://doi.org/10.1038/s41467-020-14875-z>

Solid-state lighting (SSL) is defined as light emitted by solid-state electroluminescence¹. Its current power efficiency, i.e., the optical output power of the SSL device per unit input electrical power², is ~70% and there is no fundamental physical reason why efficiencies well beyond 70% could not be reached^{2–4}. SSL is thus expected to replace all conventional light sources by 2035⁵, including halogen, xenon, incandescent, and fluorescent lamps^{4,6–8}. At present, light emitting diodes (LEDs) are the most efficient devices for white-light generation^{2,3,6}. Their adoption is predicted to achieve a 75% reduction of energy consumption for lighting by 2035⁵ in the US alone, which would result in a total energy saving of 6.75×10^{16} TJ (equivalent to nearly \$630 billion in avoided energy costs) and thus drastically reduce greenhouse emission worldwide⁵. However, the so-called “efficiency droop” still limits the operation of LEDs to very low input power densities, with current densities $\sim 0.01 \text{ kA cm}^{-2}$ ^{2,9}. Consequently, for a higher light output the physical size of a LED has to be increased. In contrast to LEDs, laser diodes (LDs) can be operated at much higher current densities ($>10 \text{ kA cm}^{-2}$), with peak efficiencies close to that of LEDs². This results in a higher light output per unit area, e.g., a 0.1 mm^2 LD source can produce the same amount of light as a 1 cm^2 LED. Hence, the target to generate more photons at high-power densities (kW cm^{-2}) and decrease the cost per lumen can only be satisfied by using LDs^{2,4,8}. State-of-the-art LD-based lighting devices exploit a blue LD pumping, e.g., a yellow-light emitting phosphor, resulting in white light (Fig. 1a)^{2,4}. However, the performance of such systems is strongly limited by the properties of the phosphor. The efficiency of state-of-the-art light emitting phosphors, such as doped yttrium-aluminum-garnet, is mainly determined by two types of energy losses, the Stokes shift ($\sim 80\%$ efficiency) and the photoluminescence quantum yield ($\sim 90\%$)¹⁰. Both these loss mechanisms scale with temperature¹⁰ (e.g., as a result of illumination) and therefore phosphor luminescence suffers from saturation¹⁰, aging¹¹, and thermal quenching¹⁰, limiting the irradiance to $\sim 5 \text{ kW cm}^{-2}$ and thus the overall light output. Even though new concepts such as glass encapsulation^{12,13}, phosphor monoliths¹⁴, or composite ceramic phosphors^{15–17} can increase the irradiance level up to $\sim 10\text{--}20 \text{ kW cm}^{-2}$, the true potential of lasers for high-brightness lighting applications, with possible light outputs of several MW cm^{-2} , still remains unemployed.

Here, we demonstrate a tunable, disordered, cubic centimeter-sized ceramic nanoarchitecture as an efficient ($> 98\%$) broadband ($> 450\text{--}640 \text{ nm}$) diffuser, that in combination with a RGB (red-green-blue) laser system (Fig. 1b), is an alternative to the

conventional used phosphors with a single laser (Fig. 1a). The diffuser withstands ~ 10 times the irradiance level achievable by state-of-the-art phosphors, enabling a lighting system whose efficiency is mainly determined by that of the LDs used, due to the lack of any conversion effects (Fig. 1c). The concept is based on a highly porous ($> 99.99\%$), macroscopic, and translucent network of randomly arranged and interconnected hexagonal boron nitride (hBN) hollow microtubes, that we call Aero-BN. The material acts like an artificial solid fog, but with a defined hierarchical internal structure - a combination of well separated feature sizes greater than, equal to, as well as below the magnitude of the impinging wavelength. The Aero-BN diffuser enables an isotropic light distribution from a multitude of coherent laser light sources at the same time, while simultaneously reducing speckle contrast to values well below the detection limit of the human eye ($< 4\%$)¹⁸. Especially the latter is a strict requirement for LD-based lighting, that is not met by today’s commercially available diffuser systems (Supplementary Note 1 and Supplementary Table 1). Even though the current state of LD technology - with laser efficiencies $< 20\%$ for green¹⁹ and $< 40\%$ for blue^{2,19} - is still limiting the application of LD-based lighting systems, fast progress in the development of more efficient laser diodes is expected in the near future^{2–4,8}. Therefore, the development of new optical components, such as the Aero-BN discussed here, is a necessity, indicating a way to unlock the full potential of LDs for high-brightness illumination, such as needed in projector technology, automotive headlights, large room illumination, and sports lighting.

Results

Light diffuser based on interconnected hBN microtubes. The laser light diffuser is based on a macroscopically ($> \text{mm}^3$) expanded nanoarchitecture consisting of interconnected nanoscopic hBN films (thickness $< 25 \text{ nm}$) in the form of hollow tubes, see Fig. 2. hBN has a large band gap of up to 6.5 eV ²⁰, ensuring low ($< 1\%$) absorption coefficients in the visible light regime. Optical transmission up to 99% at $250\text{--}900 \text{ nm}$ was reported for thin ($1\text{--}2 \text{ nm}$) hBN films²¹. Our synthesis process (Supplementary Fig. 1) is based on a ceramic template material (Supplementary Fig. 2)²², which offers, in contrast to the common Ni templates²³ used for the synthesis of hBN and graphene foams, fabrication flexibility, as the template can be tailored²² in its density, microstructure (e.g., pore size and pore interconnectivity) as well as geometry. It consists of randomly distributed, interconnected ZnO microrods, with large (up to $100 \mu\text{m}$) voids and porosities up to

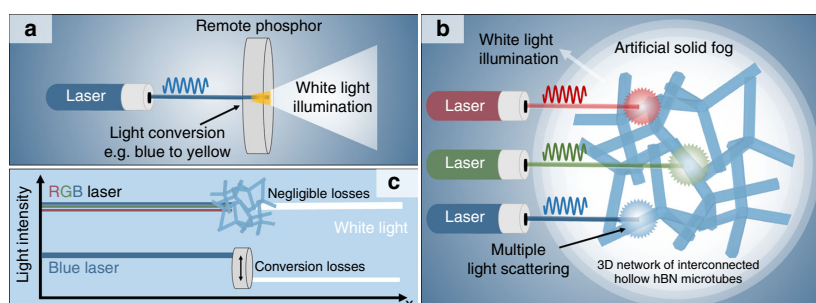


Fig. 1 Schematics of laser-based lighting concepts. **a** White-light generation by employing a remote phosphor that converts a part of the blue laser light into yellow light resulting in white light. **b** White-light generation based on an artificial solid fog in combination with an R+G+B laser system. A macroscopically expanded porous ($>99.99\%$) network of interconnected and hollow hBN microtubes with nanoscopic wall thickness is used to convert directed laser light into an isotropic high-brightness white light source, exploiting multiple light scattering. **c** Schematic comparison of efficiencies of both systems. In the case of remote phosphor, light conversion results in a strong efficiency reduction, whereas the negligible absorption and conversionless light-scattering properties of the hBN foam allow for almost zero losses in light intensity.

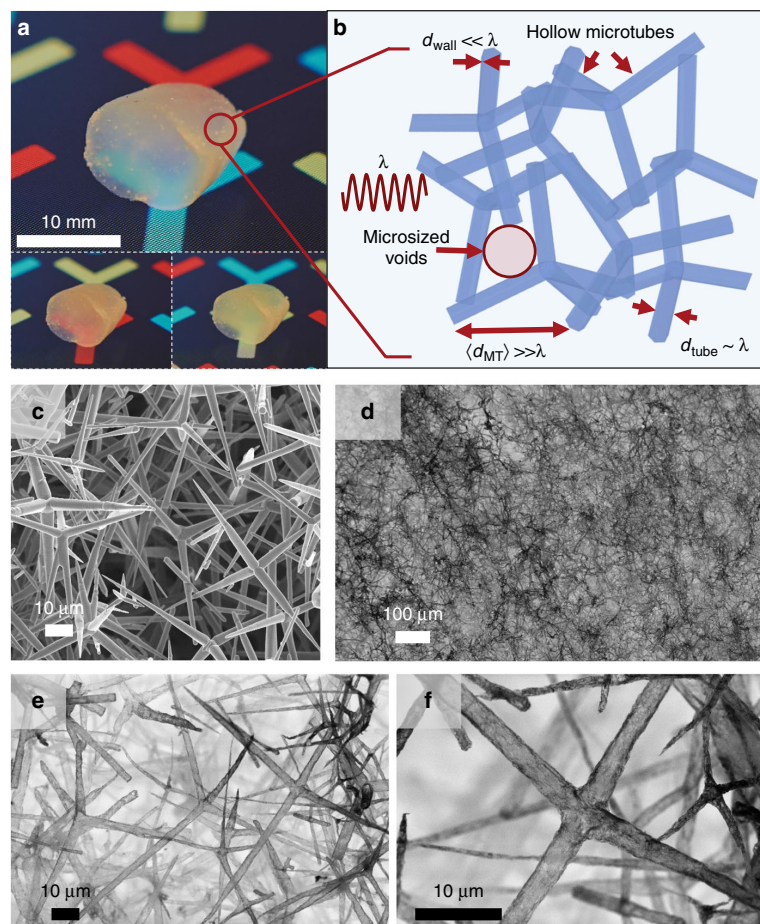


Fig. 2 Artificial solid fog. **a** Photographs of Aero-BN. A thin (< 25 nm) hBN layer is grown by CVD using macroscopically expanded templates of tetrapodal ZnO microparticles. The hBN layer encloses the entire template structure, while it is simultaneously removed by hydrogen etching, resulting in a free-standing, low density (< 1 mg cm $^{-3}$) network, consisting of interconnected hollow hBN microtubes. **b** The structure resembles an artificial solid fog, i.e., a highly optically disordered (completely randomised) photonic system with a combination of feature sizes greater than, equal to, or well below the impinging light wavelength. **c** Representative scanning electron microscopy (SEM) micrographs of the ZnO template consisting of interconnected microrods. **d–f** SEM micrographs of the resulting Aero-BN after CVD. The microtubes have an average length ~ 25 μ m, diameter between 300 and 3000 nm, and < 25 nm wall thickness.

98%²². The synthesis of the final BN network involves a one-step transformation of the ZnO microrod structure in which a thin (< 25 nm) hBN layer is formed by a chemical vapor deposition (CVD) process, while the ZnO template is simultaneously removed (Supplementary Figs. 3 and Supplementary Note 2). The final semitransparent Aero-BN (porosity $> 99.99\%$) microtube network is shown in Fig. 2a. Calculations indicate that the specific surface area of the hBN foams is in the order of 900 m 2 g $^{-1}$ (see Supplementary Note 3). Energy dispersive X-ray spectroscopy (EDX, Supplementary Fig. 5) show that the ZnO template is completely removed during CVD. The process results in a disordered²⁴ macroscopic network, Fig. 2b, consisting of interconnected hollow hBN microtubes, with individual features varying in well-defined sizes and dimensions. The as-synthesized hollow hBN microtubes have an average length ~ 25 μ m, and their diameter, d_{tube} , is between 300 and 3000 nm, depending on the geometry of the used ZnO microrods (Fig. 2c) as shown in

Fig. 2d–f. Thus, d_{tube} is of the same order of magnitude as the wavelength of visible light. The hBN CVD process results in wall-thicknesses $d_{\text{wall}} < 25$ nm. This is much smaller than the wavelength of visible light, promoting light-matter interactions that are dominated by Rayleigh-type scattering²⁵. As for Fig. 2f, the hBN microtube walls consist of randomly arranged, interconnected hBN nanoplates (see also Supplementary Fig. 6). The average distance between the individual microtubes, d_{MT} , is several μ m, larger than the visible light wavelength. The resulting Aero-BN network architecture leads thus to an optical system with microscopic (optical) density fluctuations (volumes filled with air and with hBN microtubes) throughout the macroscopic structure, as indicated in Fig. 2b. The CVD process is similar to that used to prepare macroscopically expanded nano architectures based on interconnected ZnO microrod networks^{26–28}, with the main difference that the hBN is grown here by using the sacrificial ceramic template.

ARTICLE

NATURE COMMUNICATIONS | <https://doi.org/10.1038/s41467-020-14875-z>

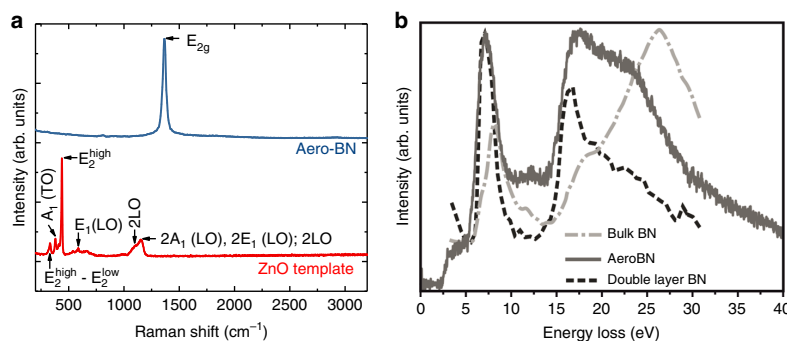


Fig. 3 Raman and EELS characterisation of the Aero-BN network. **a** Raman spectra of Aero-BN structure (blue) and ZnO template (red). **b** Low-loss EELS spectra of bulk-hBN³⁷ (dash-point), Aero-BN (solid), and double layer hBN³⁷ (dashed). The positions and shapes of the π -plasmon at ~ 6 eV match. The positions of the σ -plasmon ~ 15 eV match, while shape and relative intensity differ slightly, whereas no peak ~ 26 eV (bulk-BN) is seen. Spectra are normalized from the onset of the π -plasmon to its apex.

Figure 3a shows Raman spectra ($\lambda = 514$ nm, 1.32 mW) of Aero-BN (blue curve) and ZnO (red curve). The Aero-BN spectrum has a characteristic single peak centred ~ 1366 cm⁻¹^{29–31}. The ZnO spectrum shows several resonances. The sharp peak ~ 439 cm⁻¹ indicates the crystal quality of the sample³². The peak at ~ 335 cm⁻¹ is assigned to the difference between E_2^{high} and E_2^{low} [$E_2^{\text{high}} - E_2^{\text{low}}$], which corresponds to the high and low longitudinal optical branches of ZnO, while the feature at 384 cm⁻¹ is assigned to A₁(TO) mode³³. In addition, the black curve shows a peak at ~ 584 cm⁻¹ attributed to E₁(LO) mode. The broad, intense peak at 1158 cm⁻¹, which is found between the doubled frequencies measured for the A₁(LO) and E₁(LO) modes, contains contributions of 2A₁(LO) and 2E₁(LO) modes at the Γ point of the Brillouin zone, and possibly also of 2LO scattering³³. The weaker peak ~ 1105 cm⁻¹ can be attributed to 2LO at H and K point of the Brillouin zone³³. However, no peaks of ZnO are observed in the Aero-BN spectrum, consistent with the removal of the sacrificial ZnO template.

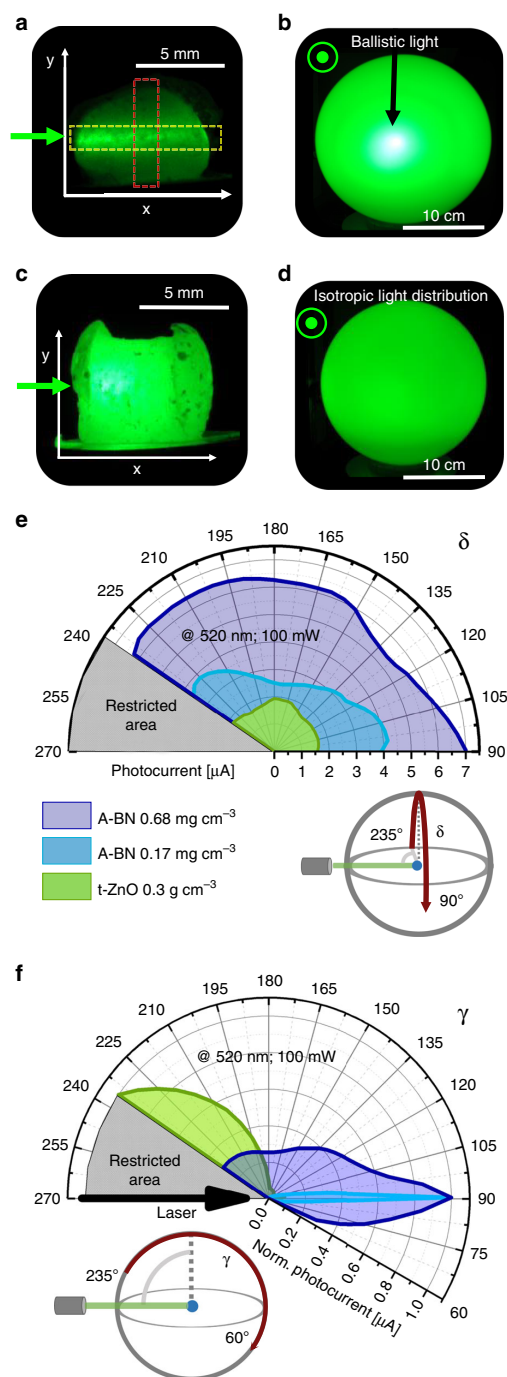
Transmission electron microscopy (TEM) investigations reveal, that the atomic structure of Aero-BN resembles that of hBN nanotubes (see Supplementary Note 4 and Supplementary Fig. 7)³⁴. Furthermore, high-resolution (HR) micrographs show the existence of numerous point and triangle defects, potentially advantageous for catalytic applications³⁵ (Supplementary Fig. 8). The wall thickness of the BN microtubes is determined via the electron energy-loss spectroscopy (EELS) log-ratio method³⁶ (Supplementary Fig. 9 and discussion) to be 4–25 nm. The EEL spectra in the plasmon region up to 40 eV are shown in Fig. 3b and compared with those of double hBN layer³⁷. The positions of the π -plasmon at 6 eV and the σ -plasmon at 15 eV match the double hBN layer reference³⁷. This confirms the nanoscale thickness of Aero-BN microtube walls, as bulk hBN shows σ -plasmon resonance peaking ~ 26 eV³⁷.

Optical absorption measurements with an integrating sphere (Supplementary Fig. 10) performed on a macroscopic Aero-BN sample ($\rho_{\text{Aero-BN}} \sim 0.68$ mg cm⁻³) give absorption ~ 4.04 , 0.85, and 0.11% for blue (450 nm), green (520 nm), and red (638 nm) laser lights, respectively. The slightly larger absorption at 450 nm might be caused by traces of ZnO, however the amount is too low to affect the measurements critically, as the measured absorption is consistent with that of 1–2 nm thick hBN structures²¹. The low absorption in combination with the structural feature sizes greater than, equal to, as well as below the magnitude of the impinging wavelength, results in a disordered system²⁴, in which the light transport properties are determined by multiple light scattering.

Light-scattering characteristics. In order to analyze the light-scattering properties and to determine the underlying mechanisms we fabricate Aero-BN with different densities $\rho_{\text{Aero-BN}}$ (0.17–0.68 mg cm⁻³) by changing the initial template density ρ_T between 0.3 and 1.2 g cm⁻³ (see Supplementary Fig. 11). This enables us to tune and control the internal light-scattering properties, key to build the envisaged laser light diffuser. For example, a template density $\rho_T \sim 300$ mg cm⁻³ results in $\rho_{\text{Aero-BN}}$ as low as ~ 0.17 mg cm⁻³ (equal to a porosity $> 99.99\%$), lower than that of other reported macroscopically expanded BN architectures^{34,38–45} (see Supplementary Table 2).

The light-scattering properties are demonstrated by illuminating an Aero-BN sample from one side with a focused laser. Figure 4a shows a photograph (perpendicular to the laser axis) of a low density ($\rho_{\text{Aero-BN}}$ of ~ 0.17 mg cm⁻³) Aero-BN illuminated at 520 nm. The resultant frontal photograph of the same sample illuminated in the centre of a semitransparent glass bulb, Fig. 4b, shows that most of the incident laser beam is transmitted through the material. Figure 4c, d display the corresponding photographs of a sample with a higher initial $\rho_{\text{Aero-BN}} \sim 0.68$ mg cm⁻³, for 520 nm illumination at 100 mW. As shown in Fig. 4d, a nearly homogeneous, isotropic light distribution, with no visible transmitted primary beam, is seen at the semitransparent glass bulb screen. The corresponding intensity plots, Supplementary Fig. 12, obtained from Fig. 4a (highlighted areas) indicate that the intensity of the incident laser beam decreases linearly through the sample along x and y directions. This can be described by a system in which the scattering mean free-path l^* is much larger than the sample dimensions⁴⁶, resulting in an overall low scattering efficiency (most light is transmitted rather than scattered), i.e., ratio of scattered to transmitted light, and a dominating ballistic transmission. For the ZnO microrod template used to prepare our Aero-BN, with the same microstructure (microrods instead of hollow microtubes), a pronounced visible backscattering is observed (Supplementary Figs. 13–15), indicating the fundamental role of the hollow tubular geometry with multiple feature sizes. A more detailed discussion on the influence of different ceramic microstructural arrangements can be found in Supplementary Note 5 and Supplementary Fig. 16.

The detailed light distribution produced by illuminating Aero-BN samples is investigated with a photo-goniometer⁴⁷ (a photodiode movable around the illuminated specimen on a spherical surface, see Supplementary Fig. 17) to characterise the broadband light-scattering properties as a function of the angle



(azimuthal and polar rotation) at 450, 520, and 638 nm, Fig. 4e, f. We also consider a network of interconnected ZnO micro-rods^{48,49} as a comparison. A perfect 3D light diffuser exhibits angle independent (isotropic) emission over the complete angular range, so that the light is uniformly emitted in all directions. Figure 4e, f show plots of both azimuthal and polar rotations,

Fig. 4 Light-scattering characterisation. **a** Photograph of $\rho_{\text{Aero-BN}} \sim 0.17 \text{ mg cm}^{-3}$ illuminated with 100 mW (spot size $\sim 1 \text{ mm}$) at 520 nm. **b** Photograph of the same sample shown in **a** when illuminated in the centre of a semitransparent glass bulb (front view). **c, d** Photograph of $\rho_{\text{Aero-BN}} \sim 0.68 \text{ mg cm}^{-3}$ illuminated with 100 mW at 520 nm, and resultant light scattering imaged using a semitransparent glass bulb (front view). **e** Angular photocurrent dependence for Aero-BN with different $\rho_{\text{Aero-BN}}$ compared with an interconnected microrod structure (t-ZnO; $\rho_{\text{T}} \sim 300 \text{ mg cm}^{-3}$) for 520 nm at 100 mW. The photodiode is polar rotated over the sample, as illustrated in the schematics. The graphs represent the photocurrent produced by scattered light only. **f** Corresponding normalised photocurrent with respect to the azimuthal rotation of the photodiode. For details of measurements see Supplementary Figs. 17–20.

extracted from the polar plots of the goniometer measurements of the laser illuminated ZnO and Aero-BN networks (see Supplementary Figs. 18–20). In both cases, the photodiode is pivoted, while the sample and the LD are stationary. These graphs provide quantitative data for the amount of scattered, reflected, and transmitted light. Figure 4e depicts the photocurrent for different samples as a function of polar angle. This represents the photocurrent produced by scattered light only, while no reflected and transmitted light reaches the detector. In contrast, Fig. 4f shows the normalised photocurrent as a function of azimuthal angle. In this case, the photocurrent detected for $90^\circ < \gamma < 180^\circ$ is caused by scattering only. The value at $\gamma = 90^\circ$ represents transmission (T) and forward scattering. For $\gamma > 180^\circ$ the photocurrent is a result of reflection and scattering. As depicted in Fig. 4e, the ZnO network with $\rho_{\text{ZnO}} \sim 300 \text{ mg cm}^{-3}$ shows only a small but homogeneous photocurrent ($\sim 1.5 \mu\text{A}$) caused mainly by back-scattered light. Thus, nearly no light is transmitted through the structure, Fig. 4f. Aero-BN, on the other hand, shows a much stronger emission and more uniform light distribution of the laser beam. The measured photocurrent caused by azimuthally scattered light from the Aero-BN (Fig. 4e) is $\sim 2.5\text{--}4 \mu\text{A}$ and $6\text{--}7 \mu\text{A}$ for $\rho_{\text{Aero-BN}} \sim 0.17$ and $\sim 0.68 \text{ mg cm}^{-3}$, respectively. Thus, for the higher density sample, the amount of scattered light is ~ 4.6 times higher than for the ZnO network, even though the density of the network structure is reduced by a factor of ~ 440 . As illustrated in Fig. 4f, the amount of light transmitted ($\gamma = 90^\circ$) through $\rho_{\text{Aero-BN}} \sim 0.68 \text{ mg cm}^{-3}$ is ~ 4 times higher than the reflected (and scattered) light ($\gamma > 180^\circ$). The ratio between transmitted and scattered light (ideal value of 1 for an isotropic diffuser) decreases with increasing network density. For $\rho_{\text{Aero-BN}} \sim 0.17 \text{ mg cm}^{-3}$ this is ~ 200 , whereas it is ~ 3.7 for $\rho_{\text{Aero-BN}} \sim 0.68 \text{ mg cm}^{-3}$. A value of 1 might be achieved by increasing $\rho_{\text{Aero-BN}}$ further. The average scattering intensity S is calculated by averaging the photocurrent intensities of the polar plots for $105^\circ < \gamma < 170^\circ$ and $100^\circ < \delta < 230^\circ$. The relative deviation of S with respect to T ($\gamma = 90^\circ$) is illustrated in Supplementary Fig. 21 as a function of the optical areal density, i.e., the density times the sample length, for three wavelengths. By increasing the optical areal density ($\rho_{\text{Aero-BN}} \times L$), the ratio $(T-S)/S$ by over three orders of magnitude, irrespective of the wavelength. Light with a shorter wavelength is scattered more effectively, as for Rayleigh scattering^{50,51} (see Supplementary Fig. 22). Further details on the light-scattering properties are in Supplementary Note 6 and Supplementary Figs. 23–27, showing that the multiple light scattering observed in Aero-BN is a result of the combination of negligible absorption losses and a control of density of scattering centres over several orders of magnitude. Furthermore, we show independent tunability of the density in all three dimensions (given the almost null equivalent Poisson's ratio of such low-density foam materials⁵², see also Supplementary Fig. 24). This

ARTICLE

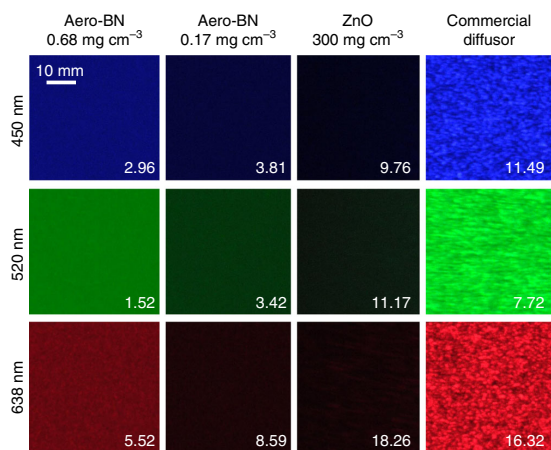
NATURE COMMUNICATIONS | <https://doi.org/10.1038/s41467-020-14875-z>

Fig. 5 Speckle contrast reduction. Objective speckle pattern at 450, 520, and 638 nm for two Aero-BN samples with high ($\rho_{\text{Aero-BN}} \sim 0.68 \text{ mg cm}^{-3}$) and low ($\rho_{\text{Aero-BN}} \sim 0.17 \text{ mg cm}^{-3}$) density, a porous ZnO microrod network ($\rho_{\text{T}} \sim 300 \text{ mg cm}^{-3}$) and a commercial plate diffuser. Values for speckle contrast are in %.

enables control of light diffusion and a nearly constant density of photons close the surface, with at most a linear decay in one dimension.

Speckle contrast reduction. The scattering behaviour also enables us to use Aero-BN for laser illumination without recognizable speckle patterns, thus solving one of the main challenges of using LDs as a light source^{18,53,54}. Speckle is the result of interference of light beams with the same frequency, but different phase and amplitude, resulting in a wave with random amplitude variations⁵⁵. The most promising approach to avoid speckle is to use an optical downstream component that superimposes multiple speckle patterns at once^{18,53,56}, so that on average no pattern is visible to the human eye, for an exposure time $\sim 1/60 \text{ s}$ ⁵⁷. In our Aero-BN, the primary laser beam is scattered multiple times. Thereby it is split into a large number of independent beams, causing multiple overlapping speckle patterns. This reduces the objective speckle contrast χ (i.e., the mean intensity of the speckle pattern divided by the standard deviation of the intensity) down to $\sim 2\%$, lower than that for the human eye (4%)¹⁸. Figure 5 plots the objective speckle pattern for different wavelengths as a function of material and Aero-BN density ($\rho_{\text{Aero-BN}}$). For high-density Aero-BN ($\rho_{\text{Aero-BN}} \sim 0.68 \text{ mg cm}^{-3}$) the speckle contrast is lowest, with minimal values $\sim 2.96\%$, 1.52% , and 5.52% for 450, 520, and 638 nm (each at 100 mW), respectively. Therefore, nearly no speckle can be observed by the human eye. Even lower speckle contrast could be achieved by using higher $\rho_{\text{Aero-BN}}$. Our Aero-BN outperforms commercially available plate diffusers like DG10-220 (Thorlabs) in terms of speckle contrast, since these have >5 times higher speckle contrasts (16%). It also surpasses that of the interconnected ZnO microrod networks, as no pure light diffusion can be reached there (see also Supplementary Fig. 15), due to missing Rayleigh-type scattering centres at the nanoscale. The lower speckle contrast for Aero-BN at lower wavelengths is a direct effect of the wavelength dependence (λ^{-4}) of Rayleigh scattering^{50,51}. Due to continuous beam splitting by multiple light-scattering processes, the low speckle contrast might also be related to small ($< 50 \text{ nm}$) thermally activated movements of the hollow microtubes with wall

thicknesses $< 25 \text{ nm}$, resulting in a time-varying speckle pattern (see also Supplementary Note 7 and Supplementary Table 4). This is similar to the speckle contrast reduction obtained by using colloidal dispersions, with values as low as 3% due to particles Brownian motion¹⁸. In comparison with other methods to reduce speckle contrast, e.g., by random lasing⁵⁸, using small moving diffusers⁵³, rotating ground glass diffusers⁵⁹ or nonmoving Hadamard matrix diffusers⁶⁰ our approach does not require complex micromechanical devices, making it easier to use and less prone to failure (see also Supplementary Note 1 and Supplementary Table 1).

Tunable RGB laser light illumination. The viability of our Aero-BN in combination with an RGB laser system as an illumination source, as an alternative to remote phosphors, is demonstrated by illuminating the $\rho_{\text{Aero-BN}} \sim 0.68 \text{ mg cm}^{-3}$ sample at different laser intensities under a translucent glass sphere screen. The resulting images are presented in Fig. 6a together with the respective International Commission on Illumination (CIE) colour space values marked in the colour map of Fig. 6b. An all-primary RGB laser wavelength mixing approach, i.e., a combination of three (red, green, and blue) or even four (red, yellow, green, and blue) laser wavelengths is known to outperform the efficiency of any other known white-light source^{2-4,8}. Furthermore, the possible colour gamut (i.e., the subset of colours which can be accurately represented) of such a system is on par to that of LEDs or LCDs⁶¹. By tuning the individual intensities of our RGB laser source, all colours in the resultant RGB triangle (Fig. 6b) can be produced. For the maximum intensity of all lasers, white light is produced, close to the CIE standard white illuminant D65⁶². The corresponding photographs of $\rho_{\text{Aero-BN}} \sim 0.68 \text{ mg cm}^{-3}$ illuminated at 450, 520, and 638 nm are in Fig. 6c, together with a photograph of the same sample illuminated with all wavelengths at once, resulting in a diffuse white-light illumination. Thus, our Aero-BN is an ideal broadband diffuser (see also Supplementary Movie 1) and can be used to fabricate tunable RGB laser light sources with a large colour gamut, depending only on characteristics of the actual laser system used, rather than on light conversion effects such as in the case of remote phosphors.

Laser damage threshold. To demonstrate that Aero-BN can overcome the irradiance levels of state-of-the-art phosphors needed for high-brightness illumination applications, such as automotive headlights or projectors, we characterised its thermal decomposition and laser damage threshold. Thermogravimetric analysis (TGA) under nitrogen atmosphere indicates nearly no change in weight ($\pm 2 \text{ wt\%}$ up to $1000 \text{ }^\circ\text{C}$). In an oxygen-containing atmosphere (nitrogen/oxygen $\sim 1/4$) the material is stable up to $700 \text{ }^\circ\text{C}$, where the formation of B_2O_3 starts⁶³ (Supplementary Fig. 28). The chemical reaction also confirms the presence of hBN over other crystalline forms of BN such as wurtzite boron nitride (wBN) and cubic boron nitride (cBN)⁶⁴. To determine the laser damage threshold we use a focused (spot diameter $\sim 8.4 \text{ } \mu\text{m}$) high-power (3 W) continuous wave laser at 450 nm. The threshold is determined by moving the focused laser beam over an individual tube and simultaneously recording the microtube with a charge-coupled device (CCD) camera. After each passage, the laser power is increased until the laser induces morphological damage (e.g., microtube destruction, see Supplementary Fig. 29). However, even at the highest power ($\sim 650 \text{ kW cm}^{-2}$) the Aero-BN network remains intact, whereas a commercially available state-of-the-art phosphor shows degradation at $\sim 80 \text{ kW cm}^{-2}$ (see Supplementary Fig. 30). In contrast to Aero-BN, the phosphor actively converts the incident laser light into energy, which leads to increased heat accumulation. To

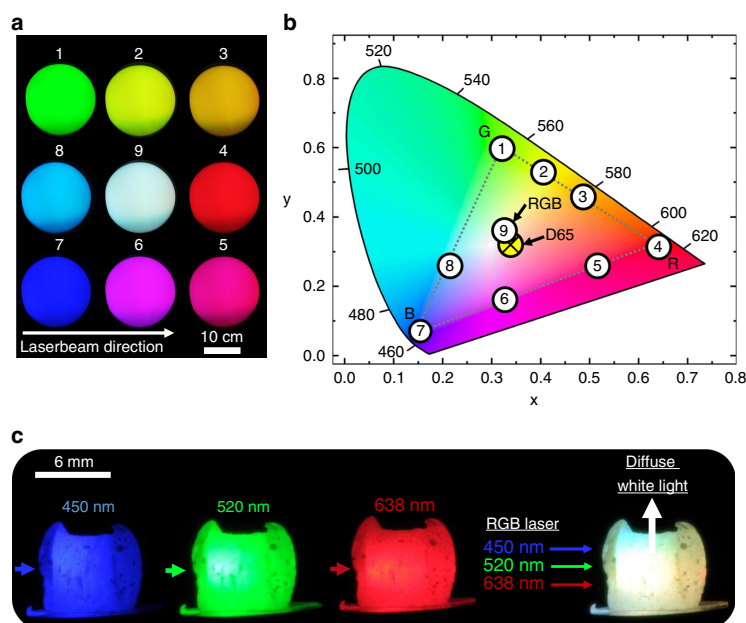


Fig. 6 Colour mixing. **a** Light distribution of a high $\rho_{\text{Aero-BN}}$ sample illuminated in the middle of a translucent glass bulb under different intensities for the each wavelength (450, 520, and 638 nm). White light is produced when all lasers (R + G + B) are at the maximum power (100 mW). **b** CIE colour map with marked values for the pictures in **a**. The value obtained for mixing R + G + B is close to the CIE standard white illuminant D65⁶² (yellow circle). **c** Photographs of a sample with $\rho_{\text{Aero-BN}} \sim 0.68 \text{ mg cm}^{-3}$ illuminated at 450, 520, and 638 nm (100 mW each, 1 mm spot size), respectively, as well as the resultant white light produced if all lasers are used at once. The arrows mark the direction of the incident laser beam.

achieve even higher power densities we use a highly focused pulsed laser (spot diameter $\sim 1 \mu\text{m}$) at 355 nm, with 100-Hz repetition rate ~ 7 -ns pulse duration (see Supplementary Fig. 29). In this configuration the Aero-BN shows a high laser damage threshold $\sim 430 \text{ MW cm}^{-2}$ ($\sim 2.65 \text{ J cm}^{-2}$), ~ 10 times higher than commercially available phosphor (see Supplementary Fig. 31)^{12,13,17}. This is directly related to the microscopic structure of the Aero-BN. The nanoscopic wall thickness leads to high transmittance of the individual tubes, meaning that only a small portion of the laser light interacts with a single tube. Furthermore, the low hBN absorption in the visible spectrum²¹, implies that a minimal amount of energy is transformed into heat. The high heat conductivity ($\sim 400 \text{ W m}^{-1} \text{ K}^{-1}$)²³ of hBN helps to quickly transport thermal energy away from the illuminated spot⁶⁵. The high porosity ($> 99.99\%$), the small wall thickness $< 25 \text{ nm}$, as well as the micrometre-sized voids enable efficient heat management, similar to that reported for other foam-like nanostructures, such as graphene foams^{66,67}, since heat can be easily transported to the surrounding air. Furthermore, the volumetric heat capacity of our Aero-BN foam is comparable with that of the surrounding air, as both have similar densities ($\rho_{\text{air}} \sim 1.2 \text{ mg cm}^{-3}$; $0.17 \text{ mg cm}^{-3} < \rho_{\text{Aero-BN}} < 1 \text{ mg cm}^{-3}$). Therefore, the damage threshold is only an estimate for the lower destruction limit. The macroscopic destruction threshold of Aero-BN is potentially much higher when a macroscopic laser beam is used, not focused to such a small spot.

Discussion

We demonstrated a concept for high-brightness and broadband laser illumination based on a diffuser consisting of a network of interconnected hollow hBN microtubes, overcoming the problems associated with inorganic phosphor materials. Their

structurally disordered arrangement, combined with the nanoscopic wall thickness, and low absorption are key to enable homogeneous light diffusion through the cm^3 -sized networks and promote light-scattering properties suitable for laser illumination applications. Our Aero-BN has efficient Rayleigh-type scattering centres arranged in a thinly spread and controlled manner, resulting in non-exponential light diffusion. By controlling the density of the aero-material system, we are able to adjust the light diffusion so that multiple scattering events result in an almost homogeneous, isotropic light illumination.

For Aero-BN densities $\sim 0.68 \text{ mg cm}^{-3}$ the speckle contrast is well below the perception threshold of the human eye. The highly porous structure, together with the low absorption in the visible range, as well as the low volumetric heat capacity and high heat conductivity, enable an efficient heat management. We achieve laser irradiance levels ~ 10 times higher than commercially available remote phosphors, unleashing the full potential of laser diodes for high-brightness illumination. Being based on multiple light scattering, rather than on light conversion effects, the broadband properties of our diffuser enable an all-primary RGB laser approach for white-light generation and full-colour range mixing with a large colour gamut⁸, without efficiency reduction, thereby overcoming the problems associated with state-of-the-art remote phosphors (see also Supplementary Note 8). With the expected increase in LD efficiencies in the near future, our concept paves the way to design a new generation of highly effective light sources.

Methods

Fabrication of highly porous ZnO networks. The t-ZnO ceramic networks are produced by a flame transport synthesis technique⁶⁸. Zinc powder with a grain size ~ 1 – $10 \mu\text{m}$ is mixed with polyvinyl butyral in a mass ratio of 1:2. The mixture is then heated in a muffle furnace at $60 \text{ }^\circ\text{C min}^{-1}$ to $900 \text{ }^\circ\text{C}$ for 30 min. After that a loose powder of ZnO tetrapods is obtained, then pressed into pellets (e.g., height $\sim 10 \text{ mm}$,

ARTICLE

NATURE COMMUNICATIONS | <https://doi.org/10.1038/s41467-020-14875-z>

diameter ~12 mm) with a density ~0.3 g cm⁻³. Reheating the pellets for 5 h at 1150 °C leads to junctions between the tetrapods and an interconnected network.

Fabrication of Aero-BN. In Supplementary Fig. 3 the computer-controlled CVD setup for the fabrication of the Aero-BN is illustrated. The highly porous (up to 98%) ZnO ceramic template is placed in the middle of a quartz tube furnace in a ceramic crucible. Next to that (~1 cm), a crucible filled with B₂O₃ is placed into the furnace. The reactor is flushed with Ar and the pressure adjusted to 30 mbar. The Ar flow is then adjusted to 30 sccm and the temperature is increased to 910 °C (heating rate ~20 °C min⁻¹). Urea is used as a nitrogen source, located in an evaporator which is connected to the quartz tube furnace as illustrated in Supplementary Fig. 3. When the quartz tube furnace reaches 910 °C the evaporator for urea is switched on. By heating to 170 °C at 30 mbar NH₃ forms⁶⁹, which decomposes to N and H₂ in the reaction zone of the reactor⁷⁰. At the process temperature (910 °C) N and B react at the surface of the ceramic template, forming a thin (<25 nm) hBN layer. Simultaneously the ZnO template is etched by hydrogen. After 3 h the urea evaporator and the quartz tube furnace are switched off. When the reactor reaches 30 °C the Ar flow is switched off and the sample is removed. A detailed discussion of the reaction is in Supplementary Note 2.

Characterisation. The morphologies of the different structures are investigated by SEM (Zeiss Supra 55VP) equipped with an EDX detector. Aero-BN is analysed by a FEI Tecnai F30 G2 STwin TEM (300 kV acceleration voltage, cs-coefficient 1.15 mm) and a FEI Titan G2 60-300 TEM equipped with a monochromator. Macroscopic aggregates of Aero-BN are tapped with TEM grids in order to transfer some tetrapods or single fragments onto the grid, minimising the breaking rate for the Aero-BN network. Unfolded BN sheets are also analysed by HRTEM to visualise atomic scale defects. The electronic structure is investigated by HR-EELS with a GIF Quantum/Enfina energy analyser. TGA measurements are performed using a TA Instruments Q50 under nitrogen and nitrogen/oxygen (1/4) at a scan rate of 10 °C min⁻¹ from 25 to 1000 °C. Raman spectroscopy is done with a Renishaw 1000 InVia micro-spectrometre at 514.5 nm for the ZnO template and a Witec Instruments Alpha300 RA at 532 nm for the Aero-BN sample.

Reflectivity calculations. Reflectivity calculations as a function of wall thickness for a hollow hBN microtube and ZnO microrods as a function of diameter for different wavelengths, respectively, follow those in ref. ⁷¹. Refractive indexes of 1.8²⁰ and 2.1⁷² are used for hBN and ZnO. The mean reflectivity is derived by averaging that for incident beam angles of 0–180° (step size of 1°). For each angle the unpolarised and polarised reflectivity is derived. This procedure is repeated for different hBN wall thicknesses as well as ZnO microrod diameters.

Light-scattering measurements. A photodiode (FDS1010, Thorlabs) is rotated around the sample with an angular step ~5° at a distance ~15 cm, using a photogoniometer. From one side the cylindrical samples are illuminated with an RGB laser (RTI OEM 300 mW RGB Modul, LaserWorld). The sample is positioned so that the laser beam illuminates it in the middle. The spot size is adjusted by a lens to ~1 mm. Each laser has a maximum output power of ~100 mW.

Absorption measurements. Absorption measurements are performed using an integrating sphere (Opsytec) with an inner diameter of 200 mm, coated with a reflective BaSO₄ thin film. The illumination intensity is measured by connecting to it a radiometer (RM-22, Opsytec). The sample is mounted on a thin (diameter of 3 mm) Al slab in the centre of the sphere. Through an opening of 2 mm, the laser is focused on the sample. The absorption is calculated as the ratio of the luminous flux measured by the radiometer with and without sample. This is integrated for at least 20 s.

Transmission measurements. Transmission measurements are performed using the same integrating sphere used for absorption. The sample is placed in front of a 2 mm opening of the sphere. The laser is adjusted to be in the same axis as the opening of the sphere and focused on the sample. The transmission is calculated as the ratio of the measured luminous flux with and without sample. For measurements as a function of compression, the sample is clamped between two highly reflective (>99%) plates to ensure as little light absorption as possible by the surrounding (clamping) material. The sample is compressed step by step using a high-precision screw. After each compression, a transmission measurement is performed as described before, using an integration time of at least 20 s. This is increased to 60 s for small fluxes.

Laser damage threshold. The sample is moved using a xy-translation stage, such that the laser beam directly hits an individual nanostructure, e.g. a microtube. The laser focus is adjusted using the back-scattered signal of the laser spot, tuned towards its highest intensity by moving the translation stage in z-direction. The laser signal is then filtered on a video camera by using a notch filter, while only the microscope image is monitored. The laser power is increased stepwise until the first morphological changes of the nanostructures become evident in the microscope (white light) image. The corresponding laser intensity (on the sample) defines the

destruction threshold of the investigated materials. The commercially used phosphor is a Intematix CL830R45XT.

Speckle pattern photography and contrast. Objective speckle patterns (i.e. the intensity pattern produced by the interference of a set of wavefronts) are obtained by illuminating with a focused laser beam with 100 mW at 450, 520, and 638 nm. The objective speckle pattern forms on a sheet of white paper at 90° with respect to the incoming laser. The distance between sample and speckle pattern is ~40 cm. The pattern is photographed using a CCD camera (Nikon D300) equipped with a lens with 120 mm focal length. The camera is positioned slightly over the sample, to avoid any light being directly scattered into the lens. The aperture of the lens is used at maximum of *f*/4 to take as much light in as possible. Since speckle patterns are time dependent⁵⁶, the exposure time is important. We use 1/60 s, close to the detection limit of the human eye⁵⁷. To avoid any overexposure of the CCD chip we use a camera sensitivity (ISO) of 800. For weakly scattering samples, this might lead to a dark speckle pattern. However, this has no influence on the speckle contrast, whereas an overexposure would result in wrong calculations. The photographs are taken at a maximum resolution of 2848 × 4288 pixels. The speckle contrast of the resultant photographs is calculated by using the Gatan Microscopy Suit. A representative quadratic area (several cm²) is chosen. The colour is converted into a black and white representation. From these images the mean intensity Φ as well as the standard deviation σ is calculated using the above mentioned software. The speckle contrast χ is then calculated as follows⁵⁶:

$$\chi = \frac{\sigma}{\Phi}.$$

FEM simulations. The FEM model developed to compute the network variation of projected porous areal density and Poisson's ratio under monoaxial compression (see Supplementary Note 6), consist of a periodic supercell ~71 × 83 × 46 μm³ (*x*, *y*, *z*) containing nine tetrapods mutually interconnected. We consider an average geometry of the tetrapod with $d_{\text{air},1} = 1.67 \mu\text{m}$, $d_{\text{air},2} = 1.00 \mu\text{m}$, $t_{\text{wall}} = 4 \text{ nm}$, and $r = 27$ or $38 \mu\text{m}$ ⁷³ to simulate networks with high or low densities, (respectively $\rho_{\text{Aero-BN}} = 0.367 \text{ mg cm}^{-3}$ and $\rho_{\text{Aero-BN}} = 0.178 \text{ mg cm}^{-3}$), similar to the ones tested in the experiments. Tetrapods are built associating the arm extremities and the central joint of the tetrapods to the vertexes and centroid of a regular tetrahedron, respectively. The tube walls are modelled with thin shell elements with selective-reduced integration, and the spurious modes effects are controlled. Monoaxial compression tests are reproduced with periodic boundary conditions along the lateral faces of the supercell (*x* and *y* directions) while the two horizontal rigid surfaces act to apply the monoaxial load on the network along *z* (displacement controlled, 0.25 μm ms⁻¹). Contact between tetrapods and within elements of the same tetrapods are implemented to prevent mutual and self-penetration. The density of the supercell is monitored along the simulations. To measure the evolution of the projected porous area, images of lateral view of the network (*xz* and *yz* planes) are extracted from simulations at a constant time sampling. The normalised projected porous area (Ω/Ω_0) is measured via a graphics software (paint.net) by selecting the void area in the lateral projection of the network ("magic wand" tool) and computing the corresponding number of pixels (ratio of the current vs. initial value).

Data availability

The data that support the findings of this study are available from the corresponding authors upon request.

Received: 16 September 2019; Accepted: 3 February 2020;

Published online: 18 March 2020

References

- Denault, K. A., Cantore, M., Nakamura, S., DenBaars, S. P. & Seshadri, R. Efficient and stable laser-driven white lighting. *AIP Adv.* **3**, 72107 (2013).
- Wierer, J. J., Tsao, J. Y. & Sizov, D. S. Comparison between blue lasers and light-emitting diodes for future solid-state lighting. *Laser Photonics Rev.* **7**, 963–993 (2013).
- Phillips, J. M. et al. Research challenges to ultra-efficient inorganic solid-state lighting. *Laser Photonics Rev.* **1**, 307–333 (2007).
- Neumann, A. et al. Four-color laser white illuminant demonstrating high color-rendering quality. *Opt. Express* **19**, A982–A990 (2011).
- Penning, J., Stober, J. K., Taylor, V. & Yamada, M. Energy savings forecast of solid-state lighting in general illumination applications (USDOE Office of Energy Efficiency and Renewable Energy (EERE) 2016). <https://www.osti.gov/biblio/1374119-energy-savings-forecast-solid-state-lighting-general-illumination-applications>.
- Basu, C., Meinhardt-Wollweber, M. & Roth, B. Lighting with laser diodes. *Adv. Opt. Technol.* **2**, 313–321 (2013).

7. Ahemen, I., Dilip, D. & Amah, N. A review of solid state white light emitting diode and its potentials for replacing conventional lighting technologies in developing countries. *Appl. Phys. Res.* **6**, 95–108 (2014).
8. Wierer, J. J. & Tsao, J. Y. Advantages of III-nitride laser diodes in solid-state lighting. *Phys. Status Solidi A* **212**, 980–985 (2015).
9. Karlicek, R., Sun, C.-C., Zissis, G., Ma, R. (eds.). *Handbook of advanced lighting technology*. (Springer International Publishing, Cham, 2017).
10. Trivellin, N. et al. *Laser-based lighting: experimental analysis and perspectives, materials*, Vol. 10 (Basel, Switzerland, 2017).
11. Mehr, M. Y., van Driel, W. D. & Zhang, G. Q. Reliability and lifetime prediction of remote phosphor plates in solid-state lighting applications using accelerated degradation testing. *J. Electron. Mater.* **45**, 444–452 (2016).
12. Yu, J. et al. High-power laser-driven phosphor-in-glass for excellently high conversion efficiency white light generation for special illumination or display backlighting. *J. Mater. Chem. C* **6**, 8212–8218 (2018).
13. Zhang, X. et al. All-inorganic light converter based on phosphor-in-glass engineering for next-generation modular high-brightness white LEDs/LDs. *ACS Photonics* **4**, 986–995 (2017).
14. Cozzan, C. et al. Monolithic translucent BaMgAl 10 O 17: Eu 2+ phosphors for laser-driven solid state lighting. *AIP Adv.* **6**, 105005 (2016).
15. Cozzan, C. et al. Stable, heat-conducting phosphor composites for high-power laser lighting. *ACS Appl. Mater. Interfaces* **10**, 5673–5681 (2018).
16. Li, S. et al. Al 2 O 3 –YAG: Ce composite phosphor ceramic: a thermally robust and efficient color converter for solid state laser lighting. *J. Mater. Chem. C* **4**, 8648–8654 (2016).
17. Song, Y. H. et al. High power laser-driven ceramic phosphor plate for outstanding efficient white light conversion in application of automotive lighting. *Sci. Rep.* **6**, 31206 (2016).
18. Riechert, F., Bastian, G. & Lemmer, U. Laser speckle reduction via colloidal-dispersion-filled projection screens. *Appl. Opt.* **48**, 3742 (2009).
19. Murayama, M. et al. Watt-class green (530 nm) and blue (465 nm) laser diodes. *Phys. Status Solidi A* **215**, 1700513 (2018).
20. Jiang, H. X. & Lin, J. Y. Review—hexagonal boron nitride epilayers: growth, optical properties and device applications. *ECS J. Solid State Sci. Technol.* **6**, Q3012–Q3021 (2016).
21. Song, L. et al. Large scale growth and characterization of atomic hexagonal boron nitride layers. *Nano Lett.* **10**, 3209–3215 (2010).
22. Mishra, Y. K. & Adelung, R. ZnO tetrapod materials for functional applications. *Mater. Today* **21**, 631–651 (2017).
23. Pakdel, A., Bando, Y. & Golberg, D. Nano boron nitride flatland. *Chem. Soc. Rev.* **43**, 934–959 (2014).
24. Wiersma, D. S. Disordered photonics. *Nat. Photon* **7**, 188–196 (2013).
25. Schittny, R. et al. Invisibility cloaking in light-scattering media. *Laser Photonics Rev.* **10**, 382–408 (2016).
26. Mecklenburg, M. et al. Aerographite: ultra lightweight, flexible nanowall, carbon microtube material with outstanding mechanical performance. *Adv. Mater.* **24**, 3486–3490 (2012).
27. Schuchardt, A. et al. Three-dimensional Aerographite-GaN hybrid networks: single step fabrication of porous and mechanically flexible materials for multifunctional applications. *Sci. Rep.* **5**, 8839 (2015).
28. Marx, J. et al. Fundamentals of the temperature-dependent electrical conductivity of a 3D carbon aerogel -aerographite. *Synth Metals* **235**, 145–152 (2018).
29. Reich, S. et al. Resonant Raman scattering in cubic and hexagonal boron nitride. *Phys. Rev. B* **71**, 1522 (2005).
30. Arenal, R. et al. Raman spectroscopy of single-wall boron nitride nanotubes. *Nano Lett.* **6**, 1812–1816 (2006).
31. Nemanich, R. J. & Solin, S. A. First- and second-order Raman scattering from finite-size crystals of graphite. *Phys. Rev. B* **20**, 392–401 (1979).
32. Calleja, J. M. & Cardona, M. Resonant Raman scattering in ZnO. *Phys. Rev. B* **16**, 3753–3761 (1977).
33. Cuscó, R. et al. Temperature dependence of Raman scattering in ZnO. *Phys. Rev. B* **75**, G3 (2007).
34. Song, Y. et al. Ultralight boron nitride aerogels via template-assisted chemical vapor deposition. *Sci. Rep.* **5**, 10337 (2015).
35. Grant, J. T. et al. Selective oxidative dehydrogenation of propane to propene using boron nitride catalysts. *Science* **354**, 1570–1573 (2016).
36. Malis, T., Cheng, S. C. & Egerton, R. F. EELS log-ratio technique for specimen-thickness measurement in the TEM. *J. Electron Microsc. Tech.* **8**, 193–200 (1988).
37. Pan, C. T. et al. Nanoscale electron diffraction and plasmon spectroscopy of single- and few-layer boron nitride. *Phys. Rev. B* **85**, 045440 (2012).
38. Yin, J., Li, X., Zhou, J. & Guo, W. Ultralight three-dimensional boron nitride foam with ultralow permittivity and superelasticity. *Nano Lett.* **13**, 3232–3236 (2013).
39. Xue, Y. et al. Multifunctional superelastic foam-like boron nitride nanotubular cellular-network architectures. *ACS Nano* **11**, 558–568 (2017).
40. Owuor, P. S. et al. Lightweight hexagonal boron nitride foam for CO₂ absorption. *ACS Nano* **11**, 8944–8952 (2017).
41. Loeblein, M. et al. High-density 3D-boron nitride and 3D-graphene for high-performance nano-thermal interface material. *ACS Nano* **11**, 2033–2044 (2017).
42. Lei, W. et al. Boron nitride colloidal solutions, ultralight aerogels and freestanding membranes through one-step exfoliation and functionalization. *Nat. Commun.* **6**, 8849 (2015).
43. Lindquist, D. A. et al. Formation and pore structure of boron nitride aerogels. *J. Am. Ceram. Soc.* **73**, 757–760 (1990).
44. Schlienger, S. et al. Micro-, mesoporous boron nitride-based materials templated from zeolites. *Chem. Mater.* **24**, 88–96 (2011).
45. Rousseas, M. et al. Synthesis of highly crystalline sp²-bonded boron nitride aerogels. *ACS Nano* **7**, 8540–8546 (2013).
46. Wiersma, D. S., Bartolini, P., Lagendijk, A. & Righini, R. Localization of light in a disordered medium. *Nature* **390**, 671–673 (1997).
47. Einaga, Y., Mitani, T., Hashizume, J., Fujita, H. & Laser, A. Scattering photogoniometer. *Polym. J.* **11**, 565–574 (1979).
48. Mishra, Y. K. et al. Versatile fabrication of complex shaped metal oxide nano-microstructures and their interconnected networks for multifunctional applications. *KONA* **31**, 92–110 (2014).
49. Mishra, Y. K. et al. Direct growth of freestanding ZnO tetrapod networks for multifunctional applications in photocatalysis, UV photodetection, and gas sensing. *ACS Appl. Mater. Interfaces* **7**, 14303–14316 (2015).
50. van de Hulst, H. C. *Light Scattering by Small Particles*. (Dover Publications, Newburyport, 2012).
51. Bohren, C. F. & Huffman, D. R. Absorption and scattering of light by small particles (Wiley-VCH, 1998). <https://onlinelibrary.wiley.com/doi/book/10.1002/9783527618156>.
52. Wu, Y. et al. Three-dimensionally bonded spongy graphene material with super compressive elasticity and near-zero Poisson's ratio. *Nat. Commun.* **6**, 6141 (2015).
53. Kuratomi, Y. et al. Speckle reduction mechanism in laser rear projection displays using a small moving diffuser. *J. Opt. Soc. Am. A Opt. Image Sci. Vis.* **27**, 1812–1817 (2010).
54. Murata, H., Shibasaki, K., Yamamoto, K. & Okamura, Y. Speckle control using high-frequency signal superposition to semiconductor laser. *OPT REV* **21**, 79–82 (2014).
55. Rabal, H. J., Braga, R. A. (eds.). *Dynamic laser speckle and applications*. (CRC Press, Boca Raton, 2009).
56. Draijer, M., Hondebrink, E., van Leeuwen, T. & Steenberg, W. Review of laser speckle contrast techniques for visualizing tissue perfusion. *Lasers Med. Sci.* **24**, 639–651 (2009).
57. Chen, H., Peng, F., Hu, M. & Wu, S.-T. Flexoelectric effect and human eye perception on the image flickering of a liquid crystal display. *Liq. Cryst.* **42**, 1730–1737 (2015).
58. Redding, B., Choma, M. A. & Cao, H. Speckle-free laser imaging using random laser illumination. *Nat. Photon* **6**, 355–359 (2012).
59. Stangner, T., Zhang, H., Dahlberg, T., Wiklund, K. & Andersson, M. Step-by-step guide to reduce spatial coherence of laser light using a rotating ground glass diffuser. *Appl. Opt.* **56**, 5427 (2017).
60. Thomas, W. & Middlebrook, C. Non-moving Hadamard matrix diffusers for speckle reduction in laser pico-projectors. *J. Mod. Opt.* **61**, S74–S80 (2014).
61. Chellappan, K. V., Erden, E. & Urey, H. Laser-based displays: a review. *Appl. Opt.* **49**, F79–F98 (2010).
62. Fan, F., Turkdogan, S., Liu, Z., Shelhammer, D. & Ning, C. Z. A monolithic white laser. *Nat. Nanotechnol.* **10**, 796–803 (2015).
63. Wang, M. et al. High yield synthesis of novel boron nitride submicro-boxes and their photocatalytic application under visible light irradiation. *Catal. Technol.* **1**, 1159 (2011).
64. Lavrenko, V. A. & Alexeev, A. F. High-temperature oxidation of boron nitride. *Ceram. Int.* **12**, 25–31 (1986).
65. Liu, L., Feng, Y. P. & Shen, Z. X. Structural and electronic properties of h-BN. *Phys. Rev. B* **68**, 582 (2003).
66. Menzel, R. et al. Joule heating characteristics of emulsion-templated graphene aerogels. *Adv. Funct. Mater.* **25**, 28–35 (2015).
67. Giorgianni, F. et al. High-efficiency and low distortion photoacoustic effect in 3D graphene sponge. *Adv. Funct. Mater.* **28**, 1702652 (2018).
68. Mishra, Y. K. et al. Fabrication of macroscopically flexible and highly porous 3D semiconductor networks from interpenetrating nanostructures by a simple flame transport approach. *Part. Part. Syst. Charact.* **30**, 775–783 (2013).
69. Schaber, P. M. et al. Thermal decomposition (pyrolysis) of urea in an open reaction vessel. *Thermochim. Acta* **424**, 131–142 (2004).
70. Mesrine, M., Grandjean, N. & Massies, J. Efficiency of NH₃ as nitrogen source for GaN molecular beam epitaxy. *Appl. Phys. Lett.* **72**, 350–352 (1998).
71. Pascoe, K. J. *Reflectivity and transmissivity through layered, lossy media. A user-friendly approach* (Biblioscholar, 2012).
72. Morkoc, H. & Ozgur, U. *Zinc oxide. fundamentals, materials and device technology* (John Wiley & Sons, 2009).

ARTICLE

NATURE COMMUNICATIONS | <https://doi.org/10.1038/s41467-020-14875-z>

73. Meija, R. et al. Nanomechanics of individual aerographite tetrapods. *Nat. Commun.* **8**, 14982 (2017).

Acknowledgements

We thank Prof. Klaus Rätzke for valuable discussions. We acknowledge funding by the Deutsche Forschungsgemeinschaft under contracts CRC 1261, AD 183/27-1, FOR 1616, and SCHU 926/25-1, European Commission under the Graphene Flagship, ERC grant Hetero2D, EPSRC grants EP/L016087/1, EP/K01711X/1, EP/R511547/1, EP/K017144/1, EP/P02534X/1, FET Proactive Neurofibres grant No. 732344, FET Open BOHEME grant No. 863179, the Italian Ministry of Education, University and Research (MIUR) under the “Departments of Excellence” grant L.232/2016, ARS01-01384-PROSCAN, PRIN-20177TTP3S, Trinity College, Cambridge, the Isaac Newton Trust, and the Institute for Basic Science (IBS-R019-D1).

Author contributions

R.A. and F.S. came up with the concept. F.S., F.T., T.C., J.C., Y.K.M., A.C.F., R.A., and N.M.P. designed the study. F.S. and H.K. fabricated the samples. F.S., R.A., S.K., J.C., and H.K. analyzed the light scattering data. J.S., N.W., L.K., H.H., and Z.L. carried out the TEM measurements and corresponding analysis. F.S. carried out SEM and EDX measurements. M.I.T., M.S., L.S., and H.K. constructed the photo goniometer setup, R.R. and M.Z. measured the laser damage threshold, T.C. and F.T. carried out the Raman measurements, J.M. and T.C. carried out the TGA measurements. N.M.P. and S.S. provided the FEM simulations and the analytical mechanical model of network compression. F.S., Y.K.M., R.A., A.C.F., and J.C. finalised the study and wrote the paper. All the authors have contributed to the discussion of the results and reviewed the paper.

Competing interests

The authors declare no competing interests.

Additional information

Supplementary information is available for this paper at <https://doi.org/10.1038/s41467-020-14875-z>.

Correspondence and requests for materials should be addressed to F.S. or R.A.

Peer review information *Nature Communications* thanks the anonymous reviewers for their contribution to the peer review of this work.

Reprints and permission information is available at <http://www.nature.com/reprints>

Publisher's note Springer Nature remains neutral with regard to jurisdictional claims in published maps and institutional affiliations.



Open Access This article is licensed under a Creative Commons Attribution 4.0 International License, which permits use, sharing, adaptation, distribution and reproduction in any medium or format, as long as you give appropriate credit to the original author(s) and the source, provide a link to the Creative Commons license, and indicate if changes were made. The images or other third party material in this article are included in the article's Creative Commons license, unless indicated otherwise in a credit line to the material. If material is not included in the article's Creative Commons license and your intended use is not permitted by statutory regulation or exceeds the permitted use, you will need to obtain permission directly from the copyright holder. To view a copy of this license, visit <http://creativecommons.org/licenses/by/4.0/>.

© The Author(s) 2020

Enhancement of antiviral drug efficacy through multimodal mechanism of Au nanoparticles complexed with ZnO tetrapods

For modern treatment in medicine nanoparticles have gained a high interest because of their ability to penetrate the cell walls and enter the metabolism of cells and bacteria. The downside of this approach is the low selectivity and the collateral damage towards other cells in the organism. Therefore, other strategies for the treatment of virus-based disease have been studied in the past years. One example is the application of zinc oxide tetrapod microparticles which possess a high amount of surface oxygen vacancies, leading to a negative surface charge. These centres act as binding points for viral envelop glycoproteins. The viruses get trapped on the microparticle surface and are then detectable by the immune system of the body. This work combines the nanoparticle treatment with this new mechanism by decorating zinc oxide tetrapods with gold nanoparticles. This increases the efficacy of virus medication, such as Acyclovir for the treatment of the herpes simplex virus. The same method shows effect on the novel human coronavirus SARS-CoV-2 and provides a large field for similar combined treatments of previously untreatable conditions.

Own contribution presented in this article

- Sample preparation
- Sample characterization via SEM and Raman Spectroscopy
- Discussion and interpretation
- Editing the manuscript

1
2
3 **Enhancement of antiviral drug efficacy through multimodal mechanism of Au nanoparticles**
4 **complexed with ZnO tetrapods**
5

6
7 Rahul K Suryawanshi^{1*}, Chandrashekhar D Patil^{1*}, Lulia Koujah^{1,2}, Pritam Kumar Panda³,
8 Sudhanshu Kumar Singh¹, Alex Agelidis^{1,2}, Ipsita Volety², Leonard Siebert⁴, Rainer Adelung⁴,
9 Rajeev Ahuja^{3,5}, Yogendra Kumar Mishra⁶, Deepak Shukla^{1,2}
10

11 **Affiliations**

12 ¹Department of Ophthalmology and Visual Sciences, University of Illinois at Chicago, Chicago IL, USA

13 ²Department of Microbiology and Immunology, University of Illinois at Chicago, Chicago, IL 60612, USA

14 ³ Condensed Matter Theory Group, Materials Theory Division, Department of Physics and Astronomy, Uppsala
15 University, Box 516, SE-751 20 Uppsala, Sweden.

16 ⁴Functional Nanomaterials, Institute for Materials Science, Kiel University, Kaiserstr. 2, D-24143, Kiel, Germany

17 ⁵ Applied Materials Physics, Department of Materials Science and Engineering, Royal Institute of Technology (KTH),
18 SE-100 44 Stockholm, Sweden.

19 ⁶ Mads Clausen Institute, NanoSYD, University of Southern Denmark, Alsion 2, DK-6400, Denmark

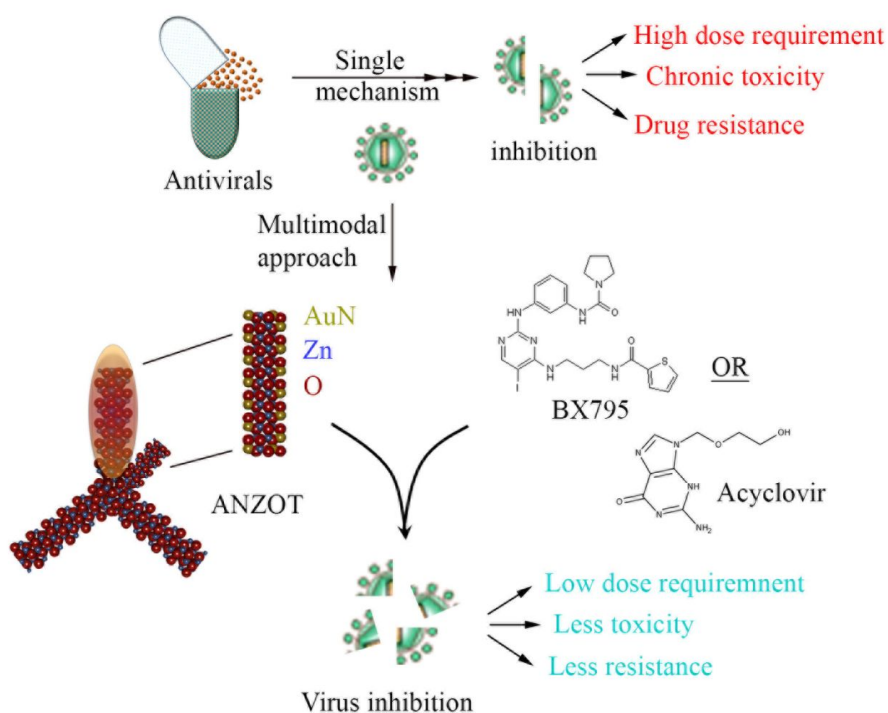
20 Correspondence: dshukla@uic.edu

21 *Equal contributors
22

23 **Abstract**

24 Nanoparticles represent an emerging treatment strategy against infectious diseases including viral
25 infections. Our previously described tetrapod shaped zinc oxide nanostructures, called ZOTEN,
26 demonstrate inherent antiviral and adjuvant-like properties. Here we investigated a novel
27 compound, gold nanoparticles decorated on ZOTEN (ANZOT), for standalone as well
28 combinatorial antiviral effects. We observed heightened inhibition of herpes simplex virus (HSV)
29 replication following combinatorial use of ANZOT with suboptimal concentrations of Acyclovir,
30 a commonly prescribed antiviral, or BX795, a promising preclinical drug. Moreover, given its
31 unique negative charge distribution, ANZOT possesses neutralizing capabilities against HSV-1
32 and the novel human coronavirus SARS-CoV-2, limiting viral entry and thus demonstrating
33 promise for broader applications in the antiviral field. A significantly enhanced drug efficacy
34 resulting from the combinatorial use of ANZOT and viral inhibitors defines an innovative strategy
35 that can be adapted to contain many viral and non-viral microbial diseases.
36
37
38

39 **Keywords:** *Herpesvirus, BX795, Zinc Oxide Tetrapod, gold nanoparticles, antiviral, virus*
40 *neutralization*
41
42
43
44
45
46
47
48
49
50
51
52
53
54
55
56
57
58
59
60



Graphical abstract

1
2
3
4
5
6
7
8
9
10
11
12
13
14
15
16
17
18
19
20
21
22
23
24
25
26
27
28
29
30
31
32
33
34
35
36
37
38
39
40
41
42
43
44
45
46
47
48
49
50
51
52
53
54
55
56
57
58
59
60

Introduction

Pathogens are known to interact with cell surface proteoglycans, which serve as a primary entry receptor or facilitator of infection.^{1,2} Heparan sulfate (HS) proteoglycans are ubiquitously expressed on the surface of many cell types and are involved in the infection of herpesviruses, papillomaviruses, flaviviruses, rhinoviruses, coronaviruses, and human immunodeficiency virus (HIV) among other viruses.³⁻⁵ Herpes simplex virus (HSV), for example, relies heavily on HS for cell attachment and entry, and is a highly contagious pathogen that causes a broad spectrum of clinical disorders ranging from oral, facial, and genital lesions to severe infection of the central nervous system (CNS).⁶⁻⁸ The World Health Organization estimate 3.7 billion, or 67%, people worldwide under the age of 50 have acquired HSV-1.⁹ Also, infection of severe acute respiratory syndrome-related coronavirus 2 (SARS-CoV-2), which is the cause of current global pandemic and unprecedented public health concerns, is facilitated through the interaction of HS and the receptor binding domain in its spike (S) protein.^{10,11} Despite the endemic prevalence of these pathogens, current antivirals suffer from serious adverse effects and do not eradicate the virus from the host. Developing an effective therapeutic strategy and mitigating the spread of these viruses is of direct global relevance. Competitive inhibition of viral attachment via nanoparticles can provide broad-spectrum antiviral benefits by reducing viral adhesion to cell surfaces and thereby, blocking entry and replication.^{1,12} Apart from sequence specific binding affinities, negatively charged moieties on HS proteoglycans plays an important role in binding of positively charged residues on viral envelop glycoproteins.

To this end, tetrapod-like zinc oxide nanoparticles (ZOTEN) were designed to mimic the negative charge density of HS through engineered oxygen vacancies.¹³ Our lab has shown virus-neutralizing capabilities of ZOTEN through electrostatic interactions, as well as adjuvant-like benefits during prophylactic or therapeutic treatment for HSV genital and ocular infections.¹⁴⁻¹⁸ Given its unique properties ZOTEN has defined a new concept in immunotherapy called microbivac. It can trap virus particles and promote the presentation of bound virions to mucosal antigen-presenting cells, which initiates and boosts adaptive immunity.^{14,15}

In this study, we test the combinatorial effect of nanostructured microparticles and antiviral drug compounds as a multimodal strategy to combat viral infections effectively. For improved activity and safe administration, we functionalized ZOTEN with gold nanoparticles (ANZOT).¹⁹ We found that this complex performed better than the independent administration of either gold nanoparticles or ZOTEN. We then probed ANZOT in a combinatorial approach to enhance drug efficacy of acyclovir (ACV), a guanosine analog commonly used to treat HSV, and BX795, a promising preclinical drug with strong activity against multiple strains of HSV-1 shown in *in-vivo*, *in-vitro*, and *in situ* ocular disease models.²⁰ We aimed to lower the threshold concentration of ACV or BX795 to increase the selectivity index and avoid adverse effects of systemic use. This is particularly important for drugs like ACV, which inherently have low bioavailability and require frequent high doses for optimal therapeutic efficacy.

This application encompasses multiple targets to combat the infection while also lowering the required concentration for optimal therapy. We observed that the administration of suboptimal concentrations of either nucleoside analogs or BX795 with ANZOT demonstrated a robust anti-HSV-1 response both *in vitro* and in a murine model of ocular infection. ANZOT, combined with

1
2
3
4
5
6
7
8
9
10
11
12
13
14
15
16
17
18
19
20
21
22
23
24
25
26
27
28
29
30
31
32
33
34
35
36
37
38
39
40
41
42
43
44
45
46
47
48
49
50
51
52
53
54
55
56
57
58
59
60

BX795, exhibits a higher efficacy in inhibiting HSV-1 replication when compared to treatments of BX795, ZnO tetrapods, or gold nanoparticles alone. The composite reduces the minimum inhibitory concentration of BX-795 by 3.9-fold with no apparent toxicity or adverse effects. Furthermore, *in-silico* and *in-vitro* experiments confirm previous findings that ZOTEN, even when complexed with gold nanoparticles, neutralizes the virus particle and inhibits viral entry.²⁰⁻²² ANZOT displayed similar neutralizing capabilities against SARS-CoV-2, suggesting a breadth of application against multiple viruses.

We also reveal new mechanistic insights into the anti-HSV-1 activity of BX795 and show that BX795 may limit the nuclear release of virions through inhibition of protein kinase C isoform PKC- α and PKC- ζ expression and perinuclear localization. Combining either ACV or BX795, which target host machinery to restrict viral replication, and ANZOT, which targets the virus itself, demonstrates a novel antiviral approach. Our study demonstrates ANZOT as a platform for the enhanced drug efficacy and safety of ACV, the most frequently prescribed antiviral, and BX795, a promising preclinical antiherpetic agent.

Results and Discussion

Synthesis and formation of gold nanoparticles complexed with tetrapod-like zinc oxide microparticles

A photographic image of pristine ZOTEN crystals fabricated by flame transport synthesis is shown, as well as images of ZOTEN coated with gold nanoparticles, which give off a distinct pink hue (Figure 1a). Images were taken with a scanning electron microscope (SEM) showing the long-legged tetrapod-shaped particles with evident specks of gold nanoparticles on the surface. Raman spectroscopy shows substantial surface enhancement visible in the uppermost spectrum, where many additional peaks can be observed (Figure 1b).

ANZOT augments the antiviral activity of BX795 both in vitro and in vivo

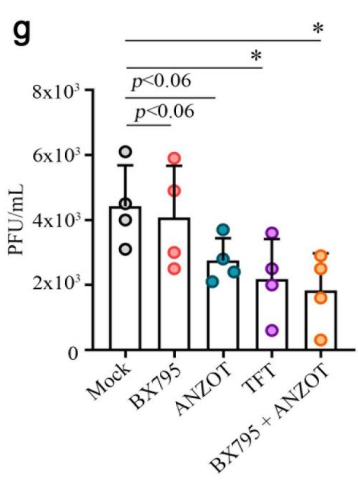
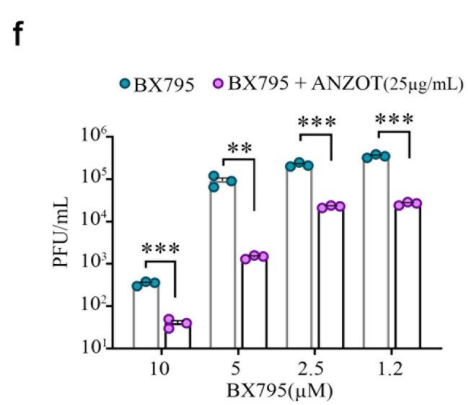
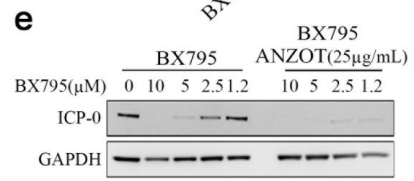
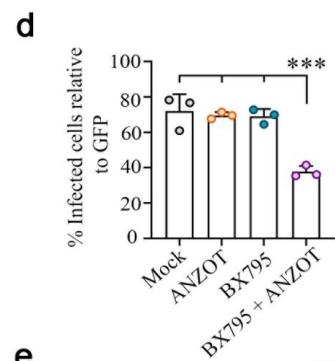
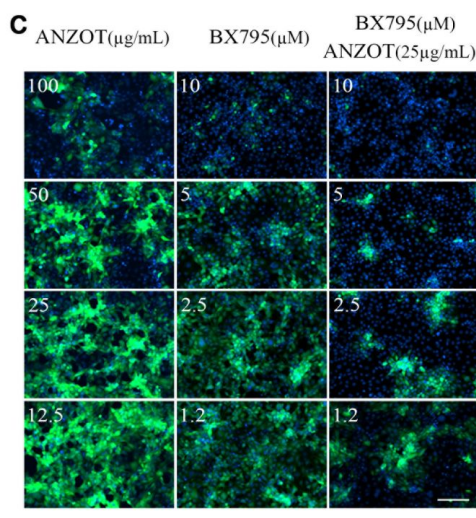
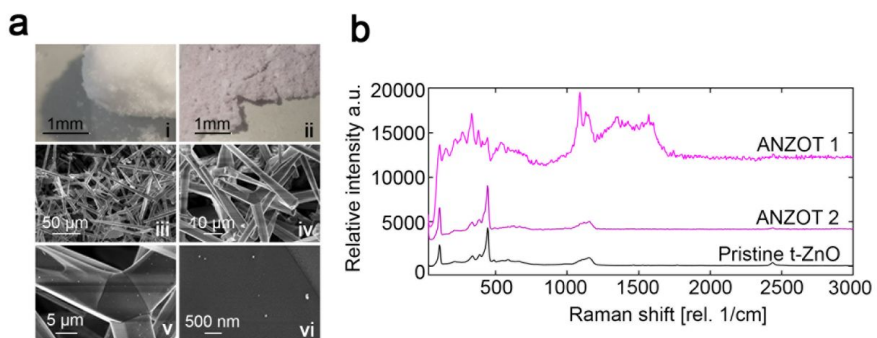
Using this new compound, we aimed our initial studies at evaluating ANZOT as a novel adjuvant for enhancing efficacy of antiviral drugs such as ACV or BX795 (Figure 1a). We have recently reported promising therapeutic and prophylactic antiviral activity of BX795 against HSV.^{21,22} Although the optimal antiviral concentration of BX795 (10 μ M) is lower than the marketed drugs, including the commonly administered nucleoside analogs acyclovir (ACV) (50 μ M) and triflurothymidine (TFT) (50 μ M), the selectivity index (SI) of BX795 remains relatively low. Therefore, in order to increase its preclinical safety, we investigated ways to lower the dose requirement of BX795 while exerting the same or enhanced antiviral efficacy.

Initially, the dose-dependent therapeutic efficacy of BX795 was assessed in vitro. Human corneal epithelial (HCE) cells were infected with 0.1 MOI (multiplicity of infection) of HSV-1 KOS strain tagged with a green fluorescent protein (GFP) (K26-GFP). The infected cells were then therapeutically treated with varying concentrations (1.2-10 μ M) at 2 hours post-infection (hpi). Fluorescence imaging and quantification of infected HCE cells show dose-dependent inhibition of HSV-1, demonstrating an optimal inhibitory concentration of BX795 at 10 μ M (Figure 1 c, d). This correlated with dose-dependent inhibition of immediate early viral protein (infected cell protein 0 (ICP0)) expression, as shown by western blot analysis. Viral plaque assay analysis was performed to quantify secreted virions. It showed inhibition of mature virus particles in response

1
2
3 to BX795 treatment (Fig 1e, f). The IC_{50} (inhibitory concentration at 50%) from the dose-response
4 curve for BX795 was estimated to be 3.55 μ M. Similarly, the independent antiviral efficacy of
5 ANZOT was assessed at varying concentrations (12.5-100 μ g/mL). MTT (-4,5-dimethylthiazol-2-
6 yl-2,5-diphenyltetrazolium bromide) assay was performed to confirm that the concentrations of
7 BX795 used did not display cytotoxicity (Supplementary Figure 1a). We also evaluated the
8 independent antiviral activity of ANZOT and showed, through MTT assay, that the concentrations
9 used did not display cytotoxicity (Supplementary Figure 1b). The cytotoxicity in conventional
10 ZnO nanostructures is mainly due to two reasons, penetration of nanoparticles themselves inside
11 cells (via membrane) and release of Zn^{2+} ions.^{23,24} The present ANZOT structures are large enough
12 to rule out the penetration mechanism. In addition, their surface to volume ratio is relatively very
13 low as compared to conventional nanoparticles and thus are least cytotoxic.

14
15
16
17 After verifying the individual and independent therapeutic activity of BX795 and ANZOT, we
18 combined different concentrations of BX795 (1.25-10 μ M) with a suboptimal ($\sim IC_{30}$)
19 concentration of ANZOT (25 μ g/mL) to probe for antiviral synergy. Through fluorescence
20 imaging, western blot analysis, and plaque assay analysis, we show that the combined treatment
21 of ANZOT with BX795 shows enhanced antiviral activity of low concentrations of BX795 (fig
22 1c-f). The combined treatment decreased the IC_{50} of BX795 to 0.9 μ M, which is a 3.9-fold decrease
23 in IC_{50} , suggesting the high synergistic antiviral potential of BX795 and ANZOT complexes
24 (Figure 1f). Moreover, the combination of BX795 with either ZOTEN or gold nanoparticles (GNP)
25 alone did not result in antiviral synergy, indicating that the observed antiviral synergy is a unique
26 property of ANZOT (Supplementary Figure 2).

27
28
29
30 The synergy between ANZOT and BX795 was further verified in a murine model of ocular
31 infection with HSV-1 Mckrae strain (1×10^5 MOI). The infected group of mice were divided into
32 five groups (n=4) and treated daily with i) Mock (DMSO), ii) BX795 (5 μ M), iii) ANZOT (100
33 μ g/mL), iv) TFT (50 μ M), and v) combination of BX795 (5 μ M) and ANZOT (100 μ g/mL) for
34 seven consecutive days post-infection (dpi). Plaque assay was performed with corneal swabs taken
35 at 2 dpi to assess the viral shedding of each treatment group. The topical combinatorial treatment
36 of BX795 and ANZOT resulted in a significantly lower amount of viral shedding compared to the
37 mock-treated group (Fig 1g). TFT, a nucleoside analog clinically used topically to treat ocular
38 HSV-1 infection, served as a positive control for this study and showed significantly decreased
39 viral shedding compared to mock-treated group (Figure 1g). The antiviral efficacy of the
40 combinatorial use of BX795 and ANZOT was comparable to that of TFT. Collectively, using in
41 vitro and in vivo models of HSV-1 infection, we show that ANZOT lowers the dose requirement
42 of BX795, thereby augmenting its antiviral efficacy and safety.



1
2
3
4
5
6
7
8
9
10
11
12
13
14
15
16
17
18
19
20
21
22
23
24
25
26
27
28
29
30
31
32
33
34
35
36
37
38
39
40
41
42
43
44
45
46
47
48
49
50
51
52
53
54
55
56
57
58
59
60

1
2
3 **Figure 1.** ANZOT enhances the antiviral efficacy of BX795 in vitro and in vivo. (a) (i) Photographic image of pristine
4 ZOTEN crystals fabricated by flame transport synthesis. The white color stems from scattering between individual
5 particles. (ii) Photographic image of ZOTEN coated with Au nanoparticles. (iii-vi) Zoom series of scanning electron
6 microscope (SEM) micrographs of the ANZOT particles. Bright gold nanoparticle clusters can be observed on the
7 ZOTEN surface in (vi). The individual, long legged tetrapods are visible in (iii) and (iv). (b) Raman spectra of two
8 samples of ANZOT particles and one spectrum of pristine ZOTEN can be seen. Strong surface enhancement is visible
9 in the upper most spectrum, where many additional peaks can be observed. (c) HCE cells infected with HSV-1 K26-
10 GFP at 0.1 MOI and therapeutically treated with different concentrations of either i) ANZOT ii) BX795 or iii) ANZOT
11 (25 µg/mL) with BX795. At 24 hpi the extent of HSV-1 infection was analyzed by fluorescence imaging which shows
12 expression of GFP (indicator of early viral gene transcription) using Biotek Lionheart FX automated microscope under
13 10X objective (scale bar, 200 µm). (d) Percent infection from (c) at indicated treatment groups (BX795 (1.25 µM),
14 ANZOT (12.5 µg/mL)) and combination of BX795 (1.25 µM) and ANZOT (12.5 µg/mL) was quantified using Biotek
15 image analysis software. (e) Lysates were collected at 24 hpi and subjected to western blot analysis. Representative
16 micrograph showing immunoblots for HSV-1 protein ICP0 and GAPDH. (f) Graph showing mature virus particle
17 formation in indicated treatment groups represented as PFU/mL. (g) Secreted virus titers of eye wash samples collected
18 at 2 dpi following ocular infection of mice with HSV-1 McKrae strain at 10⁵ MOI which were therapeutically treated
19 with i) Mock (DMSO) ii) BX795 (5 µM) iii) ANZOT (100 µg/mL) iv) TFT (50 µM) and v) combination of BX795
20 (5 µM) and ANZOT (100 µg/mL). All the experiments were performed in triplicates and the significance between the
21 treatment and control groups was statistically analyzed using unpaired student t test.

22 **ANZOT decreases the minimum inhibitory concentration of acyclovir**

23 Poor bioavailability (15-20%) of ACV requires high concentration (50 µg/mL) and frequent
24 dosing, which is 4-5 times daily. Prolonged topical administration of TFT or oral administration
25 of ACV has been reported to cause toxicity issues.²⁵ Furthermore, ACV's long-term systemic
26 treatment has resulted in ACV-resistant HSV strains.²⁶ For that reason, lowering the therapeutic
27 dose of a commonly used antiviral drug by combining it with ANZOT may provide enhanced relief
28 while reducing the risk of side effects. After observing significant enhancement of BX795 potency
29 through the combined use with ANZOT, we sought to determine if ANZOT could also enhance
30 ACV's antiviral efficacy. Initially, HCE cells were infected with HSV-1 KOS strain with 0.1 MOI
31 and therapeutically treated with varying doses of ACV (0.04-0.35 µg/mL) in combination with
32 either DMSO or ANZOT (25 µg/mL). Fluorescence images taken 24 hpi show robust inhibition
33 of HSV-1 infection with the combinatorial use of ACV and ANZOT, compared to ACV only
34 treatment (Figure 2a, b). Western blot analysis also showed significant inhibition of virus protein
35 production of ICP0 even with the use of 1.2 µg/mL of ACV, compared to ACV only treatment,
36 which required 5 µg/mL concentration for full inhibition of ICP0 protein production (Figure 2c).
37 Plaque assay analysis also demonstrated that mature virus particle formation in the combination
38 treatment group was significantly suppressed, even at the lowest concentration tested (1.7 µg/mL)
39 (Figure 2d). Cells treated with a combination of ACV and ANZOT showed an IC₅₀ of 0.01 µg/mL,
40 which is 7-fold less than the IC₅₀ of ACV only treatment. This is a significant reduction with high
41 clinical application considering the known adverse effects reported with the current dose
42 requirement prescribed to patients with herpes.
43
44
45
46
47
48
49
50
51
52
53
54
55
56
57
58
59
60

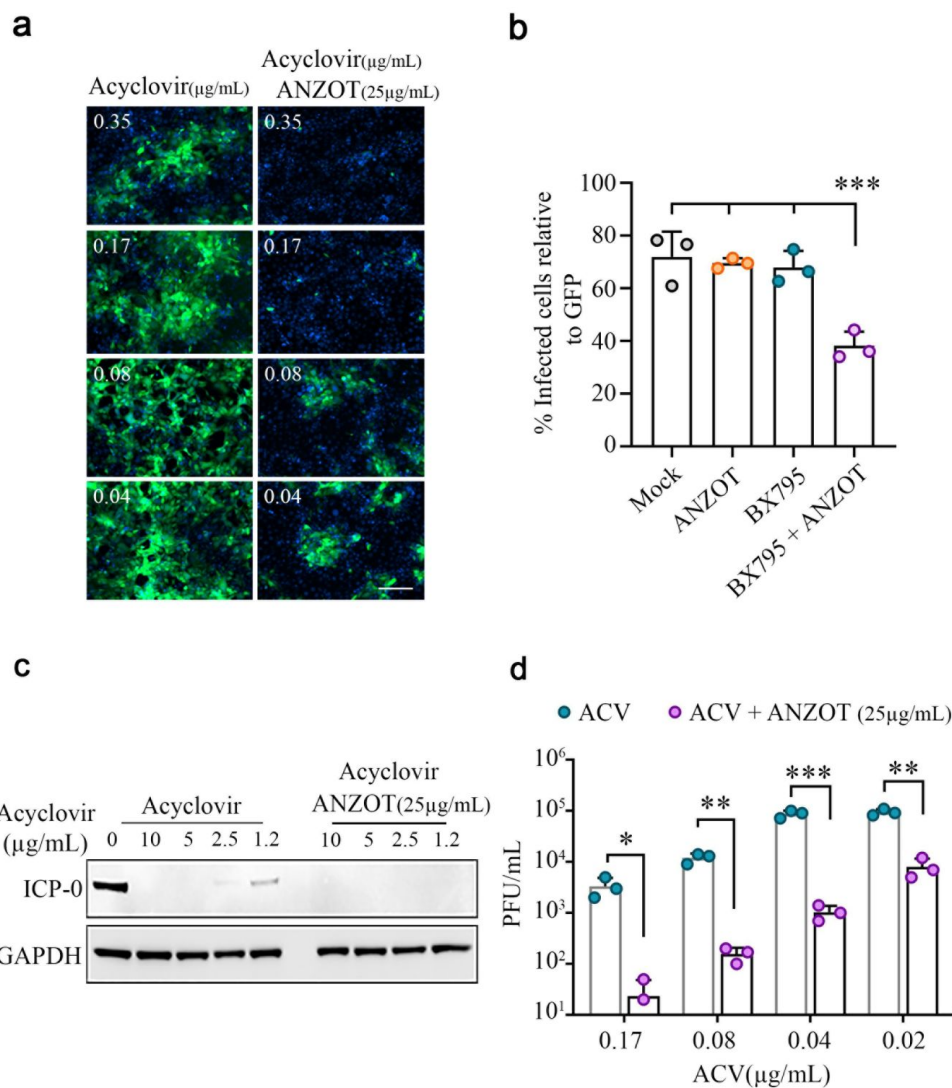


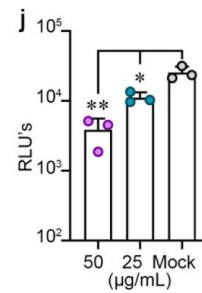
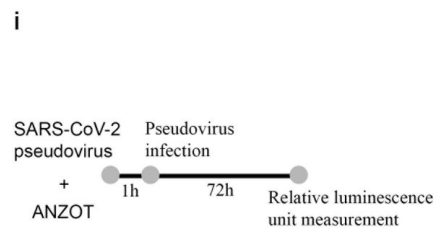
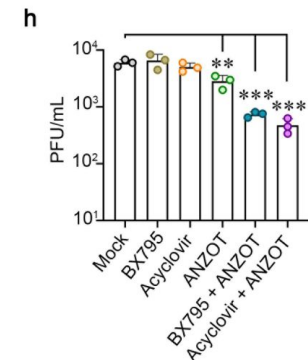
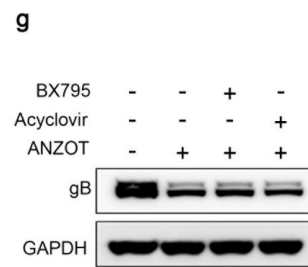
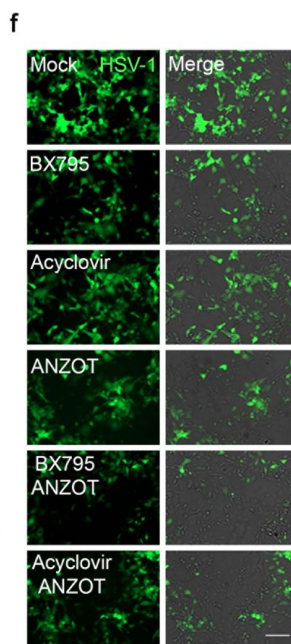
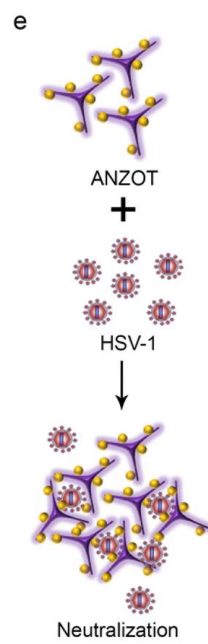
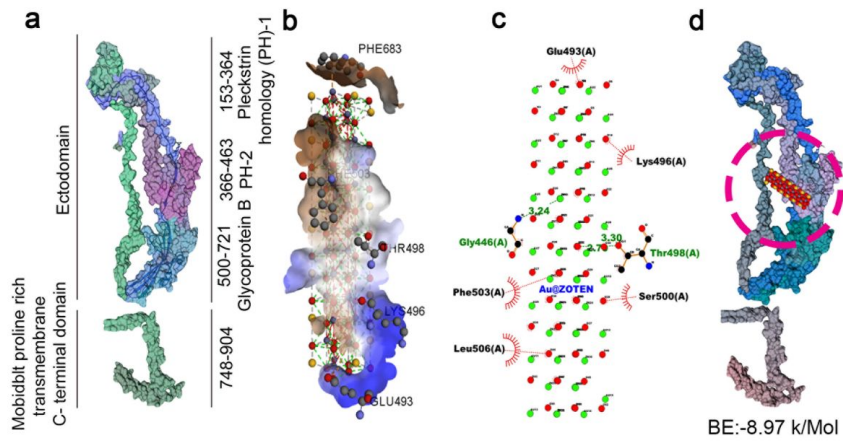
Figure 2. ANZOT decreases the minimum inhibitory concentration of acyclovir by 7-fold. (a) HCE cells infected with HSV-1 K26-GFP at 0.1 MOI and therapeutically treated with suboptimal concentration of ACV (0.35 to 0.04 μg/mL) with or without ANZOT (25 μg/mL). Fluorescence images were captured using Biotek Lionheart FX automated microscope under 10X objective. (Scale bar, 200 μm). (b) Graph showing percent of HSV-1 infected HCE cells in treatment groups (ACV (0.17 μg/mL) and ANZOT (25 μg/mL)) was quantified using Biotek image analysis software. (c) HCE cells were infected at 0.1 MOI and therapeutically treated with suboptimal concentrations of either ACV or a combination of ACV and ANZOT. Lysates were collected at 24 hpi and subjected to western blot analysis. Representative micrograph of immunoblots showing expression of HSV-1 ICP0 and GAPDH. (d) Similar to previous

1
2
3 conditions, cell lysates were collected and subjected to plaque assay, indicating mature virus particle formation in
4 different treatment groups.
5

6 **ANZOT neutralizes HSV-1 glycoprotein B and SARS-CoV-2 spike protein**

7 While the antiviral cytokine response is one of the most critical intrinsic defense mechanisms, the
8 anti-HSV response attributed to the test combinations used in the study is independent of cytokine
9 induction (Supplementary figure 3). Instead, we show that the therapeutic efficacy of this
10 combined treatment is mediated through a multimodal mechanism that includes the virus
11 neutralization capabilities exerted by ANZOT and cellular host kinase inhibition by BX795. In-
12 silico molecular docking studies support our previous finding that ZOTEN neutralizes HSV-1 and
13 also demonstrate that ANZOT is capable of binding HSV1 gB with the binding energy of -
14 8.97k/mol (Figure 3a-d).^{15,23} The molecular structure of HSV-1 glycoprotein B (gB) is shown, as
15 well as the predicted hydrophobic interactions of the ectodomain with ANZOT. To verify the
16 neutralization capabilities of ANZOT in vitro, the following combinations: i) DMSO ii) ANZOT
17 iii) BX795 and ANZOT and iv) ACV and ANZOT were incubated with 0.1 MOI of HSV- 1 KOS
18 strain for 1 hour. The mixtures were then overlaid on a monolayer of HCE cells. The media was
19 replaced at 2 hpi and incubated for 24 hpi (Fig 3e). The following test groups: i) ANZOT, ii)
20 BX795 and ANZOT, and iii) ACV and ANZOT show suppression of HSV-1 replication through
21 inhibition of gB expression (Figure 3f, g). Similarly, the production of mature virus particles was
22 significantly reduced in these treatment groups compared to DMSO treatment (Figure 3h). The
23 data suggests that the presence of ANZOT is responsible for HSV-1 neutralization and restriction
24 of viral entry into the cells. The results indicate that, compared to ANZOT treatment alone, the
25 combination of ANZOT with BX795 either ACV is more effective in this mode of infection.
26
27
28
29

30 To test a potentially broad-spectrum application of ANZOT, we evaluated its ability to neutralize
31 the spike protein of SARS-CoV-2 and block entry. We incubated ANZOT with a SARS-CoV-2
32 pseudo typed virus for one hour at room temperature followed by a 72-hour incubation with Vero
33 cells (Fig 3i). We observed significant entry inhibition, assessed through luminescence production,
34 with both concentrations of ANZOT used (Figure 3j). Our observations may be useful for
35 increasing the efficacy of SARS-CoV-2 treatment regimen and for developing topical, e.g.
36 intranasal or ocular surface preventative therapies against the virus.
37
38
39
40
41
42
43
44
45
46
47
48
49
50
51
52
53
54
55
56
57
58
59
60



1
2
3 **Figure 3.** ANZOT neutralizes HSV-1 and SARS-Cov-2 to restrict viral entry.

4 (a-d) The results inferred from molecular docking analyses depicts the probable interaction mechanism of ZOTEN
5 and ANZOT with the ecto domain of HSV-1 glycoprotein B (gB) receptor. The binding energy was found to be -8.97
6 kcal/mol. (e) Schematic for the proposed antiviral mechanism of ANZOT showing its HSV-1 neutralizing ability. (f)
7 0.1 MOI of HSV-1 was incubated with indicated treatment groups for 1 hr at 37 °C and the resulting mixture was
8 overlaid on a monolayer of HCE cells. The media was replaced at 2 hpi and the extent of HSV-1 replication was
9 analyzed at 24 hpi. Representative monographs of fluorescence imaging of different treatment groups where GFP
10 indicates HSV-1 infected cells (early gene transcription). (g) Lysates collected were subjected to western blot analysis.
11 Representative immunoblots show expression of late HSV-1 protein (HSV-1 gB) and GAPDH. (h) Lysates were also
12 collected for plaque assay to determine mature virus particle formation in different treatment groups. Significance of
13 treatment groups to mock was determined by unpaired student t test (n=3). (i) Schematic for the neutralization assay
14 using SARS-CoV-2 pseudovirus and the (j) relative luminescence intensity measured to determine entry of the
15 pseudovirus following neutralization assay with either mock (DMSO), 25 µg/mL or 50 µg/mL of ANZOT.

16 **BX795 inhibits protein kinase C, a crucial player during HSV-1 infection**

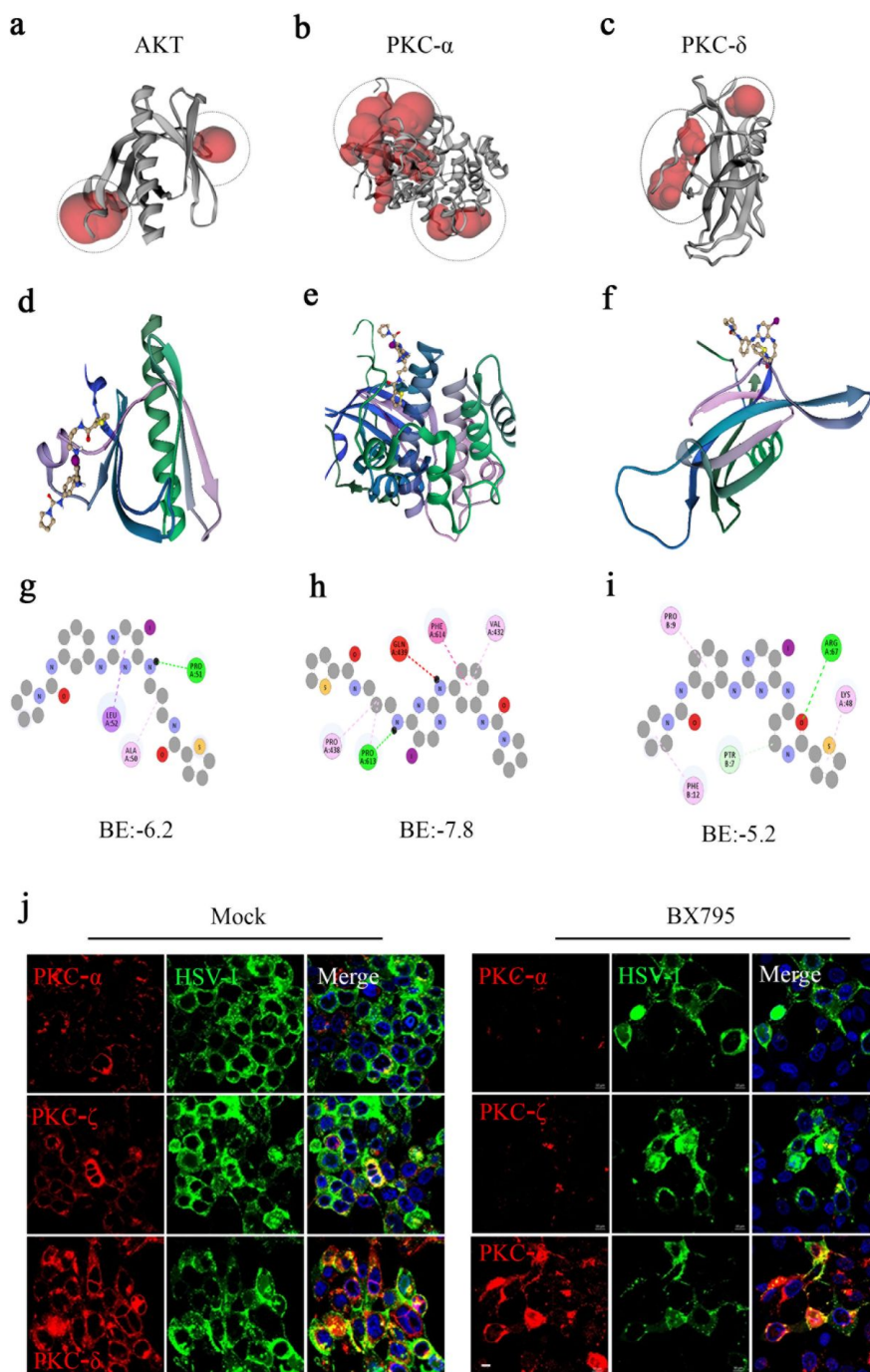
17
18 The first line of defense against HSV-1 infection is provided by innate, humoral, and cellular
19 responses. At first, we examined whether combined BX795 and ANZOT treatment affected
20 cytokine production during infection, resulting in the inhibition of viral replication. To determine
21 whether BX795 and ANZOT differentially affected cytokine production, we performed
22 quantitative real-time polymerase chain reaction (qRT-PCR) to evaluate the expression of IFN- α ,
23 IFN- β , and TNF- α . Transcript levels of IFN- α , IFN- β , and TNF- α were significantly lower in the
24 treatment groups than DMSO treatment, showing that their observed antiviral activity is
25 independent of cytokine production (Supplementary Figure 3).
26

27
28 We have previously shown that BX795 inhibits the phosphorylation and activation of protein
29 kinase B (AKT), leading to the blockage of viral protein synthesis.²⁰⁻²² During HSV-1 infection,
30 protein kinase C (PKC) isoforms (α and ζ) also play a pro-viral role by modifying the nuclear
31 lamina to enhance nucleocapsids' budding through phosphorylation of lamin B.²⁷⁻²⁹ PKC is a
32 family of serine/threonine kinases whose function is influenced by their phosphorylation, which
33 determines intracellular localization of the enzyme.³⁰ With inherent phosphorylation potential,
34 PKC enzymes play a crucial role in several signaling cascades. For the viral capsid to egress from
35 the nucleus, PKC is activated and recruited to the nuclear membrane, increasing the
36 phosphorylation of lamin B, which ultimately destabilizes nuclear lamina and promotes budding
37 of nucleocapsids at the inner nuclear membrane.²⁸⁻³⁰ We hypothesized that BX795 might regulate
38 PKC isoform's expression and perinuclear localization to generate a nonpermissive host
39 environment for viral replication. Structural analysis of AKT and PKC isoforms α and δ reveals
40 that BX795 interacts with the catalytically active sites (shown in red), respectively (Figure 4a-c).
41 The predicted binding of BX795 with kinases is also demonstrated and expected to inhibit their
42 activity (Figure 4d-f). Furthermore, binding energies for these interactions are shown (Figure 4g-
43 i).
44
45
46
47

48 *In vitro* confirmation was initially carried out with confocal microscopy to assess the effect of
49 BX795 on the expression and localization of PKC α , ζ , and δ (Figure 4j). During infection, PKC
50 isoforms are recruited to the nuclear envelope by viral proteins required for lamina disruption.
51 Using confocal microscopy, we confirm perinuclear localization of PKC α , ζ , and δ following
52 HSV-1 infection (Figure 4j). When therapeutically treated with BX795, infected cells resulted in
53 significant downregulation of both PKC α and ζ expression and restriction of perinuclear
54 localization (Figure 4j). Only PKC δ was observed to be similar in both treatment groups. Similar
55 results were obtained with therapeutic treatment of BX795 and ANZOT, suggesting that even in
56
57
58
59
60

1
2
3 combination with ANZOT, BX975 exerts its antiviral effect through the same mechanism
4 (Supplementary Figure 4a). In conclusion, Bx795 suppressed the expression and limited the
5 perinuclear localization of PKC- α and ζ in HSV-1 infected cells.
6
7
8
9
10
11
12
13
14
15
16
17
18
19
20
21
22
23
24
25
26
27
28
29
30
31
32
33
34
35
36
37
38
39
40
41
42
43
44
45
46
47
48
49
50
51
52
53
54
55
56
57
58
59
60

1
2
3
4
5
6
7
8
9
10
11
12
13
14
15
16
17
18
19
20
21
22
23
24
25
26
27
28
29
30
31
32
33
34
35
36
37
38
39
40
41
42
43
44
45
46
47
48
49
50
51
52
53
54
55
56
57
58
59
60



1
2
3 **Figure 4.** BX795 binds to the catalytically active domains of PKB and PKC isoforms

4 (a) Crystal protein structure of the Pleckstrin Homology Domain of Protein Kinase B/AKT, (b) PKC- α and (c) PKC- δ . Catalytically active domains where BX795 is predicted to bind are highlighted in red. Molecular docking studies show predicted binding of (d) AKT, (e) PKC- α , (f) PKC- δ with BX795. Binding energies of the interaction of (g) AKT, (h) PKC- α , (i) PKC- δ with BX795 (in kcal/mol). (j) Representative monographs of confocal microscopy images taken of HCE cells infected with HSV-1 17 strain (GFP labeled), treated with mock or BX795 and stained with PKC- α , PKC- ζ and PKC- δ (Red-Alexa flour 647). DAPI used for nuclear staining. Scale bar- 10 μ m.

11 To further probe this novel mode of antiviral action by BX795, western blot analysis was carried
12 out where we observed significant suppression of PKC- α and PKC- ζ protein expression when
13 treated with BX795, in the presence and absence of infection (Figure 5a). However, the expression
14 of PKC- δ remains similar under both treatment conditions (Figure 5a-d). For further confirmation,
15 we used Bisindolylmaleimide I (BIM I), a potent inhibitor of PKC- α . After demonstrating in-silico
16 binding affinity (figure 5e-f) the therapeutic treatment of BIM I (10 μ M) showed significant
17 antiviral activity against the HSV-1 17 strain, as determined by fluorescence microscopy
18 (Supplementary Figure 4b). This finding was also supported by the observed decrease in HSV-1
19 glycoprotein B (gB) expression and decreased mature virus particle formation upon treatment with
20 BIM I (Figure 5g-h). Our results confirm that BX795, even when in combination with ANZOT,
21 limits the activity of protein kinase C isoforms α and ζ and may thereby inhibit the nuclear release
22 of virions leading to restriction of viral replication (Figure i).
23
24
25
26
27
28
29
30
31
32
33
34
35
36
37
38
39
40
41
42
43
44
45
46
47
48
49
50
51
52
53
54
55
56
57
58
59
60

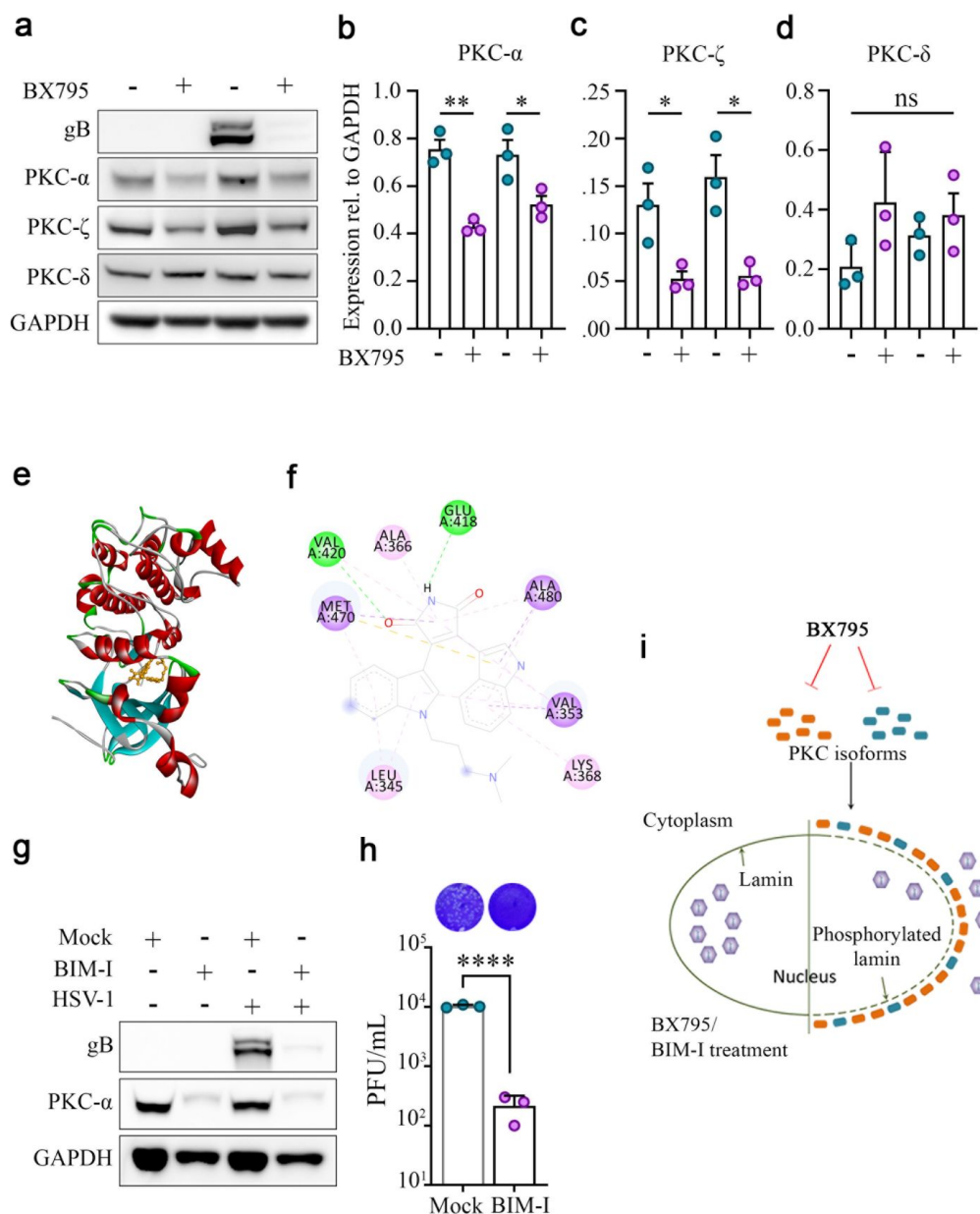


Figure 5. BX795 suppresses the expression and activation of PKC- α and PKC- ζ
 (a) HCE cells were infected with mock or 0.1 MOI of HSV-1 KOS and treated with either DMSO or BX795 (10 μ M) at 2hpi. At 24 hpi cells were processed for protein expression analysis. Representative immunoblots show the expression of HSV-1 gB, PKC- α , PKC- ζ , PKC- δ , GAPDH. Graph showing quantification of (b) PKC- α , (c) PKC- ζ , and (d) PKC- δ was performed using ImageJ software. (e) Depiction of BIM-I binding to PKC- α and (f) binding energy

1
2
3 of the interaction. (g) HCE cells were infected with HSV-1 KOS at 0.1 MOI and treated with mock or BIM I at 2hpi.
4 Representative immunoblots show expression of HSV-1 gB, PKC- α and GAPDH. (h) A graph showing mature virus
5 particle production in mock or BIM-I treated HCE cells. Plaque image shows PFU observed at 10^3 dilutions. (i)
6 Schematic representing proposed antiviral mechanism of BX795. All the experiments were carried out in triplicates
7 and statistical significance between the groups was determined using the unpaired student t-test.
8

9 **Conclusion**

10 Here, we provide proof-of-concept for a novel, nanoparticle-based approach to enhance efficacy
11 of existing as well as highly promising preclinical antiviral drugs. Our nanostructured
12 microparticles demonstrate standalone antiviral effect by neutralizing virus particles and an even
13 stronger combinatorial antiviral efficacy in conjunction with small molecule inhibitors. The latter
14 results in a robust and enhanced control of viral replication through multivalent interactions. We
15 investigated the administration of ANZOT with either ACV or BX795 to combat HSV-1 infection.
16 The findings in this study demonstrate that ANZOT enhances the activity of small molecule
17 inhibitors while also exerting antiviral effects through its ability to neutralize virus particles.
18 Molecular docking studies confirmed the binding of an HSV glycoprotein and ANZOT. Further
19 *in vitro* experiments verified the ability of ANZOT to neutralize HSV-1 and restrict its entry. The
20 neutralization occurs as the charge density of ANZOT matches with that of HS, a cell attachment
21 receptor that establishes electrostatic interactions with many viruses. Since multiple viruses rely
22 on HS for initial attachment and entry, we also examined the effect of ANZOT on SARS-CoV-2
23 pseudo typed virus and found that ANZOT was also able to restrict its entry. The epitome of our
24 findings supports the use of ANZOT as an adjuvant to reduce the minimum essential drug
25 concentration and increase their selectivity index without prompting cytotoxicity while restricting
26 viral replication in cell culture and a murine model of ocular infection.
27
28
29
30

31 **Materials and Methods**

32 **Cell lines and viruses**

33 Human corneal epithelial (HCE) cell line (RCB1834 HCE-T) was procured from Kozaburo
34 Hayashi (National Eye Institute, Bethesda, MD) and used for HSV-1 infection. HCE cells were
35 cultured in Dulbecco modified Eagle medium (DMEM; Gibco) supplemented with 10% fetal
36 bovine serum (FBS) (Life Technologies) and 1% penicillin/streptomycin (P/S) (Life
37 Technologies). HSV-1 KOS strain was procured from Dr. Patricia G. Spear (Northwestern
38 University, Chicago, IL), and HSV-1 17 strain was supplied by Dr. Richard Thompson (University
39 of Cincinnati, Cincinnati, OH). All virus stocks were made and tittered in Vero cells and stored at
40 -80°C .
41
42
43
44

45 **Chemicals**

46 ZnO tetrapods (ZOTEN) were synthesized in the previously developed flame transport synthesis.
47 ³¹ In brief, a mixture of commercially obtained spherical zinc microparticles (sized $<10\ \mu\text{m}$),
48 polyvinyl butyral (PVB) powder, and ethanol was burned together at 900°C in air. Burning of
49 polymer PVB results in consuming oxygen and suppressing the reaction through which Zn vapor
50 can form in high concentrations.^{23,31,32} Once the PVB is completely burned, oxygen is again
51 introduced through diffusion and the ZOTEN start growing from a surplus of Zn in the atmosphere
52 but the exact mechanism is yet to be disclosed.
53
54
55
56
57
58
59
60

1
2
3 Further, the decomposition of PVB continues to form CO₂ and results in an actual yield of 99.9%
4 of ZOTEN. The coating of ZOTEN was done by pipetting standard gold nanoparticle dispersion
5 onto ZOTEN powder in a filter cup.¹⁹ Afterwards the ZOTEN were rinsed with water to remove
6 glucose residues and dried for 24 h in 80 °C.
7

8 9 **Material characterization**

10 The uniformity of the ZOTEN and the ANZOT materials has been investigated using an Ultra 55
11 Zeiss FEG scanning electron microscope (SEM) at an acceleration voltage of 5 kV. Micro-Raman
12 was utilized to investigate the chemical composition of ZOTEN and ANZOT at room temperature
13 with a WITec system in a backscattering configuration. The Nd:YAG laser used had a wavelength
14 of $\lambda_{\text{ex}} = 532$ nm and for each spectrum 10 accumulations at an integration time of 0.5 s were taken.
15

16 17 **Antibodies**

18 Antibodies for protein detection and immunofluorescence of PKC- α (SC#8393), PKC- ζ
19 (SC#17781) and HSV-1 ICP0 (sc-53070) were purchased from Santa Cruz Biotechnology, (Dallas,
20 TX). GAPDH (10494-1-AP) was purchased from Proteintech Group, Inc., (Rosemont, IL). PKC-
21 δ (#9616) was purchased Cell Signaling Technology (Danvers, MA). whereas HSV-1 gB (ab6506)
22 antibody was purchased from Abcam (Cambridge, United Kingdom).
23

24 25 **Quantitative real-time polymerase chain reaction (qRT-PCR)**

26 RNA extraction was performed using TRIzol (Life Technologies). Isolated RNA was used to
27 prepare cDNA using High Capacity cDNA Reverse Transcription kit (Applied Biosystems Foster
28 City, CA). The resultant cDNA was used for Real-time quantitative polymerase chain reaction
29 (qPCR) performed on QuantStudio 7 Flex system (Life Technologies) using Fast SYBR Green
30 Master Mix (Life Technologies).
31

32 The primers used in this study are as follows:

33 Human GAPDH qPCR forward: 5'- TCCACTGGCGTCTTCACC-3', Human GAPDH
34 qPCR reverse: 5'- GGCAGAGATGATGACCCTTTT-3', Human TNF- α Forward: 5'-
35 AGCCCATGTTGTAGCAAACCC-3', Human TNF- α Reverse: 5'-GCA
36 CCTGGGAGTAGATGAGGT-3', Human IFN- β Forward: 5'- TCCACTACAGCTCTTTCCAT-
37 3', Human IFN- β Reverse: 5'-GTCAAAGTTCATCTGTCCTT-3', HSV-1 gB Forward: 5'-
38 GCCTTTTGTGTGTGGG-3', HSV-1 gB Reverse: 5'AGGAAAGAGGAAACAGGCC-3'
39
40

41 42 **Immunoblotting**

43 Hanks Cell Dissociation buffer was used to dissociate cells from culture plate and
44 radioimmunoprecipitation assay (RIPA) buffer (Sigma Aldrich, St Louis, MO) was used for
45 protein isolation. To digest the proteins samples, they were mixed with LDS loading buffer and β -
46 mercaptoethanol (5%) (Bio-Rad, Hercules, CA) and denatured at 95°C for 9 min followed by an
47 electrophoretic run on InvitrogenTMMini Gel Tank (Thermo fisher) using pre-cast gels (4-12%).
48 Nitrocellulose membrane (Thermo Fisher) was used to transfer proteins with an iBlot2 (Invitrogen)
49 assembly. After successful transfer of proteins on nitrocellulose membrane, non-specific sites on
50 the membrane were blocked using 5% milk/TBS-T for 1 h and incubated overnight with respective
51 primary antibody at 4°C. Unbound antibodies on the membrane were removed by washing with
52 TBS-T and incubated with respective horseradish peroxidase (HRP) conjugated secondary
53 antibody for 1h at room temperature. The membranes were washed before developing the blot with
54 SuperSignal West PICO plus chemiluminescent substrate (34577) and or SuperSignal West Femto
55
56
57
58
59
60

1
2
3 maximum sensitivity substrate. The protein bands were further visualized with Image-Quant LAS
4 4000 biomolecular imager (GE Healthcare Life Sciences, Pittsburgh, PA).
5
6

7 **Virus titer (plaque formation) assay**

8 HSV-1 infected HCE cells were sonicated at 30% amplification for 15 s to release intracellular
9 infectious virus particles. The resultant was used to make respective dilution in Opti-MEM
10 medium and was overlaid on a monolayer of Vero cells. After 2h Opti-MEM was replaced with a
11 complete medium (DMEM with 10% FBS and 1% P/S) containing 0.5% w/v methylcellulose
12 (Thermo Fisher). The culture plates for plaque assay were incubated at 37°C, with 5% CO₂, for 72
13 h. After incubation, the cells were fixed by adding 100% methanol and kept at room temperature
14 for 20 minutes. Finally, all media was removed, and plaques were visualized by crystal violet
15 solution and counted as plaque-forming units/mL.
16
17

18 **Cell viability (MTT) assay**

19 MTT assay was performed on HCE cells to measure the percent viability of cells at different
20 concentrations of BX795 and ANZOT. A monolayer of HCE cells was incubated with different
21 concentrations of BX795 and ANZOT starting at 80µM and 200 µg/mL, respectively. DMSO (at
22 vehicle concentration) served as a control for these experiments. After 24 h of treatment, 5µL of
23 MTT reagent (5mg/mL) was added to each reaction well and incubated for 3 hrs at 37°C in dark.
24 Further, the formazan crystals were dissolved in acidified isopropanol by shaking the plate at
25 25rpm for 15 min in the dark. Appropriate volume of supernatant was transferred to a new 96-well
26 plate to measure its optical density at 550 nm and 630 nm. The percent viability was calculated
27 using the following formula.
28
29

$$30 \quad \text{Percent viability} = \frac{\text{Mean OD of treatment}}{\text{Mean OD of control}} \times 100$$

31
32

33 **SARS-CoV-2 pseudotyped virus particles formation**

34 Pseudotyped virus particles (SARS-COV2) were prepared as per Millet et al., 2019. Briefly,
35 HEK293T cells were cultured in 6 well plates overnight to reach 40-50% confluency. The cells
36 were further transfected with gag-pol plasmid (0.3 µg), Luciferase encoding plasmid (0.4 µg) and
37 SARS-CoV-2 spike protein encoding plasmid (0.3µg) in Opti-MEM. The culture plates were
38 incubated 37 °C with 5% CO₂ in a cell culture incubator for 6h and added with DMEM containing
39 10% FBS and 1% P/S and further incubated for 72 h. Pseudotyped virus containing cell
40 supernatant were collected and filtered through a 0.45 µm filter to make the aliquots. Aliquots
41 were stored at -80 °C until use.
42
43

44 **Entry assay**

45 To check the virus neutralization potential of ANZOT on SARS-CoV-2 pseudotyped particle, the
46 at 25 and 50µg/mL concentrations were mixed with SARS-CoV-2 pseudotyped particle and placed
47 on shaker for 1 h at room temperature. After incubation the culture of Vero cells was infected with
48 mock of ANZOT treated pseudotyped virus particles for two hours and the media was replaced by
49 DMEM containing 10% FBS and 1% P/S and incubated for 72 h. After incubation, the pseudo
50 typed virus entry was evaluated by measuring chemiluminescence by luminometer.
51
52

53 **Computational methods**

54
55
56
57
58
59
60

1
2
3 Protein crystal structures of the Pleckstrin Homology Domain of Protein Kinase B/Akt (PDB ID
4 1UNQ), PKC α (PDB ID: 3IW4), C2 Domain of PKC δ (PDB ID: 1YRK), and glycoprotein B from
5 HSV-1 (PDB ID: 5V2S) were retrieved from Protein Data Bank (PDB) and were subjected to
6 initial target receptor preparation for molecular docking analyses. The ligand small molecules
7 Acyclovir and BX795 were retrieved from PubChem database and were refined using Marvin
8 sketch. The molecules ZOTEN and ANZOT were constructed using Atomic Simulation
9 Environment (ASE) and structural minimizations were performed based on first principles density
10 functional theory (DFT) using the Vienna Ab initio Simulation Package (VASP) software. The
11 projector-augmented-wave (PAW) method is used to describe the interaction between valence
12 electrons and ions. The exchange-correlation interactions used in our calculations are based on the
13 generalized gradient approximation (GGA) with the Perdew–Burke–Ernzerhof (PBE). The
14 Brillouin zone has been sampled with a $7 \times 7 \times 7$ k-mesh for a unit cell and $3 \times 3 \times 1$ for supercells.
15 The structures are optimized until the Hellman–Feynman forces are smaller than 0.001 eV/\AA .
16 Furthermore, the computational molecular docking was performed to investigate the probable
17 interaction of small molecules, ZOTEN and ANZOT with target receptors for elucidating the
18 probable binding mechanisms. To understand the molecular level, experimental analyses were
19 used to impart the atomic reaction to understand the interaction mechanism. To determine the
20 binding efficacy of the ligands and the target receptors, in silico molecular docking approach was
21 efficiently used to find the preferred binding orientations of ligand that confers minimum binding
22 energy. Molecular docking analysis was performed using both Autodock Vina and Autodock tool
23 as the metal ions e.g. Audo not have the AutoDock (AD4) element type in Autodock Vina tool.
24 Therefore, ANZOT binding interaction with target receptors was performed using Autodock 4.2
25 tool. UCSF Chimera, Discovery Studio Visualizer and LigPlot+ were used to visualize, analyze
26 and depict 2D interaction plots.^{33,34}

Statistics Analysis:

27
28 Error bars of all figures represent SEM of three independent experiments ($n=3$). The experimental
29 dataset between the two groups was compared using the two-tailed unpaired Student's t-test.
30 Differences between values were considered significant when $*p<0.05$, $**p<0.01$, $***p<0.001$,
31 $****p<0.0001$.

Acknowledgments

32
33 This work was supported by the National Institutes of Health RO1 grants EY029426, AI139768,
34 EY024710, AI133557 (to DS) and a NEI core grant (EY001792) and Illinois Society for the
35 Prevention of Blindness. This work was partially supported by the German Research Foundation
36 (DFG) in the Research Training Group “Materials for Brain” (GRK 2154). P.K.P. and R.A. thanks
37 Swedish Research Council (VR-2016-06014) for financial support and SNIC and HPC2N, Sweden
38 are acknowledged for providing the computing facilities.

Author Contributions

39
40 Conceptualization, R.K.S., C.D.P. and D.S.; Methodology, R.K.S., C.D.P., I.V.; Investigation,
41 R.K.S., D.S., L.S.; Writing Original Draft, R.K.S., C.D.P., L.K., A.A. and D.S.; P. K. P. and R.A
42 – computational calculations; Writing – Review and Editing, R.K.S., C.D.P., A.A., L.S., R.A. Y.
43 K.M. and D.S.; Funding Acquisition, D.S.; Supervision, D.S.

Declaration of Interests

1
2
3 The authors declare no competing interests.
4

5
6 **References**
7

- 8 1. Shukla, D.; Spear, P. G. Herpesviruses and heparan sulfate: an intimate relationship in aid of
9 viral entry. *J. Clin. Invest.* **2001**, *108*, 503-510.
10
11 2. Agelidis, A. M.; Shukla, D. Cell entry mechanisms of HSV: what we have learned in recent
12 years. *Future virology* **2015**, *10*, 1145-1154.
13
14 3. Liu, J.; Thorp, S. C. Cell surface heparan sulfate and its roles in assisting viral infections.
15 *Medicinal research reviews* **2002**, *22*, 1-25.
16
17 4. Cagno; Tseligka; Jones; Tapparel Heparan Sulfate Proteoglycans and Viral Attachment: True
18 Receptors or Adaptation Bias? *Viruses* **2019**, *11*, 596.
19
20 5. Connell, B. J.; Lortat-Jacob, H. Human Immunodeficiency Virus and Heparan Sulfate: From
21 Attachment to Entry Inhibition. *Frontiers in immunology* **2013**, *4*, 385.
22
23 6. Koujah, L.; Suryawanshi, R. K.; Shukla, D. Pathological processes activated by herpes simplex
24 virus-1 (HSV-1) infection in the cornea. *Cell Mol. Life Sci.* **2018**.
25
26 7. Whitley, R. J.; Roizman, B. Herpes simplex virus infections. *Lancet* **2001**, *357*, 1513-1518.
27
28 8. Roizman, B., Knipe, D.M., Whitley, R.J. Herpes simplex viruses. *Fields Virology (Lippincott*
29 *Willians and Wilkins)* **2007**, 2503-2602.
30
31 9. AnonymousGLOBALLY, An Estimated Two-Thirds Of The Population Under 50 Are Infected
32 With Herpes Simplex Virus Type 1. *States News Service* **2015**.
33
34 10. AnonymousSARS-CoV-2 spike protein binds heparan sulfate in a length- and sequence-
35 dependent manner. *Obesity, fitness, & wellness week* **2020**, 423.
36
37 11. Clausen, T. M.; Sandoval, D. R.; Spliid, C. B.; Pihl, J.; Perrett, H. R.; Painter, C. D.; Narayanan,
38 A.; Majowicz, S. A.; Kwong, E. M.; McVicar, R. N.; Thacker, B. E.; Glass, C. A.; Yang, Z.;
39 Torres, J. L.; Golden, G. J.; Bartels, P. L.; Porell, R.; Garretson, A. F.; Laubach, L.; Feldman,
40 J.; Yin, X.; Pu, Y.; Hauser, B.; Caradonna, T. M.; Kellman, B. P.; Martino, C.; Gordts, P. L.
41 S. M.; Chanda, S. K.; Schmidt, A. G.; Godula, K.; Leibel, S. L.; Jose, J.; Corbett, K. D.; Ward,
42 A. B.; Carlin, A. F.; Esko, J. D. SARS-CoV-2 Infection Depends on Cellular Heparan Sulfate
43 and ACE2. *Cell (Cambridge)* **2020**.
44
45 12. Ali, M. M.; Karasneh, G. A.; Jarding, M. J.; Tiwari, V.; Shukla, D. A 3-O-sulfated heparan
46 sulfate binding peptide preferentially targets herpes simplex virus 2-infected cells. *J. Virol.*
47 **2012**, *86*, 6434-6443.
48
49
50
51
52
53
54
55
56
57
58
59
60

- 1
2
3
4
5
6
7
8
9
10
11
12
13
14
15
16
17
18
19
20
21
22
23
24
25
26
27
28
29
30
31
32
33
34
35
36
37
38
39
40
41
42
43
44
45
46
47
48
49
50
51
52
53
54
55
56
57
58
59
60
13. Mishra, Y. K.; Adelung, R.; Rohl, C.; Shukla, D.; Spors, F.; Tiwari, V. Virostatic potential of micro-nano filopodia-like ZnO structures against herpes simplex virus-1. *Antiviral Res.* **2011**, *92*, 305-312.
 14. Agelidis, A.; Koujah, L.; Suryawanshi, R.; Yadavalli, T.; Mishra, Y. K.; Adelung, R.; Shukla, D. An Intra-Vaginal Zinc Oxide Tetrapod Nanoparticles (ZOTEN) and Genital Herpesvirus Cocktail Can Provide a Novel Platform for Live Virus Vaccine. *Frontiers in immunology* **2019**, *10*, 500.
 15. Antoine, T. E.; Hadigal, S. R.; Yakoub, A. M.; Mishra, Y. K.; Bhattacharya, P.; Haddad, C.; Valyi-Nagy, T.; Adelung, R.; Prabhakar, B. S.; Shukla, D. Intravaginal Zinc Oxide Tetrapod Nanoparticles as Novel Immunoprotective Agents against Genital Herpes. *J. Immunol.* **2016**, *196*, 4566-4575.
 16. Yadavalli, T.; Shukla, D. Could zinc oxide tetrapod nanoparticles be used as an effective immunotherapy against HSV-2? *Nanomedicine (Lond)* **2016**, *11*, 2239-2242.
 17. Duggal, N.; Jaishankar, D.; Yadavalli, T.; Hadigal, S.; Mishra, Y. K.; Adelung, R.; Shukla, D. Zinc oxide tetrapods inhibit herpes simplex virus infection of cultured corneas. *Mol. Vis.* **2017**, *23*, 26-38.
 18. Antoine, T. E.; Mishra, Y. K.; Trigilio, J.; Tiwari, V.; Adelung, R.; Shukla, D. Prophylactic, therapeutic and neutralizing effects of zinc oxide tetrapod structures against herpes simplex virus type-2 infection. *Antiviral Res.* **2012**, *96*, 363-375.
 19. Suvarna, S.; Nairy, R.; KC, S.; Yerol, N. Cytotoxicity Studies of Functionalized Gold Nanoparticles Using Yeast Comet Assay. *Fermentation technology* **2017**, *7*.
 20. Jaishankar, D.; Yakoub, A. M.; Yadavalli, T.; Agelidis, A.; Thakkar, N.; Hadigal, S.; Ames, J.; Shukla, D. An off-target effect of BX795 blocks herpes simplex virus type 1 infection of the eye. *Sci. Transl. Med.* **2018**, *10*.
 21. Iqbal, A.; Suryawanshi, R.; Yadavalli, T.; Volety, I.; Shukla, D. BX795 demonstrates potent antiviral benefits against herpes simplex Virus-1 infection of human cell lines. *Antiviral research* **2020**, *180*, 104814.
 22. Hopkins, J.; Yadavalli, T.; Suryawanshi, R.; Qatanani, F.; Volety, I.; Koganti, R.; Iqbal, A.; Shukla, D. In Vitro and In Vivo Activity, Tolerability, and Mechanism of Action of BX795 as an Antiviral against Herpes Simplex Virus 2 Genital Infection. *Antimicrobial agents and chemotherapy* **2020**, *64*.
 23. Mishra, Y. K.; Adelung, R. ZnO tetrapod materials for functional applications. *Materials today (Kidlington, England)* **2018**, *21*, 631-651.
 24. Maudgal, P. C.; Van Damme, B.; Missotten, L. Corneal epithelial dysplasia after trifluridine use. *Graefes Arch. Clin. Exp. Ophthalmol.* **1983**, *220*, 6-12.

- 1
2
3
4
5
6
7
8
9
10
11
12
13
14
15
16
17
18
19
20
21
22
23
24
25
26
27
28
29
30
31
32
33
34
35
36
37
38
39
40
41
42
43
44
45
46
47
48
49
50
51
52
53
54
55
56
57
58
59
60
25. Piret, J.; Boivin, G. Resistance of herpes simplex viruses to nucleoside analogues: mechanisms, prevalence, and management. *Antimicrob. Agents Chemother.* **2011**, *55*, 459-472.
26. Wu, S.; Pan, S.; Zhang, L.; Baines, J.; Roller, R.; Ames, J.; Yang, M.; Wang, J.; Chen, D.; Liu, Y.; Zhang, C.; Cao, Y.; He, B. Herpes Simplex Virus 1 Induces Phosphorylation and Reorganization of Lamin A/C through the γ 134.5 Protein That Facilitates Nuclear Egress. *Journal of virology* **2016**, *90*, 10414-10422.
27. Leach, N. R.; Roller, R. J. Significance of host cell kinases in herpes simplex virus type 1 egress and lamin-associated protein disassembly from the nuclear lamina. *Virology (New York, N.Y.)* **2010**, *406*, 127-137.
28. Richard Park; Joel D. Baines Herpes Simplex Virus Type 1 Infection Induces Activation and Recruitment of Protein Kinase C to the Nuclear Membrane and Increased Phosphorylation of Lamin B. *Journal of Virology* **2006**, *80*, 494-504.
29. Freeley, M.; Kelleher, D.; Long, A. Regulation of Protein Kinase C function by phosphorylation on conserved and non-conserved sites. *Cellular signalling* **2011**, *23*, 753-762.
30. Mishra, Y. K.; Modi, G.; Cretu, V.; Postica, V.; Lupan, O.; Reimer, T.; Paulowicz, I.; Hrkac, V.; Benecke, W.; Kienle, L.; Adlung, R. Direct Growth of Freestanding ZnO Tetrapod Networks for Multifunctional Applications in Photocatalysis, UV Photodetection, and Gas Sensing. *ACS Appl. Mater. Interfaces* **2015**, *7*, 14303-14316.
31. Wang, B.; Xie, J.; Yuan, Q.; Zhao, Y. Growth mechanism and joint structure of ZnO tetrapods. *Journal of Physics D: Applied Physics* **2008**, *41*, 102005.
32. Dong, C. L.; Persson, C.; Vayssieres, L.; Augustsson, A.; Schmitt, T.; Mattesini, M.; Ahuja, R.; Chang, C. L.; Guo, J. -. Electronic structure of nanostructured ZnO from x-ray absorption and emission spectroscopy and the local density approximation. *Physical review. B, Condensed matter and materials physics* **2004**, *70*.
33. Guo, J.; Vayssieres, L.; Persson, C.; Ahuja, R.; Johansson, B.; Nordgren, J. Polarization-dependent soft-x-ray absorption of highly oriented ZnO microrod arrays. *Journal of Physics: Condensed Matter* **2002**, *14*, 6969-6974.

Wear behaviour of additive manufactured polymer-polymer sliding combinations

Tribology remains a subject of high interest because many engineering tasks require sliding between two materials or depend on the friction two surfaces exert on each other. In friction bearings so called sliding combinations of two materials with low dynamic friction are used. While a typical candidate is polytetrafluoroethylene (PTFE), commonly known as Teflon, other combinations may be desired because of additional boundary conditions like processability, toughness or price. For modern engineering applications arbitrary geometries are desired and the difficult processing of pure Teflon limits its range of uses. Additively manufactured sliding combinations become more and more attractive and some companies offer their own low friction filament with added PTFE particles in an FDM-ready matrix. The exact mechanisms for friction between two polymers remain unclear and additively manufactured sliding combinations have so far not been studied extensively. This work presents findings on the sliding combinations of two commercial low friction filaments and their unfilled counterparts. A ball prism wear test has been used to determine influences of the printing parameters, the material choice and the test geometry arrangement. By means of SEM and confocal microscopy the friction surfaces have been investigated qualitatively after the wear test. It was found that the printing geometry although exhibiting steps of the individual layers does not impact the friction behaviour significantly, which is important for the applicability of this approach. It was also found that the PTFE filled polymers exceeded their unfilled counterpart in their wear behaviour regardless of the matrix polymer. This opens up some room for investigating other PTFE filled polymers tailoring the matrix polymer for the desired application while reducing the friction with added particles.

Own contribution presented in this article

- Sample characterisation via SEM
- Discussion and interpretation
- Editing of the manuscript

Harden, F.; Schädel, B.; Kral, R.; Siebert, L.; Adelung, R.; Jacobs, O.

Verschleißverhalten von additiv gefertigten Kunststoff-Kunststoff Gleitpaarungen

Zusammenfassung:

Vor dem Hintergrund der rasant steigenden Bedeutung der additiven Fertigung in der industriellen Anwendung und der sich daraus ergebenden Freiheit in Design und Materialkombinationen, sind additiv gefertigte Kunststoff-Kunststoff Gleitpaarungen von zunehmendem Interesse. Idealerweise sollten maßgeschneiderte Compounds zum Einsatz kommen, um das volle Potential von additiv gefertigten Kunststoff-Kunststoff Gleitpaarungen auszuschöpfen. In Anbetracht des additiven Fertigungsverfahrens spielen jedoch nicht nur die Materialpaarungen, sondern auch ein Verständnis des Einflusses unterschiedlicher Druckparameter eine entscheidende Rolle. In dieser Arbeit werden daher die Einflüsse von Druckorientierung und Materialpaarungen auf das Verschleißverhalten mittels des Kugel-Prisma-Verschleißtests untersucht. Des Weiteren wird deren wechselseitige Abhängigkeit diskutiert. Ergänzend werden die Besonderheiten und Herausforderungen der Prüfkörperherstellung sowie der Verschleißmessung betrachtet.

Schlüsselwörter: 3D-Druck, Additive Fertigung, FDM, FLM, Gleitverschleiß, Kugel-Prisma-Tribometer, Kunststoff-Kunststoff, Materialextusion

Wear behavior of additive manufactured polymer-polymer sliding combinations

Abstract:

For industrial applications, additive manufacturing becomes more and more important due to its unrivaled design and materials freedom. In this light, additively manufactured polymer-polymer sliding combinations gain increasing interest for manifold tribological applications. This potential can be fully exploited, e.g., by using tribologically tailored compounds. For additive manufacturing not only the sliding combinations but also the understanding of the influence of printing parameters are important. Thus, this work investigates influences of printing orientation and material combination on the wear behavior by means of the ball prism wear test. In addition, cross-relations of these parameters will be discussed. Finally, the challenges of test specimen production as well as wear measurements are considered.

Keywords: 3D-printing, additive manufacturing, FDM, FLM, sliding wear, ball prism wear test, polymer-polymer, material extrusion

Einleitung

Kunststoffe durchdringen dank ihrer vielfältigen Eigenschaften beinahe alle Bereiche des Lebens. Aufgrund ihrer Eigenschaften wie beispielsweise hohe chemische Beständigkeit und gute Notlauf- sowie Dämpfungseigenschaften werden Kunststoffe immer wieder in tribologisch beanspruchten Systemen verwendet [1]. Dabei kommen speziell additivierte Kunststoffe, häufig mit Zusätzen von PTFE, Graphit oder Silikonöl, zum Einsatz [2].

In den letzten Jahren wurden additive Fertigungsverfahren, allgemein bekannt als „3D-Druck“, zunehmend auch Bestandteil industrieller Produktionsketten [3]. Ein entscheidender Faktor hierfür ist, dass sich mittels additiver Fertigungsverfahren eine nahezu beliebige Bauteilkomplexität ohne teure Formwerkzeuge herstellen lässt, was sie gerade auch für kleine Stückzahlen interessant macht. Zudem eröffnet die additive Fertigung ganz neue Möglichkeiten, wie beispielsweise die Verarbeitung mehrerer Materialien im selben Prozess, auch bekannt als „Multimaterialdruck“ [4]. Somit können beispielsweise tribologische Paarungen hinsichtlich der Druckparameter und Materialkombination frei designet werden. Um das volle Potential additiv gefertigter Kunststoff-Kunststoff Verschleißpaarungen zu nutzen, ist eine gründliche Untersuchung spezifischer Paarungen, der Additivierung der Kunststoff-Compounds sowie des Einflusses der Druckparameter auf das Verschleißverhalten unabdingbar. Vor diesem Hintergrund sind aufeinander abgestimmte Kunststoff-Kunststoff-Gleitpaarungen für die Verarbeitung mittels additiver Fertigung von großem Interesse. Trotz der in der Praxis recht weit verbreiteten Paarungen von Kunststoffen unter tribologischen Beanspruchungen sind bisher nur wenige experimentelle Untersuchungen auf diesem Gebiet unternommen worden. Die wohl bekannteste und umfassendste Studie von Erhard [5] stammt bereits

aus dem Jahr 1980. Bei dieser Arbeit wurde der Fokus allerdings mehr auf das Reib- als auf das Verschleißverhalten gelegt. Zudem wurden nur nicht additivierte Kunststoffe verwendet.

Zu den am weitesten verbreiteten additiven Fertigungsverfahren zählen die Materialextrusionsverfahren für Kunststoffe, auch bekannt unter dem Markennamen „Fused Deposition Modeling – FDM®“ von Stratasys oder „Fused Layer Modelling – FLM“ nach der VDI-Richtlinie 3405 [6], [7]. Die Studie von Angelopoulos et al. [8] gibt einen guten Überblick über den Stand der Forschung in Bezug auf funktionelle Füllstoffe und deren Auswirkung auf die Materialeigenschaften im Bereich der FLM-Verfahren. Hier wird nochmals deutlich, dass insbesondere in dem Bereich der Materialien für FLM-Verfahren nur sehr wenige Erkenntnisse über tribologische Zusammenhänge vorliegen.

Daher stellt die vorliegende Arbeit den Beginn einer systematischen Untersuchung verschiedener, mittels FLM-Verfahren additiv gefertigter, tribologischer Kunststoff-Kunststoff Paarungen dar. Im Folgenden werden entscheidende Einflussfaktoren identifiziert und damit die Grundlagen für umfangreichere Untersuchungen gelegt.

Materialien

Um den Einfluss der Materialpaarung zu untersuchen, wurden für die jeweiligen Kunststoff-Kunststoff Paarungen vier verschiedene Materialien verwendet, welche bereits als Filament (aufgewickelter Strangmaterial, optimiert für das FLM-Verfahren) kommerziell erhältlich sind. Bei den Materialien handelt es sich zum einen um zwei bereits für tribologische Anwendungen modifizierte Materialien der Firma Igus GmbH, sowie jeweils eine nicht tribologisch optimierte Variante desselben Kunststoffs anderer Hersteller. Tabelle 1 zeigt die Materialien und Bezeichnungen, die im Weiteren verwendet werden.

Tabelle 1: Materialien und Bezeichnung

Bezeichnung	Material	Hersteller
I150	PETG/PTFE	Igus GmbH
I170	ASA/PTFE	Igus GmbH
PETG	PETG	Filamentworld
ASA	ASA	Fillamentum Manufacturing

Prüfkörperherstellung

Die Prüfkörperherstellung erfolgte im FLM Verfahren mit einem Ultimaker 2+ der Firma Ultimaker BV. Da sich die unterschiedlichen Materialien nicht mit identischen Parametern verarbeiten lassen, wurden diese mit einem jeweils auf das Material angepassten Parametersatz verarbeitet. Basierend auf den Untersuchungsergebnissen von Kuznetsov et al. [9] wurden die Prüfkörper mit möglichst hoher Verarbeitungstemperatur sowie ohne Bauteilkühlung gefertigt, um maximale Festigkeit zu erzielen. Für die Verschleißversuche wurden sowohl Kugeln als auch Plättchen gedruckt. In Anlehnung an die Norm DIN ISO 7148-2 [10] wurden Kugeln mit dem Durchmesser von 12,7 mm mit einer Aufnahme zur Einspannung in den Prüfstand gedruckt. Die Plättchen wurden ebenfalls nach den maßlichen Standards der Norm angefertigt mit Abmessungen von 10 mm x 12 mm und 2 mm Dicke. Anschließend wurden diese in Aluminiumträger eingeklebt, um die für die Verschleißversuche benötigten Prismen zu erhalten. Vor jedem Verschleißversuch wurden sowohl die Prismen als auch die Kugeln mit unvergälltem Ethanol gereinigt.

Bedingt durch das FLM-Verfahren entstehen anisotrope Bauteile. Gründe hierfür liegen in den fertigungsbedingt bereits anisotropen Werkstoffeigenschaften der Filamente und in deren gerichteter Ablage sowohl in der Fertigungsebene (x-y-Ebene), als auch in der

Schichtungsrichtung (z-Richtung) senkrecht dazu. Als Folge entsteht unter anderem eine Ausrichtung der gedruckten Oberflächenstruktur (wie in Abbildung 6 a) zu sehen). Um deren Einfluss auf das Verschleißverhalten zu untersuchen, wurden die Plättchen unterschiedlich im Prisma orientiert, sodass sich zwei unterschiedliche Ausrichtungen der aufeinander einwirkenden Oberflächenorientierungen ergeben. Abbildung 1 zeigt schematisch die Druckgeometrien im Verschleißprüfstand. Links ist die Ausrichtung der Oberflächenorientierungen des Prismas parallel zur Rotationsrichtung zu sehen, im Folgenden als Längsausrichtung (bzw. längs) bezeichnet, im rechten Teil der Abbildung die Ausrichtung der Oberflächenorientierungen des Prismas rechtwinklig zur Rotationsrichtung, im Weiteren als Querausrichtung (quer) bezeichnet. Alle möglichen Materialkombinationen (vergl. Tabelle 1) wurden sowohl in Längs-, als auch in Querrichtung getestet.

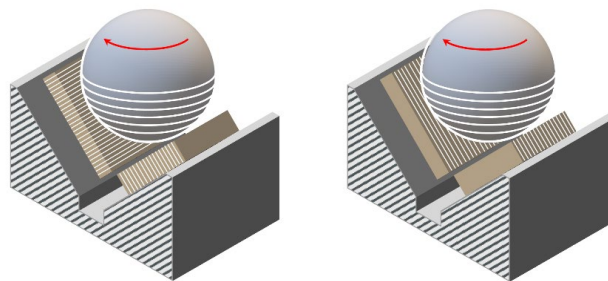


Abbildung 1: Geometrie des Verschleißkontakts mit Oberflächenorientierung der Plättchen; links: längs, rechts: quer

Untersuchungsmethoden

Die Verschleißversuche fanden in VPS 6-fach Verschleißprüfständen (Kugel-Prisma-Prüfstände) von Dr. Tillwisch GmbH Werner Stehr statt. Diese wurden mit induktiven Wegaufnehmern zur digitalen Datenerfassung ausgerüstet. Das schematische Versuchsprinzip ist in Abbildung 2 zu sehen. Der Versuchsaarm wird mit einem Gewicht belastet, welches das Prisma gegen den rotierenden Kugelprüfkörper gedrückt. Der induktive Wegaufnehmer zeichnet die Eindringtiefe beider Prüfkörper ineinander auf. Pro Paarung wurden zur Ermittlung der Verschleißdaten jeweils drei Versuche durchgeführt. Geprüft wurde dabei nach DIN ISO 7148-2 [10] über 100 h mit einer Belastung von 30 N und 1 Hz Rotationsfrequenz im Trockenlauf. Aufgrund der Prüfkörpergeometrien ergibt sich daraus eine Normalkraft von 21,21 N pro Plättchen und eine Gleitgeschwindigkeit von 28 mm/s zu Beginn des Versuchs. Aufgrund der kugelförmigen Kontaktfläche nimmt die Flächenpressung kontinuierlich während des Versuchs ab, ebenso – wenn auch in deutlich geringerem Maße – die Gleitgeschwindigkeit bei Verschleiß der Kugel. Zusätzlich zu den Versuchen mit 100 h Versuchsdauer wurden zur Ermittlung der Veränderung der Oberflächenstruktur an sechs Armen an einer ausgewählten Materialpaarung Versuche mit ansonsten identischen Bedingungen durchgeführt, bei denen mit Taktung von 10 min über die ersten 60 min jeweils ein Prüfkörper entnommen wurde. Dies wurde exemplarisch anhand der Kombination von PETG Kugeln gegen I150 Prismen längs sowie quer durchgeführt.

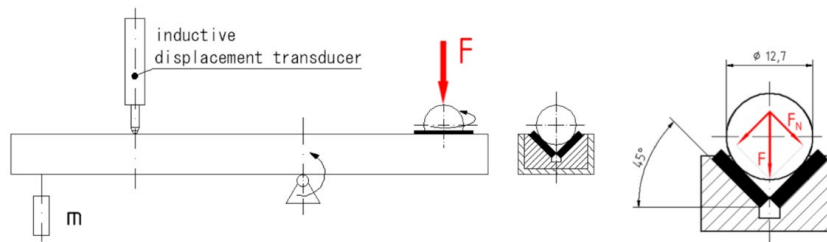


Abbildung 2: Versuchsprinzip Kugel-Prisma Verschleißtest [11]

Wie bereits in einer früheren Arbeit von Schädel et al. [11] mit demselben Versuchsaufbau dargestellt, wird die Auswertung von Kunststoff-Kunststoff Verschleißuntersuchungen wesentlich komplexer als bei gängigen Verschleißuntersuchungen von Kunststoff gegen einen metallischen oder keramischen Gegenpartner. Dort kann in der Regel der auftretende Verschleiß des Gegenpartners vernachlässigt werden, sodass Kontaktgeometrie und Verschleißvolumen eindeutig aus der Eindringtiefe ermittelt werden können. Bei einer Kunststoff-Kunststoff Paarung verschleifen dagegen beide Partner. Somit kann die Eindringtiefe nicht eindeutig einem der beiden Verschleißpartner zugeordnet werden.

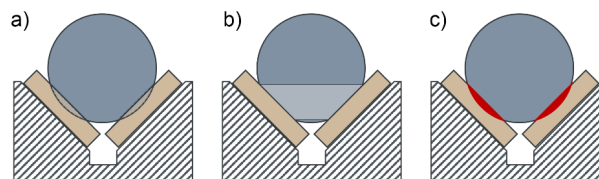


Abbildung 3: Mögliche Verschleißszenarien; a) nur Prismaverschleiß, b): nur Kugelverschleiß, c): projizierte Verschleißfläche

Abbildung 3 zeigt die beiden möglichen Extremfälle der Verschleißszenarien sowie deren projizierte Verschleißfläche. Links in der Abbildung (a) ist der Fall des verschleißenden Prismas zu sehen, in der Mitte (b) der Fall der verschleißenden Kugel. Die projizierte Verschleißfläche ist rechts (c) in der Abbildung dargestellt. Sie ist für beide Szenarien bei gleicher Eindringtiefe identisch. Das Verschleißvolumen, welches sich aus der projizierten Verschleißfläche ermitteln lässt, ist dagegen für beide Szenarien stark unterschiedlich. Verschleißt nur das Prisma, bildet sich im Eingriff jedes der Plättchen eine Kalotte aus. Verschleißt wiederum nur die Kugel, wird die projizierte Verschleißfläche umlaufend von der Kugel abgetragen. Somit ergibt sich bei derselben Eindringtiefe ein deutlich höheres Verschleißvolumen, wenn nur die Kugel verschleißt. Betrachtet man Abbildung 4, wird dieser Unterschied der beiden Extremfälle nochmal deutlich. Das wahre Verschleißverhalten setzt sich aus beiden Szenarien zusammen und liegt somit zwischen theoretischem reinem Kugel- und reinem Prismaverschleiß. Um Rückschlüsse auf das real vorliegende Verschleißszenario sowie die Oberflächenstruktur zu ermöglichen, wurden die Verschleißflächen nachträglich mit einem chromatischen Weißlicht-Sensor der Firma FRT GmbH abgerastert.

Für die Berechnungen der Verschleißkennwerte wird das Verschleißvolumen in Abhängigkeit es Weges betrachtet. Zur Bestimmung der spezifischen Verschleißrate wird zuerst der stationäre Bereich des Verschleißes ermittelt. Für diesen Bereich gilt ein linearer Zusammenhang zwischen Verschleißvolumen und Reinweg. Anhand der Daten innerhalb dieses Bereichs lässt sich die spezifische Verschleißrate

$$k = \frac{\Delta V}{F_N * \Delta L} \left[\frac{mm^3}{Nm} \right]$$

ermitteln. Der Bereich bis zum Erreichen des stationären Bereichs ist der Einlaufbereich. Hier wird das Gesamtvolumen im Einlaufbereich bezogen auf die Normalkraft ermittelt.

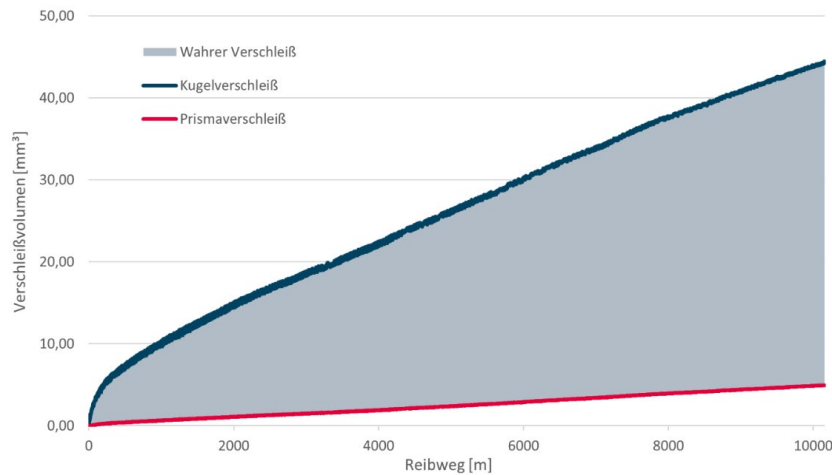


Abbildung 4: Vergleich von theoretischem, reinem Kugel- und Prismaverschleiß bei gleicher Eindringtiefe anhand der beim Versuch von 1150 Kugeln gegen ASA Prismen gemessenen Eindringtiefen.

Um ein besseres Verständnis einiger Verschleißuntersuchungen zu erhalten, wurden zusätzlich an ausgewählten Materialkombinationen mit quer ausgerichtetem Prisma Untersuchungen zum Reibungskoeffizienten mit einem Universal-Tribometer UMT-3MT der Firma Center for Tribology, Inc. (CETR) durchgeführt. Dazu wurden die Geometrien, Eingriffsverhältnisse und Belastungen der Kugel-Prisma-Verschleißuntersuchungen einseitig nachgebildet. Abbildung 5 zeigt den Versuchsaufbau. Die Kugel wird zentrisch auf einen rotierenden Tisch gespannt und das Plättchen auf einer 45° abgeschrägten Ebene des Prüfdorns befestigt. Dieser wiederum ist an dem Kraftaufnehmer befestigt, welcher sowohl vertikale (Prüf-) als auch einachsige horizontale (Reib-) Kräfte aufnehmen kann. Um die Reibkräfte messen zu können, konnte daher lediglich eine Hälfte des Prismas gegen die Kugel gedrückt werden. Dies hat zur Folge, dass die Prüfkraft lediglich 15 N betrug, um die Normalkraft auf das Prisma identisch zum Kugel-Prisma-Versuch zu halten. Auch die Drehzahl wurde entsprechend gewählt. Aus der gemessenen Prüfkraft (F) wurde die wirkende Normalkraft (F_N) berechnet. Durch Division der gemessenen Reibkraft (F_R) durch die zuvor ermittelte Normalkraft lässt sich der Reibungskoeffizient errechnen.

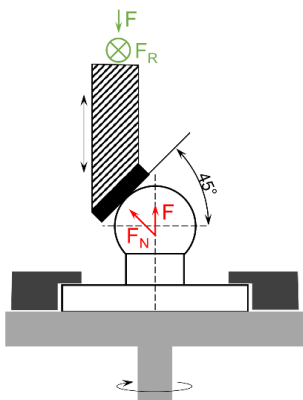


Abbildung 5: Versuchsschema Universaltribometer; grün: Messgrößen, rot: Prüfkräfte, schwarz: Bewegungen

Um einen Eindruck von den beteiligten Oberflächen – sowohl gedruckt als auch tribologisch beansprucht – und den wirkenden Verschleißmechanismen zu erlangen, wurden ausgewählte Proben mit einem Rasterelektronenmikroskop (Zeiss Supra 55VP) untersucht.

Ergebnisse & Diskussion

Die in Abbildung 6 exemplarisch dargestellten Rasterelektronenmikroskop-Aufnahmen zeigen zwei verschlissene Plättchen aus I150 (a und b) mit Längsausrichtung sowie mit Querausrichtung (c und d) des Prismas. Diese wurden in Kombination mit ASA Kugeln im Kugel-Prisma-Verschleißtest verschlissen. In Abbildung 6 a) ist die durch das Herstellungsverfahren in Bahnen strukturierte Oberfläche gut zu erkennen. Ebenfalls erkennbar sind die beim I150 eingebetteten PTFE-Partikel (beispielsweise rot umrandet). Da es sich um eine bereits verschlissene Probe handelt, sind auch Abriebpartikel zu erkennen.

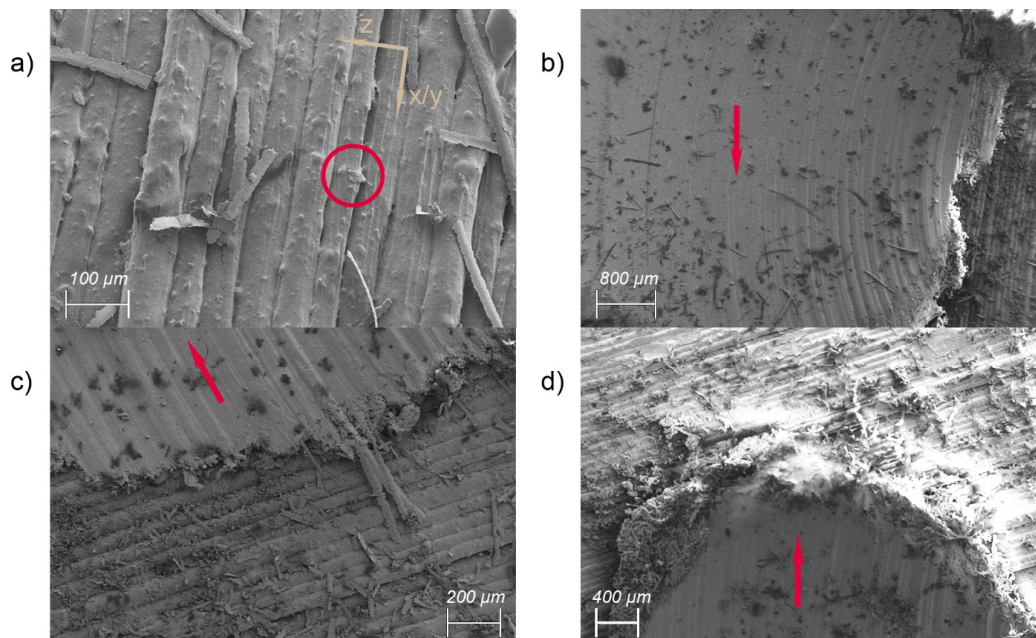


Abbildung 6: REM Aufnahmen verschlissener I150 Plättchen mit ASA als Gegenpartner; a) gedruckte Oberflächenstruktur von I150, b) Verschleißmarke eines Plättchens mit Längsausrichtung, c) Eintrittsseite der Kugel auf einem Plättchen mit Querausrichtung, d) Austrittsseite der Kugel auf einem Plättchen mit Querausrichtung; roter Pfeil: Rotationsrichtung der Kugel, rot umrandet: eingebettet PTFE Partikel, beige: Fertigungsrichtungen

Die Verschleißkalotte desselben Plättchens ist in Abbildung 6 b) zu sehen. Am rechten Rand befinden sich Teile der nicht verschlissenen Oberfläche des Plättchens. Die Verschleißkalotte selbst weist Verschleißriefen in Rotationsrichtung des Gegenpartners (roter Pfeil) auf, jedoch keine ausgerichteten Oberflächenstrukturen, bedingt durch das Herstellungsverfahren der Prüfkörper. Betrachtet man Abbildung 6 c), wird dies nochmals deutlich. Hier zu sehen ist die Eintrittsseite des Gegenpartners in das quer zur Rotationsrichtung ausgerichtete Plättchen. Die sich ausbildenden Riefen verlaufen senkrecht zur Oberflächenorientierung und sind somit eine Folge des Verschleißvorganges. Abbildung 6 d) zeigt die Austrittsseite des Gegenpartners. Auch hier ist die Ausrichtung der Riefen zur Rotationsrichtung zu erkennen. Zusätzlich findet auf der Austrittsseite vermehrt eine Anhäufung des Abriebs statt.

Anhand der genaueren Untersuchungen der sich ausbildenden Verschleißflächen mit dem chromatischen Weißlicht-Sensor erfolgte eine Zuordnung der primär vorliegenden Verschleißszenarien, wie Abbildung 7 exemplarisch an zwei verschiedenen Verschleißpaarungen zeigt. Zur Bestimmung des primären Verschleißpartners wurden Schnitte an höchster, respektive tiefster Stelle durch die dreidimensionalen Topografiedaten gelegt und mit der Sollkontur verglichen.

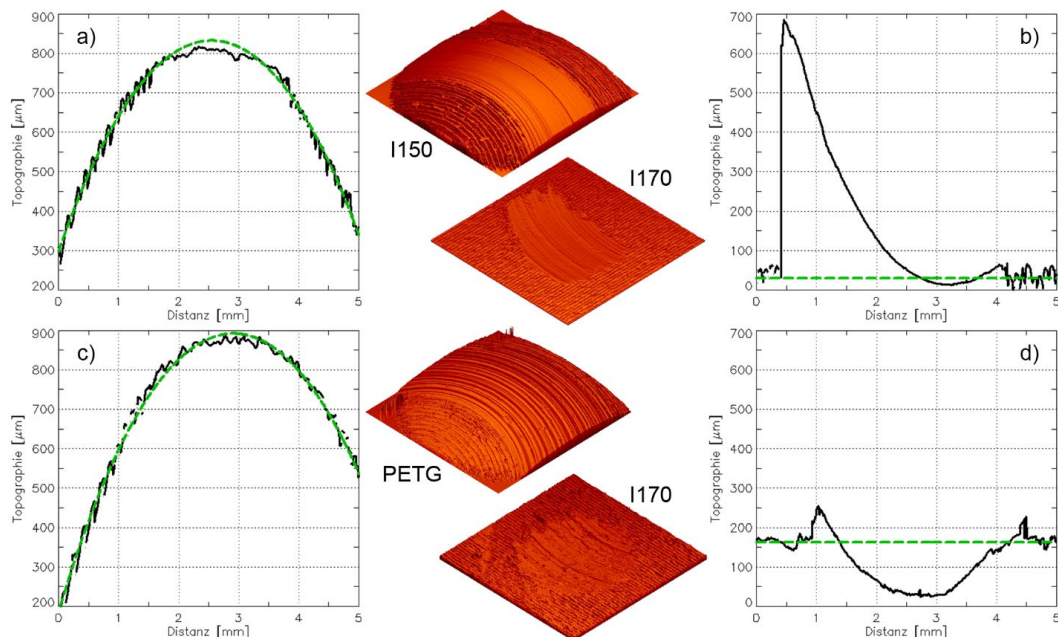


Abbildung 7: 3D-Darstellung und Schnitt der Verschleißspur einer Verschleißpaarung aus a) I150 Kugel und b) I170 Prisma mit Querausrichtung sowie einer Verschleißpaarung aus c) PETG Kugel und d) I170 Prisma mit Längsausrichtung; grün: Ideal-Kontur, schwarz: Ist-Kontur

Betrachtet man die Profilschnitte der Verschleißpaarung oben in der Abbildung 7, fällt eine Abweichung der Kontur des Kugelprüfkörpers (a) von der idealen Kugelkontur auf. Der Profilschnitt des Prismas (b) weist im Wesentlichen lediglich eine Materialanhäufung des Abriebs auf. Hier verschleißt primär die Kugel. Betrachtet man nun die beiden unteren Topografiedatensätze lässt sich kaum eine Abweichung des Kugelprüfkörpers (c) von seiner Idealkontur feststellen. Das Prisma (d) hingegen weist eine deutliche Vertiefung auf. Bei dieser Paarung verschleißt primär das Prisma. Die Ergebnisse der Zuordnung der Verschleißszenarien sind in Tabelle 2 für alle Paarungen dargestellt. Drei der untersuchten Verschleißpaarungen verschlissen allerdings vollständig vor dem Erreichen des geplanten Versuchsendes (100 h). Die Verschleißpaarungen aus PETG Kugel und PETG Prisma versagten bereits nach wenigen Minuten unter starker thermischer Verformung. Somit ließ sich diese Paarung weder einem Verschleißszenario zuordnen noch lassen sich weitere Auswertungen vornehmen. Die Verschleißpaarungen aus ASA und I170 verschlissen in den ersten etwa 10 Stunden komplett. Trotz des vorzeitigen Versagens ließen sich die Verschleißszenarien eindeutig zuordnen, weitere Auswertungen sind allerdings auch hier nicht möglich.

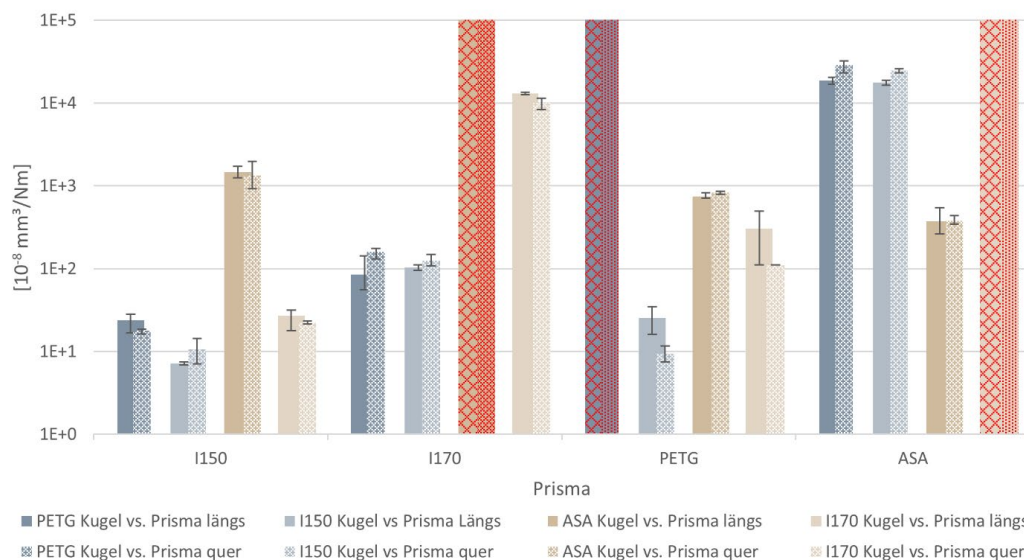
Tabelle 2: Primärer Verschleißpartner; Prisma: V – Kugel: O – vorzeitig verschlissen: x

		Prisma							
		I150		I170		PETG		ASA	
		längs	quer	längs	quer	längs	quer	längs	quer
Kugel	I150	V	V	O	O	V	V	O	O
	I170	V	V	OV	OV	V	V	xV	xV
	PETG	V	V	V	V	x	x	O	O
	ASA	V	V	xO	xO	V	V	OV	OV

Für die Auswertung der Verschleißvolumina und damit auch der Verschleißraten aus den gemessenen Eindringtiefen wurden die zuvor ermittelten Verschleißszenarien berücksichtigt. In Abbildung 8 sind die Verschleißraten, die in dem stationären Bereich nach Beendigung der Einlaufphase ermittelt wurden, dargestellt.

Der Einfluss der Additivierung mit PTFE ist stark abhängig von der Kombination der Verschleißpartner. Betrachtet man die Paarungen aus PETG und I150 fällt auf, dass die Additivierung nur eines Verschleißpartners mit PTFE zu einer drastisch verringerten Verschleißrate führt, dabei ist irrelevant welcher der beiden Partner additiviert wird. Eine Additivierung beider Partner senkt die Verschleißrate – in geringerem Maße – noch weiter.

Anders stellt es sich bei den Paarungen mit Kugeln aus PETG bzw. I150 gegen ASA Prismen dar. Die Additivierung der Kugel mit PTFE führt hier zu keiner Reduzierung der Verschleißrate. Dieselbe Beobachtung lässt sich für Paarungen aus PETG bzw. I150 Kugel mit I170 Prismen machen. Hier führt jedoch die Additivierung des Prismas zu einer drastisch verringerten Verschleißrate im Vergleich zum reinen ASA Prisma. Zusätzlich ändert sich für die Paarung mit PETG Kugel das Verschleißszenario von Kugelverschleiß beim Versuch gegen das ASA Prisma zu Prismaverschleiß beim I170 Prisma.

**Abbildung 8: spezifische Verschleißraten verschiedener Materialpaarungen im Kugel-Prisma Verschleißtest; rot schraffiert: keine Messwerte, da vorzeitig verschlissen**

Im Gegensatz zu den Ergebnissen beider Verschleißpartner aus I150 führt eine Paarung beider Verschleißpartner aus I170 zu einer deutlich erhöhten Verschleißrate im Vergleich zu beiden Partnern aus reinem ASA. Welche Ursachen zu diesem hohen Verschleiß von I170-I170 Paarungen führen, ist noch zu klären.

Im Hinblick auf die Ausrichtung der Oberflächenstruktur wurde ein Einfluss auf das Verschleißverhalten, insbesondere auf den Einlaufverschleiß, erwartet. Betrachtet man die Ergebnisse der Auswertung des Einlaufverschleißvolumens, dargestellt in Abbildung 9, kann jedoch keine solche Korrelation festgestellt werden. Ebenso zeigt sich auch keine Korrelation zwischen der Ausrichtung der Oberflächenstruktur und der Verschleißrate.

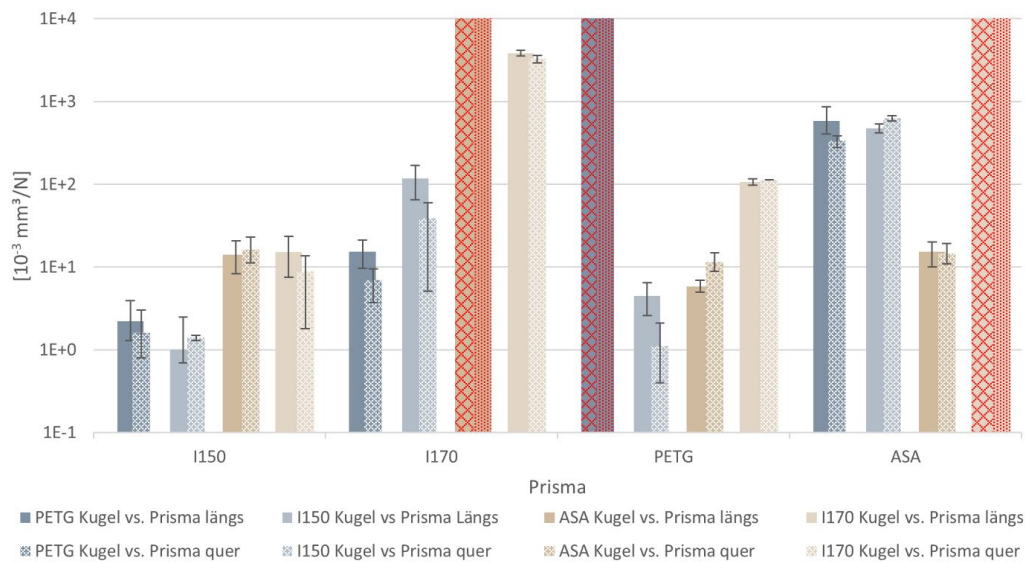


Abbildung 9: Kraftbezogenes Einlaufverschleißvolumen verschiedener Materialpaarungen im Kugel-Prisma Verschleißtest

Eine mögliche Erklärung ist, dass die Oberflächenstrukturen durch die zu Beginn des Versuchs sehr kleine Kontaktfläche bereits kurz nach Beginn des Versuches geebnet werden. Im weiteren Verlauf haben diese lediglich im Randbereich des Eingriffs eine untergeordnete Rolle. Die Untersuchungen der Verschleißflächen in den ersten 60 min der Einlaufphase bestätigen diese Vermutung. In Abbildung 10 ist bereits nach 20 min eine deutliche Einebnung der Oberflächenstrukturen sowohl für längs als auch für quer ausgerichtete Prismen zu erkennen.

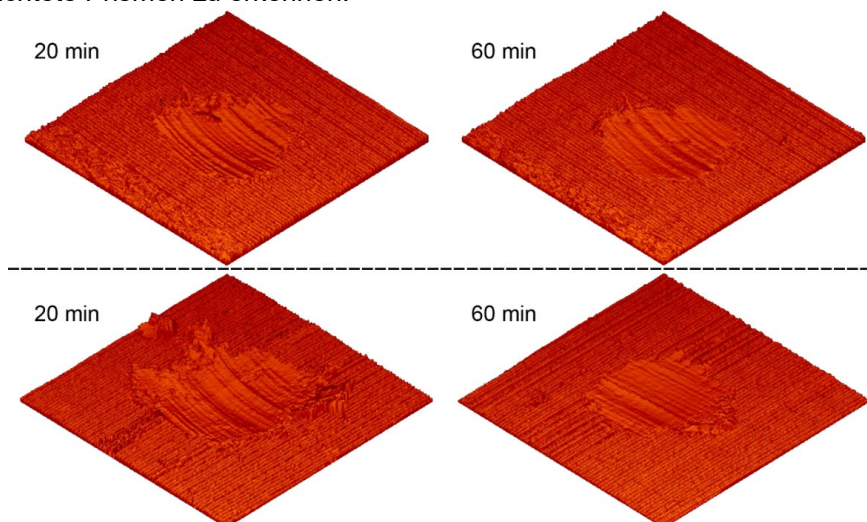


Abbildung 10: 3D-Darstellung der Verschleißspuren (Oberflächenausschnitt 4x4 mm) nach 20 min und 60 min von I150 mit ASA Kugeln als Gegenpartner; oben: Prisma mit Längsausrichtung, unten: Prisma mit Querausrichtung

Abbildung 11 zeigt die Ergebnisse der Untersuchungen im Universaltribometer. Diese liefern eine Erklärung für das vorzeitige Versagen der PETG-PETG Paarung. Der Reibkoeffizient, welcher sich in der ersten Minute vor dem vollständigen Versagen ermitteln lässt, ist circa achtmal so hoch wie bei Paarungen aus PETG und I150. Proportional zum Reibkoeffizienten steigt auch die eingetragene thermische Energie (Reibenergie), welche durch den Werkstoff dissipiert werden muss. In Kombination mit der schlechten Wärmeleitfähigkeit kann es somit zu einer kontinuierlichen Erwärmung des Materials kommen, welche schlussendlich zum thermischen Versagen führt. Der hohe ermittelte Reibungskoeffizient bei der PETG-PETG Paarung steht in Einklang mit den Erkenntnissen von Erhard [5], welcher nachwies, dass der Reibungskoeffizient in Korrelation mit der Oberflächenspannung und somit wiederum der Polarität des Materials steht.

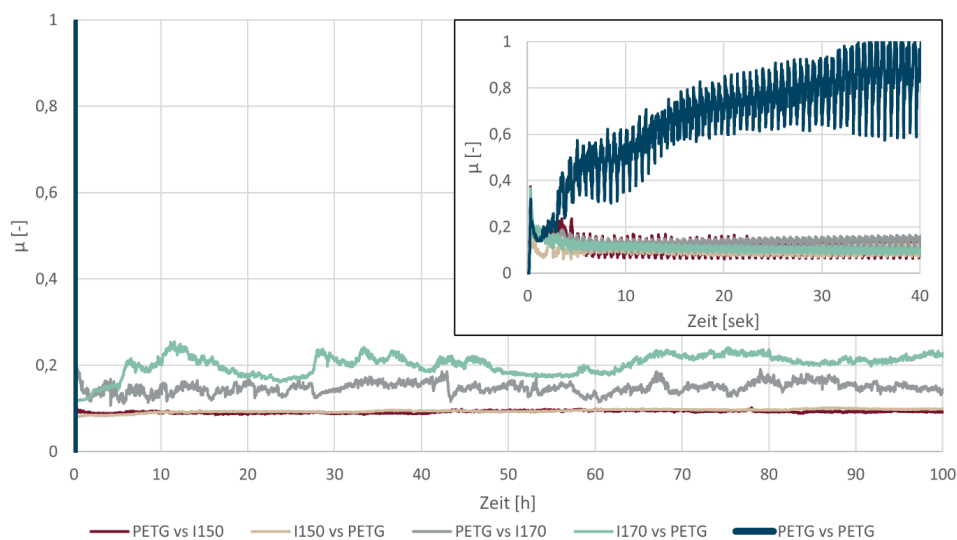


Abbildung 11: Zeitabhängige Reibungskoeffizienten von ausgewählten Verschleißpaarungen aus PETG, I150 und I170

Fazit

Insbesondere die Ergebnisse der PETG-PETG Paarungen im Vergleich mit den I150-I150 Paarungen haben gezeigt, dass es mittels Additivierung möglich ist, eine Kunststoff-Kunststoff Paarung für den tribologischen Einsatz nutzbar zu machen, obwohl die nicht additivierte Variante keineswegs dafür geeignet ist. Somit ist es nicht möglich, anhand der intrinsischen tribologischen Eigenschaften eines Basiskunststoffs abzuschätzen, ob dieses Material mit weiterer Additivierung für den tribologischen Einsatz geeignet ist oder nicht. Zudem haben die Untersuchungen gezeigt, dass eine Additivierung mit PTFE nicht immer den gewünschten Effekt auf das Verschleißverhalten erzielen kann. Somit ist es von entscheidender Bedeutung, Kunststoff-Kunststoff-Verschleißpaarungen aufeinander abzustimmen und systematisch zu untersuchen. Diese systematischen Untersuchungen verschiedenster Kunststoff-Kunststoff Verschleißpaarungen mit unterschiedlichen Additivierungen sollen in nachfolgenden Arbeiten folgen.

In Bezug auf die Ausrichtung der Oberflächenstruktur konnten keine signifikanten Einflüsse auf das Verschleißverhalten festgestellt werden, da die ausgeprägten Oberflächenstrukturen bereits sehr schnell zu Beginn des Versuchs eingeebnet werden. Im Hinblick auf den Kugel-Prisma-Verschleißtest mit simultanem Verschleiß beider Verschleißpartner zeigt sich einmal mehr das Verbesserungspotential. Zur besseren Bestimmung des Verschleißvolumens sowie der Aufteilung auf beide Verschleißpartner ist eine weitere Messinformation notwendig. Eine solche Modifikation des VPS 6-fach

Verschleißprüfstandes ist in der Entwicklung und soll für zukünftige Untersuchungen von Kunststoff-Kunststoff Verschleißpaarungen Anwendung finden.

Quellenangaben

- [1] Myshkin, N.K.; Pesetskii, S.S.; Grigoriev, A.Ya. Polymer Tribology: Current State and Applications. *Tribology in Industry* **2015**, 37 (3), 284-290
- [2] Uetz H., Wiedemeyer J. Tribologie der Polymere: Grundlagen u. Anwendungen in d.Technik; Reibung – Verschleiß – Schmierung. *Carl Hanser Verlag GmbH Co KG* **1985**
- [3] Deutscher Bundestag Ausschuss für Bildung, Forschung und Technikabschätzungen, Technikfolgenabschätzung (TA) Additive Fertigungsverfahren „3-D-Druck“. *Bundesanzeiger Verlag GmbH* **2017**
- [4] Gebhardt, A. 3D-Drucken: Grundlagen und Anwendungen des Additive Manufacturing (AM). *Carl Hanser Verlag GmbH Co KG* **2014**
- [5] Erhard, G. Zum Reibungs-und Verschleißverhalten von Polymerwerkstoffen [Dissertation], *University Karlsruhe* **1980**
- [6] Gibson, I.; Rosen, D. W.; Stucker, B. Additive manufacturing technologies. *New York: Springer* **2015**
- [7] VDI 3405:2014-12, Additive Fertigungsverfahren Grundlagen, Begriffe, Verfahrensbeschreibungen
- [8] Angelopoulos, P.M.; Samouhos, M.; Taxiarchou, M. Functional fillers in composite filaments for fused filament fabrication; a review. *Materials Today: Proceedings* **2020**
- [9] Kuznetsov, V.; Solonin, A.; Tavitov, A.; Urzhumtsev, O.; Vakulik, A. Increasing strength of FFF three-dimensional printed parts by influencing on temperature-related parameters of the process. *Rapid Prototyping Journal* **2020** 26 (1), 107-121.
- [10] DIN ISO 7148-2:2014-07, Gleitlager – Prüfung des tribologischen Verhaltens von Gleitlagerwerkstoffen – Teil 2: Prüfung von polymeren Gleitlagerwerkstoffen (ISO 7148-2:2012)
- [11] Schädel, B.; Rüdiger, G.; Jacobs, O.; Kowtun, A.; Beneke, T. Verschleißverhalten von Kunststoff-Kunststoff-Paarungen. *Tribologie und Schmierungstechnik* **2012**, 59 (3), 29-34.

Autoren

Harden, Felix M.Sc. Technische Hochschule Lübeck, Fachbereich Maschinenbau und Wirtschaft, Mönkhofer Weg 239, 23562 Lübeck, +49 451 300-5075, felix.harden@th-luebeck.de

Schädel, Birgit Dipl.-Ing. (FH) Technische Hochschule Lübeck, Fachbereich Maschinenbau und Wirtschaft, 23562 Lübeck

Kral, Roland Prof. Dr.-Ing. Technische Hochschule Lübeck, Fachbereich Maschinenbau und Wirtschaft, 23562 Lübeck

Siebert, Leonard M.Sc. Christian-Albrechts-Universität zu Kiel, Institut für Materialwissenschaft, 24143 Kiel

Adelung, Rainer Prof. Dr. rer. nat. Christian-Albrechts-Universität zu Kiel, Institut für Materialwissenschaft, 24143 Kiel

Jacobs, Olaf Prof. Dr.-Ing. Dipl.-Phys. Technische Hochschule Lübeck, Fachbereich Maschinenbau und Wirtschaft, 23562 Lübeck

Part V

Appendix B

Additional Information

List of Abbreviations

CNT	Carbon nanotube
FDM	Fused Deposition Modelling
DIW	Direct Ink Writing
SLA	Stereolithographic Apparatus
MWD	Molecular Weight Distribution
CNC	Computer Numerical Control
CAD	Computer Aided Design
ZnO	Zinc Oxide
t-ZnO	tetrapodal Zinc Oxide
CuO	Cupric Oxide
Cu₂O	Copper Oxide
Al	Aluminum
3D	Three dimensional
2D	Two dimensional
1D	One dimensional
0D	Zero dimensional
PEEK	Poly Ether Ether Ketone
PDMS	Poly dimethyl siloxane
PLA	Poly(lactic acid)
ABS	Acrylonitrile Butadiene Styrene
PA	Polyamide
PTFE	Polytetrafluoroethylene
AM	Additive Manufacturing

List of Publications and Patents

- [LS1] **L. Siebert**, T. Schaller, F. Schütt, S. Kaps, J. Carstensen, S. Shree, J. Bahr, Y.K. Mishra, H.-H. Sievers, R. Adelung, Perfect polymer interlocking by spherical particles: capillary force shapes hierarchical composite undercuts, *Nanoscale Horizons* 4, pp. 947-952 (2019)
- [LS2] R. Colaco, S. Shree, **L. Siebert**, C. Appiah, M. Dowds, S. Schultzke, R. Adelung, A. Staubitz, Mechanochromic Microfibers Stabilized by Polymer Blending, *ACS Applied Polymer Materials* 2, pp. 2055-2062 (2020)
- [LS3] D. Smazna, J. Rodrigues, S. Shree, V. Postica, G. Neubüser, A. F. Martins, N. B. Sedrine, N. K. Jena, **L. Siebert**, F. Schütt, O. Lupan, R. Ahuja, M. R. Correia, T. Monteiro, L. Kienle, Y. Yang, R. Adelung, Y. K. Mishra, Buckminsterfullerene hybridized zinc oxide tetrapods: defects and charge transfer induced optical and electrical response, *Nanoscale* 10, pp. 10050-10062 (2018)
- [LS4] F. Schütt, M. Zapf, S. Signetti, J. Strobel, H. Krüger, R. Röder, J. Carstensen, N. Wolff, J. Marx, T. Carey, M. Schweichel, M.-I. Terasa, **L. Siebert**, H.-K. Hong, S. Kaps, B. Fiedler, Y. K. Mishra, Z. Lee, N. M. Pugno, L. Kienle, A. C. Ferrari, F. Torrisi, C. Ronning, R. Adelung, Conversionless efficient and broadband laser light diffusers for high brightness illumination applications, *Nature Communications* 11, 1437 (2020)
- [LS5] **L. Siebert**, O. Lupan, M. Mirabelli, N. Ababii, M.-I. Terasa, S. Kaps, V. Cretu, A. Vahl, F. Faupel, R. Adelung, 3D-Printed Chemiresistive Sensor Array on Nanowire CuO/Cu₂O/Cu Heterojunction Nets, *ACS applied materials & interfaces* 11, pp. 25508-25515 (2019)
- [LS6] **L. Siebert**, N. Wolff, N. Ababii, M.-I. Terasa, O. Lupan, A. Vahl, V. Duppel, H. Qiu, M. Tienken, M. Mirabelli, V. Sontea, F. Faupel, L. Kienle, R. Adelung, Facile fabrication of semiconducting oxide nanostructures by direct ink writing of readily available metal microparticles and their application as low power acetone gas sensors, *Nano Energy* 70, 104420 (2019)
- [LS7] S. B. Gutekunst, K. Siemsen, S. Huth, A. Möhring, B. Hesseler, M. Timmermann, I. Paulowicz, Y. K. Mishra, **L. Siebert**, R. Adelung, C. Selhuber-Unkel, 3D Hydrogels Containing Interconnected Microchannels of Subcellular Size for Capturing Human Pathogenic *Acanthamoeba Castellani*, *ACS Biomaterials Science & Engineering* 5, 4, pp. 1784-1792 (2019)
- [LS8] **L. Siebert**, M.-I. Terasa, N. Ababii, O. Lupan, R. Adelung, 3D-Printed Sensor Array of Semiconducting Oxides, in *International Conference on Nanotechnologies and Biomedical Engineering*, pp. 3-6 (2019)

- [LS9] L. O. Akinsinde, S. Scheitz, L. Zimoch, J. K. Sierck, **L. Siebert**, R. Adelung, U. Schürmann, M. A. Rübhausen, T. Dankwort, L. Kienle, Resistivity Response to Stress and Strain of a Flexible Bi₂Te₃ Based Thermoelectric Material, *in International Conference on Nanotechnologies and Biomedical Engineering*, pp. 57-60 (2019)
- [LS10] "Thermoplast-Extrusions- und/oder 2-Komponentenpolymer-Additiv sowie Herstellungsverfahren dazu und Additiv-Verwendung dafür", Filed Patent, PCT/DE2020/100693
- [LS11] "Polymerkomposit sowie Herstellungsverfahren dazu", Filed Patent, PCT/DE2020/100694

List of Prepared and Submitted Manuscripts

- [LS12] **L. Siebert**, E. Luna-Cerón, L. E. García-Rivera, J. Oh, J. Jang, D. A. Rosas-Gómez, M. D. Pérez-Gómez, G. Maschkowitz, H. Fickenscher, D. Ocegüera-Cuevas, C. G. Holguín-León, B. Byambaa, M. A. Hussain, N. Sobahi, A. Hasan, D. P. Orgill, Y. K. Mishra, R. Adelung, E. Lee, S. R. Shin, Light controlled growth factors release on tetrapodal ZnO incorporated 3D printed hydrogels for developing smart wound scaffold, (**submitted manuscript**)
- [LS13] F. Harden, B. Schädel, R. Kral, **L. Siebert**, R. Adelung, O. Jacobs, Wear behavior of additive manufactured polymer-polymer sliding combinations, (**submitted manuscript**)
- [LS14] R. K. Suryawanshi, C. D. Patil, L. Koujah, P. K. Panda, S. K. Singh, A. Agelidis, I. Volety, **L. Siebert**, R. Adelung, R. Ahuja, Y. K. Mishra, D. Shukla, Enhancement of antiviral drug efficacy through multimodal mechanism of Au nanoparticles complexed with ZnO tetrapods, (**submitted manuscript**)
- [LS15] **L. Siebert**, J. Carstensen, P. Schadte, M. Gerhardt, J. Bahr, K. Rätzke, R. Adelung, Homogeneous polymerization realized by only trace amounts of crushed microcrystals, (**prepared manuscript**)

Acknowledgements

This section is reserved to express the sincerest gratitude towards all of the people, I was blessed enough to grow with in the last decade.

The first man I would like to thank is Rainer Adelung. Every day you inspire me with your humility, your eagerness to promote understanding, your never-ending care for and patience with us and your incredible creativity. You treat everybody you meet in a way that makes me proud to learn from you and you never stopped believing in me. I feel a deep gratitude to be able to continue learning from you.

My sincerest gratitude also goes to both Jörg Bahr and Jürgen Carstensen. In countless instances of tireless lessons and personal support you have tried your best to make me become a human to be proud of. I value the scientific and the interpersonal training I have received from you in the highest regard.

On a similarly level I value every lesson I have learned from my friends and mentors like Sören Kaps, Maik-Ivo Terasa, Klaus Rätzke, Franz Faupel, Anne Staubitz, Su Ryon Shin and Yogendra Kumar Mishra, who always took their time to openly and thoroughly discuss important academic and personal issues with me.

Equally, I would like to thank the people with whom I could study the fascinating world of materials science for their trust and support that made every day at work a day I looked forward to. Thank you, Lukas Zimoch, Philipp Schadte and Martha Gerhardt. In you I have found friendship and loyalty for many years and I am happy to continue our relationship in the years to come.

Towards my best friends Roderich von Thun and Marius Kamp I would like to express my gratitude for supporting me on a personal level even during the most challenging of times. Your encouragements are highly appreciated.

In deep gratitude I also think of my student research assistants Gunnar Ehlers, Alina Kuntze and Oliver Rothe who always tried to realise all of the unconventional ideas that peaked our interest in the past years.

Furthermore I thank all of my thesis students Dennis Seidler, Yannick Bockholt, Paul Simon, Maik Tienken, Tim Pogoda, Erwin Schröder, Andreas-Jost Meyer, Ruchira Colaco, Tobias Spratte, Julia Sierck, Mattia Mirabelli, Armin Reimers, Philip Schäfer, Senol Feldmann, Nadine Depri and Isabell Teegen. Without your trust and support this thesis would have never come to the same fruition. It was a pleasure teaching you and simultaneously learning from you.

From my time in Harvard I would like to thank all of the people that have made my stay a beautiful personal and academic experience. Many thanks go out to Mitzi Damara Perez Gomez, Daniel Vela Jarquin Diego Rosas, Ludivina De la Garza Hernández, Luis García, Angel Huidobro, Yasamin Aliashrafi Jodat are Kiavash Kiaee.

Additionally, I would like to thank all of my colleagues including Florian Rasch, Mete Hauck, Lena Saure, Chima Obobi Kalu, Catarina Schmidt, Helge Krüger, Sandra Hansen, Beate Minten, Vivian Wehr, Katrin Brandenburg, Martina Baum, Fabian Schütt, Haoyi

Qiu, Anna Gapeeva, Sindu Shree, Heather Cavers, Jan-Martin Wagner, Monja Gronenberg, Kerstin Meurisch, Tehseen Riaz, Peter Sommer, Oleg Lupan, Ingo Paulowicz, Daria Smazna, Jorit Gröttrup, Victor Kaidas, Mathias Hoppe and George Popkirov. Working with you has always been a pleasure to me.

Finally, I want to thank my family for helping me to become the man I am today. I have seldom felt anything else than love and support from you and I am grateful for my parents, my siblings and my late grandparents. I would also like to express my gratitude towards Sonja Vogt, who despite our personal differences is a good mother to our beloved daughter Nora, whom I would like to thank for motivating me to always do the best I can.

Contributions

Contributions The contributions to the presented publications and manuscripts can be categorized according to the following criteria: **C**onceptual **D**esign, **M**ethodology and **M**easurements, **D**ata **A**nalysis, **V**isualization, **W**riting and **R**eview/**E**ditng. In the following table, the estimated own contribution, as a subjective value, to each publication is given in percentage.

Publications	CD	MM	DA	V	W	RE
L. Siebert , T. Schaller, F. Schütt, S. Kaps, J. Carstensen, S. Shree, J. Bahr, Y. K. Mishra, H.-H. Sievers, R. Adelung, Perfect polymer interlocking by spherical particles: capillary force shapes hierarchical composite undercuts, <i>Nanoscale Horizons</i> 4, pp. 947-952 (2019)	40	30	80	80	60	50
R. Colaco, S. Shree, L. Siebert , C. Appiah, M. Dowds, S. Schultzke, R. Adelung, A. Staubitz, Mechanochromic Microfibers Stabilized by Polymer Blending, <i>ACS Applied Polymer Materials</i> 2, pp. 2055-2062 (2020)	30	10	20	30	20	30
D. Smazna, J. Rodrigues, S. Shree, V. Postica, G. Neubüser, A. F. Martins, N. B.Sedrine, N. K. Jena, L. Siebert , F. Schütt, O. Lupan, R. Ahuja, M. R. Correia, T. Monteiro, L. Kienle, Y. Yang, R. Adelung, Y. K. Mishra, Buckminsterfullerene hybridized zinc oxide tetrapods: defects and charge transfer induced optical and electrical response, <i>Nanoscale</i> 10, pp. 10050-10062 (2018)	5	0	0	15	5	5
F. Schütt, M. Zapf, S. Signetti, J. Strobel, H. Krüger, R. Röder, J. Carstensen, N. Wolff, J. Marx, T. Carey, M. Schweichel, M.-I. Teresa, L. Siebert , H.-K. Hong, S. Kaps, B. Fiedler, Y. K. Mishra, Z. Lee, N. M. Pugno, L. Kienle, A. C. Ferrari, F. Torrisi, C. Ronning, R. Adelung, Conversionless efficient and broadband laser lightdiffusers for high brightness illumination applications, <i>Nature Communications</i> 11, 1437 (2020)	5	0	5	0	5	5

L. Siebert , O. Lupan, M. Mirabelli, N. Ababii, M.-I. Terasa, S. Kaps, V. Cretu, A.Vahl, F. Faupel, R. Adelung, 3D-Printed Chemiresistive Sensor Array on Nanowire CuO/Cu ₂ O/Cu Heterojunction Nets, ACS applied materials & interfaces 11, pp. 25508-25515 (2019)	70	40	60	70	60	70
L. Siebert , N. Wolff, N. Ababii, M.-I. Terasa, O. Lupan, A. Vahl, V. Duppel, H. Qiu, M. Tienken, M. Mirabelli, V. Sontea, F. Faupel, L. Kienle, R. Adelung, Facile fabrication of semiconducting oxide nanostructures by direct ink writing of readily available metal microparticles and their application as low power acetone gas sensors, Nano Energy 70, 104420 (2019)	70	40	60	70	60	70
S. B. Gutekunst, K. Siemsen, S. Huth, A. Möhring, B. Hesseler, M. Timmermann, I. Paulowicz, Y. K. Mishra, L. Siebert , R. Adelung, C. Selhuber-Unkel, 3D Hydrogels Containing Interconnected Microchannels of Subcellular Size for Capturing Human Pathogenic <i>Acanthamoeba Castellanii</i> , ACS Biomaterials Science & Engineering 5,4, pp. 1784-1792 (2019)	5	5	0	0	5	5
L. Siebert , M.-I. Terasa, N. Ababii, O. Lupan, R. Adelung, 3D-Printed Sensor Array of Semiconducting Oxides, in International Conference on Nanotechnologies and Biomedical Engineering, pp. 3-6 (2019)	70	40	60	70	60	70
L. O. Akinsinde, S. Scheitz, L. Zimoch, J. K. Sierck, L. Siebert , R. Adelung, U. Schürmann, M. A. Rübhausen, T. Dankwort, L. Kienle, Resistivity Response to Stress and Strain of a Flexible Bi ₂ Te ₃ Based Thermoelectric Material, in International Conference on Nanotechnologies and Biomedical Engineering, pp. 57-60 (2019)	70	30	50	30	30	30

L. Siebert , E. Luna-Cerón, L. E. García-Rivera, J. Oh, J. Jang, D. A. Rosas-Gómez, M. D. Pérez-Gómez, G. Maschkowitz, H. Fickenscher, D. Ocegüera-Cuevas, C. G. Holguín-León, B. Byambaa, M. A. Hussain, N. Sobahi, A. Hasan, D. P. Orgill, Y. K. Mishra, R. Adelung, E. Lee, S. R. Shin, Light controlled growth factors release on tetrapodal ZnO incorporated 3D printed hydrogels for developing smart wound scaffold, (submitted manuscript)	50	30	30	40	70	70
F. Harden, B. Schädel, R. Kral, L. Siebert , R. Adelung, O. Jacobs, Wear behavior of additive manufactured polymer-polymer sliding combinations, (submitted manuscript)	10	30	20	20	20	30
R. K. Suryawanshi, C. D. Patil, L. Koujah, P. K. Panda, S. K. Singh, A. Agelidis, I. Volety, L. Siebert , R. Adelung, R. Ahuja, Y. K. Mishra, D. Shukla, Enhancement of antiviral drug efficacy through multimodal mechanism of Au nanoparticles complexed with ZnO tetrapods, (submitted manuscript)	5	15	10	10	15	10
L. Siebert , J. Carstensen, P. Schadte, M. Gerhardt, J. Bahr, K. Rätzke, R. Adelung, Homogeneous polymerization realized by only trace amounts of crushed microcrystals, (prepared manuscript)	70	40	60	80	80	70

Leonard Siebert

Rainer Adelung

Eidesstattliche Erklärung

Hiermit erkläre ich an Eides statt, die Dissertation "Additive and Self-Organised Manufacturing" eigenständig, d.h. insbesondere selbständig und ohne Hilfe eines kommerziellen Promotionsberaters, angefertigt und keine anderen als die von mir angegebenen Quellen und Hilfsmittel verwendet zu haben. Ich erkläre außerdem, dass die Dissertation weder in gleicher noch in ähnlicher Form bereits in einem anderen Prüfungsverfahren vorgelegen hat und unter Einhaltung der Regeln guter wissenschaftlicher Praxis der Deutschen Forschungsgemeinschaft entstanden ist. Des Weiteren erkläre ich, dass mir bislang kein akademischer Grad entzogen wurde.

Ort, Datum

Unterschrift

Affidavits

I hereby confirm that my thesis entitled "Additive and Self-Organised Manufacturing" is the result of my own work. I did not receive any help or support from commercial consultants. All sources and/or materials applied here are listed and specified in the thesis. Furthermore, I confirm that this thesis has not yet been submitted as part of another examination process neither in identical nor in similar form and has been prepared subject to the Rules of Good Scientific Practice of the German Research Foundation. Furthermore, I declare that no academic degree has been revoked from me in the past.

Place, Date

Signature